SUPERSONIC TURBULENT BOUNDARY LAYERS WITH PERIODIC MECHANICAL NON-EQUILIBRIUM

A Dissertation

by

ISAAC WESLEY EKOTO

Submitted to the Office of Graduate Studies of
Texas A&M University
in partial fulfillment of the requirements for the degree of

DOCTOR OF PHILOSOPHY

December 2006

Major Subject: Aerospace Engineering

SUPERSONIC TURBULENT BOUNDARY LAYERS WITH PERIODIC MECHANICAL NON-EQUILIBRIUM

A Dissertation

by

ISAAC WESLEY EKOTO

Submitted to the Office of Graduate Studies of
Texas A&M University
in partial fulfillment of the requirements for the degree of

DOCTOR OF PHILOSOPHY

Approved by:

Chair of Committee,	Rodney Bowersox
Committee Members,	Sharath Girimaji
	Othon Rediniotis
	Simon North
Head of Department,	Helen Reed

December 2006

Major Subject: Aerospace Engineering

ABSTRACT

Supersonic Turbulent Boundary Layers with

Periodic Mechanical Non-Equilibrium. (December 2006)

Isaac Wesley Ekoto, B.S., Fayetteville State University

Chair of Advisory Committee: Dr. Rodney Bowersox

Previous studies have shown that favorable pressure gradients reduce the turbulence levels and length scales in supersonic flow. Wall roughness has been shown to reduce the large-scales in wall bounded flow. Based on these previous observations new questions have been raised. The fundamental questions this dissertation addressed are: (1) What are the effects of wall topology with sharp versus blunt leading edges? and (2) Is it possible that a further reduction of turbulent scales can occur if surface roughness and favorable pressure gradients are combined? To answer these questions and to enhance the current experimental database, an experimental analysis was performed to provide high fidelity documentation of the mean and turbulent flow properties along with surface and flow visualizations of a high-speed ($M = 2.86$), high Reynolds number ($\mathrm{Re}_\theta \approx 60,000$) supersonic turbulent boundary layer distorted by curvature-induced favorable pressure gradients and large-scale ($k_s^+ \approx 300$) uniform surface roughness. Nine models were tested at three separate locations. Three pressure gradient models strengths (a nominally zero, a weak, and a strong favorable pressure gradient) and three roughness topologies (aerodynamically smooth, square, and diamond shaped roughness elements) were used. Highly resolved planar measurements of mean and fluctuating velocity components were accomplished using particle image velocimetry. Stagnation pressure profiles were

acquired with a traversing Pitot probe. Surface pressure distributions were characterized using pressure sensitive paint. Finally flow visualization was accomplished using schlieren photographs.

Roughness topology had a significant effect on the boundary layer mean and turbulent properties due to shock boundary layer interactions. Favorable pressure gradients had the expected stabilizing effect on turbulent properties, but the improvements were less significant for models with surface roughness near the wall due to increased tendency towards flow separation. It was documented that proper roughness selection coupled with a sufficiently strong favorable pressure gradient produced regions of “negative” production in the transport of turbulent stress. This led to localized areas of significant turbulence stress reduction. With proper roughness selection and sufficient favorable pressure gradient strength, it is believed that localized relaminarization of the boundary layer is possible.

ACKNOWLEDGMENTS

I want to extend my deepest thanks to all who made the present research possible. First and foremost, I would like to thank my advisor, Dr. Rodney Bowersox. Without his seemingly limitless knowledge base, vast technical expertise, and infectious enthusiasm the research would not have been possible. I thank my committee for their input and support throughout my project. I also thank Dr. Tom Beutner from the Air Force Office of Scientific Research (AFOSR) for providing financial support for the project.

I thank Dr. Larry Goss and his staff and Innovative Scientific Solutions Inc. Their on sight technical assistance and willingness to create or modify existing equipment and data processing software per my requests was invaluable.

I extend my thanks to all employees at the Oran Nicks Low Speed Wind Tunnel. Specifically I would like to single out the tunnel director Jorge Martinez for his technical assistance and willingness to incorporate our lab into his facility along with Will Seward, Chris Adcock, and Mike Sperry for their assistance in constructing and maintaining the high-speed facilities. They worked many hours of overtime and provided design assistance which greatly expedited facility construction. They would also reliably turn a complicated CAD drawing into a tangible part in no time.

I am thankful to Ravichandra Srinivasan, Justin McLellan, Jason Garcia, Dipankar Sahoo, and Michael Semper for provided testing assistance. Finally, I would like to thank my parents Edith Trimmer and Thomas Brill along with all family and friends who have supported me throughout. They kept my spirits high, and for that, I am sincerely grateful.

TABLE OF CONTENTS

Page

CHAPTER Page

LIST OF TABLES

TABLE Page

TABLE Page

LIST OF FIGURES

FIGURE Page

FIGURE Page

FIGURE Page

FIGURE Page

FIGURE Page

FIGURE Page

FIGURE Page

FIGURE Page

FIGURE Page

FIGURE Page

FIGURE Page

CHAPTER I

INTRODUCTION

Motivation

Knowledge of the nature and characteristics and of turbulent supersonic boundary layers is important in many fields of science and engineering. Reduced viscous drag, enhanced mixing, and increased propulsion efficiency have long been identified as key enabling technologies for the advancement of new flight vehicle concepts[1]. Achieving these goals requires the ability to accurately predict and quantify the complicated internal and external flow field characteristics present in modern flight vehicle concepts. These characteristics include but are not limited to compressibility, pressure gradients, wall curvature, high Reynolds numbers, elevated turbulence levels, surface roughness, shocks, and combustion. Insight into the fundamental physical processes and their interacting mechanisms will allow engineers to more accurately predict flow field behavior.

According to the Air Force Office of Scientific Research in their Broad Agency Announcement (AFOSR BAA) 2006-1[1] in the Unsteady Aerodynamics and Hypersonics section, hypersonic aerodynamics research is critical to the Air Force's renewed interest in long-range and space operations. The current thrust of hypersonic flight vehicle research has been in Scramjets, which are flight vehicles that use atmospheric air as the

---

This dissertation follows the style of *AIAA Journal.*

oxidizer. They have the advantages of increased payload capacity, reusability, and lower operating costs versus conventional rockets.

There are however, several engineering issues that must be resolved. Current vehicle designs are expected to operate with a thrust to drag ratio that is near unity, thus drag reduction is a major design consideration. Combustor design is another issue. The incoming oxidizer will be traveling at supersonic speeds meaning the transient time for mixing is on the order of a microsecond. The ability to produce a combustor that has adequate turbulent mixing of injected fuel, while maintaining heat transfer rates that are low enough that excessive thermal shielding is not required is essential.

Turbulence reduction has applications for reentry vehicles. On their undersurface they have a heat shield that is composed of uniformly shaped materials (e.g. tiles, ablative materiel, etc.). Shape selection that can reduce turbulent heat transfer will lead to thinner heat shields and thus increased payload capacity.

Regardless of the application, modern designs must increasingly rely on computational fluid dynamics to evaluate performance, due to the difficulty in reproducing complex flows in ground testing and the exorbitant costs for wind tunnel testing. It is therefore essential that the numerical solutions correctly reproduce the flow field physics. Because the small scales of turbulence require unrealistically fine computational grids for realistic flow fields via direct numerical simulation (DNS), turbulence models that simulate the turbulence physics are necessary. Unfortunately the current experimental and DNS database for compressible turbulent flow fields is insufficient to create satisfactory models. To rectify this problem, the BAA suggests

current research should emphasize the characterization, prediction and control of high-speed fluid dynamic phenomena including boundary layer transition, shock/boundary layer, and shock/shock interactions, and other phenomena associated with airframe propulsion integration.

Unanswered Questions

It has been shown in previous studies[3,4,5] that for compressible turbulent boundary layers, favorable pressure gradients have a stabilizing effect on flowfield turbulent properties. This is believed to be due to the reduction in turbulent production due to an increase in the secondary gradients $d\tilde{u}/dx$ and $d\tilde{v}/dy$, and a decrease in the primary gradient $d\tilde{u}/dy$ along with the secondary gradient $d\tilde{v}/dx$. Spectra data indicates that the largest turbulent eddies are disintegrated, transferring energy to the smaller ones, leading to faster dissipation rates. Up to a 25% reduction of Reynolds shear stresses have been observed. Numerical simulations using two-equation eddy viscosity models were found to be inadequate to successfully simulate the flow field.

Similarly it has been observed [6,7,8] that surface roughness significantly increases flowfield turbulent properties. Reynolds shear stress increases of up to 250% have been observed. The bursting process that is believed to be the source of smooth wall turbulence is disrupted by surface roughness protrusions into the flow field, and the associated shock boundary layer interactions that occur turning elongated eddies into highly energetic smaller ones. Turbulent values have been found to vary by up to 20% for different wall topology, suggesting shock boundary layer interactions are important.

Based on these previous observations new questions have been raised. Both surface roughness and favorable pressure gradients reduce the turbulent scales within the flow. It is not known what will happen if the local production mechanisms due to surface roughness are combined with the global production mechanisms due to favorable streamwise pressure gradients. It has been hypothesized that the combination of a sufficiently strong favorable pressure gradient and large scale surface roughness may enhance the negative production mechanisms, shrinking the turbulent scales to the point where relaminarization is possible.

Wall geometry and the associated shock boundary layer interactions appear to have significant effects on overall boundary layer structure. A survey of the literature reveals roughness elements with sharp leading edges have not been explored. Much could be revealed by an investigation into a these type of roughness elements. The thought is that the blunt shaped roughness elements used in the past (e.g. square and irregular sand grain roughness) have produced weak detached bow shocks. An element with a sharp leading edge will would be expected to produce an attached oblique shock potentially reducing the pressure losses behind the shock, and thus reducing overall turbulence levels.

Objectives

Based on the unanswered questions from the previous section, the principal objective of the current research is to experimentally characterize highly strained turbulent supersonic boundary layers with large scale uniform surface. The surface roughness will be uniform in shape, and both sharp and blunt leading edges will be used.

From the experimental characterization the essential flow physics will be obtained. Specific objectives necessary to meet the principal objective are as follows:

1. Design and construct a supersonic facility, test section, and models. A total of nine test section models will be constructed. The test matrix will have three different strength pressure gradients (zero, weak, and strong favorable pressure gradients), and three different surface roughness conditions (smooth wall, square shaped roughness elements, and diamond shaped roughness elements). The roughness element height and model curvature will be based on previous research and available manufacturing capabilities.
2. Record all data on the strained non-equilibrium supersonic turbulent boundary layers with uniform roughness. The database will include flow visualizations, mean and turbulent measurements, turbulent production, stagnation pressure, and surface pressure.
3. Identify and document the salient flow features, to include: flow velocities and their gradients, kinematic turbulent properties, thermodynamic properties, roughness element shock structure, turbulent production mechanisms, and length scale measurements.
4. Analyze the flow physics and interacting mechanisms present from acquired measurements.

Approach

To meet the outlined objectives, construction of a quality research facility was required. Individual components such as air dryers, heaters, and the high pressure pipe

were incorporated into the preexisting storage tank and compressors. The settling chamber, nozzle, diffuser, and all other tunnel components were designed and built. A data acquisition system was installed to monitor tunnel operating conditions. Once the tunnel was completed, preliminary testing was performed to establish flow conditions, and test the diagnostic equipment.

Surface topology and wall curvature for the tunnel models was selected based on its ability to be compared to previous studies[3,4,6,7,8] and its ease of construction. The wall curvature was selected based on a parameter which was analytically found from the ratio of the turbulent production to the pressure work terms from the Reynolds stress transport equation. In addition to a zero pressure gradient (ZPG) model, there was a weak and strong pressure gradient model. The parameter was zero for the ZPG model and there was an order of magnitude difference between the weak and strong pressure gradient models. The roughness element shape selected was a diamond roughness element with a sharp leading and trailing edge and a square roughness element that had a blunt shape. The idea was that shockwaves would attach to the leading edge of the diamond roughness element, while they would become detached bow shocks for the square roughness elements. The associated mean flow and turbulent properties could then be analyzed to determine shock boundary layer interactions.

Different measurement techniques were necessary to produce the requisite mean flow measurements, turbulent measurements, and flow visualizations. Schliren photography and Pressure Sensitive Paint (PSP) provided mean flow visualization of flow field transverse density gradients and surface pressure distributions. From these

visualizations it is possible to examine shock boundary layer interactions due to surface roughness.

Mean flow quantities were gathered by Particle Image Velocimetry (PIV), Pitot, and PSP. Planar PIV produces mean velocity field and gradient fields. From these fields, velocity profiles, defect law plots, and law of the wall plots, were generated. Pitot measurements measure the stagnation pressure behind the normal shock. From this velocity and Mach number can be calculated. PSP measurements give the mean surface pressure distributions and their gradients.

Turbulent quantities were measured by the PIV. Second order turbulent statistics such as the normal and axial turbulent stresses and the Reynolds stress were measured. Because PIV supplies two dimensional field measurements the calculation of gradients and thus the turbulent stress production are possible. Integral length scale and Taylor microscale information was found using two dimensional cross and autocorrelation maps from the velocity fluctuation fields.

Research Contributions

The fluid mechanical contributions base on the acquired data and flow visualizations are as follows:

1. Extensive addition of the current supersonic turbulent boundary layer database, specifically focusing on strained environments with varying surface topology. The database includes direct measurements of the mean and kinematic turbulent flow properties, mean surface and flowfield thermodynamic properties, and flow visualizations have been. Additionally

indirect measurements such as turbulent production, Mach number, and length scale spectra have been included.

2. Flow visualizations of all models were obtained. From these it was determined that roughness elements with sharp leading elements produce strong attached oblique shocks at the leading edge while the sharp trailing edges produced acted as expansion regions. Conversely the square roughness elements have are believed to have recirculation regions within the preceeding channels, which are the disturbance sources.
3. Velocity and production fields produced by PIV reveal that the expansion regions the trailing edge of the trailing edges of diamond roughness elements act as an expansion region where the local flow is accelerated leading to a reduction of turbulence. Conversely the weak disturbance from the square roughness elements appear to continually act as a loss on the system, and source of turbulent energy.
4. Revelation that strong favorable pressure gradients coupled with diamond shaped surface roughness produced production terms that destroyed turbulence within certain regions. Relaminarization appears possible in these regions if sufficient strength favorable pressure gradient and roughness topology are selected.

Dissertation Overview

A brief overview of the research motivation, concept, and methodologies is presented above. In chapter II a summary of the relevant governing equations is

covered. Chapter III presents a literature review which states the current existing database on compressible turbulent boundary layers. Chapter IV describes in detail all diagnostic techniques while chapter V describes the research facilities. In chapter VI the experimental results are explained. Finally in chapter VII presents a complete flowfield description, makes conclusions, and suggests recommendations for future research.

CHAPTER II

GOVERNING EQUATIONS

The following subsections present the governing equations of fluid mechanics in integral and differential form.

Integral Form

The integral form of the combined system of governing equations for a generic flow involving a single species is given in terms of the conserved quantities $\mathbf{Q}$, the inviscid surface forces $\mathbf{F_I}(\mathbf{Q})$, the viscous surface forces $\mathbf{F_V}(\mathbf{Q})$, and the body forces $\mathbf{F_B}(\mathbf{Q})$.

$$\frac{\partial}{\partial t}\iiint_V \mathbf{Q}dV + \iint_S \left(\mathbf{F_I}(\mathbf{Q})\cdot\hat{\mathbf{n}}\right)dS = \iint_S \left(\mathbf{F_V}(\mathbf{Q})\cdot\hat{\mathbf{n}}\right)dS + \iiint_V \mathbf{F_B}dV \tag{2.1}$$

where the vector of the conserved quantities is

$$\mathbf{Q} = \begin{Bmatrix} \rho \\ \rho\mathbf{V} \\ \rho e_0 \end{Bmatrix} \tag{2.2}$$

the inviscid flux term is

$$\mathbf{F_I}(\mathbf{Q})\cdot\hat{\mathbf{n}} = \begin{Bmatrix} \rho(\mathbf{V}\cdot\hat{\mathbf{n}}) \\ \rho\mathbf{V}(\mathbf{V}\cdot\hat{\mathbf{n}}) + p\hat{\mathbf{n}} \\ \rho h_0(\mathbf{V}\cdot\hat{\mathbf{n}}) \end{Bmatrix} \tag{2.3}$$

and the viscous flux term on the right hand side is given by

$$\mathbf{F_V}(\mathbf{Q})\cdot\hat{\mathbf{n}} = \begin{Bmatrix} 0 \\ \mathbf{T}\cdot\hat{\mathbf{n}} \\ (\mathbf{TV}-\mathbf{q})\cdot\hat{\mathbf{n}} \end{Bmatrix} \tag{2.4}$$

where $\mathbf{T}$ is the second order stress tensor which for a Newtonian fluid is defined as

$$\mathbf{T} = 2\mu\left[\mathbf{S}+\mathbf{S}^T\right]+\lambda(\nabla\cdot\mathbf{V})\mathbf{I} \tag{2.5}$$

In the stress tensor $\mathbf{T}$, the tensor $\mathbf{S}$ is the strain rate tensor given by

$$\mathbf{S} = \frac{1}{2}\nabla\mathbf{V} \tag{2.6}$$

μ is the dynamic viscosity and λ is the bulk viscosity. The heat flux vector $\mathbf{q}$ is given by the Fourier heat-conduction relationship:

$$\mathbf{q} = -\kappa\nabla T \tag{2.7}$$

For the current flow the body forces are assumed to be negligible, thus the source term vector $\mathbf{F_B}(\mathbf{Q})$ is zero.

Differential Form

The integral form of the conservation equations can be converted into a differential form using the Gauss divergence theorem which states that

$$\iiint_V(\nabla\cdot\mathbf{F})\,dV = \iint_S(\mathbf{F}\cdot\hat{\mathbf{n}})\,dS \tag{2.8}$$

for a vector $\mathbf{F}$ with continuous partial derivatives enclosed by a volume *V* with a surface *S* and a normal vector $\hat{\mathbf{n}}$.

Using equation (2.8), equation (2.1) can be rewritten as

$$\frac{\partial}{\partial t}\iiint_V \mathbf{Q}\,dV + \iiint_V\left(\nabla\cdot\mathbf{F_I}(\mathbf{Q})\right)dV = \iiint_V\left(\nabla\cdot\mathbf{F_V}(\mathbf{Q})\right)dV + \iiint_V \mathbf{F_B}\,dV \tag{2.9}$$

Ignoring the source vector $\mathbf{F_B}$ and accumulating terms under a single integral the following relation is obtained:

$$\iiint_V \left[\frac{\partial \mathbf{Q}}{\partial t} + \left(\nabla \cdot \mathbf{F_I}(\mathbf{Q}) \right) - \left(\nabla \cdot \mathbf{F_V}(\mathbf{Q}) \right) \right] dV = 0 \tag{2.10}$$

which is true for any arbitrary control volume. Therefore

$$\frac{\partial \mathbf{Q}}{\partial t} + \left(\nabla \cdot \mathbf{F_I}(\mathbf{Q}) \right) - \left(\nabla \cdot \mathbf{F_V}(\mathbf{Q}) \right) = 0 \tag{2.11}$$

For simplicity the remaining equations will be written in index notation in a Cartesian coordinate system. Equation (2.11) contains three separate physical principles i.e., conservation of mass, conservation of momentum, and conservation of energy which are presented below:

$$\frac{\partial \rho}{\partial t} + \frac{\partial \rho u_i}{\partial x_i} = 0 \tag{2.12}$$

$$\rho \frac{\partial u_i}{\partial t} + \rho u_j \frac{\partial u_i}{\partial x_j} = -\frac{\partial p}{\partial x_i} + \frac{\partial \tau_{ij}}{\partial x_j} \tag{2.13}$$

$$\rho \frac{\partial e_0}{\partial t} + \rho u_j \frac{\partial h_0}{\partial x_j} = \frac{\partial u_i \tau_{ij}}{\partial x_j} - \frac{\partial q_j}{\partial x_j} \tag{2.14}$$

Equations (2.13) and (2.14) can be written in conservative form by incorporating equation (2.12) to produce the conservative form of the momentum and energy equations respectively:

$$\frac{\partial \rho u_i}{\partial t} + \frac{\partial \rho u_j u_i}{\partial x_j} = -\frac{\partial p}{\partial x_i} + \frac{\partial \tau_{ij}}{\partial x_j} \tag{2.15}$$

$$\frac{\partial \rho e_0}{\partial t} + \frac{\partial \rho u_j h_0}{\partial x_j} = \frac{\partial u_i \tau_{ij}}{\partial x_j} - \frac{\partial q_j}{\partial x_j} \tag{2.16}$$

Thermodynamic Relations

From quantum and statistical mechanics it is known that when the rates of change in velocity, pressure, or temperature are sufficiently large, the flow will not have time to achieve a local equilibrium, thus making the equation of state time dependent. Generally, for non-reacting continuum flows the assumption of thermodynamic equilibrium is acceptable. Thus the air will be assumed to be a calorically perfect gas where pressure, temperature, and density are related by the ideal gas law given as:

$$p = \rho RT \tag{2.17}$$

where R is the gas constant which for air is $287.03 m^2 s^2 K$. The specific internal energy, *e*, is

$$e = c_v T \tag{2.18}$$

The stagnation internal energy is defined as

$$e_0 = e + \frac{1}{2} u_i u_i \tag{2.19}$$

And the stagnation enthalpy is

$$h_0 = e_0 + \frac{p}{\rho} \tag{2.20}$$

For a calorically perfect gas the heat flux vector from equation (2.7) can be rewritten as

$$q_j = -\frac{\mu}{\mathrm{Pr}} \frac{\partial T}{\partial x_j} \tag{2.21}$$

Turbulence

All non-reacting turbulent flows with the appropriate thermodynamic properties are governed by the equations above; however, it is often impractical to use the

instantaneous form of the governing equations to numerically simulate even the most simplistic turbulent flows. The range of scales is dependent on the Reynolds number of the flow. In order to completely capture all spatial structures in the flow a numerical grid should be on the order of $\mathrm{Re}^{9/4}$. Thus for a flow with a Reynolds number of 1.0×10^{6}, the total number of grid points should be approximately 31×10^{12}. The time step will also be prohibitively small if the smallest length scales are to be captures. Presently, girds of this size cannot be accommodated using existing computer technology where memory is limited to a few hundred gigabytes in the best of cases.

Instead an averaged form of the Navier-Stokes equations is used. Currently the two most commonly used forms of averaging are Reynolds and Favre averaging techniques.

Reynolds Averaging

Reynolds averaging is a time averaged process where the mean value of a fluctuating flow quantity is obtained. Three different Reynolds averaging procedures are commonly used in studying turbulent flows: time averaging, spatial averaging, and ensemble averaging. Spatial averaging can only be used in flows where the mean and fluctuating quantities don't change in a spatial direction. This is not the case for the flows presented here and thus a discussion about this subject would be unnecessary. Instead only time and ensemble averaging processes will be reviewed.

Any instantaneous flow quantity can be split into a mean and fluctuating value.

$$f = \overline{f} + f' \tag{2.22}$$

The instantaneous value f and the fluctuation f' are functions of the spatial coordinate and time while the mean value $\overline{f}$ is a function of only the spatial coordinate. The mean value $\overline{f}$ is obtained by time averaging the instantaneous flow quantity

$$\overline{f}(\mathbf{r}) \equiv \lim_{T\to\infty} \frac{1}{T} \int_{t}^{t+T} f(\mathbf{r},t)\, dt \tag{2.23}$$

The time average the fluctuating components are zero. For time averaging long-term variations within the flow state are assumed to be absent.

For the present experiment it is not possible to perform a continuous integration, and therefore the quantities are ensemble averaged. Ensemble averaging is used where there are long –term variations within the flow state. The definition of the ensemble average $\hat{f}$ is

$$\hat{f} \equiv \lim_{N\to\infty} \frac{1}{N} \sum_{n=1}^{N} n f_n \tag{2.24}$$

It is important that N is sufficiently large such that a statistical mean that is within a reasonable error bound is achieved, however long enough so that can

The following identities for the Reynolds averaged for all spatially and temporally continuous variables can readily be shown from the definition of the averaging process given from the definition of the averaging process in equation (2.23) and the assumption that the variables are sufficiently regular so that the operations of differentiation, integration, and averaging may be inverted in order.

$$\overline{f+g} = \overline{f} + \overline{g} \tag{2.25}$$

$$\overline{\overline{f}} = \overline{f} \tag{2.26}$$

$$\overline{f \cdot \overline{g}} = \overline{f} \cdot \overline{g} \tag{2.27}$$

$$\overline{\frac{\partial \overline{f}}{\partial x}} = \frac{\partial \overline{f}}{\partial x} \tag{2.28}$$

$$\overline{\int f dx} = \int \overline{f} dx \tag{2.29}$$

From relations (2.25) and (2.26) it can be shown that

$$\overline{fg} = \overline{\left(\overline{f} + f'\right)\left(\overline{g} + g'\right)} = \overline{\overline{f}\overline{g} + f'\overline{g} + \overline{f}g' + f'g'} = \overline{f}\overline{g} + \overline{f'g'} \tag{2.30}$$

Favre Averaging

Because the flows of interest are compressible, the density fluctuations will be non-zero and Reynolds averaging leads to additional unknowns within the governing equations including triple correlations which are difficult to measure accurately within a given set of experiments. In order to avoid these complications a density weight averaging technique known as Favre averaging is applied. This leads to a set of equations similar in form to those governing mean incompressible flows. The density weighed average of a flow quantity is defined as

$$f = \tilde{f} + f'' \tag{2.31}$$

Where

$$\tilde{f} = \frac{\overline{f\rho}}{\overline{\rho}} \tag{2.32}$$

From the definition of a Favre averaged quantity given in equations (2.31) and (2.32), and the identities given in (2.25) and (2.26) two additional relations can be shown to hold for a Favre averaged quantity

$$\overline{f''} = -\frac{\overline{\rho' f'}}{\overline{\rho}} \tag{2.33}$$

$$\overline{\rho f''} = 0 \tag{2.34}$$

Applying the Favre averaged definitions to equations (2.12), (2.15), and (2.16), and averaging produces the Favre Averaged Navier Stokes (FANS) equations

$$\frac{\partial \overline{\rho}}{\partial t} + \frac{\partial \overline{\rho} \tilde{u}_i}{\partial x_i} = 0 \tag{2.35}$$

$$\frac{\partial \overline{\rho} \tilde{u}_i}{\partial t} + \frac{\partial \overline{\rho} \tilde{u}_i \tilde{u}_j}{\partial x_j} = -\frac{\partial \overline{p}}{\partial x_i} + \frac{\partial}{\partial x_i}\left[\overline{\tau}_{ij} + \tau_{ij}^T\right] \tag{2.36}$$

$$\frac{\partial \overline{\rho} \tilde{e}_0}{\partial t} + \frac{\partial \overline{\rho} \tilde{h}_0 \tilde{u}_k}{\partial x_k} = -\frac{\partial}{\partial x_k}\left[\overline{q}_k + q_k^T\right] + \frac{\partial}{\partial x_l}\left[\tilde{u}_k \overline{\tau}_{kl}\right] \tag{2.37}$$

Where the turbulent shear stress τ_{ij}^T is given as

$$\tau_{ij}^T = -\overline{\rho u_i'' u_j''} \tag{2.38}$$

And the turbulent heat flux q_k^T is

$$q_k^T = \overline{\rho h'' u_k''} \tag{2.39}$$

Generally the last two terms on the right hand side of equation (2.39) are negligibly small. Even if these terms are neglected this still leaves 9 additional unknowns without any corresponding equations.

CHAPTER III

COMPRESSIBLE TURBULENT BOUNDARY LAYERS

Compressible Turbulent Boundary Layers

Incompressible smooth wall zero pressure gradient (ZPG) turbulent boundary layer flow is understood to the point that flowfields are considered canonical and the semi-empirical correlations (law of the wall, defect law, and energy spectra scaling) and turbulent kinetic energy transport data are routinely used to validate turbulence modeling concepts. Numerous complete reviews of this subject are available [e.g., Schlichting[9], Schetz [10], White[11], Sherman[12], Wilcox[13], Cebeci and Smith[14], and Pope[15]].

The fundamental thermodynamic characteristics for compressible flowfields are inherently different than their incompressible counterparts. Defining the shear stress and Reynolds shear stress tensors as:

$$\tau_{ij} = \mu\left(\frac{\partial u_i}{\partial x_j} + \frac{\partial u_j}{\partial x_i}\right) - \frac{2}{3}\mu\frac{\partial u_k}{\partial x_k}, \quad \tau_{ij}^T = -\overline{\rho u_i'' u_j''} \tag{3.1}$$

The complete compressible form of the Reynolds Stress Transport Equation is then given as

$$\underbrace{\frac{\partial \tau_{ij}^T}{\partial t}+\frac{\partial \tilde{u}_k \tau_{ij}^T}{\partial x_k}}_{C_{ij}}=-\underbrace{\left(\tau_{jk}^T\frac{\partial \tilde{u}_i}{\partial x_k}+\tau_{ik}^T\frac{\partial \tilde{u}_j}{\partial x_k}\right)}_{P_{ij}}-\underbrace{\left(\overline{u_i''}\frac{\partial \overline{\tau}_{jk}}{\partial x_k}+\overline{u_j''}\frac{\partial \overline{\tau}_{ik}}{\partial x_k}\right)}_{VW_{ij}}+$$

$$\underbrace{\left(\overline{u_i''}\frac{\partial \overline{p}}{\partial x_j}+\overline{u_j''}\frac{\partial \overline{p}}{\partial x_i}\right)}_{PW_{ij}}-\underbrace{\overline{p'\left(\frac{\partial u_i''}{\partial x_j}+\frac{\partial u_j''}{\partial x_i}\right)}}_{R_{ij}}-\underbrace{\frac{\partial}{\partial x_k}\left(\overline{u_i''\tau_{jk}'}+\overline{u_j''\tau_{ik}'}\right)}_{D_{ij}^V}+ \tag{3.2}$$

$$\underbrace{\frac{\partial}{\partial x_k}\left(\overline{p'u_i''}\delta_{jk}+\overline{p'u_j''}\delta_{ik}+\overline{\rho u_i''u_j''u_k''}\right)}_{D_{ij}^T}+\underbrace{\left(\overline{\tau_{jk}'\frac{\partial u_i''}{\partial x_k}}+\overline{\tau_{ik}'\frac{\partial u_j''}{\partial x_k}}\right)}_{\varepsilon_{ij}}$$

The term on the right hand side represents the convection of the turbulent stresses. The first term on the left hand side is the turbulent stress production while the second and third terms are the viscous and pressure work terms respectively. The fourth term is the pressure strain correlation term, the fifth and sixth terms are the viscous and turbulent diffusion respectively, and the final term is the viscous dissipation.

Morkovin[16] was the first to observe that many of the differences in the turbulent statistical properties across supersonic and subsonic smooth plate boundary layers can be explained, or at least correlated, by the thermodynamic property variations across the layer. This observation, termed Morkovin's hypothesis, was based on smooth wall zero pressure gradient data and the flat plate form of the turbulent kinetic energy transport equation (i.e. a contraction of equation (3.2) neglecting the pressure work terms), and has provided the rationale for using incompressible turbulence models for flows up to Mach 5. Scaling for compressibility has been found to correlate the mean velocity with the low-speed database across smooth boundary layers [Van Driest [17]]. More recent analysis of turbulent smooth wall data [Fernholz *et al.*[18], Smits *et al.*[19], Spina *et al.*[20],

Dussuage *et al.*[21] and Smits and Dussuage[22]] indicates that the current database was insufficient to confirm turbulent property scaling and the realm of applicability of Morkovin's hypothesis might be more restrictive than originally believed. In addition, supersonic flows often possess features that do are not present in subsonic flowfields such as shock-boundary layer interaction.

Surface Roughness

To find if the thermodynamic scaling still holds for rough wall zero pressure gradient flows, numerous experiments have been performed. An extensive database of the mean and turbulent flow properties already exists for low-speed rough-wall flows [Corrsin and Kistler[23], Perry *et al.*[24], Simpson[25], Antonia and Wood[26], Schlichting[9] and Nikuradse[27],], and the associated flow scaling has provided the foundation for turbulence models suitable for low-speed zero-pressure-gradient flow [Fan and Bowersox[28] and Wilcox[13]]. From the experiments, surface roughness has been shown to have a direct effect on the inner region of the law of the wall and is typically described by a single parameter; namely the roughness Reynolds number k^+ (where $k^+ \equiv ku^*/\upsilon$). Three roughness regimes have been identified for low-speed flow [Aerodynamically smooth ($k^+ < 4\text{-}5$), transitional ($4\text{-}5 < k^+ < 60\text{-}70$) and fully rough ($k^+ > 60\text{-}70$)]. Nikuradse[27] demonstrated that sand-grain generated roughness increased the velocity defect and skin friction and shifted the logarithmic region of the law of the wall downward. However, the same defect law scaling was found to hold for rough and smooth walls. The amount of downward shift of the logarithmic region of the boundary layer was shown to be a function of k^+. Schlichting[9] introduced the concept of equivalent sand-grain roughness

k_s^+ to correlate any surface roughness to the equivalent Nikuradse sand-grain roughness for comparison. Because the equivalent sand-grain roughness does not include roughness topology, investigations of the influence of the roughness geometry have also been performed [Perry *et a.l*[24], Simpson[25], Antonia and Wood[26]], but has not in general been solved.

The basic trend in the turbulence results of Corrsin and Kistler[23] for a fully rough flow was that the axial turbulence intensity levels increased by about 30-40% and the Reynolds shear stresses increased by nearly a factor of 2. These data lead to obvious statement that roughness significantly alters the production and dissipation of turbulence. Grass[29] concluded that a different dominant mode of near wall instability "might prevail" for rough walls. The laser Doppler velocimetry data confirmed the defect law scaling and the shift in the logarithmic region of the boundary layer, and provided quantification of the bursting process.

Goddard[30] and Berg[31] found that for Mach numbers in the range of 0.7 - 6.0, the shift in the law of the wall velocity profile followed the same law as the incompressible case when the Van Driest II compressibility transformation was used. Latin and Bowersox[6] also noted that when the roughness elements were observed to protrude into the supersonic portion of the boundary layer, the corresponding shock and expansion waves distorted the boundary edge. Liepmann and Goddard[32] conjectured that for fully rough flow, the wall shear force is primarily the result of the drag on the roughness elements. Based on this argument, they showed that the ratio of compressible to incompressible skin friction is equal to the wall-to-freestream density ratio. The force

balance data of Goddard[30] confirmed the Liepmann and Goddard skin friction correlation over a Mach number range of 0.7-4.54.

Latin and Bowersox[7], Latin and Bowersox[6], Fan and Bowersox[28] and Pritchett and Bowersox[33] extended the above database to include detailed turbulence information over a range of Mach numbers (M = 0.2 – 2.8). A subset of important results that directly support the need for the present research is given here. Focusing only on the supersonic condition, the roughness elements were observed to protrude into the supersonic portion of the boundary layer, and the corresponding shock and expansion waves distorted the boundary edge and interacted with the boundary layer turbulence. The trends in the mean flow, observed for incompressible rough wall flow, were found to hold for the present study when Van Driest II scaling was used. In general, the rough wall kinematic statistical turbulent flow properties measured with the laser Doppler velocimetry system, collapsed on to a single curve when scaled with outer flow variables. The only exception was the 2-D plate, and it was expected that the turbulence production mechanisms associated with the d-type cavity were significantly different than for the remaining plates, which all had 3-D roughness patterns. Roughness was found to extend the region of inner scaling applicability for the kinematic properties further out into the boundary layer. The turbulent flow statistical properties with the explicit thermodynamic dependence did not collapse when scaled by local mean quantities, and increased almost linearly with k_s^+. The transverse-velocity-density correlation increased rapidly with roughness height. It was shown that the influence of smaller roughness elements increased the skin frictional losses more than the boundary

layer turbulence levels. However, as the roughness height was increased, the turbulence production relative to the frictional losses increased. The equivalent sand-grain roughness was found to be an effective parameter to characterize the overall effects of roughness on the turbulent flow properties. The machined 2-D and 3-D plate results were in reasonable agreement with the sand-grain trends, however significant variances (up to 25%) were observed and related back to roughness topology. Hence, it was concluded that the roughness topology was an important factor in the turbulence production. Three algebraic rough-wall turbulence models (van Driest, Kragstad and Cebeci-Chang) were tested. In summary, all three models produced mean, integral and turbulence results that agreed well with the experimental data.

Pressure Gradients

The effects of pressure gradient on low-speed boundary layers have also been the subject of numerous investigations; e.g., reviews are presented in [Bradshaw[34], Sherman[12], White[11] and Schetz[10]]. In summary, the inner region boundary layer scaling (i.e., law of the wall) has been shown to hold in the presence favorable and adverse pressure gradients. The logarithmic region termination height has been shown to depend on the strength of the pressure gradient; for favorable pressure gradients, the height increases and for adverse pressure gradients it decreases. Near separation, the inner scaling breaks down. The outer region of the boundary layer is very sensitive to pressure gradient, and in general the defect law does not hold. However, Clauser[35] defined a pressure gradient strength parameter (β) as the product of the axial pressure gradient (dp/dx) and the ratio of the boundary layer displacement thickness (δ^*) and wall

shear stress (τ_{wall}) [i.e., $\beta = -(\delta^*/\tau_{wall})(dp/dx)$], and when β is constant, the boundary layers are in equilibrium; i.e., the defect scaling laws hold and the corresponding profiles are independent of axial location). Coles[36] used this idea to generalize the law of the wall for equilibrium pressure gradient flows. For very strong adverse pressure gradients, the velocity profile is such that maximum shear stress moves away from the wall, and usual defect law scaling breaks down. Perry *et al.*[24] introduced a new outer scaling law for strong adverse equilibrium and quasi-equilibrium (flows where the pressure gradients are mild enough that β depends only on local flow conditions) flows. Power law axial velocity distributions produce equilibrium (or quasi-equilibrium flows).

For laminar flow, concave surfaces can produce Görtler vortices [White[11]]. Stable Görtler vortices have been documented as difficult to produce in fully turbulent flow with elevated freestream turbulence. Smits and Dussuage[22] describe a criterion to avoid the formation of Görtler vortices for low freestream turbulence levels.

For diffusers and nozzles favorable pressure gradients without wall curvature (i.e., accelerating flows) reduce turbulence levels; the opposite is true for adverse pressure gradients. Concave and convex curvature, with and without [Thomann[37]] an associate pressure gradient, have been shown to have de-stabilizing and stabilizing effects, respectively, on the turbulent flow properties of across low-speed boundary layers [Bradshaw[38,34]]. For convex curvature, the turbulence levels, turbulent shear stresses and wall friction all decrease relative to canonical flat surface values; the opposite is observed for concave curvature. These trends are explained by simple angular momentum arguments. The angular momentum terms in the Navier-Stokes

equations for planar flow over curved surfaces are on the order of the ratio of the boundary layer thickness and radius of curvature of the wall turning; hence, the effects are first order. For laminar flow, the effects have been shown to be first order. However for turbulent flows, the effects of wall curvature are significantly larger (approximately a factor of 10) than expected, where heuristic empirical corrections are required to account for this effect in predictions [Bradshaw[38,39]]. The effects of wall curvature are most pronounced in the outer region of the boundary layer, where for strong wall curvatures (e.g., ratio of the boundary thickness and wall radius of curvature of order 0.1), negative Reynolds shear stresses have been observed [Shivaprasad and Ramaprian[40]]. Kim and Simon[41] report that the turbulent heat flux was affected by curvature more than the turbulent shear stress.

Many of the observed differences between distorted supersonic and subsonic boundary layers can be explained in terms of the fluid property changes across the boundary layer [Spina *et al.* [20], Smith and Smits[5], and Bradshaw[39]]. However, supersonic flows possess phenomena that do not have incompressible counterparts. For example, wave (expansion or compression) boundary layer interactions, where the longitudinal pressure gradients can lead to compression or dilatation, which in turn affects the velocity, pressure and density fluctuations, are not present in subsonic flow.

When a streamwise favorable pressure gradient is imposed on a supersonic boundary layer, the flow is distorted by both the effects of pressure gradient and by bulk pressure gradient [Bradshaw[34]]. A distortion is generally considered mild if $d_{max} \approx 0.01$ and strong for $d_{max} \approx 0.1$ [Spina *et al.*[20]]. If the distortion is applied for a time that is

comparable to an eddy lifetime, then the impulse parameter (I), the time-integrated strain rate, may be a better choice [Smith and Smits (1994)]. For an impulsive perturbation resulting from a region of bulk compression, $I_p = ln(p2/p1)/\gamma$ [Smith and Smits[5] and Hayakawa *et al*[42]]. For an impulse as a result of curvature, $I_\phi = \Delta\phi$ [Smits *et al.*[22]]. Even though the interactions between the strain rates are most likely nonlinear, the linear addition of the perturbation strengths is usually accepted for crude comparisons among different flows. Luker *et al.*[3] present a generalization of the pressure gradient strength definition

Collectively, the available turbulence data [Smith and Smits[43], Donovan[44], Jarayam *et al.*[45], Dussuage and Gaviglio[46] and Thomann[37]] indicate that the axial turbulence intensities decrease by 70-90% for I_p and I_ϕ values $\in$ (-0.4,-1.0) and (-0.1,-0.3), respectively. Because of the reduction in the fluctuating properties, as well as reductions in the skin friction and heat transfer, favorable pressure gradients are often characterized as having a stabilizing effect. Relaminarization of part of the boundary layer is believed possible if the pressure gradient is strong enough [Spina *et al*[20] and Jarayam *et al.*[45]]. Smith and Smits[43] and Dussauge and Gaviglio[46] estimated, using a rapid distortion analysis, that the majority of the turbulence reduction was the result of mean bulk dilatation.

Arnette *et al.*[17] showed that the overall magnitude of the kinematic Reynolds shear stress was dramatically decreased across the entire boundary layer for 7.0 and 14.0 deg. centered and gradual expansions. They further defined an "apparent reverse transition," where the normal energy transfer from the mean flow had been reversed, to

describe a sign changing of the Reynolds shear stress. Although the Arnette *et al.*[47] study provided detailed turbulence information throughout the expansion, the axial spacing was not refined enough to resolve the stream wise strain rates.

Luker *et al.*[3], Bowersox *et al.*[48], Luker *et al*[3], and Bowersox and Buter[49] performed detailed investigations of the influence of the wall curvature driven pressure gradients on the turbulent flowfield including the turbulent shear stress transport. A subset of important results to support the need for the present research is listed here. Focusing only on the favorable pressure gradient flow, the turbulence data indicated that the present favorable pressure gradient had the expected stabilizing effect on the turbulent quantities. The magnitude of the Reynolds shear stress was also reduced by the favorable pressure gradient; in the near-wall region it was approximately 25% of the zero pressure gradient value, and in the outer region $(y/\delta > 0.5)$, the kinematic Reynolds shear stresses *were negative and the principle strain rates were positive*. The three-dimensional strain rate measurements and the associated extra production indicated that the overall turbulence production was also negative in the outer half of the favorable pressure gradient boundary layer. In addition, the use of a body-intrinsic coordinate system contributed to the reduced shear stress levels. Also, the present data collectively indicated that the favorable pressure gradient was disintegrating the large-scale eddies into smaller ones. This redistribution of energy increased the amount of turbulent energy available for dissipation by the flow, which in turn had the observed stabilizing effect on the boundary layer. Numerical simulations using two-equation turbulence modeling demonstrated that the eddy viscosity approach was inadequate for these very

mild pressure gradient flows. Hence, in addition to the important physical information provided, this first AFOSR sponsored project provided strong evidence to support the contention that for the Reynolds Averaged Navier-Stokes approach to solving wall bounded flow, a full second order turbulent transport model is required.

Unanswered Questions

It is unclear what will happen when the localized turbulent stress production mechanisms present in the large scale surface roughness are combined with the global turbulent stress production mechanisms that are produced by curvature driven favorable pressure gradients. From the spectra data, the larger eddies are destroyed by the surface roughness creating the smaller more energetic eddies while the favorable pressure gradients tend to have a relaxing influence on the turbulent stress production. It has been theorized that the combination of a sufficiently strong favorable pressure gradient and large scale surface roughness may enhance the negative production mechanisms and possibly producing a laminar flow, but the current state of published data doesn't is inconclusive.

What effect will there be on the production of turbulent stresses due to wall geometry and surface roughness? What effect will the "extra production" mechanisms have on rough walls? Will favorable pressure gradients further disintegrate the structures towards even smaller scales? What is the effect of roughness topology? Will there be detached bow shocks produced by the square roughness? Will there be attached oblique shocks produced by the diamond roughness. What effect will the shock-boundary layer interactions have on the production of turbulent stresses?

CHAPTER II

EXPERIMENTAL TECHNIQUES

Particle Image Velocimetry

Particle Image Velocimetry (PIV) is a non-intrusive diagnostic technique that uses tracer particles illuminated by a light source (usually a laser) and up to four digital cameras to create a highly resolved velocity field in a variety of different applications[50]. Two successive images of the tracer particles are possible using short pulse lasers and high speed interline transfer cameras in high speed flows. A two-dimensional cross correlation of the image intensity taken over the same region in both images will produce a correlation map. The location of the correlation map peak will correspond to the average displacement of the pixels within a particular box. Adaptive correlation calculations can be used to produce better results in using smaller box sizes. For this process the original box size is rather large so that despite the fact some particles that were in the first box may have left the second box, the average will still be fairly close. The software will then use an interpolation function to determine were a smaller successive interrogation spot sizes will have moved to creating a more accurate correlation of a smaller spot size. This process can be repeated up to 2 more times before the small size of the spot sizes produce large cross correlation error.

Experimental Setup

For the current experiment it was not practical to paint the model surfaces because it was not known if the large shear stresses would remove the paint from the

roughness elements. Instead various hardware setups and experimental techniques aimed at eliminating wall reflections while enhancing the visibility of the smaller tracer particles was used. A schematic of the PIV setup for both arrangements during a supersonic boundary layer experiment is shown in Figure 1. The tunnel is seeded by a TSI Six-jet Atomizer Model 9306[51] using Bertolli extra light olive oil producing particles with diameters on the order of 1.0 μm. All six jets are opened with the input pressure set at 1.14 MPa which produces an approximate aerosol output of 4.51 x 10^{14} particles per second.

Tracer particles are illuminated in the tunnel using a dual port/dual head New-Wave Solo 120XT PIV laser designed to provide a highly stable green light source (532 nm) for PIV applications. Each laser head has a maximum energy output of 120 mJ at 532 nm. The pulse width is 4 ns with a $\pm$ 1 ns jitter and a maximum frequency of 15 Hz. Perpendicular polarization of the beam coming out of port 2 is achieved by using a half wave plate. The plate is a crystal quartz optic designed to differentially retard the phase of a polarized beam. In front of the first laser port there is a high-energy polarizing cube beamsplitter that provides efficient narrowband polarization. The polarizer consists of a pair of precision right-angle prisms optically contacted together and has a damage threshold up to 10 J/cm^2. A high energy mirror is used to reflect Laser 1 into the high-energy polarizing cube beamsplitter. After the beams have been aligned there will be two coincident beams; one with parallel polarization (Laser 1) and the other with perpendicular polarization (Laser 2).

The laser beams are guided to the test section using 90º bending prisms constructed of BK7 glass with AR coatings. A BK7 focus lens with a focal length of 500 mm is used to focus the beam so that the waist is located just above the test section floor. A laser sheet that is approximately 1.5 cm wide and 1 mm thick is formed on the test section floor using a BK7 Plano-concave cylindrical lens.

The camera used was a Cooke Corp. PCO 1600 high dynamic 14bit cooled interline-transfer CCD camera system with 1600 x 1200 pixel resolution, and the ability to perform image windowing. The image memory is integrated into the camera enabling image recording at 160MB/s. It features thermo-electrical cooling at -50°C below the ambient which is capable of a maximum dynamic range of 70dB. Image data are transferred to the computer via an IEEE 1394 (firewire) camera link. The cameras had an intrinsic delay time of the camera is 5.3 μs and a trigger delay time of 200 ns +- 13 ns. The camera trigger, laser Q-switch and laser flashlamp are all controlled by a Quantum Composers Model 9618 pulse generator. The camera frame grabbing software was Camware version 2.13. A Nikon 60 mm lens was used to focus the camera onto the illuminated particles.

Post Processing

Velocity fields are created by calculating the displacements of particle ensembles from consecutive images using Innovative Scientific Solutions' dPIV 32-bit Analysis Code[52]. A three-step adaptive correlation calculation using successive interrogation spot sizes of 128×64, 64×32, and 32×16 pixels, respectively, with 50% overlap was used to determine velocity vectors. In order to enhance the intensity of correlation peaks

relative to random noise, a correlation multiplication process filter with all four correlation maps was turned on. A consistency post processing filter and a nearest neighbor dependency filter were turned on to improve the adaptive correlation calculation during the first and second steps and eliminate incorrect vectors during the third step.

First and second order turbulent statistics are created using an in house computer code that ensemble averages the averages the velocity vector fields. In order to minimize the effects of fluctuations in total temperature and pressure while the tunnel is running, the program bins the average velocity data and computes the fluctuating velocities relative to the average velocity from in the corresponding bin. The equation for the bin mean velocity is given below, where n is the number of samples per bin, and J_{max} is the total number of bins.

$$\overline{u}_{bin,j} = \frac{1}{n} \sum_{i=(j-1)n+1}^{j \cdot n} u_i, \quad j = 1 \ldots J_{\max} \tag{4.1}$$

The computed mean velocity is simply the ensemble average of the *bin* velocity:

$$\overline{u} = \frac{1}{J_{\max}} \sum_{j=1}^{J_{\max}} \overline{u}_{bin,j} \tag{4.2}$$

And the fluctuating velocity is give as:

$$\overline{u'u'} = \frac{1}{N-1} \sum_{i}^{N} \left(u_i - \overline{u}_{bin,j} \right)^2, \quad 1 \le i \le n \Rightarrow j = 1, \ldots, \left(J_{\max} - 1 \right) n + 1 \le i \le J_{\max} n \Rightarrow j = J_{\max} \tag{4.3}$$

$$\overline{u'v'} = \frac{1}{N-1} \sum_{i}^{N} \left(u_i - \overline{u}_{bin,j} \right) \left(v_i - \overline{v}_{bin,j} \right), \quad 1 \le i \le n \Rightarrow j = 1, \ldots, \left(J_{\max} - 1 \right) n + 1 \le i \le J_{\max} n \Rightarrow j = J_{\max} \tag{4.4}$$

Wall Reflection

Near planar surfaces it becomes increasingly difficult to make accurate measurements. Smaller seed particles (0.5 – 1.0 μm) have very low Mie scattering signatures and are usually not detectable. Since the seed particles are usually injected into the freestream portion of the flow and entrained into the viscous region, in the near-wall region the seed density will thus be much lower and can become insufficient for accurate particle ensembles. Often it is not practical to increase the particle density from the flow seeder because seed accumulation on the windows can obscure the view of the test area. A possible solution is to be able to detect the previously invisible smaller particles. An additional complication is laser reflection from the surfaces. The reflection intensity can be so great that image blooming, a situation where neighboring pixels are saturated with excess charges producing a white band in the image, can occur making all particles in this region undetectable. Correcting for the first problem by increasing laser power has the undesirable effect that it also increases the wall reflection and hence image blooming. Conversely a reduction in laser power can reduce laser reflection, but also leads to a reduction in the visibility of the tracer particles. A current method in use to eliminate surface reflection is to coat the surfaces with fluorescent paint capable of absorbing up to 99% of the incoming light and scatters the remaining light at a different wavelength. Using appropriate color filters it is possible to eliminate virtually all wall reflection[53].

Stagnation Pitot

Stagnation pressure is measured by an Omega PX303 (0 – 0.69 *MPa*) pressure transducer. The transducer is connected to a pressure probe by fittings. The pressure probe is attached to a 1.6 mm diameter tube with an inner diameter of 0.8 mm. The end of the tube is crimped so that the entrance diameter is 0.16 mm. The probe is moved in the transverse direction by a Velmex model MA2508P40 linear translation stage that contains a turn screw that has 15.75 turns per centimeter. The translation stage is moved by a Vexta PK2608-02A Stepper motor that has 400 steps per revolution. The stepper motor is operated by an S100 3 channel stepper motor controller which is controlled by a personal computer running the S100 SMC software. The motor revolves at 30 revolutions per second, translating the probe 1.9 cm per minute.

Pressure Sensitive Paint

Measurements of surface pressure distributions are possible using Pressure Sensitive Paint (PSP). PSP is based on the oxygen and thermal quenching processes of luminescence which are reversible processes in molecular photoluminescence. The advantages of using PSP are its ability for remote sensing, high spatial resolution, and fast data acquisition which can leads to reduced wind tunnel time.

The inducement of photoluminescence of paint via an external light source and the subsequent dynamic quenching of the process due to the presence of oxygen is the major physical process that occurs with PSP[54]. The degree of quenching depends on the oxygen concentration in the paint layer which is directly related to the air pressure above the paint. After external stimulation of the Lumiphor molecules, the energy in the

excited electronic states is dissipated back down to the ground state by radiative and non-radiative transitions. Emission occurs through the radiative process called luminescence. The radiant transition from the lowest excited singlet state to the ground stated is called fluorescence which is a spin-allowed radiative transition between two states of the same multiplicity, and has lifetimes that typically are around for 10^{-9} seconds. The radiative transition from the triplet state to the ground state is called phosphorescence, which is a spin-forbidden radiative transition between two states of different multiplicity and has lifetimes of around 10^{-4} and longer.

$$\begin{aligned} \tau_f &= \frac{1}{k_f + k_{nr,s} + k_{q,s}\eta_{O_2}} \\ \tau_p &= \frac{1}{k_p + k_{nr,t} + k_{q,t}\eta_{O_2}} \end{aligned} \tag{4.5}$$

The oxygen quenching process, given by the last term in the denominator for both expressions, is isolated from the other non-radiative decay processes and is proportional to the diffused oxygen concentration in the permeable binder. The radiative decay rates, k_f and k_p are independent of η_{O_2}. The amount of diffused oxygen is related to the partial pressure of oxygen above the paint by a linear form of Henry's law.

$$\eta_{O_2} = \sigma p_{O_2} = \sigma \chi_{O_2} p \tag{4.6}$$

For this study, the phosphorescent decay dominated the light radiation and the intensity of the radiated light can be modeled by:

$$I(t) = Ae^{-t/\tau}; \quad \tau = \tau_p >> \tau_f \tag{4.7}$$

This phenomena is used to measure the surface pressure on items covered with the pressure sensitive paint.

Unfortunately the non-radiative and quenching process produce a simultaneous temperature dependence. When the temperature effects are included, the following substitution in the governing equations is required

$$\eta_{O_2} = \left[\sigma_1(T) + \sigma_2(T)\right] P_{O_2} \tag{4.8}$$

which is similar to the original equation but sigma which was considered a constant is now a function of temperature and the partial pressure of the oxygen.

The pressure paint used in this study is a UniCoat PSP (UNC405) produced by Innovative Scientific Solutions Inc. (ISSI). This paint, when excited in the uv emits in the visible between 400-500 nm.

The PSP was sprayed via a spray can directly onto each test section model. A total of 6 coats which each are approximately 10 μm thick were added. Normal application and calls for between 5 and 15 coats. A smaller number was used so as to minimize changes in the shape of the roughness elements. The models were cured with a heat gun for approximately 15 minutes after the final coat was applied. Four to eight reference dots were placed on the models using a black marker, and the models were then wrapped in aluminum foil to prevent photo-degradation of the paint.

PSP calibration required generating calibration coefficients using sets of images taken at known pressures and temperatures. Averaged intensity data from a region of interest from the bitmaps, applying necessary flat field correction, and using Least Square Approximation Methods, creates calibration a calibration function. The

calibration function is pressure approximated by a tw0 dimensional 2nd order approximation having relative intensity I_r and temperature T as arguments:

$$P(I_r, T) = \sum_{l=1}^{l=3} \sum_{j=1}^{j=3} \gamma_{jl} \, (I_r^{j-1} \quad T^{l-1}) \ , \tag{4.9}$$

Where, γ_{ji} are the calibration coefficients and I_r is calculated as I_0/I, where I_0 is the signal at reference pressure P_o and temperature T_o.

The camera used was the same Cooke Corp. PCO 1600 high dynamic 14bit cooled interline-transfer CCD camera system that was used to obtain the PIV images. The software used to process the images was Innovative Scientific Solution's OMS Lite version 1.1. An Innovative Scientific Solutions LED array was used as the light source. An image of the setup can be seen in Figure 4.

A background image was first recorded with the lab completely darkened in order to determine the level of noise within the camera images. A "wind-off1" image was taken just prior to the running the tunnel. The lab remained darkened from ambient light, but the LED light was on. This established the reference intensity maps. The tunnel was started and ten "wind-on" images were taken at 1 second intervals to ensure that the relative intensity remained constant throughout the runs. After the tunnel was stopped, an additional "wind-off2" image was taken. The reference dots were located on all four images that were used to correct for any possible movement or vibration that may have occurred. The OMS software would then produce a relative intensity field, which when the calibration coefficients and the reference pressures and temperatures were incorporated would produce a surface pressure distribution. The major difficulty was

determining the surface temperature, since this was not being measured, and accounted for the major sources of error.

Schlieren

The German word "schlier" refers to a transparent medium where there is a local inhomogeneity which results in light deflection. The schlieren permits both the qualitive observation and the quantitative measurement of light deflection[55]. The principal of this method was developed over a century ago by Foucalt in 1859 to check the quality of lenses and mirrors. Toeppler improved the system in 1864 by introducing the concept of the knife edge for visualizing density gradients.

Our eyes can only see amplitude and color contrast, but have no way to discern phase differences in a light beam[55]. Schlieren and shadowgraph methods convert phase differences into visible amplitude differences. Light slows upon interacting with matter. The refractive index n, or the amount of change in the speed of light of a transparent medium, is given by $n = c_0 / c$ where c is the light speed in the medium and c_0 is the universal speed limit of light in a vacuum. For gases there exists a linear relationship between the refractive index and the gas density:

$$n - 1 = k\rho \tag{4.10}$$

For air at standard conditions the Gladstone-Dale coefficient, k, is about 2.3×10^{-4} m^3/kg. From equation (4.10), it is apparent that n is only weakly dependent upon ρ, thus small density variations require very sensitive optics.

Schlieren and systems are based on the principle of light refraction. Optical inhomogeneities refract or bend light rays proportional to their gradients of refractive

index. The lateral plane is the normal direction, represented by the z axis, and is the propagation direction of undisturbed rays. The resulting ray curvature is given by:

$$\frac{\partial^2 y}{\partial z^2} = \frac{1}{n}\frac{\partial n}{\partial y} \tag{4.11}$$

Integrating once, the component of the angular ray deflection in the y direction is

$$\varepsilon_y = \frac{1}{n}\int \frac{\partial n}{\partial y} dz \tag{4.12}$$

For schlieren of extent L along the optical axis, this becomes:

$$\varepsilon_y = \frac{L}{n_0}\frac{\partial n}{\partial y} \tag{4.13}$$

where n_0 is the refractive index of the surrounding medium. The schlieren system will allow direct measurement of the angular ray deflection, and thus the density gradient, $\partial\rho/\partial y$. In a likewise manor, the density gradient in the axial direction can be obtained.

For most supersonic wind tunnel applications due to its ease with setup and low optical distortion characteristics, a *Z*-type 2-mirror schlieren system is used. A schematic of this setup is shown in Figure 5. A condenser lens with a focus length of 91.44 cm focused a white light source down to a point where a slit has been placed. The light would then pass through a horizontal slit, created out of two razor blades painted black and separated by about 1 mm, into a parabolic mirror with a focal length of 91.44 cm. The distance from the slit to the parabolic mirror will be equal to the focal length of the mirror. The parabolic mirror was aligned so that the light beam was normal to the test section. For minimum optical distortion the angle that the between the light source and the collimated light beam was minimized.

An additional parabolic mirror with the same focal length was placed in the collimated light beam after the test section. The second mirror focused the light to a point, where a horizontal knife edge was introduced. This knife edge was simply a razor blade that was painted black. A schematic of the function of a knife edge is illustrated in Figure 6. In the test section, light rays from the collimated light beam that were refracted (both upward and downward) away from their original paths. Both refracted rays miss the focus of the optical system. The upward-deflected ray is allowed to pass producing a light point relative to the background while the downward-deflected ray hits the knife-edge which corresponds to a dark point in the background. The phase difference resulted in a vertical gradient of the refractive index which was converted to viewable amplitude difference. This difference was recorded by directing the schlieren image directly onto the CCD array of a Nikkon D50 SLR camera without a lens. In order to shrink the schlieren image to a size viewable by the CCD array, a telescoping lens was placed between the camera and knife edge.

CHAPTER V

EXPERIMENTAL FACILITIES

Experimental characterization of turbulent supersonic boundary layers has been performed on a Mach 2.86 supersonic wind tunnel located at Texas A&M University. The tunnel is a blowdown facility. A finite-radius, half-nozzle was used to produce a freestream Mach number at the nozzle exit of 2.86 with a $\pm 1.0\%$ variation across the test section. The contoured side of the nozzle was located along the tunnel ceiling. The stagnation pressure and temperature were 689 KPa ($\pm 5.0\%$) and 315K ($\pm 3.5\%$) respectively.

Compressed Air

Compressed Air is supplied by 2 four-stage Chicago Pneumatic TCB-4 compressors illustrated Figure 9 that were formerly installed in a NASA rocket vehicle test facility. Each unit is powered by a 112 kilowatt motor and is rated to provide a mass flow rate of 0.13 kg/s at 24.0 MPa. The maximum discharge pressure fore each compressor is limited to 15.5 MPa. Moisture, oil, and other particulates produced by the compressors are removed by passing the air through a Domnick Hunter HDL-500 High Pressure Heatless Regenerative Air Dryer. The dryer is a high pressure dual tower heatless regenerative desiccant air dryer. Compressed air is dried by the desiccant in one tank while the other tank is regenerated. The tanks are alternated from a drying cycle to a regeneration cycle and visa-versa automatically every 5 minutes. The rated mass flow rate of the dryer is 0.28 kg/s at 13.8 MPa.

Compressed air is stored in an A. D. Smith high pressure storage tank, which has an internal volume of 23.3 cubic meters and a maximum operating pressure of 19.3 MPa. Between the wind tunnel and the storage tank, there is approximately 65 m of pipe. The pipe is made of sch XX A105 carbon steel. It has an outer diameter of 11.4 cm, an inner diameter of 8.0 cm, and a maximum rated pressure of 27.9 MPa.

A 4-1500 full bore Virgo Engineers Trunion Mounted Ball Valve controlled by a B-270U-S100 Morin Series B pneumatic actuator has been placed between the storage tank and the wind tunnel. The actuator is a spring return quarter-turn model which requires a supply pressure of 0.69 MPa which is controlled by an ASCO 3-way normally closed solenoid valve that uses shop air.

Pressure from the main line is regulated down to the tunnel operating pressure using a Straval model PRH-0022-20T dome loaded pressure regulator. The regulator has a maximum inlet pressure of 20.7 MPa, and an adjustable outlet pressure of 0.45 – 1.31 MPa with a maximum flow rate of 3.36 kg/s.

In order to eliminate heat transfer from model surfaces to the boundary layer, the incoming air is heated using a Chromalox 535 kW circulation heater so that the boundary layer adiabatic wall temperature closely matches the actual wall temperature. The adiabatic wall temperature is found by the following relation between adiabatic wall, boundary layer edge, and stagnation temperatures:

$$r = \frac{T_{aw} - T_\infty}{T_0 - T_\infty} \tag{5.1}$$

Where *r* is the *adiabatic recovery factor* which is approximated as $r \approx \sqrt[3]{\Pr}$ and Pr is the turbulent Prandtl number. For air with a Mach number of 2.9, $\Pr \approx 0.71$ and $r \approx 0.892$. The boundary layer edge temperature can be calculated in terms of the stagnation temperature using the isentropic temperature relation.

$$\frac{T_0}{T_\infty} = 1 + \frac{\gamma - 1}{2} M^2 \tag{5.2}$$

Combining equations (5.1) and (5.2) gives the following relation for the adiabatic wall temperature in terms of the total temperature, the adiabatic recovery factor, and the freestream Mach number.

$$\frac{T_{aw}}{T_0} = \frac{1 + r\dfrac{(\gamma - 1)}{2} M^2}{1 + \dfrac{(\gamma - 1)}{2} M^2} \tag{5.3}$$

Because of the small duration of the tunnel run times (> 90 seconds) and the low thermal conductivity of Plexiglas ($1.2 \times 10^{-4}\ cal/cm - \mathrm{s} - {}^{o}C$) it has been assumed that the tunnel surface temperatures remained constant at the lab temperature which was maintained at 296 K.

Settling Chamber

Smooth uniform flow with is produced by passing the compressed air a through a settling chamber. The external structure of the settling chamber is constructed of 14" sch 160 pipe carbon steel pipe 0.91m long, 0.36m in diameter, and with a wall thickness of 4.0cm. It is designed for a maximum working pressure of 1.55MPa. The settling chamber exterior is capped at each end by class 1500 blind and slip on flanges. The inlet

blind flange has a 3" NPT hole placed where it connects with the main line, and the exit blind flange has a 7.62cm by 7.62cm square hole for the transition to the nozzle. A schematic of the settling chamber interior is given below in Figure 12. Initially air is passed through a 12.7cm diameter cylinder that is 12.7 cm long to quickly redistribute the mass of the air away from the chamber centerline. It has 56 evenly spaced holes that are 12.7mm in diameter. The flow is straightened by passing it through a reverse cone that has 225 evenly spaced 4.8 mm diameter holes. Finally the turbulence intensities are minimized by passing the flow through 3 wire mesh screens evenly spaced 3.81cm apart. The mesh made of woven stainless steel wire with a diameter of 88.9μm with 28 x 28 strands per cubic centimeter. The open area of the mesh is 55% and the wire Reynolds number is $\mathrm{Re}_w = 263$. The exit is constructed of 4 pieces of pipe that have been halved along their centerline, cut at 45 degree angles, and joined together to form a square. The outer diameter of the pipe is 6.03cm, the dimension of the inner square is 7.62cm x 7.62cm, and the dimension of the outer square is 16.2cm x 16.2cm. It was designed so that the inviscid core of the pipe flow is allowed to pass through, so that boundary layer growth doesn't begin until the inlet of the nozzle.

Tunnel Control and Monitoring System

Total pressure is measured in the settling chamber via a Pitot probe using an Omega PX303 voltage output pressure transducer. The transducer is capable of measuring 0 – 0.69 MPa and outputs this value a DC voltage between 0.5 – 5.5 volts DC. The total temperature is measured using an Omega JQSS model thermocouple and the signal is amplified by an OMNI AMP-IV thermocouple amplifier. The tunnel static

pressure is measured by 5 Omega PX303 voltage output pressure transducers with a range of 0 – 0.10 MPa. The accuracy of the transducers is 0.25% full scale. The first transducer is located at the nozzle exit, and the other 4 are distributed along the centerline of the testsection sidewall. Data from the pressure transducers and thermocouples is collected in a personal computer and processed by a KPCI-3110 data acquisition board with a sampling rate of 1.25 MS/s. The board has 12 bit resolution and can support up to 32 single ended or 16 differential channels. The software used to process the data is TestPoint version 4.

Nozzle

The nozzle is Mach 2.86 half-nozzle with 3 characteristic Mach wave reflections. The nozzle was constructed using aluminum 6061 and a schematic is listed in Figure 13. The nozzle inlet and exit height are 7.62cm, and the throat height is 1.68cm. The side walls of the nozzle are 2.54cm thick and the entire nozzle assembly is held together with 42 grade 8 bolts with a diameter of 1.27cm. Grooves for 3.81mm diameter o-rings have been created 4.45mm above the nozzle surface. A groove for an o-ring has also been milled around the nozzle exit.

Diffuser

A variable throat diffuser is used to reduce the required stagnation pressure required for running the wind tunnel. The inlet height of the diffuser is 7.62cm and the exit height increases to 14.0cm. An exhaust muffler has been placed at the end of the diffuser to reduce noise. The muffler has four chambers, and has a maximum mass flow rate of 20.2 kg/s at 0.62 MPa. Noise from the diffuser is reduced by 17 to 22 decibels.

Test Section

The test section was designed so that DPIV measurements could be accurately and efficiently obtained. The sidewall is constructed of aluminum and is 71.1 cm long, 17.8 cm wide, and 1.27 cm thick. Symmetric mounting brackets are used to connect the sidewall to the nozzle exit and diffuser inlet. There are three different measurement locations located 15.9 cm, 29.8 cm, and 41.3 cm downstream of the nozzle exit respectively.

The DPIV sidewall has two fused silica windows placed along the testsection's axial centerline. The first window is 10.2 cm in diameter and has been placed 15.9 cm downstream from the nozzle exit while the second window is 15.2 cm in diameter and is 29.8 cm downstream from the nozzle exit. Within each window hole there are two o-ring grooves for 2.38 mm thick o-rings. Because the sidewall mounts are symmetric, the location of the windows can be adjusted by rotating the sidewall about its lateral axis creating the third measurement location. The second sidewall is used to obtain static pressure measurements along the testsection's axial centerline. On the outer side of the sidewall 1/8" NPT threaded holes have been distributed at 23 locations beginning 7.62 cm down from the nozzle exit, spaced 2.54 cm apart, and are 9.53 mm deep. On the tunnel side of the sidewall each NPT hole is joined by a 1.59 mm static pressure port hole. The Omega pressure transducers can be screwed into the sidewalls via a 1/4" - 1/8" F/M NPT adapter while the unused ports are plugged.

The ceiling and floors are constructed of Plexiglas most of the laser light is allowed to pass through them (~92%), minimizing wall reflection during PIV. The

models vary between 2.54 and 4.45 cm in thickness depending on the model and the location of the curvature. The models contain seven 7.94 mm holes that are 1.27 cm up from the base of each model that are used to join the testsection sidewalls and the floor and ceiling together.

Test Section Inlet Conditions

The Mach number at the nozzle exit was 2.86. The Mach number was measured using the stagnation Pitot probe in the settling chamber, and a static pressure port located 1.27 cm from the nozzle exit. The static pressure was measured using an Omega PX303 0 – 0.69 MPa pressure transducer and the KPCI 3116 data acquisition board.

To verify that the incoming flow field has no lateral variation, Pitot pressure profiles of the testsection inlet floor boundary layers. The profiles were taken at 3 locations that were centered along the tunnels lateral axis and spaced 1.27 cm apart. From Figure 15 it can be seen that all profiles are identical. Based on the Pitot profiles the boundary layer was 0.9 cm.

Tunnel Models

The tunnel models were designed to incorporate the combined effects of surface roughness and favorable pressure gradient consistent with the goals presented in the introduction.

Large Scale Periodic Surface Roughness

An aerodynamically smooth plate and fully rough regularly spaced surface roughness pattern with k_s^+ values similar to those used in Latin and Bowersox (2000). The roughness elements used 3-D uniformly distributed squares that were cut with a

1.59 mm ball end mill to a depth of 0.794 mm. Because production mechanisms that more closely resembled sandgrain roughness was desired, the 3-D elements were used. The uniform roughness was selected because it is simple to manufacture and to grid for CFD applications that use DES or LES rather than rough wall boundary conditions.

Curvature Driven Favorable Pressure Gradients

The primary mechanisms in the Reynolds Stress Transport Model we are concerned with are the production and pressure work terms from equation (3.2). The mean flow velocity and velocity gradients are negligible in the lateral direction. The resulting 2D component of the production and pressure work terms becomes respectively

$$P_{xy} \approx -\bar{\rho}\overline{v'^2}\frac{\partial \bar{u}}{\partial y} \tag{5.4}$$

$$PW_{xy} = -\overline{v''}\frac{\partial \bar{p}}{\partial x} \tag{5.5}$$

The relationship between the fluctuating velocities has been approximated by the $v' = Cu'$ where $C \approx -0.7$ based on experimental data. Production can thus be approximated as

$$P_{xy} = -C\bar{\rho}\overline{u'v'}\frac{\partial \bar{u}}{\partial y} \tag{5.6}$$

The equation of state for an ideal gas for fluctuating thermodynamic properties and the isentropic relations for fluctuating temperature are give as follows:

$$\frac{p'}{\bar{p}} = \frac{\rho'}{\bar{\rho}} + \frac{T'}{\bar{T}} \tag{5.7}$$

$$C_p\left(\bar{T}_t + T_t'\right) = C_p\left(\bar{T} + T'\right) + \frac{\bar{u}^2 + 2\bar{u}u' + u'^2}{2} \tag{5.8}$$

Following Kistler[23], it was assumed that $p' = 0$, thus

$$\frac{\rho'}{\bar{\rho}} = -\frac{T'}{\bar{T}} \tag{5.9}$$

An additional assumption that can be made using the SRA is that $T_t' = 0$. Using this assumption and equation (5.8) the following is obtained.

$$\frac{T'}{\bar{T}} = -\frac{\bar{u}u'}{C_p\bar{T}} \tag{5.10}$$

Which can be rewritten as:

$$\frac{T'}{\bar{T}} = -(\gamma - 1)\bar{M}^2\frac{u'}{\bar{u}} \tag{5.11}$$

Combining equations (5.9) and (5.11) multiplying both sides by v' and averaging produces

$$\frac{\overline{\rho'v'}}{\bar{\rho}} = \frac{(\gamma - 1)}{2}\bar{M}^2\frac{\overline{u'v'}}{\bar{u}} \tag{5.12}$$

Which can be rewritten as

$$\bar{\rho}\overline{u'v'} = \frac{2\bar{u}}{(\gamma - 1)\bar{M}^2}\overline{\rho'v'} \tag{5.13}$$

The production can now be written in terms of (5.6) and (5.13) to produce:

$$P_{xy} \approx -C\frac{2\bar{u}}{(\gamma - 1)\bar{M}^2}\overline{\rho'v'}\frac{\partial\bar{u}}{\partial y} \tag{5.14}$$

The velocity gradient can be approximated by

$$\frac{\partial\bar{u}}{\partial y} \approx \frac{\bar{u}}{\delta} \tag{5.15}$$

Boundary layer growth rates need to be estimated for the different pressure gradients, but assuming there is no separation, to a first order approximation flat plate turbulent boundary layer assumptions are valid. The production now has the approximate form:

$$P_{xy} \approx -C\frac{1}{\delta}\frac{2\overline{u}^2}{(\gamma-1)\overline{M}^2}\overline{\rho' v'} \tag{5.16}$$

For any Favre-averaged quantity, the following relation can be used.

$$\overline{f''} = -\frac{\overline{f'\rho'}}{\overline{\rho}}$$

Combining the above relation along with equation (5.5) gives the following expressing for the pressure work

$$PW_{xy} \approx \frac{\overline{v'\rho'}}{\overline{\rho}}\frac{\partial \overline{p}}{\partial x} \tag{5.17}$$

The pressure gradient is approximated by

$$\frac{\partial \overline{p}}{\partial x} \approx \frac{p_2 - p_1}{L}$$

where L is the distance between the beginning and end the streamwise curvature. A first order approximation of the pressure work using the estimate for the pressure gradient and equation (5.17) is

$$PW_{xy} \approx \frac{\overline{v'\rho'}}{\overline{\rho}}\frac{p_2 - p_1}{L} \tag{5.18}$$

Taking the ratio between the 2D pressure work (5.18) and production terms (5.16) produces a pressure work influence parameter ζ which is defined as the ratio between the pressure work and the turbulent production.

$$\zeta \equiv \frac{PW_{xy}}{P_{xy}} \approx -\frac{1}{C}(\gamma-1)\bar{M}^2 \frac{p_2 - p_1}{2\bar{\rho}\bar{u}^2}\frac{\delta}{L} \tag{5.19}$$

The average Mach number can be estimated by assuming the pressure gradient in the transverse direction is negligible which implies that

$$\frac{T_w}{\bar{T}} \approx \frac{\bar{\rho}}{\rho_w} \tag{5.20}$$

Using equation (5.20) the average Mach number is given as

$$\bar{M}^2 = \frac{\bar{u}^2}{\gamma R T_w}\frac{\bar{\rho}}{\rho_w} \tag{5.21}$$

The final approximate form of equation (5.19) is given as

$$\zeta \approx -\frac{1}{C}(\gamma-1)\frac{p_2 - p_1}{2\rho_w a_w{}^2}\frac{\delta}{L} \tag{5.22}$$

Because the wall temperature is adiabatic, equations (5.2) and (5.3) can be used with equation (5.20) and the equation of state (2.17) to find all thermodynamic properties at the wall. The boundary layer height is estimated using simple flat plate turbulent boundary layer growth rates with corrections for the favorable pressure gradient based on experimental data and using an inviscid technique such as Method of Characteristics to estimate the thermodynamic properties at the boundary layer edge.

A flat plate zero pressure gradient (ZPG) model, weak pressure gradient (WPG) model, and strong pressure gradient (SPG) model were created based on the parameter ζ. The curvature for the WPG model and the SPG model was created using a third order polynomial with the boundary conditions that the slope and the start and end points are zero, while the curvature began at 0 and ended and -1.91 cm in the *y*-direction. The

length L was varied in equation (5.22) until the desired value of ζ was obtained. Table 2 lists the distance between the beginning and the end locations for the wall curvature along with the estimated values of ζ, $d_{\max}$, I_p, and I_ϕ. The freestream Mach number has been calculated using static pressure ports that are distributed along the tunnel centerline. The Mach number is computed from the isentropic pressure relation:

$$M = \sqrt{\left[\left(\frac{p_0}{p}\right)^{\frac{\gamma}{\gamma-1}} - 1\right]\frac{2}{\gamma-1}} \tag{5.23}$$

The locations of the pressure taps from the nozzle exit are presented in Table 1. Note that the first pressure tap is placed just before the nozzle exit, while the remaining four taps are located within the test section. The local freestream Mach number computed using equation (5.23) is given below at each static pressure port location.

CHAPTER VI

RESULTS AND DISCUSSION

The main objective of this study was to improve upon the understanding of the fundamental physics of high-speed turbulent boundary layer with imposed global and local mechanical non-equilibrium. To meet this goal a series of experiments designed to provide the necessary data, as discussed in chapter IV, have been performed. The first two sections in this chapter present the results along with a detailed analysis of all acquired data. The *Mean Flow Data* section presents schlieren images, mean flow velocity and thermodynamic measurements generated from the stagnation Pitot, pressure sensitive paint (PSP), and particle image velocimetry (PIV). The *Turbulent Flow Data* section presents turbulence data acquired from the PIV. Finally the *Flowfield Description* presents a brief overview of the overall influence of surface roughness and curvature driven pressure gradients on the turbulent boundary layer flowfield and their implications. The purpose of the last section is to assimilate the empirical information provided in the first two sections into a complete description of the salient flow properties.

Flow Visualization

In order to ascertain qualitative information regarding flow structure for the different models, schlieren photographs and pressure sensitive paint distributions were obtained. The schlieren photographs were taken for each of the nine models at the second test location, while pressure sensitive paint distributions were acquired for each

model at all three test locations. These visualizations combined with the quantitative boundary layer information provide a more complete picture of the flow field characteristics.

Schlieren Images

Schlieren photographs were taken using the system described in chapter IV. An illustration of the setup is given in Figure 7. Because the dominant gradients in the boundary layer regardless of pressure gradient strength were in the transverse direction, a horizontal knife edge was used. The knife edge was adjusted in the transverse direction such that the greatest amount of contrast was supplied allowing a more complete visualization of the salient flow features.

Smooth wall schlieren images for the zero, weak, and strong favorable pressure gradients are given in Figure 21. The dark crisscrossing lines were nozzle characteristic waves. The dark band at the bottom of the image, and the light band at the top of the image represent the floor and ceiling boundary layers respectively. The shades were different because the density gradients were in opposite directions. It was seen that an increase in the pressure gradient strength produced a corresponding acceleration in the growth rate of the boundary layer thickness. For the weak and strong pressure gradient models, characteristic expansion waves were visible.

Schlieren images for the models with square surface roughness are shown in Figure 22. The nozzle characteristic waves were still visible. The floor and ceiling boundary layers were also visible however were slightly thicker. Boundary layer distortion was also observed as weak characteristic waves that originated on the surface

began to permeate the boundary layer and extend into the freestream. For the zero pressure gradient model these waves ran parallel with one another, but the waves for the weak and strong pressure gradient models separated from one another in a pattern similar to expansion waves. As would be expected, this effect is more pronounced for the strong pressure gradient model. The waves were strong enough that they extend into the ceiling boundary layer and were reflected back into the freestream, creating a cross-hatch pattern.

The schlieren images in Figure 23 are for the models with diamond. Large density gradients, that appear to have been shocks, were seen emanating off the leading edge of the roughness elements. The nozzle characteristic waves were no longer visible as the waves generated by the roughness elements were so much more significant. The ceiling boundary layer was still clearly visible; however, the floor boundary layer was no longer clearly defined. Instead the boundary layer edge can be crudely estimated as the location where the Mach lines lose their curvature, and thus the wall normal density gradient was no longer dominant. As for the square roughness models, shock reflection off the ceiling was still visible. Additionally the shock waves for the models with curvature spread out in an expansion fan pattern. In the freestream, the light and dark regions denoting positive and negative density gradients respectively appear to have equal thickness amongst the shocks, however in the boundary layer, the regions of negative density gradients become larger relative to the positive density gradients.

Surface Pressure

The schlieren system produces an image which was an integration of the density gradients across the lateral span. Variations in the lateral span will not be detected by the schlieren images, and thus it was uncertain if the flow field properties, specifically at the surface, were three dimensional. To determine the variation of thermodynamic properties at the surface, pressure distributions of the floor were generated using PSP. Variations in surface temperature and paint thickness led to a large uncertainty for each of the different test cases. Nevertheless, the salient thermodynamic trends were apparent.

Surface pressure distributions for the zero, weak, and strong pressure gradient models of all surface conditions are shown in Figure 24, 25, and 26 respectively. It should be noted that the small lines visible in the smooth wall images of Figure 25 c) and Figure 26 b) were abrasions that were created by vibrations of the stagnation Pitot probe on the surface of the Plexiglas during Pitot measurements.

For models with identical surface conditions, the pressure distributions in the first test locations were similar, regardless of the surface curvature. There was no change in the global trends of surface pressure trend lines in either the lateral or axial direction, and thus the initial thermodynamic conditions regardless of pressure gradient strength were constant. In the second test location, the zero pressure gradient models' trends haven't changed, however a small decrease in surface pressure was observed in the axial direction for the weak pressure gradient models. This effect was amplified for the strong pressure gradient models, where clear locations of high and low pressure were visible. At the third test location, the zero and weak pressure gradient models were still not

showing any change. The weak pressure gradient, due to the fact that it was located at the inflection point of the streamline curvature shows little axial pressure variation. The strong pressure gradient models in the third location appeared to be under an adverse pressure gradient.

The surface pressure distributions for the smooth wall models were uniform in both the lateral and axial direction regardless of the test location, the square roughness models given uniform high pressure regions on roughness elements upper surface, with a sharp favorable pressure gradient at the interface between the surface edge and the adjacent channel. The low pressure region within the channel was fairly uniform. Lateral thermodynamic properties thus depended on whether the location was at the element surface or within the channels of the elements. In the second and third test locations the pressure distributions appear to become more uniform and two dimensional, as the magnitude of the pressure difference between the roughness element surface and channel was reduced. The pressure gradient strength seems to magnify this effect.

The models with diamond roughness reveal strong pressure gradients which were not restricted to the interface between the roughness edge and the channels. There was a broad triangular shaped pressure increase located at the leading edge of each diamond roughness element consistent with a lateral oblique shock. This oblique shock produced a high pressure region that surrounded the outer leading edge of the roughness element. On the surface of the leading edge there was a sharp triangular shaped wake located immediately behind the oblique shock. Both the oblique shock and the wake terminated about a third of the way down the element. A low pressure triangular shaped region

orientated in the opposite direction of the oblique shock was then encountered. This region spans the middle third of the roughness element, with the region of minimum pressure located at its center. This region was followed by a high pressure region that was formed by the adjacent roughness elements located at the trailing edge in a staggered formation as described in chapter V. In the channel between the trailing tip of the element and the leading edge of the following element there was another low pressure region that was located in the expansion region of the adjacent elements. The high and low pressure regions of the individual elements would overlap with adjacent elements producing pressure gradients that exhibited large axial variation, but minimal lateral variation. Exemptions were the leading and trailing edge tips. At the leading edge the sharp wake region of the oblique shock produced a small pressure valley in the lateral direction within a large high pressure region. At the trailing edge, oblique shocks from the upstream adjacent elements would converge, creating a high pressure point within a lateral band of low pressure. Like the square roughness models, the magnitude of the difference in surface pressure at the high and low pressure regions seems to be reduced the farther downstream the measurement location. Pressure gradient strength appears to magnify this effect.

Mean Flow Measurements

This section presents surface pressure profiles, stagnation Pitot pressure profiles, velocity distributions and profiles, and velocity gradient distributions and profiles for each of the nine models at all three measurement locations. When appropriate, duplicate information from different test conditions has been grouped together for comparison.

Surface Pressure Profiles

Profiles of the surface pressure were extracted from the surface pressure distributions and are given for the zero, weak, and strong pressure gradient models respectively. The difference between the trend lines for the different surface conditions was within the measurement error. The smooth wall profiles did not exhibit any large fluctuations, however, the diamond and square roughness elements show a large amount of fluctuation that spans the individual elements. The profiles of the square roughness confirm the observations from the pressure distributions that peak pressure was nearly constant on the surface of the element and drops rapidly within the channels. The gradients exhibited by the square roughness elements were far larger than those generated by the streamline curvature. It also was clearly visible that the amplitude of the fluctuations decreased with increased axial location downstream and increased favorable pressure gradient strength.

Profiles were extracted from the roughness element centerline The dual cycles observed in the pressure distributions were more distinct in the surface pressure profiles. The first cycle located at the leading edge of the roughness element exhibited a sort of square wave behavior where there was a rapid increase in pressure followed by a broad, nearly constant peak, and finally concluding with a rapid decrease towards its minimum. The second cycle on the other hand appeared as more of a sine wave. The peak for the second cycle was about 10% greater than the first, but the valley region was nearly the same; however, the first cycle had a period that was 20 – 30% greater than the second.

Stagnation Pressure Profiles

Stagnation pressure profiles were created using data collected from the traversing Pitot probe described in chapter IV. The Pitot pressure was normalized by the inflow stagnation pressure, while the traverse distance was normalized by the reference boundary layer height δ_{ref} which was 1.0 cm or the smooth wall boundary layer thickness at the first test location. For the zero pressure gradient models a single profile was taken at each test location. For the weak and strong pressure gradient models a single profile was taken at the first test location, while five profiles were taken at the other two test locations. The location where these profiles were taken is presented test section coordinates in Table 3.

Figure 30 displays the zero pressure gradient profiles. The profiles for each surface condition show little variation with a change of test location. The only difference of note was a slight increase in the boundary layer thickness as the test location progresses. The profiles for the smooth wall were fuller than those with square roughness. Both the square roughness and smooth wall profiles show a nearly linear variation from the wall to the boundary layer edge, with a constant value in the freestream. The surface value of p_{0_2}/p_{0_1} was 0.08 for the smooth wall model and 0.06 for the square roughness model while in the freestream was 0.37 and 0.38 for the smooth wall and square roughness models respectively. The profiles for the diamond roughness contain a zigzag pattern throughout the boundary layer and into the freestream due to the probe traversing across the shocks generated by the surface roughness. The amplitude of

the fluctuations remained constant regardless of profile location, while the period became elongated the deeper into the boundary layer the measurements were taken. The boundary layer for the diamond roughness was less full than the smooth wall model, but fuller than for the square roughness model. The surface value of p_{0_2}/p_{0_1} was 0.07 while the average freestream value was 0.37.

Normal shock relations were used to compute the freestream Mach number. For the diamond roughness model, the average freestream value of p_{0_2}/p_{0_1} was used.

$$\frac{p_{0_2}}{p_{0_1}} = \left[\frac{(\gamma+1)M_1^2}{(\gamma-1)M_1^2+2}\right]^{\frac{\gamma}{\gamma-1}} \left[\frac{\gamma+1}{2\gamma M_1^2-(\gamma-1)}\right]^{\frac{1}{\gamma-1}} \tag{6.1}$$

Once the Mach number was known, the static pressure was computed from isentropic relations. For boundary layers without pressure gradients the stagnation temperature and the static pressure were nearly constant. The Mach number was then computed using the Raleigh Pitot Formula.

$$\frac{p_{o_2}}{p_1} = \left[\frac{(\gamma+1)M_1^2}{2}\right]^{\frac{\gamma}{\gamma-1}} \left[\frac{\gamma+1}{2\gamma M_1^2-(\gamma-1)}\right]^{\frac{1}{\gamma-1}} \tag{6.2}$$

Mach number profiles are given in Figure 31. Again the smooth wall models have fuller profiles than the square roughness models. The fluctuations observed in the Pitot pressure profiles for the diamond roughness were still present but the magnitude of the amplitude has been reduced due to the Mach numbers exponential dependence upon the measured stagnation pressure. Again, the Mach number profiles for the diamond roughness were less full than those for the smooth wall, but fuller than those for the

square roughness model. The Mach number at the wall was 1.2 for the smooth wall, 0.8 for the square roughness model, and 0.9 for the diamond roughness model. The measured freestream Mach number for all surface conditions was 2.9.

The weak and strong pressure gradient model profiles are given in Figure 32 thorugh 37. There were consistent trends that exist regardless of the surface roughness. For both the weak and strong pressure gradient models, the profile at the first test location matched the trends from the first test location of the zero pressure gradient models, confirming that the inflow boundary layer thermodynamic properties were consistent. For the weak pressure gradient models the boundary layer growth was rapid. In both the second and third test locations, the profiles steadily became less full the further down the measurement location. Profile variation within the boundary layer was negligible. Strong pressure gradient models contained an expansion region at the second test location, and a recompression region at the third test location. Significant boundary layer growth was seen from the first to the second test location, but appears to decrease slightly from the second to the third test location. As like the weak pressure gradient models, in the second test location the profiles became steadily less full as successive profiles were taken further downstream. This profile variation however extended into the boundary layer. In contrast to the weak pressure gradient models at the third test location, the strong pressure gradient model profiles became fuller due to the recompression region. Again, the profile variation between successive profiles was most pronounced in the freestream.

There were profile differences due to changes in surface conditions that were observed. The profiles for the square and diamond roughness show that successive profile variation was reduced at each of the individual test locations relative to the smooth wall profiles. This was especially true within the boundary layer. With the exception of the strong pressure gradient model in the recompression region, the smooth wall models exhibited a sharp spike in the stagnation pressure in the near wall region. This characteristic was not present in any of the profiles with either diamond or square surface roughness. In fact, the profiles for the recompression region showed a slow increase in the stagnation pressure for both the square and diamond roughness models, consistent with the onset of boundary layer separation. This effect was more noticeable for the square roughness model.

The profiles for the diamond roughness exhibit the characteristic zigzag pattern present in the zero pressure gradient models was present for most of the profiles. Like the zero pressure gradient models, the magnitude of the fluctuations decreased the further downstream the profiles were extracted. Increasing the pressure gradient strength accelerated the loss of the fluctuations, and in fact the fluctuations completely disappeared in the recompression region of the strong pressure gradient model.

Mean Velocity Measurements

Fields of the mean velocity measured using the PIV techniques discussed in chapter IV. Contour plots were produced using the PIV data for both $\overline{u}$ and $\overline{v}$ velocity components for each of the nine models and each of the three test locations. The velocity components were normalized by the reference velocity ($1/U_{ref}$) which was the freestream

velocity of the smooth wall zero pressure gradient model at the first test location. For the present study this value was measured to be 625 m/s. The coordinates of the field plots were in the tunnel coordinate system described in chapter V, and the length scales were normalized by the reference boundary layer thickness δ_{ref}, described above. From these fields, velocity profiles were extracted. All profiles were extracted normal to the surface of the wall. For the diamond roughness models, it was observed that there were regions of high and low shear stress at the surface, which would change the characteristics of the profile depending upon where it was extracted. Two profiles were thus extracted for all diamond roughness models: one at the location of a shear stress peak, and one at the location of a shear stress valley.

Velocity profiles were also created for the zero pressure gradient models using the stagnation Pitot measurements that were taken for each of the three different surface roughness conditions at all three of the test locations. The mean velocity was found from the adiabatic relations for temperature.

$$\overline{u} = M\sqrt{\gamma R\left[T_0 - \frac{(\gamma-1)}{2}M^2\right]} \tag{6.3}$$

Van Driest II scaling was used so that comparisons to incompressible flowfields would be possible.

$$\overline{u}_{eff} = \frac{\overline{u}_e}{a^2}\sin^{-1}\left(a\frac{\overline{u}}{\overline{u}_e}\right); \quad a = \sqrt{\frac{(\gamma-1)}{2}M^2\frac{T_e}{T_w}} \tag{6.4}$$

For the near zero pressure gradient models inner variable scaling in the form of the law of the wall was used to plot the mean velocity.

$$\bar{u}_{eff}^{+} = \begin{cases} y^{+}, & y^{+} < 10 \\ \dfrac{1}{\kappa}\ln\left(y^{+}\right) + B + \dfrac{2\Pi}{\kappa}\sin^{2}\left(\dfrac{\pi}{2}\dfrac{y}{\delta}\right), & y^{+} \geq 10 \end{cases} \tag{6.5}$$

Where $B \approx 5.0$, $\kappa = 0.41$, where from White[11] the parameter Π was estimated as $0.8(\beta + 0.5)^{3/4} \approx 0.48$. The defect law is given by

$$\frac{\bar{u}_{eff} - \bar{u}_{e,eff}}{u^{*}} = -\frac{1}{\kappa}\ln\left(\frac{y}{\delta}\right) + \frac{2\Pi}{\kappa}\left[1 - \sin^{2}\left(\frac{\pi}{2}\frac{y}{\delta}\right)\right] \tag{6.6}$$

The pressure gradient in the near wall region was not measured accurately enough to obtain a reasonable law of the wall plot for the favorable pressure gradient models, and thus outer variable scaling was used for those models.

Contours of the $\bar{u}$ and $\bar{v}$ velocity components for the zero pressure gradient models at each test location have been plotted in Figure 38 through Figure 40, while velocity profiles, law of the wall plots, and defect law plots using both PIV and Pitot measurements are given in Figure 41 through 46. All line plots contain a plot of with incompressible theory for comparison purposes.

From the contour plots for the smooth wall and square roughness models, the only difference observed in subsequent test locations was the increase in the boundary layer thickness. There was a negligible $\bar{v}$ component for both of these models. The diamond roughness contour plots on the other hand exhibited a wavy pattern in the $\bar{u}$ component, throughout the boundary layer and into the freestream, due to gradients from the shocks generated off the roughness elements. The contour plots of $\bar{v}$ contain bands of negative and positive velocity where the flow alternates between alternating compression and expansion regions on the surface due to the surface geometry. The

bands were thicker in the near wall region that they were in the freestream, with the biggest magnitude occurring at $y/\delta = 0.25$. The values varied between $\pm 3\%$ of the freestream velocity. The only apparent differences between contour plots at successive test locations was the boundary layer growth, also noted for the smooth wall and square roughness models, and a slight decrease in the intensity of the velocity fluctuations that were similarly noted for the Pitot data.

The smooth wall velocity profiles, law of the wall plots, and defect law plots extracted from PIV and those generated from stagnation Pitot data showed strong agreement with theory. Both the square roughness and diamond roughness profiles were less full than the smooth wall profiles. The diamond roughness profiles assumed an intermediate location between the square roughness and smooth wall values. For the velocity profiles extracted from the diamond roughness model, the profile shape was independent of extraction location.

Square roughness led to a downward shift in the law of the wall plots for both PIV and Pitot data. Law of the wall plots extracted at the stress peaks and valley from the PIV data varied between square roughness and smooth wall conditions respectively, indicating the mean flowfield undergoes a rapid change from smooth wall to fully rough test conditions. For the Pitot profiles however, the diamond roughness models all assumed an intermediate profile. The probe volume and roughness element size was on the same order, causing the probe to average the profiles over the roughness element. Periodic fluctuations were observed throughout the profiles including in the logarithmic region of the boundary layer.

From the defect law plots, it was seen that the Pitot data essentially collapsed onto the incompressible theory, regardless of the surface condition or the location the profile was taken. From the PIV data, the smooth wall and square roughness profiles show good agreement with incompressible theory but the diamond roughness did not. Plots extracted from a stress peak region exhibited an upward shift characteristic of a favorable pressure gradient while the profiles extracted from a location of lower wall stress exhibit a downward shift characteristic of an adverse pressure gradient.

Weak pressure gradient contour plots of the $\overline{u}$ and $\overline{v}$ for all surface conditions are presented in Figure 47, Figure 48, and Figure 49. The trends in the first location for all surface conditions closely match those from the zero pressure gradient models, and thus will not be discussed. A small component negative $\overline{v}$ component existed in the second test location and third test location for the smooth wall and square roughness models due to the mean flow velocity vector being turned as the flow crossed expansion waves. The $\overline{v}$ component had a larger magnitude in the smooth wall model than the square roughness contour plots. The $\overline{u}$ velocity component at the second and third test locations for the diamond roughness model continued to exhibit periodic fluctuations in the streamlines, although the farther downstream the amplitude was reduced while the period was elongated. The diamond roughness $\overline{v}$ velocity component still exhibits periodic changes, however it remained largely negative due the globally imposed curvature driven favorable pressure gradient.

The weak pressure gradient model velocity profiles are shown in Figure 50. Again, the profiles in the first location closely match those from the zero pressure

gradient models, confirming that the inlet mechanical properties were the same regardless of pressure gradient strength. Smooth wall profiles at the second location showed a fuller profile. This effect was even more pronounced in the third location, which had more curvature. The rough wall models however, had profiles that steadily became less full with increasing favorable pressure gradient strength.

Contour plots for the strong pressure gradient models are given in Figure 51, Figure 52, and Figure 53. As with the weak pressure gradient models, the mean velocity contours from the first test location exhibited trends similar to the zero pressure gradient models. A significant negative $\bar{v}$ velocity component exists in the second test location for the smooth wall and square roughness model. The $\bar{u}$ velocity component at the for the diamond roughness model continued to exhibit periodic fluctuations in the streamlines which like the weak pressure gradient model decreased in amplitude and increased in period compared to the inlet conditions. The diamond roughness $\bar{v}$ velocity component still exhibits periodic changes, but the values remained negative. In the recompression region the $\bar{v}$ component transitioned back to zero for all models including the diamond roughness model. The compression shock was visible in the upper portion of the contour plots. For the diamond roughness model in the third region, the velocity fluctuations had completely disappeared.

In Figure 54 velocity profiles for the strong pressure gradient models are shown. The inlet velocity profiles continue to show trends consistent with the zero and weak pressure gradient inlet conditions. At the second test location, the smooth wall profile was much fuller profile than at the inlet location, while the square and diamond

roughness profiles continued to follow the incompressible profile. In the third region all profiles regardless of surface conditions were less full than incompressible theory. At $y/\delta = 0.1$ the smooth wall profiles were while 13% less full than flat plate theory, while the diamond and square roughness models were 34% and 56% less full than flat plate theory respectively.

Velocity Gradient Measurements

Velocity gradient contours were produced using PIV data as discussed in chapter IV. Streamwise and transverse gradients of the $\bar{u}$ and $\bar{v}$ velocity components were created using a second order explicit forward differencing scheme. From the gradients, mean strain rate and the vorticity were calculated. Contour plots of the primary velocity gradient, $d\bar{u}/dy$, and the extra strain rates $d\bar{u}/dx$, $d\bar{v}/dx$, and $d\bar{v}/dy$ were produced for each of the nine models at all three test locations along with field plots of the mean vorticity and mean strain rate. The values were normalized by the reference length scale δ_{ref} and the reference velocity U_{ref}. From these contours, velocity gradient profiles were extracted.

The contour plots for the zero pressure gradient models are shown in Figure 55 through Figure 62. As with the mean velocity fields, the velocity gradient fields were consistent regardless of test location. The primary velocity gradient was the dominant gradient regardless of the surface roughness. For the smooth wall model, the extra strain rates components were negligible. This was true for the square roughness model as well, except within the bottom 20% of the boundary layer, where there were square shaped regions of alternating positive and negative gradients. The gradients were still not as

strong as the primary gradient. The diamond roughness patterns had triangular shaped extra strain rates that alternated between negative and positive, and corresponded to the triangular shaped regions of negative and positive $\bar{v}$ velocity components. The triangular shaped regions of changing gradients was observed even in the primary gradient, however the gradient never became negative, but rather fluctuated between regions of higher and lower positive gradients. The primary gradient and the $d\bar{v}/dx$ secondary gradient contained regions of positive and negative gradients which were in phase with each other, while the other secondary gradients $d\bar{u}/dx$ and $d\bar{v}/dy$ were in phase with each other and $180°$ out of phase with the other two gradients.

The ZPG velocity gradient profiles for all 3 test locations are given in Figure 63 through 65. Again it was seen that the primary gradient was dominant regardless of the surface conditions, and the square and smooth wall models had negligible components of the secondary gradients. The profiles for the diamond roughness extracted and a stress peak and a stress valley exhibited periodic fluctuations about its mean for all gradients. The fluctuations were $180°$ out of phase with each other and were about equal in magnitude regardless of the gradient. The maximum value of any of the secondary gradients was $0.2 \cdot (U_{ref}/\delta)$.

Contour plots for the weak pressure gradient models are shown in Figure 66 through Figure 74. The trends for the velocity gradient field at the first test location were consistent with the zero pressure gradient models and thus will not be discussed further. The primary velocity gradient remained the dominant gradient regardless of the surface roughness or test location. For both the second and third test locations of the smooth

wall and square roughness models, the extra strain rates remained negligible with the exception of the bottom 20% of the boundary layer for the square roughness model, where the regions of alternating positive and negative gradients remained. In the second and third test locations the triangular patterns formed by the extra strain rates were still present, however, the triangles have been elongated, and were thinner at the base. The diamond roughness contours also exhibited a larger change in the gradients relative to the zero pressure gradient case was observed in the primary gradient contours.

The weak pressure gradient model velocity gradient profiles for all 3 test locations are given in Figure 75 through Figure 77. The primary gradient continued to dominate. A slight positive tilt was observed for the $\bar{v}$ component gradients in both the second and third test locations. The inflection point of the primary gradient at the second test location was located at $y/\delta = 0.2$, while at the third test location it was at $y/\delta = 0.1$, due to the fuller velocity profile. The out of phase diamond roughness profiles were seen for the gradient fields. The diamond roughness extra strain rates experienced a small increase with the new maximum value equal to $0.25 \times \left(U_{ref}/\delta\right)$.

Contour plots for the strong pressure gradient models are shown in Figure 78 through Figure 86. As with the weak pressure gradient models, the trends at the first location were consistent with the zero pressure gradient models and thus will not be discussed further. The primary velocity gradient was still the dominant gradient, but the extra strain rates $d\bar{v}/dx$ and $d\bar{v}/dy$ for the diamond roughness models became much more significant. In the second test location of the smooth wall and square roughness models, the extra strain rates were small in the upper 90% of the boundary layer. Within

the bottom 10% large positive gradients of the $\bar{u}$ component and negative gradients of the $\bar{v}$ component were observed. The square roughness models no longer contain the alternating positive and negative patterns observed for the zero and weak pressure gradient models. The triangular patterns were present in all gradient plots, with the triangles containing the long slender profiles observed for the weak pressure gradient models. As with the smooth wall and square roughness models, the bottom 10% contained large positive and negative gradients for the $\bar{u}$ and $\bar{v}$ components respectively. In the third test location, or the recompression region, strong velocity gradients exist at the location of the recompression shock. Beneath the shock, the extra strain rates again approach zero, while the extra strain rate becomes much larger. This was true for the diamond roughness model as well, with the characteristic alternating gradients disappearing. The square roughness model, once again had a resumption of the alternating square pattern in the bottom 10% of the boundary layer for the $d\bar{u}/dx$ secondary gradient, while a similar pattern was observed for the diamond roughness model for the same gradient.

The SPG model velocity gradient profiles for the first, second, and third test locations are given in Figures 87, 88 and 89 respectively. At the second test location, the primary gradient continued to dominate, but a 50% increase of the $d\bar{v}/dx$ gradient and a 100% increase $d\bar{v}/dy$ gradient was observed for the diamond roughness model. With the upper portion of the boundary layer: the $d\bar{v}/dx$ extra strain rate was negligible in the second test location and positive in the third test location, the $d\bar{v}/dy$ extra strain rate

was positive in the second test location and negative in the third, while the $d\bar{u}/dx$ gradient was nearly zero in both test locations. The characteristic fluctuations typically observed in the velocity gradient profiles have disappeared in the third test location. The primary gradient becomes much larger in the third test location, and extends higher into the boundary layer, with the inflection point moving up to $y/\delta = 0.35$, from a value of $y/\delta = 0.2$ at the second test location.

Turbulent Measurements

All turbulent flow quantities in this section were acquired using PIV. The first and second order turbulent statistics are presented in the first two subsections. The third section presents turbulent stress production along with all of its components. Finally in the fourth section, individual instantaneous velocity fields are used to create length scale spectra using auto and cross correlations of the instantaneous velocity fluctuations. A detailed description of each of the turbulent quantities is presented in each section along with an explanation for differences when appropriate.

Turbulence Intensities

The turbulence intensities were measured using PIV. The velocity fluctuations were found from by subtracting the instantaneous velocity fields from the mean velocity field measurements using the techniques described in chapter IV. Fields plots of *u* and *v* turbulence intensities were generated for each of the nine models at all three test locations. The square root of the turbulence intensities were taken, and were then normalized by the reference velocity ($\sqrt{}/U_{ref}$). From these fields, turbulence intensity

profiles were extracted. All profiles were extracted normal to the surface of the wall. The profiles were normalized with the magnitude of the local velocity vector $\overline{V}$.

The contour plots for the zero pressure gradient turbulence intensity fields at test locations 1, 2, and 3 are shown in Figure 90, Figure 91, and Figure 92 respectively. Regardless of the surface roughness, the axial turbulence intensity, $\sqrt{\overline{u'^2}}$, has a value that was 100% greater than $\sqrt{\overline{v'^2}}$. The characteristic fluctuations noted for the diamond roughness were still present in the turbulence intensity contour plots. The turbulence intensity values fluctuate between the smooth wall and rough wall values depending on its proximity to the stress peak.

The ZPG model turbulence intensity profiles for all 3 test locations are given in Figure 93. The profile variation for diamond roughness diamond roughness models exhibited little profile fluctuation and the profiles were nearly identical regardless of extraction location. From Table 4 through Table 14 it was seen that in the near wall region ($y/\delta < 0.2$) the turbulence intensities for the square roughness models were 100% greater than the smooth wall values, while the diamond roughness turbulence intensities were 40 - 60% greater. Outside of the near wall region, the profiles converged to a turbulence intensity of less than 1% in the freestream.

The contour plots for the WPG turbulence intensity fields at test locations 1, 2, and 3 are shown in Figure 94, Figure 95, and Figure 96 respectively while the profiles are shown in Figure 97, and discrete values are given in Table 15 through Table 26. Like the mean flow quantities, turbulent measurements at the first location closely resemble

those of the zero pressure gradient models. Axial turbulence intensity values continued to be double the transverse turbulence intensities. Throughout the boundary layer a slight reduction of the smooth wall turbulence intensities was noted at the second test location with the reduction being magnified at the third location. This trend remained with the rough wall models, however, near the wall ($y/\delta < 0.1$) there was a slight but noticeable increase.

From the tables at $y/\delta = 0.2$ the turbulence intensities experienced a 20% reduction at the second test location and a 30% reduction at the third location relative to the zero pressure gradient models. From the profiles the values up to the point $y/\delta = 0.2$ appear to closely match those of the smooth wall, however this point was near the location of the inflection point for most of the models, and at the inflection point the dramatic increases in turbulence intensity were observed very near the wall.

The turbulence intensity contour plots for the strong pressure gradient models are shown in Figure 98 through Figure 100 with the profiles given in Figure 101, and discrete values in Table 27 through Table 36. As with the weak pressure gradient models, turbulent measurements taken at the first location were very near to the zero pressure gradient models and thus require no further discussion. The axial turbulence intensity values remained double the transverse turbulence intensities. At the second test location at $y/\delta = 0.2$, a 40% reduction of the turbulence intensities was observed for all models. In the near region of the smooth wall models there was a narrow band of high turbulence intensity, but this is believed to be experimenter error resulting from oil accumulation on the window near the wall. In the third location, a 30, 40, and 110%

increase was observed for the smooth wall, diamond, and square roughness models respectively. There was an upward shift of the inflection point to $y/\delta = 0.35$.

Turbulent Stress

The turbulent stress was measured using PIV. The velocity fluctuations were found from by subtracting the instantaneous velocity fields from the mean velocity field measurements using the techniques described in chapter IV. Fields plots of the turbulent stress were generated for each of the nine models at all three test locations. The values were normalized by the square of the reference velocity ($1/U_{ref}^2$). From these fields, turbulence intensity profiles were extracted. All profiles were extracted normal to the surface of the wall.

Turbulent shear stress contour plots for the zero pressure gradient models are shown in Figure 102 through Figure 104. The distinctive finger shaped contours were clearly visible diamond roughness model. At successive downstream test locations, the peaks became elongated, with steeper angles. In Figure 105 turbulence stress profiles are shown, and in Table 4 through Table 14 display shear stress values at discrete locations. Like the turbulence intensities, the profile variation for diamond roughness models exhibited little profile fluctuation, however, the profile shape was more heavily dependent on extraction location. It was seen that in the near wall region ($y/\delta < 0.2$). At $y/\delta = 0.2$ the turbulent stress for the square roughness models was 270% greater than the smooth wall values, while the diamond roughness peak and valley turbulent stress values were only 25% and 50% greater respectively. In Figure 106 through Figure 108 the turbulent stress contour plots for the weak pressure gradient models are shown.

While the turbulent stress values for the smooth wall models appeared to decease in both the second and third test locations, in the near wall region the roughness models had a significant turbulent stress increase in the near wall region. For the diamond roughness model, at the stress peak locations along the wall, small circular shaped stress concentrations were visible in the bottom 20% boundary layer. The stress peaks became elongated, but the angles did not change significantly.

In Figure 105 through Figure 109 turbulence stress profiles are shown, and Table 4 through Table 36 display shear stress values at discrete locations. Inspection of the turbulent stress profiles confirms that the smooth wall profiles experienced a reduction of turbulent stress, especially in the near wall region, while the roughness models produced an increase. At $y/\delta = 0.2$ there was a 30% decrease of the smooth wall turbulent stress values at the second test location, and a 40% decrease at the third test location, relative to the zero pressure gradient model. The square roughness experienced a 10% decrease at both the second and third test locations, while the diamond roughness models experienced a 30% increase at both test locations. From the contour plots and the profiles the major increases in turbulent stress occur in the bottom 10% of the boundary layer.

In Figure 110 through Figure 112 the turbulent stress contour plots for the strong pressure gradient models are shown with the profiles shown in Figure 113. Inspection of the plots reveals a clear reduction of turbulent stress for the all models in the expansion region, followed by a dramatic rise in turbulent stress in the recompression region. The exception seemed to be in the bottom 10% of the boundary layer where there was a band

of increased turbulence stress. The distinct finger shaped stress regions were present in the diamond roughness model expansion region, with the stress values at the wall in the stress valleys nearly zero. But within the recompression region these peaks and valleys have completely disappeared. From Table 4 through Table 36 at $y/\delta = 0.2$ there was a 70% decrease of the smooth wall turbulent stress and a 50% decrease for the rough wall models at the second test location. Conversely there was a 100%, 240% and 420% increase in the turbulent stress for the smooth wall, diamond roughness, and square roughness models respectively relative to the zero pressure gradient models.

Turbulent Production

The turbulent stress production was measured using PIV. The turbulent production required both the mean flow gradients and the turbulent stress measurements, and the techniques for obtaining these measurements are described in chapter IV. It was assumed that all lateral velocities, and lateral velocity gradients were negligible. This assumption was confirmed by the uniformity of the nozzle exit profiles measured in different lateral directions in Figure 15, and pressure distributions created using pressure sensitive paint. Lateral variation on surface pressure was negligible even for the diamond roughness patterns, implying that the disturbance structure coming from the roughness elements merged into a uniform wave. From this assumption only 3 of the 9 production terms remained; the axial turbulent stress production term P_{xx}, the transverse turbulent stress production term P_{yy}, and the turbulent shear stress production term P_{xy}. With the assumption of negligible lateral velocity and lateral velocity gradients, each production term contained 4 components. Contour plots of the turbulent stress production and its

components were generated for each of the nine models at all three test locations and were presented in Figure 114 through 129 for the zero pressure gradient models, Figure 136 through 153 for the weak pressure gradient models, and Figure 160 thorugh 177 for the strong pressure gradient models. The values were normalized by the reference length scale divided by the cube of the reference velocity (δ_{ref}/U_{ref}^3). From these fields, turbulent stress production profiles were extracted, and the profiles are given in Figure 114 through 129 for the zero pressure gradient models Figure 154 through 159 for the weak pressure gradient models and figure 178 through 183 for the strong pressure gradient models. Tables 27 through 36 contain turbulent stress production at discrete locations for all models.

The zero pressure gradient contour plots exhibit little difference between the three test locations. The differences that have been noted were the increases in boundary layer thickness that were seen from the velocity and turbulent fields, and a slight increase in all production terms in the smooth wall model in the downstream test location. The first test location production fields for the weak and strong pressure gradient models were also similar to the first test location zero pressure gradient models.

For the smooth wall models the dominant production terms were the axial production term P_{xx} and the turbulent shear stress production term P_{xy}. The transverse turbulent stress term P_{yy} was an order of magnitude lower than the other two. This was primarily due the axial stress production's dependence on $\tau_{xy}\, d\overline{u}/dy$ and turbulent shear stress production term's dependence on the on $\tau_{yy}\, d\overline{u}/dy$, which were the only terms comprised of the primary velocity gradient. In a likewise fashion, the dominant

production terms for the square roughness model were P_{xx} and P_{xy}. The exception occurs in the bottom 15% of the boundary layer where the large velocity gradients due to the surface roughness in the extra strain rates resulted in increased production from the other production terms. The distinctive square alternating patterns were present, and this led to alternating regions of creation and destruction of turbulent stress. Most production occurred in the bottom 20% of the boundary layer, which corresponded with the inflection point seen in the turbulence stress profiles.

The decrease of $d\overline{u}/dy$ and $d\overline{v}/dx$, along with an increase in $d\overline{u}/dx$ and $d\overline{v}/dy$ led to an increase in the turbulent stress production components when a favorable pressure gradient was imposed. This was visible in the smooth wall weak pressure gradient models at the second and third location and the effect was amplified for the strong pressure gradient model at the second test location. This increase in turn led to a decrease in all production terms and thus a reduction in turbulence stress throughout the boundary layer. In the weak pressure gradient model at the second and third test location there was a 70% and 80% reduction of P_{xx} and P_{xy} respectively at $y/\delta = 0.2$, while the production term P_{yy} remained negligible. For the smooth wall strong pressure gradient model at test location 2, the reduction of P_{xx} was 100% while the reduction of P_{xy} was 90%.

The reduction of the P_{xx} and P_{xy} production terms was not as significant for the square roughness. For the WPG model, the reduction of P_{xx} was 30% at the second test location and 40% at the third, while the P_{xy} production term was reduced by 10% at the

second test location, and 30% at the third. The SPG model experienced a 90% reduction in P_{xx} and a 50% reduction in P_{xy}.

The analysis for production field for the diamond roughness model needed to be different. The oblique alternating velocity gradients, noted in previous sections, created production fields that would have simultaneous production and destruction of turbulence. Production components that contained the primary gradient remained dominant in the production terms, but the addition of extra strain rates that were no longer negligible meant that terms that contained these gradients could no longer be ignored. This also meant the transverse turbulent stress production term P_{yy} was no longer insignificant. Each component of the axial and transverse turbulent stress production terms were at a minimum or maximum at the same location. The turbulent shear stress production terms were at a maximum where the axial and transverse were minimum, and vice-versa. Normalization by the mean helped to eliminate profile fluctuations visible in the contour plots, but the velocity gradient dependence meant this wasn't totally eliminated. Changes in the oblique shock angle due to Mach number changes in the near wall region for the different models meant that directed comparison was largely impossible.

The combined global gradients produced by surface curvature and the local gradients produced by the diamond surface roughness produced turbulence production fields that varied greatly from location to location. In the expansion region of the strong pressure gradient model, the axial and transverse stress production terms were positive in some locations, while the turbulent shear stress production term was negative in some

places. This was not the case for any other model with a smooth wall or square surface roughness. These regions correspond with regions of reduces turbulence.

In the recompression region of the strong pressure gradient, regardless of the surface conditions, the increase in turbulence production was present. This was primarily due to the strength of the primary gradient which was huge, while the extra strain rates became inconsequential. Thus the P_{yy} term became negligible again for the diamond roughness model. The only patterns from square and diamond roughness models from the contour plots that could be distinguished from the smooth wall model was the alternating pattern present in the bottom 20% of the boundary layer. The smooth wall model experienced a 230% increase in P_{xx} and a 30% increase in P_{xy}. The square roughness on the other hand had an astounding 10 fold increase in P_{xx} and a 12 fold increase in P_{xy}. The diamond models were more difficult to determine because of their profile fluctuations, the increase seemed be about the middle ground of the square and smooth wall models with about a 500% increase in both P_{xx} and P_{xy}.

Length Scale Correlations

Length scale spectra was computed using auto and cross-correlations of the fluctuating velocity quantities generated from the *u* and *v* velocity fluctuations from the PIV data. Contour plots of the auto and cross-correlations were produced at each measurement location for all nine models. The *u'* and *v'* auto correlation maps were normalized by the local turbulent stress, while the cross-correlations were normalized by $-\sqrt{\overline{u'^2}}\sqrt{\overline{v'^2}}$. The two-dimensional correlation maps were taken at 4 discrete locations:

$y/\delta = 0.2$, $y/\delta = 0.5$, $y/\delta = 0.7$, and $y/\delta = 0.9$. For the diamond roughness models, only the diamond peak profiles were used.

The shape of the correlation map at the top was of a two dimensional osculating parabola. The curvature at the vertex was determined by the smallest eddies, and thus was a measure of the smallest eddies. The location where the parabola intercepts the *x*- or *y*- axis was then the measure of the smaller or Taylor micro scales. The length of the microscales was thus found from the following equation:

$$\frac{1}{\lambda_R} = -\frac{1}{2}\frac{d^2R}{dy^2} \tag{6.7}$$

If the area of half the curve is integrated,

$$\Lambda_R = \int_0^\infty R(x)dx \tag{6.8}$$

which obtains the integral length scale Λ_R. This was an approximate measure of the largest length scales within the boundary layer.

Correlation maps for the first test location are shown in Figure 184 through Figure 192. The R_{uu} and R_{vv} auto correlation maps for the zero pressure gradient models produced sharp peaks. These peaks were circular in shape, and were similar in shape for both the R_{uu} and R_{vv} indicating the scales were isotropic. The R_{uv} cross-correlation maps however produced peaks that were always less than one. These peaks tended to be broad and flat, thus leading to a smaller second order gradient and in turn a larger estimated microscale. In the lower portion of the correlation peaks, the R_{uu} correlation peaks had elongated regions in the axial direction with a relatively narrow base in the transverse direction. The R_{vv} correlation peaks on the other hand tended to be circular in shape. The

axial base was nearly the same shape as the R_{uu} base in the axial direction. Which was in line with the bursting process observed by Kim and Kline where elongated horseshoe shaped vorticies hold their correlation over a longer region in the axial direction, in the near wall region. These overall trends held regardless of the surface roughness.

An additional characteristic the diamond roughness correlation maps had were waves within the correlation maps. The waves were located in regions where there normally was no correlation, including the freestream. The waves were smaller if the correlation was taken at a location near the wall. The waves were relatively mild for the R_{uu} correlation map compared to the R_{vv} and R_{uv} correlation maps.

The plots of the Taylor microscales at the first test location are shown in Figure 193. From the R_{uu} and R_{vv} autocorrelation plots, the microscales were 0.5 mm, in the near wall region and 0.6 mm in the outer portion of the boundary layer. This remained true, regardless of the surface roughness. The axial microscales were a constant 0.8 mm based on the R_{vv} correlations. From the R_{uu} autocorrelations the axial microscales were 1.1 mm in the lower potion of the boundary layer. At $y/\delta = 0.7$ the values increased to 1.2 mm, and decreased back to 1.1 mm at $y/\delta = 0.9$. The axial microscales based on cross-correlations ranged between 2.0 to 2.5 mm, and the transverse microscales were between 1.0 and 2.0 mm. The microscales showed no dependence on surface roughness.

Plots of the integral length scales at the first test location are shown in Figure 194. The transverse integral length scale plots produced from the R_{uu} and R_{vv} autocorrelation plots were identical. The values were 1.1 mm through out the boundary layer. There was no surfaces roughness dependence. The axial integral length scales in

the bottom half of the boundary layer mm based on the R_{vv} correlations were the same, regardless of the surface roughness. In the upper half of the boundary layer at $y/\delta = 0.7$ and $y/\delta = 0.9$ the smooth wall and square roughness decreased to 1.3 and 1.1 mm respectively. Conversely the diamond roughness model values remained at 1.5 mm at $y/\delta = 0.7$, and increased to 2.0 mm at $y/\delta = 0.9$. From the R_{uu} autocorrelations the axial integral length scales steadily increased from between 2.5 and 5.0 mm at $y/\delta = 0.2$ to between 3.5 and 8.0 mm at $y/\delta = 0.9$. In the lower portion of the boundary layer the square roughness models were in general smaller than the smooth wall and diamond roughness models. The ZPG diamond roughness model was believed to show smaller integral length scales, because the interrogation region didn't extend far enough in the axial direction to capture the entire autocorrelation region. The axial and transverse integral length scales based on cross-correlations were much smaller. They were relatively isotropic, and were between 0.5 and 1.0 mm at all location with little dependence on surface roughness.

The correlation maps for the second and third test locations for all models are shown in Figure 195 through Figure 202 and Figure 205 through Figure 213 respectively. The WPG model at the second and third test locations did not exhibit any noticeable variation from the ZPG models. The same was true for the SPG models regardless of the roughness condition. Favorable pressure gradients had little effect on the overall shape of the correlation maps. In the recompression region, again the correlation maps were largely the same, except for the smooth wall models. There was

some distortion in the correlation maps extracted from the upper portion of the boundary layer due to the recompression shock.

Plots of the microscales in Figure 203 indicate that the trends from the ZPG models remain consistent. There was virtually no variation between the axial or transverse microscale plots for either the autocorrelation plots or the auto correlation plots at the second test location. Trends for the integral length scales from Figure 204 were also similar. The only differences noted were the axial length scales based on the R_{vv} autocorrelations did not show an increase in the outer portion of the boundary layer like they did in the first location, but instead followed the square roughness and smooth wall pattern. Additionally the axial length scales based on the R_{uu} autocorrelations show that the WPG models had larger length scales that the ZPG models, while the SPG models had smaller length scales. As the length scales were obtained further from the wall, this effect was more pronounced. Surface roughness did not appear to play a role in the integral length scale.

In the third test location the recompression region from the SPG model did not alter either the microscales or the integral length scales as the trends were consistent with the first and second test locations.

CHAPTER VII

CONCLUSIONS

Flow Field Description

Chapter VI presented a comprehensive and detailed analysis of each measurement technique. The influence of roughness and curvature driven favorable pressure gradients has been extensively covered. The results will not be repeated here. Instead, the purpose of this section is to assimilate that information into an overview description of the influence of surface roughness on the boundary layer flow. This section starts by examining the effects of the surface roughness on the overall structure of the boundary layer. This analysis was then used to explain the observations noted in the previous sections. The section has been broken down in to three subsections: *Surface Roughness*, *Streamline Driven Pressure Gradients* and *Combined Effects*.

Surface Roughness

Flow visualizations from the schlieren images and the PSP pressure distributions immediately illustrated the importance of surface roughness topology. Three-dimensional oblique shocks were generated off the tip of the diamond surface roughness elements while the only very weak Mach lines were visible from the square roughness elements. This was counter to the initial hypothesis that square roughness elements would create strong detached bow shocks while the diamond roughness would have relatively weaker attached oblique shocks. It was believed that the reason the bow shocks never materialized for the square roughness models was that the spacing was

insufficient between the elements. Instead the concave grooves before the roughness elements end up being filled with small recirculation vorticies. These vorticies created disturbances within the flow field, but those disturbances were much milder than would be created if the supersonic flow field directly encountered the roughness element step and formed a shock. If the spacing between elements was increased, the vorticies would have a more difficult time sustaining themselves, and the faster supersonic flow would become entrained into the roughness element cavities, thus producing the expected bow shocks off the elements. This would explain in the pressure distributions why there was an increase in surface pressure within the channels, suggesting a flow deceleration. The overall flowfield never encounters the sharp leading edge of the square roughness elements.

The diamond roughness elements on the other hand have channels which were not aligned normal to the freestream. Within the channels, there were no visible surface pressure increases implying the flow was not significantly being decelerated. The vorticies were allowed to proceed down the channels unimpeded, and thus the vorticies were unable to keep the incoming supersonic flow from interacting with roughness surface. A three-dimensional oblique shock was generated off of the surface, and the flow behind this shock will be slowed. Because the diamond roughness elements were arranged in a staggered formation the flowfield will quickly encounter the trailing edge of the diamond elements. This acts as an expansion region, which will then accelerate the flow back to its original velocity. This explains the four bands of alternating high and low surface pressure that span a single roughness element. Because the elements were

arranged so closely, there ends up being little lateral variation (with the exception occurring at the leading edge tips of the roughness elements), and thus the assumption of a two-dimensional flowfield remains valid.

As would be expected, the oblique shocks become a source of locally generated velocity gradients. The distinctive zigzag pattern in the mean velocity and stagnation Pitot profiles suggest that these gradients were quite strong. The velocity gradient profiles and contour plots confirm this. There was a small decrease in the magnitude of the fluctuations for both the Pitot profiles and the velocity profiles at successive downstream test locations. The reason for this was that as the boundary layer grows, the subsonic portion of the boundary layer becomes thicker. As the flow around the elements begins to decelerate, the angle of the shock will increase. Additionally blockage area seen by the incoming supersonic flow will be reduced, thus reducing the strength of the shocks.

The square roughness models have faint shocks, but the disturbances were much smaller and thus the effects were limited to the very near wall region of the boundary layer (i.e. $y/\delta < 0.15$). It has been repeatedly shown in supersonic flowfields, that flow decelerations have destabilizing effects on turbulence while flow accelerations have a stabilizing effect. The schlieren images thus explain why the square roughness elements lead to increases in the turbulence levels. They act as a series of very weak oblique shocks which lead to a steady loss of momentum and the implied turbulence destabilization. The turbulence intensity and turbulent stress profiles illustrated this point

because greatest increases in the turbulence stress were in the near wall region, where the gradients were strongest.

The diamond roughness elements on the other hand have a series of alternating gradients that lead to rapid acceleration and deceleration. The deceleration was more significant than what was experienced by the square roughness elements, but because the flow was subsequently accelerated, the turbulence levels were reduced back to their original levels as can be seen in the turbulence intensities and turbulent stress contours. The general lack of waves in the turbulent stress profiles suggests that the increase and reduction in turbulence was inversely proportional to the local mean velocity.

The production plots reinforced this explanation. The terms in each turbulent stress production term minimums and maximums at the same location. The production and destruction of turbulent stress was then magnified. Turbulence creation was thus very strong, while the destruction, though mild, was present. This was not the case for the square roughness or smooth wall models.

For the ZPG smooth wall models the turbulence intensities in the axial direction were double the transverse turbulence intensities. This was largely true for the ZPG square roughness model as well, and can be explained by the fact that there was negligible production of transverse turbulent stress due to the lack of pressure gradients, and thus the only source of transverse stress came from the pressure strain correlation, which redistributed the normal stresses. While the diamond roughness models contained large extra strain rates, they were still at least an order of magnitude smaller than the

primary gradient and thus produced changes that were within the margin of experimental error.

The length scale data appears to be inconclusive. The grid appears to have insufficient resolution do determine the Taylor microscales sufficiently. Smaller box sizes could be used, but the associated error from such a small box size would be prohibitively large. The transverse integral length scales appeared to be accurately measured, however, the interrogation region in the axial direction couldn't span the R_{uu} autocorrelation maps, and thus the integral length scales were under predicted. Additionally the length scale spectra produced by the cross-correlations didn't appear to be very accurate, and thus will not be discussed.

Nevertheless, certain observations about the flowfield can be made from the correlation maps. Regardless of the surface condition the R_{vv} autocorrelation maps tended to be axis-symmetric, implying all scales were the same size in all directions, or isotropic. By contrast the R_{uu} correlation maps were elongated in the axial direction, implying anisotropic turbulence. This has been explained by the 'bursting' process or the entire process which carries the flow from a relatively quiescent wall-model structure to a more random chaotic turbulent character, and for flat plate smooth wall boundary layer turbulence, it has been though that in the inner region the production of turbulence was mostly due to this process. In this process unsteady hairpin shaped eddies, dominate the lower region of the buffer region of the boundary layer ($y^+ > 40$). These eddies would hold the *u'* velocity correlations well downstream, but the *v'* correlations would rapidly disappear.

R_{uu} autocorrelations by Latin and Bowersox[6] indicated that that the disturbances generated by surface roughness would disrupt this process, and thus the roughness disturbances became the primary generation mechanism for turbulence. The elongation of the current correlation maps suggests the bursting process was still present, although it was impossible to determine how long the length scales were.

The present data was insufficient to clearly indicate the physical structure of the wave pattern present in the diamond roughness model correlation plots. A possible explanation may come from the intermittency within the boundary layer. The wavy pattern becomes larger the closer to the freestream the correlation map was taken. Large eddies passing through the interrogation region will often have freestream fluid passing through it its wake. Because the shocks were creating non-uniform velocity distributions, the velocity could be correlating to the low turbulence intensity fluid throughout the upper portion of the boundary layer and the freestream.

Overall, the Reynolds stresses for the smooth wall model was less than half those for the square roughness models. The diamond roughness values tended to alternate between both. The turbulence intensities for the square roughness were increased by over fifty percent over the smooth wall values. Detailed examination of the production indicated that the flow for the diamond case was responding to local deceleration and acceleration and the associated pressure gradients.

Streamline Driven Pressure Gradients

Curvature driven favorable pressure gradients had the expected stabilizing affect on turbulence values. The smooth wall models exhibited small reductions in the

turbulent quantities for the WPG models and significant reductions in the expansion region of the SPG model. From the production fields this was due to a reduction of the primary gradient and the extra strain rate $d\bar{v}/dx$, along with simultaneous increases in the extra strain rates $d\bar{u}/dx$ and $d\bar{v}/dy$, which led to reductions in all production components. Unlike the diamond surface roughness, it wasn't possible to have destruction of turbulence however because the curvature necessary to produce extra strain rates that were stronger in magnitude than the primary gradient would have led to flow separation. It can be seen from the surface pressure profiles that the pressure gradients generated from surface roughness were several orders of magnitude greater than those from wall curvature.

The Pitot profiles became steadily less full and with strong boundary layer growth with stronger favorable pressure gradients. The expansion was distributing the boundary layer momentum over a wider area. This led to a reduction in the energy available for turbulence production. Still, the boundary layer fluid remained attached,even for the SPG model expansion condition.

In the recompression region of the SPG model, there was a large increase in the turbulence properties was observed, characteristic of a flow deceleration. The stagnation pressure profiles became fuller, but the stagnation pressure gradient at the wall $dp_{0_2}/dy\big|_w$ decreased. Boundary layer fluid was being moved away from the wall, and the onset of separation appeared to be occurring.

Combined Effects

Surface roughness combined with streamline driven pressure gradients had significant affects on the turbulent structure in the near wall region. From the diamond SPG model in the diamond roughness the addition of the globally imposed favorable pressure gradient was enough to create regions of destruction of turbulent stress. This was visible in the turbulent shear stress contour plots were the regions of low, nearly laminar flow, extend almost to the wall.

It was also interesting to note that in both the square and diamond roughness for both the WPG and SPG models, in the bottom 10% of the boundary layer there appears a region of large shear stress. The diamond roughness model had circular shaped regions at the stress peaks, while the square roughness was a solid band of high shear stress. From the Pitot profiles, it appears the surface roughness and the favorable pressure gradients were both pushing fluid away from the wall, and making the near wall region much more unstable. This was especially true for the square roughness models. The concave inflection point in the bottom 5% of the boundary layer for the ZPG model became a convex inflection point with $dp_{0_2}/dy\big|_w$ quickly approaching zero. The progression towards separation continued into the recompression region.

The increased rate of boundary layer growth meant the fluctuations in the Pitot and velocity profiles shrank at an increased rate. In the strong pressure gradient model at the recompression region they had completely disappeared altogether. The velocity profiles indicate the velocity was less than a quarter of the freestream value, well below Mach one.

The turbulence values in the outer region were reduced by the surface curvature, but not by the same magnitude as the smooth wall values. The exception of course being the low turbulence regions in the diamond roughness models, already described above.

Within the stress valleys of the diamond roughness elements, the production of turbulent stress was reduced due to the influence of the velocity gradients, but it was never altogether eliminated. This was due to the strength of the primary gradient. When the diamond surface roughness was combined with a sufficiently strong pressure gradient, within the contours of turbulent stress production, in certain regions the production would be reduced to the point where there was a sign change in the turbulent stress production. This "negative" production, at the particular location would instead of being the conventional source term, instead became a sink term that would cause the destruction of turbulence stress.

As stated before, the correlation maps were extracted at the stress peak locations. For the diamond roughness SPG model in the expansion region, since the shocks were nearly normal to the wall, the correlations were all taken at areas of elevated shear stress. Regardless of this fact, from the R_{vv} autocorrelation maps, the waves have started appearing in the $y/\delta = 0.2$ location. The shear stress contours, with their large regions of low stress, suggest that the intermittency effect would extend well into the boundary layer. This reinforces the idea that it was boundary layer intermittency causing the wave patterns in the correlation maps.

Conclusions

The schlieren and PSP flow visualizations performed demonstrated that surface roughness topology makes important contributions to the entire boundary layer flowfield. These contributions have been found to extend into the freestream. Rapid changes in the kinematic turbulent quantities (e.g. turbulence intensities, kinematic Reynolds shear stresses, etc.) was possible. Because the overall turbulence levels from the square roughness models were reduced by switching to diamond roughness, in spite of the fact that the roughness elements had the same blockage area, indicates that it is possible to tailor the roughness in such a way that further reductions (or increases, depending on the application) are possible with proper roughness design.

From the schlieren photographs and the PSP surface pressure distributions, vorticies are believed to have developed within the channels of the roughness elements. It was the disturbances caused by these vorticies that are believed to be the major source of perturbation within the square roughness flow field. This would explain the nonlinear relationship with changes blockage area compared to changes kinematic turbulent variables observed in previous studies[6]. While these disturbances are small, they nevertheless rapidly add extra strain rates which increase the turbulence production.

Favorable pressure gradients had the expected stabilizing effect while adverse pressure gradients had the expected destabilizing effect. Pitot and velocity profile data indicate that combining the favorable pressure gradients leads to the acceleration of separation because they have the combined effect pushing boundary layer fluid away from the wall. If the favorable pressure gradients are combined with the correct wall

topology the “negative” production terms can be enhanced in certain regions. Targeted areas of low turbulent stress can then be created and enhanced. The reduced shear stress and turbulent heat flux into the wall would allow engineers to reduce weight needed for thermal protective shielding while simultaneously increasing performance by reducing drag.

While the pressure work terms were not directly measured, with the large local and global pressure gradients that exist within the flow due to wall topology and streamline curvature, this term will become quite significant. The alternating adverse and favorable pressure gradients produced by the diamond surface roughness suggests that this term will alternate between a source and sink term much like the turbulent stress production term does with the alternating gradients. It would thus be desirable to be able to make this term a sink term in order to reduce turbulence stress. While the mean flow pressure gradients have been measured, the mean Favre averaged fluctuating velocity is unknown. It however can be obtained by measuring the turbulent mass flux from equation (7.1).

$$\overline{u_i''} = -\frac{\overline{-\rho' u_i'}}{\bar{\rho}} \tag{7.1}$$

Recommendations

The database and improved understanding gathered from this research provided a detailed characterization of the combined influence of curvature driven pressure gradients and surface roughness on supersonic turbulent boundary layer flow. This study will be a valuable aid to researchers and engineers in the development of semi-empirical

relations and turbulence models. However, three areas of further research are recommended.

The first recommendation is for accurate measurement of the local wall shear stress over the rough surface. Non-intrusive measurement techniques such as shear sensitive paint would provide a highly resolved shear stress distribution of the models. They would also allow for accurate Law of the Wall and Defect Law plots that were unable to be generated due to the level of uncertainty in the near wall Reynolds stress measurements.

Hot-film measurements should be taken so that the pressure work term from the Reynolds Stress Transport Equation can be obtained. It is known that this term will have a significant effect on the transport of turbulence, but experimental quantification will illustrate how much. The only term that is required that hasn't yet been measured is the turbulent mass flux, which can be obtained by cross-film measurements. The hot-film measurements will also give a more precise measurement of the energy spectra. Finally a hot-film placed in the channel of the square and diamond roughness elements will indicate the amount of vorticity, and the size of the recirculation regions within the respective channels.

The second recommendation is to alter the topology of the square and diamond roughness models. The axial spacing of the elements should be increased so that the channel vorticies are not the sources of the disturbances. Ideally a model with removable rows of roughness elements could be employed to determine the adequate spacing. Once this spacing is determined using schlieren photography, PIV measurements should then

be taken and compared to the original measurements. Due to machining simplicity, a staggered formation of diamonds was used. Unfortunately the resulting flow was exceedingly complicated and many interacting mechanisms were in play, without the basic knowledge of how they worked on their own. The expansion region of the trailing edge is a good example. It is not known if after passing through a single row of diamonds, whether or not it reverts back to its normal mean and turbulent flow properties. An experiment which investigates this would prove useful. Additionally the standard two-dimensional PIV doesn't provide lateral velocity information on a flow that locally appears to be three-dimensional. Stereoscopic PIV on a single diamond roughness element, along with Stereoscopic PIV on a single row of elements would answer many of the fundamental questions about the diamond roughness flowfield.

Continuing with the previous theme, the surface roughness should be adjusted to see if it is possible to tailor the roughness elements such that a reduction relative to the smooth wall, or an increase relative to the square roughness model is possible. Possible design considerations would be to have a roughness element with a blunt leading edge followed by a sharp trailing edge, yet have the elements spaced closely together. The idea would be that the weak deceleration from the blunt edge would then be subsequently followed by a strong acceleration due to the expansion region. There would then hypothetically be a situation where the low momentum near wall boundary layer fluid could constantly be accelerated, resulting in an associated reduction in turbulence shear stress. Conversely if high turbulence levels were desired (e.g. to enhance turbulent mixing) an element with a sharp leading edge could be followed by a blunt trailing edge.

This would have the added advantage that the shocks generated off the leading edge would propagate the high turbulence levels high into the freestream, and thus heat transfer from the reactions could be minimized.

Stronger favorable pressure gradient models should be used to determine if and when separation occurs, and whether surface roughness accelerates that process.

Finally computational simulations should be performed to see if the diamond roughness flow characteristics can be reproduced. The ability to successfully perform accurate numerical simulations will save money and reduce the required experiment time. It would more than likely be necessary to use a LES or DNS simulation.

REFERENCES

[1] Air Force, *New World Vistas, Aircraft and Propulsion Technologies*, 1995.

[2] Air Force Office of Scientific Research, *Research Interests of The Air Force Office of Scientific Research And Broad Agency Announcement 2006-1*, AFOSR, Department Of The Air Force, Air Force Office of Scientific Research (AFRL), Arlington VA, June 1999.

[3] Luker, J., Hale, C., and Bowersox, R., "Experimental Characterization of the Turbulent Shear Stresses for Distorted Supersonic Boundary Layers," *Journal of Propulsion and Power,* Vol. 14, No. 1, 1998, pp. 110-118.

[4] Luker, J., Bowersox, R., and Buter, T., "Influence of a Curvature Driven Favorable Pressure Gradient on a Supersonic Turbulent Boundary Layer," *AIAA Journal*, Vol. 38, No. 38, Aug 2000, pp. 1351-1359.

[5] Smith, D., and Smits, A., "The Effects of Streamline Curvature and Pressure Gradient on the Behavior of Turbulent Boundary Layers in Supersonic Flow," AIAA Paper 94-2227, June 1994.

[6] Latin, R. and Bowersox, R., "Influence of Surface Roughness on Supersonic Boundary Layer Turbulent Flow Structure," Paper No. 99-7059, *14th International Symposium on Airbreathing Engines (XIV ISABE),* Florence, Italy, Sept. 5-10, 1999a.

[7] Latin, R. and Bowersox, R., "Flow Properties of a Supersonic Boundary Layer with Wall Roughness," *AIAA Journal,* Vol. 38, No. 10, 2000, pp. 1804-1821.

[8] Latin, R. and Bowersox, R., "Temporal Turbulent Flow Structure for Supersonic Rough-Wall Boundary Layers," *AIAA Journal,* Vol. 40, No. 5, 2002, pp. 832-841.

[9] Schlichting, H., *Boundary-Layer Theory*, Springer, New York, 2003.

[10] Schetz, J.A., *Boundary Layer Analysis*, Prentice Hall, Englewood Cliffs, NJ, 1993.

[11] White, F., *Viscous Fluid Flow*, McGraw-Hill Higher Education, New York, 2006.

[12] Sherman, F., *Viscous Flow,* McGraw-Hill, New York, 1991.

[13] Wilcox, D. C. *Turbulence Modeling for CFD*, DCW Industries, Inc., La Cãnada, CA 1994.

[14] Cebeci, Tuncer and Smith, A. M. O. *Analysis of Turbulent Boundary Layers*. Applied Mathematics and Mechanics, Academic Press, New York, 1974.

[15] Pope, S., *Turbulent Flows*, Cambridge University Press, Cambridge, MA, 2000.

[16] Morkovin, M. V., "Effects of Compressibility on Turbulent Flows," *The Mechanics of Turbulence*, AGARD, Gordon and Breach, New York, 1961, pp. 367-380.

[17] Van Driest, E. R., "Turbulent Boundary Layer in Compressible Fluids", *Journal of Aeronautical Sciences*, Vol. 18, 1956, pp. 145-160.

[18] Fernholtz, I., Finley, M., and Mikulla, V., "A Further Compilation of Compressible Turbulent Boundary Layer Data with a Survey of Turbulence Data," *AGARDograph 263* NATO, Technical Editing and Reproduction, London, Nov. 1981.

[19] Smits, A. J., Spina, E. F., Alving, A. E., Smith, R. W., Fernando, E. M., and Donovan, J. F. "A Comparison of the Turbulence Structure of Subsonic and Supersonic Boundary Layers," *Physics of Fluids*, A Vol. 1 No. 11, 1989, pp. 1865-1875.

[20] Spina, E. F., Smits, A. J., and Robinson, S., "Supersonic Turbulent Boundary Layers," *Annual Review of Fluid Mechanics*, Vol. 26, 1994, pp. 287-319.

[21] Dussauge, J. P., Smith, R., Smits, A., Fernholtz, H., Finley, P., and Spina, E., "Turbulent Boundary Layers in Subsonic and Supersonic Flow," AGARDograph 335, NATO, Canada Communication Group, Hull, QC, Canada, July 1996.

[22] Smits, A. and Dussuage, J-P., *Turbulent Shear Layers in Supersonic Flow*," American Institute of Physics, Woodbury New York, 1996.

[23] Corrsin, S., and Kistler, A., "Free-Stream Boundaries of Turbulent Flow," NACA Report 1244, 1955.

[24] Perry, A. E., Schofield, W. H., and Joubert, P. N., "Rough Wall Turbulent Boundary Layers," *Journal of Fluid Mechanics*, Vol. 37, 1969, pp. 383-413.

[25] Simpson, R., "A Generalized Correlation of Roughness Density Effects on the Turbulent Boundary Layer," *AIAA Journal*, Vol. 11, No. 2, 1973, pp. 242-244.

[26] Antonia, R. A., and Wood, D. H., "Calculation of Turbulent Boundary Layer Downstream of a small Step Change in Surface Roughness," Aeronautical Quarterly, Vol. 26, Aug. 1975, pp. 202-210.

[27] Nikuradse, J., "Stromungsgesetze in Rauhen Rohren," *Forschung Arb. Ingenieurwesen*, No. 361, 1933.

[28] Fan, H. and Bowersox, "Numerical Analysis of High-Speed Flow over Rough Surfaces," AIAA-99-2381, 35th AIAA/ASME/SAE/ASEE Joint Propulsion Conference, Los Angeles CA, June 1999.

[29] Grass, A. J., "Structural Features of Turbulent Flow over Smooth and Rough Boundaries," *Journal of Fluid Mechanics*, Vol. 50, 1971 pp. 233 -255.

[30] Goddard, F., "Effects of Uniformly Distributed Roughness on Turbulent Skin-Friction Drag at Supersonic Speeds," *Journal of Aero/Space Sciences*, Vol. 26, No. 1, 1959, pp. 1-24.

[31] Berg, D., "Surface Roughness Effect on a Mach 6 Turbulent Boundary Layer," *AIAA Journal,* Vol. 17, No. 9, 1979, pp. 929, 930.

[32] Liepmann, H., and Goddard, F., "Note on Mach Number Effect upon the Skin Friction of Rough Surfaces," *Journal of Aero/Space Sciences*, Vol. 23, No. 10, 1957, pp. 784.

[33] Pritchett, V. and Bowersox, "Flow Properties of Compressible and Incompressible Subsonic Turbulent Boundary Layers with Surface Roughness," 39th AIAA Aerospace Sciences Meeting, Reno NV, Jan 2001.

[34] Bradshaw, P., *The Effect of Streamline Curvature on Turbulent Flow*, AGARDograph 169, 1973.

[35] Clauser, F. H., "The Turbulent Boundary Layer," *Advanced Applied Mechanics*, Vol. 4, 1956. pp. 1-51.

[36] Coles, D., "The Law of the Wake in the Turbulent Boundary Layer," *Journal of Fluid Mechanics*, Vol. 1, 1956, pp. 191-226.

[37] Thomann, H., “The Effects of Axial Wall Curvature on Heat Transfer in Turbulent Boundary Layers to Short Regions of Concave Surface Curvature,” *Journal of Fluid Mechanics*, Vol. 33, July 1968, pp. 283-292.

[38] Bradshaw, P., “The Analogy Between Streamline Curvature and Buoyancy in Turbulent Shear Flow.” *Journal of Fluid Mechanics*, Vol. 36, 1969, pp. 177-191.

[39] Bradshaw, P., “The Effect of Mean Compression or Dilatation on the Turbulence Structure of Supersonic Boundary Layers,” *Journal of Fluid Mechanics*, Vol. 63, No. 3, 1974, pp. 449-464.

[40] Shrivaprasad, B. G., and Ramaprian, B. R., “Turbulence Measurements in Boundary Layers Along Mildly Curved Surfaces,” *Journal of Fluids Engineering*, Vol. 100, No. 1, 1978, pp. 37-46.

[41] Kim, J., and Simon, T. W., "Measurements of the Turbulent Transport of Heat and Momentum in Convexly Curved Boundary Layers: Effects of Curvature, Recovery and Free-Stream Turbulence," *Journal of Turbomachinery*, Vol. 110, No. 1, 1988, pp. 80-87.

[42] Hayakawa, K., Smits, A., and Bogdonoff, S., “Hot-Wire Investigation of an Unseparated Shock-Wave/Boundary Layer Interaction,” *AIAA Journal*, Vol. 22, 1984, pp. 579-585.

[43] Smith, D., and Smits, A., “The Rapid Expansion of a Turbulent Boundary Layer in a Supersonic Flow,” *Theoretical Computational Fluid Dynamics*, Vol. 2, 1991, pp. 319-328.

[44] Donovan, J., Spina, E., and Smits, A., "The Structure of Supersonic Turbulent Boundary Layers Subjected to Concave Surface Curvature," *Journal of Fluid Mechanics*, Vol. 259, Jan. 1993, pp. 1-24.

[45] Jayaram, M., Taylor, M., and Smits, A., "The Response of a Compressible Turbulent Boundary Layer to Short Regions of Concave Surface Curvature," *Journal of Fluid Mechanics*, Vol. 175, Feb. 1987, pp. 343-362.

[46] Dussauge, J. P., and Gaviglio, J., "The Rapid Expansion of a Supersonic Turbulent Flow – Role of Bulk Dilatation," *Journal of Fluid Mechanics*, Vol. 174, Jan. 1987, pp. 81-112.

[47] Arnette, S. A., Samimy, M. and Elliott, G. S., "The effects of Expansion Regions on the Turbulence Structure of Compressible Boundary Layers," AIAA Paper 96-0656, Jan. 1996.

[48] Bowersox, R., Wier, R., Glawe, D., and Gogineni, S., "Measurements of Turbulent Flow Structure in Supersonic Curved Wall Boundary Layers," *Journal of Propulsion and Power,* Vol. 16, No. 1, 2000, pp. 153-154.

[49] Bowersox, R., and Buter, T., "Mass-Weighted Turbulence Measurements in a Mach 2.9 Boundary Layer with Mild Adverse and Favorable Pressure Gradient," *AIAA Journal*, Vol. 34, No. 12, 1996, pp. 2470-2483.

[50] Smits, A. and Lim, T., *Flow Visualization Techniques and Examples*, Imperial College Press, London, 2000.

[51] TSI Inc., "Model 9306A Six-Jet Atomizer Instruction Manual," 1930099, Rev. B, Shoreview, MN, Feb. 2003.

[52] dPIV, 32-Bit PIV Analysis Code, Software Package, Ver. 2.1, Innovative Scientific Solutions Inc., Dayton, OH, 2005.

[53] Ekoto, I., Bowersox, R., Srinivasan, R., and Goss, L., "Examination of Cameras for Near-Wall PIV Measurements in High Speed Flows," AIAA-06-0044, 44th AIAA Conference, Reno NV, JAN 2006.

[54] Liu, T., and Sullivan, J. P., *Pressure and Temperature Sensitive Paints*, Springer-Verlag, Berlin Germany, 2005.

[55] Settles, G. S., *Schlieren and Shadowgraph Techniques: Visualizing Phenomena in Transparent Media*, Springer-Verlag, Berlin Germany, 2001.

[56] Bowersox, R., "Combined Laser Doppler Velocimetry and Cross-Wire Anemometry Analysis for Supersonic Turbulent Flow," *AIAA Journal*, Vol. 34, 1996, pp. 2269-2275.

[57] Latin, R., *The Influence of Surface Roughness on Supersonic High Reynolds Number Turbulent Boundary Layer Flow*, Dissertation, Air Force Institute of Technology, Wright-Patterson Air Force Base, OH, 1998.

[58] Stoer, J. and R. Burlirsch. *Introduciton to Numerical Analysis, Second Edition*. Springer-Verlag, Berlin Germany, 1993.

[59] Benedict, L. H., and Gould, R. D., "Towards Better Uncertainty Estimates for Turbulence Statistics," *Experiments in Fluids*, Vol. 22, 1996, pp. 129-136.

[60] Luker, J. "Experimental Investigation of a Supersonic Boundary Layer Including Favorable Pressure Gradient Effects." Master's Thesis, Air Force Institute of Technology, Wright-Patterson Air Force Base, OH, 1995.

APPENDIX A

UNCERTAINTY ANALYSIS

Within any experimental research their will be inherent uncertainty within any obtained measurements. The uncertainty analysis will determine a priori the amount of error within each measurement, and the propagation error that results from multiple measurements that are used to determine a particular value. Any values with prohibitively high error can be reduced by targeting the primary source of propagation error. This section will identify and document all measurement and propagation error that exists for all measured values. Based upon the analysis presented in Bowersox[56] and Latin[57] this study uses the Euclidean (L_2) norm as the measure of error. The L_2 norm is defined as[58]

$$\left\| x_i \right\|_2 = \left\| x_1, x_2, ..., x_n \right\|_2 = \left[\sum_{i=1}^{n} x_i^2 \right]^{1/2} \tag{A.1}$$

For a given set of measurements, x_i. The total dimensional error is defined as

$$E_f = \left\| E_{x_i} \right\|_2 = \left[\sum_{i=1}^{n} \left(\frac{\partial f}{\partial x_i} E_{x_i} \right)^2 \right]^{1/2} \tag{A.2}$$

Where f is a function dependent on x_i and E_x is the error associated over the various applicable measurements. The percent or nondimensional error is given by

$$\varepsilon_f = \frac{E_f}{f} \tag{A.3}$$

Which is the total error nondimensionalized by the mean value. The reduced data error bounds are estimated based on the linearized reduction equations and include the propagation of measurement errors.

Three separate measurement techniques were used to collect data for this study. They are Pressure Sensitive Paint (PSP), Pitot, and Particle Image Velocimetry. Typical stagnation freestream conditions are shown in Table 52 and 53 and were used in this analysis. Both the measurement and the propagation errors have been computed and tabulated as described below. It has been assumed that all errors are random and have a Gaussian distribution.

PIV Error Analysis

Particle Image Velocimetry is used to gather instantaneous velocity fields. There are two types of associated error with these measurements: experimental and experimenter error. The experimental error is inherent error within the measurement techniques. For PIV this includes correlation mapping error and the conversion error that results from converting the pixel spacing into a dimensional measurement. In both cases the error has been estimated at 1%.

Experimenter error is error that is associated with the experimental collection techniques. For the present set of experiments, these errors include insufficient seeding density, laser reflection off the wall, and oil accumulation on the windows. While these errors are undesirable, they are often unavoidable. It is not possible to quantify these errors, but in both cases the errors will be the greatest in the near wall region. These errors would produce irregular correlations that would have smaller correlation peaks,

and larger correlation radii. Removal of these errors instead relied on post-processor filtering of the correlation maps which was incorporated into the dPIV software. The drawback is that the number of valid vectors per run would be reduced from 5,000 to as low as 3,000 in certain locations. Thus to determine statistical uncertainty the lower estimate was used for the number of valid samples.

A confidence interval determines the level of certainty that the true mean lies within an error interval from the calculated statistic. For normal distributions a 2 standard deviation or a 95% confidence interval is typically. For a 95% confidence interval a given statistic should will have the following error bound: $\pm 1.96\sqrt{\mathrm{var}(\vec{x})}$. The mean and turbulent statistics were obtained as described in chapter IV. The variance and the calculated error for the associated turbulence statistics[59] from PIV are given in Table 54. From the PIV data the wall shear stress for the zero pressure gradient values was obtained. From the *x*-component of the Favre averaged momentum equation presented in equation (2.13), neglecting convection which will be negligible in the near wall region, and assuming that the viscous stresses will be negligible compared to the turbulent stresses, the momentum equation will have the following form:

$$\frac{\partial \tau_{xx}^{T}}{\partial x} + \frac{\partial \tau_{xy}^{T}}{\partial y} + \frac{\partial \tau_{xz}^{T}}{\partial z} = 0 \tag{A.4}$$

The changes in the stresses will be negligible in the axial and lateral directions, thus after integrating with respect to *y* gives the shear stress in the near wall region as a constant:

$$\tau_{xy}^{T} = C \tag{A.5}$$

Thus the value at which the turbulent stress profiles become constant is the shear stress value and from the previous analysis, within a 95% confidence interval, the near wall shear stress values were measured to within 12%.

For the gradients, the uncertainty in the measurement of the axial direction length scale is 1.5% and the uncertainty in the transverse direction is 3%. The uncertainty of the velocity scales is estimated to be 0.5%. Finally an estimate for the finite difference scheme must be made. From the forward difference scheme that was used, the largest error is the from the Taylor series approximation is the second order gradient.

$$\left.\frac{du}{dx}\right|_{x+\Delta x} = \frac{u(x+\Delta x) - u(x)}{\Delta x} + \frac{\Delta x}{2}\left.\frac{d^2u}{dx^2}\right|_{x+\Delta x} + HOT \qquad \text{(A.6)}$$

Large changes noted in the gradient fields generated by the surface roughness suggest that the second order gradient can be an order of magnitude larger than the first order gradients. From equation (A.6) and this assumption the associated percentage error is 1.1% in the axial direction and 0.6% in the transverse direction. Propagation errors for the PIV data are presented in Table 54. These include the uncertainty in the velocity gradient measurements, along with the turbulent stress production terms and its associated components.

Pitot Measurement Error Analysis

Pitot Pressure was measured using an Omega PX303 0 – 69 kPa absolute pressure transducer. The pressure transducer had an accuracy of 0.25% full scale (FS). The pressure transducer was capable of sampling at 3 kHz. To improve the accuracy, the Pitot measurements were sampled at 1 kHz. Each individual data point was then the

average of the 100 measured points. The variance was assumed to be the transducer error.

Determining boundary layer thickness is difficult because it has large errors associated with the geometry of the problem. Near the freestream, large changes in y have small corresponding changes in velocity. Because of measurement error at the freestream points, locating the boundary layer edge can be imprecise. The uncertainty of the boundary layer height from the Pitot probe measurements is due to errors in the velocity and probe position. The velocity uncertainty was determined graphically as in Luker[60] and found to be 20%. The probe position uncertainty was as large as 2.5% giving a boundary layer height uncertainty of 21%. Boundary layer height error estimates based on PIV were difficult to ascertain and were estimated to be at least as large as the Pitot measurement. Propagated error estimates for Van Driest parameters were calculated as in Luker[60] and are given in Table 56. The value for the wall shear stress was found using the method described in the previous section and has been estimated as 12% for both the rough and smooth wall estimates.

PSP Error Analysis

The pressure sensitive paint measures surface pressure distributions. With stable thermodynamic flow conditions it is possible to obtain measurements accurate up to 300 Pa or for the present case and accuracy of 1.5%. The temperature dependence of the paint and the fluctuations in both the stagnation pressure and temperature increases the measurement uncertainty. The errors for those values are listed in Table 52. The uncertainty for the wall pressure p_w is 10.7%.

Table 1: Computed freestream Mach number at each static pressure port location.

Pressure Gradient	Roughness	M1	M2	M3	M4	M5
Zero	Smooth	2.86	2.85	2.87	2.77	2.76
Zero	Square	2.86	2.82	2.83	2.71	2.72
Zero	Diamond	2.86	2.84	2.89	2.75	2.77
Weak Favorable	Smooth	2.86	2.84	2.86	2.88	3.06
Weak Favorable	Square	2.86	2.84	2.84	2.84	2.96
Weak Favorable	Diamond	2.86	2.84	2.87	2.87	3.02
Strong Favorable	Smooth	2.86	2.82	2.89	3.05	2.33
Strong Favorable	Square	2.86	2.84	2.87	3.05	2.44
Strong Favorable	Diamond	2.86	2.85	2.89	3.05	2.43

Table 2: Wall curvature location and estimated value of the pressure work influence parameter ζ.

	$L = x_3 - x_2$	ψ	$d_{\max}$	I_p	I_ϕ
None	N/A	0	0	0	0
Weak	39.0 cm	0.016	0.010	0.16	0.074
Strong	15.2 cm	0.15	0.062	0.40	0.18

Table 3: Test section coordinates of stagnation pressure profiles for wall curvature models.

	Test Location 2	Test Location 3
A	29.21 cm	40.64 cm
B	29.53 cm	40.96 cm
C	29.85 cm	41.28 cm
D	30.16 cm	41.59 cm
E	30.48 cm	41.91 cm

Table 4: ZPG smooth wall PIV kinematic values at test location 1.

$\frac{y}{\delta}$	$\frac{U_{eff}}{U_{eff,e}}$	$\frac{\sqrt{\overline{u'^2}}}{U}$	$\frac{\sqrt{\overline{v'^2}}}{U}$	$\frac{\overline{u'v'}}{U^2}$	$\frac{d\bar{u}}{dx}\cdot\frac{\delta}{U}$	$\frac{d\bar{u}}{dy}\cdot\frac{\delta}{U}$	$\frac{d\bar{v}}{dx}\cdot\frac{\delta}{U}$	$\frac{d\bar{v}}{dy}\cdot\frac{\delta}{U}$	$P_{xx}\cdot\frac{\delta}{U^3}$	$P_{yy}\cdot\frac{\delta}{U^3}$	$P_{xy}\cdot\frac{\delta}{U^3}$
1.25	1.01	0.0133	0.0037	-4.3E-06	-5.9E-05	6.8E-06	-1.2E-05	-1.6E-05	-2.1E-08	0.0E+00	0.0E+00
1.22	1.01	0.0132	0.0038	-5.1E-06	-6.5E-05	4.0E-05	-9.8E-06	-2.6E-06	-2.2E-08	0.0E+00	0.0E+00
1.19	1.01	0.0133	0.0039	-5.9E-06	-8.1E-05	1.6E-04	-1.3E-05	-7.6E-06	-3.0E-08	0.0E+00	0.0E+00
1.17	1.01	0.0132	0.0040	-5.1E-06	-7.3E-05	1.9E-04	-2.5E-06	-3.3E-05	-3.0E-08	0.0E+00	0.0E+00
1.14	1.01	0.0133	0.0041	-5.6E-06	-6.1E-05	2.3E-04	-6.8E-06	-4.3E-05	-2.4E-08	0.0E+00	0.0E+00
1.11	1.01	0.0135	0.0042	-7.2E-06	-6.3E-05	3.0E-04	-8.4E-06	-4.1E-05	-2.5E-08	0.0E+00	4.3E-09
1.08	1.01	0.0139	0.0044	-9.6E-06	-7.6E-05	4.0E-04	-3.7E-06	-3.3E-05	-3.3E-08	0.0E+00	1.0E-08
1.06	1.01	0.0144	0.0046	-1.2E-05	-7.6E-05	5.1E-04	-1.2E-06	-2.6E-05	-4.1E-08	0.0E+00	1.1E-08
1.03	1.00	0.0150	0.0049	-1.4E-05	-6.8E-05	6.6E-04	-9.4E-06	-2.7E-05	-5.0E-08	0.0E+00	1.1E-08
1.00	1.00	0.0154	0.0053	-1.8E-05	-6.1E-05	8.0E-04	-9.9E-07	-7.2E-06	-5.9E-08	0.0E+00	2.5E-08
0.97	1.00	0.0160	0.0056	-2.1E-05	-5.3E-05	9.5E-04	3.0E-06	2.0E-05	-6.8E-08	0.0E+00	3.2E-08
0.94	0.99	0.0168	0.0061	-2.5E-05	-3.6E-05	1.1E-03	1.1E-06	3.9E-05	-7.8E-08	0.0E+00	3.8E-08
0.92	0.99	0.0179	0.0069	-3.3E-05	-7.0E-06	1.2E-03	-2.1E-08	3.6E-05	-8.7E-08	0.0E+00	5.6E-08
0.89	0.98	0.0183	0.0074	-3.4E-05	-1.0E-05	1.4E-03	1.1E-05	4.7E-05	-9.7E-08	0.0E+00	7.4E-08
0.86	0.98	0.0179	0.0077	-3.5E-05	-2.6E-05	1.4E-03	1.1E-05	7.6E-05	-1.2E-07	8.0E-09	8.5E-08
0.83	0.97	0.0186	0.0082	-4.2E-05	-2.8E-05	1.6E-03	8.3E-06	9.6E-05	-1.5E-07	1.1E-08	1.1E-07
0.81	0.96	0.0203	0.0090	-5.4E-05	-2.4E-05	1.8E-03	1.3E-05	1.0E-04	-2.2E-07	1.1E-08	1.5E-07
0.78	0.96	0.0226	0.0098	-7.0E-05	-2.1E-05	2.1E-03	2.7E-05	9.3E-05	-3.2E-07	1.1E-08	2.1E-07
0.75	0.95	0.0250	0.0105	-9.0E-05	-3.6E-05	2.4E-03	3.4E-05	6.4E-05	-4.8E-07	1.2E-08	2.9E-07
0.72	0.94	0.0278	0.0112	-1.1E-04	-5.5E-05	2.5E-03	1.5E-05	4.0E-05	-6.7E-07	1.2E-08	3.3E-07
0.70	0.93	0.0300	0.0121	-1.4E-04	-4.8E-05	2.7E-03	1.1E-05	3.7E-05	-8.5E-07	1.1E-08	4.1E-07
0.67	0.92	0.0325	0.0131	-1.7E-04	-1.1E-05	2.9E-03	2.2E-06	7.1E-05	-1.0E-06	2.7E-08	4.9E-07
0.64	0.91	0.0353	0.0141	-2.0E-04	2.8E-05	3.1E-03	-5.5E-06	1.2E-04	-1.2E-06	5.3E-08	5.7E-07
0.61	0.90	0.0376	0.0149	-2.4E-04	1.9E-05	3.0E-03	1.1E-05	1.5E-04	-1.4E-06	6.3E-08	6.5E-07
0.59	0.89	0.0384	0.0153	-2.5E-04	4.3E-06	3.2E-03	-2.5E-06	4.8E-05	-1.6E-06	2.1E-08	7.3E-07
0.56	0.88	0.0403	0.0163	-2.8E-04	-4.4E-05	3.3E-03	9.9E-06	1.1E-04	-2.0E-06	5.0E-08	8.8E-07
0.53	0.87	0.0422	0.0179	-3.3E-04	-7.4E-05	3.5E-03	2.4E-06	1.6E-04	-2.6E-06	1.0E-07	1.1E-06
0.50	0.86	0.0441	0.0199	-4.0E-04	-5.0E-05	3.7E-03	-2.0E-05	1.4E-04	-3.1E-06	1.2E-07	1.4E-06
0.47	0.85	0.0464	0.0218	-4.7E-04	2.8E-05	4.0E-03	-3.3E-05	2.9E-05	-3.6E-06	5.5E-08	1.8E-06
0.45	0.83	0.0485	0.0221	-4.8E-04	1.5E-05	4.2E-03	2.0E-05	-1.9E-06	-4.0E-06	-1.9E-08	2.1E-06
0.42	0.82	0.0515	0.0226	-5.3E-04	7.5E-05	4.4E-03	1.5E-05	-6.5E-05	-4.3E-06	-7.6E-08	2.3E-06
0.39	0.81	0.0549	0.0243	-6.3E-04	7.9E-05	4.6E-03	-2.1E-05	-7.0E-05	-5.3E-06	-4.8E-08	2.6E-06
0.36	0.79	0.0584	0.0260	-7.4E-04	9.1E-05	4.7E-03	-4.4E-05	2.2E-05	-6.2E-06	9.9E-08	2.9E-06
0.34	0.78	0.0614	0.0263	-7.9E-04	1.4E-04	4.7E-03	-3.9E-05	1.6E-04	-6.4E-06	2.9E-07	2.9E-06
0.31	0.77	0.0615	0.0245	-6.7E-04	1.2E-04	5.0E-03	-5.6E-05	1.6E-04	-5.8E-06	2.6E-07	2.6E-06
0.28	0.76	0.0669	0.0273	-8.8E-04	1.8E-04	5.5E-03	-1.1E-04	8.7E-05	-8.0E-06	3.2E-07	3.4E-06
0.25	0.74	0.0718	0.0288	-9.9E-04	1.8E-04	5.7E-03	-7.1E-05	7.3E-05	-9.5E-06	2.7E-07	4.1E-06
0.23	0.73	0.0759	0.0295	-1.1E-03	2.0E-04	5.6E-03	-5.6E-05	1.1E-04	-9.7E-06	3.1E-07	4.3E-06
0.20	0.71	0.0799	0.0304	-1.1E-03	2.2E-04	4.9E-03	-6.8E-05	1.0E-04	-8.3E-06	3.4E-07	3.7E-06
0.17	0.70	0.0851	0.0329	-1.2E-03	1.3E-04	3.3E-03	-1.9E-05	-5.8E-05	-6.3E-06	-7.4E-08	3.4E-06
0.14	0.70	0.0918	0.0388	-1.5E-03	1.5E-04	4.1E-03	-9.1E-07	-9.0E-05	-9.6E-06	-2.9E-07	6.1E-06
0.11	0.69	0.1050	0.0425	-1.5E-03	2.1E-04	2.4E-02	1.7E-05	7.5E-06	-6.5E-05	-7.5E-10	4.5E-05

Table 5: ZPG square roughness PIV kinematic values at test location 1.

$\frac{y}{\delta}$	$\frac{U_{eff}}{U_{eff,e}}$	$\frac{\sqrt{\overline{u'^2}}}{U}$	$\frac{\sqrt{\overline{v'^2}}}{U}$	$\frac{\overline{u'v'}}{U^2}$	$\frac{d\bar{u}}{dx}\cdot\frac{\delta}{U}$	$\frac{d\bar{u}}{dy}\cdot\frac{\delta}{U}$	$\frac{d\bar{v}}{dx}\cdot\frac{\delta}{U}$	$\frac{d\bar{v}}{dy}\cdot\frac{\delta}{U}$	$P_{xx}\cdot\frac{\delta}{U^3}$	$P_{yy}\cdot\frac{\delta}{U^3}$	$P_{xy}\cdot\frac{\delta}{U^3}$
1.27	1.01	0.0034	0.0032	-9.9E-07	-1.2E-05	3.4E-05	-1.3E-05	-2.3E-05	0.0E+00	0.0E+00	0.0E+00
1.24	1.01	0.0036	0.0033	-1.0E-06	-1.0E-05	3.9E-05	-9.4E-06	-3.3E-05	0.0E+00	0.0E+00	0.0E+00
1.21	1.01	0.0037	0.0034	-1.1E-06	-1.4E-05	5.1E-05	-9.0E-06	-2.2E-05	0.0E+00	0.0E+00	0.0E+00
1.18	1.01	0.0041	0.0035	-1.8E-06	-3.7E-06	6.0E-05	-8.2E-06	-2.4E-05	0.0E+00	0.0E+00	0.0E+00
1.15	1.01	0.0046	0.0038	-2.0E-06	-8.2E-06	1.1E-04	-1.2E-05	-2.2E-05	0.0E+00	0.0E+00	0.0E+00
1.12	1.01	0.0052	0.0040	-2.9E-06	-4.0E-06	2.0E-04	-1.9E-05	-1.9E-05	0.0E+00	0.0E+00	0.0E+00
1.09	1.01	0.0065	0.0043	-4.9E-06	2.2E-07	3.4E-04	-1.8E-05	-2.9E-05	-2.8E-09	0.0E+00	3.2E-09
1.06	1.01	0.0089	0.0048	-8.1E-06	-4.5E-06	5.0E-04	-1.7E-06	-5.6E-05	-9.5E-09	-1.2E-09	1.2E-08
1.03	1.00	0.0117	0.0055	-1.5E-05	3.3E-05	6.3E-04	6.6E-06	-9.9E-05	-1.0E-08	-9.2E-09	2.0E-08
1.00	1.00	0.0132	0.0066	-2.1E-05	7.4E-05	8.0E-04	-4.0E-06	-6.7E-05	-1.1E-08	-9.2E-09	3.7E-08
0.97	1.00	0.0158	0.0069	-2.5E-05	-5.1E-06	1.3E-03	-2.0E-06	-6.7E-05	-7.3E-08	-9.7E-09	6.1E-08
0.94	0.99	0.0198	0.0077	-3.8E-05	-7.4E-05	1.7E-03	1.2E-05	-9.0E-05	-2.0E-07	-1.5E-08	1.1E-07
0.91	0.98	0.0239	0.0086	-5.6E-05	-1.0E-04	1.9E-03	2.0E-05	-1.0E-04	-3.3E-07	-2.0E-08	1.7E-07
0.88	0.97	0.0272	0.0093	-7.5E-05	-7.8E-05	2.1E-03	1.2E-05	-1.1E-04	-4.3E-07	-2.7E-08	2.1E-07
0.85	0.96	0.0298	0.0104	-9.6E-05	-2.0E-05	2.4E-03	1.9E-06	-2.0E-04	-5.1E-07	-4.6E-08	2.8E-07
0.82	0.95	0.0331	0.0135	-1.5E-04	-1.8E-05	2.8E-03	2.6E-05	-1.4E-04	-8.5E-07	-5.6E-08	5.6E-07
0.79	0.94	0.0366	0.0142	-1.7E-04	2.8E-05	3.0E-03	1.5E-05	-1.6E-04	-9.8E-07	-7.3E-08	6.6E-07
0.76	0.93	0.0398	0.0170	-2.5E-04	1.4E-05	3.1E-03	1.3E-05	-1.7E-04	-1.5E-06	-1.1E-07	9.6E-07
0.73	0.92	0.0421	0.0199	-3.2E-04	-4.2E-05	3.1E-03	1.7E-05	-6.6E-05	-2.2E-06	-5.8E-08	1.3E-06
0.70	0.91	0.0445	0.0216	-3.9E-04	-5.1E-05	3.3E-03	7.9E-06	8.6E-05	-2.8E-06	7.5E-08	1.6E-06
0.67	0.89	0.0491	0.0231	-4.7E-04	8.2E-05	3.7E-03	-4.2E-05	1.2E-04	-3.1E-06	1.7E-07	1.8E-06
0.64	0.88	0.0534	0.0253	-5.4E-04	-4.3E-05	3.7E-03	3.2E-06	1.6E-04	-4.2E-06	2.0E-07	2.3E-06
0.61	0.87	0.0565	0.0272	-6.2E-04	-8.8E-05	4.0E-03	-2.7E-05	9.4E-05	-5.6E-06	1.7E-07	2.9E-06
0.58	0.85	0.0608	0.0289	-7.2E-04	-2.1E-04	4.7E-03	-1.7E-05	-1.4E-05	-8.5E-06	-6.5E-09	4.1E-06
0.55	0.84	0.0675	0.0314	-8.7E-04	-2.8E-04	5.5E-03	-2.2E-05	-7.8E-05	-1.2E-05	-1.1E-07	5.7E-06
0.52	0.82	0.0753	0.0344	-1.1E-03	-3.0E-04	6.1E-03	-3.3E-05	-6.5E-05	-1.7E-05	-7.3E-08	7.4E-06
0.49	0.80	0.0818	0.0367	-1.3E-03	-3.3E-04	6.3E-03	-1.7E-05	-6.7E-06	-2.1E-05	3.4E-08	8.9E-06
0.46	0.78	0.0871	0.0392	-1.5E-03	-1.7E-04	6.5E-03	-6.5E-05	-6.1E-06	-2.2E-05	1.7E-07	9.7E-06
0.43	0.76	0.0956	0.0417	-1.8E-03	3.7E-05	6.9E-03	-1.4E-04	1.2E-04	-2.4E-05	9.0E-07	1.0E-05
0.40	0.74	0.1038	0.0442	-2.1E-03	4.7E-05	7.5E-03	-1.6E-04	3.3E-04	-3.0E-05	2.0E-06	1.2E-05
0.37	0.72	0.1117	0.0479	-2.4E-03	-1.3E-04	8.0E-03	-1.4E-04	3.8E-04	-4.3E-05	2.4E-06	1.6E-05
0.34	0.70	0.1196	0.0525	-2.9E-03	-2.8E-04	8.3E-03	-1.3E-04	3.1E-04	-5.5E-05	2.4E-06	2.1E-05
0.31	0.68	0.1280	0.0572	-3.3E-03	-2.5E-04	8.3E-03	-1.6E-04	2.5E-04	-6.3E-05	2.7E-06	2.5E-05
0.28	0.66	0.1367	0.0599	-3.7E-03	-9.6E-05	8.1E-03	-1.8E-04	2.8E-04	-6.4E-05	3.3E-06	2.5E-05
0.25	0.64	0.1453	0.0639	-4.0E-03	-2.6E-04	5.8E-03	-1.6E-04	2.6E-05	-5.7E-05	1.5E-06	2.1E-05
0.22	0.63	0.1551	0.0725	-4.3E-03	-1.6E-04	6.0E-03	-1.6E-05	2.2E-07	-5.9E-05	1.1E-07	3.2E-05
0.19	0.62	0.1725	0.0840	-4.5E-03	2.1E-04	9.2E-03	-1.9E-04	-1.3E-04	-6.8E-05	-5.3E-07	6.1E-05
0.16	0.59	0.1978	0.0959	-4.8E-03	8.6E-04	1.3E-02	-3.9E-04	-2.9E-04	-4.9E-05	-1.6E-06	9.8E-05
0.13	0.57	0.2289	0.1077	-5.4E-03	1.6E-03	1.3E-02	-4.3E-04	-7.6E-05	3.3E-05	3.9E-06	1.2E-04
0.10	0.54	0.2544	0.1193	-6.3E-03	2.3E-03	9.9E-03	-5.6E-04	8.8E-04	1.7E-04	3.2E-05	8.5E-05
0.07	0.53	0.2472	0.1173	-5.6E-03	1.9E-03	6.8E-03	-7.3E-04	1.4E-03	1.6E-04	4.6E-05	3.1E-05

Table 6: ZPG diamond roughness peak PIV kinematic values at test location 1.

$\frac{y}{\delta}$	$\frac{U_{eff}}{U_{eff,e}}$	$\frac{\sqrt{\overline{u'^2}}}{U}$	$\frac{\sqrt{\overline{v'^2}}}{U}$	$\frac{\overline{u'v'}}{U^2}$	$\frac{d\bar{u}}{dx}\cdot\frac{\delta}{U}$	$\frac{d\bar{u}}{dy}\cdot\frac{\delta}{U}$	$\frac{d\bar{v}}{dx}\cdot\frac{\delta}{U}$	$\frac{d\bar{v}}{dy}\cdot\frac{\delta}{U}$	$P_{xx}\cdot\frac{\delta}{U^3}$	$P_{yy}\cdot\frac{\delta}{U^3}$	$P_{xy}\cdot\frac{\delta}{U^3}$
1.27	1.01	0.0040	0.0080	1.6E-06	-2.4E-05	2.0E-04	2.2E-04	-3.0E-04	0.0E+00	-3.9E-08	1.5E-08
1.24	1.01	0.0039	0.0077	9.4E-07	-5.4E-06	1.5E-04	1.0E-04	-4.1E-05	0.0E+00	-6.7E-09	9.1E-09
1.21	1.01	0.0040	0.0078	2.9E-07	2.9E-05	8.1E-05	-5.6E-05	3.9E-04	0.0E+00	5.2E-08	7.4E-09
1.18	1.01	0.0041	0.0086	-2.0E-07	5.8E-05	4.5E-05	-2.3E-04	8.7E-04	0.0E+00	1.3E-07	1.0E-09
1.15	1.01	0.0040	0.0098	9.1E-07	6.4E-05	1.7E-05	-3.1E-04	1.1E-03	0.0E+00	2.2E-07	0.0E+00
1.12	1.01	0.0044	0.0112	5.0E-07	5.6E-05	3.5E-05	-2.9E-04	1.1E-03	0.0E+00	2.7E-07	2.6E-09
1.09	1.01	0.0051	0.0127	-1.8E-06	3.9E-05	1.2E-04	-1.8E-04	7.1E-04	0.0E+00	2.2E-07	1.7E-08
1.06	1.01	0.0057	0.0138	-5.4E-06	1.2E-05	2.9E-04	3.3E-05	1.4E-04	-2.7E-09	4.9E-08	5.9E-08
1.03	1.00	0.0065	0.0145	-1.4E-05	-4.4E-05	6.4E-04	2.8E-04	-5.8E-04	-2.1E-08	-2.5E-07	1.6E-07
1.00	1.00	0.0108	0.0150	-3.5E-05	-1.0E-04	1.1E-03	4.3E-04	-1.2E-03	-1.1E-07	-5.7E-07	3.5E-07
0.97	0.99	0.0146	0.0147	-5.8E-05	-1.4E-04	1.4E-03	4.4E-04	-1.4E-03	-2.4E-07	-6.7E-07	4.9E-07
0.94	0.99	0.0182	0.0139	-7.2E-05	-2.0E-04	1.7E-03	3.3E-04	-1.4E-03	-3.8E-07	-6.0E-07	5.5E-07
0.91	0.98	0.0214	0.0132	-7.7E-05	-2.0E-04	1.9E-03	1.3E-04	-1.1E-03	-4.6E-07	-4.3E-07	4.8E-07
0.88	0.97	0.0248	0.0129	-7.8E-05	-9.9E-05	2.0E-03	-1.2E-04	-7.7E-04	-4.3E-07	-2.4E-07	3.2E-07
0.85	0.96	0.0273	0.0131	-7.1E-05	-7.2E-05	1.8E-03	-3.7E-04	-4.0E-04	-3.7E-07	-8.0E-08	6.9E-08
0.82	0.95	0.0290	0.0142	-6.6E-05	-7.7E-05	1.7E-03	-6.4E-04	-1.4E-04	-3.5E-07	3.2E-08	-2.0E-07
0.79	0.95	0.0306	0.0150	-6.6E-05	-1.1E-04	1.6E-03	-8.8E-04	2.6E-05	-4.1E-07	1.4E-07	-4.7E-07
0.76	0.94	0.0328	0.0161	-8.5E-05	-1.0E-04	1.6E-03	-1.0E-03	8.8E-05	-4.8E-07	2.1E-07	-6.6E-07
0.73	0.94	0.0353	0.0176	-1.3E-04	-8.8E-05	1.6E-03	-9.5E-04	4.0E-05	-6.6E-07	2.0E-07	-6.2E-07
0.70	0.93	0.0372	0.0197	-1.8E-04	-1.8E-04	1.9E-03	-7.5E-04	-1.7E-04	-1.2E-06	4.9E-08	-2.0E-07
0.67	0.92	0.0392	0.0220	-2.6E-04	-2.9E-04	2.3E-03	-3.9E-04	-6.2E-04	-2.1E-06	-4.5E-07	8.2E-07
0.64	0.91	0.0415	0.0236	-3.7E-04	-4.7E-04	3.1E-03	3.3E-05	-1.0E-03	-4.0E-06	-1.2E-06	2.4E-06
0.61	0.90	0.0453	0.0257	-5.0E-04	-6.1E-04	3.8E-03	4.1E-04	-1.4E-03	-6.5E-06	-2.3E-06	4.5E-06
0.58	0.88	0.0493	0.0277	-6.2E-04	-6.9E-04	4.4E-03	6.6E-04	-1.5E-03	-8.9E-06	-3.2E-06	6.4E-06
0.55	0.87	0.0534	0.0294	-7.1E-04	-7.2E-04	4.8E-03	7.4E-04	-1.5E-03	-1.1E-05	-3.7E-06	7.8E-06
0.52	0.85	0.0584	0.0307	-8.0E-04	-6.7E-04	4.9E-03	6.0E-04	-1.3E-03	-1.2E-05	-3.4E-06	8.3E-06
0.48	0.83	0.0617	0.0319	-7.6E-04	-4.3E-04	5.0E-03	3.2E-04	-7.5E-04	-1.1E-05	-2.0E-06	7.2E-06
0.45	0.82	0.0648	0.0331	-8.3E-04	-2.6E-04	4.9E-03	2.0E-05	-1.7E-04	-1.0E-05	-4.0E-07	5.8E-06
0.42	0.80	0.0687	0.0346	-8.5E-04	-9.1E-05	4.9E-03	-2.2E-04	3.3E-04	-9.1E-06	1.2E-06	4.6E-06
0.39	0.79	0.0740	0.0360	-8.3E-04	5.0E-05	5.1E-03	-4.4E-04	6.7E-04	-7.9E-06	2.5E-06	3.5E-06
0.36	0.77	0.0808	0.0380	-8.4E-04	1.6E-04	5.5E-03	-6.4E-04	8.6E-04	-7.1E-06	3.5E-06	2.9E-06
0.33	0.76	0.0871	0.0398	-9.2E-04	2.3E-04	5.7E-03	-7.4E-04	1.1E-03	-6.9E-06	4.8E-06	2.2E-06
0.30	0.74	0.0966	0.0436	-9.7E-04	3.7E-04	5.6E-03	-8.8E-04	1.5E-03	-3.8E-06	7.3E-06	5.2E-07
0.27	0.73	0.1100	0.0470	-1.0E-03	7.9E-04	1.0E-02	-1.0E-03	1.7E-03	-4.1E-07	9.8E-06	8.3E-06
0.24	0.69	0.1755	0.0548	-1.2E-03	3.5E-03	2.0E-02	-1.1E-03	1.6E-03	3.0E-04	1.2E-05	1.8E-05
0.21	0.63	0.2975	0.0629	-1.9E-03	7.2E-03	3.1E-02	-1.0E-03	1.2E-03	1.3E-03	1.3E-05	1.5E-05
0.18	0.56	0.4507	0.0676	-3.6E-03	9.8E-03	3.9E-02	-7.8E-04	9.0E-04	3.6E-03	1.3E-05	-2.1E-05
0.15	0.48	0.5888	0.0843	-6.8E-03	9.8E-03	3.8E-02	-7.0E-04	6.9E-04	5.8E-03	1.9E-05	-4.2E-05
0.12	0.43	0.6752	0.0973	-8.0E-03	1.3E-02	3.4E-02	-7.5E-04	-1.8E-04	1.0E-02	7.8E-06	-1.3E-04
0.09	0.39	0.7694	0.1230	-9.7E-03	1.6E-02	3.8E-02	-4.8E-04	-6.3E-04	1.7E-02	-1.2E-05	1.3E-04
0.06	0.34	0.8711	0.1458	-1.1E-02	1.7E-02	4.1E-02	-4.7E-05	-8.3E-04	2.4E-02	-3.5E-05	6.4E-04

Table 7: ZPG diamond roughness valley PIV kinematic values at test location 1.

$\frac{y}{\delta}$	$\frac{U_{eff}}{U_{eff,e}}$	$\frac{\sqrt{\overline{u'^2}}}{U}$	$\frac{\sqrt{\overline{v'^2}}}{U}$	$\frac{\overline{u'v'}}{U^2}$	$\frac{d\bar{u}}{dx}\cdot\frac{\delta}{U}$	$\frac{d\bar{u}}{dy}\cdot\frac{\delta}{U}$	$\frac{d\bar{v}}{dx}\cdot\frac{\delta}{U}$	$\frac{d\bar{v}}{dy}\cdot\frac{\delta}{U}$	$P_{xx}\cdot\frac{\delta}{U^3}$	$P_{yy}\cdot\frac{\delta}{U^3}$	$P_{xy}\cdot\frac{\delta}{U^3}$
1.24	1.01	0.0052	0.0072	2.7E-06	1.6E-04	-5.2E-05	-1.8E-04	1.1E-03	1.1E-08	1.1E-07	-4.2E-10
1.19	1.01	0.0056	0.0088	6.4E-06	7.8E-05	1.7E-04	1.1E-05	5.8E-04	1.1E-08	9.1E-08	1.7E-08
1.16	1.01	0.0051	0.0093	6.1E-06	2.7E-05	2.8E-04	2.1E-04	6.1E-05	7.2E-09	1.3E-08	3.0E-08
1.13	1.01	0.0050	0.0097	4.1E-06	-2.6E-05	3.5E-04	4.1E-04	-4.5E-04	0.0E+00	-8.1E-08	4.5E-08
1.08	1.01	0.0050	0.0093	-3.6E-06	-6.3E-05	4.3E-04	5.4E-04	-8.8E-04	-9.6E-09	-1.5E-07	5.5E-08
1.03	1.00	0.0071	0.0087	-1.1E-05	-2.3E-05	5.5E-04	2.3E-04	-3.2E-04	-1.1E-08	-5.3E-08	5.4E-08
1.00	1.00	0.0087	0.0089	-1.3E-05	1.9E-05	5.5E-04	3.8E-05	1.8E-04	-1.0E-08	2.9E-08	4.2E-08
0.97	1.00	0.0101	0.0095	-1.5E-05	4.5E-05	5.3E-04	-1.7E-04	7.2E-04	-6.8E-09	1.5E-07	1.7E-08
0.95	1.00	0.0114	0.0108	-1.7E-05	7.6E-05	6.5E-04	-3.8E-04	1.2E-03	-1.6E-09	3.0E-07	4.5E-09
0.92	0.99	0.0142	0.0131	-3.0E-05	7.3E-05	1.1E-03	-5.1E-04	1.5E-03	-4.1E-08	5.6E-07	3.4E-08
0.89	0.99	0.0186	0.0164	-5.7E-05	6.4E-05	1.4E-03	-3.7E-04	1.3E-03	-1.3E-07	7.2E-07	1.9E-07
0.84	0.97	0.0253	0.0200	-1.4E-04	-1.2E-04	2.5E-03	2.7E-04	-2.1E-04	-9.0E-07	-2.8E-07	1.3E-06
0.81	0.96	0.0291	0.0214	-2.1E-04	-2.2E-04	3.2E-03	5.4E-04	-9.5E-04	-1.7E-06	-1.1E-06	2.2E-06
0.79	0.95	0.0330	0.0225	-2.8E-04	-2.6E-04	3.8E-03	7.2E-04	-1.5E-03	-2.7E-06	-1.9E-06	3.2E-06
0.76	0.94	0.0353	0.0222	-2.8E-04	-2.1E-04	3.9E-03	7.0E-04	-1.6E-03	-2.7E-06	-2.0E-06	3.3E-06
0.73	0.92	0.0360	0.0209	-2.5E-04	-1.8E-04	3.8E-03	4.4E-04	-1.2E-03	-2.4E-06	-1.3E-06	2.6E-06
0.71	0.91	0.0367	0.0206	-2.2E-04	-4.7E-05	3.6E-03	1.1E-04	-6.1E-04	-1.7E-06	-5.8E-07	1.8E-06
0.68	0.90	0.0388	0.0211	-2.1E-04	7.4E-05	3.5E-03	-2.1E-04	-1.1E-04	-1.2E-06	-5.6E-09	1.2E-06
0.65	0.89	0.0409	0.0219	-1.9E-04	1.9E-04	3.5E-03	-5.4E-04	2.8E-04	-7.0E-07	4.8E-07	6.7E-07
0.62	0.88	0.0427	0.0232	-1.8E-04	2.5E-04	3.5E-03	-8.6E-04	5.5E-04	-3.8E-07	9.3E-07	1.4E-07
0.60	0.87	0.0463	0.0258	-1.9E-04	1.3E-04	3.3E-03	-1.1E-03	6.8E-04	-7.7E-07	1.3E-06	-2.2E-07
0.57	0.86	0.0497	0.0286	-2.5E-04	9.1E-05	3.2E-03	-1.3E-03	5.0E-04	-1.2E-06	1.5E-06	-7.2E-07
0.54	0.85	0.0531	0.0314	-3.6E-04	-3.3E-05	3.6E-03	-1.4E-03	1.7E-04	-2.8E-06	1.3E-06	-3.3E-07
0.52	0.84	0.0584	0.0332	-5.4E-04	-1.7E-04	4.1E-03	-1.3E-03	-2.0E-04	-5.7E-06	8.4E-07	5.0E-07
0.49	0.82	0.0644	0.0358	-7.7E-04	-4.8E-04	4.9E-03	-9.2E-04	-8.3E-04	-1.2E-05	-9.7E-07	3.8E-06
0.46	0.81	0.0713	0.0394	-1.1E-03	-9.5E-04	6.0E-03	-4.1E-04	-1.6E-03	-2.3E-05	-4.4E-06	1.0E-05
0.44	0.79	0.0792	0.0428	-1.5E-03	-1.4E-03	7.2E-03	1.9E-04	-2.2E-03	-3.8E-05	-8.8E-06	2.0E-05
0.41	0.77	0.0865	0.0443	-1.9E-03	-1.4E-03	7.9E-03	6.0E-04	-2.6E-03	-5.0E-05	-1.2E-05	2.7E-05
0.38	0.75	0.0924	0.0477	-2.1E-03	-1.8E-03	8.6E-03	9.3E-04	-2.7E-03	-6.5E-05	-1.6E-05	3.7E-05
0.36	0.73	0.1019	0.0517	-2.2E-03	-1.7E-03	9.3E-03	1.0E-03	-2.2E-03	-7.6E-05	-1.6E-05	4.4E-05
0.33	0.71	0.1097	0.0567	-2.3E-03	-1.4E-03	9.7E-03	9.3E-04	-1.4E-03	-7.8E-05	-1.3E-05	4.9E-05
0.30	0.68	0.1206	0.0629	-2.3E-03	-1.1E-03	9.9E-03	7.1E-04	-8.1E-04	-7.9E-05	-9.7E-06	5.4E-05
0.28	0.66	0.1342	0.0692	-2.2E-03	-1.0E-03	1.0E-02	4.2E-04	-5.0E-04	-8.2E-05	-6.8E-06	6.0E-05
0.25	0.64	0.1418	0.0737	-2.4E-03	-5.6E-04	1.0E-02	2.0E-04	-8.6E-05	-7.4E-05	-2.0E-06	6.2E-05
0.22	0.62	0.1612	0.0794	-3.2E-03	-5.0E-04	1.2E-02	2.4E-04	5.1E-04	-9.9E-05	4.9E-06	7.9E-05
0.20	0.60	0.1790	0.0875	-3.0E-03	-1.9E-04	9.9E-03	-1.4E-04	1.5E-04	-7.1E-05	2.7E-06	7.1E-05
0.17	0.59	0.1908	0.1022	-2.5E-03	-2.5E-04	1.0E-02	-4.1E-04	-6.9E-05	-6.8E-05	-1.1E-07	9.3E-05
0.14	0.57	0.2180	0.1238	-1.1E-03	-4.3E-04	1.7E-02	-3.4E-04	8.7E-04	-6.5E-05	3.5E-05	2.6E-04
0.12	0.53	0.2821	0.1426	3.9E-04	-1.4E-03	3.4E-02	-2.0E-04	2.6E-03	-2.8E-04	1.1E-04	6.5E-04
0.09	0.47	0.4090	0.1466	9.2E-04	-5.6E-03	5.8E-02	-5.6E-04	3.7E-03	-2.1E-03	1.7E-04	1.2E-03
0.06	0.36	0.6408	0.1387	1.6E-03	-1.8E-02	7.2E-02	-2.0E-03	2.4E-03	-1.5E-02	8.0E-05	5.3E-04

Table 8: ZPG square roughness PIV kinematic values at test location 2.

$\frac{y}{\delta}$	$\frac{U_{eff}}{U_{eff,e}}$	$\frac{\sqrt{\overline{u'^2}}}{U}$	$\frac{\sqrt{\overline{v'^2}}}{U}$	$\frac{\overline{u'v'}}{U^2}$	$\frac{d\bar{u}}{dx}\cdot\frac{\delta}{U}$	$\frac{d\bar{u}}{dy}\cdot\frac{\delta}{U}$	$\frac{d\bar{v}}{dx}\cdot\frac{\delta}{U}$	$\frac{d\bar{v}}{dy}\cdot\frac{\delta}{U}$	$P_{xx}\cdot\frac{\delta}{U^3}$	$P_{yy}\cdot\frac{\delta}{U^3}$	$P_{xy}\cdot\frac{\delta}{U^3}$
1.17	1.01	0.0041	0.0048	-3.1E-06	-5.1E-06	1.1E-04	3.7E-05	4.1E-05	0.0E+00	0.0E+00	0.0E+00
1.15	1.01	0.0045	0.0049	-3.4E-06	-1.0E-05	1.4E-04	3.3E-05	2.2E-05	0.0E+00	0.0E+00	0.0E+00
1.12	1.01	0.0052	0.0052	-4.4E-06	-2.5E-05	2.2E-04	3.0E-05	-9.2E-06	0.0E+00	0.0E+00	3.2E-09
1.10	1.01	0.0069	0.0058	-6.9E-06	-2.0E-05	3.6E-04	2.5E-05	-5.0E-05	-2.2E-09	-2.2E-09	1.6E-08
1.07	1.01	0.0087	0.0066	-1.1E-05	4.9E-05	5.1E-04	-2.7E-06	-1.1E-04	-5.1E-09	-1.2E-08	2.9E-08
1.02	1.00	0.0127	0.0080	-1.9E-05	4.9E-05	7.2E-04	-1.3E-05	3.7E-05	-1.4E-08	0.0E+00	4.1E-08
1.00	1.00	0.0152	0.0079	-1.8E-05	6.7E-05	1.3E-03	-6.8E-06	-7.6E-05	-2.1E-08	-1.1E-08	8.5E-08
0.98	0.99	0.0206	0.0093	-3.6E-05	3.5E-06	1.8E-03	-2.1E-05	-1.2E-04	-1.3E-07	-2.3E-08	1.5E-07
0.95	0.99	0.0242	0.0108	-5.4E-05	5.0E-06	1.9E-03	-2.6E-05	-9.5E-05	-1.9E-07	-2.4E-08	2.1E-07
0.93	0.98	0.0274	0.0128	-8.0E-05	4.7E-05	2.4E-03	-2.9E-05	-1.2E-04	-3.2E-07	-4.1E-08	3.9E-07
0.90	0.97	0.0324	0.0150	-1.3E-04	7.3E-05	3.0E-03	-4.2E-05	-1.8E-04	-6.3E-07	-7.3E-08	6.7E-07
0.85	0.95	0.0407	0.0209	-2.5E-04	-1.8E-05	3.3E-03	-4.9E-05	-9.6E-05	-1.7E-06	-5.7E-08	1.4E-06
0.83	0.94	0.0439	0.0222	-3.0E-04	7.5E-05	3.7E-03	-8.2E-05	-3.7E-05	-1.9E-06	6.7E-09	1.7E-06
0.80	0.92	0.0489	0.0251	-3.9E-04	8.8E-05	4.2E-03	-5.4E-05	-9.7E-06	-2.8E-06	2.4E-08	2.5E-06
0.75	0.90	0.0569	0.0298	-6.3E-04	-1.1E-04	4.1E-03	1.4E-05	2.1E-04	-5.8E-06	3.6E-07	3.6E-06
0.73	0.89	0.0590	0.0312	-6.5E-04	1.5E-04	4.4E-03	-6.1E-05	3.0E-04	-4.7E-06	6.5E-07	3.7E-06
0.70	0.87	0.0629	0.0336	-8.0E-04	1.1E-04	5.3E-03	-4.8E-05	-4.7E-05	-7.7E-06	-4.0E-08	5.8E-06
0.68	0.86	0.0711	0.0370	-1.1E-03	-1.9E-05	5.5E-03	-4.5E-05	-5.4E-05	-1.2E-05	-5.0E-08	7.4E-06
0.65	0.84	0.0750	0.0386	-1.2E-03	1.3E-04	5.4E-03	-1.2E-04	7.0E-05	-1.1E-05	4.9E-07	7.2E-06
0.63	0.83	0.0806	0.0408	-1.4E-03	5.8E-06	5.8E-03	-1.2E-04	1.5E-04	-1.6E-05	8.3E-07	8.7E-06
0.60	0.81	0.0855	0.0435	-1.6E-03	-6.2E-05	6.0E-03	-8.6E-05	1.4E-04	-2.0E-05	7.9E-07	1.1E-05
0.58	0.80	0.0897	0.0467	-1.9E-03	-1.3E-04	6.1E-03	-7.0E-05	1.6E-04	-2.5E-05	9.4E-07	1.3E-05
0.55	0.78	0.0936	0.0493	-2.1E-03	-1.2E-04	6.3E-03	-5.8E-05	1.9E-04	-2.8E-05	1.2E-06	1.5E-05
0.50	0.75	0.1032	0.0538	-2.6E-03	1.2E-04	6.6E-03	-1.1E-04	1.0E-04	-3.2E-05	1.1E-06	1.8E-05
0.48	0.74	0.1080	0.0569	-2.9E-03	2.7E-04	7.0E-03	-1.9E-04	1.6E-05	-3.4E-05	1.2E-06	2.0E-05
0.45	0.72	0.1137	0.0589	-3.2E-03	5.2E-05	7.4E-03	-1.2E-04	-9.0E-05	-4.6E-05	1.9E-07	2.4E-05
0.43	0.70	0.1171	0.0607	-3.3E-03	1.2E-04	7.3E-03	-1.4E-04	6.9E-05	-4.5E-05	1.4E-06	2.4E-05
0.40	0.69	0.1206	0.0629	-3.6E-03	8.6E-05	7.2E-03	-5.5E-05	1.8E-04	-4.9E-05	1.8E-06	2.7E-05
0.38	0.67	0.1236	0.0645	-3.7E-03	1.5E-04	8.0E-03	-1.0E-04	1.4E-04	-5.5E-05	2.0E-06	3.1E-05
0.35	0.66	0.1315	0.0674	-3.9E-03	2.4E-04	9.1E-03	-6.0E-05	1.9E-04	-6.2E-05	2.2E-06	3.9E-05
0.33	0.64	0.1397	0.0706	-4.1E-03	-8.9E-05	9.6E-03	-2.4E-05	2.7E-04	-8.2E-05	2.9E-06	4.7E-05
0.30	0.62	0.1473	0.0729	-4.6E-03	-3.6E-05	1.0E-02	1.7E-05	3.9E-04	-9.5E-05	4.0E-06	5.3E-05
0.28	0.60	0.1578	0.0778	-5.2E-03	-2.0E-04	1.0E-02	2.6E-05	5.5E-04	-1.2E-04	6.4E-06	6.2E-05
0.25	0.59	0.1679	0.0812	-5.6E-03	-2.5E-04	1.1E-02	-4.9E-06	6.4E-04	-1.3E-04	8.4E-06	6.9E-05
0.23	0.57	0.1826	0.0854	-5.8E-03	-1.0E-05	1.2E-02	1.5E-04	5.2E-04	-1.4E-04	5.8E-06	8.8E-05
0.20	0.55	0.2057	0.0954	-6.2E-03	2.8E-04	1.1E-02	4.0E-04	-1.2E-05	-1.2E-04	-6.0E-06	1.2E-04
0.18	0.53	0.2345	0.1111	-6.1E-03	8.4E-04	9.9E-03	2.9E-04	-5.6E-04	-2.4E-05	-1.8E-05	1.4E-04
0.15	0.52	0.2791	0.1347	-5.4E-03	1.7E-03	1.2E-02	4.1E-05	2.3E-04	1.3E-04	9.2E-06	2.2E-04
0.13	0.50	0.3312	0.1604	-6.9E-03	1.7E-03	1.7E-02	-1.3E-04	5.5E-04	1.3E-04	3.3E-05	4.1E-04
0.10	0.48	0.3584	0.1816	-6.7E-03	9.9E-04	2.2E-02	4.3E-04	-1.3E-04	-5.7E-05	-8.9E-06	7.8E-04
0.08	0.44	0.4312	0.1855	-9.3E-03	-6.5E-04	2.8E-02	-1.4E-06	9.3E-04	-7.9E-04	6.5E-05	9.7E-04

Table 9: ZPG diamond roughness peak PIV kinematic values at test location 2.

$\frac{y}{\delta}$	$\frac{U_{eff}}{U_{eff,e}}$	$\frac{\sqrt{\overline{u'^2}}}{U}$	$\frac{\sqrt{\overline{v'^2}}}{U}$	$\frac{\overline{u'v'}}{U^2}$	$\frac{d\bar{u}}{dx}\cdot\frac{\delta}{U}$	$\frac{d\bar{u}}{dy}\cdot\frac{\delta}{U}$	$\frac{d\bar{v}}{dx}\cdot\frac{\delta}{U}$	$\frac{d\bar{v}}{dy}\cdot\frac{\delta}{U}$	$P_{xx}\cdot\frac{\delta}{U^3}$	$P_{yy}\cdot\frac{\delta}{U^3}$	$P_{xy}\cdot\frac{\delta}{U^3}$
1.26	1.01	0.0025	0.0043	-1.9E-06	-1.1E-05	1.1E-04	7.7E-05	-2.1E-04	0.0E+00	-1.1E-08	0.0E+00
1.23	1.01	0.0028	0.0043	-2.3E-06	-2.6E-05	1.5E-04	1.2E-04	-3.2E-04	0.0E+00	-1.1E-08	0.0E+00
1.20	1.01	0.0032	0.0041	-2.9E-06	-3.1E-05	1.8E-04	1.1E-04	-3.2E-04	0.0E+00	-1.1E-08	4.1E-10
1.17	1.01	0.0036	0.0037	-2.9E-06	-2.5E-05	2.1E-04	7.2E-05	-2.2E-04	0.0E+00	-8.7E-09	8.2E-10
1.14	1.01	0.0043	0.0036	-3.1E-06	-7.0E-06	2.3E-04	1.4E-05	-5.7E-05	0.0E+00	-4.1E-10	4.1E-10
1.12	1.01	0.0050	0.0036	-4.0E-06	2.1E-05	2.5E-04	-5.2E-05	9.9E-05	0.0E+00	1.2E-09	0.0E+00
1.09	1.01	0.0061	0.0039	-4.1E-06	5.4E-05	2.8E-04	-1.2E-04	2.8E-04	0.0E+00	1.1E-08	0.0E+00
1.03	1.00	0.0091	0.0055	-8.7E-06	4.3E-06	6.1E-04	-2.0E-04	4.9E-04	-1.0E-08	3.3E-08	0.0E+00
1.00	1.00	0.0120	0.0067	-1.4E-05	5.4E-05	1.1E-03	-1.3E-04	3.7E-04	-1.1E-08	3.4E-08	3.0E-08
0.97	0.99	0.0165	0.0078	-3.1E-05	-6.0E-05	1.9E-03	-5.4E-06	1.4E-04	-1.6E-07	1.7E-08	1.2E-07
0.94	0.98	0.0222	0.0101	-7.8E-05	-2.0E-04	2.5E-03	1.2E-04	-2.5E-04	-6.0E-07	-7.7E-08	3.6E-07
0.91	0.97	0.0257	0.0107	-1.0E-04	-2.8E-04	2.6E-03	2.2E-04	-6.1E-04	-9.1E-07	-1.9E-07	5.4E-07
0.88	0.96	0.0275	0.0102	-1.1E-04	-3.1E-04	2.7E-03	2.6E-04	-6.8E-04	-1.1E-06	-2.0E-07	5.8E-07
0.86	0.95	0.0289	0.0103	-1.1E-04	-2.9E-04	2.9E-03	2.1E-04	-5.2E-04	-1.2E-06	-1.6E-07	5.8E-07
0.83	0.94	0.0308	0.0104	-1.2E-04	-2.5E-04	3.1E-03	1.1E-04	-2.9E-04	-1.2E-06	-9.2E-08	5.0E-07
0.80	0.93	0.0329	0.0104	-1.2E-04	-1.2E-04	3.0E-03	-2.9E-05	-8.0E-06	-9.5E-07	5.7E-09	3.0E-07
0.77	0.92	0.0345	0.0107	-1.2E-04	-5.9E-06	2.9E-03	-1.7E-04	3.0E-04	-7.1E-07	1.1E-07	1.1E-07
0.74	0.91	0.0361	0.0119	-1.4E-04	5.9E-05	2.9E-03	-3.1E-04	6.5E-04	-6.2E-07	2.8E-07	-9.5E-08
0.71	0.90	0.0385	0.0145	-1.8E-04	1.8E-04	3.0E-03	-4.8E-04	1.0E-03	-5.0E-07	6.2E-07	-3.0E-07
0.68	0.89	0.0411	0.0171	-2.3E-04	2.4E-04	3.1E-03	-5.5E-04	1.3E-03	-6.3E-07	1.0E-06	-3.7E-07
0.65	0.88	0.0442	0.0190	-3.1E-04	2.5E-04	3.1E-03	-4.9E-04	1.3E-03	-9.4E-07	1.3E-06	-3.2E-07
0.62	0.87	0.0451	0.0223	-4.2E-04	2.0E-04	3.6E-03	-3.2E-04	9.3E-04	-2.2E-06	1.2E-06	6.9E-07
0.60	0.85	0.0493	0.0254	-6.1E-04	-7.6E-05	4.4E-03	9.4E-05	5.5E-05	-5.8E-06	-5.7E-08	3.1E-06
0.57	0.84	0.0523	0.0272	-7.4E-04	-6.8E-04	5.1E-03	6.7E-04	-9.1E-04	-1.1E-05	-2.4E-06	6.8E-06
0.54	0.82	0.0561	0.0303	-9.6E-04	-8.1E-04	6.4E-03	8.8E-04	-1.8E-03	-1.7E-05	-5.0E-06	1.1E-05
0.51	0.80	0.0648	0.0330	-1.3E-03	-8.6E-04	6.8E-03	9.9E-04	-1.9E-03	-2.5E-05	-6.6E-06	1.5E-05
0.48	0.78	0.0677	0.0331	-1.3E-03	-7.8E-04	6.4E-03	9.0E-04	-1.5E-03	-2.4E-05	-5.7E-06	1.4E-05
0.45	0.76	0.0690	0.0331	-1.3E-03	-4.7E-04	6.4E-03	5.9E-04	-1.2E-03	-2.1E-05	-4.2E-06	1.2E-05
0.42	0.75	0.0697	0.0332	-1.2E-03	-7.7E-05	6.5E-03	2.3E-04	-7.2E-04	-1.7E-05	-2.2E-06	9.4E-06
0.39	0.73	0.0715	0.0334	-1.2E-03	1.3E-04	6.3E-03	-9.5E-05	-1.9E-04	-1.4E-05	-2.9E-07	6.7E-06
0.36	0.71	0.0730	0.0344	-1.2E-03	3.0E-04	6.0E-03	-3.5E-04	3.2E-04	-1.2E-05	1.6E-06	4.6E-06
0.34	0.70	0.0751	0.0355	-1.2E-03	4.4E-04	6.0E-03	-5.2E-04	7.1E-04	-9.8E-06	3.1E-06	3.2E-06
0.31	0.69	0.0788	0.0365	-1.3E-03	7.8E-04	5.8E-03	-7.3E-04	8.8E-04	-5.0E-06	4.2E-06	9.6E-07
0.28	0.67	0.0825	0.0374	-1.4E-03	1.3E-03	5.4E-03	-1.0E-03	1.1E-03	3.4E-06	5.9E-06	-2.7E-06
0.25	0.66	0.0854	0.0382	-1.4E-03	1.7E-03	5.2E-03	-1.2E-03	1.4E-03	1.0E-05	7.7E-06	-5.8E-06
0.22	0.65	0.0893	0.0397	-1.5E-03	1.9E-03	5.2E-03	-1.3E-03	1.4E-03	1.5E-05	8.6E-06	-7.5E-06
0.19	0.64	0.0958	0.0420	-1.6E-03	-3.6E-03	5.3E-03	-1.2E-03	1.0E-03	-9.7E-05	7.4E-06	2.8E-06
0.16	0.63	0.1101	0.0466	-1.7E-03	-2.5E-02	1.0E-02	-6.1E-04	6.2E-04	-6.7E-04	4.6E-06	6.2E-05
0.13	0.60	0.1750	0.0602	-2.6E-03	-3.1E-02	4.0E-02	-5.3E-04	-4.3E-05	-2.8E-03	1.5E-06	2.3E-04
0.10	0.47	0.5167	0.0986	-9.3E-03	-5.0E-02	8.6E-02	7.8E-05	-1.4E-03	-3.0E-02	-3.0E-05	1.4E-03
0.08	0.35	0.8006	0.1728	-1.8E-02	-6.9E-02	1.1E-01	6.3E-04	-1.6E-03	-9.4E-02	-1.2E-04	5.2E-03
0.05	0.23	1.1576	0.2521	-2.6E-02	-7.2E-02	1.9E-01	8.1E-04	-3.3E-03	-2.0E-01	-4.6E-04	1.5E-02

Table 10: ZPG diamond roughness valley PIV kinematic values at test location 2.

$\frac{y}{\delta}$	$\frac{U_{eff}}{U_{eff,e}}$	$\frac{\sqrt{\overline{u'^2}}}{U}$	$\frac{\sqrt{\overline{v'^2}}}{U}$	$\frac{\overline{u'v'}}{U^2}$	$\frac{d\bar{u}}{dx}\cdot\frac{\delta}{U}$	$\frac{d\bar{u}}{dy}\cdot\frac{\delta}{U}$	$\frac{d\bar{v}}{dx}\cdot\frac{\delta}{U}$	$\frac{d\bar{v}}{dy}\cdot\frac{\delta}{U}$	$P_{xx}\cdot\frac{\delta}{U^3}$	$P_{yy}\cdot\frac{\delta}{U^3}$	$P_{xy}\cdot\frac{\delta}{U^3}$
1.25	1.01	0.0021	0.0035	-9.8E-07	2.6E-05	-1.8E-05	-1.2E-04	2.4E-04	0.0E+00	8.3E-09	0.0E+00
1.22	1.01	0.0022	0.0038	-9.8E-07	2.7E-05	-3.4E-06	-1.2E-04	2.5E-04	0.0E+00	1.1E-08	0.0E+00
1.20	1.01	0.0023	0.0043	-9.8E-07	1.9E-05	2.9E-05	-8.1E-05	1.6E-04	0.0E+00	6.1E-09	0.0E+00
1.17	1.01	0.0026	0.0046	-1.5E-06	1.2E-06	1.0E-04	-1.2E-05	-1.8E-06	0.0E+00	-3.1E-09	0.0E+00
1.14	1.01	0.0033	0.0050	-3.3E-06	-3.8E-06	2.1E-04	6.6E-05	-1.7E-04	0.0E+00	-1.0E-08	5.4E-09
1.11	1.01	0.0044	0.0052	-5.7E-06	4.6E-06	3.1E-04	1.2E-04	-3.0E-04	-1.5E-09	-1.8E-08	1.3E-08
1.08	1.01	0.0054	0.0051	-7.3E-06	-1.4E-05	4.2E-04	1.3E-04	-3.4E-04	-5.5E-09	-2.4E-08	1.7E-08
1.06	1.01	0.0070	0.0050	-8.5E-06	-4.6E-05	5.9E-04	9.9E-05	-2.9E-04	-1.5E-08	-1.6E-08	2.5E-08
1.03	1.00	0.0092	0.0049	-1.0E-05	2.5E-05	7.5E-04	2.5E-05	-1.4E-04	-1.0E-08	-1.2E-08	1.8E-08
1.00	1.00	0.0117	0.0047	-1.1E-05	1.5E-04	9.8E-04	-5.9E-05	2.8E-05	1.6E-08	-4.1E-10	1.3E-08
0.97	1.00	0.0148	0.0052	-1.5E-05	1.5E-04	1.3E-03	-1.4E-04	2.2E-04	2.4E-08	1.4E-08	4.7E-10
0.94	0.99	0.0184	0.0059	-2.2E-05	2.2E-04	1.9E-03	-2.2E-04	4.4E-04	6.8E-08	3.8E-08	-2.5E-08
0.91	0.98	0.0241	0.0083	-5.0E-05	1.6E-04	2.0E-03	-2.6E-04	6.2E-04	-1.4E-08	1.1E-07	-5.1E-08
0.89	0.97	0.0265	0.0100	-7.5E-05	1.3E-04	1.7E-03	-2.3E-04	6.0E-04	-6.6E-08	1.5E-07	-5.0E-08
0.83	0.96	0.0296	0.0127	-1.4E-04	-1.4E-04	2.7E-03	1.0E-04	-4.7E-05	-1.0E-06	-5.7E-08	5.7E-07
0.80	0.95	0.0320	0.0141	-1.9E-04	-2.7E-04	3.2E-03	3.1E-04	-5.3E-04	-1.8E-06	-3.5E-07	1.1E-06
0.77	0.93	0.0335	0.0148	-2.1E-04	-3.3E-04	3.5E-03	4.1E-04	-8.4E-04	-2.2E-06	-5.4E-07	1.5E-06
0.75	0.92	0.0350	0.0151	-2.3E-04	-2.8E-04	3.7E-03	3.9E-04	-8.4E-04	-2.4E-06	-5.7E-07	1.6E-06
0.72	0.91	0.0370	0.0152	-2.4E-04	-2.3E-04	3.8E-03	3.0E-04	-6.6E-04	-2.5E-06	-4.6E-07	1.5E-06
0.69	0.89	0.0393	0.0154	-2.5E-04	-1.1E-04	3.9E-03	1.3E-04	-3.7E-04	-2.3E-06	-2.5E-07	1.3E-06
0.66	0.88	0.0412	0.0156	-2.6E-04	9.6E-05	3.9E-03	-9.7E-05	3.6E-05	-1.7E-06	5.1E-08	7.9E-07
0.63	0.87	0.0432	0.0163	-2.6E-04	2.3E-04	4.1E-03	-2.8E-04	4.4E-04	-1.3E-06	3.9E-07	4.0E-07
0.61	0.86	0.0461	0.0185	-3.1E-04	3.0E-04	4.3E-03	-4.5E-04	7.5E-04	-1.4E-06	8.1E-07	1.9E-07
0.58	0.84	0.0516	0.0215	-4.2E-04	3.5E-04	4.1E-03	-6.3E-04	1.1E-03	-1.6E-06	1.6E-06	-4.4E-07
0.55	0.83	0.0537	0.0231	-4.6E-04	6.5E-04	3.9E-03	-8.1E-04	1.5E-03	1.3E-07	2.3E-06	-1.3E-06
0.52	0.82	0.0557	0.0248	-5.5E-04	8.3E-04	4.1E-03	-8.9E-04	1.4E-03	6.7E-07	2.8E-06	-1.5E-06
0.49	0.81	0.0588	0.0278	-7.1E-04	7.9E-04	4.3E-03	-8.1E-04	1.3E-03	-6.8E-07	3.1E-06	-9.5E-07
0.47	0.79	0.0619	0.0298	-9.1E-04	2.7E-04	4.8E-03	-4.0E-04	7.3E-04	-6.8E-06	1.9E-06	2.0E-06
0.44	0.78	0.0656	0.0325	-1.2E-03	-1.9E-04	5.6E-03	2.1E-04	-2.7E-04	-1.5E-05	-1.4E-06	7.8E-06
0.41	0.76	0.0699	0.0356	-1.4E-03	-6.6E-04	6.7E-03	7.3E-04	-1.2E-03	-2.6E-05	-5.4E-06	1.5E-05
0.38	0.74	0.0748	0.0383	-1.7E-03	-9.9E-04	7.4E-03	1.2E-03	-1.6E-03	-3.7E-05	-8.9E-06	2.2E-05
0.35	0.73	0.0773	0.0388	-1.8E-03	-1.1E-03	7.9E-03	1.3E-03	-1.8E-03	-4.1E-05	-1.0E-05	2.5E-05
0.33	0.71	0.0811	0.0394	-1.9E-03	-9.5E-04	8.5E-03	1.2E-03	-1.8E-03	-4.4E-05	-1.0E-05	2.6E-05
0.30	0.69	0.0863	0.0409	-2.0E-03	-8.4E-04	8.5E-03	1.0E-03	-1.4E-03	-4.7E-05	-9.0E-06	2.6E-05
0.27	0.67	0.0901	0.0418	-2.1E-03	-6.9E-04	8.2E-03	7.9E-04	-9.9E-04	-4.5E-05	-6.9E-06	2.4E-05
0.24	0.65	0.0938	0.0424	-2.1E-03	-5.5E-04	8.1E-03	4.5E-04	-5.7E-04	-4.3E-05	-4.0E-06	2.1E-05
0.21	0.63	0.0998	0.0445	-2.2E-03	-4.6E-04	8.2E-03	1.7E-04	-8.5E-05	-4.6E-05	-1.0E-06	1.9E-05
0.19	0.62	0.1070	0.0476	-2.4E-03	-1.9E-04	7.3E-03	-3.9E-05	1.3E-04	-3.9E-05	7.3E-07	1.6E-05
0.16	0.60	0.1152	0.0520	-2.5E-03	4.3E-05	5.6E-03	-2.0E-04	-7.1E-05	-2.7E-05	5.9E-07	1.3E-05
0.13	0.60	0.1340	0.0606	-2.6E-03	-8.4E-04	9.2E-03	-3.3E-04	3.2E-04	-8.9E-05	4.2E-06	3.0E-05
0.10	0.57	0.1835	0.0684	-2.4E-03	-4.9E-03	2.5E-02	-5.4E-04	1.1E-03	-3.9E-04	1.3E-05	1.2E-04
0.07	0.51	0.3345	0.0946	-1.5E-03	-2.7E-03	5.8E-02	-4.8E-04	1.3E-03	-7.6E-04	2.4E-05	4.7E-04

Table 11: ZPG smooth wall PIV kinematic values at test location 3.

$\frac{y}{\delta}$	$\frac{U_{eff}}{U_{eff,e}}$	$\frac{\sqrt{\overline{u'^2}}}{U}$	$\frac{\sqrt{\overline{v'^2}}}{U}$	$\frac{\overline{u'v'}}{U^2}$	$\frac{d\bar{u}}{dx}\cdot\frac{\delta}{U}$	$\frac{d\bar{u}}{dy}\cdot\frac{\delta}{U}$	$\frac{d\bar{v}}{dx}\cdot\frac{\delta}{U}$	$\frac{d\bar{v}}{dy}\cdot\frac{\delta}{U}$	$P_{xx}\cdot\frac{\delta}{U^3}$	$P_{yy}\cdot\frac{\delta}{U^3}$	$P_{xy}\cdot\frac{\delta}{U^3}$
1.20	1.01	0.0062	0.0141	-1.1E-06	-4.2E-05	3.3E-05	-4.2E-04	-2.9E-05	0.0E+00	-8.2E-09	-7.6E-09
1.15	1.01	0.0073	0.0151	-1.0E-05	-4.5E-05	2.4E-04	-4.5E-04	-1.9E-04	-1.2E-08	-7.8E-08	3.7E-08
1.13	1.01	0.0093	0.0161	-2.3E-05	-2.1E-05	3.4E-04	-4.9E-04	-2.8E-04	-1.5E-08	-1.3E-07	5.9E-08
1.10	1.01	0.0111	0.0163	-3.1E-05	-5.4E-05	4.2E-04	-4.8E-04	-3.5E-04	-4.0E-08	-1.5E-07	6.8E-08
1.05	1.01	0.0150	0.0180	-6.9E-05	-9.1E-06	7.0E-04	-4.9E-04	-3.2E-04	-1.1E-07	-1.3E-07	1.4E-07
1.00	1.00	0.0205	0.0189	-1.3E-04	-2.1E-04	1.1E-03	-3.4E-04	-2.1E-04	-4.8E-07	-6.3E-08	3.2E-07
0.97	1.00	0.0228	0.0192	-1.6E-04	-2.4E-04	1.3E-03	-3.2E-04	-1.1E-04	-6.7E-07	1.9E-08	3.7E-07
0.95	0.99	0.0260	0.0199	-2.0E-04	-1.9E-04	1.5E-03	-3.2E-04	-4.2E-05	-8.5E-07	9.3E-08	4.2E-07
0.92	0.99	0.0281	0.0202	-2.3E-04	-1.4E-04	1.5E-03	-3.0E-04	9.7E-05	-9.3E-07	2.2E-07	4.1E-07
0.90	0.98	0.0298	0.0202	-2.5E-04	-1.1E-04	1.7E-03	-2.5E-04	1.7E-04	-1.0E-06	2.6E-07	4.4E-07
0.85	0.96	0.0345	0.0213	-3.4E-04	-1.1E-04	2.4E-03	-1.5E-04	2.4E-05	-1.9E-06	1.2E-07	9.7E-07
0.82	0.96	0.0373	0.0224	-4.0E-04	-1.5E-04	2.5E-03	-1.1E-04	7.9E-05	-2.4E-06	1.7E-07	1.1E-06
0.80	0.95	0.0392	0.0230	-4.4E-04	-1.9E-04	2.3E-03	-8.5E-05	2.1E-04	-2.6E-06	3.0E-07	1.1E-06
0.77	0.94	0.0405	0.0233	-4.8E-04	-2.1E-04	2.4E-03	-6.9E-05	3.0E-04	-3.0E-06	3.8E-07	1.2E-06
0.75	0.93	0.0421	0.0238	-5.1E-04	-1.7E-04	2.7E-03	-5.8E-05	2.6E-04	-3.3E-06	3.5E-07	1.4E-06
0.72	0.92	0.0442	0.0247	-5.7E-04	-1.4E-04	2.7E-03	-6.3E-05	3.1E-04	-3.6E-06	4.5E-07	1.4E-06
0.70	0.92	0.0454	0.0252	-5.9E-04	-1.5E-04	2.7E-03	-7.3E-05	4.0E-04	-3.8E-06	6.0E-07	1.5E-06
0.67	0.91	0.0472	0.0257	-6.1E-04	-1.8E-04	2.9E-03	-4.2E-05	3.2E-04	-4.3E-06	4.8E-07	1.7E-06
0.65	0.90	0.0493	0.0267	-6.6E-04	-1.2E-04	2.8E-03	-4.9E-05	3.5E-04	-4.3E-06	5.6E-07	1.7E-06
0.62	0.89	0.0508	0.0275	-6.9E-04	-1.1E-04	2.9E-03	-5.6E-05	3.4E-04	-4.5E-06	5.8E-07	1.9E-06
0.60	0.88	0.0521	0.0279	-7.2E-04	-1.1E-04	3.1E-03	-4.3E-05	3.5E-04	-5.0E-06	6.0E-07	2.1E-06
0.57	0.87	0.0537	0.0281	-7.6E-04	-1.1E-04	3.3E-03	-2.6E-05	3.8E-04	-5.6E-06	6.4E-07	2.3E-06
0.55	0.86	0.0558	0.0287	-8.0E-04	-8.0E-05	3.4E-03	-8.8E-06	3.4E-04	-6.0E-06	5.8E-07	2.6E-06
0.52	0.85	0.0579	0.0296	-8.5E-04	-4.1E-05	3.5E-03	4.0E-05	2.5E-04	-6.2E-06	3.7E-07	3.0E-06
0.50	0.84	0.0605	0.0309	-9.2E-04	-1.8E-04	3.5E-03	4.0E-05	2.8E-04	-7.8E-06	4.5E-07	3.4E-06
0.47	0.83	0.0619	0.0310	-9.4E-04	-9.4E-05	3.5E-03	-5.2E-06	3.6E-04	-7.3E-06	6.9E-07	3.1E-06
0.45	0.82	0.0637	0.0309	-9.5E-04	-2.3E-04	3.6E-03	9.4E-05	4.7E-04	-8.7E-06	7.2E-07	3.6E-06
0.42	0.81	0.0653	0.0312	-9.7E-04	-2.0E-04	3.8E-03	5.0E-05	4.6E-04	-9.0E-06	7.9E-07	3.7E-06
0.40	0.80	0.0673	0.0319	-1.0E-03	-1.3E-04	4.0E-03	-1.3E-06	4.3E-04	-9.3E-06	8.7E-07	3.7E-06
0.37	0.79	0.0693	0.0325	-1.1E-03	-7.4E-05	4.0E-03	-4.7E-05	4.5E-04	-9.1E-06	1.0E-06	3.6E-06
0.35	0.78	0.0710	0.0335	-1.1E-03	-6.8E-05	4.0E-03	-6.8E-05	4.6E-04	-9.3E-06	1.2E-06	3.7E-06
0.32	0.77	0.0728	0.0345	-1.1E-03	-1.5E-04	4.2E-03	-2.2E-05	4.9E-04	-1.1E-05	1.2E-06	4.5E-06
0.30	0.76	0.0754	0.0357	-1.1E-03	-1.1E-04	4.7E-03	-4.9E-05	5.5E-04	-1.2E-05	1.5E-06	5.1E-06
0.25	0.74	0.0809	0.0374	-1.2E-03	-1.4E-04	5.7E-03	-8.8E-05	5.4E-04	-1.5E-05	1.7E-06	6.9E-06
0.22	0.73	0.0842	0.0381	-1.2E-03	-2.2E-04	6.1E-03	-1.1E-04	5.9E-04	-1.8E-05	2.0E-06	7.7E-06
0.20	0.71	0.0873	0.0388	-1.2E-03	-2.5E-04	6.8E-03	-1.1E-04	7.0E-04	-2.0E-05	2.4E-06	8.9E-06
0.17	0.70	0.0897	0.0380	-1.2E-03	-2.3E-04	5.3E-03	-8.2E-05	3.9E-04	-1.6E-05	1.4E-06	7.1E-06
0.15	0.69	0.1006	0.0456	-1.2E-03	-1.5E-04	4.1E-03	-7.0E-05	-1.1E-05	-1.3E-05	-2.6E-08	8.8E-06
0.12	0.68	0.1166	0.0587	-1.2E-03	5.6E-05	6.1E-03	-4.5E-05	9.8E-05	-1.4E-05	1.0E-06	2.1E-05
0.10	0.66	0.1241	0.0607	-1.3E-03	2.4E-04	1.1E-02	4.4E-05	6.2E-04	-2.1E-05	4.4E-06	3.9E-05
0.07	0.64	0.1251	0.0518	-1.5E-03	1.3E-04	1.5E-02	-1.4E-05	7.6E-04	-4.0E-05	4.2E-06	3.6E-05

Table 12: ZPG square roughness PIV kinematic values at test location 3.

$\frac{y}{\delta}$	$\frac{U_{eff}}{U_{eff,e}}$	$\frac{\sqrt{\overline{u'^2}}}{U}$	$\frac{\sqrt{\overline{v'^2}}}{U}$	$\frac{\overline{u'v'}}{U^2}$	$\frac{d\bar{u}}{dx}\cdot\frac{\delta}{U}$	$\frac{d\bar{u}}{dy}\cdot\frac{\delta}{U}$	$\frac{d\bar{v}}{dx}\cdot\frac{\delta}{U}$	$\frac{d\bar{v}}{dy}\cdot\frac{\delta}{U}$	$P_{xx}\cdot\frac{\delta}{U^3}$	$P_{yy}\cdot\frac{\delta}{U^3}$	$P_{xy}\cdot\frac{\delta}{U^3}$
1.14	1.01	0.0088	0.0078	-7.7E-06	6.4E-05	2.1E-04	2.6E-05	1.2E-04	2.7E-09	1.5E-08	1.5E-08
1.12	1.01	0.0093	0.0082	-1.0E-05	7.4E-05	2.9E-04	2.0E-05	1.5E-04	7.9E-09	1.7E-08	1.7E-08
1.09	1.01	0.0102	0.0086	-1.3E-05	8.5E-05	3.7E-04	5.7E-06	1.5E-04	1.3E-08	2.2E-08	2.4E-08
1.05	1.01	0.0128	0.0095	-2.3E-05	1.4E-04	7.0E-04	-8.2E-06	1.5E-04	1.1E-08	3.1E-08	5.8E-08
1.02	1.00	0.0147	0.0101	-2.8E-05	1.4E-04	9.6E-04	-2.1E-05	1.6E-04	5.0E-09	3.4E-08	8.1E-08
1.00	1.00	0.0175	0.0106	-4.3E-05	1.1E-04	1.3E-03	-1.1E-08	1.3E-04	-3.5E-08	2.7E-08	1.3E-07
0.98	1.00	0.0208	0.0113	-5.7E-05	8.6E-05	1.5E-03	8.3E-06	1.6E-04	-9.4E-08	4.5E-08	1.7E-07
0.95	0.99	0.0235	0.0120	-7.5E-05	7.3E-05	1.6E-03	1.3E-05	1.7E-04	-1.6E-07	4.6E-08	2.2E-07
0.93	0.98	0.0261	0.0134	-9.5E-05	8.4E-05	1.9E-03	8.8E-06	1.7E-04	-2.4E-07	5.5E-08	3.2E-07
0.91	0.98	0.0287	0.0138	-1.1E-04	9.9E-05	2.3E-03	1.2E-05	1.6E-04	-3.3E-07	5.7E-08	4.2E-07
0.88	0.97	0.0325	0.0156	-1.4E-04	2.2E-04	2.8E-03	-2.3E-05	1.2E-04	-3.2E-07	6.5E-08	6.1E-07
0.84	0.95	0.0411	0.0182	-2.4E-04	2.1E-04	3.2E-03	-2.3E-05	1.7E-04	-8.1E-07	1.2E-07	9.3E-07
0.81	0.94	0.0440	0.0195	-2.8E-04	1.7E-04	3.1E-03	-3.7E-05	1.8E-04	-1.0E-06	1.6E-07	1.0E-06
0.79	0.93	0.0460	0.0217	-3.2E-04	1.5E-04	3.4E-03	-2.2E-05	1.5E-04	-1.5E-06	1.5E-07	1.5E-06
0.77	0.92	0.0488	0.0251	-4.1E-04	9.6E-05	3.8E-03	3.2E-05	1.3E-04	-2.7E-06	1.3E-07	2.4E-06
0.74	0.91	0.0522	0.0281	-5.1E-04	9.4E-05	4.2E-03	4.6E-05	1.3E-04	-3.9E-06	1.6E-07	3.4E-06
0.72	0.90	0.0560	0.0303	-6.3E-04	1.3E-04	4.4E-03	2.9E-05	2.2E-04	-4.7E-06	3.8E-07	3.9E-06
0.70	0.88	0.0593	0.0316	-7.0E-04	1.5E-04	4.3E-03	5.9E-05	3.2E-04	-4.9E-06	5.5E-07	4.2E-06
0.67	0.87	0.0616	0.0334	-7.8E-04	1.8E-04	4.3E-03	7.7E-05	2.7E-04	-5.3E-06	4.6E-07	4.7E-06
0.63	0.85	0.0680	0.0376	-1.0E-03	1.9E-04	5.1E-03	4.8E-05	1.3E-04	-8.8E-06	2.7E-07	7.1E-06
0.61	0.83	0.0727	0.0395	-1.2E-03	2.0E-04	5.2E-03	4.4E-06	6.8E-05	-1.0E-05	2.0E-07	7.9E-06
0.58	0.82	0.0758	0.0405	-1.3E-03	1.4E-04	5.2E-03	3.0E-05	1.7E-05	-1.2E-05	-2.1E-08	8.5E-06
0.56	0.81	0.0783	0.0427	-1.4E-03	1.6E-04	5.3E-03	-1.3E-05	9.9E-05	-1.3E-05	4.0E-07	9.2E-06
0.54	0.80	0.0805	0.0444	-1.4E-03	1.4E-04	5.4E-03	3.0E-05	1.3E-04	-1.4E-05	4.1E-07	1.1E-05
0.51	0.78	0.0835	0.0454	-1.5E-03	9.0E-05	6.0E-03	-6.9E-05	-6.8E-05	-1.7E-05	-8.6E-08	1.2E-05
0.49	0.77	0.0887	0.0471	-1.7E-03	-8.3E-06	5.9E-03	-4.2E-05	-4.7E-07	-2.0E-05	1.4E-07	1.3E-05
0.47	0.76	0.0920	0.0485	-1.9E-03	-1.3E-04	6.2E-03	6.8E-05	-1.7E-05	-2.5E-05	-3.3E-07	1.5E-05
0.44	0.74	0.0982	0.0511	-2.2E-03	-3.1E-05	6.6E-03	5.8E-05	1.1E-05	-3.0E-05	-1.6E-07	1.8E-05
0.42	0.73	0.1035	0.0549	-2.5E-03	8.0E-05	6.6E-03	-4.4E-05	1.7E-04	-3.1E-05	1.2E-06	1.9E-05
0.40	0.72	0.1059	0.0557	-2.6E-03	-1.0E-05	7.1E-03	3.6E-05	1.0E-04	-3.7E-05	4.3E-07	2.2E-05
0.35	0.69	0.1169	0.0605	-3.2E-03	2.5E-04	8.6E-03	-9.5E-05	3.9E-05	-4.8E-05	8.8E-07	2.9E-05
0.33	0.67	0.1219	0.0639	-3.5E-03	2.2E-04	9.0E-03	-3.5E-05	3.1E-05	-5.7E-05	4.9E-07	3.5E-05
0.30	0.65	0.1270	0.0670	-3.8E-03	3.7E-04	8.6E-03	-6.4E-05	8.4E-05	-5.3E-05	1.3E-06	3.6E-05
0.28	0.64	0.1352	0.0698	-4.3E-03	3.9E-04	7.8E-03	-1.6E-04	2.1E-04	-5.3E-05	3.4E-06	3.3E-05
0.26	0.63	0.1441	0.0718	-4.8E-03	8.9E-05	8.4E-03	-5.9E-05	1.9E-04	-7.7E-05	2.5E-06	4.1E-05
0.23	0.61	0.1505	0.0740	-5.1E-03	2.1E-04	9.7E-03	3.7E-05	3.3E-04	-8.9E-05	3.2E-06	5.1E-05
0.21	0.60	0.1587	0.0751	-5.3E-03	4.4E-04	1.0E-02	-6.3E-05	5.4E-04	-8.4E-05	6.8E-06	5.0E-05
0.19	0.58	0.1661	0.0776	-5.7E-03	6.0E-04	1.0E-02	-5.0E-05	3.8E-04	-8.1E-05	5.2E-06	5.4E-05
0.16	0.57	0.1755	0.0803	-5.9E-03	-2.7E-04	1.0E-02	5.6E-06	2.9E-04	-1.4E-04	3.8E-06	6.5E-05
0.14	0.55	0.1848	0.0817	-6.0E-03	-6.9E-03	1.1E-02	2.6E-05	-3.2E-04	-6.2E-04	-5.0E-06	1.2E-04
0.12	0.54	0.2119	0.0941	-7.2E-03	-1.1E-02	4.4E-02	-9.9E-05	-1.1E-03	-1.8E-03	-1.8E-05	4.6E-04

Table 13: ZPG diamond roughness peak PIV kinematic values at test location 3.

$\frac{y}{\delta}$	$\frac{U_{eff}}{U_{eff,e}}$	$\frac{\sqrt{\overline{u'^2}}}{U}$	$\frac{\sqrt{\overline{v'^2}}}{U}$	$\frac{\overline{u'v'}}{U^2}$	$\frac{d\bar{u}}{dx}\cdot\frac{\delta}{U}$	$\frac{d\bar{u}}{dy}\cdot\frac{\delta}{U}$	$\frac{d\bar{v}}{dx}\cdot\frac{\delta}{U}$	$\frac{d\bar{v}}{dy}\cdot\frac{\delta}{U}$	$P_{xx}\cdot\frac{\delta}{U^3}$	$P_{yy}\cdot\frac{\delta}{U^3}$	$P_{xy}\cdot\frac{\delta}{U^3}$
1.15	1.01	0.0062	0.0067	-6.7E-06	-1.6E-05	3.1E-04	1.2E-04	-2.0E-04	-3.8E-09	-1.8E-08	2.0E-08
1.12	1.01	0.0068	0.0068	-7.2E-06	4.0E-06	3.1E-04	6.3E-05	-3.2E-05	-3.8E-09	-4.9E-09	1.4E-08
1.10	1.01	0.0076	0.0068	-8.2E-06	1.9E-05	3.3E-04	-4.8E-06	2.0E-04	-1.9E-09	1.4E-08	1.2E-08
1.07	1.01	0.0085	0.0065	-8.7E-06	1.7E-05	3.2E-04	-9.6E-05	4.3E-04	0.0E+00	3.7E-08	4.8E-09
1.05	1.00	0.0096	0.0062	-9.5E-06	7.5E-05	3.5E-04	-1.9E-04	5.6E-04	3.9E-09	4.5E-08	-1.4E-08
1.02	1.00	0.0109	0.0063	-1.0E-05	1.9E-04	5.7E-04	-2.4E-04	5.6E-04	2.7E-08	5.1E-08	-1.7E-08
1.00	1.00	0.0133	0.0069	-1.7E-05	1.2E-04	8.8E-04	-1.8E-04	5.2E-04	3.7E-09	5.1E-08	6.3E-10
0.97	1.00	0.0164	0.0072	-2.5E-05	-1.1E-04	1.4E-03	-7.4E-05	3.7E-04	-1.2E-07	4.1E-08	4.7E-08
0.95	0.99	0.0212	0.0081	-5.0E-05	-1.1E-04	1.9E-03	-5.0E-07	1.1E-04	-2.9E-07	1.8E-08	1.2E-07
0.93	0.98	0.0241	0.0096	-7.9E-05	-1.2E-04	2.0E-03	1.4E-04	-1.0E-04	-4.7E-07	-4.8E-08	2.9E-07
0.88	0.97	0.0289	0.0130	-1.4E-04	-2.7E-04	2.9E-03	2.6E-04	-5.1E-04	-1.3E-06	-2.6E-07	8.4E-07
0.85	0.96	0.0310	0.0141	-1.7E-04	-3.8E-04	3.5E-03	2.7E-04	-5.9E-04	-1.9E-06	-3.3E-07	1.1E-06
0.83	0.94	0.0344	0.0165	-2.3E-04	-3.1E-04	3.7E-03	1.8E-04	-4.1E-04	-2.4E-06	-3.0E-07	1.4E-06
0.80	0.93	0.0367	0.0175	-2.5E-04	-8.1E-05	3.1E-03	-2.1E-05	1.7E-04	-1.8E-06	1.1E-07	9.0E-07
0.78	0.92	0.0373	0.0155	-2.0E-04	4.6E-05	2.6E-03	-1.8E-04	6.8E-04	-9.5E-07	3.7E-07	2.7E-07
0.75	0.92	0.0380	0.0143	-1.7E-04	9.2E-05	2.6E-03	-2.7E-04	8.7E-04	-6.0E-07	4.5E-07	-6.8E-09
0.70	0.90	0.0418	0.0184	-2.2E-04	2.0E-04	3.1E-03	-4.6E-04	1.2E-03	-6.5E-07	1.0E-06	-6.7E-08
0.68	0.89	0.0440	0.0213	-2.8E-04	1.6E-04	3.2E-03	-4.3E-04	1.2E-03	-1.2E-06	1.3E-06	2.8E-07
0.65	0.88	0.0468	0.0240	-3.8E-04	1.6E-04	3.7E-03	-3.0E-04	8.2E-04	-2.2E-06	1.0E-06	1.2E-06
0.63	0.87	0.0510	0.0279	-5.6E-04	2.3E-05	4.4E-03	-3.4E-05	2.2E-04	-4.9E-06	2.1E-07	3.4E-06
0.60	0.85	0.0552	0.0313	-7.8E-04	-3.2E-04	4.7E-03	3.6E-04	-4.6E-04	-9.5E-06	-1.6E-06	6.5E-06
0.58	0.84	0.0587	0.0335	-9.8E-04	-6.6E-04	5.4E-03	6.6E-04	-1.1E-03	-1.5E-05	-3.9E-06	1.0E-05
0.56	0.83	0.0645	0.0354	-1.2E-03	-7.8E-04	5.9E-03	8.8E-04	-1.6E-03	-2.1E-05	-6.0E-06	1.4E-05
0.53	0.81	0.0671	0.0362	-1.3E-03	-8.7E-04	6.1E-03	8.5E-04	-1.6E-03	-2.3E-05	-6.4E-06	1.5E-05
0.51	0.79	0.0694	0.0377	-1.4E-03	-5.2E-04	6.1E-03	6.5E-04	-1.5E-03	-2.2E-05	-6.0E-06	1.4E-05
0.48	0.78	0.0704	0.0375	-1.3E-03	-3.6E-04	6.0E-03	4.3E-04	-9.3E-04	-1.9E-05	-3.8E-06	1.2E-05
0.46	0.77	0.0730	0.0379	-1.3E-03	-1.3E-04	6.0E-03	1.2E-04	-4.0E-04	-1.6E-05	-1.5E-06	9.9E-06
0.43	0.75	0.0736	0.0386	-1.2E-03	1.9E-04	5.7E-03	-2.7E-04	1.1E-04	-1.2E-05	9.6E-07	6.6E-06
0.41	0.74	0.0745	0.0388	-1.2E-03	4.1E-04	5.3E-03	-5.9E-04	6.3E-04	-8.1E-06	3.2E-06	3.6E-06
0.36	0.72	0.0769	0.0404	-1.1E-03	8.2E-04	5.1E-03	-1.1E-03	1.3E-03	-2.1E-06	6.8E-06	-5.7E-07
0.33	0.71	0.0794	0.0417	-1.2E-03	9.9E-04	5.0E-03	-1.3E-03	1.7E-03	5.5E-08	9.1E-06	-2.8E-06
0.31	0.70	0.0821	0.0439	-1.3E-03	1.2E-03	4.7E-03	-1.4E-03	2.1E-03	3.0E-06	1.2E-05	-5.1E-06
0.28	0.69	0.0853	0.0464	-1.4E-03	1.3E-03	4.6E-03	-1.5E-03	2.2E-03	5.8E-06	1.4E-05	-6.2E-06
0.26	0.68	0.0904	0.0484	-1.6E-03	1.3E-03	5.2E-03	-1.5E-03	1.9E-03	4.6E-06	1.4E-05	-5.4E-06
0.23	0.67	0.0982	0.0517	-1.9E-03	1.2E-03	6.1E-03	-1.3E-03	1.9E-03	-4.5E-07	1.4E-05	-1.6E-06
0.21	0.66	0.1137	0.0575	-2.3E-03	8.6E-04	1.2E-02	-9.1E-04	1.4E-03	-4.0E-05	1.2E-05	2.9E-05
0.16	0.55	0.3803	0.0773	-6.2E-03	-5.7E-03	3.6E-02	2.0E-04	-4.6E-04	-2.1E-03	-1.1E-05	2.9E-04
0.14	0.52	0.4305	0.0940	-8.9E-03	-6.2E-03	5.1E-02	5.6E-04	-2.1E-03	-3.2E-03	-4.8E-05	6.4E-04
0.11	0.41	0.6203	0.1079	-1.5E-02	-1.4E-02	1.1E-01	1.7E-03	-5.4E-03	-1.4E-02	-1.8E-04	2.2E-03
0.09	0.29	0.8520	0.1278	-2.3E-02	-2.0E-02	1.2E-01	2.4E-03	-6.8E-03	-3.3E-02	-3.3E-04	4.5E-03
0.06	0.22	1.1507	0.1508	-2.2E-02	-2.9E-02	1.1E-01	3.2E-03	-4.8E-03	-7.7E-02	-3.7E-04	7.6E-03

Table 14: ZPG diamond roughness valley PIV kinematic values at test location 3.

$\frac{y}{\delta}$	$\frac{U_{eff}}{U_{eff,e}}$	$\frac{\sqrt{\overline{u'^2}}}{U}$	$\frac{\sqrt{\overline{v'^2}}}{U}$	$\frac{\overline{u'v'}}{U^2}$	$\frac{d\bar{u}}{dx}\cdot\frac{\delta}{U}$	$\frac{d\bar{u}}{dy}\cdot\frac{\delta}{U}$	$\frac{d\bar{v}}{dx}\cdot\frac{\delta}{U}$	$\frac{d\bar{v}}{dy}\cdot\frac{\delta}{U}$	$P_{xx}\cdot\frac{\delta}{U^3}$	$P_{yy}\cdot\frac{\delta}{U^3}$	$P_{xy}\cdot\frac{\delta}{U^3}$
1.12	1.01	0.0063	0.0063	-8.4E-06	7.8E-07	1.9E-04	7.1E-05	7.1E-05	0.0E+00	-3.7E-10	8.4E-09
1.10	1.01	0.0066	0.0067	-1.0E-05	-2.8E-05	3.8E-04	1.6E-04	-1.7E-04	-7.5E-09	-1.9E-08	2.8E-08
1.07	1.01	0.0075	0.0071	-1.3E-05	-2.8E-05	5.5E-04	2.0E-04	-3.4E-04	-1.5E-08	-3.5E-08	4.8E-08
1.05	1.01	0.0087	0.0075	-1.6E-05	3.4E-06	6.8E-04	2.0E-04	-3.8E-04	-2.2E-08	-4.5E-08	6.3E-08
1.02	1.00	0.0103	0.0076	-1.9E-05	2.1E-05	8.7E-04	1.4E-04	-2.5E-04	-3.2E-08	-3.6E-08	7.3E-08
1.00	1.00	0.0123	0.0075	-2.1E-05	2.7E-06	1.0E-03	5.0E-05	-2.5E-06	-3.9E-08	-5.0E-09	6.7E-08
0.95	0.99	0.0159	0.0075	-2.2E-05	2.6E-05	1.1E-03	-1.6E-04	5.2E-04	-2.8E-08	6.1E-08	4.1E-09
0.93	0.99	0.0189	0.0079	-2.5E-05	2.0E-04	1.8E-03	-2.5E-04	6.3E-04	5.3E-08	9.4E-08	-3.1E-09
0.90	0.98	0.0233	0.0092	-4.6E-05	2.2E-04	1.9E-03	-3.1E-04	7.7E-04	6.3E-08	1.6E-07	-5.7E-08
0.88	0.98	0.0251	0.0097	-5.4E-05	1.2E-04	1.7E-03	-2.5E-04	7.7E-04	-3.5E-08	1.7E-07	-3.7E-08
0.86	0.97	0.0276	0.0102	-7.4E-05	-4.8E-05	2.2E-03	-1.2E-04	5.4E-04	-4.1E-07	1.3E-07	1.1E-07
0.83	0.96	0.0311	0.0121	-1.2E-04	-2.2E-04	2.9E-03	3.5E-05	1.9E-04	-1.2E-06	3.8E-08	4.9E-07
0.79	0.94	0.0366	0.0162	-2.4E-04	-3.0E-04	3.7E-03	3.6E-04	-7.0E-04	-2.6E-06	-5.7E-07	1.7E-06
0.76	0.93	0.0392	0.0189	-3.2E-04	-3.2E-04	4.2E-03	4.2E-04	-1.0E-03	-3.7E-06	-1.0E-06	2.6E-06
0.74	0.91	0.0422	0.0210	-4.0E-04	-3.1E-04	4.1E-03	3.7E-04	-9.3E-04	-4.3E-06	-1.1E-06	2.9E-06
0.71	0.90	0.0429	0.0210	-3.9E-04	-2.4E-04	3.7E-03	1.9E-04	-5.2E-04	-3.8E-06	-6.4E-07	2.3E-06
0.69	0.89	0.0435	0.0209	-3.7E-04	-1.2E-04	3.8E-03	-2.2E-05	-7.3E-05	-3.3E-06	-4.1E-08	1.7E-06
0.67	0.88	0.0459	0.0210	-3.8E-04	-6.8E-06	4.0E-03	-2.4E-04	3.3E-04	-3.1E-06	4.5E-07	1.2E-06
0.64	0.87	0.0482	0.0213	-3.8E-04	9.7E-05	4.0E-03	-4.4E-04	7.1E-04	-2.6E-06	9.9E-07	4.8E-07
0.62	0.86	0.0502	0.0236	-4.3E-04	2.5E-04	3.7E-03	-6.3E-04	1.1E-03	-1.9E-06	1.8E-06	-1.0E-07
0.57	0.84	0.0537	0.0269	-4.9E-04	3.8E-04	3.6E-03	-9.2E-04	1.5E-03	-1.4E-06	3.0E-06	-9.5E-07
0.55	0.83	0.0571	0.0293	-6.3E-04	3.9E-04	4.1E-03	-7.8E-04	1.4E-03	-2.5E-06	3.4E-06	-1.6E-07
0.52	0.82	0.0621	0.0327	-8.8E-04	5.0E-04	4.3E-03	-5.5E-04	1.2E-03	-3.7E-06	3.5E-06	1.1E-06
0.50	0.81	0.0646	0.0350	-1.0E-03	-1.3E-04	4.5E-03	3.1E-05	6.6E-04	-1.0E-05	1.5E-06	5.2E-06
0.48	0.80	0.0677	0.0374	-1.2E-03	-6.3E-04	5.9E-03	5.4E-04	-2.9E-04	-2.1E-05	-2.3E-06	1.2E-05
0.45	0.78	0.0738	0.0414	-1.6E-03	-8.1E-04	6.9E-03	9.6E-04	-1.1E-03	-3.1E-05	-7.2E-06	2.0E-05
0.43	0.77	0.0786	0.0447	-1.9E-03	-1.1E-03	7.2E-03	1.3E-03	-1.8E-03	-4.1E-05	-1.2E-05	2.8E-05
0.41	0.75	0.0810	0.0459	-2.0E-03	-1.3E-03	7.7E-03	1.5E-03	-2.1E-03	-4.9E-05	-1.5E-05	3.3E-05
0.38	0.73	0.0828	0.0460	-2.1E-03	-1.1E-03	7.9E-03	1.4E-03	-1.9E-03	-4.8E-05	-1.4E-05	3.3E-05
0.36	0.72	0.0850	0.0455	-2.0E-03	-9.5E-04	7.9E-03	1.1E-03	-1.5E-03	-4.6E-05	-1.1E-05	2.9E-05
0.33	0.70	0.0881	0.0456	-1.9E-03	-7.1E-04	8.0E-03	7.5E-04	-1.1E-03	-4.2E-05	-7.7E-06	2.6E-05
0.31	0.69	0.0923	0.0474	-1.9E-03	-3.4E-04	8.1E-03	4.0E-04	-6.6E-04	-3.7E-05	-4.5E-06	2.4E-05
0.29	0.67	0.0957	0.0487	-2.0E-03	9.7E-05	8.1E-03	-8.5E-06	-9.2E-05	-3.0E-05	-5.1E-07	1.9E-05
0.26	0.66	0.0977	0.0494	-2.0E-03	4.5E-04	8.0E-03	-3.5E-04	5.4E-04	-2.3E-05	4.1E-06	1.4E-05
0.24	0.64	0.1006	0.0511	-2.1E-03	7.8E-04	7.9E-03	-6.6E-04	1.0E-03	-1.7E-05	8.0E-06	1.0E-05
0.19	0.61	0.1080	0.0535	-2.1E-03	1.6E-03	6.6E-03	-1.3E-03	1.0E-03	9.0E-06	1.1E-05	-1.7E-06
0.17	0.61	0.1139	0.0575	-2.1E-03	1.8E-03	4.5E-03	-1.4E-03	6.2E-04	2.6E-05	1.0E-05	-8.1E-06
0.14	0.60	0.1311	0.0742	-1.9E-03	1.8E-03	6.2E-03	-1.7E-03	6.8E-04	3.8E-05	1.4E-05	9.6E-07
0.12	0.59	0.1480	0.0819	-2.1E-03	2.1E-03	1.1E-02	-1.7E-03	1.1E-03	4.6E-05	2.2E-05	3.0E-05
0.10	0.57	0.1723	0.0862	-2.8E-03	1.4E-03	1.7E-02	-2.0E-03	5.0E-04	-8.5E-06	1.9E-05	6.0E-05
0.07	0.54	0.2416	0.0939	-1.7E-03	-6.4E-03	1.9E-02	-6.6E-04	6.3E-04	-8.8E-04	1.4E-05	1.4E-04

Table 15: WPG smooth wall PIV kinematic values at test location 1.

$\frac{y}{\delta}$	$\frac{U_{eff}}{U_{eff,e}}$	$\frac{\sqrt{\overline{u'^2}}}{U}$	$\frac{\sqrt{\overline{v'^2}}}{U}$	$\frac{\overline{u'v'}}{U^2}$	$\frac{d\bar{u}}{dx}\cdot\frac{\delta}{U}$	$\frac{d\bar{u}}{dy}\cdot\frac{\delta}{U}$	$\frac{d\bar{v}}{dx}\cdot\frac{\delta}{U}$	$\frac{d\bar{v}}{dy}\cdot\frac{\delta}{U}$	$P_{xx}\cdot\frac{\delta}{U^3}$	$P_{yy}\cdot\frac{\delta}{U^3}$	$P_{xy}\cdot\frac{\delta}{U^3}$
1.19	1.00	0.0094	0.0078	2.4E-07	-3.0E-05	4.5E-05	1.4E-06	2.5E-05	-3.1E-09	5.5E-09	0.0E+00
1.17	1.00	0.0098	0.0083	2.2E-07	-4.4E-05	4.7E-05	-2.5E-05	-2.4E-05	-1.0E-08	-2.9E-09	-6.2E-10
1.14	1.00	0.0100	0.0084	1.6E-06	-3.0E-05	6.8E-06	-5.7E-05	-7.6E-05	-1.0E-08	-1.1E-08	-8.4E-09
1.11	1.00	0.0103	0.0082	1.2E-06	-5.4E-05	4.7E-05	-8.6E-05	-1.7E-04	-1.0E-08	-2.7E-08	-9.5E-09
1.08	1.00	0.0106	0.0086	2.5E-07	-7.5E-05	1.3E-04	-1.0E-04	-2.8E-04	-1.6E-08	-4.3E-08	-4.4E-09
1.06	1.00	0.0110	0.0090	-2.1E-06	-8.6E-05	2.3E-04	-1.1E-04	-3.4E-04	-2.2E-08	-5.5E-08	4.1E-09
1.03	1.00	0.0116	0.0093	-4.5E-06	-9.1E-05	3.3E-04	-1.2E-04	-3.3E-04	-2.5E-08	-6.1E-08	1.4E-08
1.00	1.00	0.0125	0.0094	-2.9E-06	-1.2E-04	4.8E-04	-1.1E-04	-3.3E-04	-4.0E-08	-6.1E-08	3.0E-08
0.97	1.00	0.0140	0.0100	-1.1E-05	-1.0E-04	6.7E-04	-8.2E-05	-3.5E-04	-5.6E-08	-6.8E-08	5.6E-08
0.94	0.99	0.0148	0.0103	-1.6E-05	-7.1E-05	8.7E-04	-5.0E-05	-3.1E-04	-5.9E-08	-6.2E-08	8.8E-08
0.92	0.99	0.0162	0.0107	-2.7E-05	-7.6E-05	1.1E-03	-2.1E-05	-2.5E-04	-1.0E-07	-5.4E-08	1.3E-07
0.89	0.99	0.0178	0.0111	-4.0E-05	-1.1E-04	1.4E-03	8.1E-06	-1.7E-04	-1.8E-07	-4.3E-08	1.8E-07
0.86	0.98	0.0193	0.0116	-5.1E-05	-1.6E-04	1.7E-03	4.3E-05	-8.8E-05	-3.0E-07	-3.0E-08	2.6E-07
0.83	0.97	0.0222	0.0117	-6.6E-05	-1.3E-04	2.1E-03	4.4E-05	-1.0E-04	-4.1E-07	-3.1E-08	3.3E-07
0.81	0.96	0.0249	0.0128	-9.8E-05	-1.7E-04	2.2E-03	5.0E-05	-6.9E-05	-6.6E-07	-3.3E-08	4.3E-07
0.78	0.95	0.0269	0.0133	-1.1E-04	-1.4E-04	2.4E-03	5.9E-05	-2.4E-05	-7.5E-07	-2.2E-08	4.9E-07
0.75	0.95	0.0292	0.0139	-1.4E-04	-1.1E-04	2.7E-03	5.8E-05	-3.1E-05	-9.3E-07	-2.9E-08	6.0E-07
0.72	0.93	0.0320	0.0150	-1.8E-04	-1.1E-04	3.0E-03	5.2E-05	-8.7E-05	-1.3E-06	-5.8E-08	7.8E-07
0.69	0.92	0.0352	0.0160	-2.2E-04	-1.0E-04	3.3E-03	5.4E-05	-7.4E-05	-1.7E-06	-6.1E-08	9.6E-07
0.67	0.91	0.0379	0.0173	-2.7E-04	1.1E-05	3.1E-03	2.8E-05	6.1E-05	-1.7E-06	2.1E-08	9.6E-07
0.64	0.90	0.0388	0.0170	-2.7E-04	5.9E-05	3.2E-03	2.2E-05	6.5E-05	-1.6E-06	2.1E-08	9.3E-07
0.61	0.89	0.0400	0.0174	-2.9E-04	3.0E-05	3.3E-03	4.3E-05	2.1E-05	-1.8E-06	-1.4E-08	1.1E-06
0.58	0.88	0.0414	0.0182	-3.2E-04	-6.1E-05	3.6E-03	8.1E-05	-5.1E-05	-2.5E-06	-8.4E-08	1.3E-06
0.56	0.87	0.0431	0.0191	-3.6E-04	-1.3E-04	3.7E-03	1.0E-04	-9.0E-05	-3.1E-06	-1.5E-07	1.6E-06
0.53	0.86	0.0464	0.0209	-4.3E-04	-4.1E-05	4.1E-03	2.3E-05	-1.4E-04	-3.7E-06	-1.4E-07	1.9E-06
0.50	0.84	0.0505	0.0223	-5.2E-04	-3.5E-05	4.3E-03	3.8E-06	-6.3E-05	-4.6E-06	-6.0E-08	2.2E-06
0.47	0.83	0.0534	0.0236	-6.0E-04	-1.0E-05	4.2E-03	1.4E-05	3.0E-05	-5.1E-06	2.4E-08	2.4E-06
0.45	0.82	0.0550	0.0244	-6.3E-04	-2.5E-05	4.3E-03	2.5E-05	5.5E-05	-5.6E-06	3.4E-08	2.6E-06
0.42	0.81	0.0562	0.0247	-6.4E-04	-1.0E-04	4.6E-03	3.1E-05	-6.1E-06	-6.5E-06	-4.8E-08	3.0E-06
0.39	0.79	0.0611	0.0261	-7.4E-04	-9.6E-05	5.0E-03	2.3E-05	-9.4E-05	-8.1E-06	-1.6E-07	3.6E-06
0.36	0.78	0.0647	0.0274	-8.3E-04	-3.4E-05	5.0E-03	2.7E-06	2.7E-05	-8.5E-06	4.0E-08	3.7E-06
0.33	0.77	0.0671	0.0282	-8.6E-04	-7.1E-05	5.1E-03	-1.7E-05	2.1E-04	-9.4E-06	3.6E-07	3.9E-06
0.31	0.75	0.0704	0.0290	-8.9E-04	-5.7E-05	5.5E-03	-9.2E-06	2.7E-04	-1.0E-05	4.7E-07	4.4E-06
0.28	0.74	0.0755	0.0314	-9.8E-04	-3.4E-05	5.9E-03	-6.8E-07	2.5E-04	-1.2E-05	5.0E-07	5.6E-06
0.25	0.72	0.0814	0.0361	-1.1E-03	-7.8E-05	5.8E-03	-4.1E-05	2.4E-04	-1.4E-05	7.0E-07	7.1E-06
0.22	0.71	0.0884	0.0396	-1.2E-03	-1.5E-04	3.6E-03	4.1E-05	-3.5E-05	-1.1E-05	-2.4E-07	6.2E-06
0.20	0.71	0.1016	0.0539	-1.3E-03	1.3E-04	4.2E-03	2.6E-05	4.2E-05	-8.1E-06	2.2E-07	1.3E-05
0.17	0.69	0.1200	0.0679	-1.5E-03	-1.2E-04	7.9E-03	4.3E-05	1.0E-04	-2.9E-05	8.9E-07	4.0E-05
0.14	0.67	0.1477	0.0827	-2.0E-03	-8.0E-04	1.1E-02	4.4E-05	8.4E-06	-8.6E-05	-4.3E-07	7.9E-05
0.11	0.64	0.1889	0.0939	-2.7E-03	-1.4E-03	1.1E-02	-1.9E-05	-4.7E-04	-1.7E-04	-7.2E-06	1.0E-04
0.08	0.62	0.2448	0.0866	-2.1E-03	-1.9E-03	8.0E-03	-1.8E-04	-1.6E-03	-2.6E-04	-2.3E-05	5.6E-05
0.06	0.61	0.2443	0.0392	1.8E-05	-7.7E-04	6.3E-03	6.4E-04	-3.0E-03	-9.8E-05	-8.1E-06	5.3E-05

Table 16: WPG square roughness PIV kinematic values at test location 1.

$\frac{y}{\delta}$	$\frac{U_{eff}}{U_{eff,e}}$	$\frac{\sqrt{\overline{u'^2}}}{U}$	$\frac{\sqrt{\overline{v'^2}}}{U}$	$\frac{\overline{u'v'}}{U^2}$	$\frac{d\bar{u}}{dx}\cdot\frac{\delta}{U}$	$\frac{d\bar{u}}{dy}\cdot\frac{\delta}{U}$	$\frac{d\bar{v}}{dx}\cdot\frac{\delta}{U}$	$\frac{d\bar{v}}{dy}\cdot\frac{\delta}{U}$	$P_{xx}\cdot\frac{\delta}{U^3}$	$P_{yy}\cdot\frac{\delta}{U^3}$	$P_{xy}\cdot\frac{\delta}{U^3}$
1.24	1.01	0.0029	0.0036	-5.4E-07	-2.5E-05	1.5E-05	-4.8E-05	-1.2E-04	0.0E+00	0.0E+00	0.0E+00
1.21	1.01	0.0035	0.0039	-1.1E-06	-2.5E-05	8.1E-06	-4.9E-05	-1.4E-04	0.0E+00	0.0E+00	0.0E+00
1.18	1.01	0.0038	0.0040	-1.8E-06	-2.6E-05	-2.0E-06	-4.9E-05	-1.4E-04	0.0E+00	0.0E+00	0.0E+00
1.15	1.01	0.0044	0.0040	-1.9E-06	-1.8E-05	3.8E-05	-4.1E-05	-1.1E-04	0.0E+00	0.0E+00	0.0E+00
1.12	1.01	0.0050	0.0043	-2.8E-06	-1.9E-05	9.8E-05	-2.2E-05	-8.9E-05	0.0E+00	0.0E+00	0.0E+00
1.09	1.01	0.0058	0.0047	-4.1E-06	-2.5E-05	2.0E-04	-1.2E-05	-7.1E-05	-5.0E-09	0.0E+00	6.1E-09
1.06	1.00	0.0069	0.0051	-6.7E-06	-2.5E-05	3.3E-04	-1.2E-05	-5.1E-05	-8.8E-09	0.0E+00	9.9E-09
1.03	1.00	0.0086	0.0056	-9.9E-06	-2.6E-05	5.1E-04	-1.4E-05	-2.1E-05	-1.5E-08	0.0E+00	1.4E-08
1.00	1.00	0.0108	0.0061	-1.3E-05	-4.8E-05	7.8E-04	-9.6E-06	9.7E-07	-3.5E-08	0.0E+00	2.6E-08
0.97	1.00	0.0140	0.0064	-2.0E-05	-9.5E-05	1.3E-03	2.5E-06	-3.1E-05	-8.8E-08	0.0E+00	5.7E-08
0.94	0.99	0.0188	0.0076	-3.9E-05	-7.8E-05	1.7E-03	6.0E-06	-3.3E-05	-2.0E-07	-7.0E-09	1.1E-07
0.91	0.98	0.0230	0.0082	-5.7E-05	-6.3E-05	1.8E-03	6.4E-06	-1.0E-05	-2.7E-07	-2.4E-09	1.3E-07
0.88	0.97	0.0259	0.0091	-7.2E-05	-6.4E-05	2.0E-03	1.7E-05	-4.0E-05	-3.8E-07	-9.2E-09	1.9E-07
0.85	0.96	0.0285	0.0103	-9.3E-05	-7.5E-05	2.4E-03	3.5E-05	-8.9E-05	-5.6E-07	-2.5E-08	3.0E-07
0.82	0.95	0.0316	0.0117	-1.2E-04	-6.9E-05	2.7E-03	3.8E-05	-8.4E-05	-8.1E-07	-3.1E-08	4.3E-07
0.79	0.94	0.0353	0.0128	-1.6E-04	-6.3E-05	2.8E-03	1.8E-05	-4.0E-05	-1.0E-06	-1.8E-08	4.9E-07
0.76	0.93	0.0369	0.0149	-1.9E-04	-2.6E-04	2.9E-03	8.8E-05	-8.4E-06	-1.8E-06	-4.2E-08	8.4E-07
0.73	0.92	0.0393	0.0166	-2.3E-04	-2.4E-04	3.2E-03	8.3E-05	5.4E-05	-2.2E-06	-5.1E-09	1.1E-06
0.70	0.91	0.0416	0.0175	-2.6E-04	-1.6E-04	3.4E-03	4.1E-05	1.3E-04	-2.3E-06	6.0E-08	1.1E-06
0.67	0.90	0.0442	0.0181	-2.9E-04	-1.2E-04	3.8E-03	1.7E-05	1.6E-04	-2.7E-06	9.3E-08	1.3E-06
0.64	0.88	0.0482	0.0199	-3.6E-04	-1.7E-04	4.3E-03	4.4E-05	1.3E-04	-3.9E-06	6.8E-08	1.8E-06
0.61	0.87	0.0537	0.0243	-5.1E-04	-2.7E-04	4.5E-03	3.1E-05	1.1E-04	-6.2E-06	9.4E-08	2.9E-06
0.58	0.85	0.0578	0.0265	-6.0E-04	-2.6E-04	4.9E-03	4.7E-05	1.4E-04	-7.6E-06	1.3E-07	3.7E-06
0.55	0.83	0.0634	0.0282	-7.3E-04	-2.2E-04	5.6E-03	4.3E-05	1.1E-04	-1.0E-05	1.1E-07	4.7E-06
0.52	0.82	0.0710	0.0308	-9.5E-04	-3.9E-04	6.2E-03	7.1E-05	1.0E-04	-1.6E-05	5.8E-08	6.6E-06
0.49	0.80	0.0790	0.0336	-1.2E-03	-4.2E-04	6.5E-03	7.3E-05	1.4E-04	-2.1E-05	1.5E-07	8.1E-06
0.47	0.78	0.0860	0.0363	-1.4E-03	-2.1E-04	6.6E-03	4.6E-05	1.7E-04	-2.2E-05	3.2E-07	9.1E-06
0.44	0.76	0.0920	0.0385	-1.6E-03	-1.4E-04	7.2E-03	4.6E-05	1.1E-04	-2.6E-05	1.7E-07	1.1E-05
0.41	0.74	0.1004	0.0408	-1.9E-03	-3.3E-04	7.8E-03	4.5E-05	1.5E-04	-3.7E-05	3.1E-07	1.4E-05
0.38	0.72	0.1080	0.0447	-2.2E-03	-1.2E-04	8.2E-03	-1.4E-06	6.9E-05	-3.9E-05	2.9E-07	1.7E-05
0.35	0.70	0.1167	0.0490	-2.8E-03	-1.1E-04	8.4E-03	-3.7E-06	9.1E-05	-4.9E-05	4.6E-07	2.0E-05
0.32	0.68	0.1243	0.0508	-3.1E-03	-7.0E-05	8.6E-03	2.5E-05	2.5E-04	-5.5E-05	1.1E-06	2.2E-05
0.29	0.66	0.1317	0.0511	-3.2E-03	2.5E-05	8.9E-03	3.6E-05	4.5E-04	-5.6E-05	2.1E-06	2.2E-05
0.26	0.64	0.1410	0.0536	-3.6E-03	5.4E-05	9.8E-03	-3.1E-05	5.2E-04	-6.8E-05	3.2E-06	2.6E-05
0.23	0.62	0.1559	0.0623	-4.4E-03	-1.1E-04	1.0E-02	-1.1E-04	5.0E-04	-9.8E-05	4.9E-06	3.6E-05
0.20	0.59	0.1733	0.0661	-4.8E-03	-2.5E-03	1.4E-02	8.1E-05	-3.0E-04	-2.4E-04	-3.5E-06	7.7E-05
0.17	0.56	0.2548	0.0741	-5.4E-03	-2.4E-04	2.3E-02	1.3E-04	-2.5E-04	-1.1E-04	-4.1E-06	1.4E-04
0.14	0.51	0.3589	0.0835	-6.7E-03	1.4E-03	3.0E-02	2.3E-04	2.7E-04	1.7E-04	6.8E-07	2.3E-04
0.11	0.46	0.4552	0.0937	-8.4E-03	2.1E-03	3.3E-02	3.6E-04	7.9E-04	4.6E-04	7.9E-06	3.3E-04
0.08	0.41	0.5258	0.1080	-9.4E-03	1.6E-03	3.2E-02	3.3E-04	5.2E-04	4.1E-04	5.5E-06	4.5E-04
0.05	0.38	0.5908	0.1283	-1.0E-02	-5.1E-06	5.0E-02	2.6E-04	-4.8E-04	-9.1E-04	-2.0E-05	9.4E-04

Table 17: WPG diamond roughness peak PIV kinematic values at test location 1.

$\frac{y}{\delta}$	$\frac{U_{eff}}{U_{eff,e}}$	$\frac{\sqrt{\overline{u'^2}}}{U}$	$\frac{\sqrt{\overline{v'^2}}}{U}$	$\frac{\overline{u'v'}}{U^2}$	$\frac{d\bar{u}}{dx}\cdot\frac{\delta}{U}$	$\frac{d\bar{u}}{dy}\cdot\frac{\delta}{U}$	$\frac{d\bar{v}}{dx}\cdot\frac{\delta}{U}$	$\frac{d\bar{v}}{dy}\cdot\frac{\delta}{U}$	$P_{xx}\cdot\frac{\delta}{U^3}$	$P_{yy}\cdot\frac{\delta}{U^3}$	$P_{xy}\cdot\frac{\delta}{U^3}$
1.20	1.01	0.0039	0.0040	-2.0E-06	3.6E-05	2.1E-05	-1.3E-04	3.5E-04	0.0E+00	1.0E-08	0.0E+00
1.17	1.01	0.0039	0.0041	-2.0E-06	2.1E-05	8.3E-05	-9.3E-05	2.2E-04	0.0E+00	7.0E-09	0.0E+00
1.14	1.01	0.0040	0.0042	-2.2E-06	-1.0E-05	1.2E-04	-3.5E-05	3.3E-05	0.0E+00	-2.7E-09	9.0E-10
1.11	1.01	0.0043	0.0046	-2.4E-06	-5.0E-05	2.0E-04	5.7E-05	-1.9E-04	-4.4E-11	-1.2E-08	2.0E-09
1.08	1.01	0.0049	0.0048	-4.8E-06	-3.4E-05	3.5E-04	1.3E-04	-3.9E-04	-1.1E-09	-2.1E-08	1.1E-08
1.06	1.00	0.0053	0.0050	-7.2E-06	-5.9E-05	4.6E-04	1.7E-04	-4.6E-04	-8.2E-09	-2.9E-08	2.0E-08
1.03	1.00	0.0063	0.0051	-9.8E-06	-7.7E-05	5.6E-04	1.7E-04	-4.3E-04	-1.6E-08	-2.6E-08	2.8E-08
1.00	1.00	0.0075	0.0052	-1.2E-05	-5.3E-05	5.8E-04	1.2E-04	-3.1E-04	-1.7E-08	-1.6E-08	2.7E-08
0.97	1.00	0.0087	0.0052	-1.2E-05	2.3E-05	5.5E-04	2.7E-05	-9.7E-05	-6.5E-09	-3.6E-09	1.7E-08
0.94	1.00	0.0100	0.0052	-1.3E-05	1.3E-04	5.6E-04	-6.6E-05	1.6E-04	9.2E-09	1.3E-08	8.3E-09
0.92	0.99	0.0119	0.0052	-1.4E-05	1.3E-04	7.5E-04	-1.5E-04	3.6E-04	1.8E-08	2.2E-08	-8.7E-09
0.89	0.99	0.0145	0.0061	-1.7E-05	2.2E-04	9.7E-04	-1.9E-04	5.3E-04	6.8E-08	4.5E-08	-1.8E-08
0.86	0.99	0.0173	0.0069	-2.2E-05	1.9E-04	1.3E-03	-1.9E-04	5.7E-04	5.6E-08	6.2E-08	-1.4E-08
0.83	0.98	0.0206	0.0076	-3.4E-05	1.0E-04	1.7E-03	-1.3E-04	4.7E-04	-4.5E-08	6.0E-08	3.0E-08
0.80	0.97	0.0240	0.0085	-5.3E-05	-4.0E-06	2.1E-03	-1.5E-05	2.4E-04	-2.5E-07	2.4E-08	1.5E-07
0.78	0.96	0.0271	0.0103	-8.7E-05	-9.1E-05	2.6E-03	1.5E-04	-1.0E-04	-5.9E-07	-5.4E-08	4.1E-07
0.75	0.95	0.0298	0.0115	-1.3E-04	-2.3E-04	3.0E-03	3.1E-04	-5.6E-04	-1.2E-06	-2.3E-07	7.8E-07
0.72	0.94	0.0315	0.0123	-1.6E-04	-3.7E-04	3.4E-03	4.1E-04	-9.0E-04	-1.8E-06	-4.1E-07	1.1E-06
0.69	0.93	0.0318	0.0134	-1.8E-04	-3.8E-04	3.7E-03	4.6E-04	-9.3E-04	-2.1E-06	-5.0E-07	1.4E-06
0.66	0.91	0.0322	0.0138	-1.8E-04	-3.3E-04	3.8E-03	3.9E-04	-7.3E-04	-2.1E-06	-4.1E-07	1.3E-06
0.64	0.90	0.0334	0.0134	-1.7E-04	-2.3E-04	3.7E-03	1.7E-04	-4.2E-04	-1.8E-06	-2.0E-07	9.5E-07
0.61	0.89	0.0349	0.0143	-1.9E-04	2.0E-05	3.5E-03	-1.0E-04	-9.3E-05	-1.3E-06	-6.2E-09	6.0E-07
0.58	0.88	0.0376	0.0150	-2.1E-04	2.7E-04	3.4E-03	-3.5E-04	2.8E-04	-6.7E-07	2.7E-07	1.6E-07
0.55	0.87	0.0395	0.0160	-2.2E-04	2.8E-04	3.6E-03	-4.6E-04	6.2E-04	-6.9E-07	5.2E-07	2.9E-08
0.52	0.85	0.0419	0.0172	-2.3E-04	3.4E-04	3.6E-03	-5.5E-04	1.0E-03	-4.6E-07	8.5E-07	-2.1E-07
0.50	0.84	0.0445	0.0191	-2.6E-04	4.2E-04	3.5E-03	-6.7E-04	1.4E-03	-1.7E-07	1.4E-06	-5.2E-07
0.47	0.83	0.0478	0.0219	-3.4E-04	4.9E-04	3.5E-03	-7.9E-04	1.6E-03	-1.3E-07	2.1E-06	-8.1E-07
0.44	0.82	0.0523	0.0249	-4.6E-04	5.1E-04	3.7E-03	-8.3E-04	1.7E-03	-6.9E-07	2.8E-06	-9.3E-07
0.41	0.81	0.0553	0.0273	-6.0E-04	4.0E-04	4.3E-03	-6.6E-04	1.3E-03	-2.7E-06	2.8E-06	1.1E-07
0.38	0.80	0.0606	0.0305	-8.6E-04	2.1E-06	5.3E-03	-1.9E-04	5.9E-04	-9.3E-06	1.3E-06	3.9E-06
0.36	0.78	0.0678	0.0345	-1.2E-03	-3.5E-04	6.4E-03	3.3E-04	-3.0E-04	-1.9E-05	-1.8E-06	1.0E-05
0.33	0.76	0.0755	0.0374	-1.6E-03	-7.5E-04	7.5E-03	8.3E-04	-1.2E-03	-3.3E-05	-6.1E-06	1.9E-05
0.30	0.74	0.0841	0.0400	-1.9E-03	-1.1E-03	8.4E-03	1.2E-03	-1.8E-03	-4.9E-05	-1.1E-05	2.8E-05
0.27	0.72	0.0930	0.0436	-2.3E-03	-1.4E-03	8.8E-03	1.5E-03	-1.9E-03	-6.5E-05	-1.4E-05	3.7E-05
0.24	0.70	0.1002	0.0450	-2.4E-03	-1.4E-03	8.8E-03	1.4E-03	-1.5E-03	-7.2E-05	-1.3E-05	3.9E-05
0.22	0.68	0.1028	0.0454	-2.4E-03	-1.3E-03	5.8E-03	1.2E-03	-1.2E-03	-5.6E-05	-1.1E-05	3.1E-05
0.19	0.67	0.1071	0.0506	-2.5E-03	-1.4E-03	5.7E-03	1.2E-03	-9.7E-04	-6.0E-05	-1.1E-05	3.4E-05
0.16	0.66	0.1158	0.0556	-2.6E-03	-1.2E-03	8.8E-03	1.1E-03	-7.4E-04	-7.8E-05	-1.0E-05	4.7E-05
0.13	0.63	0.1281	0.0605	-2.9E-03	-9.0E-04	1.3E-02	7.8E-04	-4.2E-04	-1.0E-04	-7.2E-06	6.2E-05
0.10	0.61	0.1422	0.0676	-3.2E-03	-6.8E-04	1.4E-02	5.4E-04	1.8E-04	-1.1E-04	-1.7E-06	7.5E-05
0.08	0.58	0.1590	0.0739	-3.2E-03	4.7E-05	1.4E-02	4.5E-04	1.1E-03	-8.4E-05	9.1E-06	8.2E-05

Table 18: WPG diamond roughness valley PIV kinematic values at test location 1.

$\frac{y}{\delta}$	$\frac{U_{eff}}{U_{eff,e}}$	$\frac{\sqrt{\overline{u'^2}}}{U}$	$\frac{\sqrt{\overline{v'^2}}}{U}$	$\frac{\overline{u'v'}}{U^2}$	$\frac{d\bar{u}}{dx}\cdot\frac{\delta}{U}$	$\frac{d\bar{u}}{dy}\cdot\frac{\delta}{U}$	$\frac{d\bar{v}}{dx}\cdot\frac{\delta}{U}$	$\frac{d\bar{v}}{dy}\cdot\frac{\delta}{U}$	$P_{xx}\cdot\frac{\delta}{U^3}$	$P_{yy}\cdot\frac{\delta}{U^3}$	$P_{xy}\cdot\frac{\delta}{U^3}$
1.32	1.01	0.0028	0.0043	-1.3E-06	-2.0E-05	2.3E-04	1.0E-04	-3.5E-04	0.0E+00	-1.2E-08	9.3E-09
1.29	1.01	0.0032	0.0044	-2.1E-06	-5.0E-05	1.4E-04	1.2E-04	-3.6E-04	0.0E+00	-1.6E-08	9.1E-09
1.25	1.01	0.0037	0.0044	-3.6E-06	-3.8E-05	1.3E-04	8.4E-05	-2.5E-04	0.0E+00	-9.9E-09	7.5E-09
1.22	1.01	0.0038	0.0042	-3.7E-06	-1.9E-05	1.1E-04	2.0E-05	-8.5E-05	0.0E+00	-2.5E-09	1.3E-09
1.19	1.01	0.0040	0.0041	-3.7E-06	-4.0E-06	6.0E-05	-5.4E-05	1.0E-04	0.0E+00	5.4E-09	0.0E+00
1.16	1.01	0.0043	0.0040	-3.7E-06	1.5E-05	4.3E-05	-1.1E-04	2.5E-04	0.0E+00	9.4E-09	0.0E+00
1.13	1.01	0.0046	0.0041	-3.9E-06	4.6E-05	8.4E-05	-1.3E-04	3.3E-04	0.0E+00	1.1E-08	0.0E+00
1.10	1.01	0.0052	0.0045	-4.2E-06	6.9E-05	1.3E-04	-1.2E-04	3.5E-04	0.0E+00	1.6E-08	5.4E-10
1.06	1.01	0.0058	0.0050	-5.2E-06	1.9E-05	2.0E-04	-7.3E-05	2.5E-04	0.0E+00	1.6E-08	2.2E-09
1.03	1.00	0.0071	0.0052	-7.8E-06	-2.2E-05	5.3E-04	5.5E-06	8.0E-05	-9.1E-09	1.3E-09	1.8E-08
1.00	1.00	0.0106	0.0066	-1.9E-05	-7.2E-05	9.8E-04	9.2E-05	-1.5E-04	-6.0E-08	-2.2E-08	6.3E-08
0.97	0.99	0.0147	0.0076	-3.6E-05	-1.2E-04	1.4E-03	1.7E-04	-3.7E-04	-1.6E-07	-5.8E-08	1.4E-07
0.94	0.99	0.0189	0.0079	-5.5E-05	-1.6E-04	1.8E-03	2.2E-04	-5.0E-04	-3.1E-07	-8.8E-08	2.2E-07
0.90	0.98	0.0226	0.0080	-7.1E-05	-1.7E-04	2.0E-03	2.1E-04	-4.8E-04	-4.5E-07	-9.4E-08	2.8E-07
0.87	0.97	0.0256	0.0085	-8.3E-05	-7.1E-05	2.1E-03	1.5E-04	-3.5E-04	-4.4E-07	-7.4E-08	2.9E-07
0.84	0.96	0.0272	0.0086	-7.9E-05	-8.5E-06	2.1E-03	2.6E-05	-1.3E-04	-3.4E-07	-2.3E-08	1.9E-07
0.81	0.95	0.0283	0.0087	-8.0E-05	2.2E-05	2.1E-03	-1.0E-04	1.6E-04	-2.9E-07	4.4E-08	5.9E-08
0.78	0.94	0.0288	0.0091	-8.1E-05	1.3E-04	2.2E-03	-2.1E-04	4.5E-04	-1.4E-07	1.2E-07	-3.7E-08
0.75	0.93	0.0290	0.0102	-8.5E-05	1.9E-04	2.3E-03	-3.1E-04	7.1E-04	-5.0E-08	2.1E-07	-9.9E-08
0.71	0.92	0.0297	0.0118	-9.4E-05	1.4E-04	2.2E-03	-3.8E-04	8.9E-04	-1.6E-07	3.3E-07	-1.2E-07
0.68	0.92	0.0335	0.0130	-1.3E-04	1.7E-04	2.1E-03	-3.8E-04	1.0E-03	-1.4E-07	4.3E-07	-2.1E-07
0.65	0.91	0.0352	0.0171	-1.9E-04	1.1E-04	2.2E-03	-2.4E-04	8.6E-04	-5.9E-07	5.9E-07	1.7E-07
0.62	0.90	0.0367	0.0194	-2.6E-04	-1.3E-05	2.7E-03	1.2E-05	2.4E-04	-1.5E-06	1.5E-07	1.0E-06
0.59	0.89	0.0377	0.0197	-3.0E-04	-2.0E-04	3.4E-03	3.2E-04	-4.4E-04	-2.6E-06	-5.4E-07	2.0E-06
0.55	0.87	0.0409	0.0206	-3.7E-04	-4.1E-04	4.1E-03	6.1E-04	-9.9E-04	-4.6E-06	-1.4E-06	3.4E-06
0.52	0.86	0.0453	0.0221	-4.9E-04	-5.9E-04	4.7E-03	8.1E-04	-1.3E-03	-7.0E-06	-2.1E-06	4.9E-06
0.49	0.84	0.0492	0.0238	-5.9E-04	-6.6E-04	5.1E-03	8.6E-04	-1.5E-03	-9.3E-06	-2.7E-06	6.3E-06
0.46	0.82	0.0539	0.0247	-6.8E-04	-6.3E-04	5.6E-03	7.4E-04	-1.4E-03	-1.1E-05	-2.7E-06	7.0E-06
0.43	0.80	0.0584	0.0255	-7.2E-04	-5.9E-04	5.9E-03	4.8E-04	-1.0E-03	-1.3E-05	-2.0E-06	6.6E-06
0.39	0.78	0.0639	0.0266	-7.9E-04	-3.1E-04	5.9E-03	1.9E-04	-5.2E-04	-1.2E-05	-1.0E-06	5.6E-06
0.36	0.77	0.0685	0.0285	-8.6E-04	-8.8E-05	6.0E-03	-7.9E-05	-9.0E-06	-1.1E-05	1.7E-07	4.6E-06
0.33	0.75	0.0737	0.0309	-9.8E-04	1.3E-04	6.2E-03	-2.9E-04	4.5E-04	-1.1E-05	1.5E-06	3.7E-06
0.30	0.73	0.0798	0.0336	-1.1E-03	3.8E-04	6.1E-03	-4.5E-04	8.7E-04	-9.1E-06	3.0E-06	2.6E-06
0.27	0.71	0.0832	0.0360	-1.2E-03	4.2E-04	6.5E-03	-6.4E-04	1.2E-03	-9.6E-06	4.7E-06	2.0E-06
0.24	0.70	0.0888	0.0377	-1.2E-03	-3.2E-04	9.4E-03	-9.1E-04	1.5E-03	-2.8E-05	6.4E-06	4.8E-06
0.20	0.67	0.1165	0.0384	-1.3E-03	-6.6E-03	8.8E-03	-1.0E-03	9.5E-04	-3.3E-04	5.5E-06	4.5E-06
0.17	0.65	0.1421	0.0446	-1.6E-03	-1.0E-02	1.6E-02	-1.1E-03	7.1E-04	-6.2E-04	6.3E-06	2.3E-05
0.14	0.60	0.1923	0.0525	-1.9E-03	-1.2E-02	2.6E-02	-1.2E-03	1.1E-03	-1.2E-03	1.1E-05	4.3E-05
0.11	0.53	0.2617	0.0612	-2.4E-03	-1.2E-02	3.4E-02	-1.2E-03	1.5E-03	-2.0E-03	1.7E-05	6.5E-05
0.08	0.48	0.2288	0.0692	-2.8E-03	-7.1E-03	3.3E-02	-1.1E-03	9.8E-04	-9.4E-04	1.5E-05	1.2E-04

Table 19: WPG smooth wall PIV kinematic values at test location 2.

$\frac{y}{\delta}$	$\frac{U_{eff}}{U_{eff,e}}$	$\frac{\sqrt{\overline{u'^2}}}{U}$	$\frac{\sqrt{\overline{v'^2}}}{U}$	$\frac{\overline{u'v'}}{U^2}$	$\frac{d\bar{u}}{dx}\cdot\frac{\delta}{U}$	$\frac{d\bar{u}}{dy}\cdot\frac{\delta}{U}$	$\frac{d\bar{v}}{dx}\cdot\frac{\delta}{U}$	$\frac{d\bar{v}}{dy}\cdot\frac{\delta}{U}$	$P_{xx}\cdot\frac{\delta}{U^3}$	$P_{yy}\cdot\frac{\delta}{U^3}$	$P_{xy}\cdot\frac{\delta}{U^3}$
1.43	1.01	0.0078	0.0049	1.9E-06	6.2E-05	9.7E-05	1.2E-05	5.7E-05	9.1E-09	0.0E+00	0.0E+00
1.40	1.01	0.0076	0.0050	1.8E-06	7.8E-05	1.1E-04	1.1E-05	6.4E-05	1.1E-08	0.0E+00	0.0E+00
1.37	1.01	0.0076	0.0050	1.1E-06	8.1E-05	2.8E-05	3.7E-06	8.1E-05	1.3E-08	0.0E+00	0.0E+00
1.33	1.01	0.0075	0.0050	8.8E-07	7.3E-05	1.3E-05	-9.3E-06	8.1E-05	1.1E-08	0.0E+00	0.0E+00
1.30	1.01	0.0078	0.0052	-8.4E-07	9.6E-05	4.1E-05	-2.9E-06	7.0E-05	1.1E-08	0.0E+00	0.0E+00
1.27	1.01	0.0077	0.0053	-1.0E-06	6.7E-05	6.1E-05	-2.7E-05	6.2E-05	1.1E-08	0.0E+00	4.5E-10
1.23	1.01	0.0078	0.0053	-1.1E-06	4.3E-05	4.4E-05	-8.6E-06	6.5E-05	1.0E-09	0.0E+00	0.0E+00
1.20	1.01	0.0080	0.0055	-2.1E-06	6.4E-05	9.9E-05	-1.6E-05	7.7E-05	9.1E-09	0.0E+00	0.0E+00
1.17	1.01	0.0081	0.0058	-3.2E-06	7.1E-05	9.6E-05	-2.7E-05	6.7E-05	6.1E-09	0.0E+00	0.0E+00
1.13	1.01	0.0085	0.0060	-4.2E-06	1.2E-04	1.4E-04	-5.0E-05	8.2E-05	1.8E-08	4.0E-09	0.0E+00
1.10	1.01	0.0092	0.0064	-5.3E-06	7.8E-05	2.2E-04	-5.8E-05	1.1E-04	6.8E-09	1.1E-08	0.0E+00
1.07	1.00	0.0100	0.0068	-6.5E-06	2.0E-05	2.8E-04	-5.5E-05	9.7E-05	-3.4E-09	1.1E-08	5.3E-09
1.03	1.00	0.0108	0.0073	-8.8E-06	8.7E-06	4.3E-04	-7.6E-05	1.1E-04	-7.4E-09	1.1E-08	1.1E-08
1.00	1.00	0.0118	0.0078	-1.4E-05	1.7E-05	6.4E-04	-9.4E-05	1.7E-04	-1.6E-08	2.6E-08	2.1E-08
0.97	1.00	0.0138	0.0091	-2.1E-05	3.5E-05	8.6E-04	-9.2E-05	2.2E-04	-2.4E-08	4.2E-08	5.1E-08
0.93	0.99	0.0160	0.0098	-3.0E-05	3.0E-05	9.4E-04	-1.3E-04	2.4E-04	-4.3E-08	5.5E-08	5.0E-08
0.90	0.99	0.0173	0.0100	-3.2E-05	-1.8E-05	1.1E-03	-1.5E-04	2.8E-04	-8.2E-08	6.9E-08	5.8E-08
0.87	0.98	0.0198	0.0105	-4.6E-05	1.9E-05	1.7E-03	-1.8E-04	4.0E-04	-1.4E-07	1.1E-07	1.0E-07
0.83	0.97	0.0244	0.0129	-8.4E-05	4.4E-05	1.9E-03	-2.1E-04	5.0E-04	-2.7E-07	2.0E-07	1.5E-07
0.80	0.96	0.0274	0.0141	-1.2E-04	8.6E-05	1.9E-03	-2.4E-04	4.5E-04	-3.0E-07	2.3E-07	1.3E-07
0.77	0.95	0.0297	0.0147	-1.4E-04	9.1E-05	2.0E-03	-2.4E-04	4.6E-04	-4.2E-07	2.7E-07	1.4E-07
0.73	0.95	0.0325	0.0161	-1.9E-04	1.0E-04	2.2E-03	-1.9E-04	4.1E-04	-6.1E-07	2.8E-07	2.7E-07
0.70	0.94	0.0345	0.0172	-2.3E-04	9.9E-05	2.4E-03	-1.5E-04	3.0E-04	-8.4E-07	2.5E-07	4.5E-07
0.67	0.92	0.0370	0.0184	-2.7E-04	2.8E-05	2.5E-03	-9.0E-05	2.3E-04	-1.3E-06	2.0E-07	6.6E-07
0.63	0.91	0.0391	0.0191	-3.2E-04	4.9E-05	2.7E-03	-7.4E-05	1.9E-04	-1.6E-06	1.9E-07	8.0E-07
0.60	0.90	0.0410	0.0201	-3.6E-04	1.1E-04	2.8E-03	-7.2E-05	1.4E-04	-1.7E-06	1.6E-07	9.4E-07
0.57	0.89	0.0427	0.0212	-4.1E-04	7.7E-05	3.0E-03	-4.1E-05	7.0E-05	-2.2E-06	9.5E-08	1.2E-06
0.53	0.88	0.0445	0.0216	-4.3E-04	1.3E-04	3.3E-03	-3.7E-05	3.2E-05	-2.3E-06	5.8E-08	1.4E-06
0.50	0.87	0.0481	0.0227	-5.0E-04	1.2E-04	3.4E-03	-2.6E-05	3.4E-05	-2.9E-06	6.2E-08	1.6E-06
0.47	0.85	0.0497	0.0240	-5.6E-04	1.3E-04	3.3E-03	3.7E-06	8.0E-05	-3.0E-06	9.1E-08	1.8E-06
0.43	0.84	0.0508	0.0241	-5.7E-04	1.9E-04	3.5E-03	-1.1E-05	6.9E-05	-3.0E-06	9.4E-08	1.8E-06
0.40	0.83	0.0527	0.0250	-6.1E-04	2.0E-04	3.7E-03	1.1E-05	8.6E-06	-3.4E-06	1.7E-09	2.3E-06
0.37	0.81	0.0543	0.0263	-6.6E-04	1.9E-04	3.8E-03	1.2E-05	-1.7E-05	-3.8E-06	-4.1E-08	2.5E-06
0.33	0.80	0.0567	0.0272	-7.0E-04	1.8E-04	4.1E-03	-2.5E-05	-6.0E-05	-4.6E-06	-4.6E-08	2.8E-06
0.30	0.79	0.0604	0.0281	-8.0E-04	1.6E-04	4.3E-03	-1.6E-05	-2.8E-05	-5.8E-06	-1.7E-08	3.3E-06
0.27	0.77	0.0633	0.0288	-8.6E-04	1.8E-04	4.5E-03	-3.6E-06	-2.3E-05	-6.3E-06	-3.1E-08	3.6E-06
0.23	0.76	0.0655	0.0282	-8.6E-04	2.0E-04	4.9E-03	5.1E-06	-1.5E-05	-6.8E-06	-3.1E-08	3.8E-06
0.20	0.74	0.0687	0.0289	-9.2E-04	3.0E-04	5.4E-03	-1.2E-05	1.6E-04	-7.2E-06	2.9E-07	4.1E-06
0.17	0.73	0.0729	0.0300	-9.7E-04	2.1E-04	6.2E-03	-3.8E-07	2.2E-04	-9.7E-06	3.8E-07	5.1E-06
0.13	0.71	0.0792	0.0308	-1.1E-03	2.5E-04	7.2E-03	2.6E-05	3.3E-04	-1.2E-05	5.8E-07	6.4E-06
0.10	0.69	0.0900	0.0329	-1.1E-03	5.7E-04	6.6E-03	-3.8E-05	-2.8E-04	-4.9E-06	-5.3E-07	6.5E-06
0.07	0.67	0.1115	0.0493	-1.3E-03	1.3E-03	1.0E-02	-1.4E-04	-5.0E-04	7.4E-06	-2.0E-06	2.2E-05

Table 20: WPG square roughness PIV kinematic values at test location 2.

$\frac{y}{\delta}$	$\frac{U_{eff}}{U_{eff,e}}$	$\frac{\sqrt{\overline{u'^2}}}{U}$	$\frac{\sqrt{\overline{v'^2}}}{U}$	$\frac{\overline{u'v'}}{U^2}$	$\frac{d\bar{u}}{dx}\cdot\frac{\delta}{U}$	$\frac{d\bar{u}}{dy}\cdot\frac{\delta}{U}$	$\frac{d\bar{v}}{dx}\cdot\frac{\delta}{U}$	$\frac{d\bar{v}}{dy}\cdot\frac{\delta}{U}$	$P_{xx}\cdot\frac{\delta}{U^3}$	$P_{yy}\cdot\frac{\delta}{U^3}$	$P_{xy}\cdot\frac{\delta}{U^3}$
1.24	1.01	0.0069	0.0060	-1.2E-06	2.6E-05	-1.7E-05	-8.5E-06	6.6E-05	0.0E+00	1.6E-09	0.0E+00
1.21	1.01	0.0073	0.0066	-3.2E-07	3.2E-05	-2.5E-05	-1.7E-05	6.3E-05	0.0E+00	0.0E+00	0.0E+00
1.18	1.01	0.0077	0.0069	-1.8E-06	1.9E-05	1.9E-06	-2.7E-05	6.4E-05	0.0E+00	1.8E-09	0.0E+00
1.15	1.01	0.0084	0.0067	-2.9E-06	2.2E-05	6.3E-05	-5.6E-05	8.5E-05	0.0E+00	1.2E-08	0.0E+00
1.12	1.01	0.0089	0.0071	-4.0E-06	-1.5E-05	1.9E-04	-5.6E-05	1.4E-04	0.0E+00	1.3E-08	0.0E+00
1.09	1.01	0.0114	0.0079	-7.9E-06	3.2E-06	4.6E-04	-5.6E-05	1.4E-04	-1.1E-08	1.5E-08	2.4E-08
1.07	1.01	0.0140	0.0089	-1.6E-05	2.1E-05	4.5E-04	-6.5E-05	1.7E-04	-1.1E-08	2.6E-08	1.5E-08
1.04	1.01	0.0127	0.0088	-1.2E-05	2.8E-05	6.6E-04	-8.1E-05	1.9E-04	-6.8E-09	2.8E-08	3.3E-08
1.01	1.00	0.0158	0.0098	-2.4E-05	-6.8E-06	1.1E-03	-7.0E-05	2.5E-04	-5.6E-08	4.7E-08	8.1E-08
0.98	1.00	0.0182	0.0108	-3.3E-05	-4.6E-06	1.2E-03	-9.4E-05	3.2E-04	-7.9E-08	8.0E-08	9.9E-08
0.95	0.99	0.0199	0.0117	-4.3E-05	5.2E-05	1.5E-03	-1.2E-04	3.1E-04	-8.9E-08	8.8E-08	1.5E-07
0.93	0.99	0.0236	0.0131	-6.4E-05	1.1E-04	2.0E-03	-1.2E-04	3.3E-04	-1.4E-07	1.3E-07	2.6E-07
0.90	0.98	0.0274	0.0151	-9.4E-05	1.3E-04	2.1E-03	-1.3E-04	3.4E-04	-1.9E-07	1.8E-07	3.3E-07
0.87	0.97	0.0297	0.0160	-1.2E-04	1.8E-04	2.1E-03	-1.4E-04	3.8E-04	-1.7E-07	2.2E-07	3.4E-07
0.84	0.96	0.0320	0.0165	-1.4E-04	2.2E-04	2.6E-03	-1.2E-04	3.8E-04	-2.7E-07	2.4E-07	5.3E-07
0.81	0.95	0.0366	0.0181	-2.0E-04	2.5E-04	3.1E-03	-1.3E-04	3.0E-04	-5.5E-07	2.5E-07	7.4E-07
0.78	0.94	0.0408	0.0195	-2.6E-04	2.1E-04	3.2E-03	-1.2E-04	3.0E-04	-9.5E-07	3.0E-07	8.7E-07
0.76	0.93	0.0443	0.0214	-3.3E-04	8.6E-05	3.8E-03	-8.4E-05	2.6E-04	-2.2E-06	2.9E-07	1.5E-06
0.73	0.91	0.0504	0.0247	-4.7E-04	9.8E-05	4.2E-03	-4.9E-05	2.6E-04	-3.5E-06	3.6E-07	2.3E-06
0.70	0.90	0.0555	0.0274	-6.2E-04	1.7E-04	4.0E-03	-2.0E-06	3.9E-04	-3.9E-06	5.9E-07	2.7E-06
0.67	0.88	0.0583	0.0282	-6.4E-04	2.9E-04	3.9E-03	-5.6E-05	4.9E-04	-3.1E-06	8.5E-07	2.5E-06
0.64	0.87	0.0606	0.0300	-7.5E-04	2.2E-04	4.3E-03	-3.3E-05	4.1E-04	-4.8E-06	7.9E-07	3.3E-06
0.62	0.86	0.0640	0.0315	-8.8E-04	4.3E-04	4.8E-03	-1.2E-04	2.4E-04	-4.8E-06	7.0E-07	3.6E-06
0.59	0.84	0.0677	0.0346	-1.0E-03	8.9E-05	5.7E-03	7.7E-06	-2.1E-06	-1.1E-05	-3.6E-08	6.9E-06
0.56	0.82	0.0769	0.0395	-1.4E-03	3.0E-04	6.1E-03	-7.1E-05	-7.0E-05	-1.4E-05	-1.7E-08	8.8E-06
0.53	0.81	0.0809	0.0422	-1.6E-03	3.6E-04	5.9E-03	-1.4E-04	1.2E-05	-1.4E-05	4.8E-07	8.9E-06
0.50	0.79	0.0863	0.0446	-1.8E-03	3.5E-04	5.8E-03	-1.2E-04	-1.4E-05	-1.6E-05	3.8E-07	9.9E-06
0.47	0.77	0.0889	0.0460	-2.0E-03	6.0E-04	5.9E-03	-1.4E-04	6.3E-05	-1.4E-05	8.0E-07	1.0E-05
0.45	0.76	0.0946	0.0487	-2.2E-03	4.8E-04	6.6E-03	-9.6E-05	-4.5E-05	-2.1E-05	2.0E-07	1.4E-05
0.42	0.74	0.1010	0.0516	-2.4E-03	4.4E-04	6.7E-03	-8.6E-05	-5.3E-05	-2.4E-05	1.5E-07	1.6E-05
0.39	0.72	0.1051	0.0541	-2.6E-03	4.3E-04	6.8E-03	-1.3E-05	1.4E-04	-2.6E-05	8.4E-07	1.8E-05
0.36	0.71	0.1103	0.0560	-2.9E-03	3.7E-04	7.2E-03	1.9E-05	-6.8E-05	-3.2E-05	-5.6E-07	2.2E-05
0.33	0.69	0.1169	0.0591	-3.1E-03	2.6E-04	7.7E-03	2.1E-05	-2.2E-04	-4.1E-05	-1.6E-06	2.7E-05
0.30	0.67	0.1235	0.0629	-3.5E-03	1.0E-04	8.0E-03	4.4E-05	-9.4E-06	-5.2E-05	-3.4E-07	3.2E-05
0.28	0.65	0.1291	0.0656	-3.7E-03	2.9E-06	8.3E-03	5.9E-05	1.1E-05	-6.2E-05	-3.4E-07	3.7E-05
0.25	0.64	0.1371	0.0699	-4.1E-03	1.1E-05	9.2E-03	3.0E-05	-1.1E-04	-7.5E-05	-1.4E-06	4.6E-05
0.22	0.62	0.1441	0.0734	-4.6E-03	2.5E-04	1.0E-02	1.3E-04	-3.5E-05	-8.2E-05	-1.6E-06	5.5E-05
0.19	0.60	0.1563	0.0780	-5.0E-03	3.8E-05	1.1E-02	1.0E-04	5.2E-05	-1.1E-04	-4.2E-07	6.7E-05
0.16	0.58	0.1705	0.0807	-5.3E-03	-1.7E-04	1.5E-02	2.9E-04	1.2E-04	-1.7E-04	-1.5E-06	1.1E-04
0.14	0.54	0.2403	0.0876	-6.5E-03	-5.2E-03	2.7E-02	2.9E-04	-5.8E-04	-9.8E-04	-1.3E-05	2.6E-04
0.11	0.49	0.3628	0.1043	-9.3E-03	-4.2E-03	2.8E-02	4.4E-04	-9.2E-04	-1.6E-03	-2.8E-05	4.1E-04
0.08	0.46	0.4189	0.1257	-1.1E-02	8.1E-04	3.5E-02	2.0E-04	-1.8E-03	-4.8E-04	-6.2E-05	6.0E-04

Table 21: WPG diamond roughness peak PIV kinematic values at test location 2.

$\frac{y}{\delta}$	$\frac{U_{eff}}{U_{eff,e}}$	$\frac{\sqrt{\overline{u'^2}}}{U}$	$\frac{\sqrt{\overline{v'^2}}}{U}$	$\frac{\overline{u'v'}}{U^2}$	$\frac{d\bar{u}}{dx}\cdot\frac{\delta}{U}$	$\frac{d\bar{u}}{dy}\cdot\frac{\delta}{U}$	$\frac{d\bar{v}}{dx}\cdot\frac{\delta}{U}$	$\frac{d\bar{v}}{dy}\cdot\frac{\delta}{U}$	$P_{xx}\cdot\frac{\delta}{U^3}$	$P_{yy}\cdot\frac{\delta}{U^3}$	$P_{xy}\cdot\frac{\delta}{U^3}$
1.36	1.01	0.0065	0.0049	-3.0E-06	-7.8E-05	2.3E-04	8.5E-05	-2.6E-04	-1.3E-08	-1.3E-08	1.3E-08
1.30	1.01	0.0063	0.0047	-2.7E-06	6.3E-06	1.0E-04	-1.4E-05	3.9E-05	0.0E+00	1.4E-09	-4.3E-10
1.27	1.01	0.0065	0.0047	-1.1E-06	5.1E-05	-1.3E-05	-9.1E-05	2.4E-04	2.1E-09	1.5E-08	-2.4E-09
1.24	1.01	0.0064	0.0049	-2.2E-06	8.0E-05	-7.5E-05	-1.5E-04	4.4E-04	1.3E-08	2.6E-08	-1.3E-08
1.22	1.01	0.0065	0.0053	-2.9E-06	7.2E-05	-4.4E-05	-1.4E-04	4.5E-04	8.6E-09	2.6E-08	-8.6E-09
1.16	1.01	0.0064	0.0062	-5.4E-06	-2.1E-05	2.3E-04	6.6E-05	-6.7E-05	-6.1E-09	-1.2E-08	1.3E-08
1.13	1.01	0.0066	0.0066	-7.1E-06	-5.6E-05	3.8E-04	1.7E-04	-3.4E-04	-1.2E-08	-3.2E-08	2.5E-08
1.10	1.01	0.0066	0.0067	-9.9E-06	-5.7E-05	4.5E-04	2.0E-04	-4.5E-04	-1.3E-08	-4.7E-08	3.5E-08
1.07	1.00	0.0069	0.0068	-1.2E-05	-2.2E-05	4.5E-04	1.3E-04	-3.0E-04	-1.3E-08	-3.4E-08	3.0E-08
1.04	1.00	0.0074	0.0067	-1.2E-05	3.0E-05	3.6E-04	-2.3E-05	6.8E-05	-3.1E-09	2.9E-09	1.7E-08
1.01	1.00	0.0078	0.0067	-1.3E-05	8.6E-05	2.9E-04	-1.6E-04	4.8E-04	-4.9E-10	4.5E-08	-7.0E-09
0.98	1.00	0.0088	0.0068	-1.4E-05	1.5E-04	3.3E-04	-2.8E-04	7.8E-04	1.3E-08	7.6E-08	-2.4E-08
0.96	1.00	0.0101	0.0072	-1.6E-05	1.8E-04	4.4E-04	-3.0E-04	8.7E-04	2.6E-08	1.1E-07	-2.5E-08
0.93	1.00	0.0117	0.0079	-2.1E-05	1.2E-04	8.4E-04	-2.1E-04	7.2E-04	3.6E-11	9.7E-08	5.3E-09
0.90	0.99	0.0150	0.0092	-3.4E-05	2.7E-05	1.5E-03	-4.8E-05	3.7E-04	-9.7E-08	6.2E-08	1.1E-07
0.87	0.98	0.0190	0.0106	-6.0E-05	-4.3E-05	2.2E-03	1.9E-04	-1.9E-04	-3.1E-07	-7.5E-08	3.5E-07
0.81	0.96	0.0265	0.0118	-1.2E-04	-1.8E-04	3.0E-03	4.1E-04	-8.1E-04	-9.7E-07	-3.2E-07	8.2E-07
0.78	0.95	0.0283	0.0120	-1.3E-04	-1.3E-04	3.1E-03	3.3E-04	-5.7E-04	-9.8E-07	-2.5E-07	8.0E-07
0.75	0.94	0.0297	0.0123	-1.3E-04	-2.2E-05	3.1E-03	1.3E-04	-1.6E-04	-8.5E-07	-9.5E-08	6.2E-07
0.72	0.93	0.0306	0.0122	-1.2E-04	1.9E-04	3.1E-03	-1.2E-04	3.5E-04	-4.0E-07	1.3E-07	3.0E-07
0.70	0.91	0.0314	0.0130	-1.1E-04	4.0E-04	3.2E-03	-4.8E-04	9.5E-04	7.1E-08	4.4E-07	-8.3E-08
0.67	0.90	0.0337	0.0151	-1.2E-04	5.0E-04	3.2E-03	-8.0E-04	1.8E-03	3.3E-07	1.0E-06	-4.4E-07
0.64	0.89	0.0351	0.0193	-1.5E-04	5.1E-04	3.0E-03	-1.0E-03	2.6E-03	3.7E-07	2.3E-06	-6.4E-07
0.58	0.87	0.0403	0.0261	-3.1E-04	5.8E-04	3.0E-03	-8.3E-04	2.1E-03	-5.6E-08	3.3E-06	3.4E-08
0.55	0.86	0.0453	0.0285	-4.8E-04	3.4E-04	4.0E-03	-3.1E-04	1.0E-03	-2.6E-06	1.8E-06	2.2E-06
0.52	0.85	0.0519	0.0312	-7.1E-04	1.1E-04	5.1E-03	3.3E-04	-4.2E-04	-7.0E-06	-1.6E-06	6.4E-06
0.49	0.83	0.0581	0.0344	-9.8E-04	-2.9E-04	6.6E-03	9.2E-04	-2.0E-03	-1.5E-05	-6.8E-06	1.4E-05
0.46	0.81	0.0656	0.0379	-1.3E-03	-6.5E-04	7.4E-03	1.4E-03	-2.7E-03	-2.5E-05	-1.2E-05	2.1E-05
0.41	0.76	0.0740	0.0392	-1.4E-03	-4.8E-04	7.4E-03	9.6E-04	-2.0E-03	-2.7E-05	-8.9E-06	2.0E-05
0.38	0.75	0.0757	0.0376	-1.3E-03	-2.2E-04	7.1E-03	4.9E-04	-1.1E-03	-2.1E-05	-4.7E-06	1.5E-05
0.35	0.73	0.0800	0.0397	-1.3E-03	1.0E-04	1.2E-02	-1.9E-05	-3.3E-04	-3.1E-05	-9.5E-07	2.0E-05
0.32	0.68	0.1808	0.0419	-1.6E-03	1.6E-03	2.3E-02	-5.1E-04	5.5E-04	-1.6E-05	3.5E-06	2.3E-05
0.29	0.62	0.3163	0.0458	-2.7E-03	3.0E-03	4.4E-02	-8.1E-04	7.4E-04	4.2E-04	7.7E-06	-3.6E-06
0.26	0.51	0.5448	0.0520	-6.5E-03	5.0E-03	4.8E-02	-1.5E-03	9.7E-04	2.3E-03	2.5E-05	-3.5E-04
0.23	0.46	0.6184	0.0560	-1.0E-02	2.4E-03	3.6E-02	-1.8E-03	1.4E-03	1.1E-03	4.8E-05	-6.3E-04
0.20	0.41	0.7218	0.0628	-1.8E-02	3.1E-03	3.7E-02	-2.0E-03	1.7E-03	1.8E-03	8.5E-05	-9.8E-04
0.18	0.37	0.7906	0.0695	-2.6E-02	1.2E-04	3.7E-02	-2.0E-03	8.7E-04	-1.8E-03	1.1E-04	-1.1E-03
0.15	0.33	0.8874	0.0808	-3.5E-02	-2.6E-03	3.5E-02	-2.0E-03	-8.4E-05	-6.6E-03	1.4E-04	-1.2E-03
0.12	0.30	0.9513	0.0955	-4.4E-02	-6.7E-03	3.8E-02	-1.8E-03	2.5E-04	-1.5E-02	1.6E-04	-1.0E-03
0.09	0.26	1.0222	0.1084	-5.8E-02	-1.6E-02	5.7E-02	-7.0E-04	-1.3E-03	-4.0E-02	5.7E-05	8.7E-04
0.06	0.21	1.0692	0.1139	-6.6E-02	-2.4E-02	6.2E-02	-1.5E-04	-3.9E-03	-6.4E-02	-7.9E-05	2.5E-03

Table 22: WPG diamond roughness valley PIV kinematic values at test location 2.

$\frac{y}{\delta}$	$\frac{U_{eff}}{U_{eff,e}}$	$\frac{\sqrt{\overline{u'^2}}}{U}$	$\frac{\sqrt{\overline{v'^2}}}{U}$	$\frac{\overline{u'v'}}{U^2}$	$\frac{d\bar{u}}{dx}\cdot\frac{\delta}{U}$	$\frac{d\bar{u}}{dy}\cdot\frac{\delta}{U}$	$\frac{d\bar{v}}{dx}\cdot\frac{\delta}{U}$	$\frac{d\bar{v}}{dy}\cdot\frac{\delta}{U}$	$P_{xx}\cdot\frac{\delta}{U^3}$	$P_{yy}\cdot\frac{\delta}{U^3}$	$P_{xy}\cdot\frac{\delta}{U^3}$
1.33	1.01	0.0069	0.0053	-2.2E-06	-3.0E-05	1.6E-04	4.9E-05	-1.0E-04	-1.3E-09	-6.9E-09	8.2E-09
1.24	1.01	0.0070	0.0053	-2.4E-06	-3.1E-05	1.9E-04	4.5E-05	-9.9E-05	-2.9E-09	-2.9E-09	1.2E-08
1.21	1.01	0.0070	0.0053	-2.7E-06	2.2E-05	1.0E-04	-5.9E-05	1.5E-04	0.0E+00	1.1E-08	1.7E-09
1.18	1.01	0.0070	0.0055	-3.0E-06	7.7E-05	-2.9E-06	-1.6E-04	4.5E-04	1.0E-08	3.3E-08	-1.1E-08
1.15	1.01	0.0070	0.0059	-4.6E-06	1.1E-04	-7.3E-05	-2.4E-04	6.7E-04	1.3E-08	4.9E-08	-2.3E-08
1.13	1.01	0.0069	0.0061	-5.8E-06	1.1E-04	-4.7E-05	-2.5E-04	7.1E-04	1.2E-08	5.0E-08	-1.4E-08
1.10	1.01	0.0070	0.0065	-8.7E-06	7.1E-05	9.0E-05	-1.7E-04	4.9E-04	4.9E-10	3.8E-08	-1.3E-08
1.07	1.01	0.0074	0.0071	-1.2E-05	4.0E-06	3.6E-04	-3.8E-05	1.1E-04	-1.2E-08	1.3E-08	1.2E-08
1.04	1.01	0.0082	0.0078	-1.7E-05	-6.6E-05	6.4E-04	9.8E-05	-2.8E-04	-2.7E-08	-3.9E-08	5.2E-08
1.01	1.00	0.0095	0.0082	-2.3E-05	-1.1E-04	8.8E-04	2.1E-04	-5.7E-04	-5.4E-08	-9.0E-08	9.2E-08
0.98	1.00	0.0109	0.0084	-3.0E-05	-9.0E-05	1.1E-03	2.1E-04	-6.0E-04	-8.2E-08	-1.0E-07	1.2E-07
0.95	0.99	0.0128	0.0084	-3.3E-05	-4.1E-05	1.3E-03	1.1E-04	-3.7E-04	-9.6E-08	-5.9E-08	1.2E-07
0.93	0.99	0.0154	0.0084	-3.4E-05	4.2E-05	1.4E-03	-4.4E-05	3.3E-05	-7.2E-08	8.2E-09	8.5E-08
0.90	0.98	0.0182	0.0084	-3.5E-05	1.8E-04	1.5E-03	-2.3E-04	4.9E-04	1.7E-08	8.2E-08	-3.4E-10
0.87	0.98	0.0212	0.0089	-3.8E-05	2.8E-04	1.5E-03	-3.9E-04	9.3E-04	1.4E-07	1.8E-07	-1.0E-07
0.81	0.96	0.0260	0.0122	-5.1E-05	3.7E-04	1.6E-03	-6.3E-04	1.8E-03	3.3E-07	6.0E-07	-2.8E-07
0.78	0.96	0.0281	0.0154	-7.5E-05	3.3E-04	1.9E-03	-5.9E-04	1.8E-03	2.3E-07	9.3E-07	-1.5E-07
0.75	0.95	0.0299	0.0186	-1.3E-04	2.5E-04	2.4E-03	-2.9E-04	1.3E-03	-1.8E-07	8.8E-07	4.3E-07
0.73	0.94	0.0321	0.0211	-2.0E-04	6.1E-05	3.1E-03	1.3E-04	1.8E-04	-1.2E-06	3.4E-08	1.6E-06
0.70	0.93	0.0354	0.0231	-3.2E-04	-1.4E-04	4.0E-03	5.6E-04	-9.2E-04	-3.0E-06	-1.4E-06	3.2E-06
0.67	0.91	0.0388	0.0245	-4.2E-04	-2.7E-04	4.5E-03	8.1E-04	-1.5E-03	-4.7E-06	-2.5E-06	4.7E-06
0.64	0.89	0.0409	0.0249	-4.6E-04	-2.9E-04	4.8E-03	8.5E-04	-1.5E-03	-5.3E-06	-2.7E-06	5.2E-06
0.61	0.88	0.0437	0.0243	-4.5E-04	-8.8E-05	5.1E-03	5.8E-04	-1.2E-03	-5.0E-06	-2.0E-06	4.7E-06
0.55	0.84	0.0517	0.0263	-5.3E-04	4.1E-04	4.7E-03	-2.6E-04	5.0E-04	-2.8E-06	9.6E-07	2.1E-06
0.52	0.83	0.0537	0.0274	-5.5E-04	5.9E-04	3.9E-03	-6.4E-04	1.5E-03	-8.9E-07	2.9E-06	-1.3E-08
0.50	0.82	0.0510	0.0276	-4.4E-04	6.4E-04	3.5E-03	-9.6E-04	2.1E-03	3.1E-07	4.0E-06	-1.0E-06
0.47	0.81	0.0531	0.0300	-5.1E-04	9.9E-04	3.8E-03	-1.3E-03	2.5E-03	1.7E-06	5.8E-06	-2.0E-06
0.44	0.80	0.0565	0.0315	-6.2E-04	1.1E-03	4.2E-03	-1.4E-03	2.5E-03	2.0E-06	6.8E-06	-2.5E-06
0.41	0.79	0.0620	0.0344	-8.6E-04	1.0E-03	4.4E-03	-1.1E-03	2.1E-03	1.4E-07	6.9E-06	-1.8E-06
0.38	0.77	0.0657	0.0370	-1.1E-03	8.5E-04	5.0E-03	-6.1E-04	1.2E-03	-3.8E-06	4.3E-06	2.5E-06
0.35	0.76	0.0727	0.0410	-1.5E-03	2.9E-04	6.5E-03	2.0E-04	-2.6E-04	-1.7E-05	-2.4E-06	1.3E-05
0.32	0.74	0.0795	0.0457	-2.0E-03	-5.2E-04	7.9E-03	1.1E-03	-1.9E-03	-3.9E-05	-1.4E-05	3.0E-05
0.30	0.72	0.0875	0.0508	-2.5E-03	-1.0E-03	8.8E-03	1.8E-03	-3.1E-03	-6.0E-05	-2.5E-05	4.7E-05
0.27	0.70	0.0926	0.0519	-2.7E-03	-1.3E-03	9.4E-03	2.2E-03	-3.3E-03	-7.4E-05	-3.0E-05	5.7E-05
0.24	0.67	0.0967	0.0520	-2.8E-03	-1.3E-03	9.7E-03	2.1E-03	-2.9E-03	-7.8E-05	-2.7E-05	5.8E-05
0.21	0.65	0.1029	0.0531	-2.8E-03	-1.0E-03	9.9E-03	1.7E-03	-2.2E-03	-7.8E-05	-2.2E-05	5.5E-05
0.18	0.63	0.1112	0.0544	-2.8E-03	-7.4E-04	9.1E-03	1.2E-03	-1.4E-03	-7.0E-05	-1.5E-05	4.8E-05
0.15	0.61	0.1544	0.0604	-2.8E-03	1.5E-03	1.9E-02	9.9E-04	-1.1E-03	2.9E-07	-1.4E-05	9.8E-05
0.12	0.55	0.2882	0.0683	-3.3E-03	-3.7E-04	4.3E-02	9.4E-04	-1.0E-03	-5.1E-04	-1.6E-05	2.8E-04
0.10	0.47	0.4689	0.0735	-4.9E-03	-4.7E-03	5.1E-02	3.3E-04	-3.6E-04	-2.7E-03	-7.2E-06	3.6E-04
0.07	0.41	0.5802	0.0760	-6.8E-03	-1.2E-02	4.1E-02	1.1E-04	7.2E-05	-8.3E-03	-6.1E-07	3.6E-04

Table 23: WPG smooth wall PIV kinematic values at test location 3.

$\frac{y}{\delta}$	$\frac{U_{eff}}{U_{eff,e}}$	$\frac{\sqrt{\overline{u'^2}}}{U}$	$\frac{\sqrt{\overline{v'^2}}}{U}$	$\frac{\overline{u'v'}}{U^2}$	$\frac{d\bar{u}}{dx}\cdot\frac{\delta}{U}$	$\frac{d\bar{u}}{dy}\cdot\frac{\delta}{U}$	$\frac{d\bar{v}}{dx}\cdot\frac{\delta}{U}$	$\frac{d\bar{v}}{dy}\cdot\frac{\delta}{U}$	$P_{xx}\cdot\frac{\delta}{U^3}$	$P_{yy}\cdot\frac{\delta}{U^3}$	$P_{xy}\cdot\frac{\delta}{U^3}$
1.12	1.00	0.0080	0.0161	1.1E-05	-1.2E-04	-4.5E-06	2.7E-05	9.6E-05	-1.6E-08	4.6E-08	0.0E+00
1.09	1.00	0.0078	0.0161	3.7E-06	-9.1E-05	-2.1E-05	-1.1E-06	5.9E-05	-1.6E-08	3.4E-08	-1.2E-08
1.07	1.00	0.0079	0.0160	3.1E-06	-8.9E-05	4.9E-05	-3.4E-05	7.2E-05	-1.6E-08	4.0E-08	6.4E-09
1.04	1.00	0.0085	0.0160	3.3E-07	-9.1E-05	1.3E-04	-6.3E-05	1.7E-04	-1.6E-08	8.3E-08	2.6E-08
1.02	1.00	0.0091	0.0163	-5.7E-06	-9.4E-05	1.4E-04	-1.7E-04	2.3E-04	-1.8E-08	1.2E-07	2.3E-08
1.00	1.00	0.0095	0.0166	-1.1E-05	-9.7E-05	1.9E-04	-1.2E-04	1.8E-04	-2.3E-08	9.9E-08	3.7E-08
0.97	1.00	0.0103	0.0166	-1.6E-05	-9.8E-05	3.8E-04	-6.6E-05	1.4E-04	-3.5E-08	7.9E-08	9.6E-08
0.95	1.00	0.0123	0.0168	-3.2E-05	-4.7E-05	5.6E-04	-3.5E-05	5.0E-05	-5.0E-08	3.1E-08	1.5E-07
0.92	1.00	0.0142	0.0172	-5.0E-05	-4.6E-05	6.6E-04	2.1E-05	4.6E-05	-8.2E-08	2.6E-08	2.0E-07
0.90	0.99	0.0162	0.0179	-7.0E-05	-2.6E-05	9.3E-04	-1.7E-07	1.3E-05	-1.4E-07	1.1E-08	3.0E-07
0.88	0.99	0.0185	0.0188	-1.1E-04	-1.5E-05	1.1E-03	-3.2E-05	-2.0E-04	-2.5E-07	-1.3E-07	4.0E-07
0.85	0.99	0.0205	0.0182	-1.2E-04	-3.4E-05	1.3E-03	7.0E-05	-2.0E-04	-3.6E-07	-1.4E-07	5.0E-07
0.80	0.98	0.0239	0.0185	-1.6E-04	-4.9E-05	1.8E-03	5.6E-05	-9.3E-05	-6.2E-07	-8.2E-08	6.7E-07
0.78	0.97	0.0256	0.0192	-1.7E-04	4.7E-05	2.1E-03	-5.1E-05	-7.3E-05	-6.8E-07	-3.5E-08	7.4E-07
0.76	0.96	0.0273	0.0199	-2.0E-04	2.1E-06	2.1E-03	-2.8E-05	9.5E-07	-8.5E-07	1.3E-08	8.2E-07
0.73	0.95	0.0276	0.0196	-2.0E-04	9.8E-05	2.4E-03	4.0E-05	-7.6E-05	-7.9E-07	-7.3E-08	9.3E-07
0.71	0.95	0.0293	0.0203	-2.4E-04	1.4E-04	2.6E-03	4.3E-05	-2.0E-04	-1.0E-06	-2.0E-07	1.1E-06
0.68	0.94	0.0305	0.0208	-2.7E-04	1.9E-04	2.0E-03	-4.6E-05	6.7E-05	-7.1E-07	8.6E-08	7.5E-07
0.64	0.92	0.0313	0.0216	-3.1E-04	1.9E-04	3.0E-03	-7.6E-05	-1.6E-04	-1.5E-06	-9.5E-08	1.3E-06
0.61	0.91	0.0322	0.0225	-3.2E-04	2.1E-04	2.4E-03	-9.8E-05	-1.6E-05	-1.1E-06	4.7E-08	1.1E-06
0.59	0.91	0.0332	0.0231	-3.4E-04	2.3E-04	2.4E-03	-7.1E-05	5.6E-05	-1.1E-06	1.1E-07	1.1E-06
0.54	0.89	0.0359	0.0250	-3.9E-04	3.7E-04	3.0E-03	-7.3E-05	-1.5E-05	-1.4E-06	3.8E-08	1.6E-06
0.51	0.88	0.0382	0.0256	-4.3E-04	3.1E-04	3.1E-03	-1.3E-04	-2.2E-04	-1.7E-06	-1.7E-07	1.8E-06
0.49	0.87	0.0396	0.0252	-4.5E-04	1.9E-04	3.0E-03	-9.0E-05	-2.4E-04	-2.1E-06	-2.2E-07	1.8E-06
0.47	0.87	0.0404	0.0260	-4.9E-04	2.1E-04	3.1E-03	-1.2E-04	-2.0E-04	-2.3E-06	-1.4E-07	1.9E-06
0.44	0.86	0.0419	0.0277	-5.4E-04	1.9E-04	3.1E-03	-1.1E-04	-8.8E-05	-2.7E-06	-1.0E-08	2.1E-06
0.42	0.85	0.0437	0.0285	-5.7E-04	2.2E-04	3.3E-03	-6.6E-05	-1.8E-04	-2.9E-06	-2.2E-07	2.5E-06
0.39	0.84	0.0447	0.0295	-5.9E-04	3.6E-04	3.7E-03	-7.8E-05	-6.3E-05	-3.0E-06	-7.6E-09	2.9E-06
0.37	0.83	0.0469	0.0303	-5.9E-04	5.7E-04	3.5E-03	-5.8E-05	-7.0E-05	-1.7E-06	-6.5E-08	2.8E-06
0.35	0.82	0.0483	0.0314	-6.3E-04	4.5E-04	3.4E-03	7.5E-05	-1.6E-04	-2.2E-06	-4.2E-07	3.4E-06
0.32	0.81	0.0492	0.0322	-6.5E-04	3.6E-04	3.3E-03	6.5E-05	-6.3E-05	-2.5E-06	-2.1E-07	3.4E-06
0.30	0.81	0.0494	0.0325	-6.5E-04	2.4E-04	3.2E-03	1.5E-05	1.6E-05	-3.1E-06	7.3E-09	3.3E-06
0.27	0.80	0.0497	0.0329	-6.9E-04	4.7E-05	3.3E-03	2.7E-05	9.7E-05	-4.2E-06	1.5E-07	3.5E-06
0.25	0.79	0.0531	0.0348	-6.8E-04	2.1E-04	3.3E-03	-1.5E-04	-5.2E-04	-3.2E-06	-1.1E-06	3.7E-06
0.23	0.78	0.0550	0.0352	-7.2E-04	1.2E-04	4.0E-03	-9.7E-05	-6.3E-04	-5.1E-06	-1.4E-06	5.0E-06
0.20	0.77	0.0567	0.0358	-7.9E-04	-2.0E-04	4.4E-03	-8.2E-05	-3.4E-04	-8.2E-06	-7.4E-07	5.7E-06
0.18	0.76	0.0632	0.0386	-9.0E-04	-1.6E-04	4.8E-03	-7.7E-05	-7.3E-04	-9.9E-06	-2.0E-06	7.7E-06
0.15	0.75	0.0650	0.0397	-9.2E-04	-1.9E-05	6.0E-03	1.8E-06	-5.8E-04	-1.1E-05	-1.8E-06	1.0E-05
0.13	0.74	0.0748	0.0455	-1.0E-03	-1.2E-04	7.7E-03	-1.8E-05	-3.7E-04	-1.7E-05	-1.6E-06	1.6E-05
0.11	0.72	0.0819	0.0487	-1.2E-03	-4.9E-04	8.8E-03	-1.9E-04	-2.3E-04	-2.7E-05	-8.4E-07	2.0E-05
0.08	0.70	0.0866	0.0500	-1.3E-03	-7.2E-04	9.6E-03	-2.9E-04	8.1E-04	-3.6E-05	4.9E-06	2.2E-05
0.06	0.68	0.1039	0.0561	-1.3E-03	8.2E-05	1.2E-02	-7.2E-04	-1.0E-04	-2.4E-05	4.8E-07	3.0E-05

Table 24: WPG square roughness PIV kinematic values at test location 3.

$\frac{y}{\delta}$	$\frac{U_{eff}}{U_{eff,e}}$	$\frac{\sqrt{\overline{u'^2}}}{U}$	$\frac{\sqrt{\overline{v'^2}}}{U}$	$\frac{\overline{u'v'}}{U^2}$	$\frac{d\bar{u}}{dx}\cdot\frac{\delta}{U}$	$\frac{d\bar{u}}{dy}\cdot\frac{\delta}{U}$	$\frac{d\bar{v}}{dx}\cdot\frac{\delta}{U}$	$\frac{d\bar{v}}{dy}\cdot\frac{\delta}{U}$	$P_{xx}\cdot\frac{\delta}{U^3}$	$P_{yy}\cdot\frac{\delta}{U^3}$	$P_{xy}\cdot\frac{\delta}{U^3}$
1.17	1.01	0.0083	0.0106	-1.9E-06	1.3E-05	1.6E-04	-3.9E-05	2.2E-04	5.3E-10	5.1E-08	1.5E-08
1.14	1.01	0.0085	0.0109	-3.5E-06	4.9E-05	1.7E-04	-5.0E-05	1.5E-04	3.8E-09	3.2E-08	1.6E-08
1.12	1.01	0.0091	0.0116	-3.8E-06	4.6E-05	1.7E-04	-3.0E-05	2.2E-04	2.6E-09	6.4E-08	2.2E-08
1.07	1.01	0.0101	0.0124	-8.9E-06	7.2E-05	4.6E-04	-9.9E-06	3.0E-04	3.0E-10	9.1E-08	6.9E-08
1.04	1.01	0.0108	0.0130	-9.1E-06	7.6E-05	5.2E-04	1.1E-05	3.3E-04	6.7E-09	1.1E-07	8.6E-08
1.02	1.01	0.0117	0.0136	-1.3E-05	6.7E-05	6.8E-04	-1.1E-06	3.0E-04	3.9E-09	1.1E-07	1.2E-07
0.99	1.00	0.0132	0.0146	-2.2E-05	6.2E-05	9.0E-04	-2.9E-05	2.0E-04	-1.2E-08	8.1E-08	1.8E-07
0.97	1.00	0.0150	0.0162	-3.5E-05	5.6E-05	1.2E-03	1.7E-05	1.6E-04	-5.7E-08	8.4E-08	3.2E-07
0.94	0.99	0.0176	0.0172	-5.6E-05	8.5E-05	1.4E-03	1.0E-05	2.4E-04	-1.0E-07	1.4E-07	4.0E-07
0.92	0.99	0.0186	0.0181	-7.1E-05	7.3E-06	1.5E-03	2.4E-05	2.1E-04	-2.1E-07	1.4E-07	4.8E-07
0.89	0.98	0.0211	0.0190	-9.7E-05	-4.4E-05	2.0E-03	6.9E-05	1.4E-04	-4.3E-07	8.4E-08	7.4E-07
0.87	0.98	0.0239	0.0199	-1.3E-04	-4.7E-05	2.3E-03	9.6E-05	4.9E-05	-6.5E-07	7.5E-09	9.7E-07
0.82	0.96	0.0303	0.0227	-2.3E-04	2.0E-05	2.8E-03	7.6E-05	-6.7E-05	-1.3E-06	-1.1E-07	1.5E-06
0.79	0.95	0.0347	0.0244	-3.2E-04	7.3E-05	3.2E-03	9.8E-05	-1.7E-04	-1.9E-06	-2.7E-07	2.1E-06
0.77	0.94	0.0379	0.0256	-3.9E-04	-2.4E-05	2.9E-03	1.1E-04	9.7E-05	-2.3E-06	4.6E-08	2.0E-06
0.72	0.92	0.0445	0.0279	-5.3E-04	1.5E-04	4.1E-03	4.6E-05	-2.1E-04	-3.8E-06	-3.6E-07	3.3E-06
0.69	0.91	0.0469	0.0289	-5.7E-04	1.8E-04	4.0E-03	-4.3E-05	-2.1E-04	-3.8E-06	-3.1E-07	3.3E-06
0.67	0.89	0.0503	0.0310	-6.6E-04	3.4E-05	4.2E-03	7.9E-05	-9.4E-05	-5.4E-06	-2.9E-07	4.3E-06
0.64	0.88	0.0517	0.0315	-6.9E-04	6.9E-05	4.0E-03	4.7E-05	3.5E-05	-5.1E-06	-5.6E-09	4.0E-06
0.62	0.87	0.0538	0.0328	-7.4E-04	1.0E-04	4.6E-03	4.9E-05	-1.4E-04	-6.3E-06	-3.9E-07	5.2E-06
0.59	0.86	0.0575	0.0351	-8.7E-04	1.7E-04	4.9E-03	4.9E-05	-3.5E-04	-7.5E-06	-9.4E-07	6.4E-06
0.57	0.84	0.0613	0.0386	-1.1E-03	3.2E-05	5.0E-03	1.1E-04	-3.3E-04	-1.0E-05	-1.2E-06	8.2E-06
0.54	0.83	0.0647	0.0415	-1.2E-03	-3.2E-05	4.8E-03	1.3E-04	-7.9E-05	-1.2E-05	-5.9E-07	8.9E-06
0.52	0.82	0.0652	0.0416	-1.2E-03	9.4E-05	5.2E-03	5.4E-05	-1.3E-04	-1.2E-05	-6.4E-07	9.5E-06
0.49	0.80	0.0702	0.0457	-1.5E-03	8.9E-05	5.7E-03	-2.6E-05	-1.1E-04	-1.6E-05	-4.0E-07	1.2E-05
0.47	0.79	0.0731	0.0430	-1.4E-03	2.0E-04	5.4E-03	-1.6E-05	1.5E-04	-1.3E-05	5.7E-07	9.4E-06
0.44	0.78	0.0756	0.0431	-1.5E-03	4.1E-04	6.1E-03	-1.7E-04	-2.1E-04	-1.3E-05	-2.9E-07	1.0E-05
0.42	0.76	0.0821	0.0473	-1.8E-03	5.9E-04	6.6E-03	-1.2E-04	-2.9E-04	-1.7E-05	-8.5E-07	1.4E-05
0.39	0.74	0.0888	0.0516	-2.2E-03	6.7E-04	6.9E-03	-1.2E-04	-8.7E-05	-2.0E-05	9.7E-08	1.6E-05
0.37	0.73	0.0941	0.0530	-2.4E-03	6.3E-04	6.8E-03	-1.7E-04	1.4E-04	-2.1E-05	1.6E-06	1.6E-05
0.34	0.72	0.0942	0.0542	-2.4E-03	7.4E-04	6.8E-03	-1.2E-04	2.0E-04	-2.0E-05	1.8E-06	1.7E-05
0.29	0.69	0.1030	0.0555	-2.7E-03	3.6E-04	8.1E-03	-3.8E-05	-1.0E-04	-3.6E-05	-4.3E-07	2.4E-05
0.27	0.67	0.1104	0.0593	-3.2E-03	5.7E-04	9.3E-03	-3.2E-05	-8.4E-05	-4.5E-05	-4.0E-07	3.1E-05
0.24	0.65	0.1198	0.0634	-3.9E-03	7.2E-04	9.7E-03	-1.2E-04	-4.5E-05	-5.4E-05	5.9E-07	3.5E-05
0.22	0.63	0.1256	0.0666	-4.3E-03	5.2E-04	1.0E-02	-1.3E-04	-4.6E-05	-7.0E-05	6.8E-07	4.1E-05
0.19	0.61	0.1316	0.0690	-4.6E-03	6.1E-04	1.1E-02	-2.9E-05	-2.2E-04	-8.2E-05	-1.8E-06	5.1E-05
0.17	0.59	0.1422	0.0736	-5.5E-03	1.3E-03	1.2E-02	-1.9E-04	-1.1E-04	-8.2E-05	9.2E-07	5.6E-05
0.14	0.57	0.1524	0.0781	-6.2E-03	1.5E-03	1.3E-02	-4.2E-04	-5.4E-05	-9.0E-05	4.5E-06	5.9E-05
0.12	0.55	0.1605	0.0805	-6.5E-03	1.3E-03	1.5E-02	-3.3E-04	2.2E-05	-1.2E-04	4.5E-06	7.8E-05
0.09	0.53	0.1816	0.0869	-7.0E-03	-2.9E-03	3.0E-02	7.7E-05	-2.1E-04	-6.5E-04	-4.4E-06	2.5E-04
0.07	0.47	0.3212	0.0965	-1.3E-02	1.8E-03	8.3E-02	-3.9E-04	-4.5E-03	-1.8E-03	-7.3E-05	7.7E-04

Table 25: WPG diamond roughness peak PIV kinematic values at test location 3.

$\frac{y}{\delta}$	$\frac{U_{eff}}{U_{eff,e}}$	$\frac{\sqrt{\overline{u'^2}}}{U}$	$\frac{\sqrt{\overline{v'^2}}}{U}$	$\frac{\overline{u'v'}}{U^2}$	$\frac{d\bar{u}}{dx}\cdot\frac{\delta}{U}$	$\frac{d\bar{u}}{dy}\cdot\frac{\delta}{U}$	$\frac{d\bar{v}}{dx}\cdot\frac{\delta}{U}$	$\frac{d\bar{v}}{dy}\cdot\frac{\delta}{U}$	$P_{xx}\cdot\frac{\delta}{U^3}$	$P_{yy}\cdot\frac{\delta}{U^3}$	$P_{xy}\cdot\frac{\delta}{U^3}$
1.15	1.02	0.0083	0.0112	-1.1E-05	-5.6E-05	-3.2E-05	-2.7E-04	8.1E-04	-2.7E-09	2.1E-07	-3.4E-08
1.12	1.02	0.0089	0.0108	-1.3E-05	4.9E-06	-6.4E-05	-4.0E-04	1.0E-03	1.9E-09	2.5E-07	-5.3E-08
1.10	1.02	0.0095	0.0109	-1.5E-05	3.8E-05	2.7E-04	-4.5E-04	7.4E-04	-3.1E-09	1.9E-07	-1.8E-08
1.07	1.02	0.0104	0.0112	-1.9E-05	5.1E-05	3.0E-04	-3.0E-04	5.3E-04	3.8E-09	1.4E-07	-4.9E-09
1.02	1.01	0.0122	0.0120	-3.2E-05	2.1E-04	1.2E-03	-8.8E-05	-4.9E-04	-1.3E-08	-1.3E-07	1.7E-07
1.00	1.01	0.0138	0.0129	-4.6E-05	-7.1E-05	1.4E-03	4.1E-05	-8.4E-04	-1.6E-07	-2.9E-07	2.9E-07
0.97	1.00	0.0158	0.0141	-6.4E-05	8.9E-05	1.5E-03	1.1E-04	-7.4E-04	-1.5E-07	-3.1E-07	3.7E-07
0.93	0.99	0.0189	0.0140	-7.5E-05	-5.5E-06	1.3E-03	-7.8E-05	3.0E-04	-2.0E-07	1.3E-07	2.1E-07
0.90	0.99	0.0203	0.0144	-7.7E-05	-8.2E-05	1.3E-03	-2.0E-04	8.4E-04	-2.9E-07	3.8E-07	1.4E-07
0.88	0.98	0.0204	0.0147	-7.5E-05	-2.8E-05	1.9E-03	-2.8E-04	1.0E-03	-3.1E-07	4.8E-07	2.2E-07
0.85	0.97	0.0248	0.0158	-1.3E-04	4.2E-05	2.4E-03	-1.5E-04	8.0E-04	-5.5E-07	4.3E-07	4.1E-07
0.83	0.96	0.0269	0.0174	-1.7E-04	9.1E-05	2.5E-03	1.1E-04	3.9E-04	-7.1E-07	1.8E-07	7.6E-07
0.80	0.96	0.0293	0.0189	-2.3E-04	8.8E-05	2.7E-03	3.8E-04	-1.9E-04	-1.1E-06	-3.3E-07	1.3E-06
0.78	0.95	0.0300	0.0200	-2.5E-04	-9.3E-05	3.1E-03	5.9E-04	-7.3E-04	-1.7E-06	-8.8E-07	2.0E-06
0.73	0.92	0.0348	0.0215	-3.4E-04	1.1E-05	4.1E-03	4.8E-04	-1.1E-03	-2.8E-06	-1.4E-06	2.9E-06
0.70	0.91	0.0355	0.0224	-3.6E-04	1.9E-04	3.4E-03	2.4E-04	-3.8E-04	-2.0E-06	-5.5E-07	2.1E-06
0.68	0.90	0.0375	0.0226	-3.6E-04	3.0E-04	3.3E-03	-5.4E-05	3.3E-04	-1.5E-06	3.8E-07	1.4E-06
0.66	0.89	0.0372	0.0229	-3.4E-04	3.2E-04	3.4E-03	-3.2E-04	8.8E-04	-1.4E-06	1.1E-06	9.1E-07
0.63	0.88	0.0392	0.0246	-3.8E-04	4.8E-04	2.8E-03	-5.6E-04	1.6E-03	-6.4E-07	2.4E-06	2.9E-08
0.61	0.87	0.0422	0.0258	-4.1E-04	5.1E-04	3.1E-03	-7.1E-04	2.0E-03	-7.4E-07	3.2E-06	-2.2E-07
0.58	0.86	0.0443	0.0270	-4.8E-04	5.0E-04	3.5E-03	-6.6E-04	1.6E-03	-1.5E-06	2.9E-06	3.1E-07
0.56	0.85	0.0472	0.0292	-5.9E-04	4.2E-04	3.9E-03	-2.8E-04	8.2E-04	-2.8E-06	1.6E-06	2.0E-06
0.53	0.84	0.0500	0.0314	-7.4E-04	-2.7E-04	4.6E-03	3.6E-04	-2.4E-04	-8.3E-06	-1.2E-06	6.0E-06
0.51	0.83	0.0541	0.0351	-9.7E-04	-3.9E-04	5.7E-03	8.5E-04	-1.5E-03	-1.3E-05	-5.4E-06	1.1E-05
0.48	0.81	0.0580	0.0381	-1.2E-03	-3.4E-04	6.4E-03	1.2E-03	-2.4E-03	-1.8E-05	-9.8E-06	1.7E-05
0.46	0.80	0.0609	0.0394	-1.3E-03	-4.9E-04	6.5E-03	1.3E-03	-2.5E-03	-2.0E-05	-1.1E-05	1.9E-05
0.44	0.78	0.0629	0.0400	-1.3E-03	-3.1E-04	6.5E-03	1.1E-03	-2.2E-03	-1.9E-05	-9.8E-06	1.8E-05
0.41	0.77	0.0645	0.0402	-1.3E-03	-6.1E-05	6.3E-03	7.1E-04	-1.5E-03	-1.7E-05	-6.7E-06	1.5E-05
0.39	0.75	0.0660	0.0401	-1.2E-03	3.7E-04	6.1E-03	2.7E-04	-3.6E-04	-1.2E-05	-2.0E-06	1.1E-05
0.34	0.73	0.0700	0.0423	-1.2E-03	9.5E-04	5.8E-03	-6.5E-04	8.6E-04	-4.7E-06	4.7E-06	5.0E-06
0.31	0.71	0.0716	0.0437	-1.2E-03	1.1E-03	5.9E-03	-8.7E-04	1.3E-03	-2.8E-06	7.2E-06	4.0E-06
0.29	0.70	0.0765	0.0467	-1.3E-03	1.2E-03	6.2E-03	-1.1E-03	1.5E-03	-1.5E-06	9.2E-06	4.0E-06
0.26	0.69	0.0807	0.0496	-1.4E-03	1.2E-03	6.4E-03	-1.0E-03	1.4E-03	-2.9E-06	9.6E-06	5.5E-06
0.24	0.68	0.0853	0.0513	-1.6E-03	1.0E-03	7.1E-03	-9.8E-04	1.1E-03	-8.7E-06	8.9E-06	8.5E-06
0.22	0.66	0.0916	0.0555	-2.0E-03	8.8E-04	7.9E-03	-6.3E-04	7.7E-04	-1.8E-05	6.7E-06	1.7E-05
0.19	0.65	0.1017	0.0617	-2.6E-03	5.4E-04	9.6E-03	-1.1E-04	-9.8E-05	-4.0E-05	-7.9E-07	3.5E-05
0.17	0.63	0.1138	0.0681	-3.0E-03	2.3E-04	1.2E-02	3.1E-04	-1.0E-03	-6.5E-05	-1.2E-05	6.1E-05
0.14	0.61	0.1308	0.0756	-3.5E-03	-7.9E-04	1.4E-02	1.0E-03	-1.5E-03	-1.3E-04	-2.6E-05	1.1E-04
0.12	0.58	0.1612	0.0881	-4.0E-03	-3.8E-03	2.3E-02	1.6E-03	-2.5E-03	-4.2E-04	-5.3E-05	2.6E-04
0.09	0.53	0.2574	0.1023	-6.5E-03	-5.3E-03	3.7E-02	1.9E-03	-3.3E-03	-1.2E-03	-9.4E-05	5.8E-04
0.07	0.48	0.3631	0.1193	-1.1E-02	-5.8E-03	4.9E-02	2.2E-03	-4.8E-03	-2.6E-03	-1.9E-04	1.1E-03

Table 26: WPG diamond roughness valley PIV kinematic values at test location 3.

$\frac{y}{\delta}$	$\frac{U_{eff}}{U_{eff,e}}$	$\frac{\sqrt{\overline{u'^2}}}{U}$	$\frac{\sqrt{\overline{v'^2}}}{U}$	$\frac{\overline{u'v'}}{U^2}$	$\frac{d\bar{u}}{dx}\cdot\frac{\delta}{U}$	$\frac{d\bar{u}}{dy}\cdot\frac{\delta}{U}$	$\frac{d\bar{v}}{dx}\cdot\frac{\delta}{U}$	$\frac{d\bar{v}}{dy}\cdot\frac{\delta}{U}$	$P_{xx}\cdot\frac{\delta}{U^3}$	$P_{yy}\cdot\frac{\delta}{U^3}$	$P_{xy}\cdot\frac{\delta}{U^3}$
1.11	1.01	0.0084	0.0108	-1.8E-05	1.2E-04	6.5E-04	1.3E-04	-6.3E-04	5.5E-10	-1.5E-07	9.1E-08
1.09	1.01	0.0090	0.0112	-1.9E-05	1.6E-04	4.3E-04	1.1E-04	-2.8E-04	1.5E-08	-7.5E-08	7.1E-08
1.07	1.01	0.0095	0.0109	-2.0E-05	1.2E-04	6.2E-04	-4.8E-05	2.6E-04	2.8E-10	6.7E-08	6.9E-08
1.02	1.00	0.0092	0.0109	-1.8E-05	2.8E-04	4.9E-04	-2.1E-04	1.3E-03	2.8E-08	3.1E-07	1.1E-08
1.00	1.00	0.0107	0.0110	-2.3E-05	2.3E-04	4.7E-04	-1.3E-04	1.5E-03	3.4E-08	3.7E-07	-3.6E-09
0.97	1.00	0.0092	0.0109	-1.7E-05	6.0E-05	6.1E-04	-8.5E-07	1.4E-03	-1.6E-08	3.3E-07	4.8E-08
0.95	1.00	0.0099	0.0108	-2.1E-05	1.0E-04	8.8E-04	1.4E-04	7.6E-04	-1.7E-08	1.6E-07	1.1E-07
0.92	0.99	0.0126	0.0123	-3.9E-05	1.1E-04	1.6E-03	3.1E-04	-1.0E-05	-1.3E-07	-6.2E-08	3.3E-07
0.90	0.99	0.0156	0.0135	-6.0E-05	-6.0E-05	2.0E-03	5.4E-04	-5.0E-04	-3.1E-07	-2.6E-07	5.7E-07
0.88	0.98	0.0202	0.0145	-9.6E-05	1.1E-04	2.6E-03	5.2E-04	-9.0E-04	-4.0E-07	-4.8E-07	8.4E-07
0.83	0.96	0.0257	0.0159	-1.2E-04	-1.9E-05	2.7E-03	2.3E-04	-2.7E-04	-6.8E-07	-2.0E-07	8.4E-07
0.81	0.95	0.0278	0.0169	-1.4E-04	-8.9E-05	2.9E-03	-1.8E-05	2.8E-04	-9.8E-07	1.6E-07	7.9E-07
0.78	0.94	0.0313	0.0178	-1.7E-04	4.1E-04	2.6E-03	-3.7E-04	1.3E-03	-4.7E-08	9.4E-07	1.5E-07
0.76	0.94	0.0309	0.0167	-1.4E-04	1.8E-04	3.1E-03	-5.2E-04	1.2E-03	-4.9E-07	8.2E-07	1.8E-07
0.73	0.92	0.0340	0.0200	-2.2E-04	5.3E-04	3.7E-03	-6.0E-04	7.3E-04	-4.0E-07	8.4E-07	5.2E-07
0.71	0.92	0.0349	0.0201	-2.5E-04	6.6E-04	2.5E-03	-2.6E-04	1.0E-03	3.9E-07	9.7E-07	2.4E-07
0.69	0.91	0.0364	0.0203	-2.7E-04	3.7E-04	3.1E-03	2.2E-04	-9.1E-05	-7.2E-07	-2.4E-07	1.5E-06
0.66	0.90	0.0387	0.0242	-4.1E-04	7.9E-05	4.5E-03	5.1E-04	-1.3E-03	-3.4E-06	-2.0E-06	4.0E-06
0.64	0.88	0.0426	0.0275	-5.6E-04	-4.4E-05	4.6E-03	6.7E-04	-1.8E-03	-5.3E-06	-3.5E-06	5.8E-06
0.62	0.87	0.0434	0.0292	-6.1E-04	-1.8E-04	5.1E-03	7.5E-04	-2.0E-03	-6.9E-06	-4.3E-06	7.1E-06
0.59	0.86	0.0463	0.0306	-6.7E-04	4.1E-05	5.3E-03	5.0E-04	-1.5E-03	-6.9E-06	-3.5E-06	7.0E-06
0.57	0.84	0.0473	0.0306	-6.5E-04	2.3E-04	5.2E-03	1.5E-04	-6.6E-04	-5.7E-06	-1.4E-06	5.5E-06
0.55	0.83	0.0482	0.0307	-6.2E-04	4.0E-04	4.8E-03	-2.3E-04	2.1E-04	-4.1E-06	6.9E-07	3.6E-06
0.50	0.81	0.0528	0.0323	-6.6E-04	8.2E-04	4.1E-03	-9.2E-04	1.6E-03	-8.6E-07	4.6E-06	1.1E-07
0.47	0.80	0.0541	0.0330	-6.8E-04	8.3E-04	4.3E-03	-1.2E-03	2.0E-03	-1.0E-06	5.8E-06	-5.6E-07
0.45	0.79	0.0557	0.0342	-7.5E-04	8.8E-04	4.2E-03	-1.4E-03	2.2E-03	-7.9E-07	7.1E-06	-1.6E-06
0.43	0.78	0.0578	0.0356	-8.3E-04	7.3E-04	4.2E-03	-1.2E-03	1.8E-03	-2.1E-06	6.5E-06	-7.0E-07
0.40	0.77	0.0600	0.0375	-9.4E-04	4.8E-04	4.8E-03	-7.7E-04	1.1E-03	-5.6E-06	4.3E-06	2.7E-06
0.38	0.76	0.0645	0.0408	-1.3E-03	-1.6E-04	5.8E-03	-9.7E-06	-1.2E-04	-1.6E-05	-4.4E-07	1.0E-05
0.36	0.74	0.0698	0.0443	-1.6E-03	-7.9E-04	6.9E-03	7.4E-04	-1.8E-03	-3.0E-05	-9.7E-06	2.1E-05
0.33	0.73	0.0743	0.0478	-2.0E-03	-1.1E-03	7.8E-03	1.3E-03	-3.4E-03	-4.4E-05	-2.1E-05	3.4E-05
0.31	0.71	0.0771	0.0497	-2.1E-03	-1.2E-03	8.7E-03	1.5E-03	-4.0E-03	-5.2E-05	-2.6E-05	4.1E-05
0.29	0.69	0.0824	0.0499	-2.3E-03	-1.2E-03	9.5E-03	1.4E-03	-3.9E-03	-6.1E-05	-2.6E-05	4.6E-05
0.24	0.66	0.0911	0.0504	-2.4E-03	-6.6E-04	1.0E-02	6.7E-04	-2.7E-03	-6.0E-05	-1.7E-05	3.9E-05
0.21	0.64	0.0961	0.0519	-2.6E-03	-4.7E-04	1.1E-02	1.8E-04	-1.6E-03	-6.5E-05	-9.8E-06	3.7E-05
0.19	0.62	0.1020	0.0541	-2.8E-03	-1.2E-04	1.2E-02	-9.9E-05	-6.2E-04	-6.7E-05	-3.2E-06	3.5E-05
0.17	0.60	0.1082	0.0566	-2.9E-03	3.6E-04	1.2E-02	-3.3E-04	-1.4E-04	-6.4E-05	9.5E-07	3.5E-05
0.14	0.58	0.1171	0.0593	-3.1E-03	8.7E-04	1.4E-02	-7.0E-04	1.5E-04	-6.0E-05	5.3E-06	3.5E-05
0.12	0.56	0.1316	0.0669	-3.7E-03	1.3E-03	1.4E-02	-1.0E-03	4.0E-04	-5.8E-05	1.1E-05	4.0E-05
0.10	0.54	0.1596	0.0800	-3.7E-03	1.8E-03	1.5E-02	-1.0E-03	3.5E-04	-2.1E-05	1.2E-05	6.6E-05
0.07	0.51	0.1955	0.0963	-4.7E-03	2.3E-03	2.6E-02	-1.1E-03	9.4E-06	-7.1E-05	1.0E-05	2.0E-04

Table 27: SPG smooth wall PIV kinematic values at test location 1.

$\frac{y}{\delta}$	$\frac{U_{eff}}{U_{eff,e}}$	$\frac{\sqrt{\overline{u'^2}}}{U}$	$\frac{\sqrt{\overline{v'^2}}}{U}$	$\frac{\overline{u'v'}}{U^2}$	$\frac{d\bar{u}}{dx}\cdot\frac{\delta}{U}$	$\frac{d\bar{u}}{dy}\cdot\frac{\delta}{U}$	$\frac{d\bar{v}}{dx}\cdot\frac{\delta}{U}$	$\frac{d\bar{v}}{dy}\cdot\frac{\delta}{U}$	$P_{xx}\cdot\frac{\delta}{U^3}$	$P_{yy}\cdot\frac{\delta}{U^3}$	$P_{xy}\cdot\frac{\delta}{U^3}$
1.29	1.01	0.0091	0.0056	4.2E-06	4.3E-05	1.3E-05	4.6E-05	-3.4E-06	9.4E-09	0.0E+00	0.0E+00
1.26	1.01	0.0085	0.0052	2.8E-06	3.2E-05	9.2E-05	3.2E-05	-1.9E-06	6.1E-09	0.0E+00	3.3E-09
1.23	1.01	0.0077	0.0055	2.6E-06	1.5E-05	1.2E-04	2.7E-05	-2.6E-06	4.0E-10	0.0E+00	7.7E-09
1.20	1.01	0.0081	0.0057	1.9E-06	1.8E-05	6.7E-05	3.0E-05	6.0E-07	5.6E-10	0.0E+00	2.5E-10
1.17	1.01	0.0083	0.0058	1.1E-06	3.0E-05	8.4E-05	2.0E-05	3.4E-06	4.1E-10	0.0E+00	4.1E-10
1.14	1.01	0.0093	0.0061	-5.0E-07	1.9E-06	1.8E-04	6.3E-06	-1.5E-05	0.0E+00	0.0E+00	7.9E-09
1.11	1.01	0.0099	0.0064	-1.6E-06	7.6E-06	2.8E-04	6.5E-06	-1.0E-05	0.0E+00	0.0E+00	1.6E-08
1.09	1.01	0.0101	0.0066	-2.6E-06	2.0E-05	4.1E-04	6.6E-06	9.0E-06	-4.3E-10	0.0E+00	2.0E-08
1.06	1.01	0.0107	0.0071	-4.7E-06	1.1E-05	6.0E-04	5.9E-06	1.7E-05	-5.8E-09	0.0E+00	2.9E-08
1.03	1.00	0.0130	0.0081	-9.9E-06	-2.8E-05	8.3E-04	1.9E-05	-1.4E-06	-2.4E-08	4.4E-10	5.5E-08
1.00	1.00	0.0148	0.0091	-2.3E-05	-5.7E-05	1.0E-03	1.3E-05	-5.9E-06	-6.8E-08	6.3E-10	9.0E-08
0.97	1.00	0.0165	0.0095	-3.1E-05	-5.2E-05	1.2E-03	1.0E-05	5.6E-06	-1.0E-07	9.1E-10	1.1E-07
0.94	0.99	0.0186	0.0102	-4.7E-05	-5.7E-05	1.4E-03	1.5E-05	3.0E-05	-1.7E-07	6.7E-09	1.6E-07
0.91	0.98	0.0208	0.0110	-6.1E-05	-4.7E-05	1.6E-03	1.5E-05	2.3E-05	-2.3E-07	5.2E-09	2.0E-07
0.88	0.98	0.0230	0.0117	-7.6E-05	-2.8E-05	1.8E-03	1.1E-05	-2.8E-05	-3.1E-07	-1.0E-08	2.6E-07
0.86	0.97	0.0254	0.0127	-1.0E-04	-2.5E-06	2.1E-03	9.9E-06	-8.8E-05	-4.4E-07	-3.1E-08	3.5E-07
0.80	0.95	0.0322	0.0154	-1.9E-04	-9.9E-05	2.4E-03	6.1E-05	7.0E-05	-1.1E-06	7.3E-09	6.4E-07
0.77	0.94	0.0340	0.0159	-2.0E-04	-1.3E-04	2.4E-03	5.5E-05	7.7E-05	-1.3E-06	1.2E-08	6.9E-07
0.74	0.93	0.0361	0.0168	-2.4E-04	-7.3E-05	2.7E-03	4.9E-05	3.4E-05	-1.4E-06	-9.5E-09	8.4E-07
0.71	0.92	0.0384	0.0182	-2.8E-04	-1.9E-05	2.9E-03	4.1E-05	-1.7E-05	-1.7E-06	-4.0E-08	1.0E-06
0.68	0.91	0.0407	0.0194	-3.4E-04	-3.0E-05	3.1E-03	3.2E-05	-4.9E-05	-2.2E-06	-6.1E-08	1.2E-06
0.65	0.90	0.0431	0.0204	-3.8E-04	-4.8E-05	3.2E-03	3.8E-05	-4.7E-05	-2.6E-06	-7.2E-08	1.4E-06
0.62	0.89	0.0450	0.0212	-4.1E-04	3.7E-05	3.3E-03	8.3E-06	-4.6E-05	-2.5E-06	-4.4E-08	1.5E-06
0.60	0.88	0.0467	0.0223	-4.5E-04	2.5E-05	3.5E-03	2.5E-05	-6.7E-05	-3.1E-06	-8.5E-08	1.8E-06
0.57	0.87	0.0502	0.0240	-5.4E-04	-6.1E-05	3.7E-03	5.3E-05	-8.6E-05	-4.4E-06	-1.6E-07	2.4E-06
0.54	0.85	0.0533	0.0255	-6.1E-04	-8.0E-05	3.9E-03	8.5E-05	-1.1E-04	-5.2E-06	-2.4E-07	2.9E-06
0.51	0.84	0.0557	0.0267	-6.6E-04	-3.4E-05	4.1E-03	9.7E-05	-8.6E-05	-5.6E-06	-2.4E-07	3.3E-06
0.48	0.83	0.0591	0.0282	-7.4E-04	-3.3E-05	4.3E-03	6.6E-05	1.2E-05	-6.5E-06	-7.1E-08	3.7E-06
0.45	0.82	0.0628	0.0306	-7.9E-04	2.5E-05	4.3E-03	3.2E-05	4.8E-05	-6.5E-06	4.0E-08	4.1E-06
0.42	0.80	0.0665	0.0330	-9.5E-04	-5.3E-05	4.6E-03	6.6E-05	-4.3E-05	-9.1E-06	-2.2E-07	5.4E-06
0.39	0.79	0.0703	0.0346	-9.9E-04	-1.2E-04	4.9E-03	4.3E-05	5.5E-05	-1.1E-05	5.0E-08	6.2E-06
0.37	0.78	0.0751	0.0369	-9.8E-04	-1.1E-04	5.3E-03	5.2E-05	1.8E-04	-1.2E-05	4.1E-07	7.4E-06
0.34	0.76	0.0808	0.0395	-1.0E-03	-8.2E-05	5.5E-03	3.0E-05	1.8E-04	-1.2E-05	5.3E-07	8.6E-06
0.31	0.75	0.0867	0.0421	-1.2E-03	-1.3E-04	5.4E-03	-7.1E-05	3.9E-05	-1.5E-05	3.4E-07	9.3E-06
0.25	0.72	0.1029	0.0519	-1.4E-03	-9.9E-05	4.7E-03	-9.1E-05	-2.5E-04	-1.5E-05	-1.1E-06	1.2E-05
0.22	0.71	0.1428	0.0809	-1.6E-03	-6.7E-04	5.3E-03	-9.1E-05	-6.0E-04	-4.9E-05	-8.7E-06	3.7E-05
0.19	0.70	0.1928	0.1127	-1.6E-03	-6.6E-04	5.7E-03	-2.0E-04	-2.3E-04	-6.3E-05	-1.9E-06	6.7E-05
0.16	0.68	0.2229	0.1280	-1.3E-03	-1.9E-04	6.6E-03	-2.3E-04	6.5E-04	-3.6E-05	2.1E-05	9.5E-05
0.13	0.67	0.2343	0.1267	-1.3E-03	3.2E-04	8.1E-03	-1.3E-04	1.5E-03	1.3E-05	4.9E-05	1.2E-04
0.11	0.64	0.2571	0.1263	-2.0E-03	1.9E-04	9.0E-03	-1.5E-04	1.6E-03	-1.1E-05	5.4E-05	1.3E-04
0.08	0.63	0.2119	0.0966	-2.3E-03	-2.2E-04	8.0E-03	-3.1E-04	1.1E-03	-5.4E-05	2.4E-05	6.2E-05

Table 28: SPG diamond roughness peak PIV kinematic values at test location 1.

$\frac{y}{\delta}$	$\frac{U_{eff}}{U_{eff,e}}$	$\frac{\sqrt{\overline{u'^2}}}{U}$	$\frac{\sqrt{\overline{v'^2}}}{U}$	$\frac{\overline{u'v'}}{U^2}$	$\frac{d\bar{u}}{dx}\cdot\frac{\delta}{U}$	$\frac{d\bar{u}}{dy}\cdot\frac{\delta}{U}$	$\frac{d\bar{v}}{dx}\cdot\frac{\delta}{U}$	$\frac{d\bar{v}}{dy}\cdot\frac{\delta}{U}$	$P_{xx}\cdot\frac{\delta}{U^3}$	$P_{yy}\cdot\frac{\delta}{U^3}$	$P_{xy}\cdot\frac{\delta}{U^3}$
1.43	1.01	0.0075	0.0041	-2.9E-06	3.0E-05	-7.1E-05	-9.5E-05	1.7E-04	4.2E-09	8.9E-09	-8.9E-09
1.40	1.01	0.0076	0.0044	-3.0E-06	5.6E-06	1.1E-05	-5.5E-05	6.7E-05	0.0E+00	5.3E-09	-5.3E-09
1.36	1.01	0.0077	0.0047	-3.0E-06	-1.0E-05	4.7E-05	3.5E-06	-6.4E-05	-2.3E-09	-2.3E-09	2.4E-09
1.33	1.01	0.0081	0.0049	-3.1E-06	-5.8E-05	1.6E-04	5.6E-05	-2.1E-04	-9.9E-09	-9.9E-09	9.9E-09
1.30	1.01	0.0076	0.0047	-3.9E-06	-1.1E-04	3.9E-04	8.5E-05	-2.9E-04	-1.8E-08	-1.8E-08	1.8E-08
1.26	1.00	0.0061	0.0044	-3.2E-06	-9.5E-05	3.6E-04	9.3E-05	-2.6E-04	-1.1E-08	-1.1E-08	1.1E-08
1.23	1.00	0.0055	0.0042	-3.0E-06	-7.1E-05	2.6E-04	6.3E-05	-1.8E-04	-9.0E-09	-9.0E-09	9.0E-09
1.20	1.00	0.0050	0.0041	-3.0E-06	-6.4E-05	1.5E-04	7.1E-06	-3.2E-05	-4.4E-09	-4.3E-09	4.4E-09
1.16	1.00	0.0049	0.0041	-3.4E-06	-4.4E-05	3.7E-05	-5.5E-05	1.5E-04	0.0E+00	3.5E-09	-3.3E-09
1.13	1.00	0.0054	0.0044	-4.2E-06	-2.3E-06	-3.1E-05	-1.1E-04	3.2E-04	0.0E+00	1.3E-08	-9.1E-09
1.10	1.00	0.0059	0.0050	-5.0E-06	7.8E-06	9.7E-06	-1.5E-04	4.5E-04	0.0E+00	2.8E-08	-9.1E-09
1.07	1.00	0.0061	0.0057	-5.9E-06	1.5E-05	1.2E-05	-1.5E-04	5.3E-04	0.0E+00	3.6E-08	-9.1E-09
1.03	1.00	0.0086	0.0073	-1.1E-05	-1.6E-05	2.1E-04	-7.5E-05	4.7E-04	-7.1E-09	5.0E-08	5.3E-09
1.00	1.00	0.0109	0.0092	-2.3E-05	-2.1E-05	5.5E-04	2.8E-05	2.0E-04	-3.2E-08	2.5E-08	5.6E-08
0.97	1.00	0.0131	0.0106	-3.8E-05	-5.2E-05	8.7E-04	1.5E-04	-1.5E-04	-9.0E-08	-4.9E-08	1.4E-07
0.93	0.99	0.0156	0.0116	-5.8E-05	-1.2E-04	1.2E-03	2.5E-04	-4.8E-04	-2.1E-07	-1.6E-07	2.6E-07
0.90	0.99	0.0183	0.0123	-8.3E-05	-1.8E-04	1.5E-03	3.0E-04	-7.2E-04	-3.9E-07	-2.6E-07	4.1E-07
0.87	0.98	0.0219	0.0120	-1.1E-04	-1.9E-04	2.0E-03	2.9E-04	-8.0E-04	-6.1E-07	-2.9E-07	5.3E-07
0.84	0.97	0.0261	0.0143	-1.4E-04	-4.4E-05	2.2E-03	1.3E-04	-5.6E-04	-7.0E-07	-2.7E-07	6.3E-07
0.80	0.96	0.0289	0.0149	-1.5E-04	6.2E-05	2.2E-03	-4.2E-05	-1.0E-04	-5.5E-07	-3.3E-08	4.6E-07
0.77	0.95	0.0308	0.0149	-1.4E-04	1.7E-04	2.1E-03	-2.3E-04	4.3E-04	-2.8E-07	2.5E-07	1.6E-07
0.74	0.94	0.0322	0.0144	-1.4E-04	2.3E-04	2.0E-03	-4.0E-04	8.8E-04	-6.5E-08	4.7E-07	-1.6E-07
0.70	0.93	0.0333	0.0143	-1.4E-04	2.7E-04	1.8E-03	-5.2E-04	1.2E-03	1.2E-07	6.3E-07	-4.2E-07
0.67	0.92	0.0336	0.0151	-1.5E-04	3.2E-04	1.6E-03	-5.7E-04	1.3E-03	2.6E-07	7.6E-07	-5.2E-07
0.64	0.92	0.0322	0.0164	-1.5E-04	2.4E-04	1.8E-03	-5.1E-04	1.2E-03	-4.4E-08	7.9E-07	-2.6E-07
0.60	0.91	0.0340	0.0176	-2.1E-04	1.7E-04	2.5E-03	-2.8E-04	6.3E-04	-6.4E-07	5.0E-07	2.9E-07
0.57	0.90	0.0372	0.0200	-3.2E-04	2.0E-05	3.1E-03	7.3E-05	-7.1E-06	-2.0E-06	-1.1E-07	1.4E-06
0.54	0.88	0.0408	0.0223	-4.4E-04	-2.1E-04	3.7E-03	4.1E-04	-6.2E-04	-4.0E-06	-1.0E-06	2.9E-06
0.51	0.87	0.0441	0.0243	-5.6E-04	-5.0E-04	4.2E-03	7.1E-04	-1.2E-03	-6.8E-06	-2.2E-06	4.9E-06
0.47	0.85	0.0479	0.0258	-6.9E-04	-7.0E-04	4.8E-03	9.1E-04	-1.6E-03	-9.8E-06	-3.4E-06	6.9E-06
0.44	0.83	0.0530	0.0267	-8.0E-04	-7.2E-04	5.2E-03	9.2E-04	-1.7E-03	-1.2E-05	-3.9E-06	8.2E-06
0.41	0.82	0.0556	0.0253	-7.5E-04	-7.8E-04	5.3E-03	7.7E-04	-1.4E-03	-1.3E-05	-3.0E-06	7.4E-06
0.37	0.80	0.0601	0.0264	-8.2E-04	-4.0E-04	5.5E-03	4.7E-04	-9.2E-04	-1.2E-05	-2.1E-06	6.6E-06
0.34	0.78	0.0643	0.0291	-9.2E-04	-2.0E-04	5.7E-03	2.1E-04	-4.2E-04	-1.2E-05	-1.0E-06	6.3E-06
0.31	0.76	0.0687	0.0309	-9.6E-04	-1.2E-04	5.6E-03	-7.9E-05	5.7E-05	-1.2E-05	2.7E-07	5.0E-06
0.27	0.74	0.0718	0.0315	-9.5E-04	2.5E-05	5.5E-03	-3.6E-04	5.0E-04	-1.0E-05	1.7E-06	3.1E-06
0.24	0.73	0.0744	0.0326	-9.6E-04	2.4E-04	5.5E-03	-6.0E-04	9.1E-04	-7.9E-06	3.1E-06	1.5E-06
0.21	0.71	0.0795	0.0364	-1.1E-03	3.4E-04	5.5E-03	-8.0E-04	1.1E-03	-7.2E-06	4.7E-06	6.3E-07
0.18	0.70	0.0860	0.0391	-1.2E-03	6.2E-04	3.5E-03	-1.0E-03	4.5E-04	6.2E-07	3.9E-06	-3.7E-06
0.14	0.69	0.0957	0.0480	-1.4E-03	7.7E-04	3.9E-03	-1.1E-03	6.3E-04	3.3E-06	6.1E-06	-3.1E-06
0.11	0.68	0.1112	0.0550	-1.6E-03	8.4E-04	6.5E-03	-1.3E-03	1.3E-03	-8.6E-07	1.2E-05	-7.3E-09
0.08	0.66	0.1380	0.0650	-1.6E-03	1.2E-03	2.4E-02	-1.4E-03	1.3E-03	-2.2E-05	1.5E-05	8.4E-05

Table 29: SPG diamond roughness valley PIV kinematic values at test location 1.

$\frac{y}{\delta}$	$\frac{U_{eff}}{U_{eff,e}}$	$\frac{\sqrt{\overline{u'^2}}}{U}$	$\frac{\sqrt{\overline{v'^2}}}{U}$	$\frac{\overline{u'v'}}{U^2}$	$\frac{d\bar{u}}{dx}\cdot\frac{\delta}{U}$	$\frac{d\bar{u}}{dy}\cdot\frac{\delta}{U}$	$\frac{d\bar{v}}{dx}\cdot\frac{\delta}{U}$	$\frac{d\bar{v}}{dy}\cdot\frac{\delta}{U}$	$P_{xx}\cdot\frac{\delta}{U^3}$	$P_{yy}\cdot\frac{\delta}{U^3}$	$P_{xy}\cdot\frac{\delta}{U^3}$
1.24	1.01	0.0065	0.0040	-4.0E-06	-3.6E-05	-1.0E-04	-6.6E-05	1.9E-04	3.9E-11	9.8E-09	-8.5E-10
1.21	1.01	0.0066	0.0042	-4.9E-06	1.0E-05	-2.1E-04	-1.2E-04	3.4E-04	3.9E-11	9.8E-09	-9.2E-09
1.18	1.01	0.0072	0.0046	-6.5E-06	-4.4E-05	-2.3E-04	-1.4E-04	4.3E-04	5.9E-11	1.7E-08	-1.7E-08
1.15	1.01	0.0076	0.0052	-7.5E-06	-8.0E-05	-7.9E-05	-1.0E-04	3.7E-04	-6.2E-09	1.9E-08	-1.3E-08
1.12	1.01	0.0075	0.0057	-8.3E-06	-9.7E-05	9.7E-05	-2.7E-05	1.8E-04	-9.7E-09	9.8E-09	-1.3E-10
1.09	1.01	0.0074	0.0062	-9.5E-06	-1.3E-04	2.3E-04	7.1E-05	-6.5E-05	-1.6E-08	-1.0E-08	1.6E-08
1.06	1.01	0.0076	0.0067	-1.2E-05	-1.8E-04	3.3E-04	1.6E-04	-2.9E-04	-3.1E-08	-3.3E-08	3.3E-08
1.03	1.01	0.0078	0.0071	-1.5E-05	-1.9E-04	4.7E-04	2.1E-04	-4.5E-04	-3.9E-08	-4.9E-08	4.9E-08
1.00	1.01	0.0079	0.0071	-1.7E-05	-1.6E-04	5.6E-04	2.1E-04	-5.0E-04	-3.9E-08	-5.8E-08	4.9E-08
0.97	1.00	0.0086	0.0073	-2.1E-05	-1.1E-04	6.1E-04	1.6E-04	-4.0E-04	-4.0E-08	-5.2E-08	4.9E-08
0.94	1.00	0.0095	0.0076	-2.3E-05	-7.2E-05	7.9E-04	4.6E-05	-1.9E-04	-4.6E-08	-2.6E-08	5.6E-08
0.91	1.00	0.0118	0.0084	-3.0E-05	-2.3E-05	9.9E-04	-8.9E-05	9.7E-05	-6.4E-08	2.2E-08	5.1E-08
0.88	0.99	0.0148	0.0094	-4.1E-05	5.9E-05	1.1E-03	-2.1E-04	4.5E-04	-5.9E-08	1.0E-07	2.8E-08
0.85	0.99	0.0173	0.0109	-4.6E-05	1.8E-04	1.2E-03	-3.1E-04	8.2E-04	4.0E-09	2.3E-07	1.6E-09
0.82	0.98	0.0200	0.0138	-5.4E-05	2.8E-04	1.3E-03	-4.1E-04	1.0E-03	8.1E-08	4.4E-07	1.2E-08
0.79	0.98	0.0223	0.0153	-7.2E-05	2.0E-04	1.6E-03	-3.5E-04	9.6E-04	-3.4E-08	5.0E-07	1.2E-07
0.76	0.97	0.0261	0.0171	-1.1E-04	8.4E-05	2.0E-03	-1.6E-04	5.2E-04	-3.5E-07	3.2E-07	4.4E-07
0.73	0.96	0.0295	0.0199	-1.8E-04	-2.3E-05	2.5E-03	9.0E-05	-1.7E-04	-9.6E-07	-2.5E-07	1.2E-06
0.70	0.95	0.0324	0.0219	-2.6E-04	-1.9E-04	3.0E-03	3.7E-04	-8.9E-04	-2.0E-06	-1.1E-06	2.1E-06
0.67	0.93	0.0347	0.0225	-3.2E-04	-3.8E-04	3.3E-03	5.9E-04	-1.4E-03	-3.0E-06	-1.8E-06	2.9E-06
0.64	0.92	0.0359	0.0226	-3.6E-04	-4.1E-04	3.5E-03	6.1E-04	-1.4E-03	-3.5E-06	-1.9E-06	3.2E-06
0.61	0.91	0.0360	0.0211	-3.6E-04	-4.0E-04	3.5E-03	5.4E-04	-1.2E-03	-3.6E-06	-1.5E-06	2.8E-06
0.58	0.89	0.0353	0.0188	-3.1E-04	-3.0E-04	3.6E-03	3.4E-04	-7.9E-04	-2.9E-06	-7.9E-07	2.0E-06
0.55	0.88	0.0364	0.0180	-2.9E-04	-2.3E-04	3.5E-03	1.1E-04	-2.8E-04	-2.6E-06	-2.5E-07	1.4E-06
0.52	0.87	0.0379	0.0184	-2.9E-04	-1.1E-04	3.5E-03	-1.6E-04	2.0E-04	-2.3E-06	2.4E-07	9.2E-07
0.48	0.86	0.0400	0.0193	-3.1E-04	1.2E-04	3.4E-03	-4.4E-04	6.8E-04	-1.7E-06	7.9E-07	3.0E-07
0.45	0.85	0.0424	0.0199	-3.1E-04	4.4E-04	3.3E-03	-6.8E-04	1.2E-03	-4.6E-07	1.4E-06	-4.4E-07
0.42	0.84	0.0440	0.0203	-3.1E-04	7.7E-04	3.4E-03	-8.6E-04	1.6E-03	9.2E-07	1.9E-06	-1.0E-06
0.39	0.82	0.0484	0.0225	-3.5E-04	8.6E-04	3.6E-03	-1.0E-03	1.9E-03	1.5E-06	2.7E-06	-1.5E-06
0.36	0.81	0.0521	0.0246	-4.3E-04	8.1E-04	3.4E-03	-1.0E-03	2.0E-03	1.4E-06	3.4E-06	-1.9E-06
0.33	0.80	0.0541	0.0259	-4.8E-04	5.6E-04	3.9E-03	-8.5E-04	1.8E-03	-4.6E-07	3.2E-06	-9.4E-07
0.30	0.79	0.0600	0.0290	-6.8E-04	3.2E-04	4.8E-03	-4.8E-04	1.1E-03	-4.6E-06	2.4E-06	1.7E-06
0.27	0.77	0.0681	0.0330	-1.0E-03	-5.0E-05	5.7E-03	4.9E-05	3.0E-04	-1.3E-05	3.3E-07	6.5E-06
0.24	0.76	0.0753	0.0362	-1.4E-03	-6.2E-04	6.5E-03	6.6E-04	-5.3E-04	-2.5E-05	-3.3E-06	1.4E-05
0.21	0.74	0.0851	0.0401	-1.7E-03	-9.5E-04	7.0E-03	1.1E-03	-1.0E-03	-3.8E-05	-7.1E-06	2.3E-05
0.18	0.72	0.0927	0.0445	-2.0E-03	-1.2E-03	4.5E-03	1.4E-03	-1.0E-03	-3.9E-05	-9.8E-06	2.6E-05
0.15	0.71	0.0992	0.0498	-2.3E-03	-1.5E-03	5.2E-03	1.7E-03	-1.4E-03	-5.4E-05	-1.5E-05	3.7E-05
0.12	0.70	0.1106	0.0566	-2.5E-03	-1.6E-03	8.5E-03	1.8E-03	-1.8E-03	-8.1E-05	-2.1E-05	5.8E-05
0.09	0.67	0.1250	0.0629	-2.7E-03	-1.7E-03	1.2E-02	1.6E-03	-1.4E-03	-1.2E-04	-1.9E-05	8.0E-05
0.06	0.64	0.1551	0.0711	-2.7E-03	-1.7E-03	1.4E-02	1.2E-03	-2.2E-04	-1.5E-04	-8.0E-06	1.1E-04

Table 30: SPG smooth wall PIV kinematic values at test location 2.

$\frac{y}{\delta}$	$\frac{U_{eff}}{U_{eff,e}}$	$\frac{\sqrt{\overline{u'^2}}}{U}$	$\frac{\sqrt{\overline{v'^2}}}{U}$	$\frac{\overline{u'v'}}{U^2}$	$\frac{d\bar{u}}{dx}\cdot\frac{\delta}{U}$	$\frac{d\bar{u}}{dy}\cdot\frac{\delta}{U}$	$\frac{d\bar{v}}{dx}\cdot\frac{\delta}{U}$	$\frac{d\bar{v}}{dy}\cdot\frac{\delta}{U}$	$P_{xx}\cdot\frac{\delta}{U^3}$	$P_{yy}\cdot\frac{\delta}{U^3}$	$P_{xy}\cdot\frac{\delta}{U^3}$
1.27	1.01	0.0093	0.0105	3.0E-06	4.5E-05	-2.1E-04	-2.7E-04	7.2E-04	1.5E-09	1.6E-07	-4.0E-08
1.24	1.01	0.0103	0.0108	5.0E-06	7.3E-05	-1.8E-04	-2.7E-04	8.4E-04	1.2E-08	1.9E-07	-4.1E-08
1.22	1.01	0.0102	0.0106	6.3E-06	6.8E-05	-1.2E-04	-2.7E-04	9.2E-04	1.3E-08	2.0E-07	-3.6E-08
1.19	1.01	0.0103	0.0104	8.5E-06	6.7E-05	-1.7E-05	-2.4E-04	8.8E-04	1.5E-08	1.9E-07	-2.0E-08
1.16	1.01	0.0111	0.0104	8.3E-06	9.8E-05	7.2E-05	-2.2E-04	8.7E-04	2.6E-08	1.9E-07	-1.3E-08
1.14	1.01	0.0121	0.0104	8.1E-06	1.2E-04	1.3E-04	-2.5E-04	8.4E-04	3.8E-08	1.8E-07	-1.6E-08
1.11	1.01	0.0126	0.0102	8.3E-06	1.2E-04	2.3E-04	-2.6E-04	8.2E-04	4.2E-08	1.7E-07	-9.4E-09
1.05	1.01	0.0153	0.0104	5.6E-06	1.8E-04	4.8E-04	-2.4E-04	8.1E-04	9.2E-08	1.7E-07	4.8E-09
1.03	1.00	0.0163	0.0109	3.4E-06	1.6E-04	6.7E-04	-2.4E-04	7.5E-04	9.4E-08	1.7E-07	2.0E-08
1.00	1.00	0.0178	0.0112	1.9E-06	1.8E-04	8.6E-04	-2.4E-04	8.5E-04	1.2E-07	2.1E-07	3.4E-08
0.97	1.00	0.0194	0.0123	1.5E-06	3.0E-04	8.6E-04	-2.3E-04	9.7E-04	2.3E-07	3.0E-07	4.9E-08
0.95	0.99	0.0195	0.0142	1.1E-05	2.9E-04	1.1E-03	-2.2E-04	9.5E-04	2.4E-07	3.8E-07	1.5E-07
0.92	0.99	0.0214	0.0159	-2.6E-06	2.8E-04	1.4E-03	-2.0E-04	1.0E-03	2.4E-07	5.0E-07	2.7E-07
0.89	0.98	0.0225	0.0166	-1.0E-05	1.9E-04	1.4E-03	-2.3E-04	1.0E-03	1.6E-07	5.8E-07	2.6E-07
0.86	0.98	0.0235	0.0178	-1.3E-05	3.0E-04	1.5E-03	-2.3E-04	1.0E-03	2.9E-07	6.4E-07	3.3E-07
0.84	0.97	0.0250	0.0197	-3.7E-05	4.0E-04	1.7E-03	-2.9E-04	1.1E-03	3.6E-07	8.4E-07	4.1E-07
0.81	0.97	0.0267	0.0211	-5.8E-05	3.5E-04	1.6E-03	-2.9E-04	1.0E-03	3.1E-07	9.5E-07	4.4E-07
0.78	0.96	0.0279	0.0211	-7.6E-05	3.2E-04	1.6E-03	-2.9E-04	9.3E-04	2.5E-07	8.7E-07	3.9E-07
0.76	0.95	0.0289	0.0218	-9.8E-05	3.3E-04	1.7E-03	-3.1E-04	1.0E-03	2.2E-07	1.1E-06	4.0E-07
0.73	0.95	0.0301	0.0227	-1.2E-04	3.3E-04	1.7E-03	-2.8E-04	1.0E-03	1.9E-07	1.1E-06	4.6E-07
0.70	0.94	0.0320	0.0233	-1.5E-04	3.1E-04	1.8E-03	-2.7E-04	8.7E-04	9.8E-08	1.0E-06	5.2E-07
0.68	0.94	0.0344	0.0241	-1.8E-04	3.9E-04	1.9E-03	-2.6E-04	8.8E-04	2.5E-07	1.1E-06	5.6E-07
0.65	0.93	0.0361	0.0238	-1.9E-04	4.5E-04	1.9E-03	-2.6E-04	7.7E-04	4.2E-07	9.8E-07	5.1E-07
0.62	0.92	0.0366	0.0236	-2.0E-04	4.4E-04	2.0E-03	-2.1E-04	6.5E-04	3.6E-07	8.1E-07	6.3E-07
0.59	0.92	0.0377	0.0233	-2.1E-04	4.4E-04	2.0E-03	-2.1E-04	7.5E-04	3.9E-07	9.0E-07	5.5E-07
0.57	0.91	0.0389	0.0247	-2.3E-04	4.8E-04	2.0E-03	-1.5E-04	7.2E-04	5.0E-07	9.5E-07	7.2E-07
0.54	0.90	0.0399	0.0250	-2.6E-04	5.1E-04	2.3E-03	-9.8E-05	3.8E-04	4.8E-07	5.2E-07	1.0E-06
0.51	0.90	0.0405	0.0239	-2.6E-04	4.5E-04	2.3E-03	-2.1E-04	3.4E-04	2.9E-07	5.0E-07	7.3E-07
0.46	0.88	0.0418	0.0251	-3.0E-04	4.9E-04	2.4E-03	-1.2E-04	4.5E-04	2.8E-07	6.4E-07	1.0E-06
0.43	0.87	0.0420	0.0251	-3.1E-04	5.4E-04	2.4E-03	-1.0E-04	3.5E-04	4.1E-07	5.0E-07	1.1E-06
0.40	0.87	0.0422	0.0247	-3.1E-04	5.3E-04	2.4E-03	-1.5E-04	3.2E-04	4.0E-07	4.9E-07	9.5E-07
0.38	0.86	0.0420	0.0243	-3.1E-04	6.1E-04	2.5E-03	-1.0E-04	4.1E-04	5.9E-07	5.4E-07	1.0E-06
0.35	0.85	0.0424	0.0248	-3.2E-04	5.9E-04	2.6E-03	-1.4E-04	3.4E-04	4.7E-07	5.0E-07	1.0E-06
0.32	0.84	0.0430	0.0241	-3.3E-04	5.7E-04	2.8E-03	-1.1E-04	2.9E-04	2.8E-07	4.1E-07	1.1E-06
0.30	0.83	0.0440	0.0248	-3.5E-04	5.6E-04	3.0E-03	-1.2E-04	3.0E-04	2.2E-08	4.4E-07	1.3E-06
0.27	0.83	0.0449	0.0249	-3.6E-04	6.2E-04	3.2E-03	-1.8E-04	2.0E-04	2.3E-07	3.8E-07	1.3E-06
0.24	0.82	0.0450	0.0253	-3.8E-04	5.9E-04	3.1E-03	-1.2E-04	2.6E-04	2.5E-08	4.4E-07	1.4E-06
0.21	0.81	0.0463	0.0261	-4.2E-04	6.3E-04	3.0E-03	-1.5E-04	2.6E-04	2.0E-07	4.8E-07	1.3E-06
0.19	0.80	0.0482	0.0278	-4.3E-04	6.1E-04	2.8E-03	-1.6E-04	2.1E-04	4.5E-07	4.6E-07	1.4E-06
0.16	0.79	0.0505	0.0305	-5.1E-04	7.4E-04	3.2E-03	-1.8E-04	1.2E-04	5.0E-07	4.1E-07	2.0E-06
0.13	0.78	0.0609	0.0389	-5.3E-04	8.6E-04	4.6E-03	-3.9E-04	-1.2E-03	1.4E-06	-3.7E-06	5.8E-06
0.11	0.77	0.1358	0.0843	-3.1E-04	1.4E-03	9.5E-03	-9.4E-04	-5.8E-03	5.0E-05	-9.0E-05	5.5E-05

Table 31: SPG square roughness PIV kinematic values at test location 2.

$\frac{y}{\delta}$	$\frac{U_{eff}}{U_{eff,e}}$	$\frac{\sqrt{\overline{u'^2}}}{U}$	$\frac{\sqrt{\overline{v'^2}}}{U}$	$\frac{\overline{u'v'}}{U^2}$	$\frac{d\bar{u}}{dx}\cdot\frac{\delta}{U}$	$\frac{d\bar{u}}{dy}\cdot\frac{\delta}{U}$	$\frac{d\bar{v}}{dx}\cdot\frac{\delta}{U}$	$\frac{d\bar{v}}{dy}\cdot\frac{\delta}{U}$	$P_{xx}\cdot\frac{\delta}{U^3}$	$P_{yy}\cdot\frac{\delta}{U^3}$	$P_{xy}\cdot\frac{\delta}{U^3}$
1.30	1.04	0.0101	0.0103	-1.0E-06	1.0E-04	-2.0E-04	-2.1E-04	6.1E-04	2.4E-08	1.3E-07	-4.4E-08
1.27	1.04	0.0096	0.0107	-3.6E-06	9.7E-05	-9.1E-05	-2.7E-04	6.3E-04	2.0E-08	1.4E-07	-3.3E-08
1.24	1.04	0.0111	0.0120	-4.4E-06	6.4E-05	1.7E-05	-2.4E-04	6.4E-04	1.3E-08	1.8E-07	-3.0E-08
1.21	1.04	0.0116	0.0120	-1.8E-06	5.7E-05	1.2E-04	-2.6E-04	7.0E-04	1.3E-08	2.0E-07	-2.4E-08
1.19	1.04	0.0131	0.0122	-1.8E-06	8.2E-05	3.5E-04	-2.3E-04	7.4E-04	3.1E-08	2.3E-07	1.3E-08
1.16	1.04	0.0147	0.0128	9.6E-07	1.4E-04	5.9E-04	-2.4E-04	7.8E-04	6.6E-08	2.6E-07	4.6E-08
1.13	1.03	0.0167	0.0143	3.3E-06	1.7E-04	7.7E-04	-2.6E-04	8.0E-04	9.8E-08	3.2E-07	8.5E-08
1.10	1.03	0.0183	0.0152	1.3E-06	2.0E-04	7.8E-04	-2.3E-04	8.2E-04	1.4E-07	3.8E-07	1.0E-07
1.07	1.03	0.0198	0.0154	-1.3E-06	1.5E-04	9.5E-04	-2.1E-04	7.6E-04	1.1E-07	3.6E-07	1.5E-07
1.04	1.02	0.0215	0.0154	-3.0E-07	1.6E-04	1.4E-03	-2.1E-04	7.5E-04	1.4E-07	3.6E-07	2.3E-07
1.01	1.01	0.0245	0.0168	-1.4E-05	1.5E-04	1.7E-03	-2.0E-04	7.3E-04	1.5E-07	4.1E-07	3.4E-07
0.98	1.01	0.0271	0.0184	-4.2E-05	2.2E-04	1.6E-03	-1.3E-04	6.9E-04	1.8E-07	4.8E-07	4.1E-07
0.95	1.00	0.0286	0.0192	-5.3E-05	2.1E-04	1.7E-03	-1.6E-04	6.0E-04	1.6E-07	4.6E-07	4.7E-07
0.92	0.99	0.0313	0.0199	-7.3E-05	4.7E-05	2.0E-03	-1.4E-04	4.8E-04	-2.2E-07	3.9E-07	6.3E-07
0.89	0.98	0.0342	0.0212	-1.1E-04	2.1E-04	2.1E-03	-1.4E-04	5.3E-04	1.3E-08	5.1E-07	7.0E-07
0.86	0.97	0.0360	0.0213	-1.3E-04	1.5E-04	2.0E-03	-1.4E-04	6.3E-04	-1.4E-07	6.1E-07	6.4E-07
0.83	0.97	0.0376	0.0226	-1.5E-04	8.3E-05	2.7E-03	-8.0E-05	5.7E-04	-5.7E-07	6.1E-07	1.2E-06
0.80	0.95	0.0429	0.0251	-2.4E-04	2.5E-04	3.1E-03	-1.0E-04	3.1E-04	-5.5E-07	4.5E-07	1.6E-06
0.77	0.94	0.0466	0.0278	-3.3E-04	2.4E-04	2.8E-03	-8.9E-05	4.8E-04	-8.4E-07	8.0E-07	1.7E-06
0.74	0.93	0.0485	0.0292	-4.1E-04	2.3E-04	3.1E-03	-6.3E-05	5.2E-04	-1.4E-06	9.4E-07	2.1E-06
0.71	0.92	0.0524	0.0316	-5.2E-04	3.1E-04	3.3E-03	-1.4E-04	4.6E-04	-1.7E-06	1.1E-06	2.5E-06
0.68	0.91	0.0558	0.0333	-6.1E-04	4.1E-04	3.2E-03	-1.5E-04	5.6E-04	-1.4E-06	1.4E-06	2.5E-06
0.66	0.90	0.0580	0.0347	-6.5E-04	4.6E-04	3.2E-03	-1.7E-04	5.0E-04	-1.1E-06	1.4E-06	2.7E-06
0.63	0.88	0.0603	0.0367	-7.9E-04	4.9E-04	3.3E-03	-2.4E-04	3.6E-04	-1.7E-06	1.3E-06	3.0E-06
0.60	0.87	0.0624	0.0390	-8.2E-04	6.7E-04	3.5E-03	-2.4E-04	3.5E-04	-5.4E-07	1.5E-06	3.5E-06
0.57	0.86	0.0639	0.0405	-9.4E-04	5.9E-04	3.4E-03	-2.4E-04	2.9E-04	-1.5E-06	1.4E-06	3.8E-06
0.54	0.85	0.0650	0.0414	-1.0E-03	7.1E-04	3.7E-03	-2.8E-04	2.4E-04	-1.6E-06	1.4E-06	4.2E-06
0.51	0.84	0.0683	0.0446	-1.2E-03	6.7E-04	4.0E-03	-1.4E-04	2.6E-04	-3.0E-06	1.4E-06	6.2E-06
0.48	0.82	0.0712	0.0467	-1.3E-03	6.8E-04	4.0E-03	-1.2E-04	2.0E-04	-3.3E-06	1.2E-06	7.1E-06
0.45	0.81	0.0751	0.0491	-1.4E-03	6.6E-04	4.2E-03	-2.0E-04	3.1E-05	-4.0E-06	6.8E-07	8.1E-06
0.42	0.80	0.0792	0.0525	-1.5E-03	5.9E-04	4.6E-03	-1.3E-04	1.7E-04	-6.0E-06	1.3E-06	1.1E-05
0.39	0.79	0.0823	0.0538	-1.6E-03	6.2E-04	4.4E-03	-5.5E-05	1.8E-04	-5.9E-06	1.2E-06	1.1E-05
0.36	0.77	0.0891	0.0566	-1.5E-03	5.4E-04	4.4E-03	-1.2E-04	1.3E-05	-4.5E-06	3.7E-07	1.2E-05
0.33	0.76	0.0934	0.0577	-1.5E-03	9.1E-04	5.2E-03	-4.3E-05	2.5E-05	8.4E-07	2.8E-07	1.6E-05
0.30	0.75	0.0997	0.0640	-1.7E-03	9.1E-04	5.3E-03	-1.3E-04	-3.6E-05	-7.6E-08	1.7E-07	1.9E-05
0.27	0.73	0.0968	0.0624	-2.0E-03	9.3E-04	4.6E-03	-5.3E-05	1.2E-04	-8.7E-07	1.2E-06	1.6E-05
0.24	0.72	0.1008	0.0680	-2.2E-03	8.6E-04	5.1E-03	-1.4E-04	-3.7E-04	-5.3E-06	-2.8E-06	2.1E-05
0.21	0.71	0.1118	0.0738	-2.3E-03	5.0E-04	6.3E-03	-1.0E-04	-2.9E-04	-1.7E-05	-2.5E-06	3.3E-05
0.18	0.69	0.1277	0.0847	-2.5E-03	4.9E-04	6.9E-03	-1.0E-04	-5.4E-05	-1.8E-05	-1.2E-06	4.8E-05
0.15	0.67	0.1608	0.1018	-2.7E-03	9.8E-04	7.6E-03	-3.3E-04	-4.7E-04	1.0E-05	-8.0E-06	6.9E-05
0.12	0.65	0.2024	0.1029	-4.2E-03	1.6E-03	1.1E-02	2.5E-04	2.2E-04	3.1E-05	-6.6E-07	1.2E-04

Table 32: SPG diamond roughness peak PIV kinematic values at test location 2.

$\frac{y}{\delta}$	$\frac{U_{eff}}{U_{eff,e}}$	$\frac{\sqrt{\overline{u'^2}}}{U}$	$\frac{\sqrt{\overline{v'^2}}}{U}$	$\frac{\overline{u'v'}}{U^2}$	$\frac{d\bar{u}}{dx}\cdot\frac{\delta}{U}$	$\frac{d\bar{u}}{dy}\cdot\frac{\delta}{U}$	$\frac{d\bar{v}}{dx}\cdot\frac{\delta}{U}$	$\frac{d\bar{v}}{dy}\cdot\frac{\delta}{U}$	$P_{xx}\cdot\frac{\delta}{U^3}$	$P_{yy}\cdot\frac{\delta}{U^3}$	$P_{xy}\cdot\frac{\delta}{U^3}$
1.28	1.03	0.0109	0.0103	-1.5E-05	-5.5E-05	4.6E-04	5.4E-05	6.8E-05	-2.6E-08	7.9E-09	5.6E-08
1.25	1.03	0.0108	0.0094	-1.0E-05	4.4E-05	4.6E-04	-3.3E-05	4.9E-04	2.1E-09	8.3E-08	3.4E-08
1.22	1.03	0.0109	0.0090	-4.9E-06	1.1E-04	3.3E-04	-1.6E-04	8.9E-04	2.3E-08	1.4E-07	5.7E-09
1.19	1.03	0.0115	0.0087	-6.5E-06	1.9E-04	3.2E-04	-2.9E-04	1.2E-03	5.0E-08	1.9E-07	-2.1E-08
1.16	1.03	0.0123	0.0088	-2.6E-06	2.2E-04	3.1E-04	-3.9E-04	1.5E-03	5.8E-08	2.3E-07	-3.6E-08
1.13	1.03	0.0135	0.0089	-2.3E-06	3.1E-04	3.4E-04	-4.9E-04	1.5E-03	1.1E-07	2.4E-07	-6.9E-08
1.10	1.02	0.0147	0.0094	-2.4E-06	3.2E-04	4.4E-04	-5.2E-04	1.5E-03	1.3E-07	2.7E-07	-7.3E-08
1.07	1.02	0.0155	0.0107	-2.5E-06	2.7E-04	7.2E-04	-5.0E-04	1.4E-03	1.3E-07	3.3E-07	-3.8E-08
1.04	1.02	0.0159	0.0127	-5.2E-06	1.8E-04	9.1E-04	-3.6E-04	1.1E-03	8.0E-08	3.3E-07	5.4E-08
1.01	1.01	0.0165	0.0147	-1.7E-05	7.9E-05	1.2E-03	-1.4E-04	2.8E-04	-5.1E-09	1.1E-07	2.1E-07
0.98	1.01	0.0170	0.0155	-3.4E-05	4.1E-05	1.5E-03	1.1E-04	-4.6E-04	-7.8E-08	-2.3E-07	4.1E-07
0.95	1.00	0.0200	0.0164	-5.9E-05	6.2E-06	1.9E-03	2.6E-04	-8.8E-04	-2.3E-07	-5.1E-07	6.7E-07
0.92	0.99	0.0241	0.0160	-8.4E-05	2.6E-04	2.3E-03	2.2E-04	-1.1E-03	-7.9E-08	-5.7E-07	7.7E-07
0.89	0.98	0.0260	0.0136	-6.9E-05	2.8E-04	2.1E-03	7.9E-05	-5.5E-04	6.5E-08	-2.1E-07	4.7E-07
0.86	0.97	0.0277	0.0126	-5.4E-05	3.0E-04	2.0E-03	-2.2E-04	2.8E-04	2.6E-07	1.1E-07	1.1E-07
0.83	0.96	0.0294	0.0142	-4.5E-05	3.8E-04	1.9E-03	-5.0E-04	1.4E-03	5.0E-07	6.4E-07	-1.3E-07
0.80	0.96	0.0312	0.0181	-5.5E-05	4.3E-04	1.7E-03	-7.8E-04	2.4E-03	6.5E-07	1.8E-06	-3.4E-07
0.77	0.95	0.0323	0.0221	-7.3E-05	4.9E-04	1.9E-03	-9.8E-04	3.1E-03	7.5E-07	3.2E-06	-3.4E-07
0.74	0.94	0.0362	0.0251	-1.3E-04	5.5E-04	2.4E-03	-1.0E-03	3.2E-03	8.0E-07	4.2E-06	-3.6E-07
0.71	0.93	0.0396	0.0270	-1.9E-04	6.4E-04	2.4E-03	-9.1E-04	2.6E-03	1.1E-06	4.2E-06	-3.0E-07
0.68	0.93	0.0419	0.0297	-3.1E-04	6.4E-04	2.7E-03	-5.5E-04	1.5E-03	6.0E-07	2.9E-06	7.7E-07
0.65	0.91	0.0422	0.0314	-4.6E-04	3.1E-04	2.9E-03	1.4E-04	-2.9E-04	-1.6E-06	-7.5E-07	3.2E-06
0.62	0.90	0.0434	0.0313	-5.5E-04	1.2E-04	4.0E-03	7.2E-04	-2.0E-03	-4.0E-06	-4.8E-06	6.4E-06
0.59	0.88	0.0465	0.0338	-7.2E-04	-1.7E-05	5.1E-03	9.9E-04	-3.3E-03	-7.4E-06	-8.9E-06	1.0E-05
0.56	0.87	0.0489	0.0366	-8.5E-04	4.9E-05	5.0E-03	9.5E-04	-3.1E-03	-8.2E-06	-1.0E-05	1.2E-05
0.53	0.85	0.0494	0.0345	-7.4E-04	2.6E-04	4.6E-03	5.4E-04	-2.0E-03	-5.7E-06	-5.6E-06	8.2E-06
0.50	0.83	0.0499	0.0324	-6.1E-04	4.9E-04	4.1E-03	-3.2E-05	-7.1E-04	-2.7E-06	-1.6E-06	4.5E-06
0.47	0.82	0.0492	0.0308	-4.8E-04	7.5E-04	3.9E-03	-5.4E-04	4.1E-04	-1.7E-07	1.3E-06	1.9E-06
0.44	0.81	0.0517	0.0330	-5.0E-04	9.7E-04	3.8E-03	-9.8E-04	1.5E-03	1.4E-06	4.2E-06	3.4E-07
0.41	0.80	0.0528	0.0343	-5.2E-04	1.2E-03	3.3E-03	-1.4E-03	2.9E-03	3.3E-06	8.2E-06	-2.1E-06
0.38	0.79	0.0541	0.0343	-5.4E-04	1.3E-03	2.7E-03	-1.6E-03	3.5E-03	4.7E-06	1.0E-05	-4.1E-06
0.35	0.78	0.0550	0.0371	-6.2E-04	1.5E-03	2.4E-03	-1.8E-03	4.2E-03	6.4E-06	1.4E-05	-5.7E-06
0.32	0.78	0.0552	0.0371	-6.2E-04	1.5E-03	2.4E-03	-1.9E-03	4.6E-03	6.3E-06	1.5E-05	-6.3E-06
0.29	0.77	0.0549	0.0380	-7.0E-04	1.6E-03	2.6E-03	-1.7E-03	3.9E-03	5.7E-06	1.4E-05	-5.2E-06
0.26	0.77	0.0563	0.0396	-8.8E-04	1.3E-03	3.1E-03	-1.1E-03	2.4E-03	2.4E-06	9.0E-06	-1.3E-06
0.23	0.76	0.0590	0.0414	-1.1E-03	8.3E-04	4.4E-03	-3.4E-05	2.4E-04	-4.3E-06	6.3E-07	6.5E-06
0.20	0.74	0.0630	0.0431	-1.4E-03	2.7E-04	5.8E-03	1.2E-03	-1.9E-03	-1.4E-05	-1.0E-05	1.8E-05
0.17	0.73	0.0683	0.0466	-1.8E-03	-1.1E-04	7.5E-03	2.2E-03	-3.7E-03	-2.8E-05	-2.4E-05	3.3E-05
0.14	0.70	0.0766	0.0516	-2.2E-03	-3.4E-04	9.3E-03	2.8E-03	-5.0E-03	-4.6E-05	-4.0E-05	5.3E-05
0.11	0.68	0.0887	0.0578	-2.6E-03	-5.6E-04	1.1E-02	3.0E-03	-5.5E-03	-6.5E-05	-5.3E-05	7.6E-05
0.08	0.65	0.1198	0.0675	-3.5E-03	1.2E-03	1.9E-02	2.4E-03	-5.8E-03	-6.4E-05	-7.3E-05	1.4E-04
0.05	0.59	0.2195	0.0884	-8.2E-03	8.9E-03	4.4E-02	6.9E-04	-1.1E-02	9.6E-04	-1.7E-04	2.8E-04

Table 33: SPG diamond roughness valley PIV kinematic values at test location 2.

$\frac{y}{\delta}$	$\frac{U_{eff}}{U_{eff,e}}$	$\frac{\sqrt{\overline{u'^2}}}{U}$	$\frac{\sqrt{\overline{v'^2}}}{U}$	$\frac{\overline{u'v'}}{U^2}$	$\frac{d\bar{u}}{dx}\cdot\frac{\delta}{U}$	$\frac{d\bar{u}}{dy}\cdot\frac{\delta}{U}$	$\frac{d\bar{v}}{dx}\cdot\frac{\delta}{U}$	$\frac{d\bar{v}}{dy}\cdot\frac{\delta}{U}$	$P_{xx}\cdot\frac{\delta}{U^3}$	$P_{yy}\cdot\frac{\delta}{U^3}$	$P_{xy}\cdot\frac{\delta}{U^3}$
1.39	1.05	0.0089	0.0107	-1.2E-05	1.0E-04	-1.5E-04	-2.7E-04	1.5E-03	2.3E-08	3.5E-07	-5.7E-08
1.36	1.05	0.0095	0.0115	-1.1E-05	1.3E-04	-1.1E-04	-3.0E-04	1.7E-03	2.3E-08	4.7E-07	-6.4E-08
1.33	1.05	0.0103	0.0118	-1.1E-05	1.2E-04	6.7E-05	-2.5E-04	1.5E-03	2.7E-08	4.3E-07	-3.2E-08
1.29	1.05	0.0111	0.0121	-1.1E-05	7.6E-05	3.6E-04	-1.7E-04	9.8E-04	7.0E-09	2.9E-07	2.1E-08
1.26	1.04	0.0123	0.0126	-1.8E-05	5.2E-05	6.3E-04	-2.2E-05	3.2E-04	-9.4E-09	9.4E-08	9.5E-08
1.23	1.04	0.0133	0.0124	-2.4E-05	2.3E-05	9.3E-04	9.4E-05	-2.6E-04	-3.4E-08	-8.2E-08	1.7E-07
1.20	1.03	0.0139	0.0122	-2.6E-05	2.8E-05	1.1E-03	1.3E-04	-5.4E-04	-4.8E-08	-1.7E-07	2.0E-07
1.16	1.03	0.0145	0.0118	-2.6E-05	5.4E-05	1.2E-03	9.0E-05	-5.1E-04	-3.8E-08	-1.5E-07	1.9E-07
1.13	1.02	0.0151	0.0119	-2.3E-05	7.9E-05	1.1E-03	-3.2E-05	-1.7E-04	-1.2E-08	-4.6E-08	1.5E-07
1.10	1.02	0.0156	0.0117	-1.8E-05	1.3E-04	9.8E-04	-2.2E-04	4.0E-04	2.6E-08	1.2E-07	7.3E-08
1.07	1.01	0.0161	0.0121	-1.7E-05	1.8E-04	9.7E-04	-3.8E-04	1.1E-03	6.1E-08	3.2E-07	1.8E-08
1.03	1.01	0.0173	0.0140	-1.1E-05	1.9E-04	9.5E-04	-5.2E-04	1.7E-03	1.0E-07	7.0E-07	1.1E-08
1.00	1.01	0.0188	0.0165	-1.5E-05	2.2E-04	1.1E-03	-6.7E-04	2.3E-03	1.2E-07	1.3E-06	2.4E-08
0.97	1.00	0.0216	0.0188	-2.9E-05	2.4E-04	1.4E-03	-6.6E-04	2.3E-03	1.4E-07	1.7E-06	1.2E-07
0.94	0.99	0.0254	0.0201	-6.1E-05	2.6E-04	1.6E-03	-4.5E-04	1.7E-03	1.3E-07	1.4E-06	2.7E-07
0.90	0.99	0.0279	0.0218	-1.1E-04	2.1E-04	1.9E-03	-1.3E-04	6.2E-04	-1.1E-07	5.6E-07	7.4E-07
0.87	0.98	0.0301	0.0232	-1.7E-04	1.4E-04	2.2E-03	2.3E-04	-5.6E-04	-5.0E-07	-7.3E-07	1.5E-06
0.84	0.97	0.0320	0.0246	-2.2E-04	4.0E-05	2.6E-03	5.2E-04	-1.6E-03	-1.1E-06	-2.2E-06	2.5E-06
0.81	0.95	0.0347	0.0260	-2.8E-04	1.8E-05	3.2E-03	6.5E-04	-2.1E-03	-1.8E-06	-3.2E-06	3.5E-06
0.78	0.94	0.0375	0.0263	-3.2E-04	1.9E-04	3.4E-03	4.9E-04	-1.8E-03	-1.6E-06	-2.8E-06	3.5E-06
0.74	0.92	0.0395	0.0259	-3.0E-04	1.9E-04	3.0E-03	2.0E-04	-8.8E-04	-1.1E-06	-1.3E-06	2.5E-06
0.71	0.91	0.0406	0.0262	-2.6E-04	4.0E-04	2.5E-03	-2.2E-04	2.1E-04	3.2E-10	4.0E-07	1.2E-06
0.68	0.90	0.0406	0.0271	-2.4E-04	6.6E-04	2.5E-03	-5.4E-04	1.3E-03	9.6E-07	2.2E-06	5.0E-07
0.65	0.89	0.0407	0.0284	-2.3E-04	6.9E-04	2.3E-03	-7.8E-04	2.1E-03	1.2E-06	3.8E-06	-8.7E-08
0.61	0.89	0.0424	0.0298	-2.8E-04	7.9E-04	2.0E-03	-9.5E-04	2.7E-03	1.7E-06	5.3E-06	-8.7E-07
0.58	0.88	0.0437	0.0299	-2.9E-04	9.3E-04	2.0E-03	-1.1E-03	3.0E-03	2.4E-06	6.1E-06	-1.5E-06
0.55	0.87	0.0443	0.0295	-3.0E-04	1.0E-03	1.7E-03	-1.1E-03	3.3E-03	3.0E-06	6.4E-06	-2.0E-06
0.52	0.87	0.0458	0.0310	-3.7E-04	9.9E-04	2.1E-03	-9.6E-04	2.8E-03	2.6E-06	6.0E-06	-1.3E-06
0.48	0.86	0.0491	0.0342	-5.4E-04	7.3E-04	2.8E-03	-4.4E-04	1.4E-03	4.5E-07	3.7E-06	1.1E-06
0.45	0.85	0.0525	0.0376	-8.2E-04	4.2E-04	3.4E-03	3.3E-04	-5.6E-04	-3.4E-06	-2.3E-06	6.0E-06
0.42	0.83	0.0557	0.0415	-1.1E-03	6.6E-05	4.5E-03	1.1E-03	-2.7E-03	-9.5E-06	-1.2E-05	1.4E-05
0.39	0.82	0.0587	0.0461	-1.4E-03	-2.3E-04	5.6E-03	1.8E-03	-4.3E-03	-1.8E-05	-2.4E-05	2.5E-05
0.36	0.79	0.0587	0.0456	-1.4E-03	-3.9E-05	6.0E-03	1.8E-03	-4.8E-03	-1.7E-05	-2.5E-05	2.5E-05
0.32	0.77	0.0596	0.0441	-1.3E-03	1.8E-04	5.5E-03	1.3E-03	-3.8E-03	-1.3E-05	-1.8E-05	2.0E-05
0.29	0.76	0.0608	0.0427	-1.1E-03	5.4E-04	5.2E-03	6.2E-04	-2.1E-03	-7.9E-06	-9.2E-06	1.4E-05
0.26	0.74	0.0618	0.0431	-1.1E-03	9.3E-04	5.0E-03	-9.7E-05	-5.1E-04	-3.8E-06	-1.8E-06	8.6E-06
0.23	0.73	0.0627	0.0415	-9.9E-04	1.3E-03	4.6E-03	-8.1E-04	6.0E-04	7.6E-07	3.5E-06	3.1E-06
0.19	0.72	0.0639	0.0410	-9.3E-04	1.5E-03	4.3E-03	-1.4E-03	1.7E-03	4.2E-06	8.3E-06	-1.4E-06
0.16	0.70	0.0654	0.0442	-9.4E-04	1.8E-03	4.4E-03	-2.0E-03	2.8E-03	7.2E-06	1.5E-05	-4.1E-06
0.13	0.69	0.0708	0.0478	-1.0E-03	2.3E-03	6.2E-03	-2.4E-03	2.8E-03	1.0E-05	1.8E-05	-2.8E-06
0.10	0.67	0.0785	0.0540	-1.3E-03	2.3E-03	8.1E-03	-2.9E-03	1.7E-03	7.3E-06	1.8E-05	6.4E-07
0.06	0.65	0.0992	0.0608	-2.1E-03	2.8E-03	8.4E-02	-3.3E-03	-1.1E-02	-3.2E-04	-6.9E-05	3.0E-04

Table 34: SPG smooth wall PIV kinematic values at test location 3.

$\frac{y}{\delta}$	$\frac{U_{eff}}{U_{eff,e}}$	$\frac{\sqrt{\overline{u'^2}}}{U}$	$\frac{\sqrt{\overline{v'^2}}}{U}$	$\frac{\overline{u'v'}}{U^2}$	$\frac{d\bar{u}}{dx}\cdot\frac{\delta}{U}$	$\frac{d\bar{u}}{dy}\cdot\frac{\delta}{U}$	$\frac{d\bar{v}}{dx}\cdot\frac{\delta}{U}$	$\frac{d\bar{v}}{dy}\cdot\frac{\delta}{U}$	$P_{xx}\cdot\frac{\delta}{U^3}$	$P_{yy}\cdot\frac{\delta}{U^3}$	$P_{xy}\cdot\frac{\delta}{U^3}$
1.27	1.05	0.0131	0.0125	-3.7E-05	-3.4E-04	1.0E-03	7.4E-04	-2.6E-03	-1.9E-07	-8.7E-07	4.0E-07
1.24	1.05	0.0137	0.0120	-3.8E-05	-3.5E-04	1.0E-03	6.6E-04	-2.4E-03	-2.1E-07	-7.4E-07	3.7E-07
1.21	1.04	0.0141	0.0111	-3.1E-05	-3.5E-04	1.0E-03	6.1E-04	-2.0E-03	-2.1E-07	-5.4E-07	3.3E-07
1.18	1.03	0.0152	0.0114	-3.5E-05	-3.7E-04	1.1E-03	6.0E-04	-2.0E-03	-2.5E-07	-5.6E-07	3.7E-07
1.15	1.03	0.0162	0.0131	-4.5E-05	-4.6E-04	1.4E-03	7.3E-04	-2.4E-03	-3.7E-07	-9.1E-07	5.6E-07
1.12	1.02	0.0173	0.0156	-6.3E-05	-5.1E-04	1.6E-03	9.5E-04	-2.9E-03	-5.1E-07	-1.6E-06	8.9E-07
1.09	1.01	0.0177	0.0178	-8.1E-05	-5.1E-04	2.0E-03	1.1E-03	-3.2E-03	-6.5E-07	-2.2E-06	1.3E-06
1.06	1.00	0.0157	0.0178	-6.4E-05	-6.1E-04	1.9E-03	1.1E-03	-3.1E-03	-5.8E-07	-2.1E-06	1.1E-06
1.03	0.99	0.0139	0.0161	-4.5E-05	-4.2E-04	1.6E-03	9.2E-04	-2.5E-03	-3.3E-07	-1.4E-06	7.8E-07
1.00	0.99	0.0117	0.0141	-3.0E-05	-2.7E-04	1.3E-03	7.1E-04	-1.7E-03	-1.5E-07	-7.5E-07	4.2E-07
0.97	0.98	0.0118	0.0132	-3.0E-05	-1.6E-04	1.2E-03	4.9E-04	-1.2E-03	-1.2E-07	-4.4E-07	3.3E-07
0.94	0.97	0.0139	0.0131	-4.4E-05	-1.6E-04	1.6E-03	3.5E-04	-8.2E-04	-2.0E-07	-3.1E-07	3.8E-07
0.91	0.97	0.0173	0.0130	-6.1E-05	-1.2E-04	2.1E-03	2.8E-04	-6.4E-04	-3.2E-07	-2.6E-07	4.8E-07
0.88	0.96	0.0216	0.0136	-9.6E-05	-2.0E-04	2.4E-03	2.1E-04	-4.7E-04	-6.6E-07	-2.2E-07	6.1E-07
0.84	0.95	0.0247	0.0147	-1.3E-04	-2.5E-04	2.7E-03	1.7E-04	-3.6E-04	-1.0E-06	-2.0E-07	7.6E-07
0.81	0.93	0.0271	0.0157	-1.6E-04	-2.7E-04	3.0E-03	1.6E-04	-3.3E-04	-1.3E-06	-2.1E-07	9.5E-07
0.78	0.92	0.0285	0.0165	-1.8E-04	-2.6E-04	3.2E-03	1.4E-04	-3.1E-04	-1.6E-06	-2.2E-07	1.1E-06
0.75	0.91	0.0294	0.0178	-2.1E-04	-2.9E-04	3.4E-03	1.5E-04	-3.5E-04	-1.9E-06	-2.8E-07	1.3E-06
0.72	0.90	0.0307	0.0203	-2.7E-04	-2.5E-04	3.5E-03	1.4E-04	-2.9E-04	-2.4E-06	-3.1E-07	1.7E-06
0.69	0.88	0.0320	0.0224	-3.2E-04	-2.4E-04	3.5E-03	1.4E-04	-2.6E-04	-2.7E-06	-3.6E-07	2.1E-06
0.66	0.87	0.0330	0.0233	-3.7E-04	-2.3E-04	3.4E-03	1.0E-04	-3.1E-04	-3.0E-06	-4.0E-07	2.2E-06
0.63	0.86	0.0343	0.0228	-3.9E-04	-2.5E-04	3.5E-03	9.8E-05	-2.8E-04	-3.3E-06	-3.6E-07	2.1E-06
0.60	0.85	0.0351	0.0251	-4.4E-04	-2.1E-04	3.7E-03	9.3E-05	-2.5E-05	-3.8E-06	-1.1E-07	2.6E-06
0.57	0.83	0.0364	0.0257	-4.8E-04	-1.2E-04	3.8E-03	6.9E-05	-1.6E-05	-3.9E-06	-8.9E-08	2.7E-06
0.54	0.82	0.0394	0.0257	-5.3E-04	-1.5E-04	4.0E-03	5.0E-05	-4.8E-05	-4.8E-06	-1.2E-07	2.8E-06
0.51	0.81	0.0417	0.0262	-5.9E-04	-1.6E-04	4.2E-03	9.7E-05	1.5E-04	-5.5E-06	9.5E-08	3.1E-06
0.48	0.79	0.0441	0.0265	-6.2E-04	-1.3E-04	4.3E-03	8.3E-05	3.6E-04	-5.8E-06	4.1E-07	3.1E-06
0.45	0.78	0.0470	0.0280	-6.7E-04	-1.5E-04	4.8E-03	7.7E-05	3.4E-04	-7.1E-06	4.4E-07	3.8E-06
0.42	0.77	0.0523	0.0296	-7.9E-04	-2.3E-04	5.5E-03	6.2E-05	3.1E-04	-1.0E-05	4.5E-07	5.0E-06
0.39	0.75	0.0571	0.0312	-9.0E-04	-3.2E-04	6.0E-03	6.7E-05	4.3E-04	-1.3E-05	7.2E-07	5.9E-06
0.36	0.73	0.0632	0.0329	-1.0E-03	-2.7E-04	6.9E-03	5.6E-05	3.4E-04	-1.7E-05	6.1E-07	7.6E-06
0.33	0.71	0.0721	0.0356	-1.3E-03	-2.7E-04	7.9E-03	1.0E-04	3.4E-04	-2.4E-05	6.0E-07	1.0E-05
0.30	0.69	0.0824	0.0397	-1.7E-03	-3.6E-04	9.3E-03	1.2E-04	2.6E-04	-3.6E-05	4.0E-07	1.6E-05
0.27	0.67	0.0950	0.0438	-2.0E-03	-4.4E-04	1.1E-02	3.6E-05	2.0E-04	-5.1E-05	5.5E-07	2.1E-05
0.24	0.64	0.1079	0.0491	-2.5E-03	-5.1E-04	1.1E-02	2.3E-05	1.5E-04	-7.0E-05	6.0E-07	2.9E-05
0.21	0.62	0.1179	0.0530	-2.9E-03	-5.2E-04	1.2E-02	6.4E-05	2.8E-04	-8.5E-05	1.3E-06	3.6E-05
0.18	0.59	0.1263	0.0560	-3.1E-03	-8.1E-04	8.8E-03	2.1E-04	1.0E-04	-8.1E-05	-5.6E-07	3.3E-05
0.15	0.58	0.1649	0.0800	-3.1E-03	8.4E-04	8.6E-03	2.8E-04	7.3E-05	-4.5E-06	-6.3E-07	6.3E-05
0.12	0.55	0.1820	0.0885	-3.2E-03	1.0E-02	1.5E-02	-3.6E-05	4.4E-05	6.9E-04	4.1E-07	8.2E-05
0.09	0.53	0.1940	0.0872	-3.2E-03	1.5E-02	1.5E-02	-3.1E-04	-5.4E-04	1.3E-03	-6.5E-06	5.6E-05
0.06	0.50	0.1920	0.0551	-1.9E-03	1.7E-02	1.4E-02	-2.5E-04	-1.3E-03	1.5E-03	-6.0E-06	5.7E-06

Table 35: SPG square roughness PIV kinematic values at test location 3.

$\frac{y}{\delta}$	$\frac{U_{eff}}{U_{eff,e}}$	$\frac{\sqrt{\overline{u'^2}}}{U}$	$\frac{\sqrt{\overline{v'^2}}}{U}$	$\frac{\overline{u'v'}}{U^2}$	$\frac{d\bar{u}}{dx}\cdot\frac{\delta}{U}$	$\frac{d\bar{u}}{dy}\cdot\frac{\delta}{U}$	$\frac{d\bar{v}}{dx}\cdot\frac{\delta}{U}$	$\frac{d\bar{v}}{dy}\cdot\frac{\delta}{U}$	$P_{xx}\cdot\frac{\delta}{U^3}$	$P_{yy}\cdot\frac{\delta}{U^3}$	$P_{xy}\cdot\frac{\delta}{U^3}$
1.16	1.03	0.0166	0.0235	-1.9E-05	-1.9E-04	6.6E-04	5.4E-04	-1.9E-03	-1.3E-07	-2.1E-06	5.5E-07
1.14	1.02	0.0159	0.0228	-2.8E-05	-1.1E-04	9.3E-04	6.6E-04	-2.2E-03	-1.1E-07	-2.4E-06	7.2E-07
1.09	1.01	0.0173	0.0223	-6.9E-05	-3.1E-05	1.5E-03	5.4E-04	-1.5E-03	-2.4E-07	-1.5E-06	1.0E-06
1.06	1.01	0.0181	0.0219	-9.6E-05	-2.3E-05	1.7E-03	6.7E-04	-1.6E-03	-3.5E-07	-1.6E-06	1.2E-06
1.04	1.00	0.0187	0.0215	-9.8E-05	5.1E-05	2.0E-03	5.6E-04	-1.5E-03	-3.6E-07	-1.5E-06	1.3E-06
1.01	0.99	0.0207	0.0220	-1.2E-04	-4.0E-05	2.6E-03	5.4E-04	-1.4E-03	-6.5E-07	-1.5E-06	1.7E-06
0.99	0.98	0.0236	0.0228	-1.6E-04	-7.3E-05	3.1E-03	4.6E-04	-1.3E-03	-1.0E-06	-1.5E-06	2.1E-06
0.96	0.97	0.0266	0.0234	-1.9E-04	-4.9E-05	3.5E-03	3.7E-04	-1.1E-03	-1.4E-06	-1.3E-06	2.4E-06
0.94	0.95	0.0305	0.0271	-3.0E-04	-1.2E-04	4.0E-03	4.7E-04	-9.7E-04	-2.6E-06	-1.7E-06	3.7E-06
0.91	0.94	0.0331	0.0264	-3.4E-04	-9.6E-05	4.2E-03	4.1E-04	-1.1E-03	-3.1E-06	-1.8E-06	3.8E-06
0.89	0.93	0.0358	0.0273	-4.2E-04	6.5E-05	4.4E-03	2.3E-04	-7.9E-04	-3.6E-06	-1.4E-06	3.9E-06
0.84	0.90	0.0413	0.0307	-6.0E-04	9.6E-05	4.8E-03	1.4E-04	-5.8E-04	-5.4E-06	-1.3E-06	5.0E-06
0.81	0.88	0.0431	0.0322	-6.6E-04	2.1E-04	5.0E-03	3.8E-05	-4.8E-04	-5.9E-06	-1.0E-06	5.4E-06
0.79	0.87	0.0465	0.0341	-8.0E-04	1.0E-04	5.3E-03	1.6E-04	-2.4E-04	-8.1E-06	-8.1E-07	6.7E-06
0.76	0.85	0.0490	0.0350	-8.8E-04	6.8E-05	5.5E-03	2.0E-04	-2.1E-04	-9.3E-06	-8.7E-07	7.3E-06
0.74	0.84	0.0517	0.0348	-9.2E-04	-4.4E-05	6.0E-03	1.7E-04	-2.3E-04	-1.1E-05	-8.8E-07	8.0E-06
0.71	0.82	0.0575	0.0367	-1.1E-03	-6.7E-05	6.8E-03	6.7E-05	-1.5E-04	-1.5E-05	-5.3E-07	9.6E-06
0.69	0.80	0.0639	0.0408	-1.4E-03	-8.2E-05	6.5E-03	8.4E-05	2.4E-04	-1.9E-05	5.9E-07	1.1E-05
0.66	0.79	0.0679	0.0431	-1.6E-03	-5.1E-05	6.6E-03	1.7E-05	4.2E-04	-2.1E-05	1.5E-06	1.2E-05
0.64	0.77	0.0742	0.0447	-1.8E-03	2.3E-04	7.2E-03	-8.2E-05	3.0E-04	-2.3E-05	1.5E-06	1.3E-05
0.61	0.75	0.0792	0.0460	-1.9E-03	3.6E-04	7.5E-03	-2.7E-05	2.4E-04	-2.5E-05	1.1E-06	1.5E-05
0.59	0.73	0.0864	0.0487	-2.2E-03	4.3E-04	7.7E-03	3.8E-06	4.1E-04	-2.8E-05	2.0E-06	1.6E-05
0.54	0.70	0.0964	0.0545	-2.6E-03	-2.1E-04	8.7E-03	1.8E-04	3.5E-04	-5.0E-05	1.1E-06	2.7E-05
0.51	0.68	0.1055	0.0611	-3.2E-03	-2.9E-05	1.1E-02	3.8E-05	5.0E-04	-7.1E-05	3.5E-06	4.0E-05
0.49	0.66	0.1211	0.0656	-3.9E-03	3.5E-05	1.2E-02	-3.9E-05	4.0E-04	-9.7E-05	3.8E-06	5.1E-05
0.46	0.63	0.1371	0.0711	-5.0E-03	1.8E-05	1.3E-02	-1.8E-04	-7.0E-06	-1.3E-04	1.7E-06	6.4E-05
0.44	0.61	0.1533	0.0781	-6.2E-03	2.6E-04	1.4E-02	-2.1E-04	-4.0E-05	-1.6E-04	2.2E-06	8.0E-05
0.41	0.58	0.1695	0.0850	-7.3E-03	9.4E-05	1.6E-02	-6.0E-05	3.1E-05	-2.2E-04	1.3E-06	1.1E-04
0.39	0.56	0.1920	0.0928	-9.0E-03	5.4E-04	1.8E-02	-7.6E-05	1.0E-04	-2.9E-04	3.0E-06	1.5E-04
0.36	0.53	0.2124	0.1013	-1.0E-02	3.2E-04	1.9E-02	1.2E-05	3.2E-04	-3.6E-04	6.1E-06	1.9E-04
0.34	0.50	0.2301	0.1130	-1.2E-02	-4.8E-04	2.2E-02	2.2E-04	-6.9E-04	-5.8E-04	-2.4E-05	3.0E-04
0.31	0.47	0.2546	0.1249	-1.5E-02	-9.8E-04	2.2E-02	8.8E-04	-9.3E-04	-8.2E-04	-5.6E-05	4.4E-04
0.29	0.44	0.2789	0.1369	-1.9E-02	-1.4E-03	2.2E-02	1.0E-03	-8.2E-04	-1.1E-03	-6.9E-05	5.4E-04
0.26	0.42	0.2990	0.1495	-2.1E-02	-1.3E-03	2.3E-02	7.8E-04	8.1E-04	-1.2E-03	4.4E-06	5.9E-04
0.24	0.39	0.3192	0.1594	-2.4E-02	-5.2E-04	2.7E-02	3.6E-04	-4.7E-04	-1.4E-03	-4.2E-05	7.6E-04
0.21	0.36	0.3449	0.1728	-2.7E-02	8.7E-04	2.8E-02	1.7E-04	-1.3E-03	-1.3E-03	-8.6E-05	8.8E-04
0.19	0.34	0.3730	0.1860	-2.8E-02	2.0E-03	2.7E-02	-1.1E-04	2.0E-04	-9.5E-04	1.9E-05	8.7E-04
0.16	0.31	0.4098	0.2021	-3.1E-02	2.1E-03	3.1E-02	-3.7E-05	-4.2E-04	-1.2E-03	-3.1E-05	1.2E-03
0.14	0.29	0.4638	0.2190	-3.1E-02	6.3E-03	2.2E-02	6.3E-05	-1.5E-03	1.4E-03	-1.4E-04	9.0E-04
0.11	0.28	0.5313	0.2647	-3.3E-02	8.7E-03	2.7E-02	6.8E-04	-1.5E-03	3.2E-03	-2.7E-04	1.9E-03
0.09	0.25	0.6387	0.3561	-4.8E-02	2.1E-02	6.1E-02	7.0E-04	-2.4E-03	1.2E-02	-7.3E-04	7.3E-03
0.06	0.20	0.8290	0.4349	-4.9E-02	4.6E-02	8.9E-02	-2.0E-03	-4.9E-03	5.4E-02	-1.6E-03	1.4E-02

Table 36: SPG diamond roughness PIV kinematic values at test location 3.

$\frac{y}{\delta}$	$\frac{U_{eff}}{U_{eff,e}}$	$\frac{\sqrt{\overline{u'^2}}}{U}$	$\frac{\sqrt{\overline{v'^2}}}{U}$	$\frac{\overline{u'v'}}{U^2}$	$\frac{d\bar{u}}{dx}\cdot\frac{\delta}{U}$	$\frac{d\bar{u}}{dy}\cdot\frac{\delta}{U}$	$\frac{d\bar{v}}{dx}\cdot\frac{\delta}{U}$	$\frac{d\bar{v}}{dy}\cdot\frac{\delta}{U}$	$P_{xx}\cdot\frac{\delta}{U^3}$	$P_{yy}\cdot\frac{\delta}{U^3}$	$P_{xy}\cdot\frac{\delta}{U^3}$
1.18	1.03	0.0079	0.0096	-2.2E-06	-1.4E-04	2.0E-04	2.8E-04	-1.2E-03	-1.6E-08	-2.3E-07	3.8E-08
1.13	1.02	0.0082	0.0100	-5.7E-06	-1.8E-04	4.9E-04	3.7E-04	-1.4E-03	-2.9E-08	-2.8E-07	8.3E-08
1.10	1.02	0.0093	0.0105	-7.3E-06	-2.7E-04	5.1E-04	4.5E-04	-1.6E-03	-5.4E-08	-3.5E-07	1.1E-07
1.08	1.02	0.0099	0.0111	-1.1E-05	-2.4E-04	6.6E-04	4.2E-04	-1.8E-03	-6.4E-08	-4.5E-07	1.4E-07
1.05	1.01	0.0109	0.0121	-1.4E-05	-2.8E-04	1.0E-03	5.3E-04	-2.2E-03	-9.5E-08	-6.7E-07	2.5E-07
1.00	1.00	0.0142	0.0128	-2.8E-05	-3.7E-04	1.7E-03	4.2E-04	-2.7E-03	-2.5E-07	-9.1E-07	4.5E-07
0.97	0.99	0.0166	0.0136	-3.5E-05	-4.4E-04	2.0E-03	4.6E-04	-3.1E-03	-3.9E-07	-1.2E-06	6.2E-07
0.95	0.98	0.0185	0.0140	-5.2E-05	-4.2E-04	2.2E-03	4.3E-04	-3.0E-03	-5.1E-07	-1.2E-06	7.6E-07
0.92	0.97	0.0196	0.0139	-7.0E-05	-3.5E-04	2.5E-03	4.8E-04	-3.0E-03	-6.1E-07	-1.2E-06	9.0E-07
0.90	0.96	0.0197	0.0150	-8.0E-05	-3.0E-04	2.8E-03	5.9E-04	-3.1E-03	-6.8E-07	-1.5E-06	1.1E-06
0.87	0.95	0.0192	0.0175	-1.0E-04	-2.0E-04	2.9E-03	6.7E-04	-2.7E-03	-7.3E-07	-1.8E-06	1.4E-06
0.82	0.93	0.0190	0.0214	-1.5E-04	-2.1E-04	2.9E-03	1.0E-03	-2.3E-03	-1.0E-06	-2.4E-06	2.0E-06
0.80	0.92	0.0204	0.0221	-1.7E-04	-3.0E-04	3.2E-03	9.5E-04	-1.9E-03	-1.4E-06	-2.2E-06	2.4E-06
0.77	0.91	0.0245	0.0232	-2.2E-04	-2.8E-04	3.9E-03	8.7E-04	-1.6E-03	-2.1E-06	-2.1E-06	3.1E-06
0.75	0.90	0.0283	0.0240	-2.9E-04	-2.7E-04	4.2E-03	7.8E-04	-1.3E-03	-2.8E-06	-1.9E-06	3.5E-06
0.72	0.88	0.0309	0.0250	-3.4E-04	-2.4E-04	4.6E-03	7.4E-04	-1.4E-03	-3.6E-06	-2.3E-06	4.2E-06
0.70	0.87	0.0338	0.0268	-4.3E-04	-3.3E-04	5.0E-03	7.6E-04	-1.4E-03	-5.1E-06	-2.7E-06	5.2E-06
0.67	0.86	0.0341	0.0275	-4.5E-04	-4.2E-04	5.1E-03	7.6E-04	-1.3E-03	-5.6E-06	-2.7E-06	5.5E-06
0.65	0.84	0.0380	0.0292	-5.4E-04	-2.8E-04	5.2E-03	6.1E-04	-9.8E-04	-6.4E-06	-2.3E-06	6.0E-06
0.62	0.83	0.0374	0.0273	-4.8E-04	-2.4E-04	5.1E-03	4.9E-04	-8.5E-04	-5.6E-06	-1.7E-06	5.0E-06
0.60	0.81	0.0387	0.0294	-5.4E-04	-1.7E-04	5.5E-03	4.2E-04	-6.9E-04	-6.4E-06	-1.6E-06	5.8E-06
0.57	0.80	0.0414	0.0299	-5.8E-04	-1.3E-04	5.6E-03	2.8E-04	-3.0E-04	-7.0E-06	-8.5E-07	5.7E-06
0.52	0.77	0.0454	0.0326	-7.1E-04	-2.0E-04	5.5E-03	1.8E-04	-2.2E-04	-8.6E-06	-7.2E-07	6.5E-06
0.50	0.76	0.0472	0.0333	-7.7E-04	-2.7E-04	6.4E-03	2.3E-04	-3.3E-04	-1.1E-05	-1.1E-06	8.1E-06
0.47	0.74	0.0537	0.0361	-9.6E-04	-4.5E-04	6.8E-03	4.0E-04	-4.6E-04	-1.6E-05	-1.9E-06	1.1E-05
0.45	0.73	0.0570	0.0376	-1.1E-03	-4.8E-04	6.8E-03	4.7E-04	-4.1E-04	-1.8E-05	-2.2E-06	1.2E-05
0.42	0.71	0.0600	0.0388	-1.2E-03	-5.6E-04	7.7E-03	5.8E-04	-5.7E-04	-2.3E-05	-3.1E-06	1.5E-05
0.40	0.69	0.0658	0.0407	-1.4E-03	-6.2E-04	8.8E-03	5.3E-04	-4.9E-04	-3.0E-05	-3.1E-06	1.8E-05
0.37	0.67	0.0741	0.0431	-1.7E-03	-6.2E-04	9.0E-03	5.3E-04	-1.7E-04	-3.8E-05	-2.4E-06	2.1E-05
0.35	0.66	0.0805	0.0455	-1.9E-03	-6.1E-04	9.9E-03	4.9E-04	-2.4E-04	-4.5E-05	-2.8E-06	2.5E-05
0.32	0.64	0.0909	0.0497	-2.3E-03	-7.5E-04	1.1E-02	3.9E-04	5.4E-05	-6.5E-05	-1.5E-06	3.2E-05
0.29	0.62	0.1012	0.0532	-2.7E-03	-7.2E-04	1.3E-02	2.8E-04	3.8E-06	-8.4E-05	-1.5E-06	4.1E-05
0.27	0.59	0.1171	0.0601	-3.5E-03	-3.7E-04	1.5E-02	2.4E-04	1.7E-04	-1.2E-04	-4.4E-07	5.8E-05
0.24	0.57	0.1345	0.0662	-4.4E-03	-8.2E-05	1.7E-02	1.1E-04	3.3E-04	-1.5E-04	1.9E-06	7.3E-05
0.19	0.51	0.1745	0.0803	-6.7E-03	6.6E-05	2.1E-02	9.7E-05	6.6E-04	-2.8E-04	7.2E-06	1.3E-04
0.17	0.48	0.1952	0.0866	-7.8E-03	2.7E-04	2.1E-02	2.5E-05	4.3E-04	-3.0E-04	6.1E-06	1.5E-04
0.14	0.45	0.2160	0.0986	-8.8E-03	8.5E-04	1.9E-02	-1.1E-04	3.8E-04	-2.6E-04	9.6E-06	1.7E-04
0.12	0.43	0.2333	0.1060	-9.1E-03	1.5E-03	1.6E-02	1.2E-05	-4.3E-04	-1.4E-04	-9.9E-06	1.7E-04
0.09	0.41	0.2715	0.1318	-9.5E-03	1.5E-03	2.9E-02	-6.2E-05	-1.3E-03	-3.4E-04	-3.8E-05	5.1E-04
0.07	0.37	0.4027	0.1867	-1.2E-02	-8.8E-04	4.7E-02	2.5E-04	1.4E-04	-1.6E-03	6.4E-06	1.8E-03
0.04	0.32	0.6515	0.2175	-1.1E-02	-8.4E-03	7.5E-02	7.9E-05	-3.0E-03	-9.7E-03	-2.5E-04	3.6E-03

Table 37: ZPG smooth wall Pitot data at the 1st test location.

y (mm)	y/δ	P_{01}	P_{02}	P_{02}/P_{01}	P/P_{02}	M	U	U/U_e	$\frac{U_{eff} - U_{eff,e}}{u^*}$	y^+	u^+
0.38	0.035	6.13E+05	4.87E+04	0.079	0.415	1.20	380	0.60	-1.42E+01	1.34E+02	1.72E+01
0.68	0.062	6.26E+05	5.63E+04	0.090	0.367	1.30	405	0.64	-1.29E+01	2.46E+02	1.85E+01
0.97	0.088	6.13E+05	5.84E+04	0.095	0.346	1.35	416	0.66	-1.24E+01	3.43E+02	1.91E+01
1.27	0.115	6.18E+05	6.90E+04	0.112	0.295	1.49	447	0.70	-1.08E+01	4.52E+02	2.06E+01
1.57	0.143	6.22E+05	7.61E+04	0.122	0.270	1.58	463	0.73	-9.93E+00	5.63E+02	2.15E+01
1.87	0.170	6.15E+05	7.95E+04	0.129	0.255	1.63	473	0.75	-9.39E+00	6.62E+02	2.20E+01
2.17	0.197	6.27E+05	8.67E+04	0.138	0.238	1.69	485	0.77	-8.73E+00	7.84E+02	2.27E+01
2.47	0.224	6.29E+05	8.94E+04	0.142	0.232	1.72	490	0.77	-8.46E+00	8.94E+02	2.30E+01
2.77	0.252	6.14E+05	9.12E+04	0.148	0.222	1.76	498	0.78	-8.04E+00	9.81E+02	2.34E+01
3.08	0.280	6.17E+05	9.57E+04	0.155	0.213	1.81	505	0.80	-7.62E+00	1.09E+03	2.38E+01
3.39	0.307	6.17E+05	1.00E+05	0.162	0.203	1.85	513	0.81	-7.18E+00	1.20E+03	2.43E+01
3.69	0.335	6.15E+05	1.04E+05	0.168	0.196	1.89	519	0.82	-6.82E+00	1.31E+03	2.46E+01
3.99	0.363	6.19E+05	1.10E+05	0.177	0.186	1.95	528	0.83	-6.33E+00	1.42E+03	2.51E+01
4.30	0.390	6.08E+05	1.11E+05	0.183	0.181	1.98	533	0.84	-6.04E+00	1.51E+03	2.54E+01
4.61	0.419	6.07E+05	1.16E+05	0.192	0.172	2.03	541	0.85	-5.57E+00	1.61E+03	2.59E+01
4.91	0.446	5.93E+05	1.18E+05	0.199	0.166	2.07	547	0.86	-5.23E+00	1.68E+03	2.62E+01
5.22	0.474	5.92E+05	1.22E+05	0.206	0.160	2.12	553	0.87	-4.87E+00	1.78E+03	2.66E+01
5.53	0.502	6.00E+05	1.29E+05	0.215	0.153	2.17	559	0.88	-4.48E+00	1.91E+03	2.70E+01
5.83	0.530	6.00E+05	1.33E+05	0.222	0.149	2.20	564	0.89	-4.18E+00	2.02E+03	2.72E+01
6.14	0.557	6.01E+05	1.38E+05	0.230	0.144	2.24	569	0.90	-3.85E+00	2.13E+03	2.76E+01
6.44	0.585	6.05E+05	1.43E+05	0.237	0.139	2.28	574	0.90	-3.56E+00	2.25E+03	2.79E+01
6.75	0.613	6.05E+05	1.49E+05	0.246	0.134	2.33	579	0.91	-3.21E+00	2.36E+03	2.82E+01
7.06	0.641	6.03E+05	1.52E+05	0.253	0.131	2.36	583	0.92	-2.95E+00	2.46E+03	2.85E+01
7.36	0.668	5.89E+05	1.54E+05	0.261	0.126	2.40	588	0.93	-2.65E+00	2.51E+03	2.88E+01
7.67	0.696	6.04E+05	1.61E+05	0.267	0.123	2.43	591	0.93	-2.44E+00	2.68E+03	2.90E+01
7.96	0.723	6.03E+05	1.66E+05	0.275	0.120	2.47	596	0.94	-2.16E+00	2.78E+03	2.93E+01
8.27	0.751	5.94E+05	1.70E+05	0.287	0.115	2.53	602	0.95	-1.76E+00	2.84E+03	2.97E+01
8.57	0.779	5.89E+05	1.74E+05	0.295	0.112	2.56	605	0.96	-1.52E+00	2.92E+03	2.99E+01
8.88	0.806	6.05E+05	1.80E+05	0.298	0.111	2.58	606	0.96	-1.44E+00	3.11E+03	3.00E+01
9.19	0.834	5.87E+05	1.80E+05	0.307	0.108	2.62	610	0.96	-1.17E+00	3.13E+03	3.03E+01
9.49	0.862	5.97E+05	1.88E+05	0.315	0.105	2.65	614	0.97	-9.30E-01	3.28E+03	3.05E+01
9.79	0.889	5.98E+05	1.90E+05	0.318	0.104	2.67	615	0.97	-8.48E-01	3.40E+03	3.06E+01
10.10	0.917	5.93E+05	1.94E+05	0.328	0.101	2.71	619	0.98	-5.66E-01	3.47E+03	3.09E+01
10.40	0.944	5.91E+05	1.96E+05	0.331	0.099	2.73	621	0.98	-4.63E-01	3.57E+03	3.10E+01
10.71	0.972	5.97E+05	2.02E+05	0.339	0.097	2.76	623	0.98	-2.73E-01	3.71E+03	3.12E+01
11.01	1.000	5.87E+05	2.05E+05	0.349	0.094	2.80	627	0.99	0.00E+00	3.75E+03	3.14E+01
11.31	1.027	5.93E+05	2.17E+05	0.366	0.090	2.87	633	1.00	4.19E-01	3.90E+03	3.18E+01
11.62	1.055	5.94E+05	2.26E+05	0.381	0.087	2.93	638	1.01	7.76E-01	4.01E+03	3.22E+01
11.92	1.083	5.93E+05	2.27E+05	0.382	0.086	2.94	638	1.01	7.93E-01	4.11E+03	3.22E+01
12.23	1.111	5.94E+05	2.27E+05	0.382	0.086	2.94	638	1.01	7.85E-01	4.23E+03	3.22E+01
12.53	1.138	5.85E+05	2.23E+05	0.381	0.087	2.93	637	1.01	7.58E-01	4.27E+03	3.22E+01
12.84	1.166	5.98E+05	2.26E+05	0.378	0.087	2.92	636	1.01	6.78E-01	4.47E+03	3.21E+01
13.14	1.193	5.81E+05	2.22E+05	0.383	0.086	2.94	638	1.01	7.97E-01	4.45E+03	3.22E+01

Table 38: ZPG square roughness Pitot data at the 1st test location.

y (mm)	y/δ	P_{01}	P_{02}	P_{02}/P_{01}	P/P_{02}	M	U	U/U_e	$\frac{U_{eff} - U_{eff,e}}{u^*}$	y^+	u^+
0.38	0.034	8.08E+05	4.22E+04	0.649	0.052	0.79	265	0.42	-1.42E+01	2.02E+02	8.93E+00
0.59	0.053	8.11E+05	4.37E+04	0.631	0.054	0.83	276	0.44	-1.38E+01	3.13E+02	9.32E+00
0.89	0.080	8.19E+05	4.96E+04	0.560	0.061	0.95	310	0.50	-1.26E+01	4.81E+02	1.05E+01
1.21	0.109	8.13E+05	5.42E+04	0.509	0.067	1.03	333	0.53	-1.18E+01	6.51E+02	1.13E+01
1.52	0.136	8.17E+05	6.20E+04	0.447	0.076	1.14	360	0.58	-1.08E+01	8.21E+02	1.23E+01
1.84	0.165	8.14E+05	6.66E+04	0.415	0.082	1.20	375	0.60	-1.02E+01	9.90E+02	1.29E+01
2.15	0.192	8.09E+05	7.41E+04	0.370	0.092	1.30	398	0.64	-9.35E+00	1.15E+03	1.37E+01
2.48	0.222	8.10E+05	8.02E+04	0.343	0.099	1.36	413	0.66	-8.77E+00	1.33E+03	1.43E+01
2.79	0.250	8.06E+05	8.75E+04	0.313	0.109	1.44	430	0.69	-8.11E+00	1.49E+03	1.50E+01
3.12	0.279	8.10E+05	9.48E+04	0.290	0.117	1.51	444	0.71	-7.56E+00	1.67E+03	1.55E+01
3.43	0.307	8.14E+05	1.02E+05	0.271	0.125	1.57	456	0.73	-7.07E+00	1.85E+03	1.60E+01
3.76	0.337	8.08E+05	1.09E+05	0.251	0.135	1.64	470	0.75	-6.51E+00	2.02E+03	1.66E+01
4.07	0.365	8.03E+05	1.15E+05	0.236	0.144	1.70	480	0.77	-6.08E+00	2.17E+03	1.70E+01
4.40	0.394	8.03E+05	1.23E+05	0.222	0.153	1.76	490	0.79	-5.65E+00	2.35E+03	1.74E+01
4.72	0.423	8.02E+05	1.29E+05	0.211	0.161	1.82	500	0.80	-5.26E+00	2.52E+03	1.78E+01
5.06	0.453	8.04E+05	1.40E+05	0.195	0.174	1.90	512	0.82	-4.72E+00	2.70E+03	1.84E+01
5.37	0.481	8.00E+05	1.45E+05	0.187	0.182	1.94	520	0.83	-4.40E+00	2.86E+03	1.87E+01
5.71	0.511	8.01E+05	1.54E+05	0.176	0.193	2.01	529	0.85	-3.99E+00	3.04E+03	1.91E+01
6.02	0.539	7.96E+05	1.61E+05	0.168	0.202	2.06	537	0.86	-3.65E+00	3.19E+03	1.94E+01
6.36	0.569	7.99E+05	1.71E+05	0.158	0.214	2.13	546	0.88	-3.25E+00	3.38E+03	1.98E+01
6.67	0.597	7.95E+05	1.77E+05	0.153	0.222	2.17	551	0.88	-2.99E+00	3.53E+03	2.01E+01
7.00	0.627	7.92E+05	1.86E+05	0.144	0.235	2.24	560	0.90	-2.59E+00	3.70E+03	2.05E+01
7.32	0.655	7.93E+05	1.93E+05	0.140	0.243	2.28	565	0.91	-2.36E+00	3.87E+03	2.07E+01
7.65	0.684	7.91E+05	2.02E+05	0.133	0.256	2.34	572	0.92	-2.00E+00	4.03E+03	2.11E+01
7.96	0.713	7.92E+05	2.08E+05	0.129	0.262	2.37	576	0.92	-1.84E+00	4.21E+03	2.12E+01
8.29	0.742	7.92E+05	2.15E+05	0.125	0.272	2.42	581	0.93	-1.59E+00	4.38E+03	2.15E+01
8.60	0.770	7.90E+05	2.23E+05	0.120	0.282	2.47	586	0.94	-1.33E+00	4.54E+03	2.18E+01
8.93	0.799	7.85E+05	2.28E+05	0.117	0.291	2.51	590	0.95	-1.13E+00	4.68E+03	2.20E+01
9.24	0.827	7.83E+05	2.36E+05	0.112	0.302	2.56	595	0.96	-8.86E-01	4.84E+03	2.22E+01
9.57	0.856	7.84E+05	2.42E+05	0.110	0.309	2.59	598	0.96	-7.28E-01	5.02E+03	2.24E+01
9.89	0.885	7.83E+05	2.46E+05	0.108	0.315	2.61	601	0.97	-6.07E-01	5.18E+03	2.25E+01
10.21	0.914	7.82E+05	2.56E+05	0.104	0.327	2.67	606	0.97	-3.46E-01	5.35E+03	2.27E+01
10.53	0.943	7.83E+05	2.61E+05	0.102	0.334	2.70	608	0.98	-2.17E-01	5.52E+03	2.29E+01
10.85	0.971	7.81E+05	2.65E+05	0.100	0.340	2.72	611	0.98	-9.97E-02	5.68E+03	2.30E+01
11.17	1.000	7.79E+05	2.69E+05	0.098	0.345	2.74	612	0.98	0.00E+00	5.84E+03	2.31E+01
11.49	1.029	7.75E+05	2.73E+05	0.096	0.353	2.78	615	0.99	1.45E-01	5.98E+03	2.32E+01
11.81	1.057	7.73E+05	2.80E+05	0.094	0.362	2.81	618	0.99	3.13E-01	6.13E+03	2.34E+01
12.14	1.086	7.74E+05	2.90E+05	0.091	0.374	2.86	622	1.00	5.27E-01	6.31E+03	2.36E+01
12.45	1.115	7.74E+05	2.93E+05	0.090	0.378	2.88	624	1.00	5.95E-01	6.48E+03	2.37E+01
12.78	1.144	7.70E+05	2.92E+05	0.089	0.379	2.88	624	1.00	6.08E-01	6.62E+03	2.37E+01
13.09	1.172	7.70E+05	2.92E+05	0.089	0.379	2.88	624	1.00	6.04E-01	6.78E+03	2.37E+01
13.42	1.201	7.70E+05	2.93E+05	0.089	0.381	2.89	624	1.00	6.28E-01	6.96E+03	2.37E+01
13.74	1.230	7.64E+05	2.92E+05	0.089	0.381	2.89	624	1.00	6.33E-01	7.07E+03	2.37E+01
14.06	1.259	7.66E+05	2.91E+05	0.089	0.380	2.89	624	1.00	6.10E-01	7.26E+03	2.37E+01
14.38	1.287	7.65E+05	2.89E+05	0.090	0.378	2.88	623	1.00	5.62E-01	7.42E+03	2.36E+01
14.71	1.317	7.69E+05	2.89E+05	0.090	0.376	2.87	622	1.00	5.33E-01	7.63E+03	2.36E+01

Table 39: ZPG diamond roughness Pitot data at the 1st test location.

y (mm)	y/δ	P_{01}	P_{02}	P_{02}/P_{01}	P/P_{02}	M	U	U/U_e	$\frac{U_{eff} - U_{eff,e}}{u^*}$	y^+	u^+
0.38	0.029	7.22E+05	3.97E+04	0.055	0.640	0.81	272	0.43	-1.79E+01	1.55E+02	1.11E+01
0.38	0.029	7.24E+05	4.04E+04	0.056	0.631	0.83	277	0.44	-1.76E+01	1.55E+02	1.13E+01
0.58	0.044	7.20E+05	4.66E+04	0.065	0.544	0.97	318	0.51	-1.58E+01	2.35E+02	1.31E+01
0.90	0.068	7.28E+05	5.40E+04	0.074	0.475	1.09	349	0.56	-1.45E+01	3.70E+02	1.45E+01
1.21	0.091	7.13E+05	5.92E+04	0.083	0.424	1.18	372	0.60	-1.34E+01	4.87E+02	1.56E+01
1.84	0.139	7.17E+05	7.51E+04	0.105	0.336	1.38	418	0.67	-1.13E+01	7.44E+02	1.77E+01
2.17	0.163	7.23E+05	8.39E+04	0.116	0.303	1.47	437	0.70	-1.04E+01	8.82E+02	1.86E+01
2.48	0.187	7.13E+05	8.89E+04	0.125	0.282	1.53	450	0.72	-9.72E+00	9.95E+02	1.93E+01
2.80	0.211	7.08E+05	9.46E+04	0.134	0.263	1.60	463	0.74	-9.10E+00	1.12E+03	1.99E+01
3.11	0.235	7.07E+05	9.87E+04	0.140	0.252	1.64	471	0.75	-8.70E+00	1.24E+03	2.03E+01
3.44	0.260	7.02E+05	1.01E+05	0.143	0.245	1.67	475	0.76	-8.46E+00	1.36E+03	2.05E+01
3.76	0.284	7.04E+05	1.04E+05	0.148	0.238	1.70	481	0.77	-8.19E+00	1.49E+03	2.08E+01
4.09	0.308	6.96E+05	1.07E+05	0.154	0.229	1.73	487	0.78	-7.85E+00	1.60E+03	2.11E+01
4.40	0.332	6.90E+05	1.12E+05	0.162	0.218	1.78	496	0.79	-7.39E+00	1.71E+03	2.16E+01
4.73	0.357	6.93E+05	1.20E+05	0.173	0.204	1.85	507	0.81	-6.79E+00	1.85E+03	2.22E+01
5.05	0.381	6.87E+05	1.25E+05	0.182	0.193	1.91	516	0.83	-6.32E+00	1.96E+03	2.27E+01
5.38	0.406	6.80E+05	1.33E+05	0.196	0.179	1.99	528	0.85	-5.65E+00	2.07E+03	2.33E+01
5.70	0.430	6.83E+05	1.41E+05	0.206	0.171	2.04	536	0.86	-5.22E+00	2.20E+03	2.38E+01
6.02	0.454	6.82E+05	1.48E+05	0.217	0.162	2.10	545	0.87	-4.73E+00	2.32E+03	2.42E+01
6.67	0.503	6.76E+05	1.63E+05	0.241	0.146	2.22	561	0.90	-3.80E+00	2.55E+03	2.52E+01
7.32	0.552	6.65E+05	1.76E+05	0.265	0.133	2.34	574	0.92	-2.99E+00	2.75E+03	2.60E+01
7.64	0.576	6.68E+05	1.78E+05	0.267	0.132	2.35	576	0.92	-2.91E+00	2.89E+03	2.61E+01
7.96	0.601	6.69E+05	1.78E+05	0.266	0.132	2.35	575	0.92	-2.93E+00	3.02E+03	2.60E+01
8.28	0.625	6.68E+05	1.78E+05	0.267	0.132	2.35	576	0.92	-2.92E+00	3.14E+03	2.61E+01
8.61	0.649	6.68E+05	1.82E+05	0.272	0.129	2.37	579	0.93	-2.73E+00	3.26E+03	2.62E+01
8.93	0.673	6.72E+05	1.89E+05	0.281	0.125	2.42	583	0.94	-2.45E+00	3.40E+03	2.65E+01
9.25	0.698	6.64E+05	1.95E+05	0.293	0.120	2.47	589	0.94	-2.09E+00	3.48E+03	2.69E+01
9.56	0.721	6.63E+05	2.02E+05	0.306	0.115	2.52	595	0.95	-1.73E+00	3.60E+03	2.72E+01
9.89	0.746	6.61E+05	2.11E+05	0.319	0.110	2.58	601	0.96	-1.35E+00	3.71E+03	2.76E+01
10.21	0.770	6.62E+05	2.18E+05	0.330	0.107	2.63	605	0.97	-1.07E+00	3.84E+03	2.79E+01
10.53	0.795	6.56E+05	2.24E+05	0.341	0.103	2.68	609	0.98	-7.69E-01	3.93E+03	2.82E+01
10.85	0.819	6.60E+05	2.30E+05	0.348	0.101	2.70	612	0.98	-5.97E-01	4.07E+03	2.84E+01
11.18	0.843	6.54E+05	2.32E+05	0.355	0.099	2.73	614	0.99	-4.37E-01	4.15E+03	2.85E+01
11.49	0.867	6.53E+05	2.29E+05	0.351	0.100	2.72	613	0.98	-5.37E-01	4.27E+03	2.84E+01
12.13	0.915	6.56E+05	2.34E+05	0.357	0.099	2.74	615	0.99	-3.98E-01	4.53E+03	2.86E+01
12.45	0.940	6.54E+05	2.37E+05	0.363	0.097	2.76	617	0.99	-2.57E-01	4.64E+03	2.87E+01
12.77	0.964	6.50E+05	2.40E+05	0.369	0.095	2.79	619	0.99	-1.11E-01	4.73E+03	2.89E+01
13.10	0.988	6.50E+05	2.42E+05	0.372	0.095	2.80	620	1.00	-4.91E-02	4.86E+03	2.89E+01
13.42	1.012	6.45E+05	2.44E+05	0.378	0.093	2.82	622	1.00	8.65E-02	4.94E+03	2.91E+01
13.74	1.037	6.48E+05	2.47E+05	0.381	0.092	2.84	623	1.00	1.64E-01	5.08E+03	2.91E+01
14.06	1.061	6.43E+05	2.47E+05	0.384	0.092	2.85	624	1.00	2.23E-01	5.16E+03	2.92E+01
14.36	1.083	6.49E+05	2.49E+05	0.384	0.092	2.85	623	1.00	2.09E-01	5.32E+03	2.92E+01
14.93	1.126	6.45E+05	2.37E+05	0.368	0.096	2.78	618	0.99	-1.62E-01	5.51E+03	2.88E+01

Table 40: ZPG smooth wall Pitot data at the 2nd test location.

y (mm)	y/δ	P_{01}	P_{02}	P_{02}/P_{01}	P/P_{02}	M	U	U/U_e	$\frac{U_{eff} - U_{eff,e}}{u^*}$	y^+	u^+
0.68	0.053	7.03E+05	6.68E+04	0.095	0.329	1.40	422	0.67	-1.24E+01	2.59E+02	1.93E+01
0.89	0.069	7.05E+05	6.76E+04	0.096	0.327	1.40	423	0.67	-1.23E+01	3.37E+02	1.94E+01
1.20	0.094	7.07E+05	7.12E+04	0.101	0.311	1.45	432	0.69	-1.18E+01	4.59E+02	1.99E+01
1.51	0.117	7.07E+05	8.22E+04	0.116	0.269	1.58	458	0.73	-1.05E+01	5.77E+02	2.12E+01
1.83	0.142	7.04E+05	8.95E+04	0.127	0.246	1.66	474	0.75	-9.61E+00	6.96E+02	2.21E+01
2.13	0.166	7.09E+05	9.35E+04	0.132	0.238	1.70	480	0.76	-9.27E+00	8.21E+02	2.24E+01
2.46	0.191	7.07E+05	9.79E+04	0.138	0.226	1.74	489	0.78	-8.81E+00	9.42E+02	2.29E+01
2.77	0.215	7.06E+05	9.97E+04	0.141	0.222	1.76	492	0.78	-8.63E+00	1.06E+03	2.31E+01
3.09	0.240	7.06E+05	1.05E+05	0.149	0.211	1.82	501	0.80	-8.15E+00	1.19E+03	2.35E+01
3.40	0.265	7.06E+05	1.08E+05	0.154	0.204	1.85	506	0.80	-7.85E+00	1.31E+03	2.39E+01
3.73	0.290	7.07E+05	1.13E+05	0.160	0.196	1.89	513	0.82	-7.44E+00	1.44E+03	2.43E+01
4.04	0.314	7.03E+05	1.18E+05	0.168	0.187	1.94	520	0.83	-7.03E+00	1.55E+03	2.47E+01
4.37	0.340	7.05E+05	1.22E+05	0.173	0.182	1.97	525	0.83	-6.75E+00	1.68E+03	2.49E+01
4.69	0.364	7.04E+05	1.26E+05	0.179	0.175	2.02	531	0.84	-6.39E+00	1.80E+03	2.53E+01
5.02	0.390	7.02E+05	1.31E+05	0.186	0.168	2.06	537	0.85	-6.05E+00	1.92E+03	2.56E+01
5.33	0.415	7.03E+05	1.36E+05	0.193	0.162	2.10	543	0.86	-5.70E+00	2.05E+03	2.60E+01
5.66	0.440	7.01E+05	1.39E+05	0.199	0.158	2.13	547	0.87	-5.45E+00	2.17E+03	2.62E+01
5.98	0.465	7.02E+05	1.44E+05	0.205	0.153	2.17	552	0.88	-5.17E+00	2.30E+03	2.65E+01
6.31	0.490	6.98E+05	1.50E+05	0.216	0.145	2.23	559	0.89	-4.70E+00	2.41E+03	2.70E+01
6.62	0.515	6.99E+05	1.56E+05	0.223	0.140	2.27	564	0.90	-4.39E+00	2.54E+03	2.73E+01
6.95	0.540	6.97E+05	1.61E+05	0.231	0.136	2.31	569	0.91	-4.08E+00	2.66E+03	2.76E+01
7.26	0.565	6.95E+05	1.65E+05	0.238	0.132	2.35	574	0.91	-3.82E+00	2.77E+03	2.79E+01
7.59	0.590	6.96E+05	1.72E+05	0.247	0.127	2.40	579	0.92	-3.47E+00	2.91E+03	2.82E+01
7.91	0.615	6.97E+05	1.75E+05	0.252	0.125	2.42	582	0.93	-3.31E+00	3.03E+03	2.84E+01
8.23	0.640	6.94E+05	1.81E+05	0.260	0.120	2.47	586	0.93	-3.00E+00	3.14E+03	2.87E+01
8.55	0.665	6.95E+05	1.85E+05	0.267	0.117	2.50	590	0.94	-2.79E+00	3.27E+03	2.89E+01
8.87	0.690	6.92E+05	1.90E+05	0.274	0.114	2.54	593	0.95	-2.54E+00	3.38E+03	2.92E+01
9.19	0.714	6.92E+05	1.94E+05	0.280	0.112	2.56	596	0.95	-2.35E+00	3.51E+03	2.93E+01
9.51	0.739	6.93E+05	2.00E+05	0.289	0.108	2.61	600	0.96	-2.08E+00	3.64E+03	2.96E+01
9.82	0.764	6.92E+05	2.05E+05	0.297	0.106	2.64	604	0.96	-1.86E+00	3.76E+03	2.98E+01
10.15	0.789	6.91E+05	2.09E+05	0.303	0.103	2.67	606	0.97	-1.67E+00	3.88E+03	3.00E+01
10.47	0.814	6.85E+05	2.14E+05	0.312	0.100	2.71	610	0.97	-1.42E+00	3.97E+03	3.03E+01
10.79	0.839	6.88E+05	2.16E+05	0.314	0.100	2.72	611	0.98	-1.36E+00	4.11E+03	3.03E+01
11.10	0.863	6.85E+05	2.23E+05	0.326	0.096	2.78	615	0.98	-1.05E+00	4.22E+03	3.06E+01
11.43	0.889	6.88E+05	2.25E+05	0.327	0.096	2.78	616	0.98	-1.02E+00	4.36E+03	3.07E+01
11.75	0.913	6.87E+05	2.28E+05	0.332	0.094	2.80	617	0.99	-8.98E-01	4.48E+03	3.08E+01
12.07	0.938	6.84E+05	2.32E+05	0.339	0.092	2.84	620	0.99	-7.12E-01	4.59E+03	3.10E+01
12.38	0.963	6.87E+05	2.35E+05	0.342	0.092	2.85	621	0.99	-6.42E-01	4.73E+03	3.11E+01
12.71	0.988	6.85E+05	2.37E+05	0.346	0.091	2.87	622	0.99	-5.48E-01	4.84E+03	3.11E+01
13.02	1.012	6.82E+05	2.38E+05	0.349	0.090	2.88	623	1.00	-4.81E-01	4.95E+03	3.12E+01
13.35	1.038	6.82E+05	2.40E+05	0.351	0.089	2.89	624	1.00	-4.41E-01	5.07E+03	3.13E+01
13.67	1.062	6.83E+05	2.41E+05	0.352	0.089	2.89	624	1.00	-4.20E-01	5.21E+03	3.13E+01
13.99	1.087	6.81E+05	2.42E+05	0.355	0.088	2.90	625	1.00	-3.66E-01	5.32E+03	3.13E+01
14.31	1.112	6.78E+05	2.41E+05	0.356	0.088	2.91	625	1.00	-3.48E-01	5.42E+03	3.13E+01
14.63	1.137	6.79E+05	2.42E+05	0.357	0.088	2.91	625	1.00	-3.29E-01	5.55E+03	3.14E+01
14.95	1.162	6.76E+05	2.42E+05	0.358	0.088	2.92	625	1.00	-3.09E-01	5.65E+03	3.14E+01

Table 41: ZPG square roughness Pitot data at the 2nd test location.

y (mm)	y/δ	P_{01}	P_{02}	P_{02}/P_{01}	P/P_{02}	M	U	U/U_e	$\frac{U_{eff} - U_{eff,e}}{u^*}$	y^+	u^+
0.38	0.030	7.69E+05	4.52E+04	0.059	0.628	0.83	282	0.45	-1.43E+01	1.85E+02	9.50E+00
0.63	0.050	7.68E+05	4.85E+04	0.063	0.584	0.91	304	0.48	-1.35E+01	3.04E+02	1.03E+01
0.94	0.075	7.67E+05	5.26E+04	0.069	0.538	0.98	325	0.52	-1.27E+01	4.55E+02	1.10E+01
1.25	0.099	7.69E+05	5.77E+04	0.075	0.492	1.06	345	0.55	-1.20E+01	6.03E+02	1.18E+01
1.57	0.124	7.66E+05	6.28E+04	0.082	0.450	1.13	364	0.58	-1.13E+01	7.52E+02	1.25E+01
1.88	0.148	7.68E+05	6.68E+04	0.087	0.424	1.18	377	0.60	-1.08E+01	9.04E+02	1.30E+01
2.20	0.173	7.63E+05	7.06E+04	0.093	0.399	1.23	389	0.62	-1.03E+01	1.05E+03	1.34E+01
2.51	0.198	7.66E+05	7.73E+04	0.101	0.366	1.31	407	0.65	-9.68E+00	1.20E+03	1.41E+01
2.83	0.223	7.64E+05	8.17E+04	0.107	0.345	1.36	418	0.66	-9.24E+00	1.35E+03	1.45E+01
3.14	0.248	7.63E+05	8.61E+04	0.113	0.327	1.40	428	0.68	-8.84E+00	1.50E+03	1.49E+01
3.46	0.274	7.62E+05	9.17E+04	0.120	0.307	1.46	440	0.70	-8.36E+00	1.66E+03	1.54E+01
3.78	0.298	7.63E+05	9.78E+04	0.128	0.288	1.52	452	0.72	-7.89E+00	1.81E+03	1.59E+01
4.11	0.324	7.53E+05	9.95E+04	0.132	0.279	1.54	458	0.73	-7.67E+00	1.94E+03	1.61E+01
4.42	0.349	7.53E+05	1.06E+05	0.141	0.262	1.60	470	0.75	-7.19E+00	2.09E+03	1.66E+01
4.75	0.375	7.54E+05	1.11E+05	0.147	0.250	1.65	478	0.76	-6.85E+00	2.25E+03	1.69E+01
5.07	0.400	7.55E+05	1.14E+05	0.151	0.244	1.67	483	0.77	-6.65E+00	2.40E+03	1.71E+01
5.40	0.427	7.56E+05	1.23E+05	0.162	0.228	1.74	495	0.79	-6.15E+00	2.57E+03	1.76E+01
5.72	0.452	7.50E+05	1.28E+05	0.170	0.217	1.79	503	0.80	-5.78E+00	2.70E+03	1.80E+01
6.05	0.478	7.54E+05	1.34E+05	0.178	0.207	1.83	511	0.81	-5.45E+00	2.86E+03	1.83E+01
6.37	0.503	7.42E+05	1.39E+05	0.187	0.197	1.89	520	0.83	-5.08E+00	2.97E+03	1.87E+01
6.70	0.529	7.48E+05	1.45E+05	0.194	0.190	1.92	525	0.83	-4.83E+00	3.15E+03	1.89E+01
7.02	0.554	7.46E+05	1.51E+05	0.202	0.183	1.97	532	0.85	-4.52E+00	3.29E+03	1.92E+01
7.35	0.580	7.48E+05	1.58E+05	0.211	0.175	2.01	539	0.86	-4.21E+00	3.46E+03	1.96E+01
7.67	0.605	7.44E+05	1.63E+05	0.219	0.168	2.06	545	0.87	-3.93E+00	3.59E+03	1.98E+01
7.99	0.631	7.41E+05	1.69E+05	0.228	0.162	2.10	552	0.88	-3.65E+00	3.73E+03	2.01E+01
8.32	0.656	7.45E+05	1.74E+05	0.234	0.158	2.13	556	0.88	-3.46E+00	3.90E+03	2.03E+01
8.64	0.682	7.43E+05	1.82E+05	0.245	0.151	2.18	563	0.89	-3.14E+00	4.05E+03	2.06E+01
8.96	0.707	7.42E+05	1.92E+05	0.258	0.143	2.25	571	0.91	-2.74E+00	4.19E+03	2.10E+01
9.29	0.733	7.40E+05	1.98E+05	0.267	0.138	2.29	576	0.92	-2.51E+00	4.34E+03	2.13E+01
9.61	0.759	7.40E+05	2.02E+05	0.273	0.135	2.32	579	0.92	-2.36E+00	4.49E+03	2.14E+01
9.93	0.784	7.36E+05	2.09E+05	0.284	0.130	2.37	585	0.93	-2.07E+00	4.61E+03	2.17E+01
10.25	0.809	7.36E+05	2.16E+05	0.294	0.126	2.41	590	0.94	-1.83E+00	4.76E+03	2.19E+01
10.58	0.835	7.35E+05	2.23E+05	0.304	0.122	2.45	595	0.95	-1.59E+00	4.91E+03	2.22E+01
10.90	0.861	7.30E+05	2.28E+05	0.313	0.118	2.49	599	0.95	-1.39E+00	5.03E+03	2.24E+01
11.22	0.886	7.28E+05	2.37E+05	0.325	0.114	2.54	604	0.96	-1.11E+00	5.17E+03	2.27E+01
11.54	0.911	7.34E+05	2.44E+05	0.333	0.111	2.58	607	0.97	-9.43E-01	5.35E+03	2.28E+01
11.87	0.937	7.36E+05	2.52E+05	0.342	0.108	2.61	611	0.97	-7.56E-01	5.52E+03	2.30E+01
12.19	0.962	7.25E+05	2.59E+05	0.357	0.103	2.67	617	0.98	-4.55E-01	5.59E+03	2.33E+01
12.51	0.987	7.24E+05	2.70E+05	0.373	0.099	2.74	622	0.99	-1.51E-01	5.74E+03	2.36E+01
12.83	1.013	7.28E+05	2.78E+05	0.382	0.097	2.77	625	1.00	0.00E+00	5.92E+03	2.38E+01
13.15	1.038	7.21E+05	2.81E+05	0.390	0.095	2.80	628	1.00	1.43E-01	6.01E+03	2.39E+01
13.47	1.064	7.26E+05	2.83E+05	0.389	0.095	2.80	628	1.00	1.33E-01	6.20E+03	2.39E+01
13.79	1.089	7.18E+05	2.82E+05	0.393	0.094	2.81	629	1.00	1.92E-01	6.28E+03	2.40E+01
14.12	1.115	7.20E+05	2.83E+05	0.393	0.094	2.81	629	1.00	1.94E-01	6.45E+03	2.40E+01
14.44	1.140	7.19E+05	2.84E+05	0.395	0.094	2.82	629	1.00	2.17E-01	6.60E+03	2.40E+01
14.76	1.165	7.15E+05	2.83E+05	0.396	0.093	2.82	630	1.00	2.39E-01	6.71E+03	2.40E+01

Table 42: ZPG diamond roughness Pitot data at the 2nd test location.

y (mm)	y/δ	P_{01}	P_{02}	P_{02}/P_{01}	P/P_{02}	M	U	U/U_e	$\frac{U_{eff} - U_{eff,e}}{u^*}$	y^+	u^+
0.38	0.029	7.15E+05	4.61E+04	0.064	0.510	1.03	334	0.53	-1.47E+01	1.40E+02	1.38E+01
0.61	0.046	7.19E+05	4.25E+04	0.059	0.556	0.95	314	0.50	-1.56E+01	2.25E+02	1.29E+01
0.92	0.070	7.19E+05	4.45E+04	0.062	0.532	0.99	324	0.51	-1.52E+01	3.43E+02	1.34E+01
1.24	0.094	7.20E+05	4.88E+04	0.068	0.485	1.07	345	0.55	-1.43E+01	4.60E+02	1.43E+01
1.55	0.118	7.21E+05	5.51E+04	0.077	0.430	1.17	370	0.59	-1.31E+01	5.78E+02	1.55E+01
1.86	0.142	7.22E+05	6.35E+04	0.088	0.374	1.29	398	0.63	-1.18E+01	6.97E+02	1.68E+01
2.18	0.166	7.21E+05	6.91E+04	0.096	0.343	1.36	415	0.66	-1.10E+01	8.15E+02	1.75E+01
2.50	0.190	7.18E+05	7.52E+04	0.105	0.314	1.44	432	0.69	-1.02E+01	9.31E+02	1.83E+01
2.82	0.215	7.21E+05	8.00E+04	0.111	0.296	1.49	442	0.70	-9.71E+00	1.05E+03	1.89E+01
3.14	0.239	7.19E+05	8.36E+04	0.116	0.283	1.53	451	0.72	-9.29E+00	1.17E+03	1.93E+01
3.46	0.264	7.20E+05	8.89E+04	0.124	0.266	1.59	462	0.73	-8.75E+00	1.29E+03	1.98E+01
3.78	0.288	7.24E+05	9.45E+04	0.131	0.252	1.64	472	0.75	-8.25E+00	1.42E+03	2.03E+01
4.10	0.312	7.23E+05	9.88E+04	0.137	0.241	1.68	480	0.76	-7.84E+00	1.54E+03	2.07E+01
4.42	0.337	7.33E+05	1.06E+05	0.145	0.227	1.74	490	0.78	-7.31E+00	1.68E+03	2.13E+01
4.75	0.362	7.43E+05	1.13E+05	0.152	0.216	1.79	499	0.79	-6.85E+00	1.83E+03	2.17E+01
5.07	0.386	7.58E+05	1.20E+05	0.159	0.207	1.83	506	0.80	-6.48E+00	2.00E+03	2.21E+01
5.40	0.411	7.71E+05	1.29E+05	0.167	0.197	1.89	514	0.82	-6.01E+00	2.16E+03	2.26E+01
5.72	0.436	7.88E+05	1.37E+05	0.174	0.189	1.93	521	0.83	-5.64E+00	2.34E+03	2.29E+01
6.05	0.461	8.01E+05	1.44E+05	0.180	0.183	1.97	527	0.84	-5.35E+00	2.52E+03	2.32E+01
6.36	0.485	8.19E+05	1.51E+05	0.184	0.178	1.99	531	0.84	-5.12E+00	2.71E+03	2.34E+01
6.69	0.510	8.31E+05	1.55E+05	0.187	0.176	2.01	533	0.85	-5.01E+00	2.89E+03	2.36E+01
7.01	0.534	8.43E+05	1.61E+05	0.192	0.172	2.04	537	0.85	-4.79E+00	3.07E+03	2.38E+01
7.34	0.559	8.63E+05	1.68E+05	0.195	0.169	2.05	539	0.86	-4.65E+00	3.29E+03	2.39E+01
7.65	0.583	8.76E+05	1.73E+05	0.198	0.166	2.07	542	0.86	-4.49E+00	3.49E+03	2.41E+01
7.98	0.608	8.90E+05	1.85E+05	0.208	0.158	2.13	549	0.87	-4.07E+00	3.70E+03	2.45E+01
8.30	0.632	9.04E+05	1.94E+05	0.214	0.154	2.16	554	0.88	-3.80E+00	3.91E+03	2.48E+01
8.62	0.657	9.17E+05	2.06E+05	0.225	0.146	2.22	561	0.89	-3.38E+00	4.13E+03	2.52E+01
8.94	0.681	9.32E+05	2.19E+05	0.235	0.140	2.27	568	0.90	-2.99E+00	4.35E+03	2.56E+01
9.26	0.706	9.50E+05	2.31E+05	0.243	0.135	2.32	573	0.91	-2.68E+00	4.60E+03	2.59E+01
9.58	0.730	9.66E+05	2.46E+05	0.255	0.129	2.38	580	0.92	-2.25E+00	4.84E+03	2.63E+01
9.91	0.755	9.79E+05	2.61E+05	0.267	0.123	2.44	586	0.93	-1.85E+00	5.08E+03	2.67E+01
10.23	0.779	9.97E+05	2.76E+05	0.277	0.119	2.48	591	0.94	-1.55E+00	5.35E+03	2.70E+01
10.55	0.804	1.01E+06	2.93E+05	0.291	0.113	2.55	598	0.95	-1.12E+00	5.58E+03	2.74E+01
10.86	0.828	1.03E+06	3.02E+05	0.295	0.112	2.57	599	0.96	-1.00E+00	5.85E+03	2.76E+01
11.19	0.853	1.04E+06	3.12E+05	0.301	0.109	2.59	602	0.96	-8.31E-01	6.11E+03	2.77E+01
11.51	0.877	1.05E+06	3.17E+05	0.301	0.109	2.60	602	0.96	-8.21E-01	6.37E+03	2.77E+01
11.84	0.902	1.07E+06	3.26E+05	0.303	0.108	2.61	603	0.96	-7.65E-01	6.69E+03	2.78E+01
12.15	0.926	1.09E+06	3.34E+05	0.307	0.107	2.62	604	0.96	-6.68E-01	6.98E+03	2.79E+01
12.48	0.951	1.10E+06	3.50E+05	0.317	0.104	2.67	608	0.97	-3.98E-01	7.27E+03	2.82E+01
12.80	0.975	1.12E+06	3.62E+05	0.322	0.102	2.69	610	0.97	-2.71E-01	7.61E+03	2.83E+01
13.13	1.000	1.15E+06	3.81E+05	0.332	0.099	2.73	614	0.98	0.00E+00	7.95E+03	2.86E+01
13.44	1.024	1.17E+06	3.96E+05	0.340	0.097	2.77	617	0.99	1.92E-01	8.30E+03	2.88E+01
13.77	1.049	1.18E+06	4.11E+05	0.348	0.095	2.80	620	0.99	3.74E-01	8.64E+03	2.89E+01
14.09	1.073	1.21E+06	4.21E+05	0.349	0.094	2.81	620	0.99	4.06E-01	9.02E+03	2.90E+01
14.41	1.098	1.23E+06	4.33E+05	0.353	0.093	2.82	621	0.99	4.82E-01	9.40E+03	2.91E+01
14.74	1.123	1.25E+06	4.43E+05	0.355	0.093	2.83	622	0.99	5.32E-01	9.78E+03	2.91E+01

Table 43: ZPG smooth wall Pitot data at the 3rd test location.

y (mm)	y/δ	P_{01}	P_{02}	P_{02}/P_{01}	P/P_{02}	M	U	U/U_e	$\frac{U_{eff} - U_{eff,e}}{u^*}$	y^+	u^+
0.58	0.038	7.08E+06	6.15E+05	0.087	0.368	1.30	402	0.64	-1.34E+01	2.15E+02	1.84E+01
0.88	0.058	7.10E+06	6.96E+05	0.098	0.326	1.41	425	0.67	-1.23E+01	3.29E+02	1.96E+01
1.20	0.079	7.17E+06	8.36E+05	0.117	0.274	1.56	457	0.72	-1.06E+01	4.50E+02	2.13E+01
1.51	0.099	7.18E+06	9.18E+05	0.128	0.250	1.65	473	0.75	-9.69E+00	5.68E+02	2.21E+01
1.82	0.121	7.14E+06	9.58E+05	0.134	0.238	1.69	481	0.76	-9.22E+00	6.85E+02	2.26E+01
2.13	0.141	7.14E+06	9.93E+05	0.139	0.230	1.73	488	0.77	-8.87E+00	8.01E+02	2.30E+01
2.46	0.162	7.23E+06	1.05E+06	0.146	0.219	1.78	496	0.79	-8.43E+00	9.36E+02	2.34E+01
2.77	0.183	7.22E+06	1.08E+06	0.149	0.214	1.80	500	0.79	-8.20E+00	1.05E+03	2.36E+01
3.09	0.204	7.18E+06	1.11E+06	0.154	0.207	1.84	505	0.80	-7.87E+00	1.17E+03	2.40E+01
3.41	0.225	7.13E+06	1.14E+06	0.160	0.200	1.87	511	0.81	-7.55E+00	1.28E+03	2.43E+01
3.73	0.247	7.19E+06	1.20E+06	0.167	0.192	1.92	518	0.82	-7.15E+00	1.42E+03	2.47E+01
4.21	0.278	7.12E+06	1.22E+06	0.171	0.187	1.94	521	0.83	-6.92E+00	1.59E+03	2.49E+01
4.53	0.299	7.08E+06	1.25E+06	0.177	0.180	1.98	527	0.84	-6.57E+00	1.70E+03	2.53E+01
4.86	0.321	7.17E+06	1.30E+06	0.181	0.176	2.01	531	0.84	-6.35E+00	1.85E+03	2.55E+01
5.34	0.353	7.08E+06	1.34E+06	0.189	0.169	2.05	538	0.85	-5.95E+00	2.01E+03	2.59E+01
5.66	0.374	7.13E+06	1.39E+06	0.195	0.164	2.09	542	0.86	-5.66E+00	2.14E+03	2.62E+01
5.98	0.395	7.14E+06	1.42E+06	0.199	0.161	2.11	545	0.87	-5.47E+00	2.27E+03	2.64E+01
6.31	0.417	7.12E+06	1.46E+06	0.205	0.155	2.15	551	0.88	-5.15E+00	2.39E+03	2.67E+01
6.79	0.449	7.09E+06	1.51E+06	0.213	0.150	2.19	556	0.88	-4.83E+00	2.56E+03	2.70E+01
7.11	0.470	7.04E+06	1.54E+06	0.219	0.146	2.22	560	0.89	-4.56E+00	2.66E+03	2.73E+01
7.44	0.491	7.07E+06	1.58E+06	0.224	0.143	2.25	563	0.90	-4.35E+00	2.80E+03	2.75E+01
7.91	0.523	7.09E+06	1.64E+06	0.232	0.138	2.29	568	0.90	-4.02E+00	3.00E+03	2.78E+01
8.23	0.544	7.09E+06	1.68E+06	0.238	0.134	2.32	572	0.91	-3.78E+00	3.11E+03	2.80E+01
8.56	0.565	6.98E+06	1.70E+06	0.244	0.131	2.36	576	0.92	-3.55E+00	3.19E+03	2.83E+01
8.88	0.587	7.00E+06	1.75E+06	0.249	0.128	2.39	579	0.92	-3.32E+00	3.32E+03	2.85E+01
9.36	0.618	7.03E+06	1.82E+06	0.258	0.124	2.43	584	0.93	-3.00E+00	3.52E+03	2.88E+01
9.84	0.650	6.98E+06	1.86E+06	0.266	0.120	2.47	588	0.94	-2.72E+00	3.68E+03	2.91E+01
10.16	0.671	7.01E+06	1.92E+06	0.274	0.117	2.51	592	0.94	-2.46E+00	3.82E+03	2.94E+01
10.48	0.692	7.02E+06	1.96E+06	0.280	0.114	2.54	594	0.95	-2.27E+00	3.95E+03	2.96E+01
10.95	0.724	6.94E+06	2.00E+06	0.288	0.111	2.58	598	0.95	-1.99E+00	4.09E+03	2.98E+01
11.28	0.745	6.98E+06	2.08E+06	0.297	0.107	2.62	603	0.96	-1.70E+00	4.23E+03	3.01E+01
11.60	0.766	6.96E+06	2.10E+06	0.302	0.106	2.64	605	0.96	-1.56E+00	4.34E+03	3.03E+01
11.92	0.788	6.95E+06	2.15E+06	0.309	0.103	2.67	607	0.97	-1.35E+00	4.46E+03	3.05E+01
12.40	0.819	6.92E+06	2.21E+06	0.319	0.100	2.72	611	0.98	-1.06E+00	4.62E+03	3.08E+01
12.72	0.840	6.89E+06	2.25E+06	0.327	0.098	2.76	615	0.98	-8.22E-01	4.72E+03	3.10E+01
13.04	0.862	6.88E+06	2.29E+06	0.333	0.096	2.78	617	0.98	-6.53E-01	4.83E+03	3.12E+01
13.36	0.883	6.90E+06	2.36E+06	0.341	0.094	2.82	620	0.99	-4.30E-01	4.96E+03	3.14E+01
13.68	0.904	6.88E+06	2.38E+06	0.345	0.092	2.83	622	0.99	-3.18E-01	5.07E+03	3.15E+01
14.16	0.936	6.91E+06	2.40E+06	0.347	0.092	2.84	622	0.99	-2.67E-01	5.27E+03	3.16E+01
14.49	0.957	6.92E+06	2.44E+06	0.352	0.091	2.86	624	1.00	-1.26E-01	5.40E+03	3.17E+01
14.81	0.979	6.97E+06	2.46E+06	0.353	0.090	2.87	624	1.00	-1.13E-01	5.55E+03	3.17E+01
15.14	1.000	6.90E+06	2.46E+06	0.357	0.089	2.88	626	1.00	0.00E+00	5.62E+03	3.18E+01
15.61	1.032	6.87E+06	2.48E+06	0.360	0.089	2.90	627	1.00	9.30E-02	5.76E+03	3.19E+01
15.93	1.053	6.96E+06	2.50E+06	0.360	0.089	2.89	627	1.00	8.32E-02	5.94E+03	3.19E+01
16.26	1.074	6.88E+06	2.49E+06	0.361	0.088	2.90	628	1.00	1.35E-01	6.00E+03	3.20E+01
16.57	1.095	6.91E+06	2.50E+06	0.362	0.088	2.91	628	1.00	1.65E-01	6.14E+03	3.20E+01

Table 44: ZPG square roughness Pitot data at the 3rd test location.

y (mm)	y/δ	P_{01}	P_{02}	P_{02}/P_{01}	P/P_{02}	M	U	U/U_e	$\frac{U_{eff} - U_{eff,e}}{u^*}$	y^+	u^+
0.38	0.026	6.60E+06	4.14E+05	0.063	0.559	0.95	315	0.50	-1.30E+01	1.54E+02	1.07E+01
0.47	0.031	6.59E+06	4.41E+05	0.067	0.524	1.01	331	0.52	-1.25E+01	1.87E+02	1.13E+01
0.77	0.052	6.61E+06	4.88E+05	0.074	0.476	1.09	353	0.56	-1.17E+01	3.11E+02	1.21E+01
1.08	0.073	6.62E+06	5.32E+05	0.080	0.436	1.16	371	0.59	-1.10E+01	4.36E+02	1.27E+01
1.40	0.094	6.63E+06	5.76E+05	0.087	0.404	1.22	387	0.61	-1.04E+01	5.63E+02	1.33E+01
1.71	0.115	6.65E+06	6.01E+05	0.090	0.388	1.26	395	0.62	-1.01E+01	6.91E+02	1.36E+01
2.02	0.136	6.66E+06	6.40E+05	0.096	0.365	1.31	408	0.64	-9.62E+00	8.18E+02	1.41E+01
2.34	0.157	6.68E+06	6.88E+05	0.103	0.340	1.37	421	0.66	-9.10E+00	9.50E+02	1.46E+01
2.66	0.178	6.62E+06	7.34E+05	0.111	0.316	1.43	435	0.69	-8.55E+00	1.07E+03	1.52E+01
2.98	0.200	6.57E+06	7.45E+05	0.113	0.309	1.45	439	0.69	-8.38E+00	1.19E+03	1.54E+01
3.30	0.221	6.66E+06	7.92E+05	0.119	0.295	1.49	448	0.71	-8.03E+00	1.33E+03	1.57E+01
3.62	0.243	6.56E+06	8.23E+05	0.125	0.280	1.54	458	0.72	-7.63E+00	1.44E+03	1.61E+01
3.94	0.264	6.58E+06	8.52E+05	0.129	0.271	1.57	464	0.73	-7.39E+00	1.57E+03	1.63E+01
4.26	0.286	6.64E+06	8.92E+05	0.134	0.261	1.61	471	0.74	-7.11E+00	1.72E+03	1.66E+01
4.58	0.307	6.53E+06	9.37E+05	0.143	0.245	1.67	483	0.76	-6.63E+00	1.82E+03	1.71E+01
4.91	0.329	6.55E+06	9.59E+05	0.146	0.239	1.69	486	0.77	-6.48E+00	1.95E+03	1.73E+01
5.24	0.351	6.57E+06	9.99E+05	0.152	0.231	1.73	493	0.78	-6.20E+00	2.09E+03	1.75E+01
5.56	0.373	6.52E+06	1.04E+06	0.159	0.221	1.77	501	0.79	-5.87E+00	2.20E+03	1.79E+01
6.05	0.406	6.55E+06	1.11E+06	0.169	0.207	1.83	512	0.81	-5.40E+00	2.40E+03	1.83E+01
6.38	0.428	6.54E+06	1.13E+06	0.173	0.203	1.85	515	0.81	-5.26E+00	2.53E+03	1.85E+01
6.86	0.460	6.51E+06	1.21E+06	0.186	0.188	1.93	528	0.83	-4.70E+00	2.71E+03	1.90E+01
7.51	0.504	6.48E+06	1.27E+06	0.197	0.178	1.99	537	0.85	-4.30E+00	2.95E+03	1.94E+01
8.00	0.536	6.42E+06	1.36E+06	0.211	0.166	2.07	549	0.87	-3.78E+00	3.12E+03	1.99E+01
8.32	0.558	6.51E+06	1.39E+06	0.213	0.165	2.08	550	0.87	-3.72E+00	3.29E+03	2.00E+01
8.64	0.579	6.45E+06	1.45E+06	0.224	0.156	2.14	558	0.88	-3.34E+00	3.38E+03	2.04E+01
9.12	0.612	6.41E+06	1.52E+06	0.238	0.148	2.21	567	0.90	-2.92E+00	3.55E+03	2.08E+01
9.61	0.644	6.41E+06	1.60E+06	0.250	0.140	2.27	575	0.91	-2.55E+00	3.74E+03	2.12E+01
9.93	0.666	6.40E+06	1.64E+06	0.256	0.137	2.30	579	0.91	-2.38E+00	3.86E+03	2.14E+01
10.41	0.698	6.42E+06	1.70E+06	0.265	0.132	2.35	584	0.92	-2.13E+00	4.07E+03	2.16E+01
10.74	0.720	6.36E+06	1.76E+06	0.277	0.127	2.40	590	0.93	-1.83E+00	4.16E+03	2.19E+01
11.06	0.741	6.35E+06	1.82E+06	0.286	0.122	2.44	595	0.94	-1.59E+00	4.27E+03	2.21E+01
11.70	0.784	6.35E+06	1.90E+06	0.299	0.117	2.50	601	0.95	-1.29E+00	4.52E+03	2.24E+01
12.03	0.806	6.37E+06	1.94E+06	0.305	0.115	2.53	604	0.95	-1.14E+00	4.66E+03	2.26E+01
12.34	0.827	6.34E+06	1.98E+06	0.312	0.112	2.56	607	0.96	-9.84E-01	4.76E+03	2.27E+01
12.67	0.849	6.29E+06	2.01E+06	0.320	0.110	2.59	610	0.96	-8.25E-01	4.85E+03	2.29E+01
13.14	0.881	6.29E+06	2.08E+06	0.330	0.106	2.63	614	0.97	-6.02E-01	5.04E+03	2.31E+01
13.47	0.903	6.32E+06	2.12E+06	0.335	0.105	2.66	616	0.97	-4.91E-01	5.19E+03	2.32E+01
13.79	0.925	6.32E+06	2.16E+06	0.341	0.103	2.68	619	0.98	-3.68E-01	5.32E+03	2.34E+01
14.27	0.957	6.26E+06	2.20E+06	0.351	0.100	2.72	622	0.98	-1.87E-01	5.46E+03	2.35E+01
14.60	0.979	6.24E+06	2.23E+06	0.357	0.098	2.75	625	0.99	-5.94E-02	5.56E+03	2.37E+01
14.91	1.000	6.28E+06	2.26E+06	0.361	0.097	2.76	626	0.99	0.00E+00	5.72E+03	2.37E+01
15.24	1.022	6.22E+06	2.30E+06	0.370	0.095	2.80	629	1.00	1.74E-01	5.79E+03	2.39E+01
15.56	1.043	6.26E+06	2.30E+06	0.368	0.095	2.79	628	0.99	1.33E-01	5.96E+03	2.39E+01
15.88	1.065	6.19E+06	2.32E+06	0.374	0.094	2.81	630	1.00	2.50E-01	6.01E+03	2.40E+01
16.20	1.086	6.23E+06	2.33E+06	0.374	0.094	2.81	630	1.00	2.44E-01	6.17E+03	2.40E+01
16.52	1.108	6.21E+06	2.32E+06	0.372	0.094	2.81	630	1.00	2.13E-01	6.29E+03	2.39E+01

Table 45: ZPG diamond roughness Pitot data at the 3rd test location.

y (mm)	y/δ	P_{01}	P_{02}	P_{02}/P_{01}	P/P_{02}	M	U	U/U_e	$\frac{U_{eff} - U_{eff,e}}{u^*}$	y^+	u^+
0.38	0.026	6.73E+06	4.23E+05	0.063	0.601	0.88	296	0.47	-1.60E+01	1.67E+02	1.21E+01
0.66	0.045	6.77E+06	4.60E+05	0.068	0.555	0.96	317	0.50	-1.50E+01	2.90E+02	1.30E+01
0.97	0.066	6.84E+06	5.22E+05	0.076	0.495	1.05	344	0.55	-1.39E+01	4.33E+02	1.42E+01
1.27	0.087	6.86E+06	5.74E+05	0.084	0.451	1.13	364	0.58	-1.30E+01	5.72E+02	1.51E+01
1.74	0.120	6.90E+06	6.58E+05	0.095	0.396	1.24	390	0.62	-1.18E+01	7.91E+02	1.63E+01
2.05	0.141	6.88E+06	6.99E+05	0.102	0.372	1.29	403	0.64	-1.12E+01	9.30E+02	1.69E+01
2.37	0.163	6.89E+06	7.46E+05	0.108	0.348	1.35	415	0.66	-1.06E+01	1.08E+03	1.75E+01
2.68	0.184	6.88E+06	7.78E+05	0.113	0.334	1.38	423	0.68	-1.02E+01	1.22E+03	1.79E+01
3.00	0.206	6.91E+06	8.12E+05	0.118	0.321	1.42	431	0.69	-9.89E+00	1.37E+03	1.82E+01
3.49	0.239	6.90E+06	8.66E+05	0.126	0.301	1.48	443	0.71	-9.30E+00	1.59E+03	1.88E+01
3.80	0.261	6.87E+06	9.05E+05	0.132	0.286	1.52	452	0.72	-8.87E+00	1.72E+03	1.92E+01
4.13	0.283	6.89E+06	9.43E+05	0.137	0.275	1.56	459	0.73	-8.52E+00	1.88E+03	1.96E+01
4.44	0.305	6.85E+06	9.80E+05	0.143	0.264	1.60	467	0.75	-8.14E+00	2.01E+03	2.00E+01
4.93	0.338	6.84E+06	1.05E+06	0.154	0.246	1.66	480	0.77	-7.51E+00	2.23E+03	2.06E+01
5.25	0.360	6.82E+06	1.10E+06	0.161	0.234	1.71	488	0.78	-7.07E+00	2.37E+03	2.10E+01
5.58	0.382	6.84E+06	1.14E+06	0.166	0.228	1.74	493	0.79	-6.83E+00	2.53E+03	2.13E+01
5.90	0.405	6.81E+06	1.18E+06	0.173	0.218	1.78	500	0.80	-6.46E+00	2.67E+03	2.16E+01
6.22	0.427	6.82E+06	1.23E+06	0.180	0.210	1.82	507	0.81	-6.11E+00	2.82E+03	2.20E+01
6.71	0.460	6.78E+06	1.29E+06	0.191	0.198	1.88	517	0.83	-5.60E+00	3.02E+03	2.25E+01
7.03	0.482	6.74E+06	1.33E+06	0.197	0.192	1.92	522	0.83	-5.32E+00	3.15E+03	2.28E+01
7.35	0.504	6.74E+06	1.37E+06	0.204	0.185	1.95	528	0.84	-5.02E+00	3.30E+03	2.31E+01
7.67	0.526	6.70E+06	1.40E+06	0.208	0.181	1.98	531	0.85	-4.82E+00	3.42E+03	2.33E+01
8.16	0.559	6.70E+06	1.45E+06	0.217	0.174	2.02	537	0.86	-4.49E+00	3.64E+03	2.36E+01
8.48	0.581	6.71E+06	1.48E+06	0.221	0.171	2.04	540	0.86	-4.32E+00	3.80E+03	2.38E+01
8.80	0.603	6.66E+06	1.51E+06	0.227	0.166	2.07	545	0.87	-4.09E+00	3.91E+03	2.40E+01
9.12	0.626	6.66E+06	1.55E+06	0.232	0.162	2.10	548	0.88	-3.89E+00	4.06E+03	2.42E+01
9.44	0.647	6.63E+06	1.60E+06	0.241	0.157	2.14	554	0.89	-3.57E+00	4.18E+03	2.45E+01
9.93	0.681	6.66E+06	1.68E+06	0.252	0.150	2.19	561	0.90	-3.18E+00	4.42E+03	2.49E+01
10.25	0.703	6.61E+06	1.75E+06	0.264	0.143	2.25	568	0.91	-2.78E+00	4.54E+03	2.53E+01
10.58	0.725	6.59E+06	1.86E+06	0.282	0.134	2.33	577	0.92	-2.23E+00	4.67E+03	2.59E+01
10.89	0.747	6.58E+06	1.93E+06	0.293	0.129	2.38	583	0.93	-1.89E+00	4.81E+03	2.62E+01
11.37	0.780	6.57E+06	2.02E+06	0.307	0.123	2.44	590	0.94	-1.51E+00	5.01E+03	2.66E+01
11.70	0.802	6.59E+06	2.10E+06	0.318	0.119	2.49	595	0.95	-1.19E+00	5.18E+03	2.69E+01
12.01	0.824	6.54E+06	2.14E+06	0.328	0.115	2.52	599	0.96	-9.51E-01	5.28E+03	2.71E+01
12.34	0.846	6.53E+06	2.17E+06	0.332	0.114	2.54	600	0.96	-8.56E-01	5.42E+03	2.72E+01
12.65	0.868	6.52E+06	2.20E+06	0.337	0.112	2.56	603	0.97	-7.23E-01	5.55E+03	2.74E+01
13.14	0.901	6.49E+06	2.23E+06	0.344	0.110	2.59	605	0.97	-5.63E-01	5.75E+03	2.75E+01
13.46	0.923	6.45E+06	2.27E+06	0.352	0.107	2.62	608	0.98	-3.69E-01	5.85E+03	2.77E+01
13.78	0.945	6.43E+06	2.32E+06	0.360	0.105	2.65	611	0.98	-1.77E-01	5.98E+03	2.79E+01
14.10	0.967	6.47E+06	2.34E+06	0.362	0.104	2.66	612	0.98	-1.45E-01	6.16E+03	2.79E+01
14.42	0.989	6.46E+06	2.40E+06	0.372	0.102	2.70	615	0.99	7.44E-02	6.29E+03	2.82E+01
14.74	1.011	6.46E+06	2.44E+06	0.377	0.100	2.72	617	0.99	1.90E-01	6.43E+03	2.83E+01
15.06	1.033	6.45E+06	2.48E+06	0.384	0.098	2.74	619	0.99	3.34E-01	6.57E+03	2.84E+01
15.39	1.055	6.44E+06	2.51E+06	0.390	0.097	2.77	621	1.00	4.61E-01	6.70E+03	2.86E+01
15.71	1.078	6.45E+06	2.52E+06	0.391	0.097	2.77	621	1.00	4.62E-01	6.86E+03	2.86E+01
16.03	1.099	6.43E+06	2.54E+06	0.394	0.096	2.78	622	1.00	5.37E-01	6.99E+03	2.86E+01

Table 46: WPG smooth wall Pitot data.

	Location 1	Location 2					Location 3				
		A	B	C	D	E	A	B	C	D	E
y (mm)	**p_{t2}/p_{t1}**	**p_{t2}/p_{t1}**	**p_{t2}/p_{t1}**	**p_{t2}/p_{t1}**	**p_{t2}/p_{t1}**	**p_{t2}/p_{t1}**	**p_{t2}/p_{t1}**	**p_{t2}/p_{t1}**	**p_{t2}/p_{t1}**	**p_{t2}/p_{t1}**	**p_{t2}/p_{t1}**
0.4	0.08	0.08	0.08	0.08	0.08	0.08	0.06	0.06	0.06	0.06	0.06
0.5	0.1	0.11	0.11	0.11	0.11	0.11	0.09	0.08	0.09	0.08	0.08
1.3	0.13	0.13	0.13	0.13	0.13	0.13	0.11	0.11	0.11	0.11	0.11
2.0	0.15	0.14	0.14	0.14	0.14	0.14	0.12	0.12	0.12	0.12	0.12
2.9	0.16	0.16	0.16	0.16	0.16	0.16	0.14	0.13	0.13	0.13	0.13
3.7	0.18	0.17	0.17	0.17	0.17	0.17	0.15	0.15	0.15	0.14	0.14
4.5	0.2	0.18	0.18	0.18	0.18	0.18	0.16	0.16	0.16	0.16	0.16
5.3	0.23	0.2	0.2	0.2	0.2	0.2	0.17	0.17	0.17	0.17	0.17
6.1	0.25	0.22	0.21	0.21	0.21	0.21	0.18	0.18	0.18	0.18	0.18
6.9	0.3	0.24	0.23	0.23	0.23	0.23	0.19	0.19	0.19	0.19	0.19
7.7	0.33	0.25	0.25	0.25	0.25	0.25	0.2	0.2	0.2	0.2	0.2
8.5	0.35	0.27	0.27	0.27	0.26	0.26	0.21	0.21	0.21	0.21	0.21
9.4	0.37	0.3	0.29	0.29	0.28	0.28	0.23	0.22	0.23	0.22	0.22
10.2	0.38	0.31	0.31	0.31	0.3	0.3	0.24	0.24	0.24	0.24	0.24
11.0	0.38	0.33	0.33	0.33	0.32	0.32	0.26	0.25	0.25	0.25	0.25
11.8	0.38	0.35	0.35	0.34	0.34	0.33	0.27	0.26	0.26	0.26	0.26
12.6	0.38	0.36	0.36	0.35	0.35	0.34	0.28	0.28	0.28	0.28	0.28
13.4	0.38	0.36	0.37	0.36	0.35	0.35	0.29	0.29	0.29	0.29	0.29
14.2	0.38	0.37	0.37	0.36	0.36	0.35	0.3	0.3	0.3	0.31	0.3
15.0	0.37	0.37	0.37	0.37	0.36	0.36	0.32	0.32	0.32	0.32	0.31
15.9	0.37	0.37	0.38	0.37	0.36	0.36	0.33	0.33	0.33	0.32	0.32
16.7	0.37	0.37	0.38	0.37	0.36	0.36	0.33	0.33	0.33	0.33	0.32
17.5	0.37	0.37	0.38	0.37	0.37	0.36	0.33	0.34	0.34	0.33	0.33
18.3	0.37	0.38	0.38	0.37	0.37	0.36	0.33	0.34	0.34	0.33	0.33
19.1	0.36	0.38	0.38	0.37	0.37	0.36	0.33	0.34	0.34	0.33	0.33
19.4	0.37	0.38	0.38	0.37	0.37	0.36	0.33	0.33	0.33	0.34	0.33

Table 47: WPG square roughness Pitot data.

	Location 1	Location 2					Location 3				
		A	B	C	D	E	A	B	C	D	E
y (mm)	**p_{t2}/p_{t1}**	**p_{t2}/p_{t1}**	**p_{t2}/p_{t1}**	**p_{t2}/p_{t1}**	**p_{t2}/p_{t1}**	**p_{t2}/p_{t1}**	**p_{t2}/p_{t1}**	**p_{t2}/p_{t1}**	**p_{t2}/p_{t1}**	**p_{t2}/p_{t1}**	**p_{t2}/p_{t1}**
0.4	0.05	0.05	0.05	0.05	0.05	0.05	0.04	0.04	0.04	0.04	0.04
0.5	0.05	0.06	0.05	0.05	0.05	0.05	0.05	0.05	0.05	0.05	0.05
1.2	0.07	0.07	0.07	0.07	0.07	0.07	0.05	0.06	0.06	0.06	0.06
1.9	0.08	0.08	0.08	0.08	0.08	0.08	0.06	0.06	0.07	0.07	0.07
2.7	0.1	0.1	0.1	0.1	0.1	0.1	0.07	0.07	0.08	0.08	0.08
3.4	0.12	0.11	0.11	0.11	0.11	0.11	0.09	0.08	0.09	0.09	0.09
4.1	0.15	0.13	0.12	0.12	0.12	0.12	0.09	0.09	0.1	0.1	0.1
4.9	0.17	0.14	0.14	0.14	0.14	0.14	0.1	0.1	0.11	0.11	0.11
5.6	0.19	0.15	0.15	0.15	0.15	0.16	0.11	0.11	0.12	0.12	0.12
6.3	0.22	0.17	0.17	0.17	0.17	0.17	0.13	0.12	0.13	0.13	0.13
7.1	0.25	0.19	0.19	0.19	0.19	0.19	0.14	0.14	0.14	0.14	0.14
7.8	0.28	0.21	0.21	0.21	0.21	0.21	0.15	0.15	0.15	0.15	0.16
8.5	0.29	0.23	0.22	0.23	0.22	0.23	0.16	0.16	0.17	0.17	0.17
9.2	0.33	0.25	0.25	0.24	0.25	0.25	0.18	0.18	0.18	0.18	0.18
10.0	0.36	0.28	0.27	0.26	0.27	0.27	0.19	0.19	0.2	0.19	0.19
10.7	0.37	0.3	0.29	0.29	0.29	0.29	0.21	0.21	0.21	0.21	0.21
11.4	0.38	0.31	0.31	0.31	0.31	0.31	0.22	0.22	0.22	0.22	0.22
12.2	0.38	0.33	0.33	0.33	0.32	0.32	0.24	0.23	0.24	0.24	0.24
12.9	0.37	0.34	0.34	0.34	0.33	0.33	0.25	0.25	0.26	0.26	0.25
13.6	0.38	0.35	0.35	0.35	0.34	0.34	0.27	0.27	0.27	0.27	0.27
14.3	0.37	0.35	0.35	0.35	0.35	0.35	0.29	0.29	0.29	0.29	0.29
15.1	0.38	0.35	0.35	0.35	0.35	0.35	0.31	0.3	0.31	0.3	0.3
15.8	0.37	0.36	0.35	0.35	0.35	0.36	0.32	0.32	0.32	0.31	0.31
16.5	0.37	0.36	0.35	0.35	0.36	0.36	0.32	0.33	0.33	0.33	0.32
17.2	0.37	0.36	0.35	0.36	0.36	0.36	0.34	0.33	0.33	0.34	0.33
17.4	0.38	0.36	0.35	0.35	0.36	0.36	0.34	0.34	0.34	0.34	0.33

Table 48: WPG diamond roughness Pitot data.

	Location 1	Location 2					Location 3				
		A	B	C	D	E	A	B	C	D	E
y (mm)	**p_{t2}/p_{t1}**	**p_{t2}/p_{t1}**	**p_{t2}/p_{t1}**	**p_{t2}/p_{t1}**	**p_{t2}/p_{t1}**	**p_{t2}/p_{t1}**	**p_{t2}/p_{t1}**	**p_{t2}/p_{t1}**	**p_{t2}/p_{t1}**	**p_{t2}/p_{t1}**	**p_{t2}/p_{t1}**
0.3	0.07	0.05	0.05	0.06	0.05	0.05	0.05	0.05	0.04	0.05	0.05
0.3	0.08	0.05	0.06	0.06	0.06	0.05	0.05	0.05	0.04	0.05	0.05
1.0	0.11	0.07	0.08	0.08	0.08	0.08	0.06	0.06	0.06	0.06	0.06
1.7	0.12	0.1	0.09	0.09	0.1	0.1	0.08	0.08	0.07	0.07	0.08
2.4	0.15	0.11	0.11	0.11	0.11	0.11	0.09	0.09	0.09	0.09	0.09
3.1	0.16	0.12	0.13	0.12	0.12	0.13	0.1	0.1	0.1	0.1	0.1
3.8	0.17	0.13	0.13	0.14	0.13	0.14	0.11	0.11	0.11	0.11	0.11
4.6	0.19	0.15	0.14	0.16	0.15	0.15	0.12	0.12	0.12	0.13	0.12
5.3	0.23	0.17	0.16	0.17	0.17	0.16	0.13	0.13	0.13	0.14	0.13
6.0	0.26	0.19	0.19	0.18	0.2	0.18	0.14	0.15	0.14	0.15	0.14
6.7	0.26	0.2	0.21	0.19	0.21	0.2	0.15	0.16	0.15	0.15	0.16
7.4	0.28	0.21	0.23	0.22	0.22	0.23	0.16	0.17	0.16	0.17	0.17
8.2	0.3	0.23	0.24	0.25	0.23	0.25	0.18	0.17	0.18	0.18	0.17
8.9	0.33	0.26	0.25	0.27	0.26	0.25	0.2	0.19	0.19	0.2	0.18
9.6	0.35	0.29	0.28	0.28	0.29	0.27	0.21	0.21	0.2	0.22	0.2
10.3	0.35	0.31	0.31	0.29	0.3	0.3	0.22	0.23	0.21	0.22	0.22
11.0	0.35	0.31	0.33	0.31	0.3	0.32	0.23	0.24	0.23	0.23	0.24
11.8	0.37	0.32	0.34	0.33	0.32	0.32	0.25	0.25	0.26	0.25	0.25
12.5	0.37	0.34	0.33	0.35	0.33	0.32	0.27	0.26	0.27	0.28	0.26
13.2	0.35	0.36	0.34	0.34	0.35	0.33	0.29	0.29	0.28	0.3	0.28
13.9	0.35	0.35	0.36	0.34	0.36	0.35	0.29	0.31	0.29	0.29	0.3
14.6	0.36	0.34	0.36	0.35	0.34	0.36	0.3	0.31	0.31	0.31	0.31
15.3	0.36	0.35	0.34	0.36	0.35	0.35	0.32	0.31	0.32	0.32	0.31
16.1	0.35	0.36	0.35	0.36	0.36	0.35	0.33	0.32	0.32	0.33	0.31
16.7	0.35	0.36	0.35	0.35	0.36	0.36	0.34	0.33	0.32	0.33	0.33
17.4	0.35	0.36	0.36	0.35	0.36	0.36	0.33	0.34	0.33	0.32	0.33

Table 49: SPG smooth wall Pitot data.

	Location 1	Location 2					Location 3				
		A	B	C	D	E	A	B	C	D	E
y (mm)	**p_{t2}/p_{t1}**	**p_{t2}/p_{t1}**	**p_{t2}/p_{t1}**	**p_{t2}/p_{t1}**	**p_{t2}/p_{t1}**	**p_{t2}/p_{t1}**	**p_{t2}/p_{t1}**	**p_{t2}/p_{t1}**	**p_{t2}/p_{t1}**	**p_{t2}/p_{t1}**	**p_{t2}/p_{t1}**
0.4	0.11	0.06	0.05	0.08	0.06	0.08	0.05	0.06	0.06	0.06	0.06
0.4	0.12	0.08	0.08	0.09	0.08	0.09	0.07	0.07	0.07	0.07	0.07
1.2	0.14	0.1	0.09	0.09	0.09	0.1	0.08	0.08	0.08	0.08	0.08
2.0	0.15	0.11	0.1	0.1	0.1	0.11	0.09	0.1	0.1	0.1	0.09
2.8	0.17	0.12	0.11	0.11	0.11	0.11	0.11	0.11	0.11	0.11	0.11
3.6	0.19	0.13	0.12	0.12	0.11	0.12	0.13	0.13	0.13	0.13	0.12
5.3	0.22	0.14	0.13	0.13	0.13	0.13	0.16	0.16	0.16	0.16	0.15
6.1	0.25	0.15	0.14	0.14	0.14	0.14	0.17	0.17	0.18	0.17	0.16
6.9	0.26	0.16	0.15	0.15	0.14	0.15	0.18	0.19	0.2	0.18	0.18
7.7	0.28	0.17	0.17	0.16	0.15	0.16	0.2	0.2	0.21	0.2	0.19
8.5	0.3	0.19	0.18	0.17	0.16	0.16	0.21	0.22	0.22	0.22	0.21
9.4	0.31	0.2	0.19	0.18	0.17	0.17	0.23	0.23	0.24	0.23	0.23
10.2	0.32	0.21	0.2	0.19	0.18	0.18	0.24	0.25	0.25	0.25	0.24
11.0	0.32	0.22	0.21	0.2	0.19	0.19	0.26	0.27	0.27	0.26	0.26
11.8	0.32	0.24	0.23	0.21	0.2	0.21	0.26	0.28	0.29	0.27	0.27
13.4	0.33	0.27	0.26	0.24	0.23	0.22	0.28	0.29	0.31	0.31	0.31
14.2	0.33	0.28	0.27	0.25	0.24	0.23	0.29	0.29	0.31	0.31	0.32
15.0	0.33	0.29	0.28	0.27	0.25	0.25	0.29	0.29	0.3	0.31	0.33
15.9	0.32	0.3	0.29	0.28	0.26	0.26	0.28	0.29	0.3	0.3	0.32
16.7	0.32	0.31	0.3	0.29	0.27	0.26	0.27	0.27	0.3	0.31	0.32
17.5	0.32	0.31	0.31	0.29	0.28	0.27	0.26	0.27	0.28	0.3	0.32
18.3	0.32	0.32	0.31	0.29	0.28	0.27	0.25	0.26	0.26	0.29	0.31
19.1	0.32	0.33	0.31	0.29	0.29	0.27	0.25	0.26	0.26	0.27	0.3
20.6	0.31	0.34	0.32	0.3	0.3	0.29	0.25	0.25	0.25	0.26	0.26
21.4	0.31	0.34	0.33	0.31	0.29	0.29	0.24	0.25	0.25	0.25	0.25
22.1	0.31	0.34	0.33	0.31	0.31	0.3	0.24	0.25	0.24	0.25	0.25
22.2	0.32	0.34	0.33	0.31	0.3	0.3	0.24	0.24	0.24	0.25	0.25

Table 50: SPG square roughness Pitot data.

	Location 1	Location 2					Location 3				
		A	B	C	D	E	A	B	C	D	E
y (mm)	**p_{t2}/p_{t1}**	**p_{t2}/p_{t1}**	**p_{t2}/p_{t1}**	**p_{t2}/p_{t1}**	**p_{t2}/p_{t1}**	**p_{t2}/p_{t1}**	**p_{t2}/p_{t1}**	**p_{t2}/p_{t1}**	**p_{t2}/p_{t1}**	**p_{t2}/p_{t1}**	**p_{t2}/p_{t1}**
0.4	0.06	0.04	0.04	0.04	0.04	0.04	0.04	0.04	0.04	0.04	0.04
0.6	0.07	0.04	0.04	0.04	0.04	0.04	0.04	0.04	0.04	0.04	0.04
1.3	0.08	0.06	0.06	0.05	0.06	0.05	0.04	0.04	0.05	0.05	0.05
2.1	0.1	0.07	0.07	0.07	0.07	0.06	0.04	0.05	0.05	0.05	0.05
2.8	0.12	0.08	0.08	0.08	0.08	0.08	0.05	0.05	0.05	0.05	0.05
3.5	0.13	0.09	0.09	0.09	0.09	0.08	0.05	0.06	0.06	0.06	0.06
5.0	0.18	0.11	0.11	0.1	0.1	0.1	0.06	0.08	0.08	0.08	0.08
5.8	0.2	0.12	0.12	0.11	0.11	0.11	0.07	0.09	0.09	0.09	0.09
6.5	0.22	0.13	0.12	0.12	0.12	0.12	0.08	0.1	0.1	0.1	0.1
7.3	0.24	0.14	0.14	0.13	0.13	0.13	0.1	0.12	0.12	0.11	0.12
8.0	0.26	0.15	0.14	0.14	0.14	0.14	0.11	0.13	0.13	0.13	0.13
8.8	0.28	0.16	0.16	0.15	0.15	0.15	0.13	0.15	0.15	0.14	0.15
9.5	0.29	0.17	0.17	0.16	0.16	0.16	0.14	0.16	0.17	0.16	0.16
10.3	0.31	0.19	0.18	0.17	0.18	0.17	0.16	0.18	0.18	0.18	0.18
11.0	0.31	0.2	0.2	0.19	0.19	0.18	0.17	0.2	0.2	0.2	0.2
11.7	0.31	0.22	0.21	0.2	0.2	0.19	0.19	0.22	0.22	0.22	0.22
12.5	0.31	0.24	0.23	0.21	0.22	0.21	0.2	0.23	0.24	0.24	0.24
13.2	0.31	0.25	0.24	0.23	0.23	0.22	0.22	0.25	0.26	0.26	0.26
14.0	0.31	0.27	0.26	0.25	0.25	0.24	0.24	0.27	0.28	0.28	0.28
14.7	0.31	0.28	0.27	0.26	0.26	0.25	0.25	0.29	0.3	0.31	0.3
15.4	0.3	0.3	0.29	0.27	0.28	0.27	0.27	0.31	0.32	0.32	0.32
16.2	0.3	0.31	0.3	0.29	0.28	0.28	0.29	0.33	0.33	0.34	0.34
16.9	0.3	0.32	0.31	0.3	0.29	0.29	0.31	0.34	0.34	0.34	0.34
17.6	0.3	0.33	0.31	0.3	0.3	0.29	0.32	0.34	0.34	0.34	0.34
18.3	0.31	0.33	0.32	0.31	0.31	0.3	0.33	0.33	0.33	0.33	0.34
19.0	0.31	0.34	0.32	0.31	0.31	0.31	0.33	0.32	0.33	0.33	0.34
19.7	0.31	0.34	0.33	0.32	0.32	0.31	0.32	0.31	0.32	0.33	0.34

Table 51: SPG diamond roughness Pitot data.

	Location 1	Location 2					Location 3				
		A	B	C	D	E	A	B	C	D	E
y (mm)	p_{t2}/p_{t1}	p_{t2}/p_{t1}	p_{t2}/p_{t1}	p_{t2}/p_{t1}	p_{t2}/p_{t1}	p_{t2}/p_{t1}	p_{t2}/p_{t1}	p_{t2}/p_{t1}	p_{t2}/p_{t1}	p_{t2}/p_{t1}	p_{t2}/p_{t1}
0.3	0.07	0.05	0.04	0.05	0.03	0.04	0.04	0.04	0.05	0.05	0.05
0.6	0.08	0.05	0.05	0.05	0.04	0.05	0.04	0.05	0.05	0.05	0.05
1.2	0.11	0.07	0.07	0.07	0.07	0.07	0.05	0.05	0.05	0.05	0.05
1.8	0.13	0.08	0.09	0.08	0.08	0.09	0.06	0.06	0.06	0.06	0.06
2.5	0.14	0.09	0.09	0.1	0.09	0.08	0.07	0.07	0.07	0.07	0.07
3.1	0.16	0.1	0.09	0.11	0.1	0.09	0.08	0.09	0.08	0.09	0.08
3.8	0.19	0.12	0.1	0.1	0.11	0.1	0.1	0.1	0.1	0.1	0.09
4.4	0.22	0.13	0.12	0.11	0.12	0.12	0.11	0.12	0.11	0.11	0.11
5.1	0.25	0.13	0.13	0.12	0.12	0.13	0.13	0.13	0.13	0.13	0.12
5.7	0.25	0.13	0.15	0.13	0.12	0.13	0.14	0.14	0.14	0.14	0.14
6.4	0.26	0.14	0.15	0.15	0.13	0.13	0.15	0.16	0.16	0.16	0.15
7.0	0.3	0.16	0.15	0.17	0.15	0.14	0.17	0.17	0.17	0.17	0.17
7.7	0.33	0.18	0.16	0.17	0.17	0.16	0.18	0.19	0.19	0.19	0.18
8.3	0.34	0.2	0.18	0.17	0.18	0.18	0.19	0.2	0.2	0.2	0.2
9.0	0.33	0.21	0.2	0.19	0.18	0.19	0.21	0.21	0.21	0.22	0.21
9.6	0.34	0.21	0.22	0.21	0.19	0.2	0.22	0.23	0.23	0.23	0.23
10.9	0.36	0.25	0.23	0.24	0.23	0.21	0.25	0.26	0.26	0.27	0.27
11.6	0.34	0.27	0.25	0.24	0.25	0.23	0.27	0.27	0.27	0.28	0.28
12.2	0.35	0.29	0.27	0.25	0.25	0.25	0.28	0.29	0.29	0.3	0.3
12.8	0.36	0.28	0.29	0.27	0.26	0.26	0.28	0.29	0.3	0.31	0.31
13.5	0.36	0.29	0.29	0.28	0.27	0.26	0.28	0.29	0.31	0.32	0.32
14.1	0.34	0.3	0.29	0.3	0.28	0.27	0.27	0.28	0.3	0.32	0.32
14.7	0.35	0.31	0.29	0.3	0.3	0.28	0.27	0.28	0.29	0.32	0.32
16.6	0.35	0.33	0.33	0.31	0.3	0.3	0.25	0.26	0.27	0.27	0.29
17.2	0.35	0.32	0.33	0.32	0.3	0.3	0.25	0.26	0.26	0.26	0.27
17.7	0.36	0.33	0.33	0.33	0.31	0.3	0.25	0.25	0.26	0.25	0.26
17.8	0.36	0.33	0.32	0.33	0.32	0.3	0.25	0.25	0.25	0.25	0.26

Table 52: Stagnation thermodynamic properties.

Variable	Value	Error Bound
P_0 (kPa)	68.9	$\pm 10\%$
T_0 (K)	315	$\pm 5\%$
M_e	2.86	$\pm 0.5\%$

Table 53: Freestream thermodynamic properties for all models.

		Test Loc.	*Mach*	*T (K)*	*p (Pa)*	*ρ (kg/m3)*	*dp/dx (Pa/m)*	*δ(m)*	*Re/m*	*Re$_δ$*
ZPG	**Smooth Wall**	**1**	2.85	120	23526	0.683	0.00E+00	0.0112	5.14E+07	5.78E+05
		2	2.87	119	22822	0.668	0.00E+00	0.0121	5.09E+07	6.16E+05
		3	2.82	122	24626	0.706	0.00E+00	0.0127	5.22E+07	6.61E+05
	Square Roughness	**1**	2.82	122	24626	0.706	0.00E+00	0.0099	5.22E+07	5.16E+05
		2	2.83	121	24253	0.698	0.00E+00	0.0130	5.20E+07	6.73E+05
		3	2.77	124	26580	0.745	0.00E+00	0.0146	5.36E+07	7.83E+05
	Diamond Peak	**1**	2.84	121	23887	0.690	0.00E+00	0.0094	5.17E+07	4.86E+05
		2	2.89	118	22141	0.654	0.00E+00	0.0114	5.03E+07	5.75E+05
		3	2.83	121	24253	0.698	0.00E+00	0.0134	5.20E+07	6.97E+05
	Diamond Valley	**1**	2.84	121	23887	0.690	0.00E+00	0.0111	5.17E+07	5.75E+05
		2	2.89	118	22141	0.654	0.00E+00	0.0118	5.03E+07	5.94E+05
		3	2.83	121	24253	0.698	0.00E+00	0.0140	5.20E+07	7.25E+05
WPG	**Smooth Wall**	**1**	2.84	121	23887	0.690	3.68E-04	0.0108	5.17E+07	5.57E+05
		2	2.86	120	23172	0.676	-3.90E+04	0.0117	5.11E+07	5.98E+05
		3	2.88	118	22479	0.661	1.04E+04	0.0161	5.06E+07	8.14E+05
	Square Roughness	**1**	2.84	121	23887	0.690	0.00E+00	0.0100	5.17E+07	5.14E+05
		2	2.84	121	23887	0.690	-1.65E+04	0.0129	5.17E+07	6.66E+05
		3	2.84	121	23887	0.690	-1.48E+04	0.0153	5.17E+07	7.91E+05
	Diamond Peak	**1**	2.84	121	23887	0.690	0.00E+00	0.0107	5.17E+07	5.52E+05
		2	2.87	119	22822	0.668	-8.28E+03	0.0130	5.09E+07	6.62E+05
		3	2.88	118	22479	0.661	7.18E+04	0.0151	5.06E+07	7.65E+05
	Diamond Valley	**1**	2.84	121	23887	0.690	0.00E+00	0.0095	5.17E+07	4.89E+05
		2	2.87	119	22822	0.668	-8.28E+03	0.0128	5.09E+07	6.53E+05
		3	2.88	118	22479	0.661	7.18E+04	0.0156	5.06E+07	7.88E+05
SPG	**Smooth Wall**	**1**	2.82	122	24626	0.706	0.00E+00	0.0105	5.22E+07	5.48E+05
		2	2.89	118	22141	0.654	-4.97E+04	0.0146	5.03E+07	7.35E+05
		3	2.99	113	19041	0.587	4.09E+03	0.0148	4.78E+07	7.08E+05
	Square Roughness	**1**	2.84	121	23887	0.690	0.00E+00	0.0100	5.17E+07	5.15E+05
		2	2.87	119	22822	0.668	-8.90E+04	0.0128	5.09E+07	6.49E+05
		3	2.98	113	19329	0.594	5.78E+04	0.0174	4.80E+07	8.38E+05
	Diamond Peak	**1**	2.85	120	23526	0.683	0.00E+00	0.0095	5.14E+07	4.86E+05
		2	2.89	118	22141	0.654	-7.61E+04	0.0127	5.03E+07	6.37E+05
		3	2.99	113	19041	0.587	8.08E+04	0.0169	4.78E+07	8.08E+05
	Diamond Valley	**1**	2.85	120	23526	0.683	0.00E+00	0.0100	5.14E+07	5.14E+05
		2	2.89	118	22141	0.654	-7.61E+04	0.0123	5.03E+07	6.17E+05
		3	N/A	N/A	N/A	N/A	N/A	N/A	N/A	N/A

Table 54: Estimator variances multiplied by N and maximum interval.

Statistic	Variance	Maximum Interval
$\overline{u}$	$\overline{u'u'}$	$\pm 0.5\%$
$\sqrt{\overline{u'^2}}$	$\frac{\overline{u'^2}}{2}$	$\pm 2.2\%$
$\sqrt{\overline{v'^2}}$	$\frac{\overline{v'^2}}{2}$	$\pm 2.2\%$
$\overline{u'v'}$	$\left(\overline{u'u'}\right)\left(\overline{v'v'}\right)+\left(\overline{u'v'}\right)^2$	$\pm 12\%$

Table 55: PIV propagation error values.

Variable	***% Error***
δ	15%
$d\overline{u}/dx$	1.9%
$d\overline{u}/dy$	1.9%
$d\overline{v}/dx$	3.1%
$d\overline{v}/dy$	3.1%
$\left(\tau_{xx}/\overline{\rho}\right)\cdot d\overline{u}/dx$	4.8%
$\left(\tau_{xy}/\overline{\rho}\right)\cdot d\overline{u}/dy$	11.7%
$\left(\tau_{xy}/\overline{\rho}\right)\cdot d\overline{v}/dx$	12.0%
$\left(\tau_{yy}/\overline{\rho}\right)\cdot d\overline{v}/dy$	5.4%
$\left(\tau_{xx}/\overline{\rho}\right)\cdot d\overline{v}/dx$	5.4%
$\left(\tau_{xy}/\overline{\rho}\right)\cdot d\overline{u}/dx$	11.7%
$\left(\tau_{xy}/\overline{\rho}\right)\cdot d\overline{v}/dy$	12.0%
$\left(\tau_{yy}/\overline{\rho}\right)\cdot d\overline{u}/dy$	4.8%
$P_{xx}/\overline{\rho}$	17.9%
$P_{yy}/\overline{\rho}$	18.6%
$P_{xy}/\overline{\rho}$	18.3%

Table 56: Pitot measurement and propagation error values.

Variable	*%Error*
y	2.5%
p_{02}/p_{01}	0.2%
M	0.6%
U	0.6%
U_{eff}	1.1%
y^+	5.6%
U_{eff}^+	5.1%

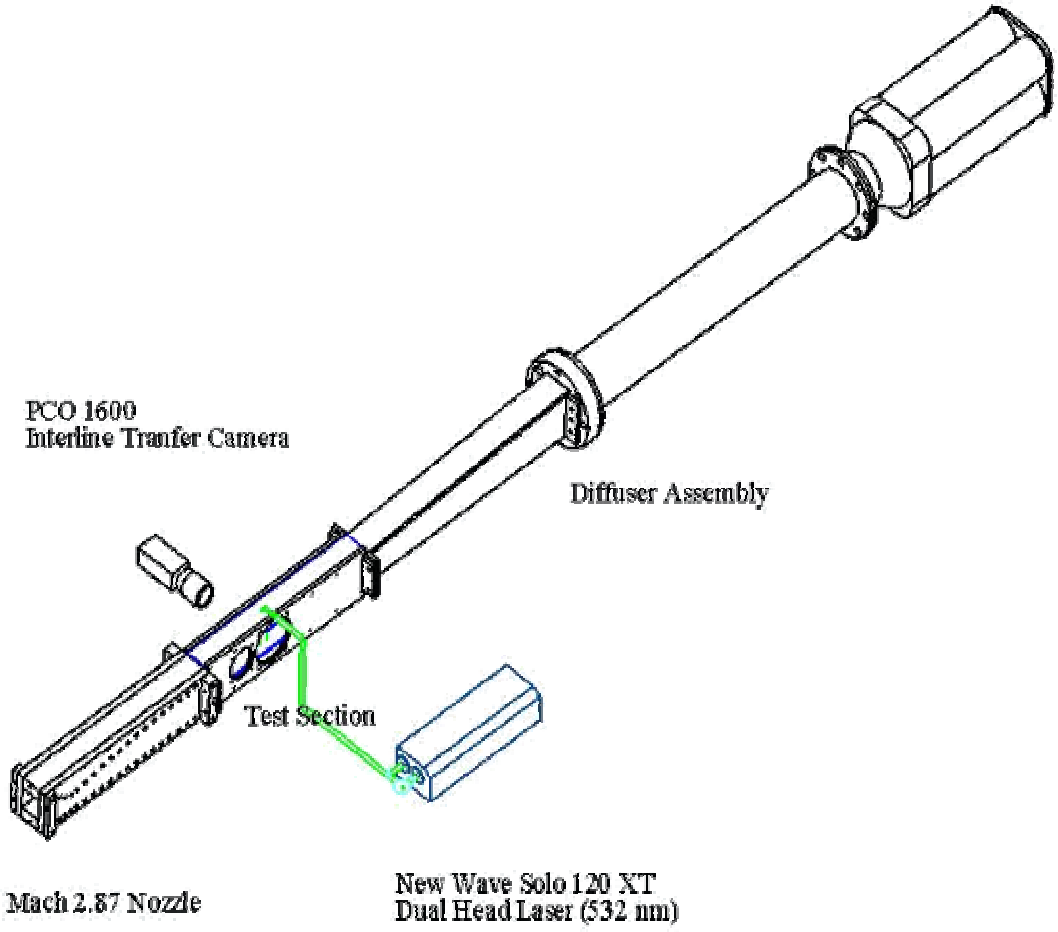

Figure 1: **Schematic of the PIV setup**

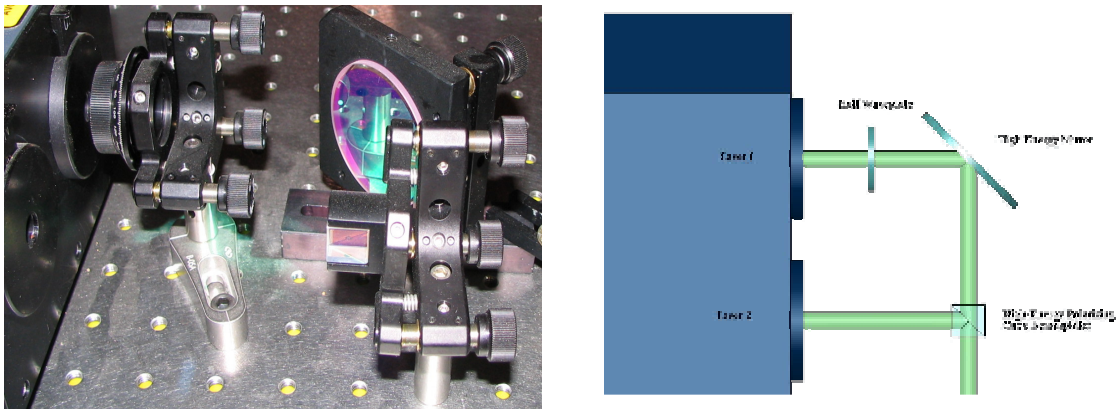

Figure 2: Laser polarization setup

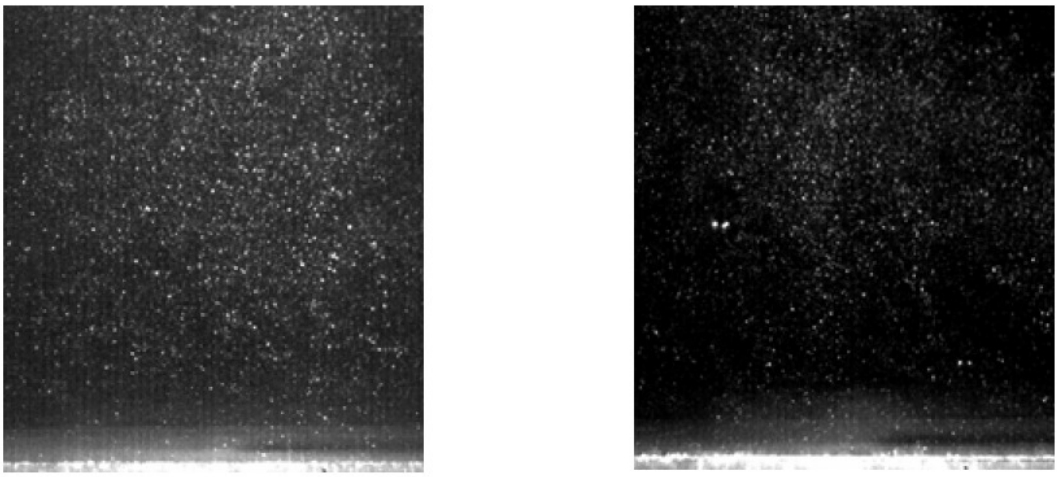

Figure 3: Sample PIV images

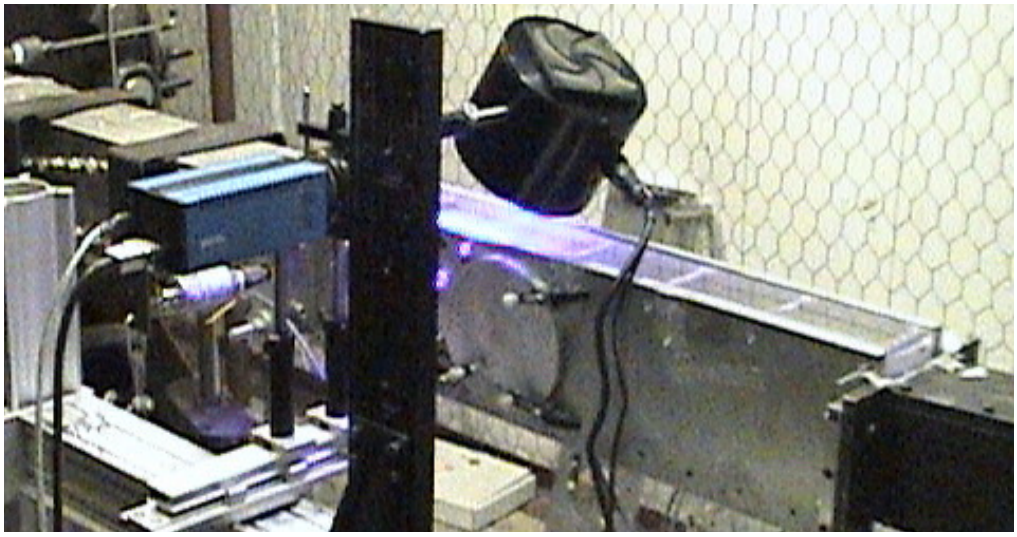

Figure 4 PSP Setup

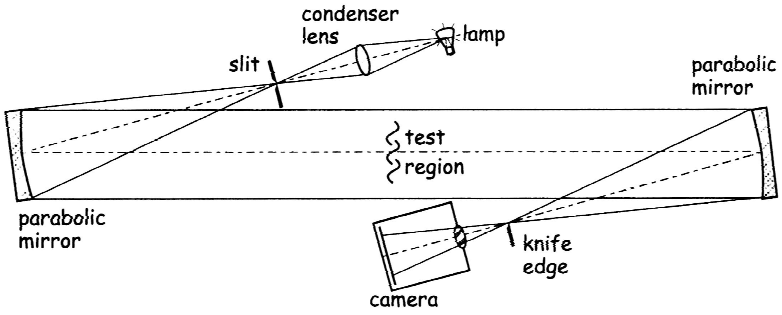

Figure 5: Schematic of a *Z*-type 2-mirror schlieren system[55]

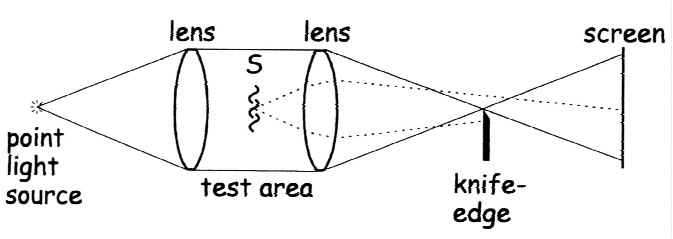

Figure 6: Schematic of the knife edge function in a schlieren system[55]

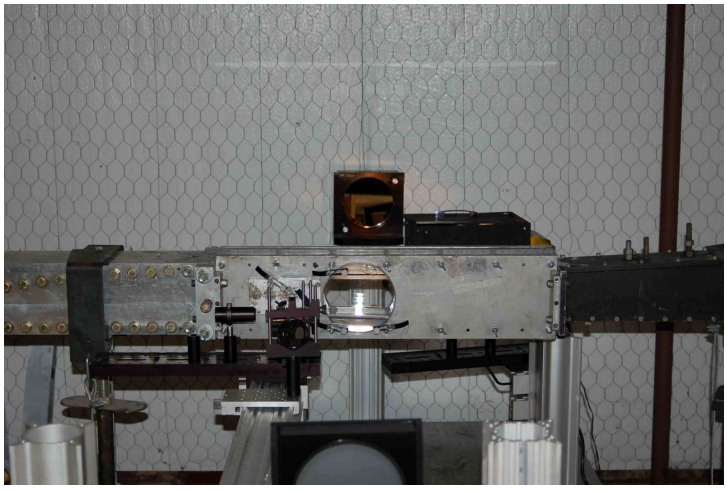

Figure 7: Schlieren Setup

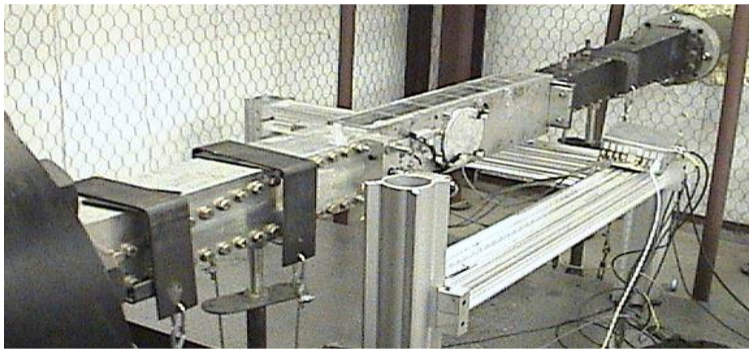

Figure 8: Mach 2.86 Supersonic Blow-Down Wind Tunnel

a) b)

Figure 9: a) Chicago Pneumatic compressor. b) Domnick Hunter air dryer

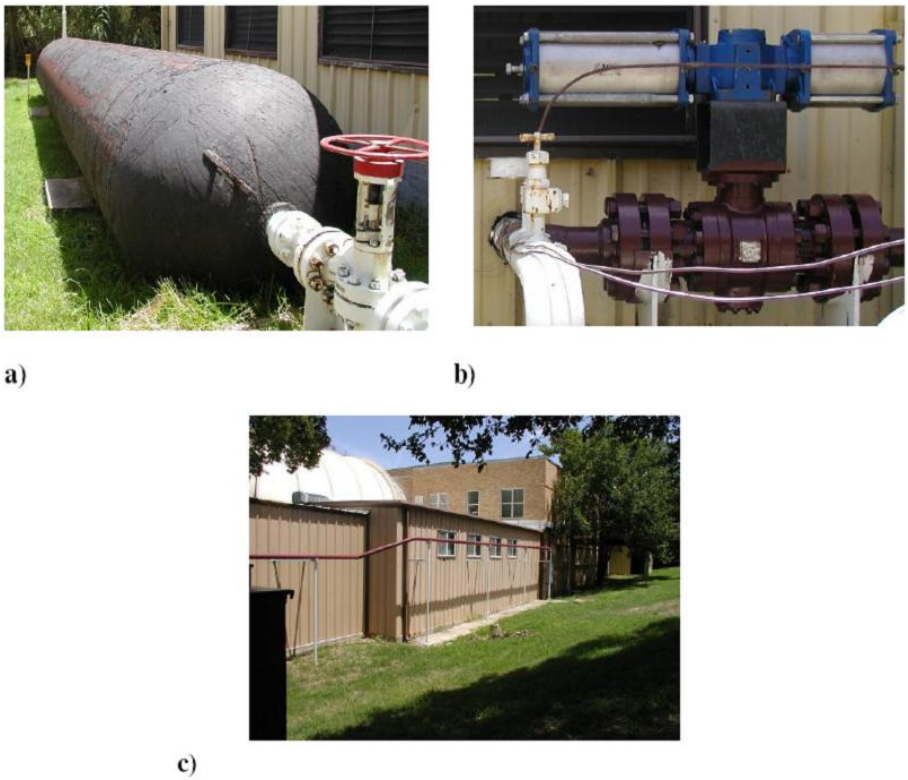

a) b) c)

Figure 10: a) Storage tank. b) Pneumatic actuator and ball valve. c) Supply line

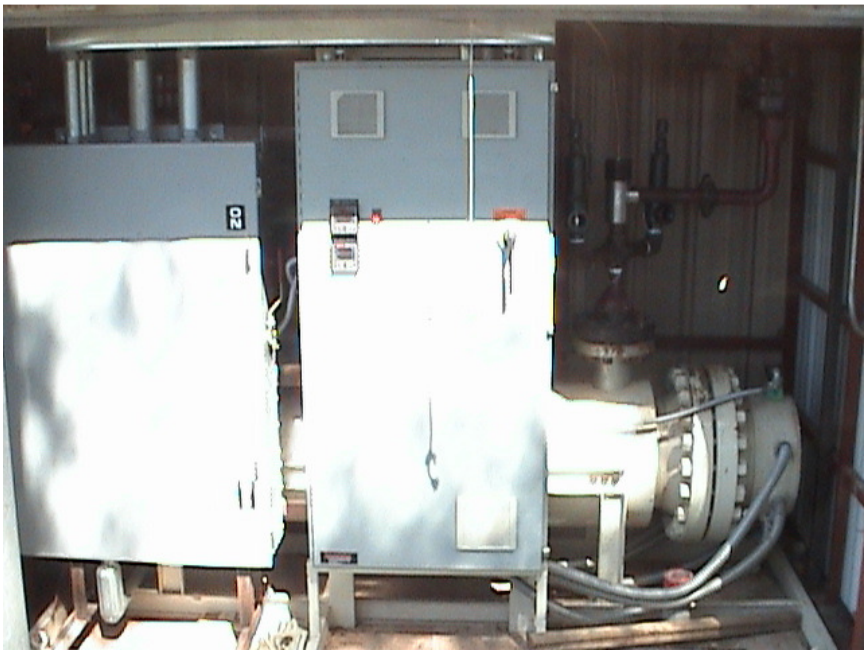

Figure 11: Chromalox 535 kW circulation heater

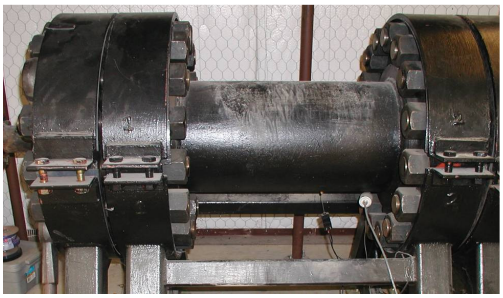

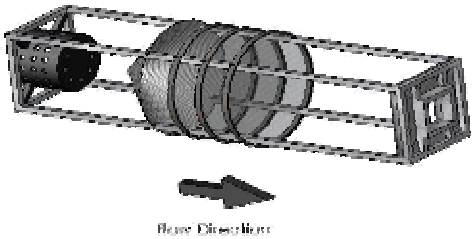

Figure 12: Settling chamber and schematic of flow straightener.

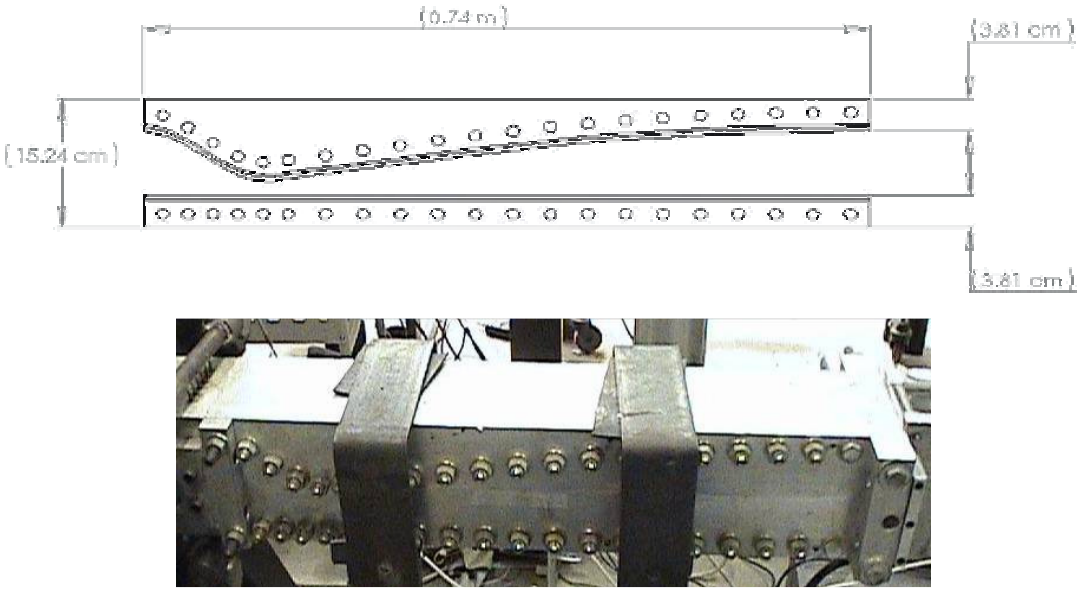

Figure 13: Mach 2.86 half-nozzle

Figure 14: Variable area diffuser and muffler

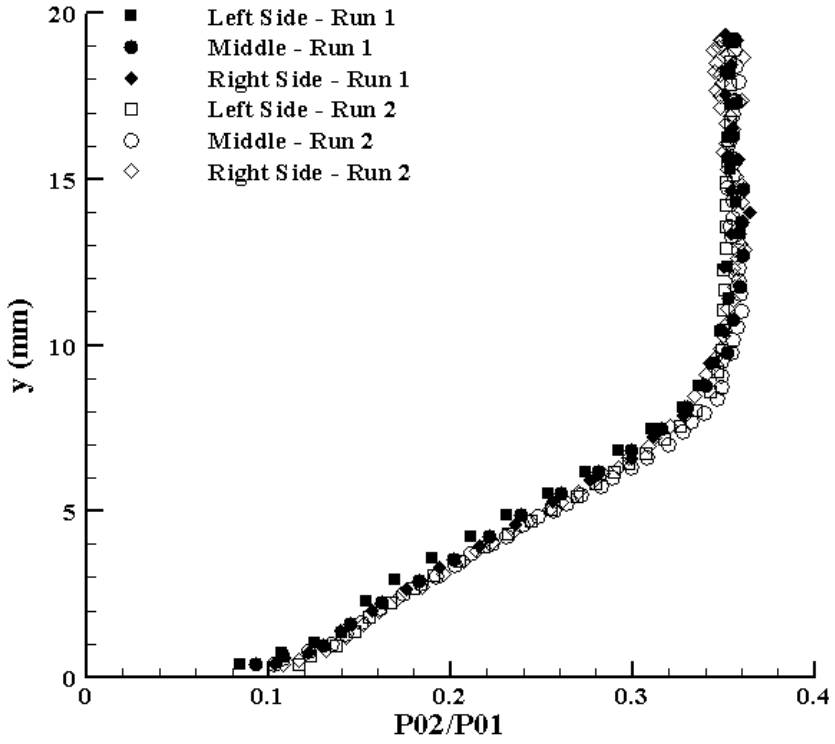

Figure 15 Pitot pressure profiles at the nozzle exit

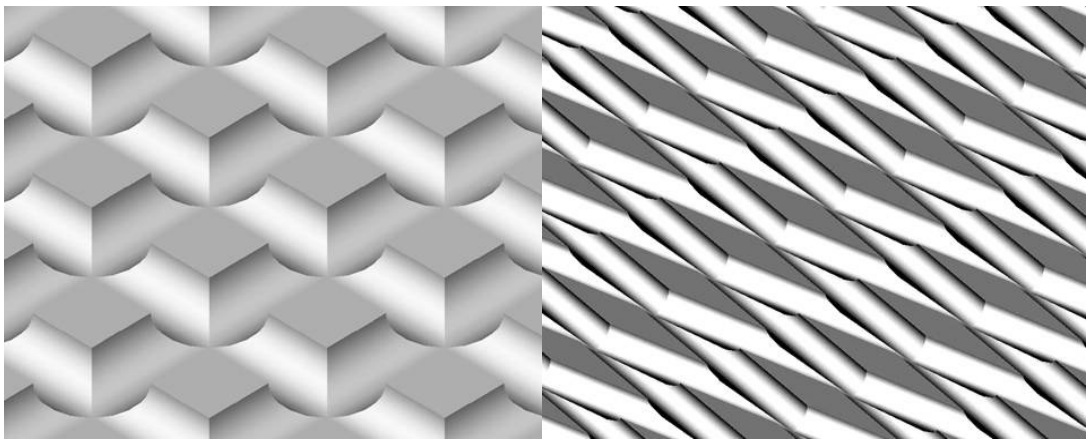

Figure 16: Periodic surface roughness pattern

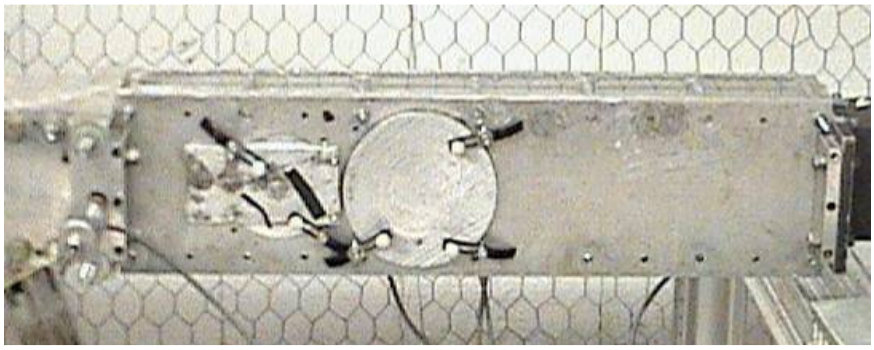

Figure 17: Mach 2.86 test section sidewall

Figure 18: Schematic of test section models

Figure 19: Tunnel models

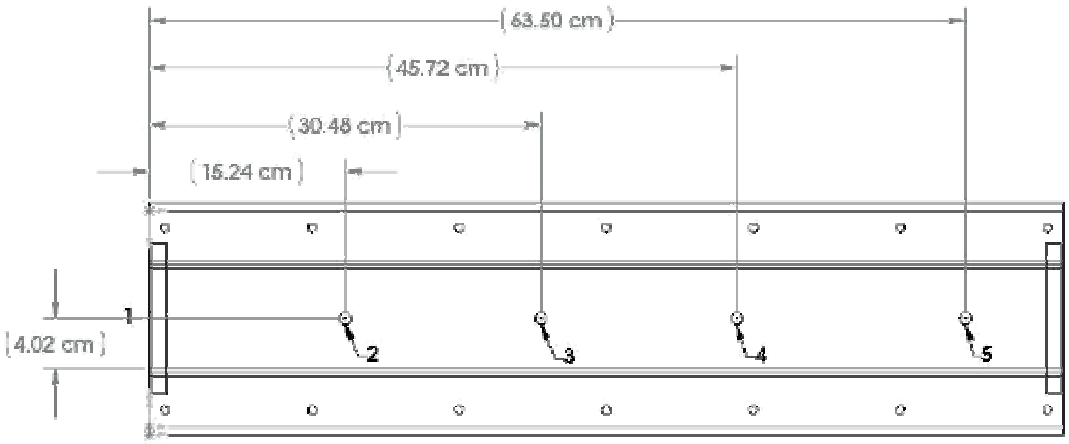

	1	2	3	4	5
Location	-1.27 cm	15.24 cm	30.48 cm	45.72 cm	63.50 cm

Figure 20: Static pressure port location

a)

b)

c)

Figure 21: Smooth wall schlieren images: a) ZPG, b) WPG, and c) SPG

a)

b)

c)

Figure 22: Square roughness schlieren images: a) ZPG, b) WPG, and c) SPG

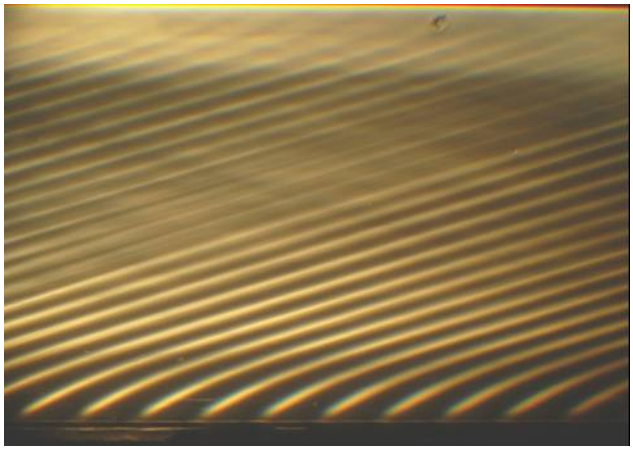

a)

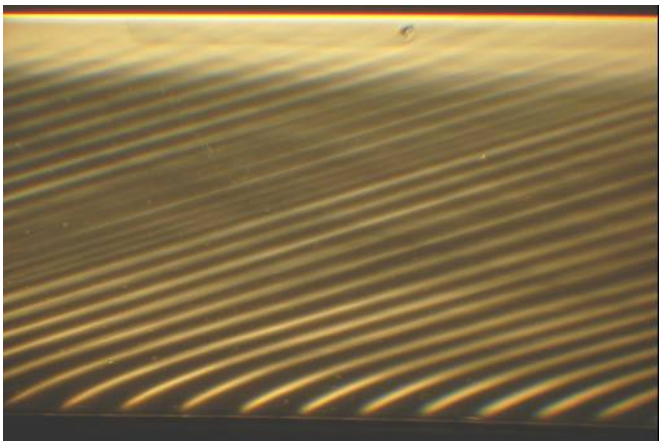

b)

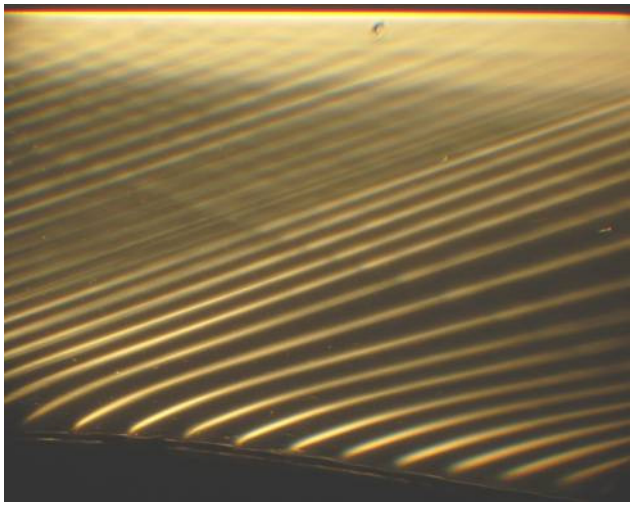

c)

Figure 23: Diamond roughness schlieren images: a) ZPG, b) WPG, and c) SPG

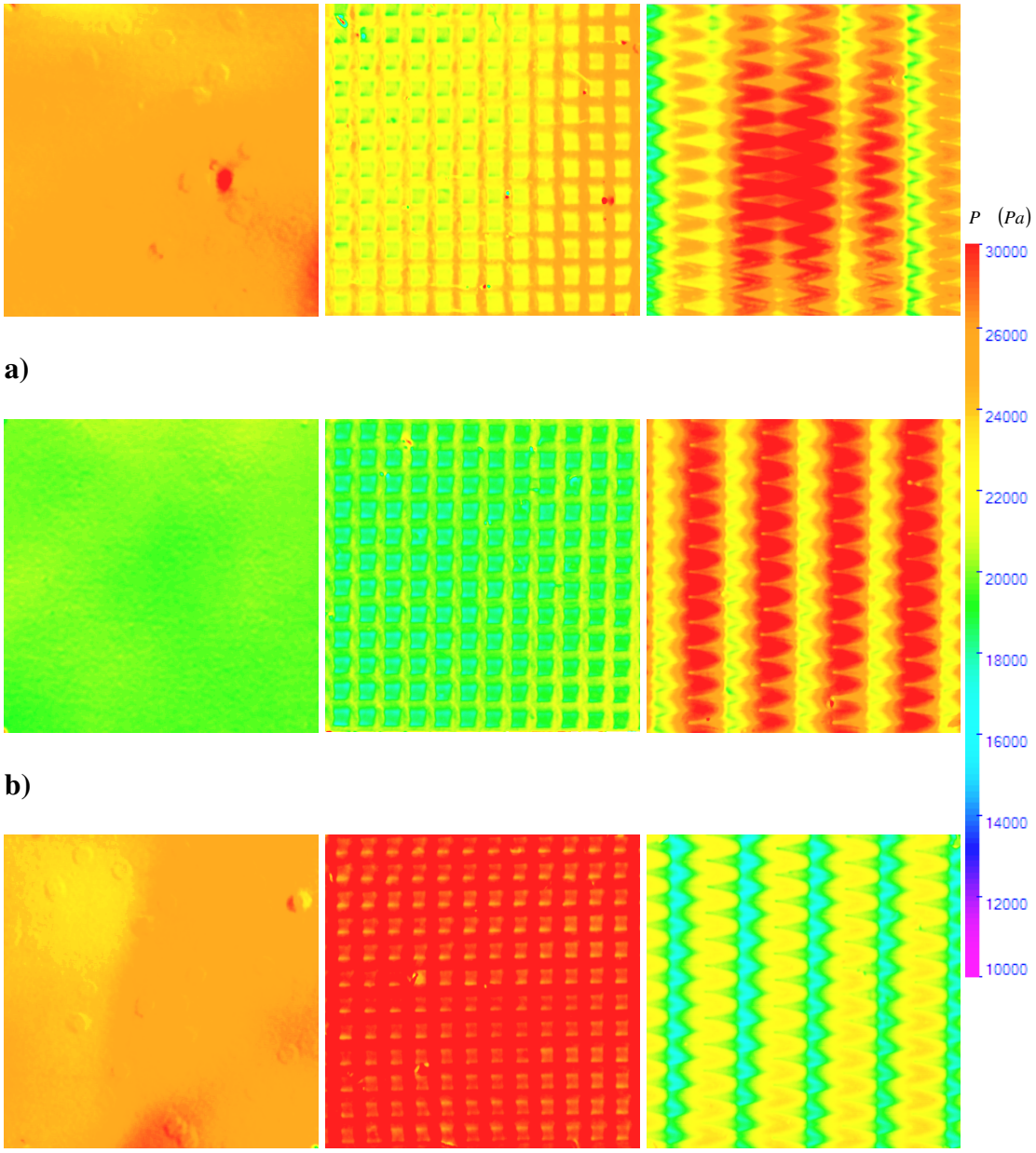

Figure 24: Surface pressure distributions for the ZPG models

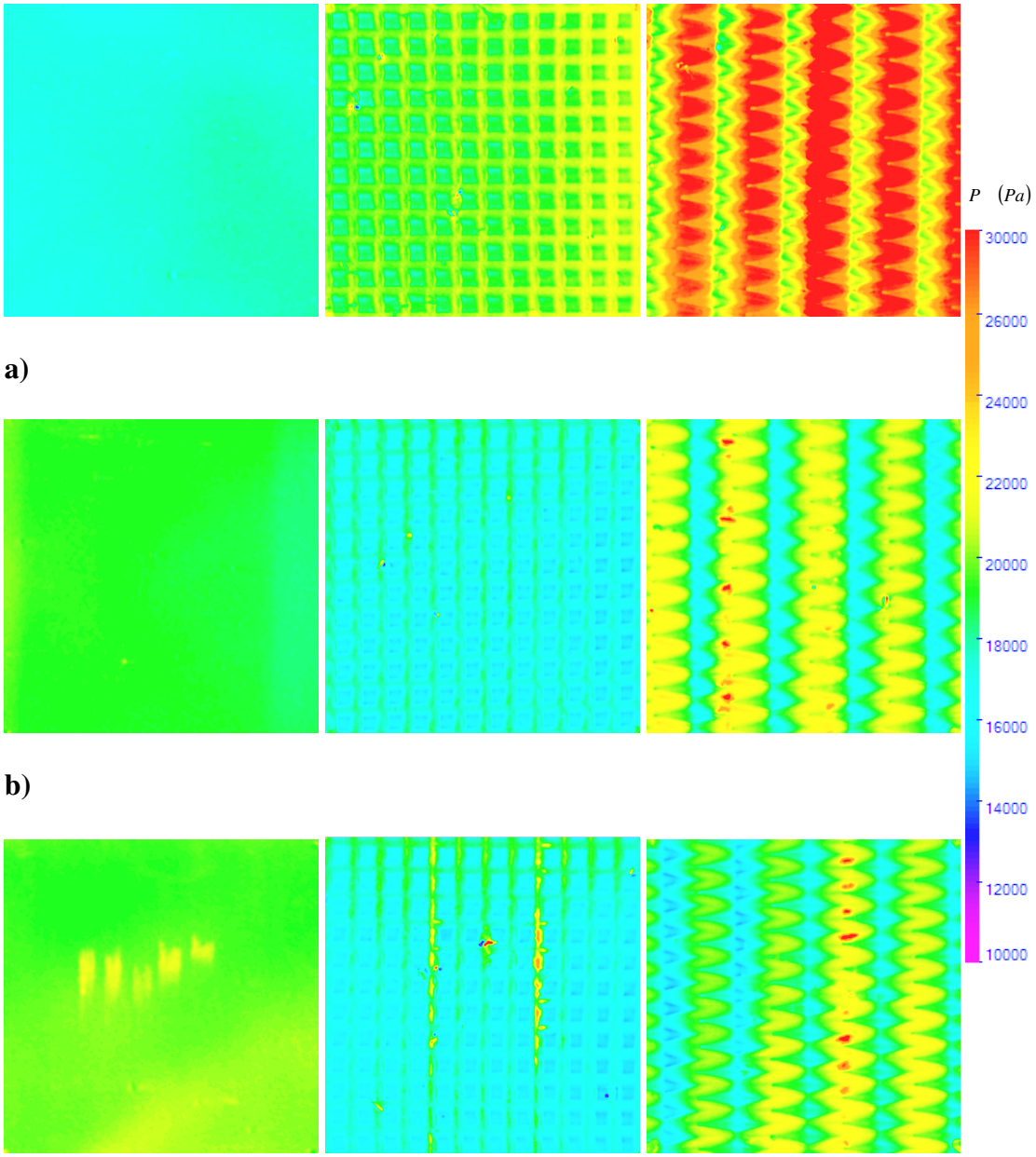

Figure 25: Surface pressure distributions for the WPG model

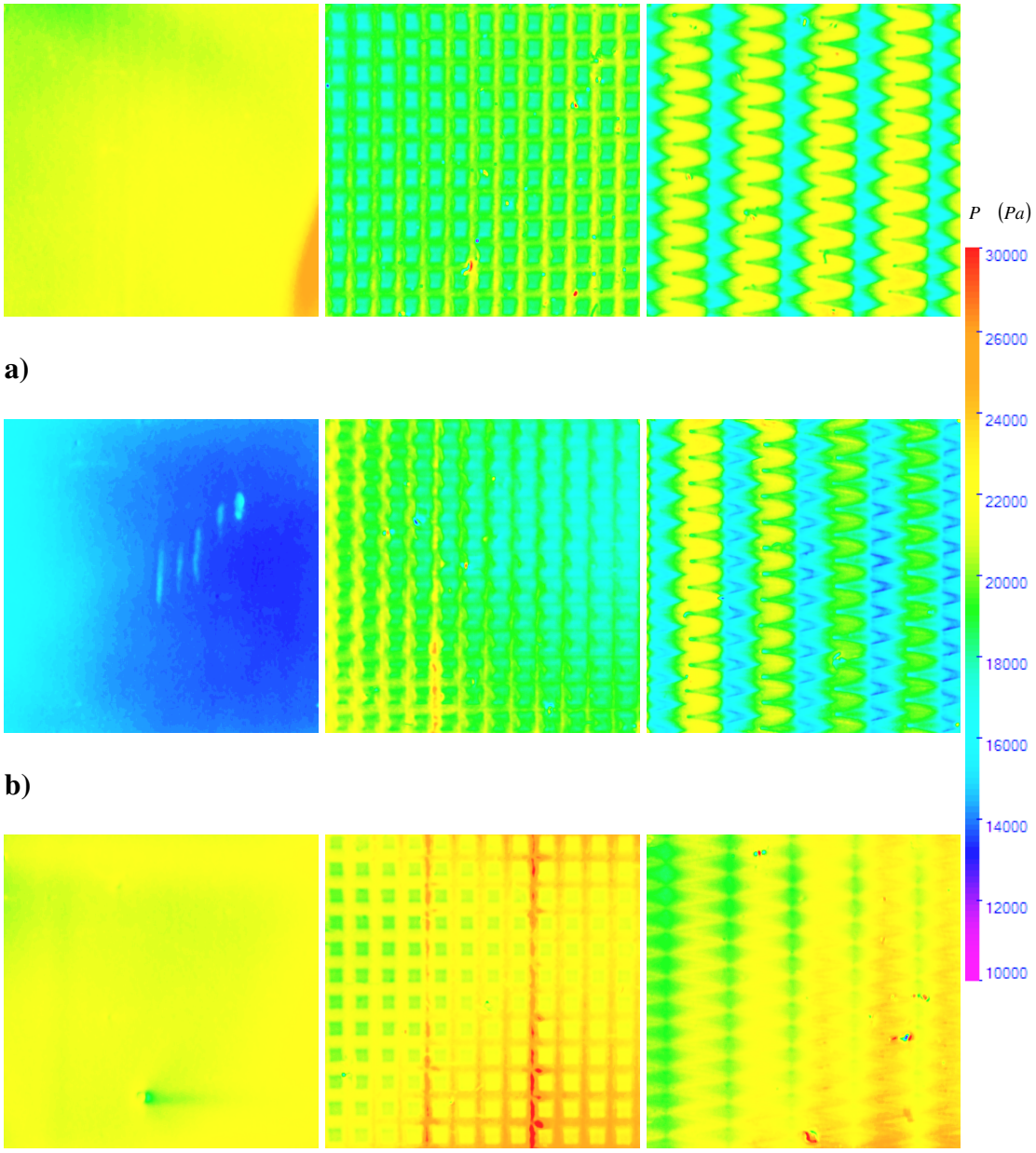

Figure 26: Surface pressure distributions for the SPG models

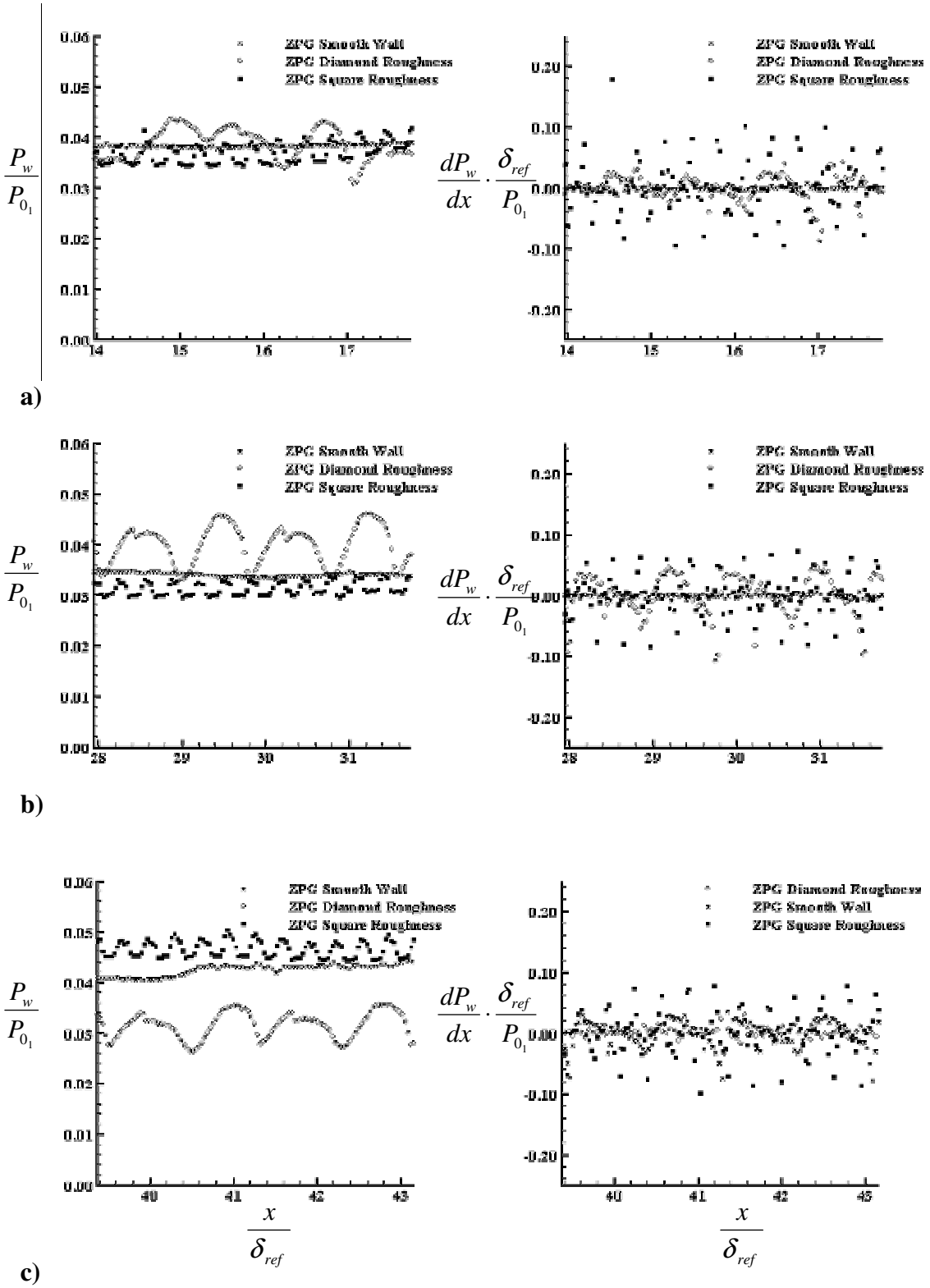

Figure 27: Streamwise pressure and pressure gradient profiles for the ZPG models

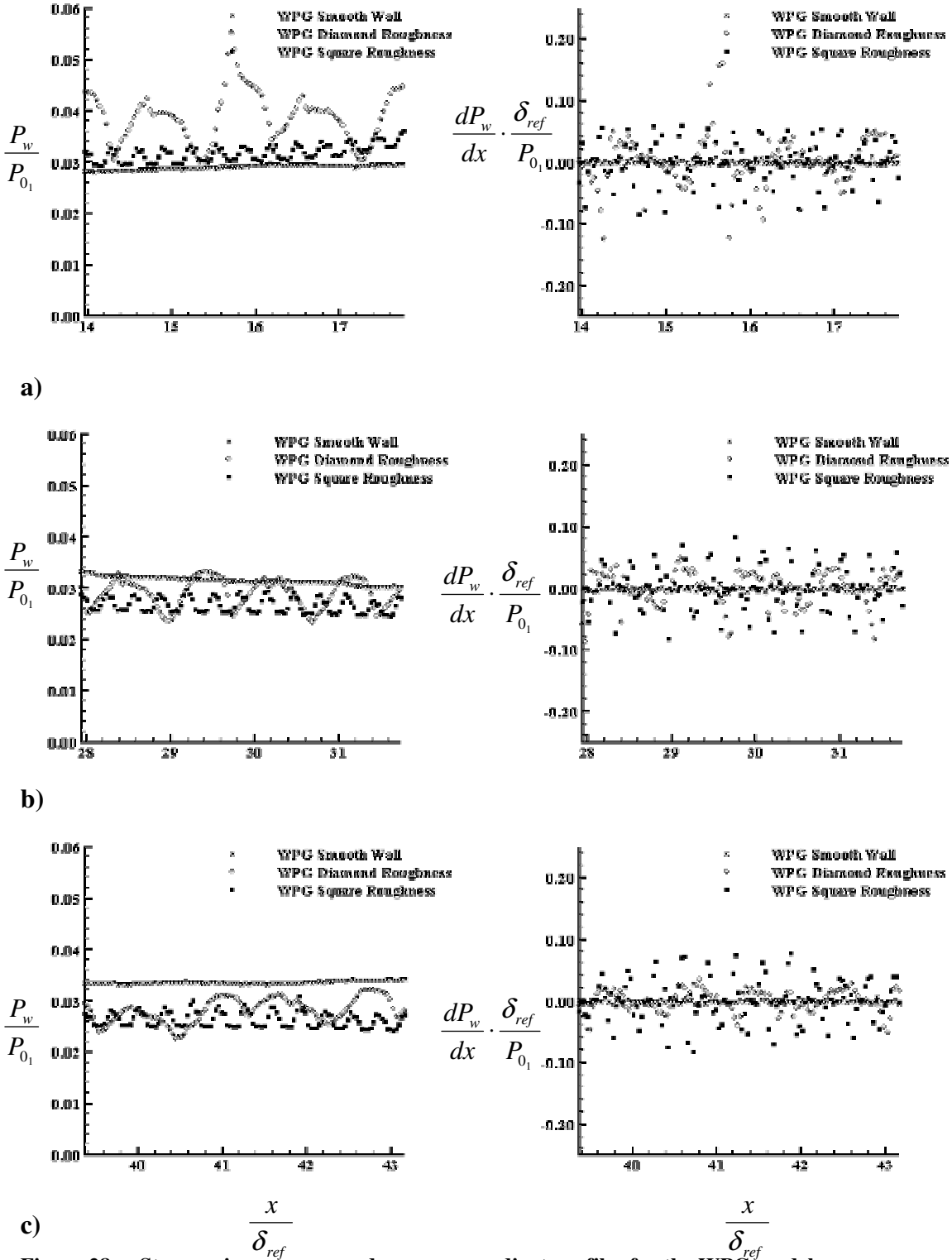

Figure 28: Streamwise pressure and pressure gradient profiles for the WPG models

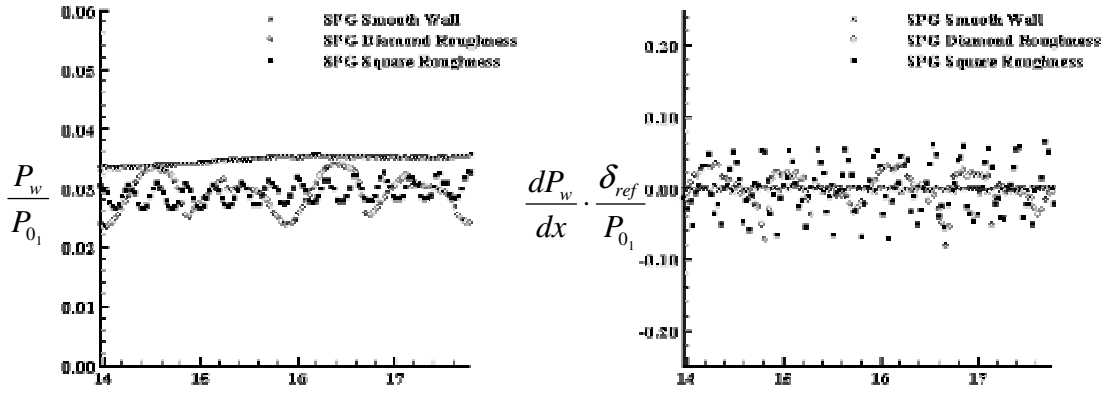

a)

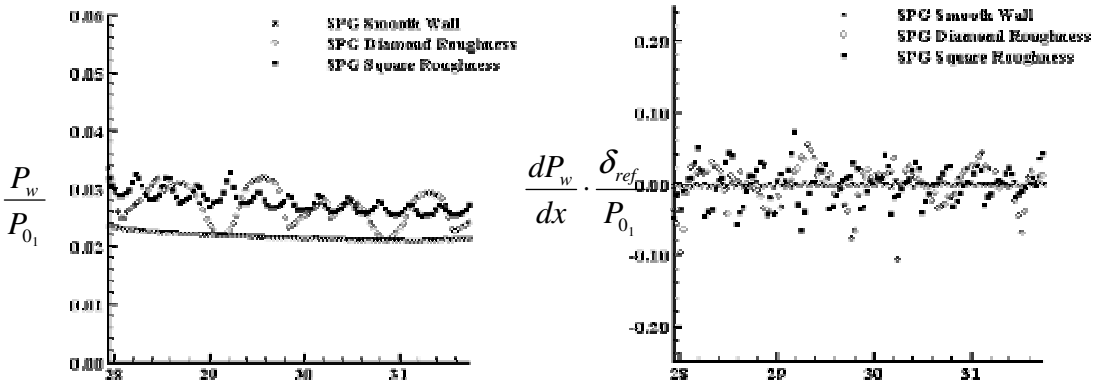

b)

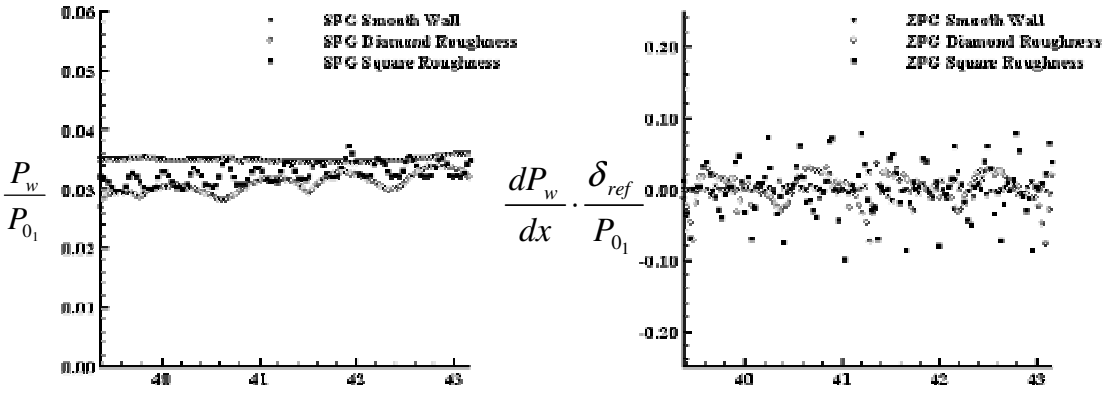

c)

Figure 29: Streamwise pressure and pressure gradient profiles for the SPG models

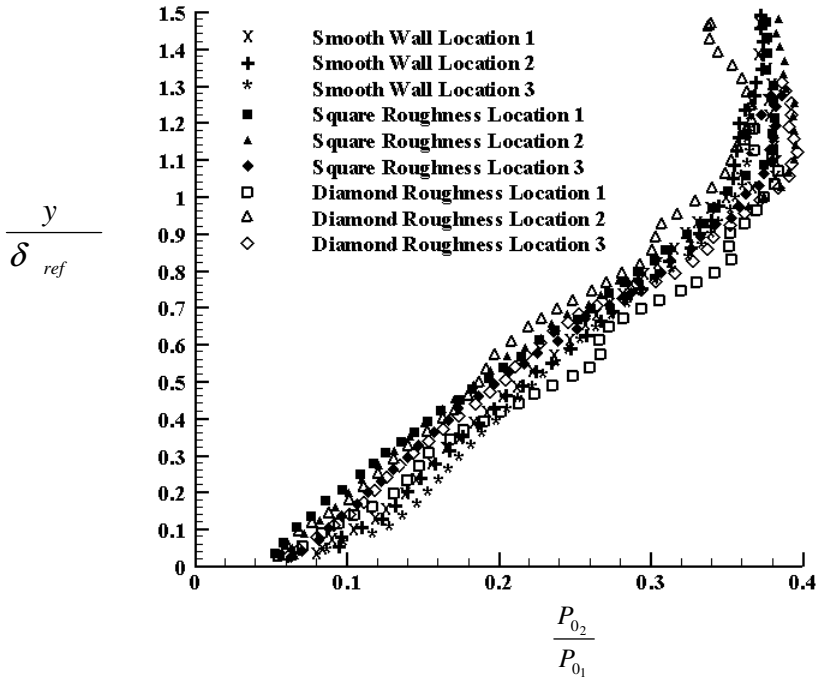

Figure 30: Stagnation pressure profiles for the ZPG models

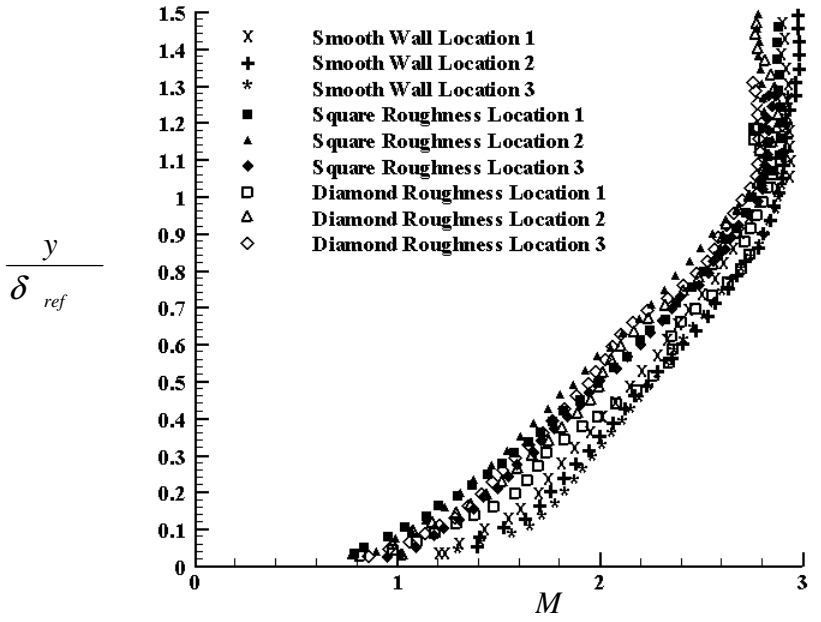

Figure 31: Mach number profiles for the ZPG models

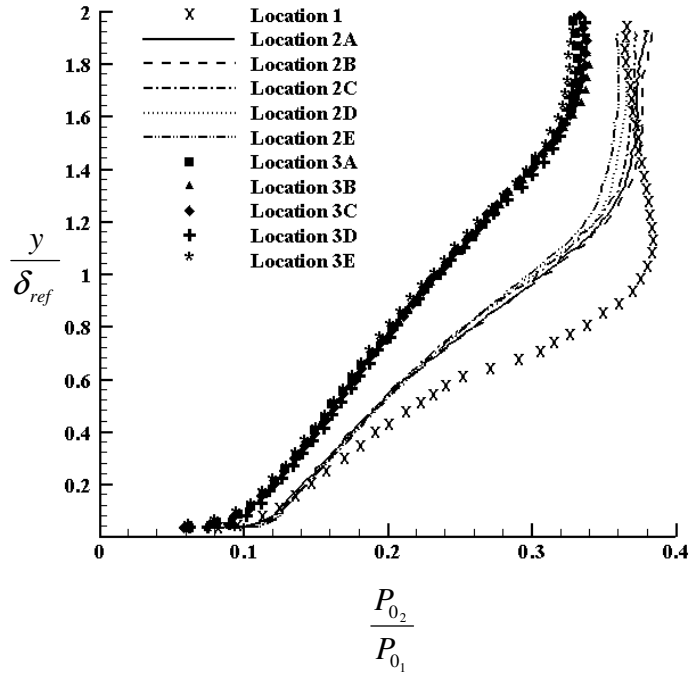

Figure 32: Stagnation pressure profiles of the smooth wall WPG model

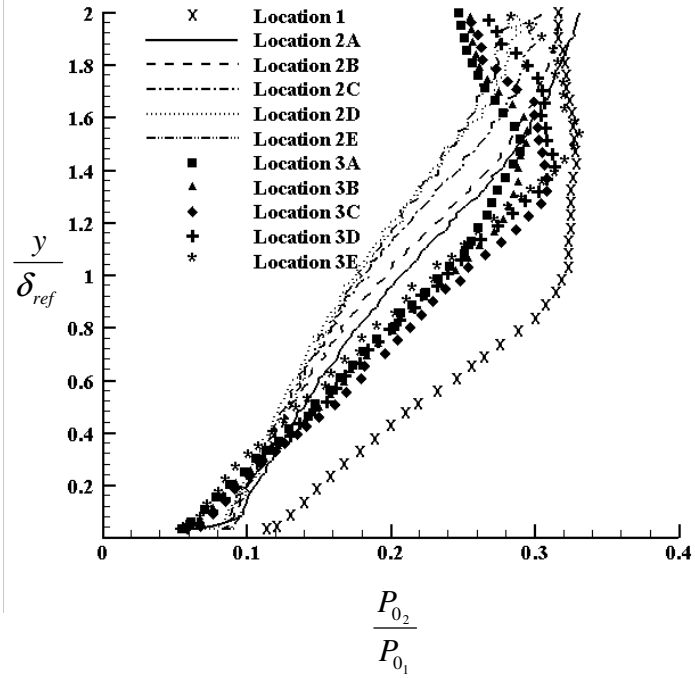

Figure 33: Stagnation pressure profiles of the smooth wall SPG model

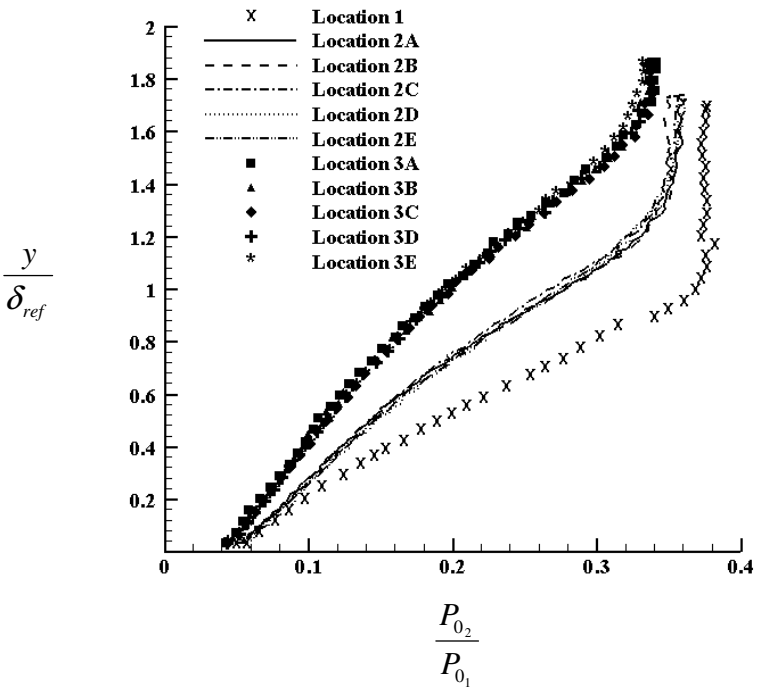

Figure 34: Stagnation pressure profiles of the square roughness WPG model

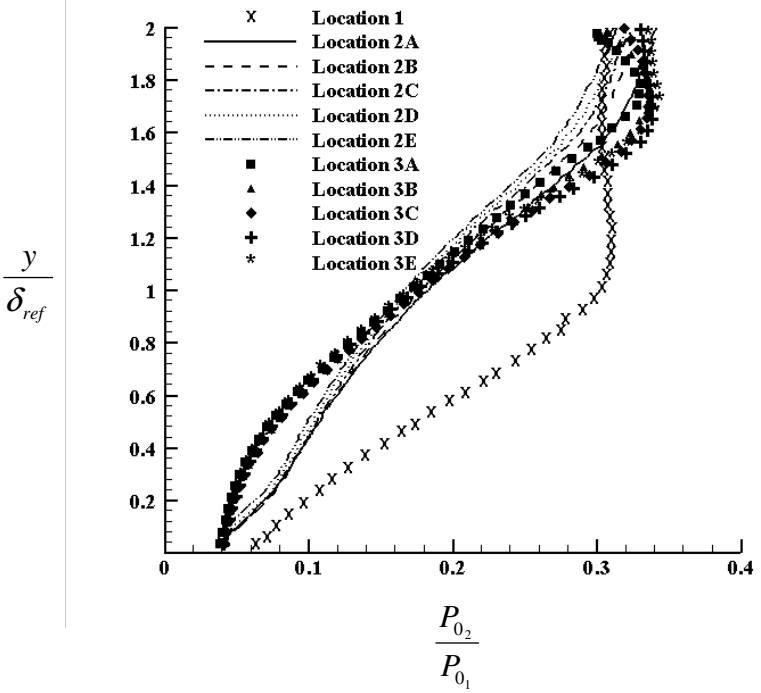

Figure 35: Stagnation pressure profiles of the square roughness SPG model

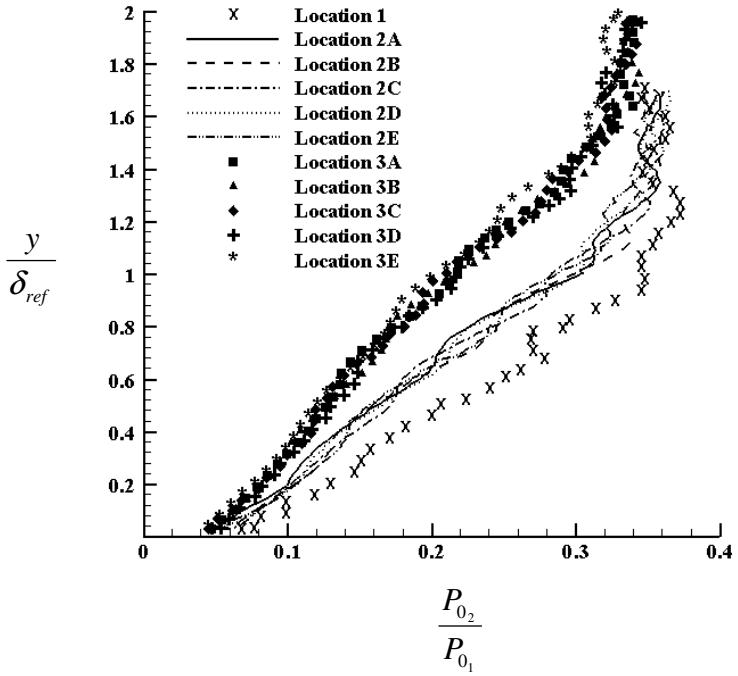

Figure 36: Stagnation pressure profiles of the diamond roughness WPG model

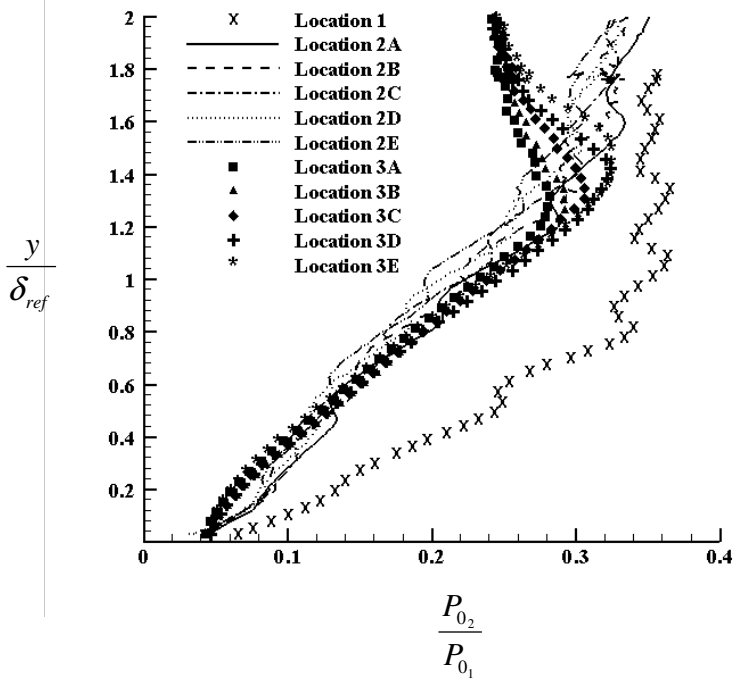

Figure 37: Stagnation pressure profiles of the diamond roughness SPG model

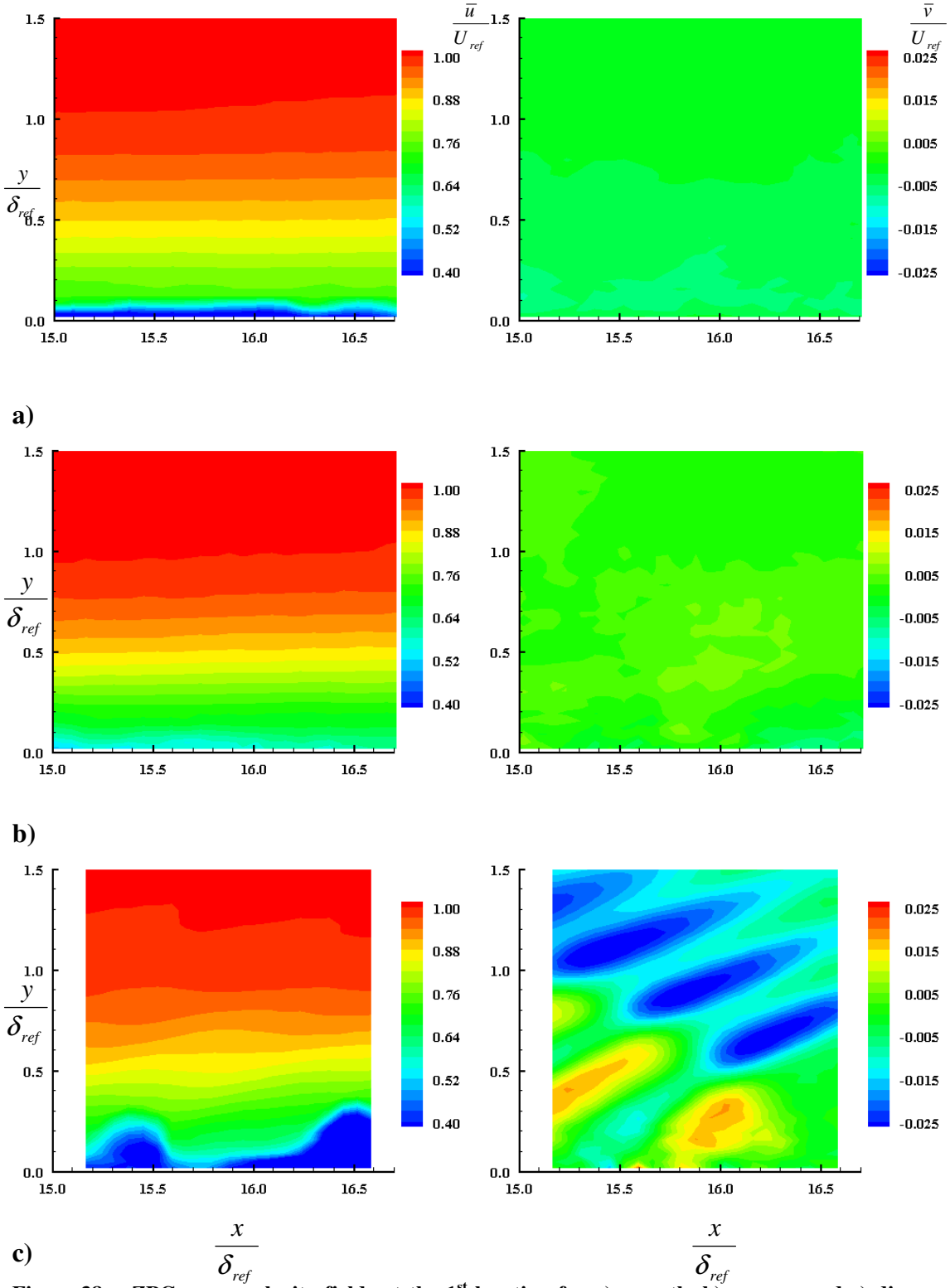

Figure 38: ZPG mean velocity fields at the 1st location for a) smooth, b) square, and c) diamond roughness

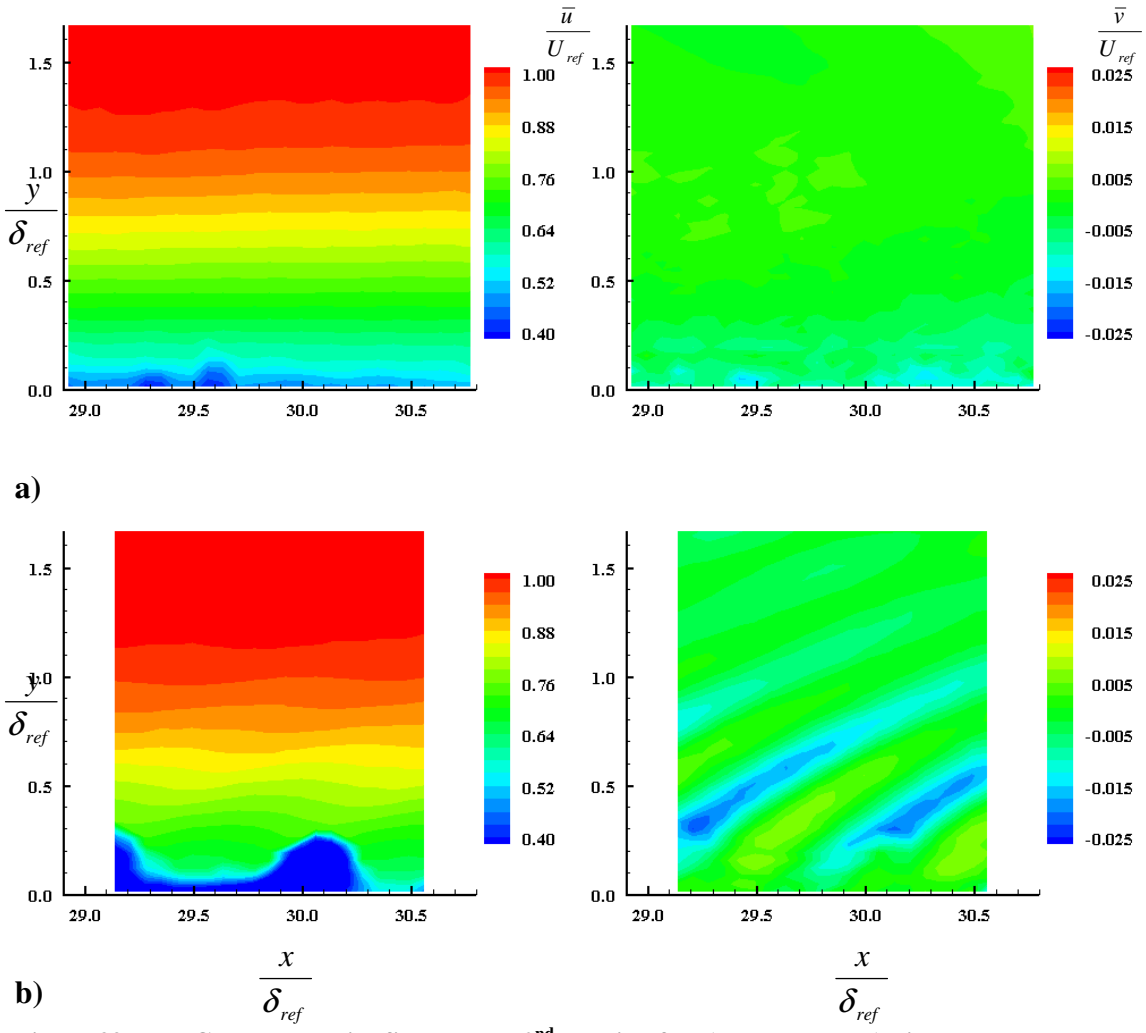

Figure 39: ZPG mean velocity fields at the 2nd location for a) square and b) diamond roughness

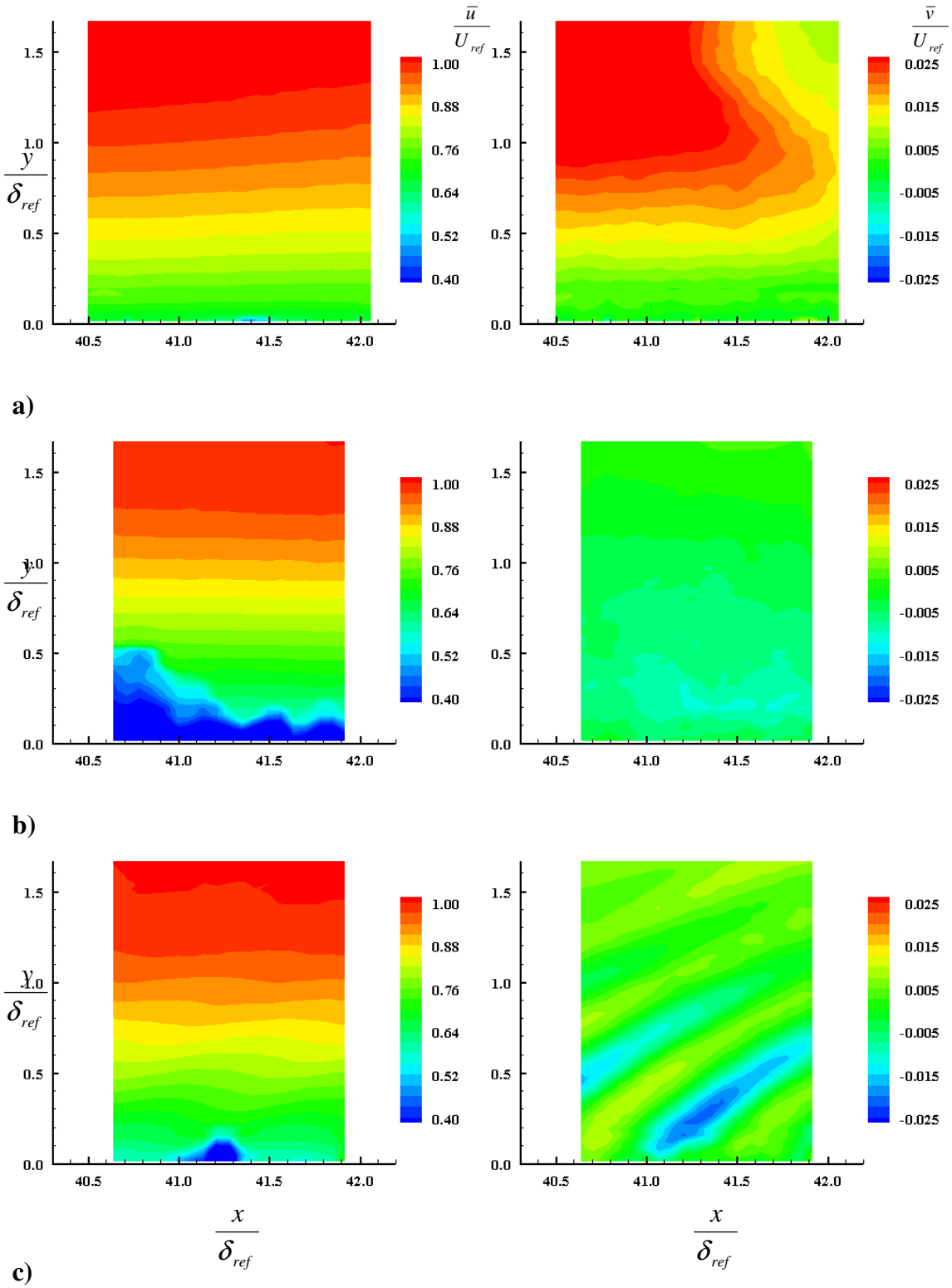

Figure 40: ZPG mean velocity fields at the 3rd location for a) smooth, b) square, and c) diamond roughness

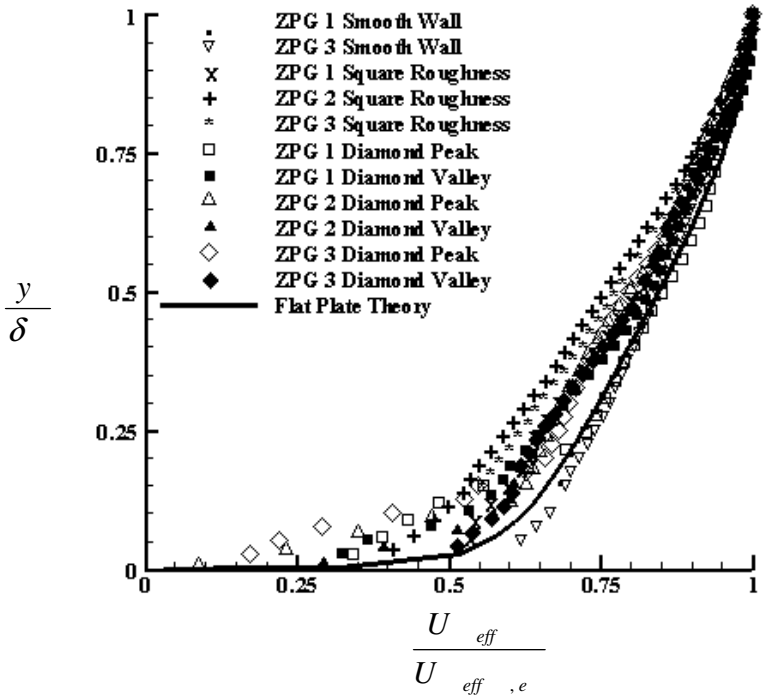

Figure 41: Zero pressure gradient velocity profiles from PIV data

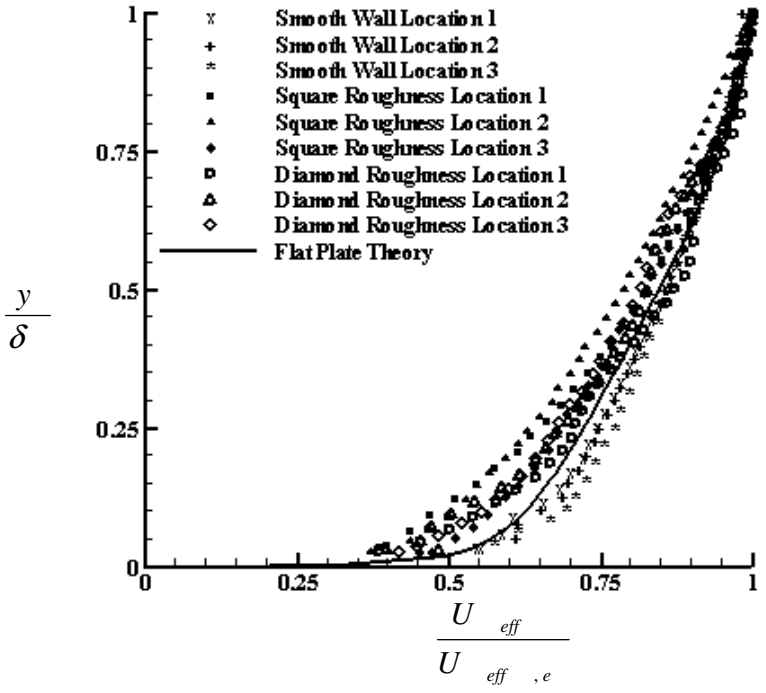

Figure 42: Zero pressure gradient velocity profiles from Pitot data

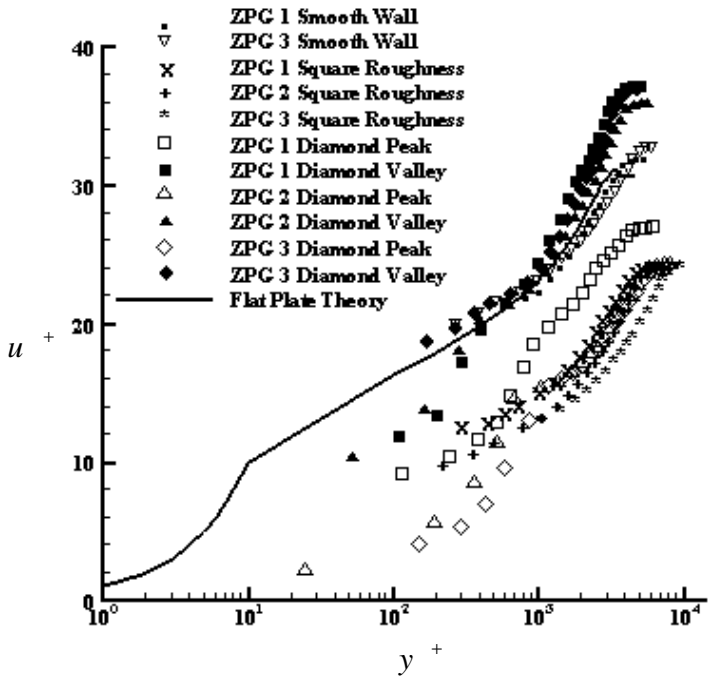

Figure 43: Law of the wall plot for the ZPG models from PIV data

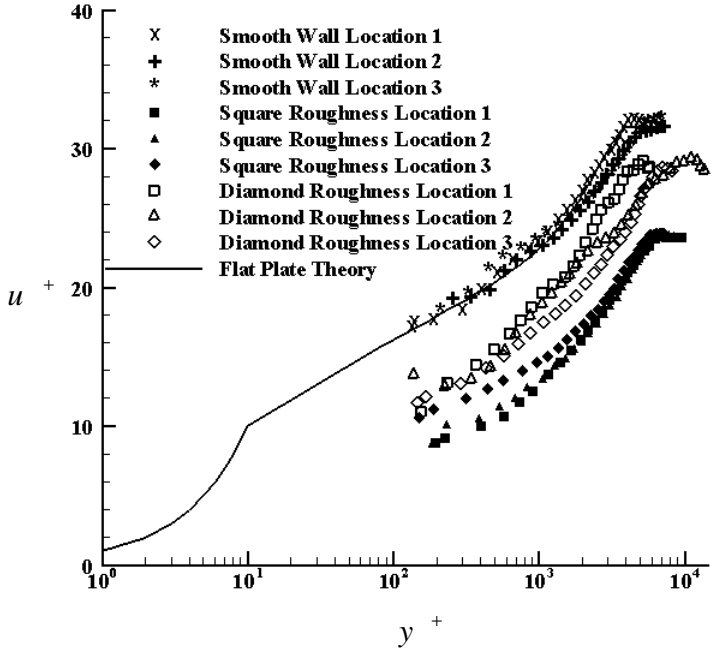

Figure 44: Law of the wall plot for the ZPG models using Pitot measurements

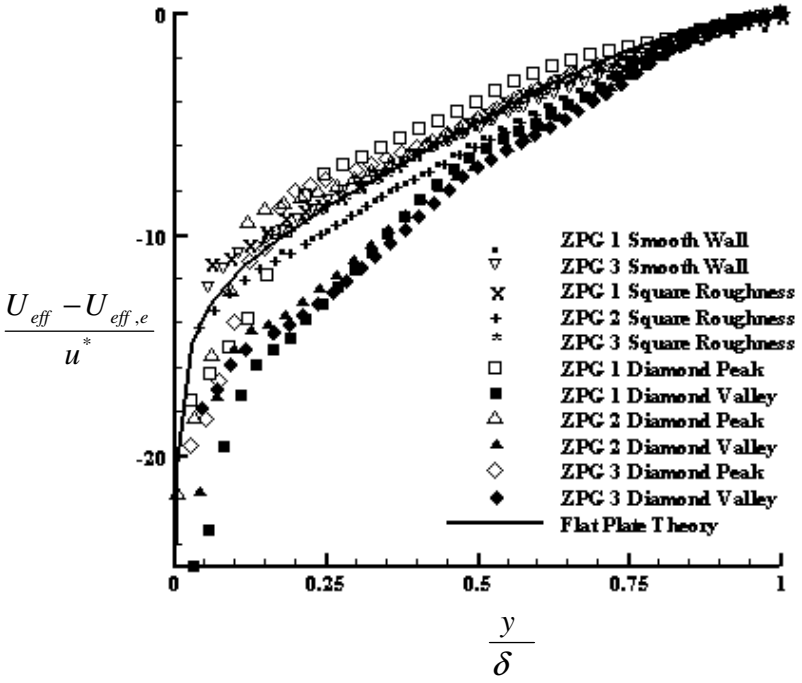

Figure 45: Defect law plot for the ZPG models from PIV data

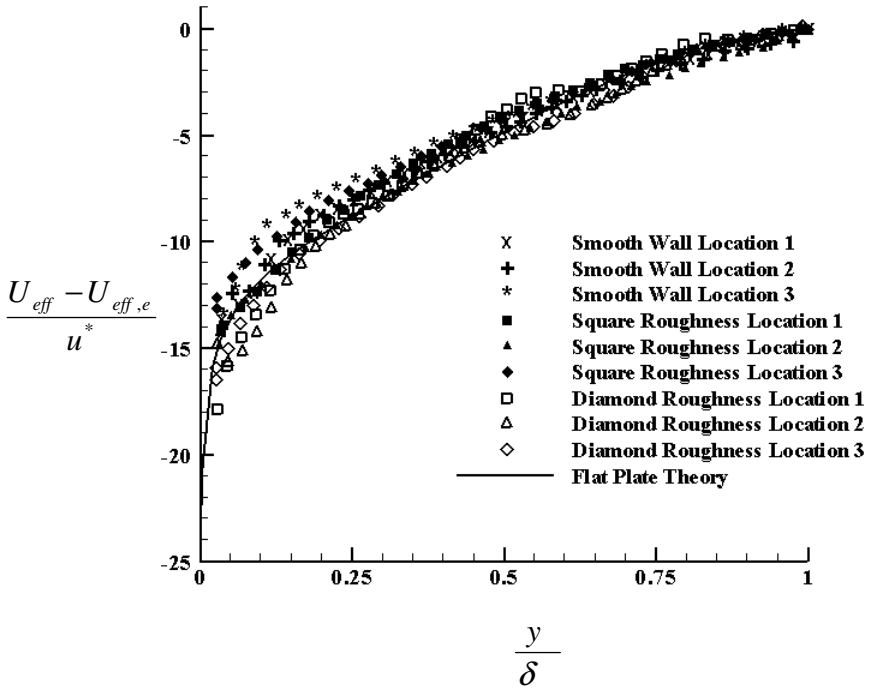

Figure 46: Defect law plot for the ZPG models using Pitot measurements

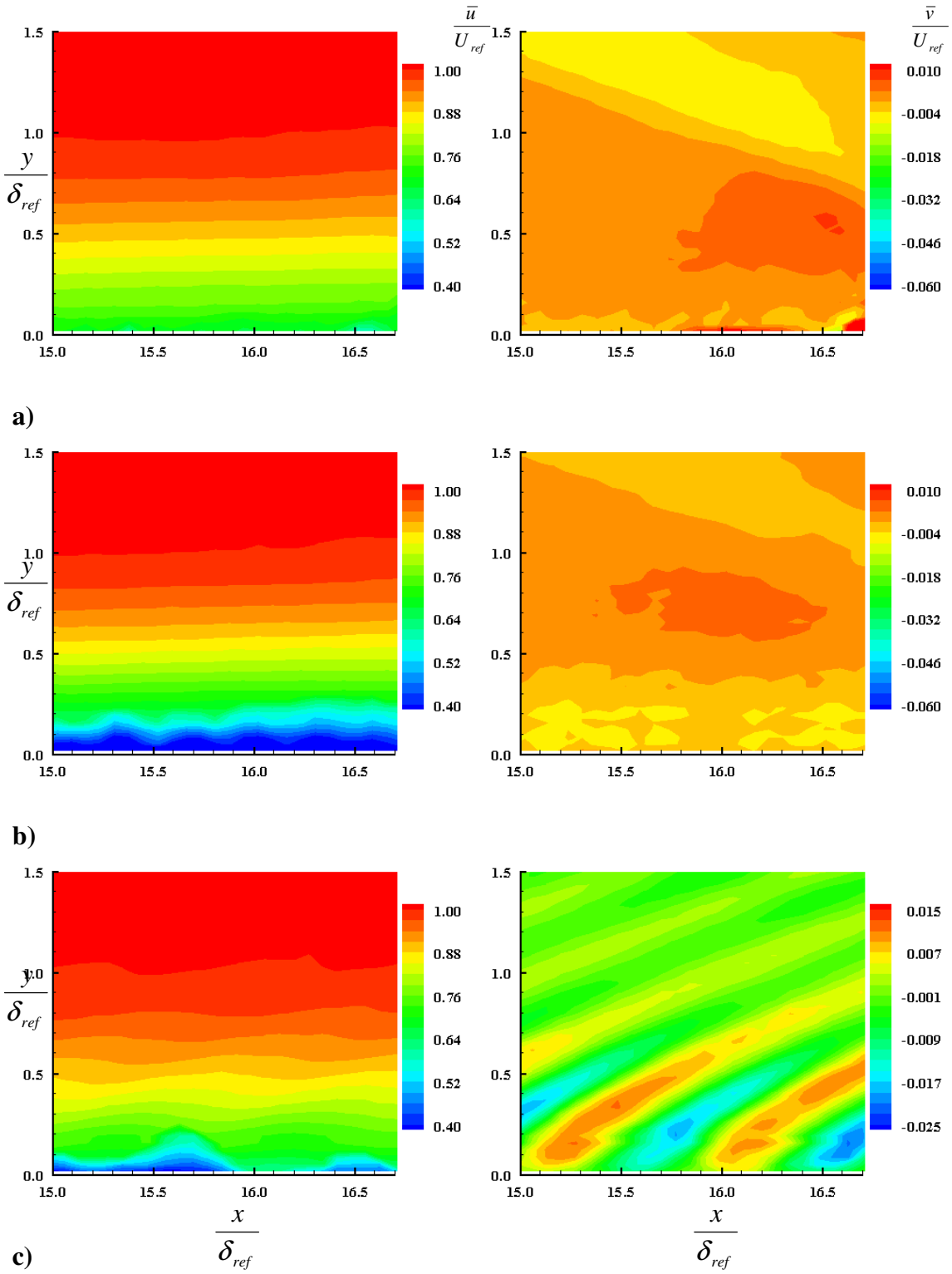

Figure 47: WPG mean velocity fields at the 1st location for a) smooth, b) square, and c) diamond roughness

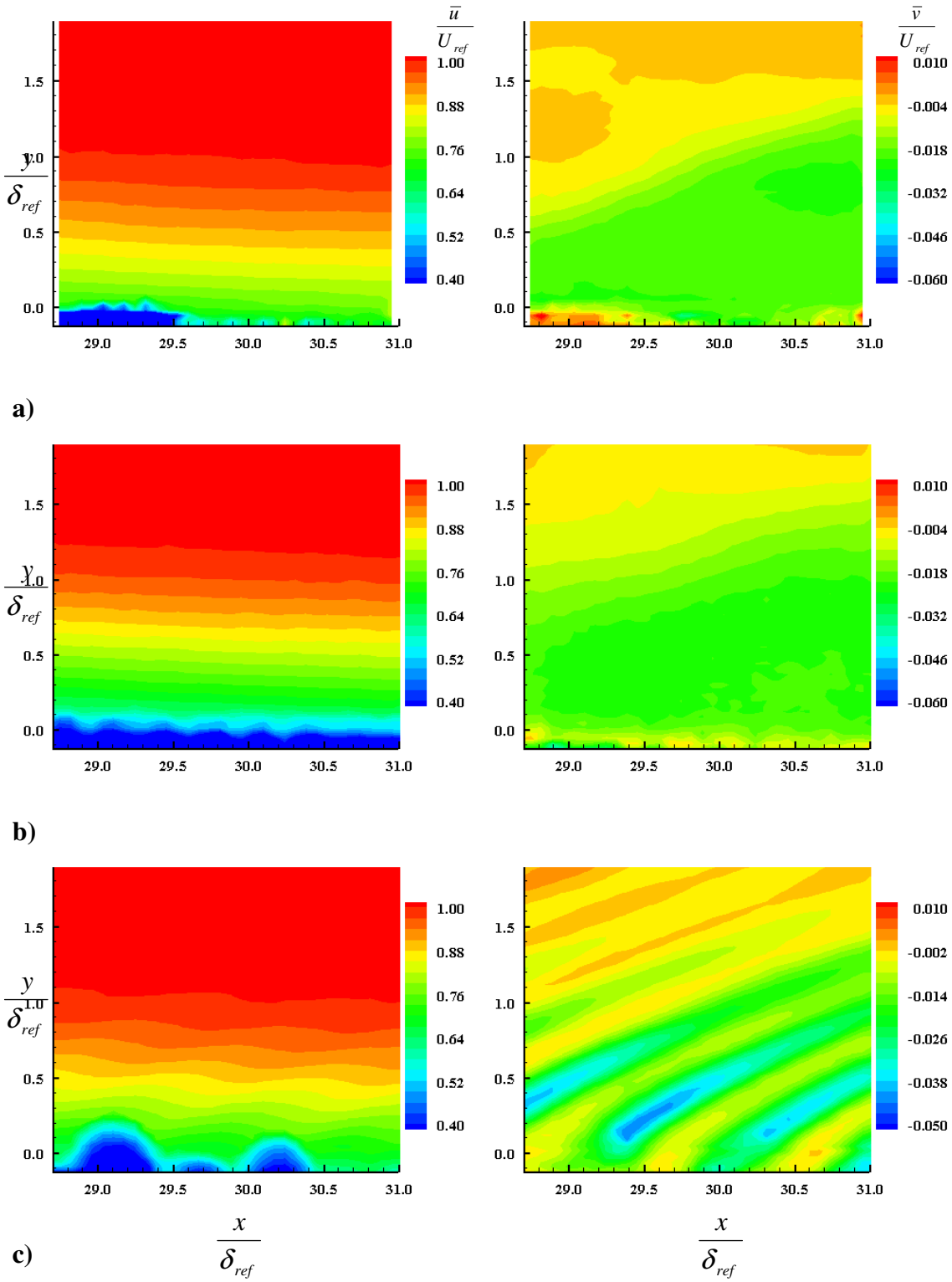

Figure 48: WPG mean velocity fields at the 2nd location for a) smooth, b) square, and c) diamond roughness

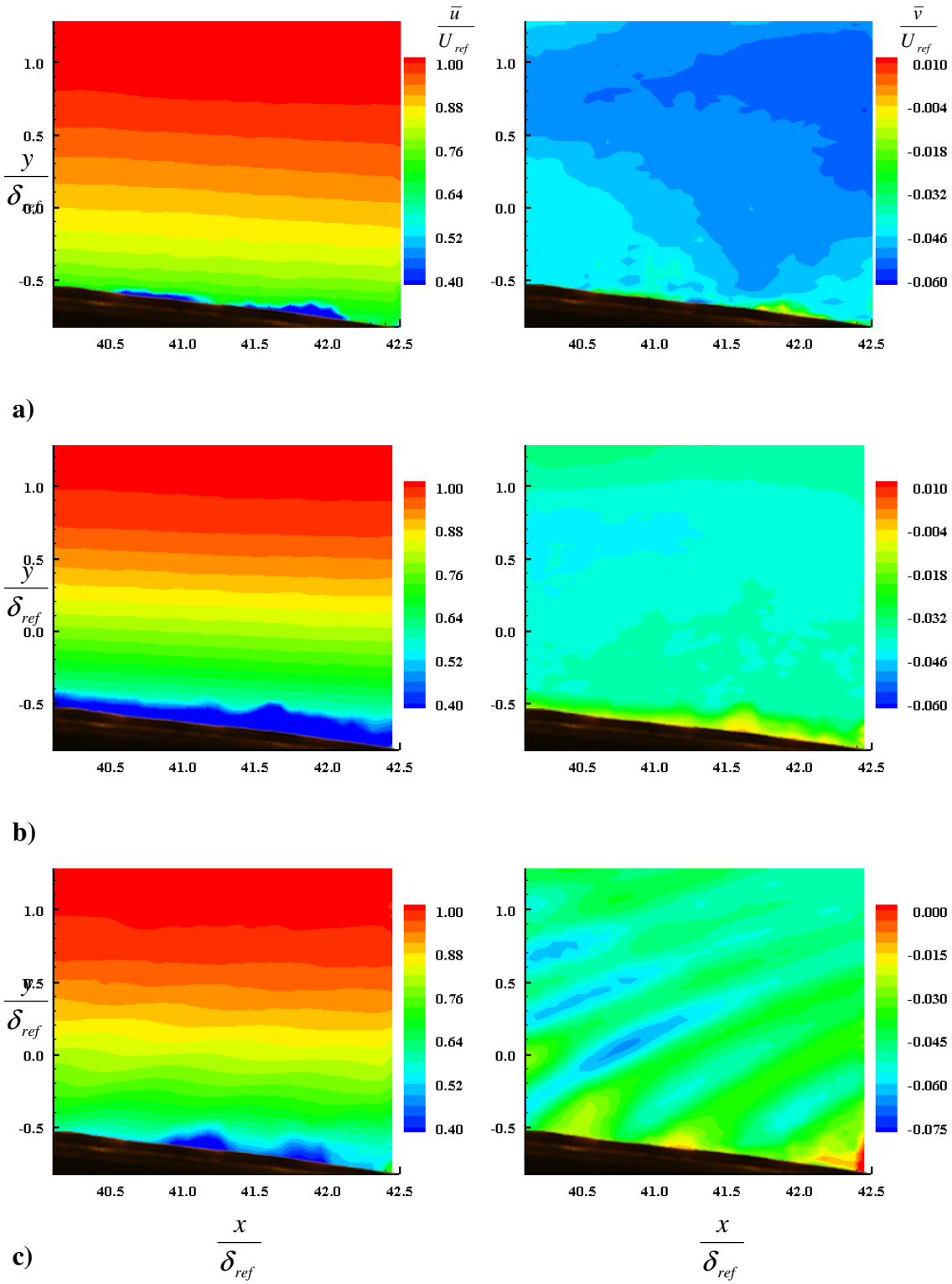

Figure 49: WPG mean velocity fields at the 3rd test location for a) smooth, b) square, and c) diamond roughness

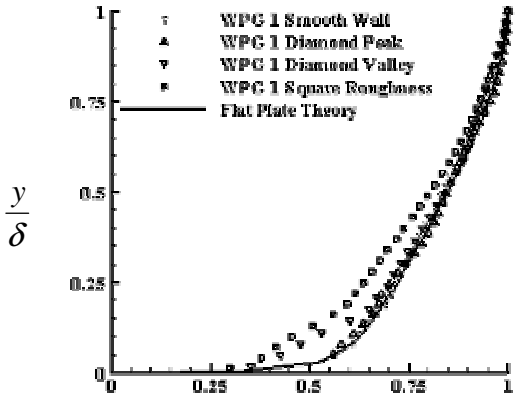

a)

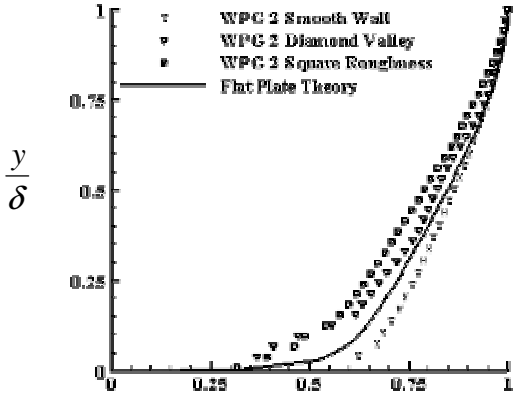

b)

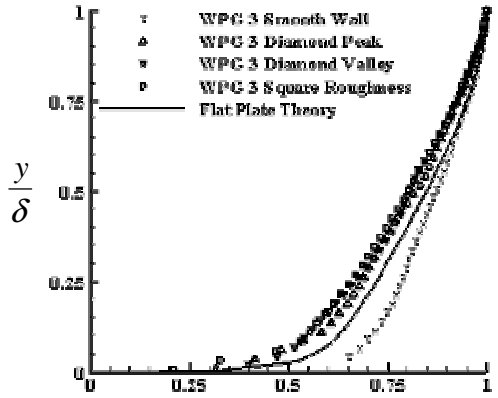

c)

Figure 50: Weak pressure gradient velocity profiles

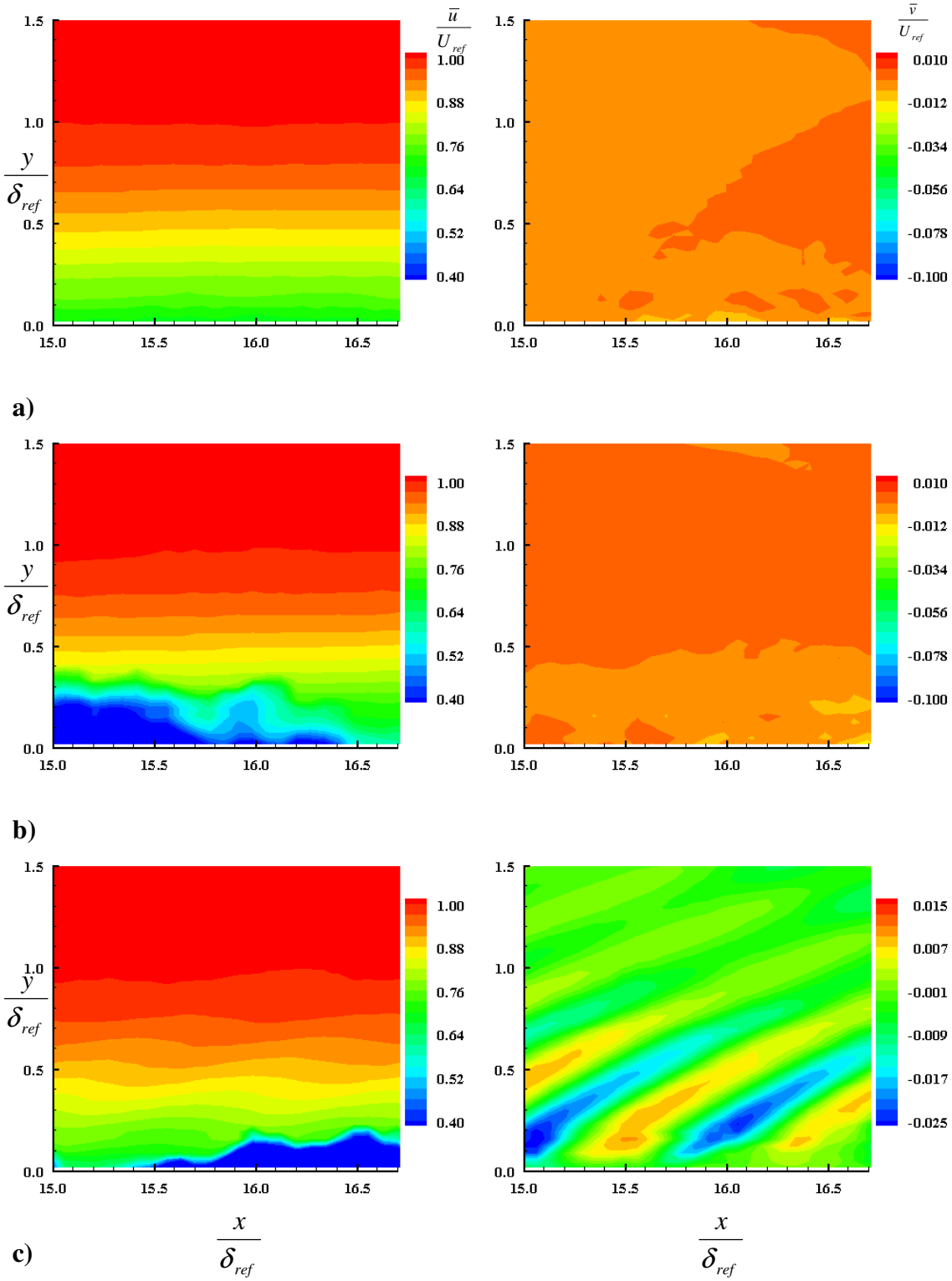

Figure 51: SPG mean velocity fields at the 1st test location for a) smooth, b) square, and c) diamond roughness

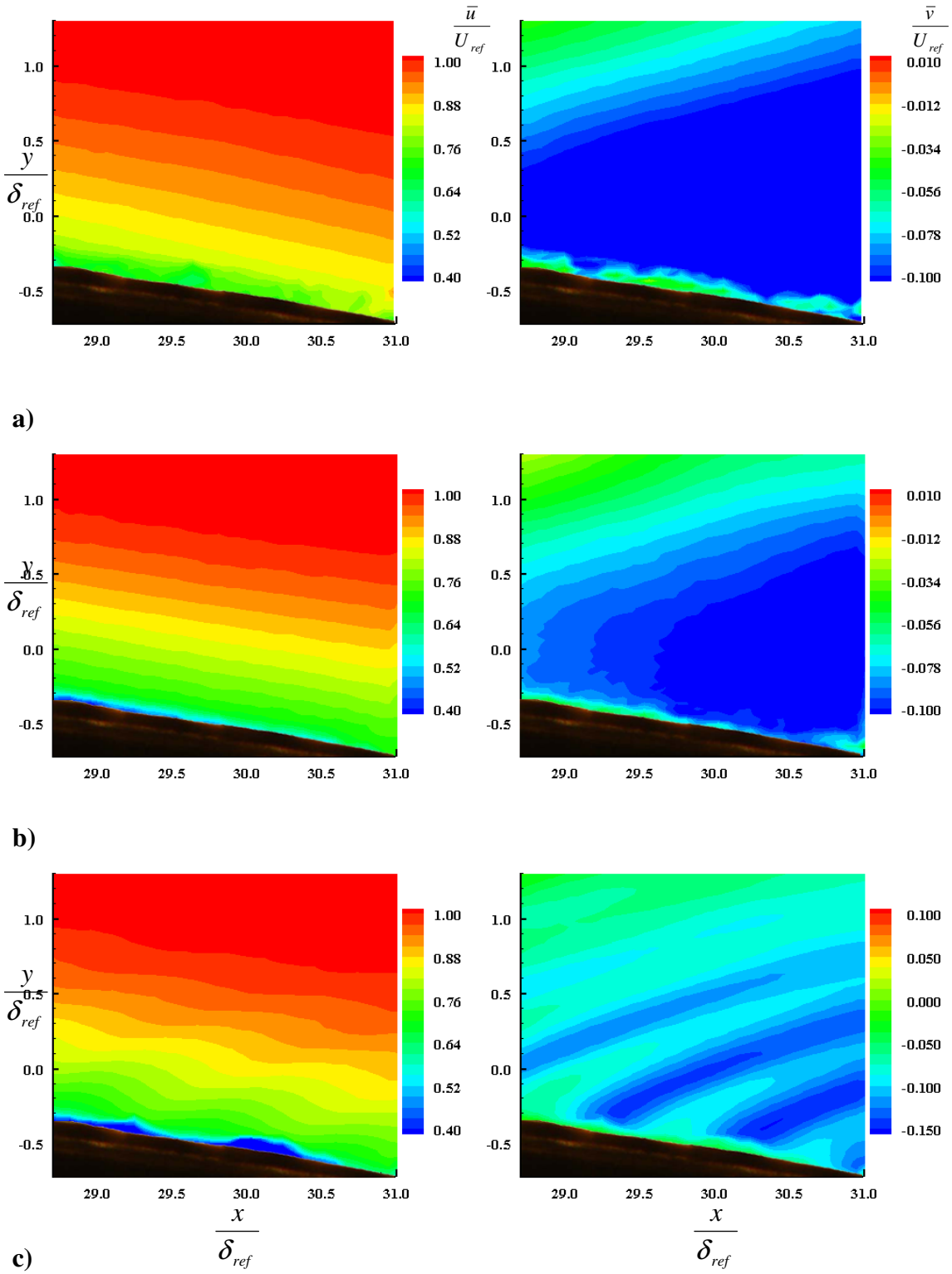

Figure 52: SPG mean velocity fields at the 2nd test location for a) smooth, b) square, and c) diamond roughness

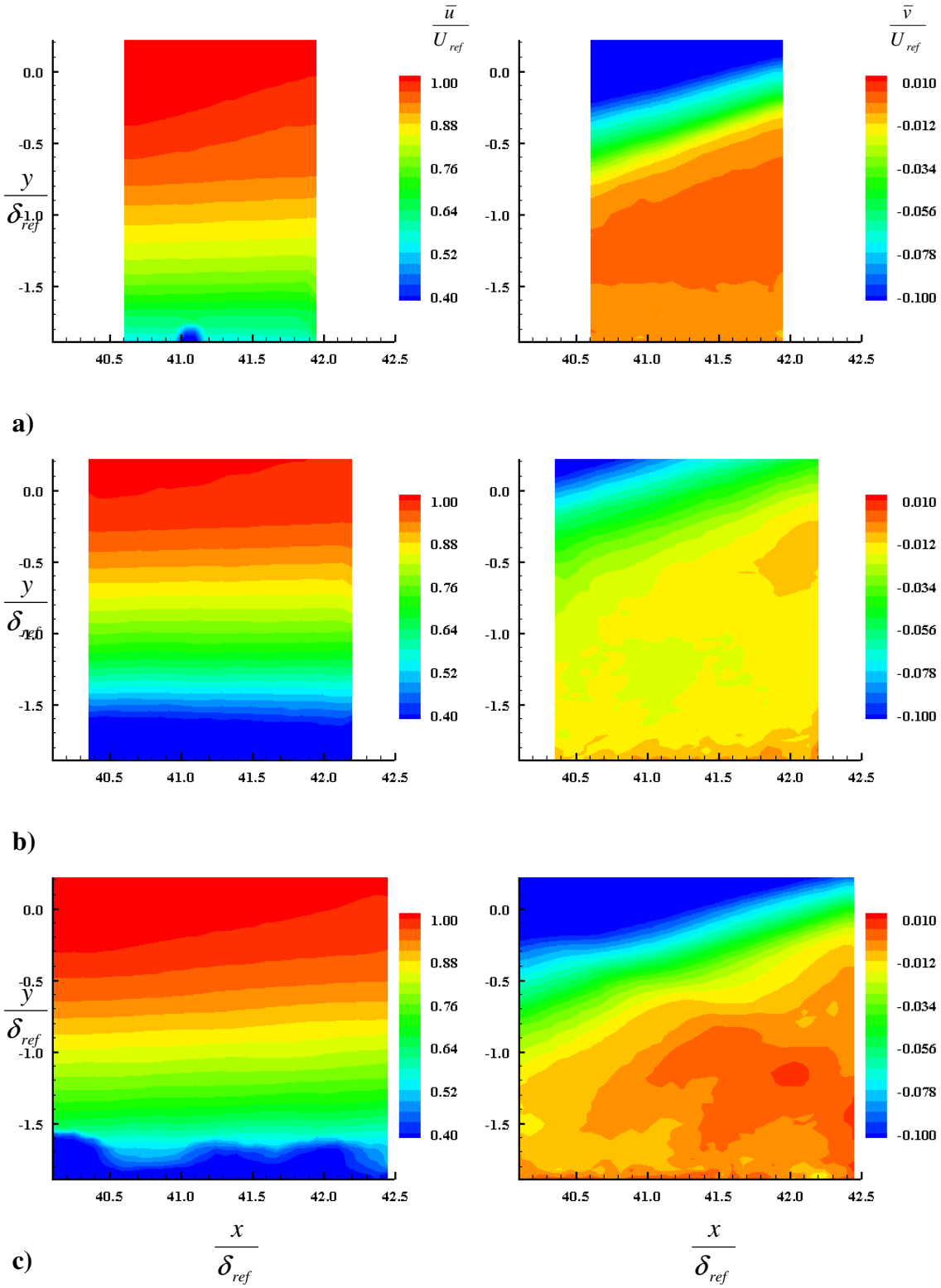

Figure 53: SPG mean velocity fields at the 3rd test location for a) smooth, b) square, and c) diamond roughness

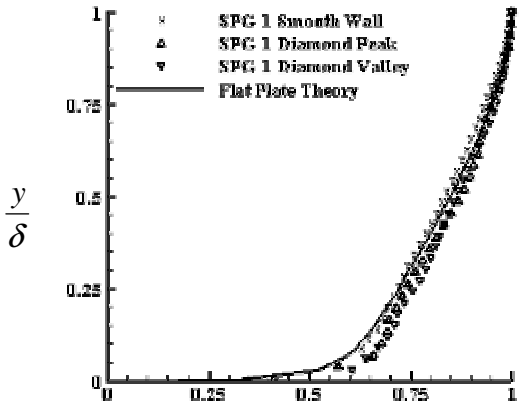

a)

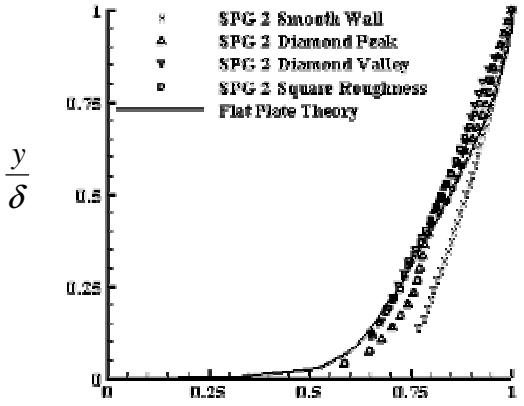

b)

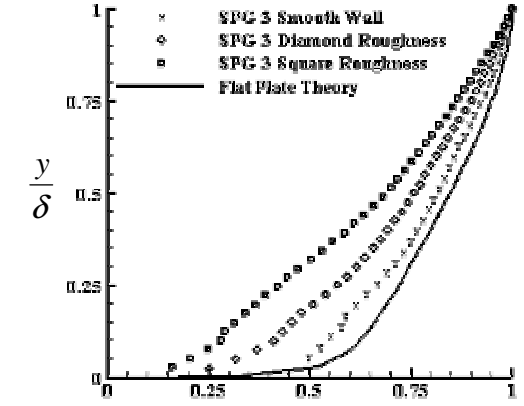

c)

Figure 54: Strong pressure gradient velocity profiles

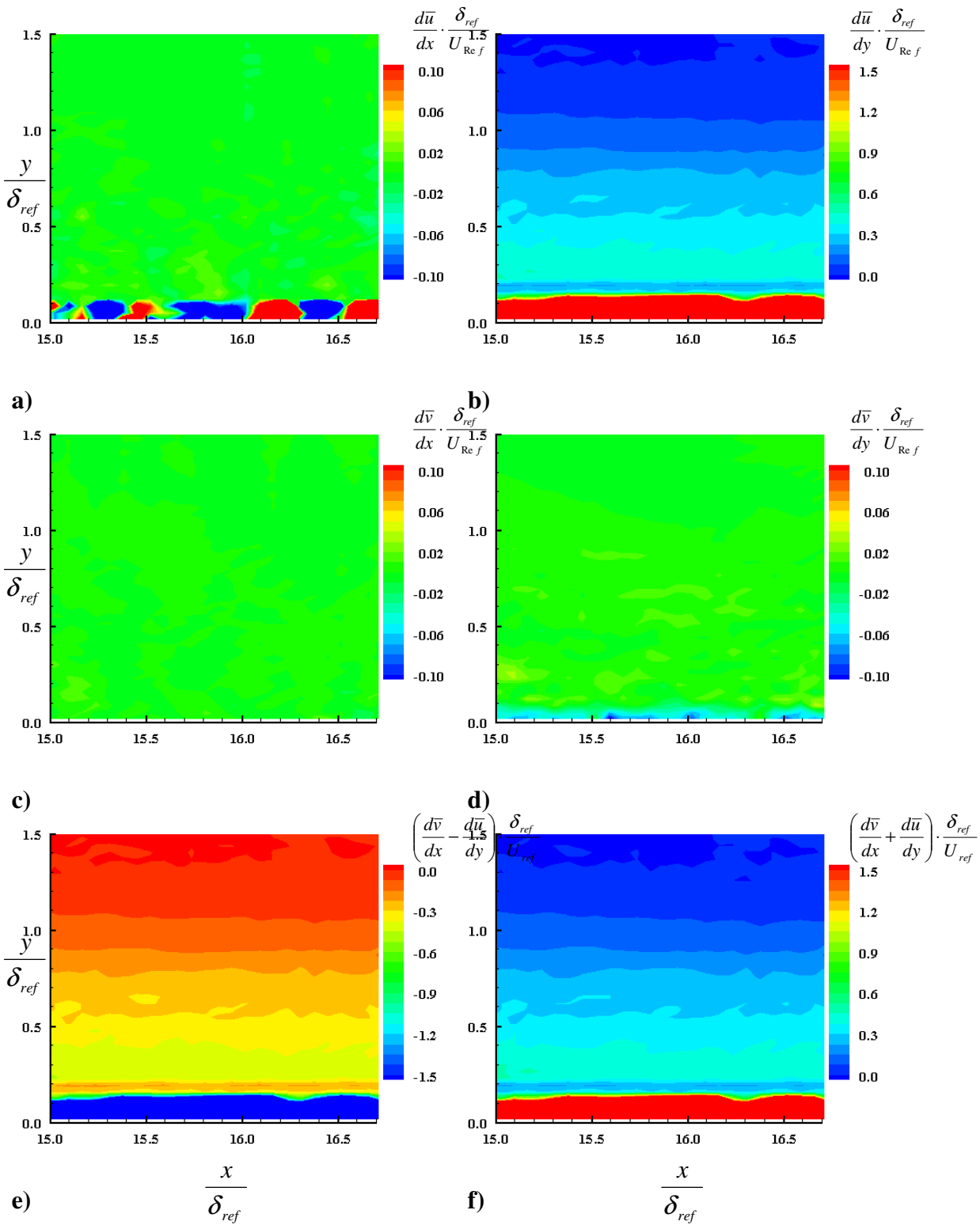

Figure 55: Velocity gradients of the ZPG smooth wall model at location 1

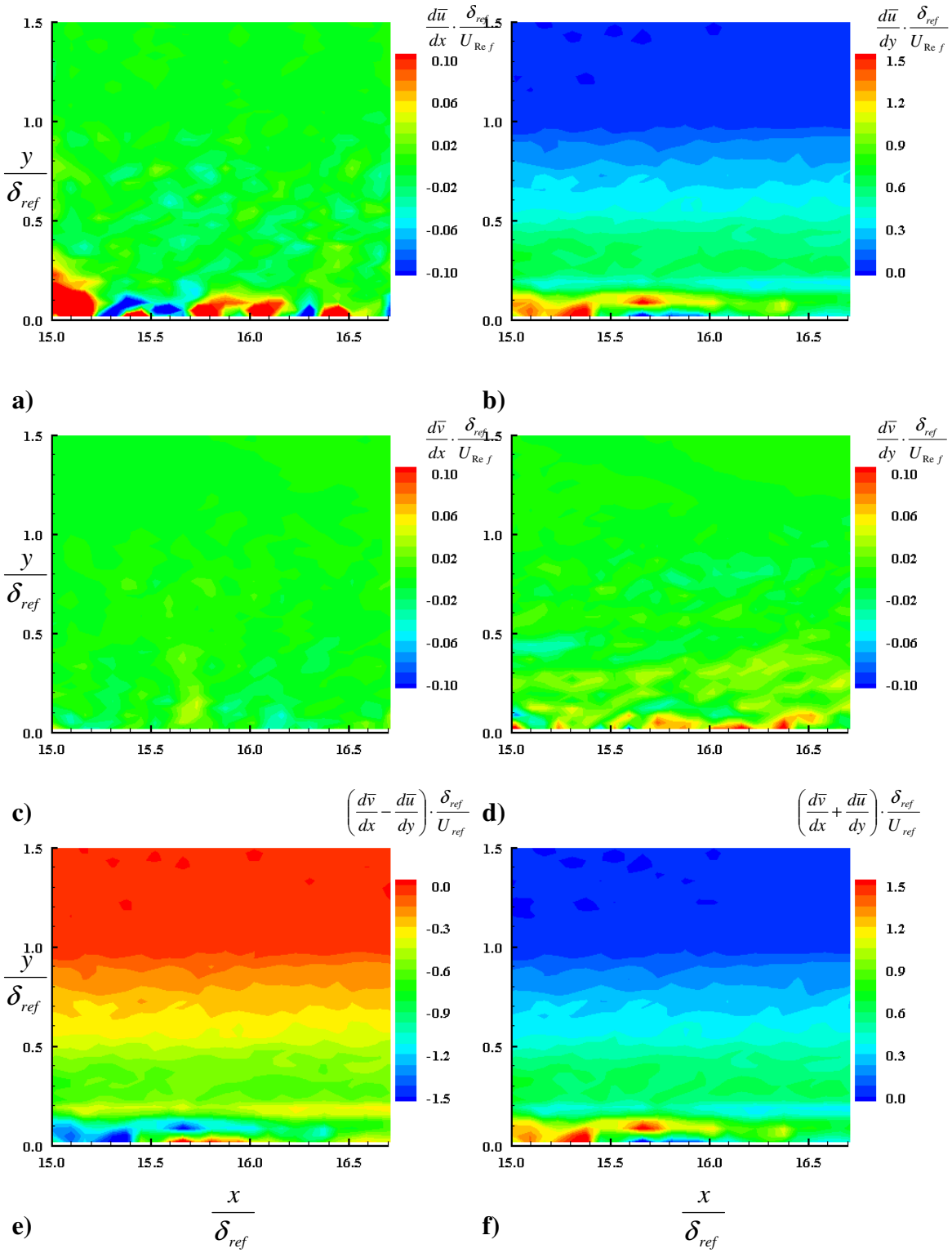

Figure 56: Velocity gradients of the ZPG square roughness model at location 1

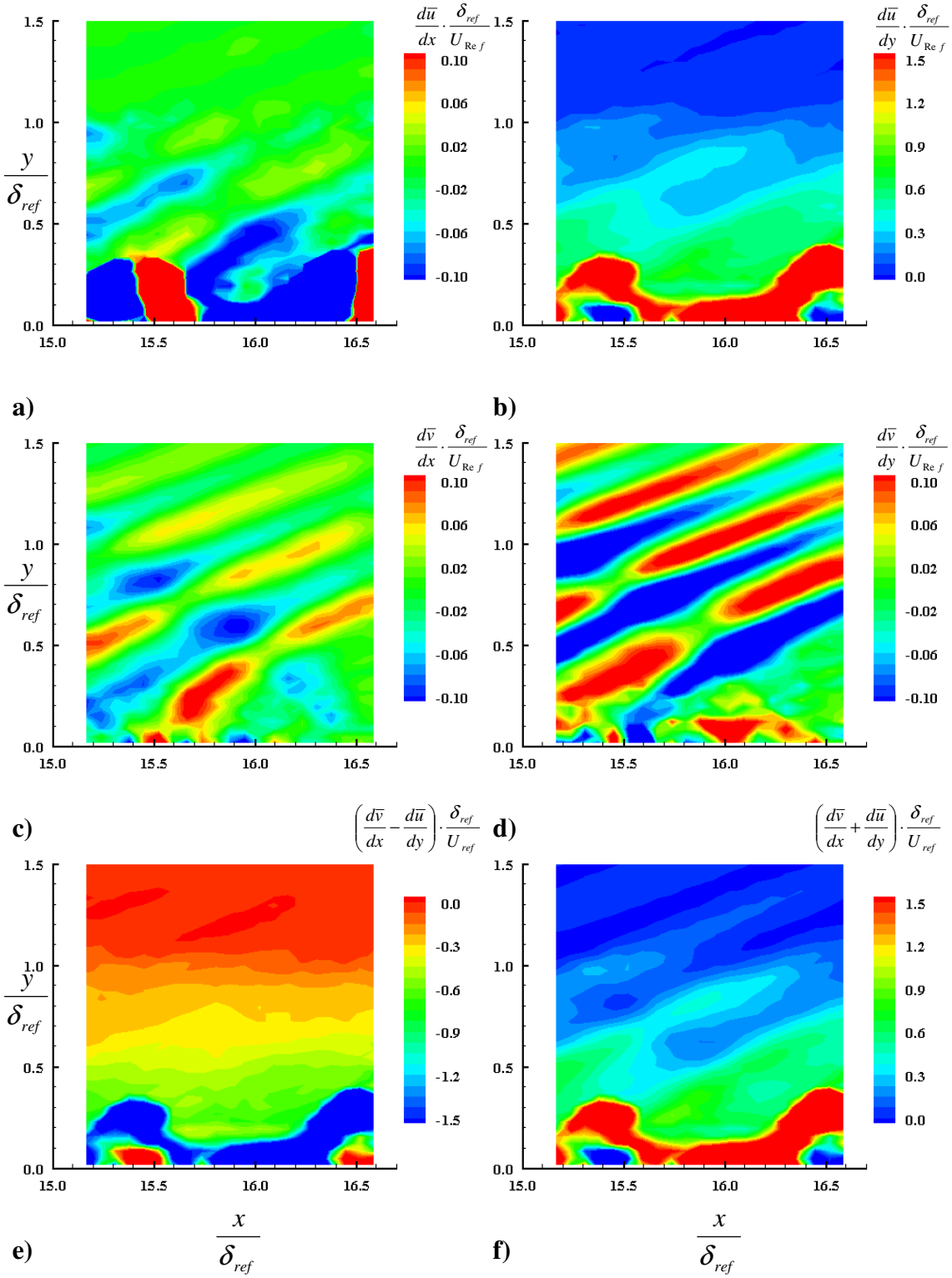

Figure 57: Velocity gradients of the ZPG diamond roughness model at location 1

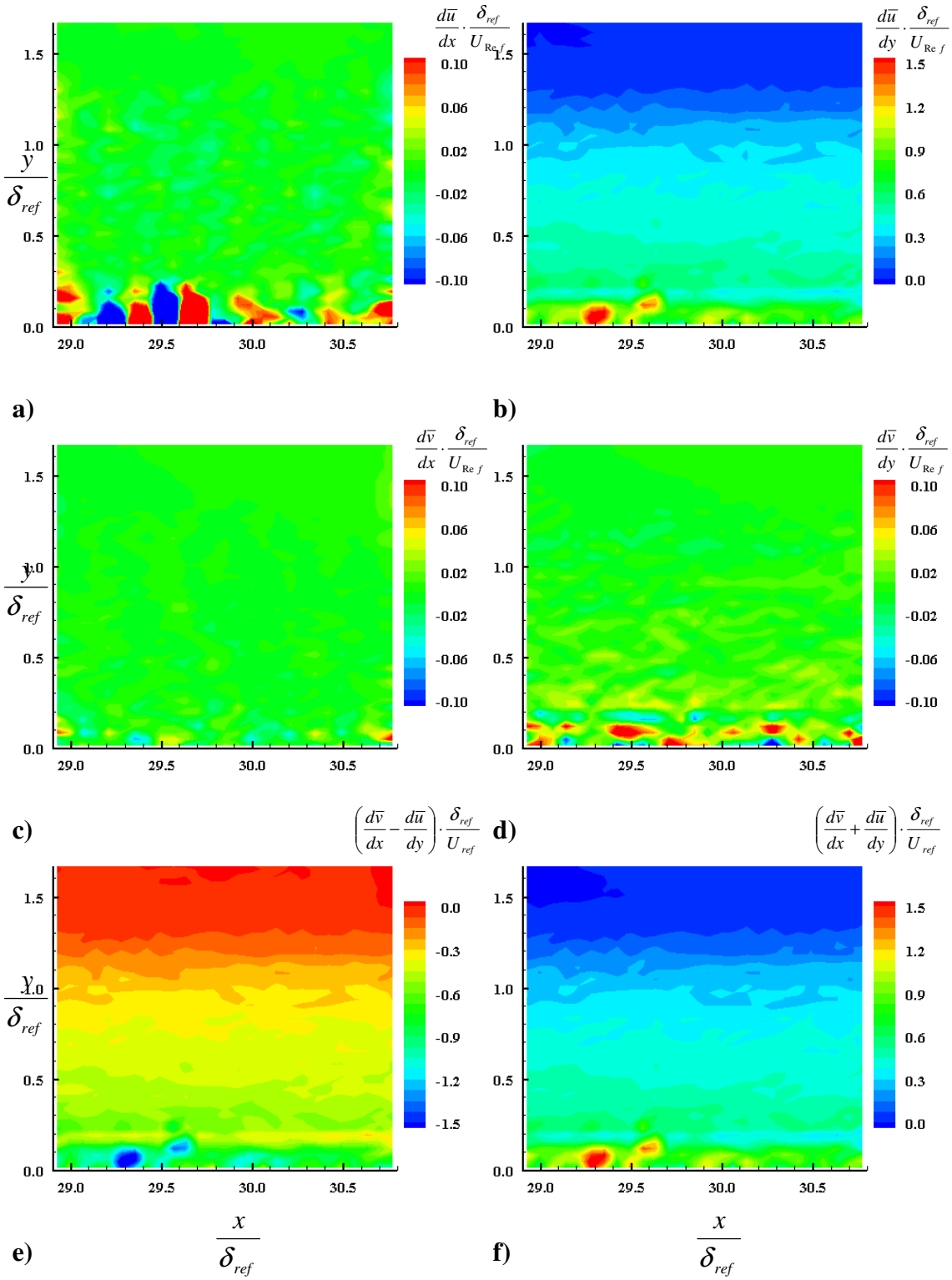

Figure 58: Velocity gradients of the ZPG square roughness model at location 2

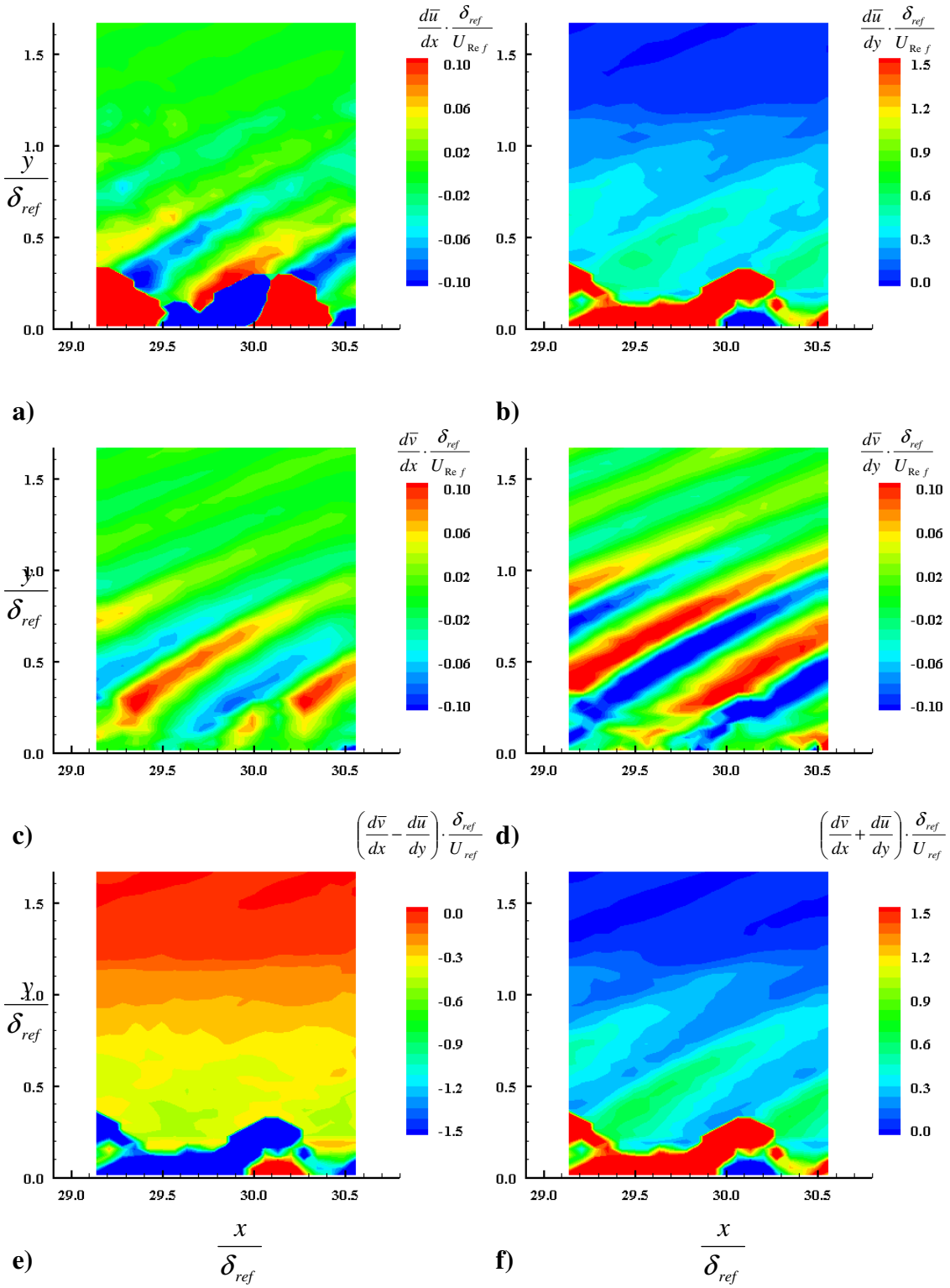

Figure 59: Velocity gradients of the ZPG diamond roughness model at location 2

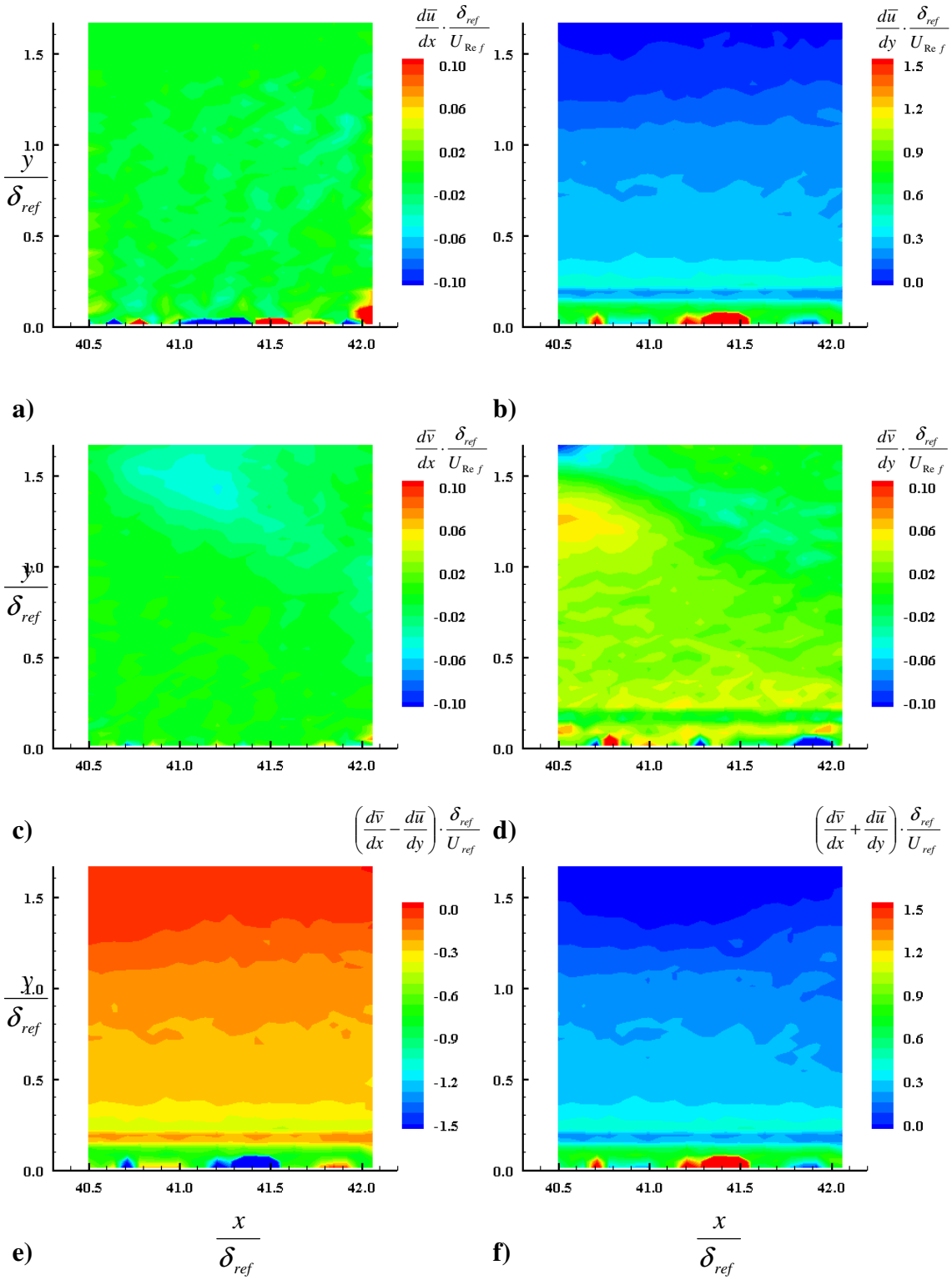

Figure 60: Velocity gradients of the ZPG smooth wall model at location 3

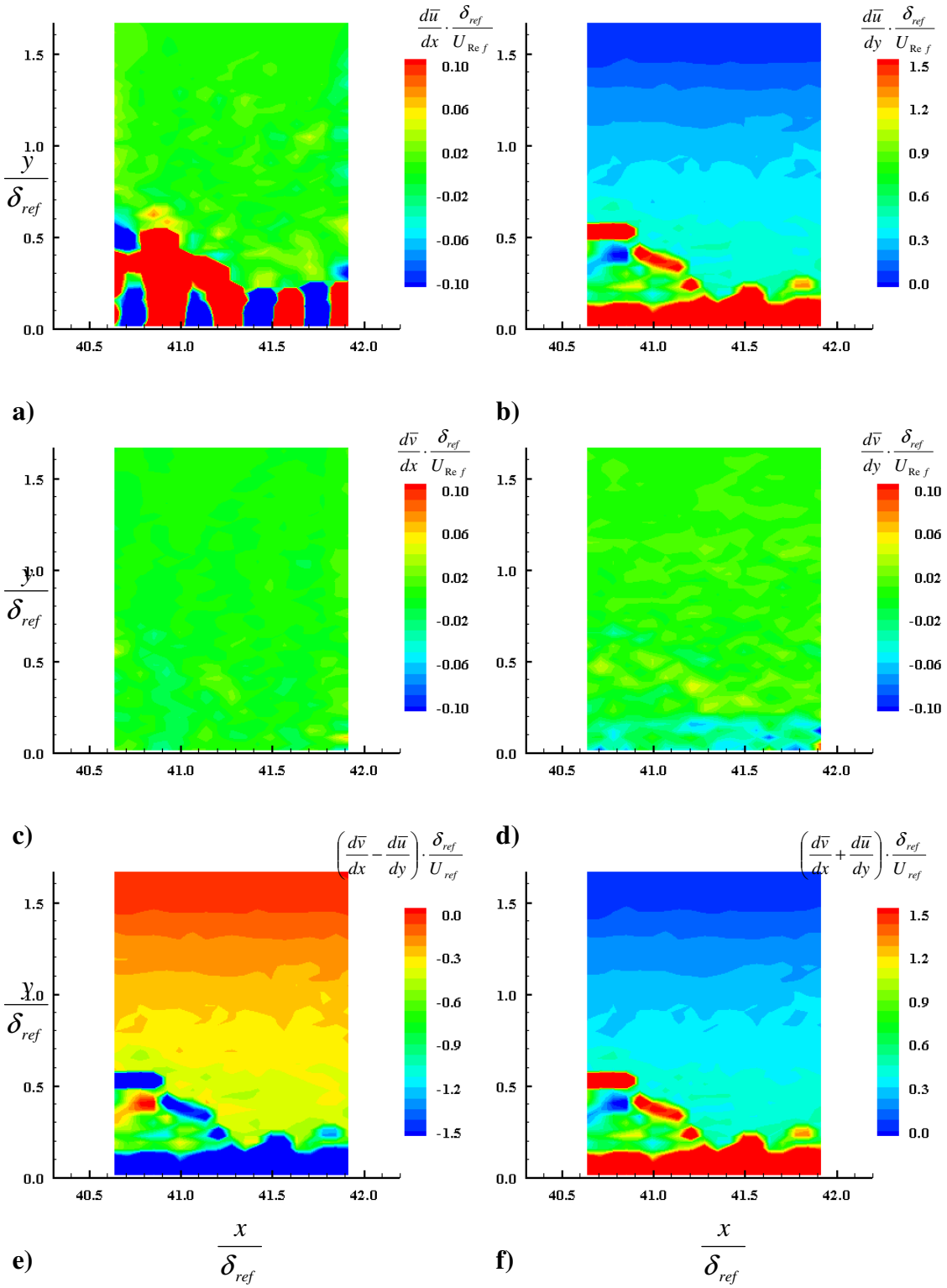

Figure 61: Velocity gradients of the ZPG square roughness model at location 3

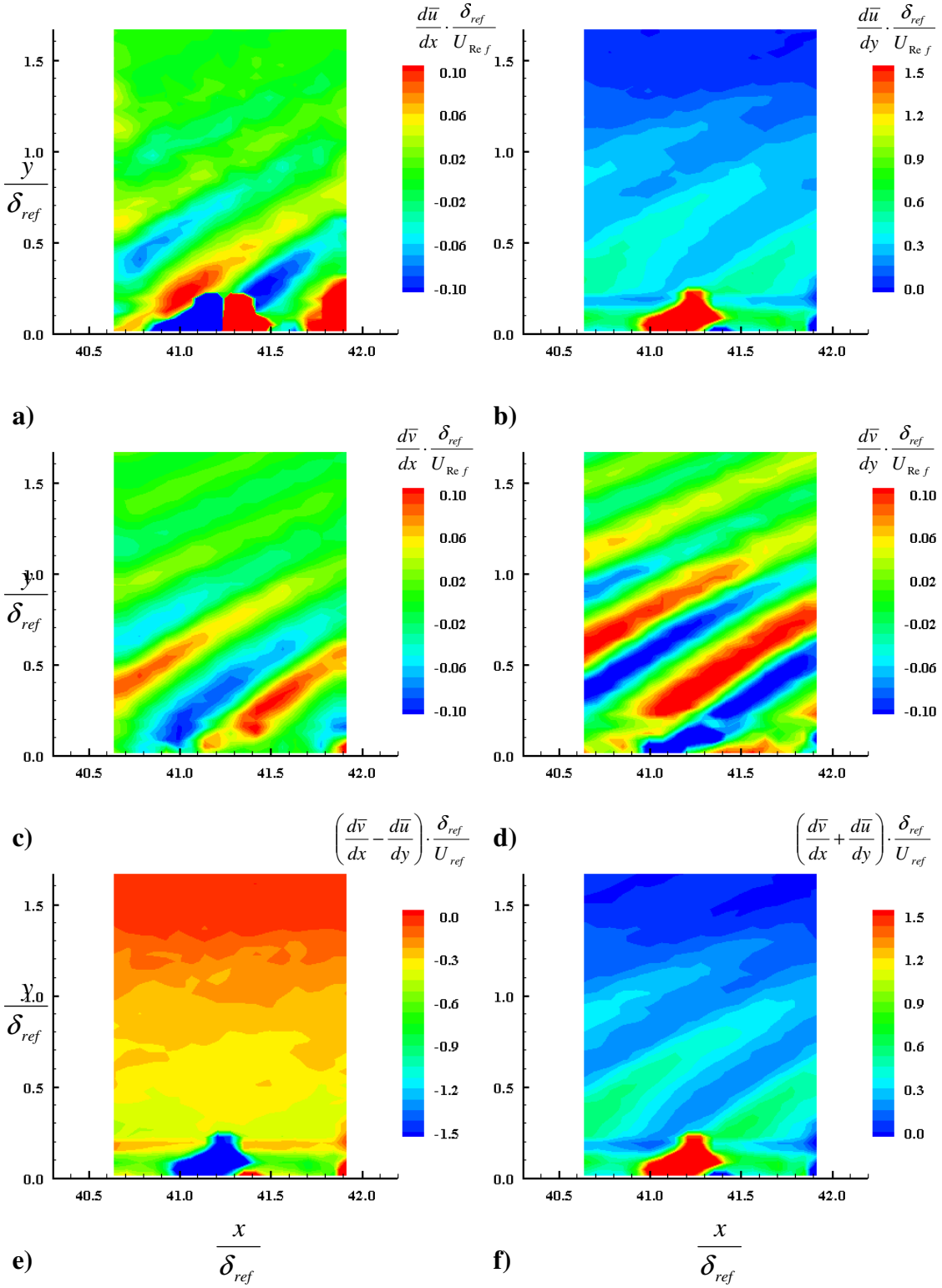

Figure 62: Velocity gradients of the ZPG diamond roughness model at location 3

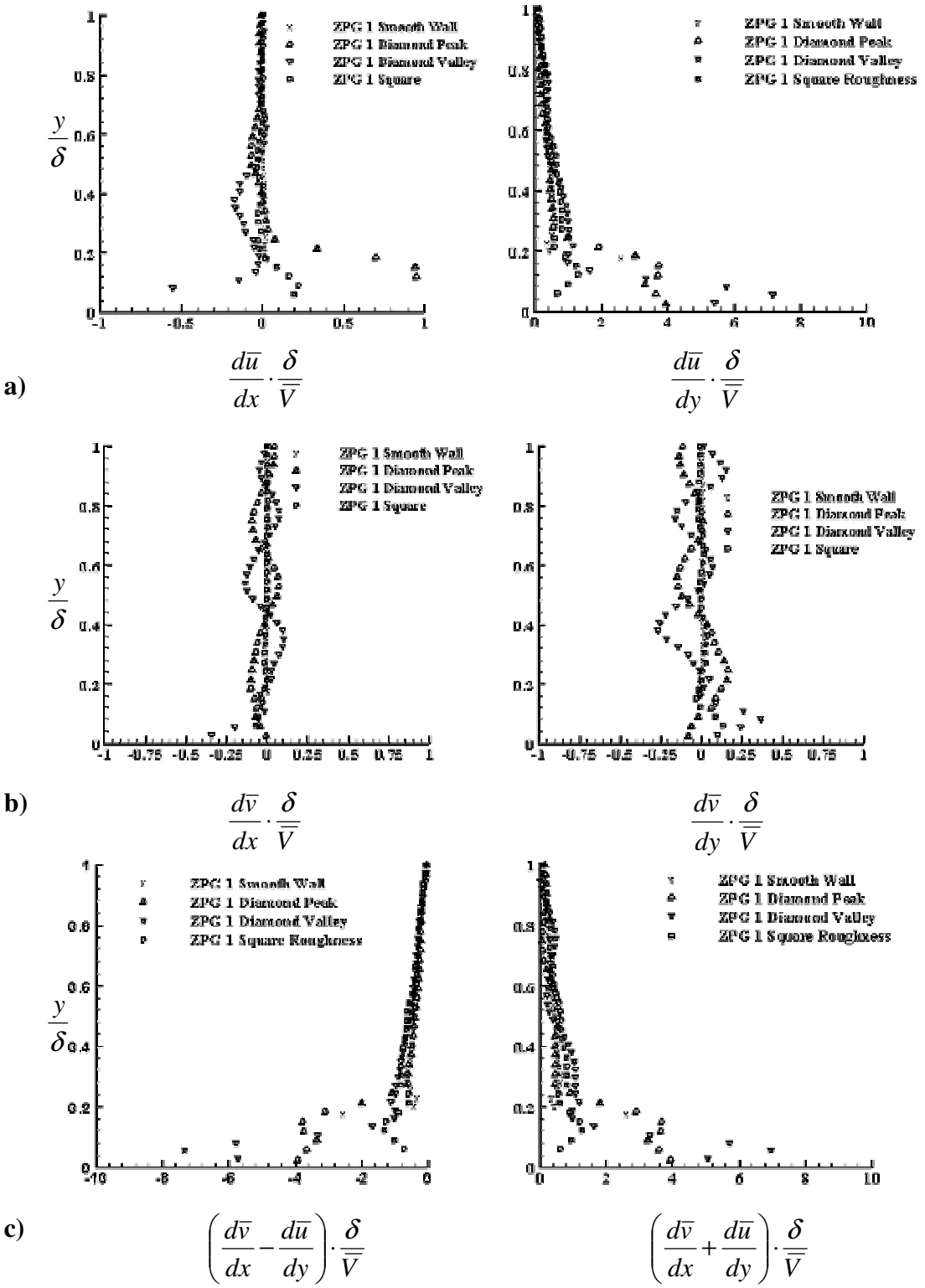

Figure 63: Velocity gradient profiles of the ZPG models at location 1

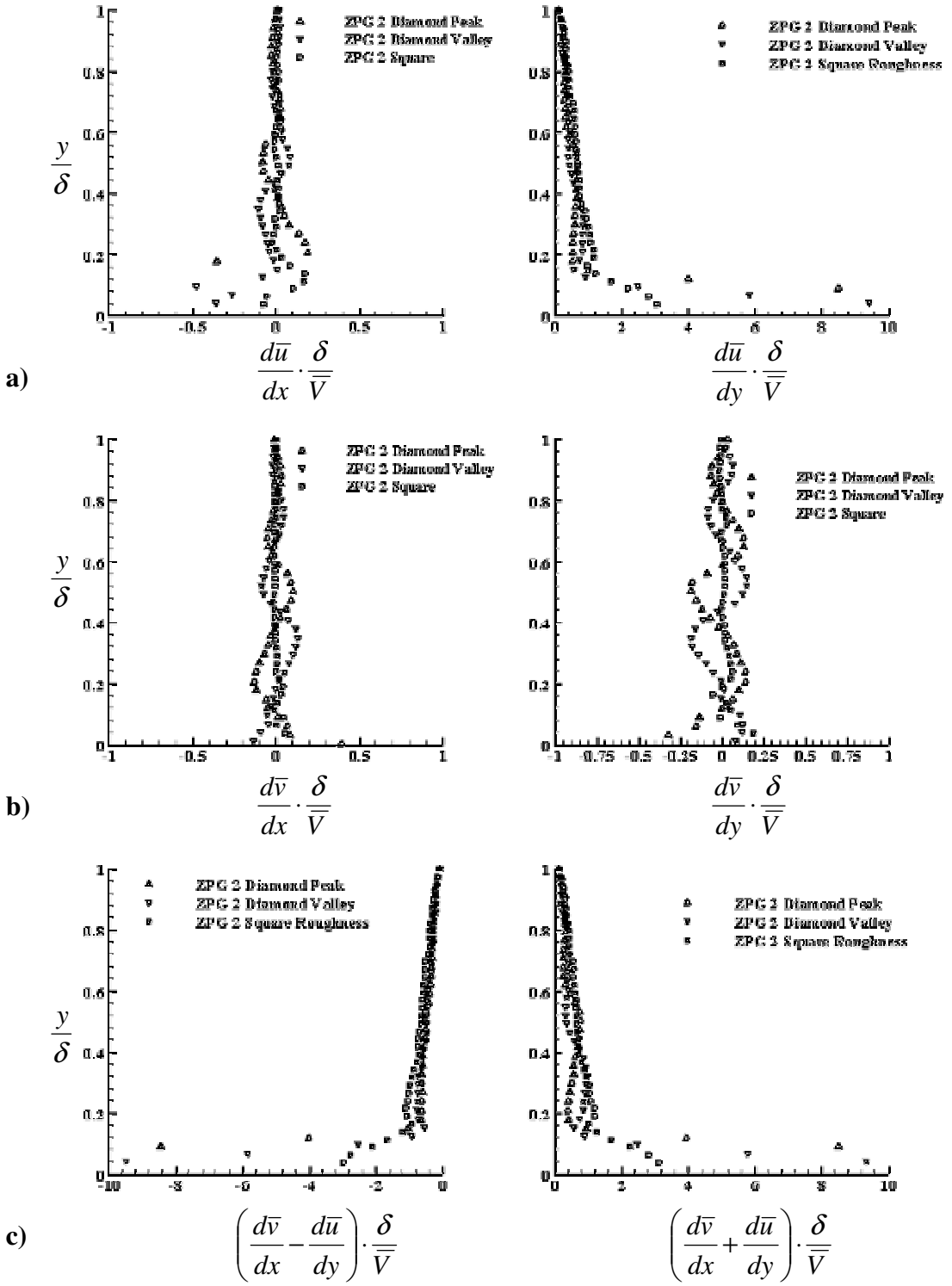

Figure 64: Velocity gradient profiles of the ZPG models at location 2

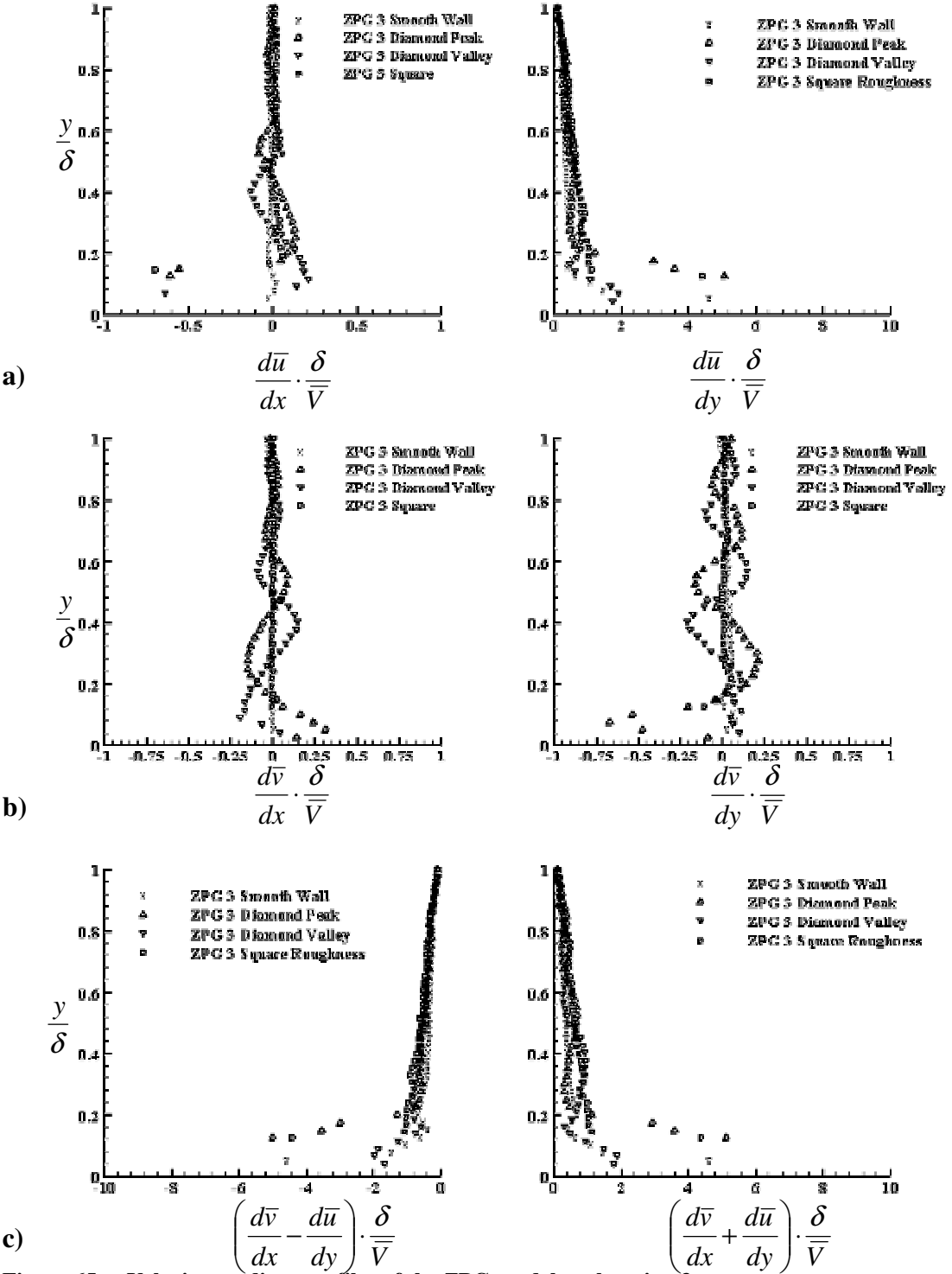

Figure 65: Velocity gradient profiles of the ZPG models at location 3

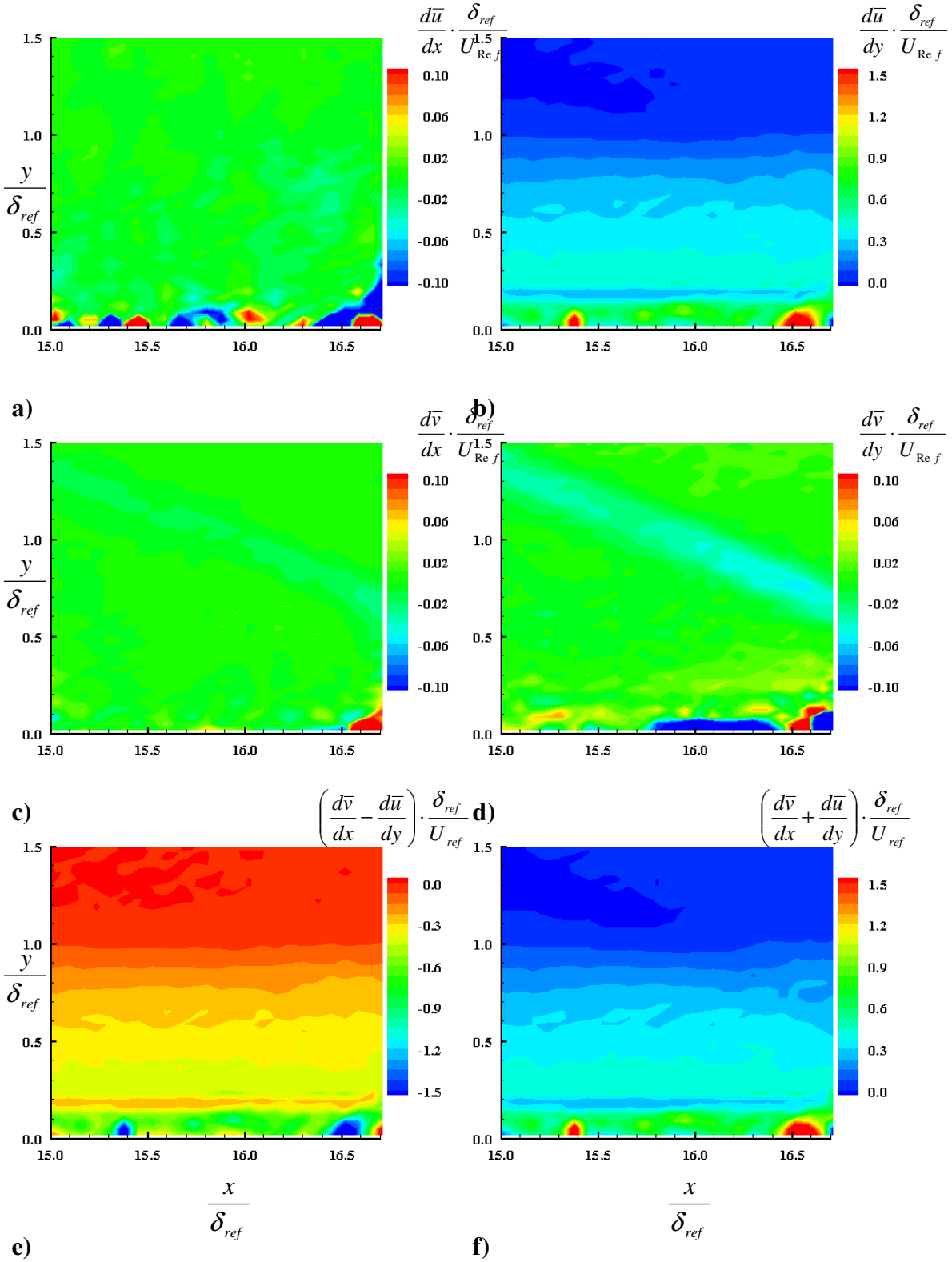

Figure 66: Velocity gradients of the WPG smooth wall model at location 1

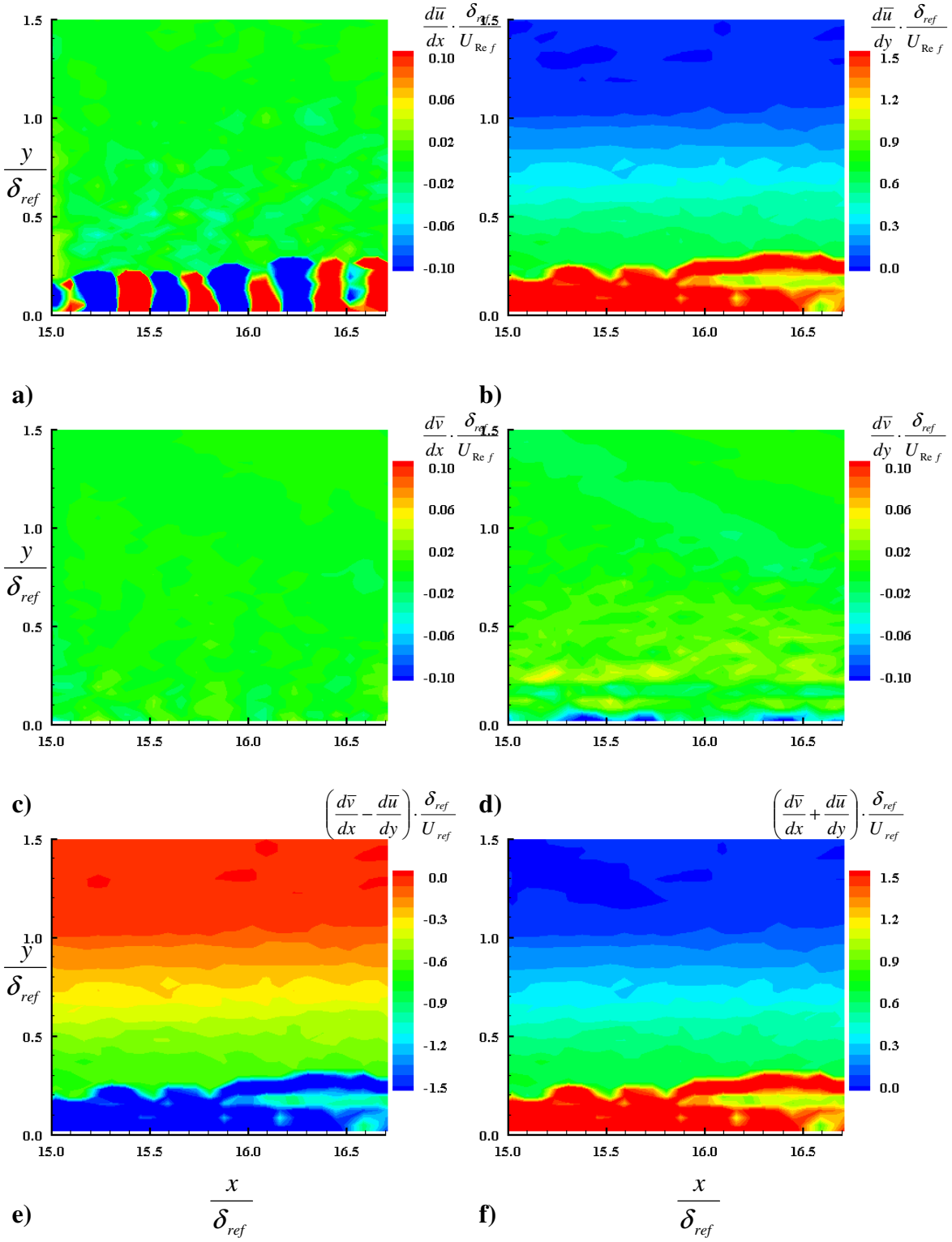

Figure 67: Velocity gradients of the WPG square roughness model at location 1

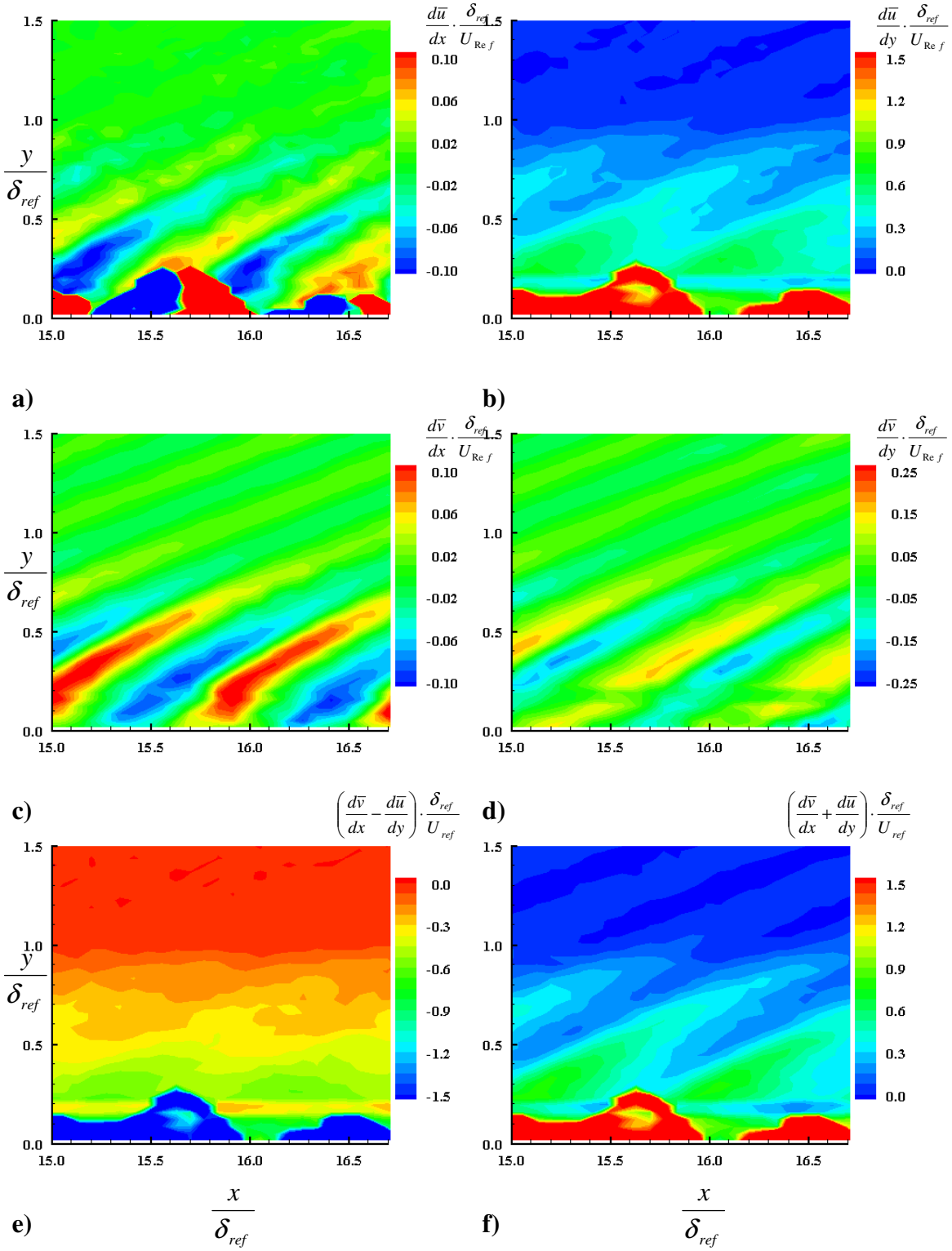

Figure 68: Velocity gradients of the WPG diamond roughness model at location 1

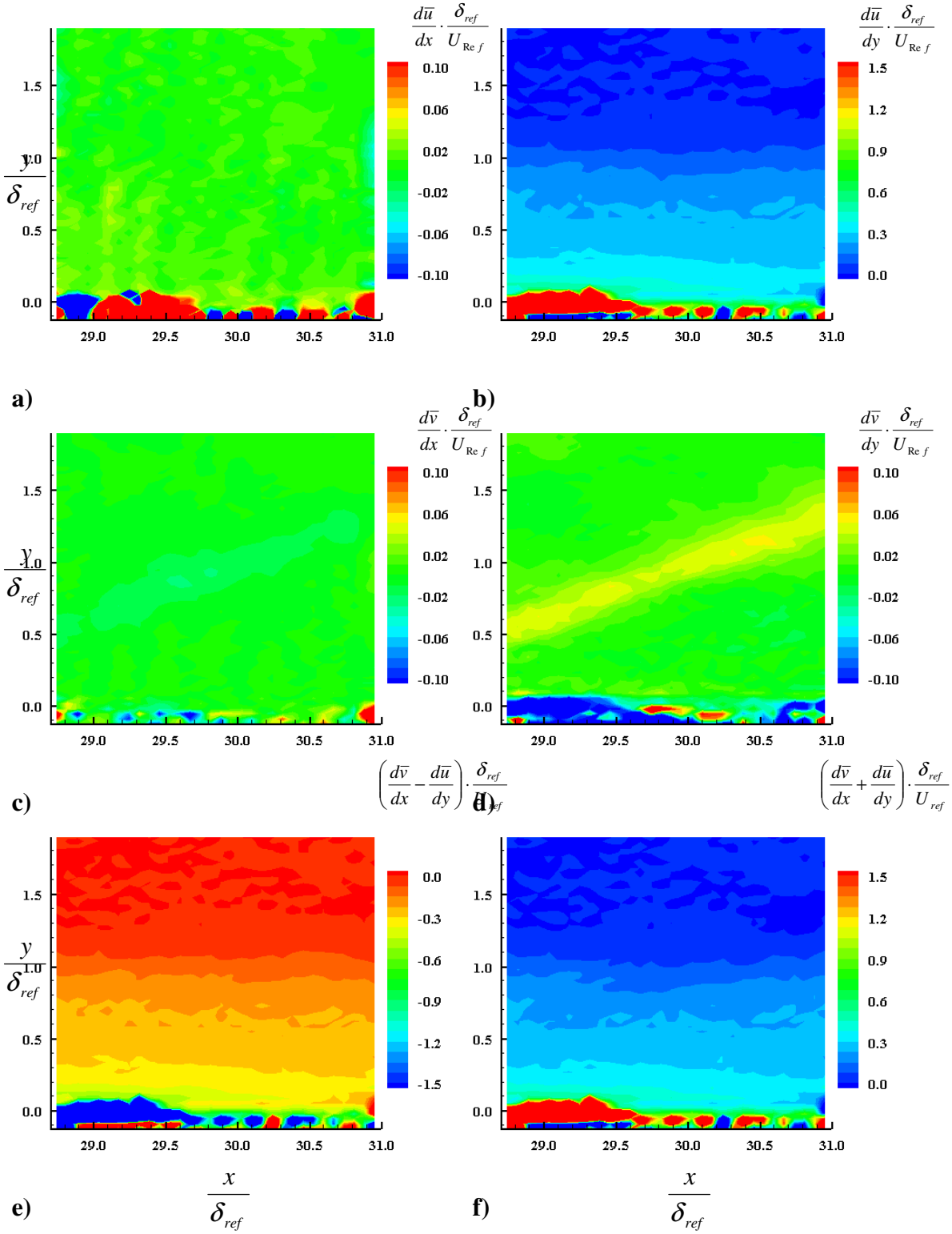

Figure 69: Velocity gradients of the WPG smooth wall model at location 2

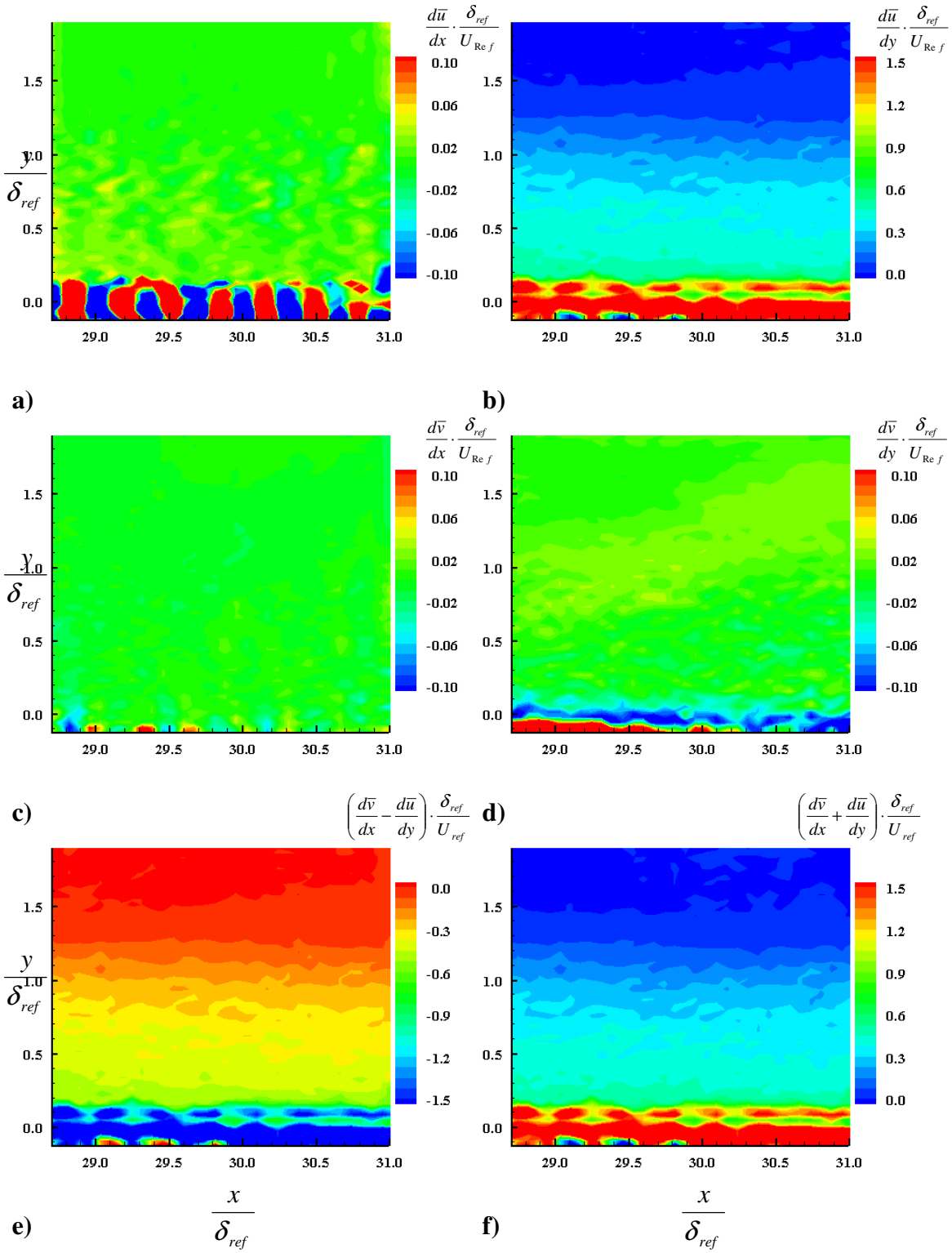

Figure 70: Velocity gradients of the WPG square roughness model at location 2

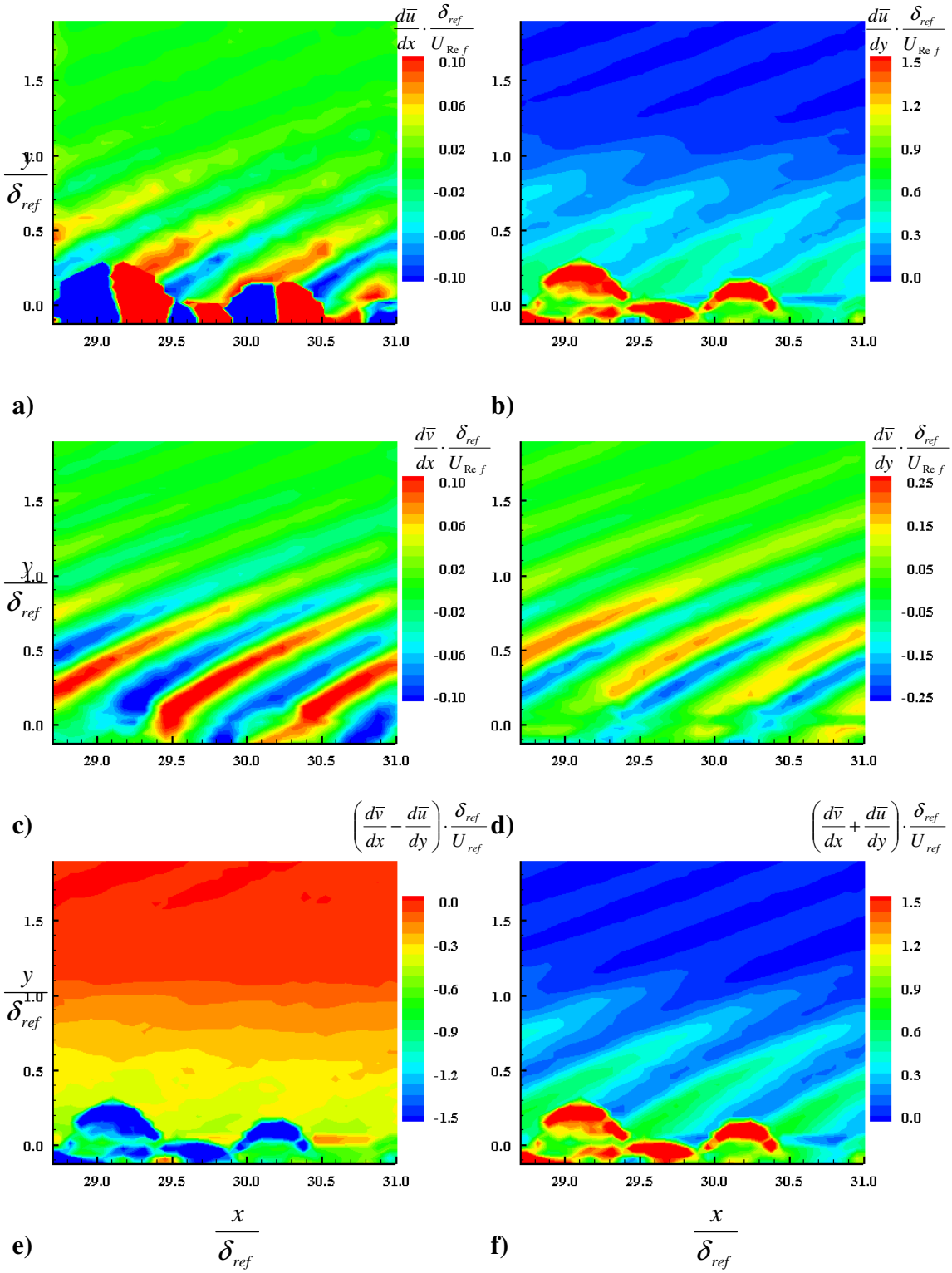

Figure 71: Velocity gradients of the WPG diamond roughness model at location 2

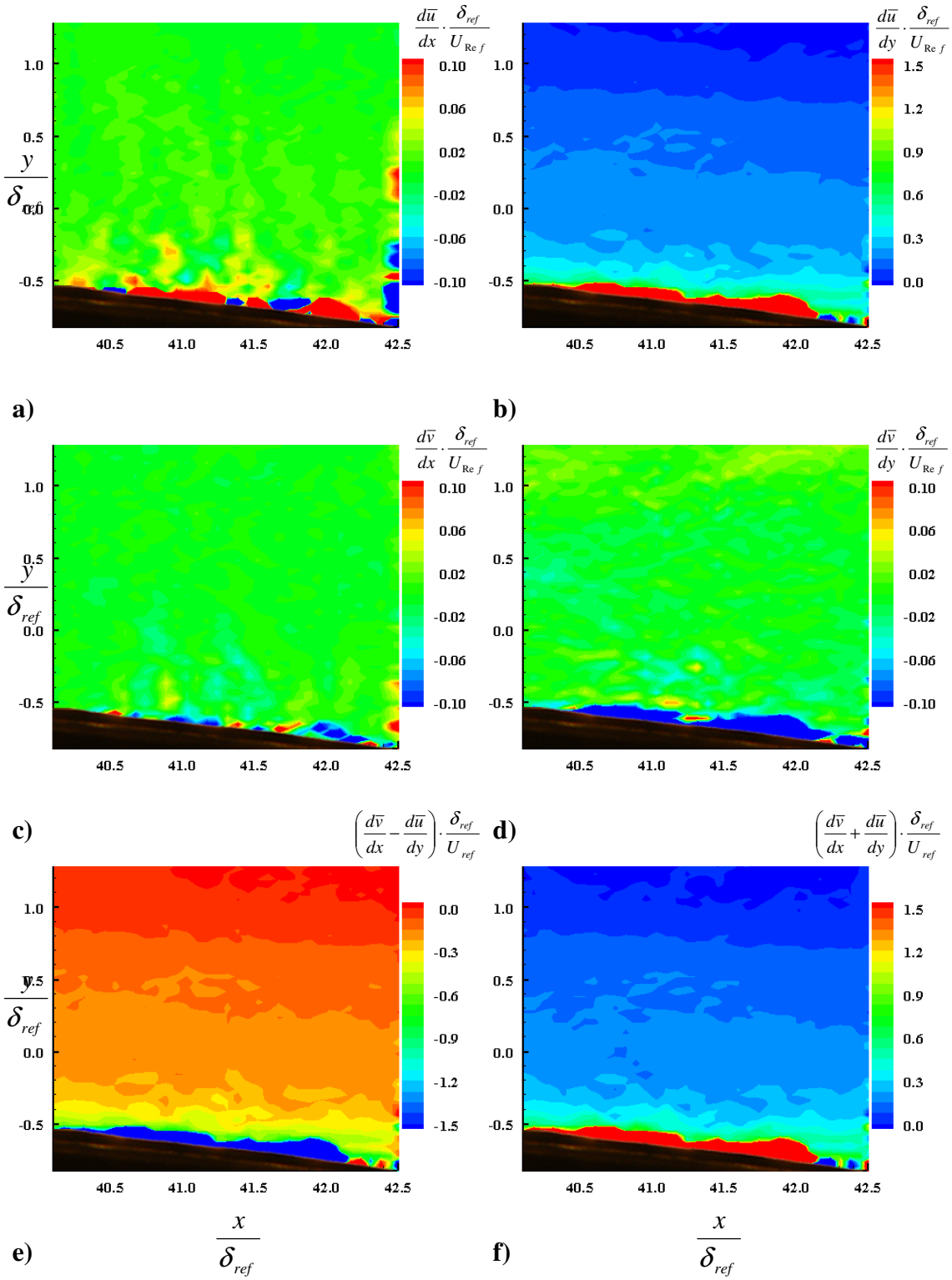

Figure 72: Velocity gradients of the WPG smooth wall model at location 3

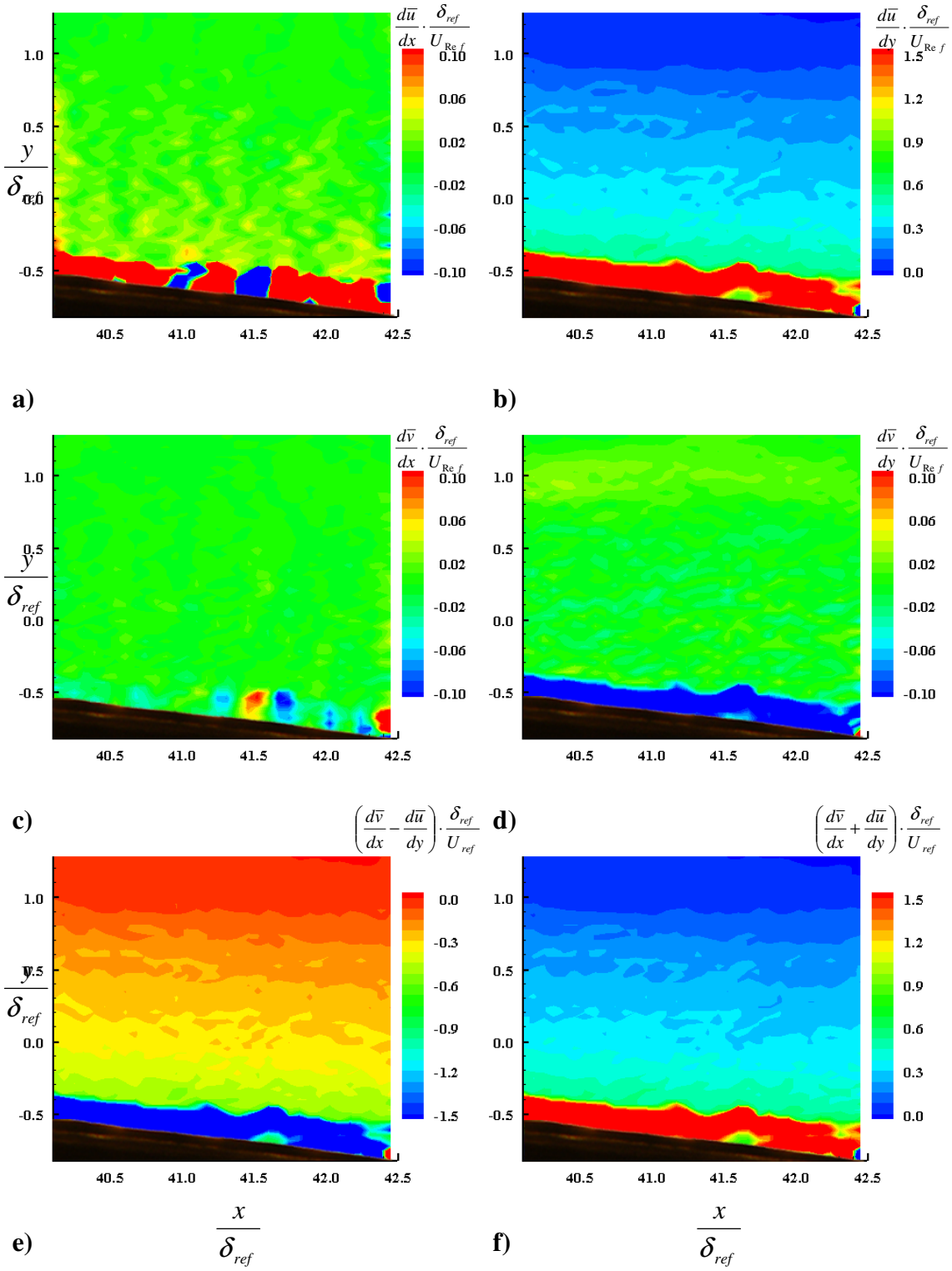

Figure 73: Velocity gradients of the WPG square roughness model at location 3

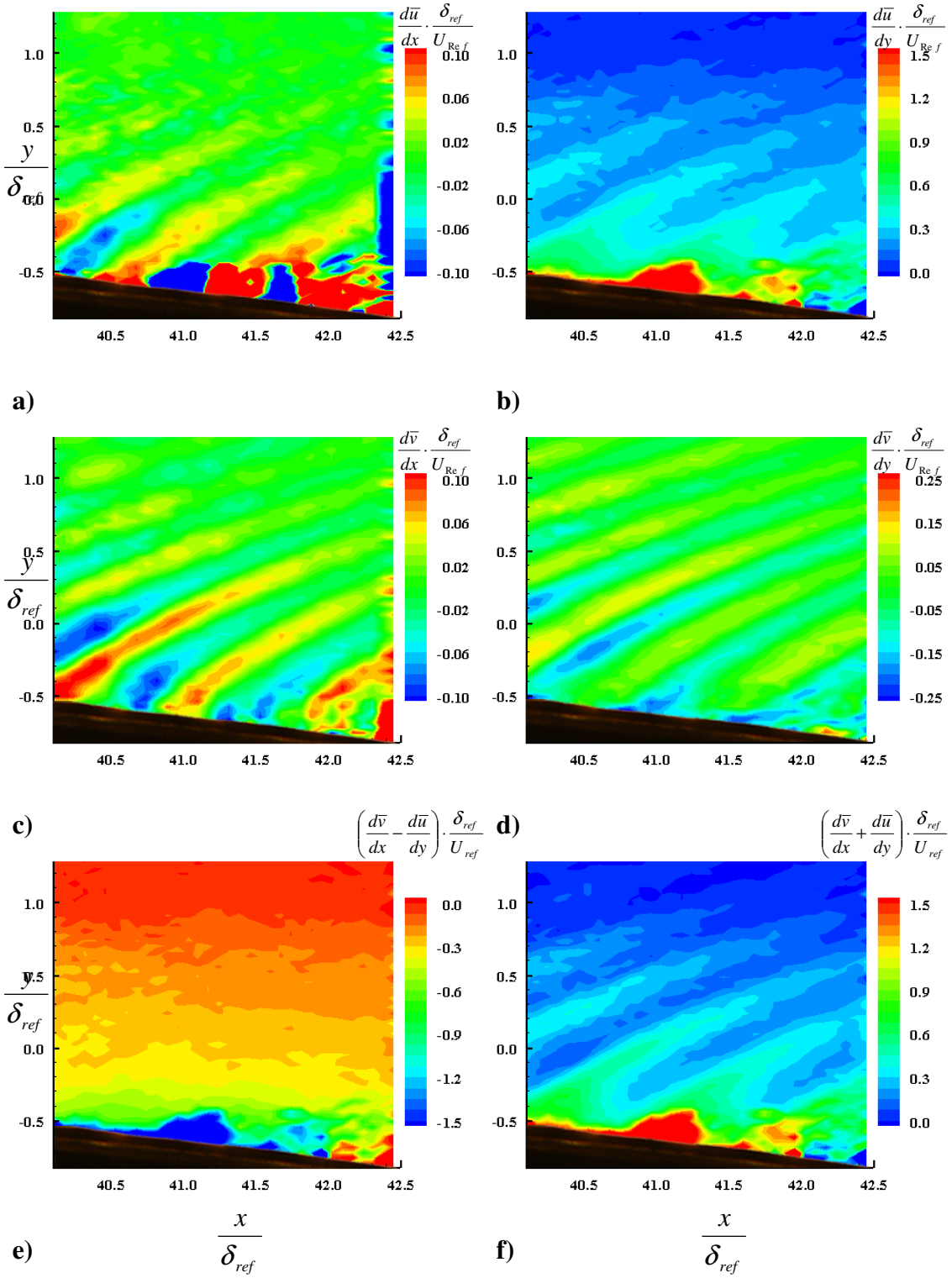

Figure 74: Velocity gradients of the WPG diamond roughness model at location 3

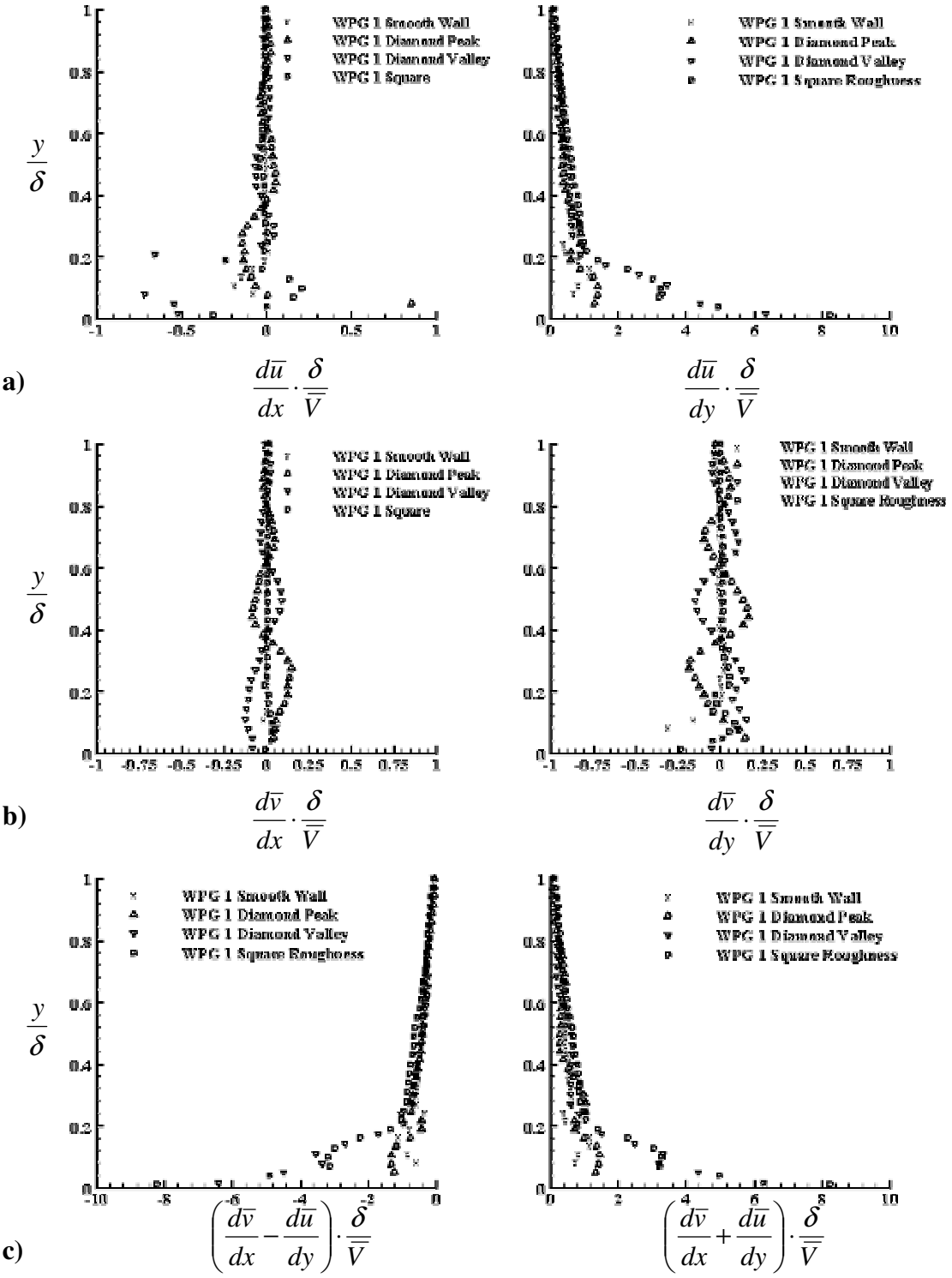

Figure 75: Velocity gradient profiles of the WPG models at location 1

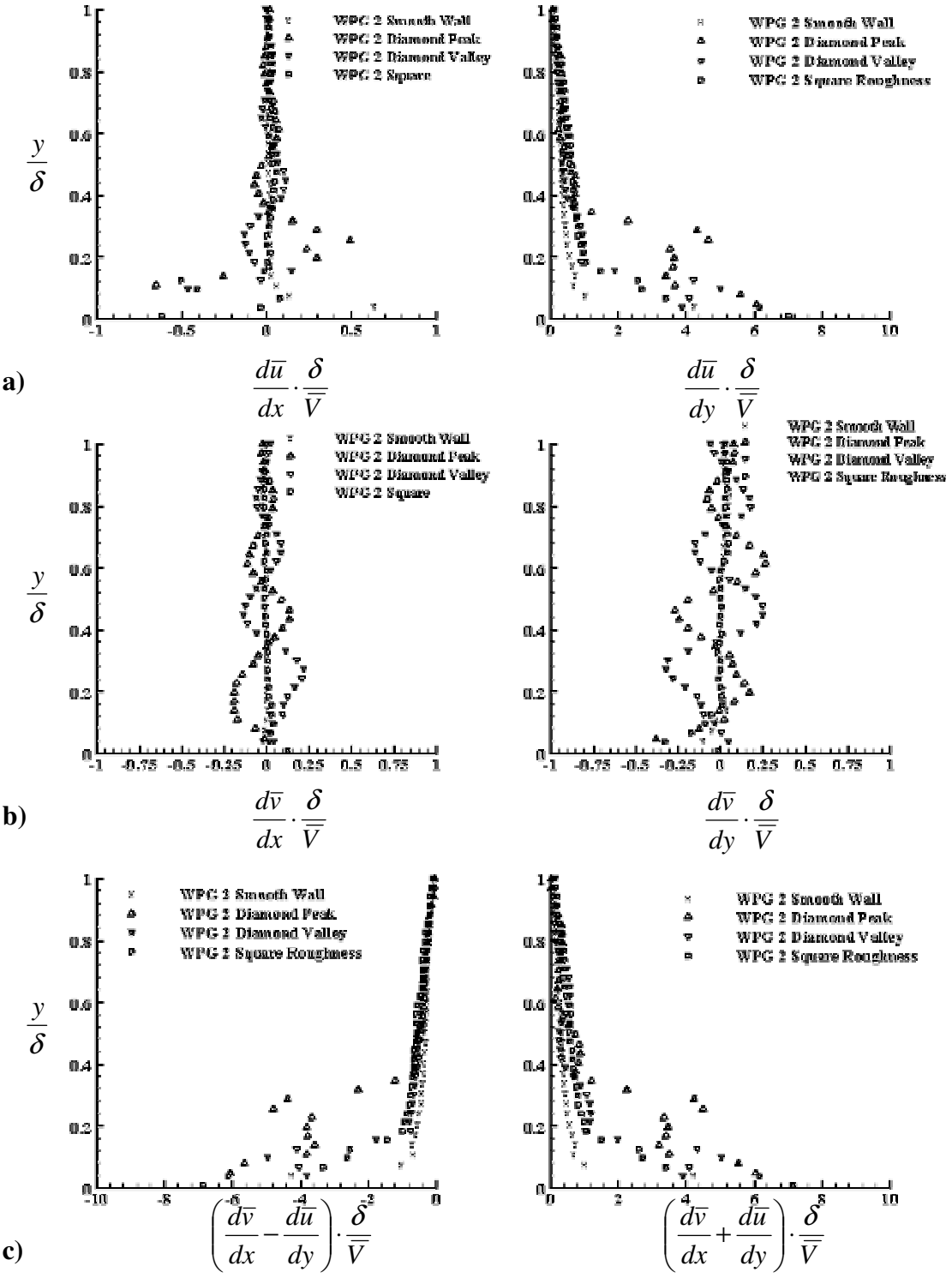

Figure 76: Velocity gradient profiles of the WPG models at location 2

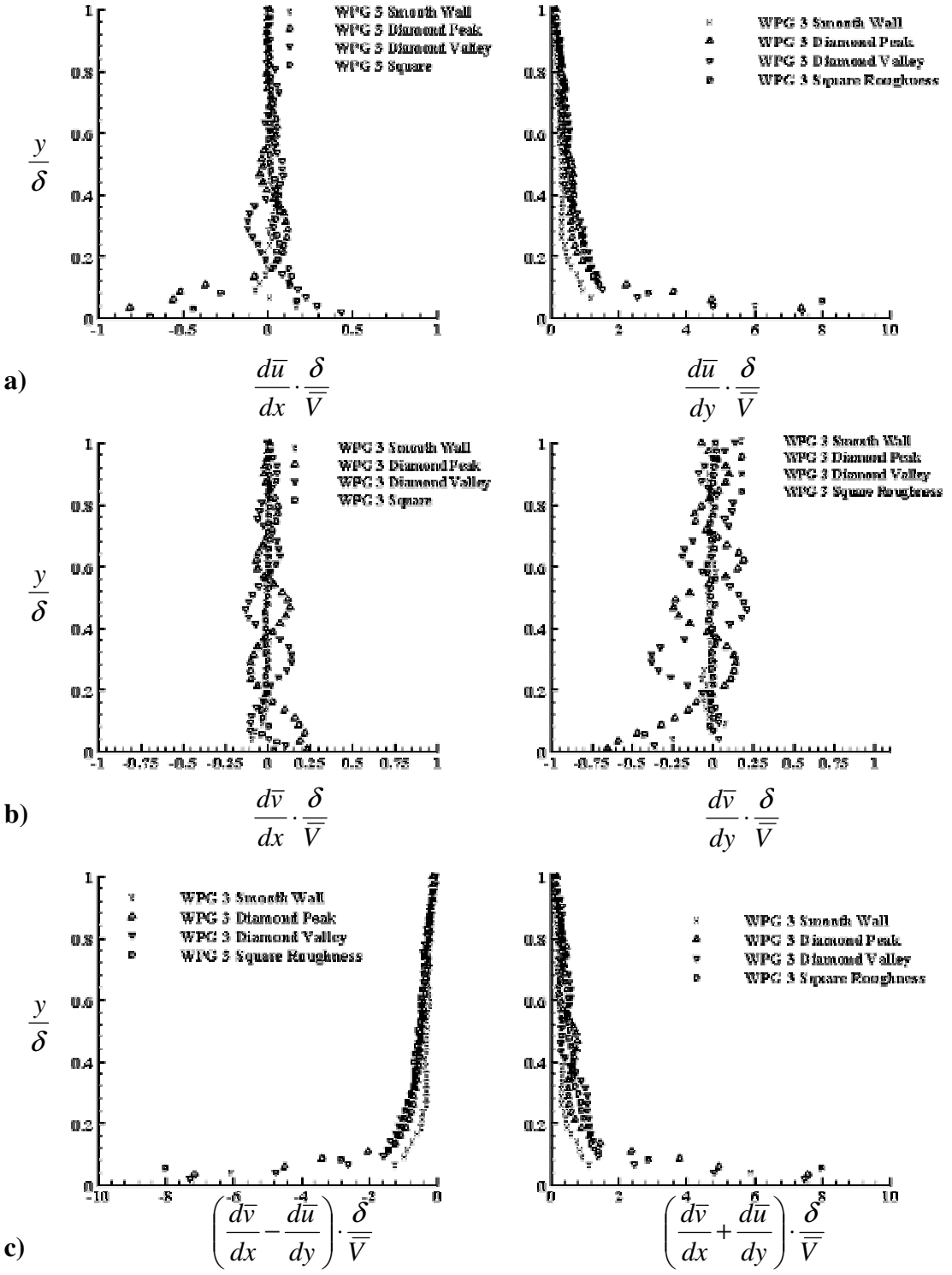

Figure 77: Velocity gradient profiles of the WPG models at location 3

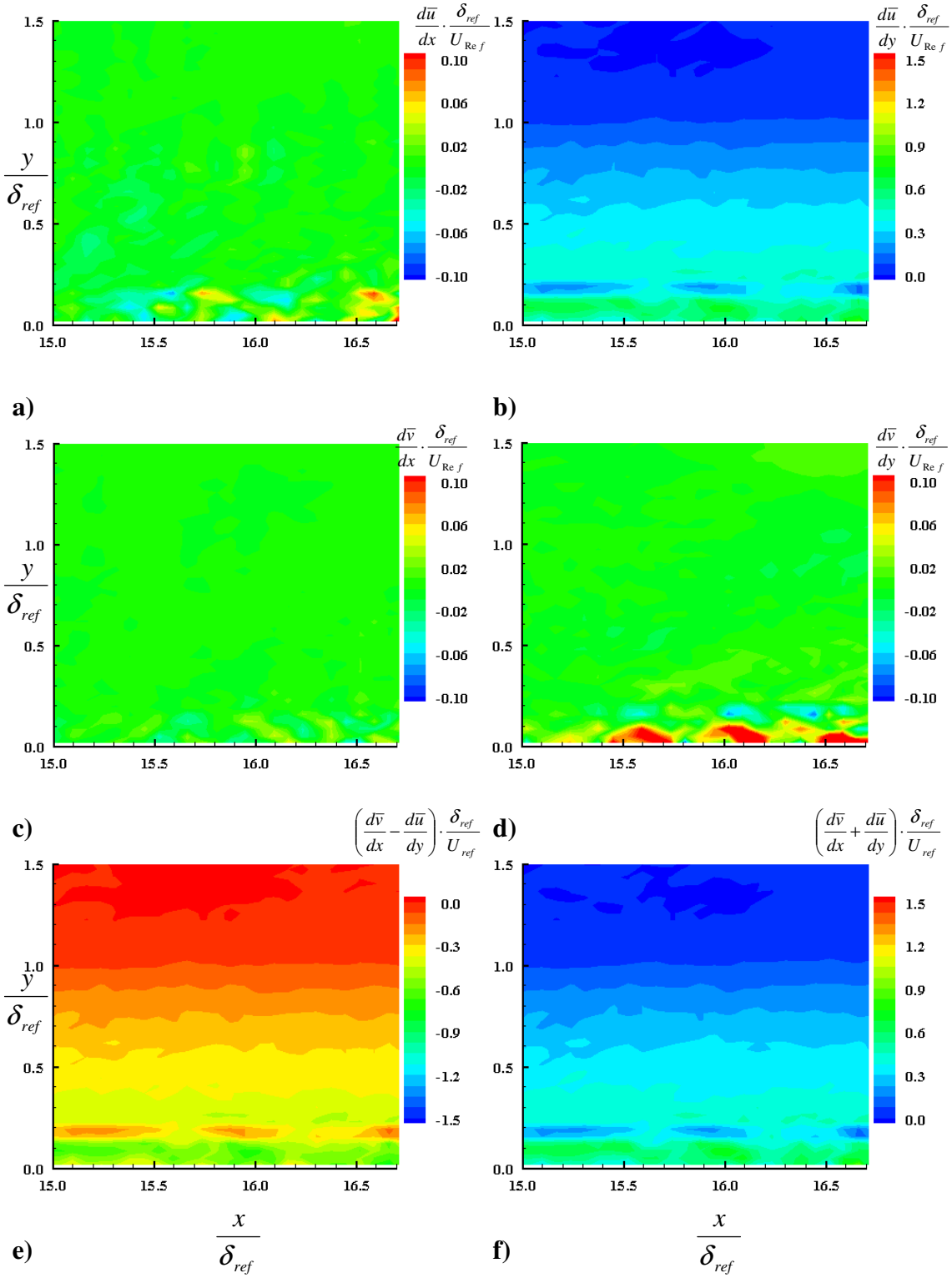

Figure 78: Velocity gradients of the SPG smooth wall model at location 1

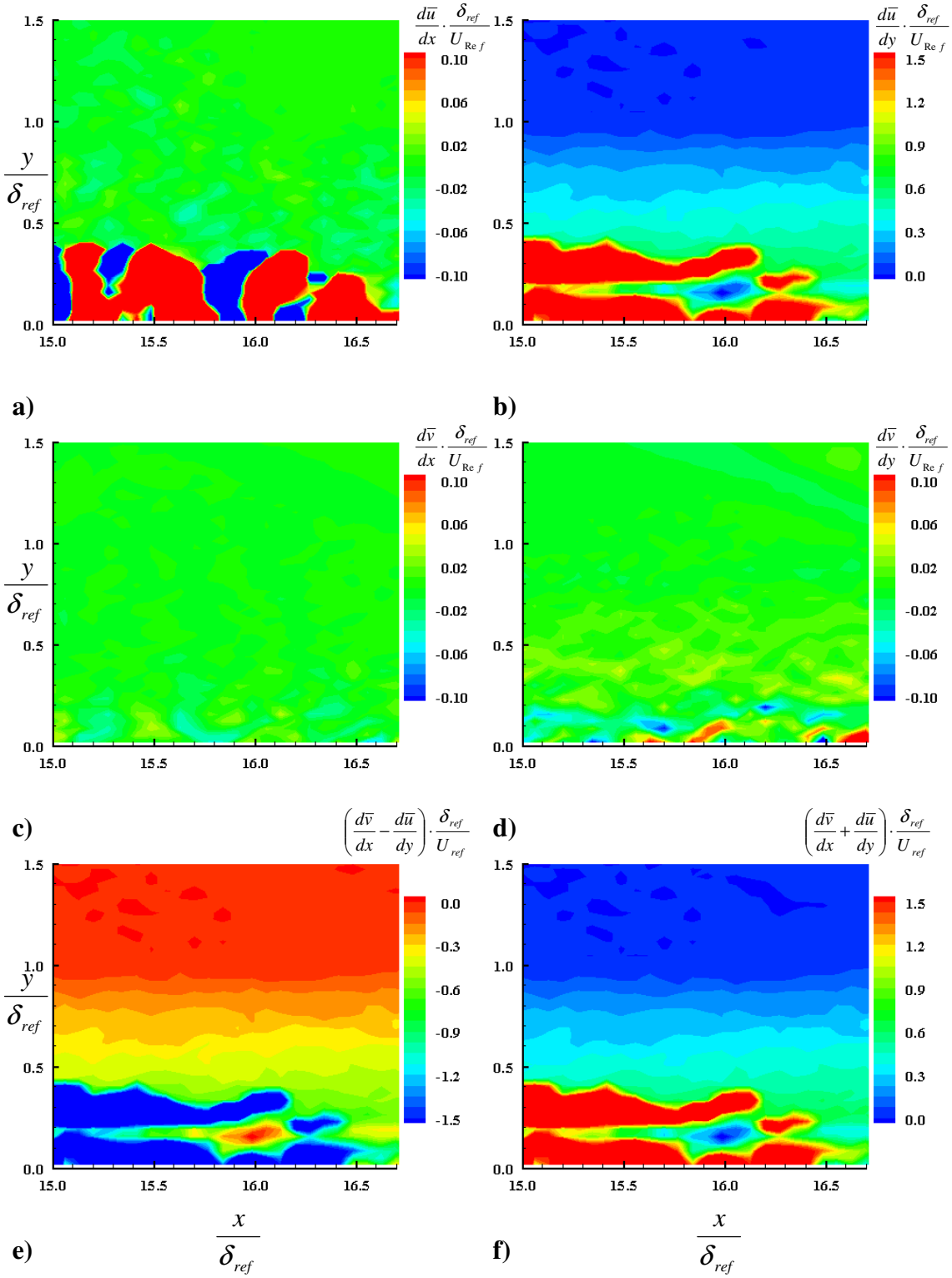

Figure 79: Velocity gradients of the SPG square roughness model at location 1

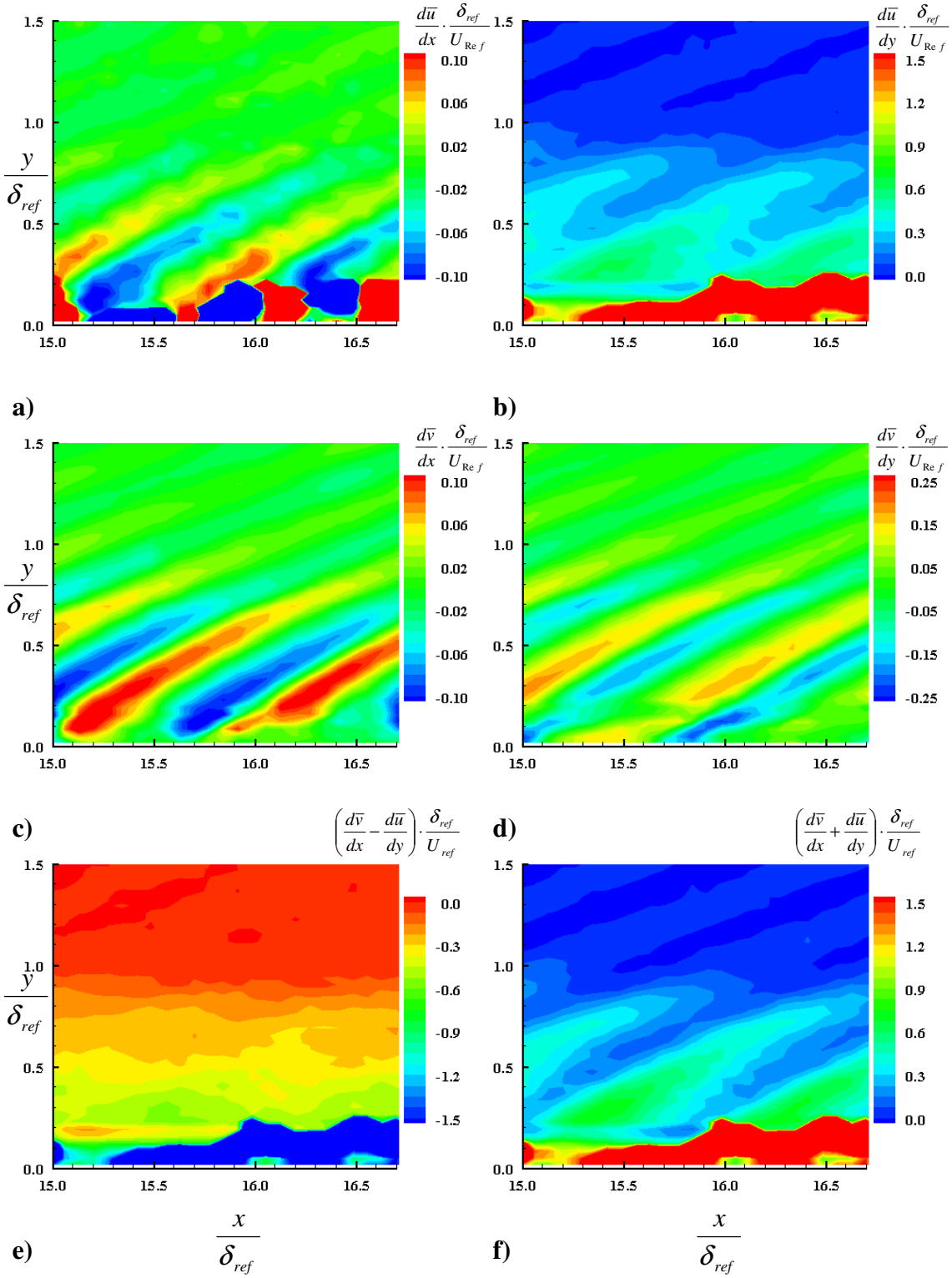

Figure 80: Velocity gradients of the SPG diamond roughness model at location 1

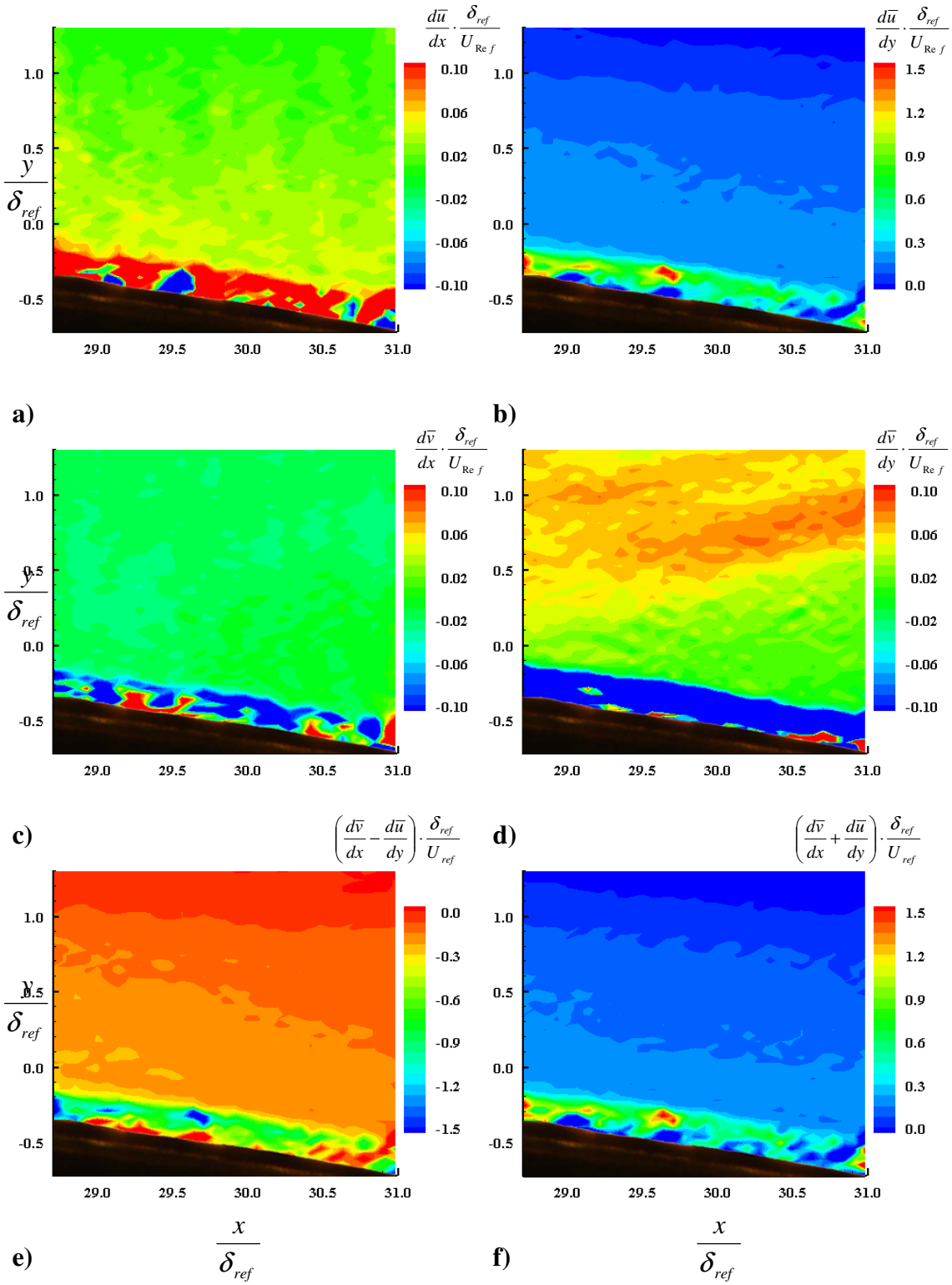

Figure 81: Velocity gradients of the SPG smooth wall model at location 2

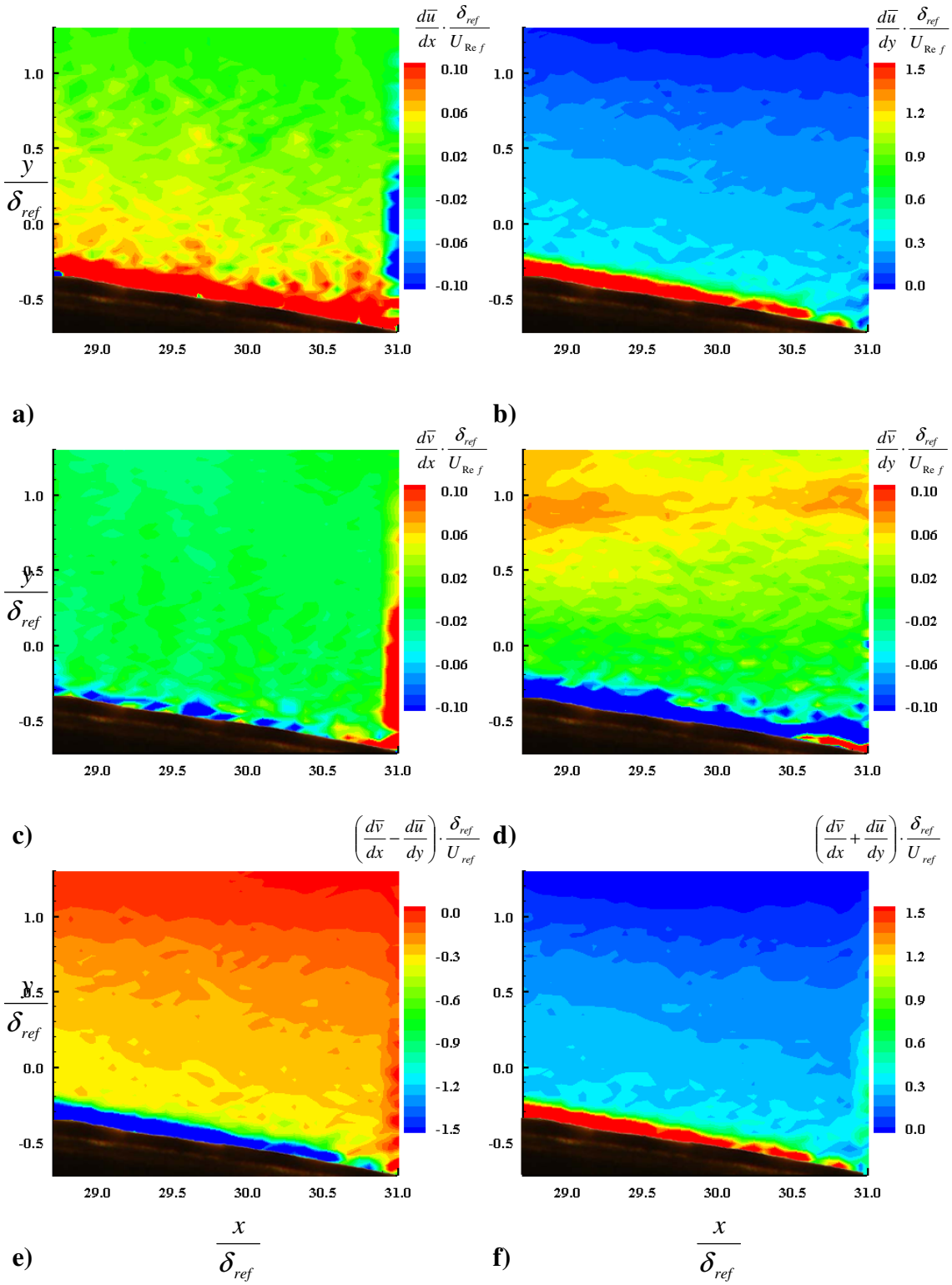

Figure 82: Velocity gradients of the SPG square roughness model at location 2

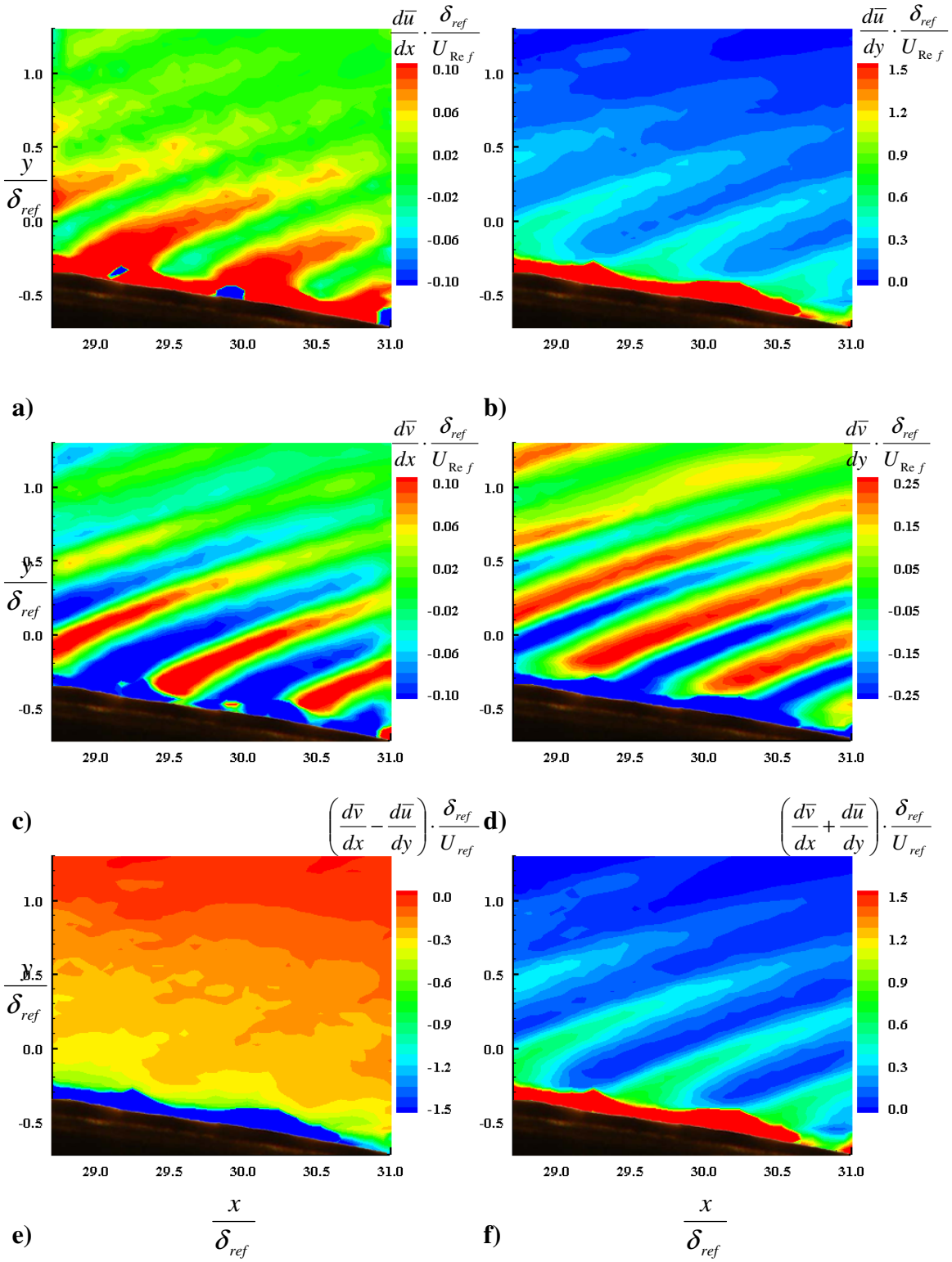

Figure 83: Velocity gradients of the SPG diamond roughness model at location 2

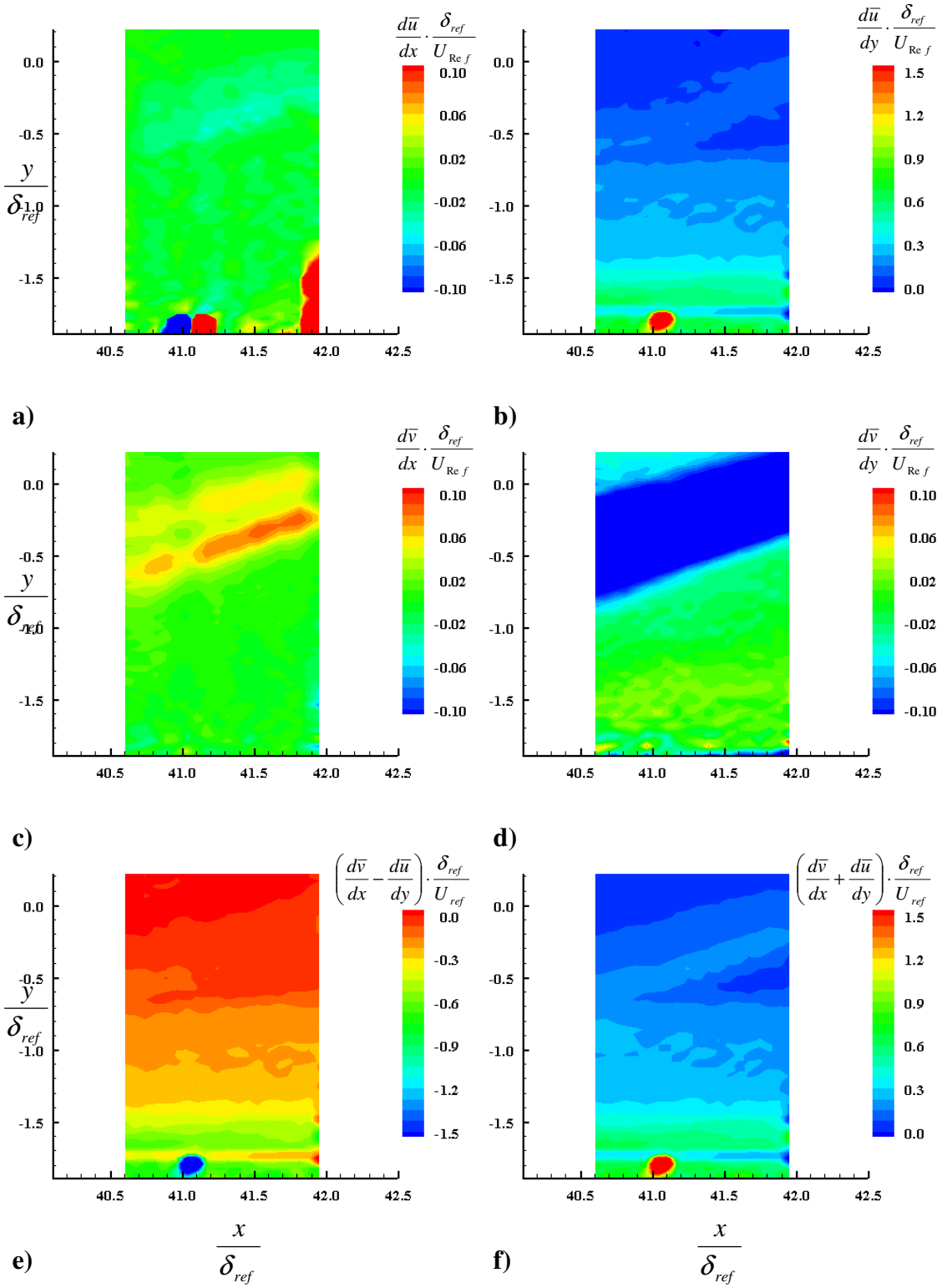

Figure 84: Velocity gradients of the SPG smooth wall model at location 3

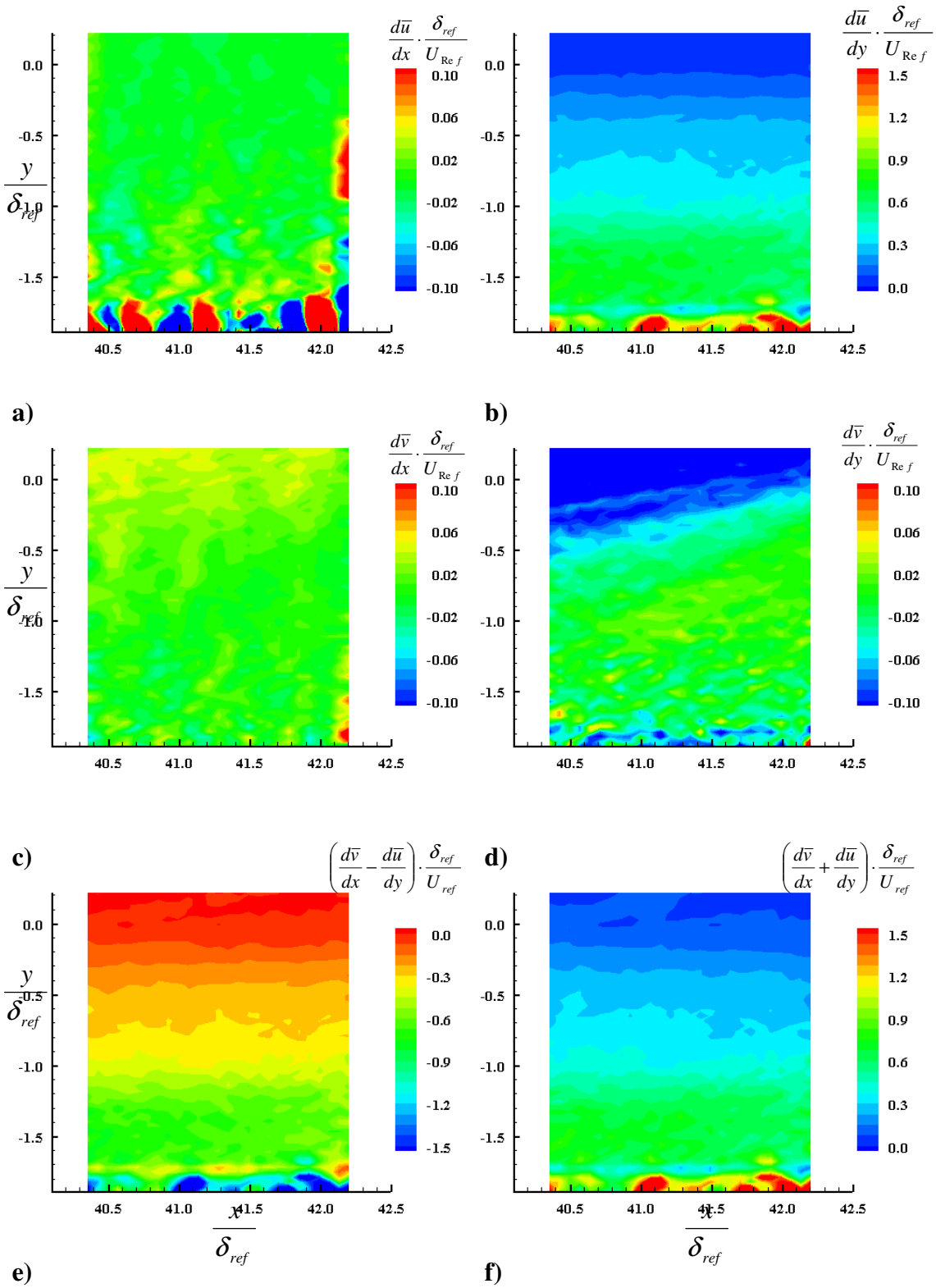

Figure 85: Velocity gradients of the SPG square roughness model at location 3

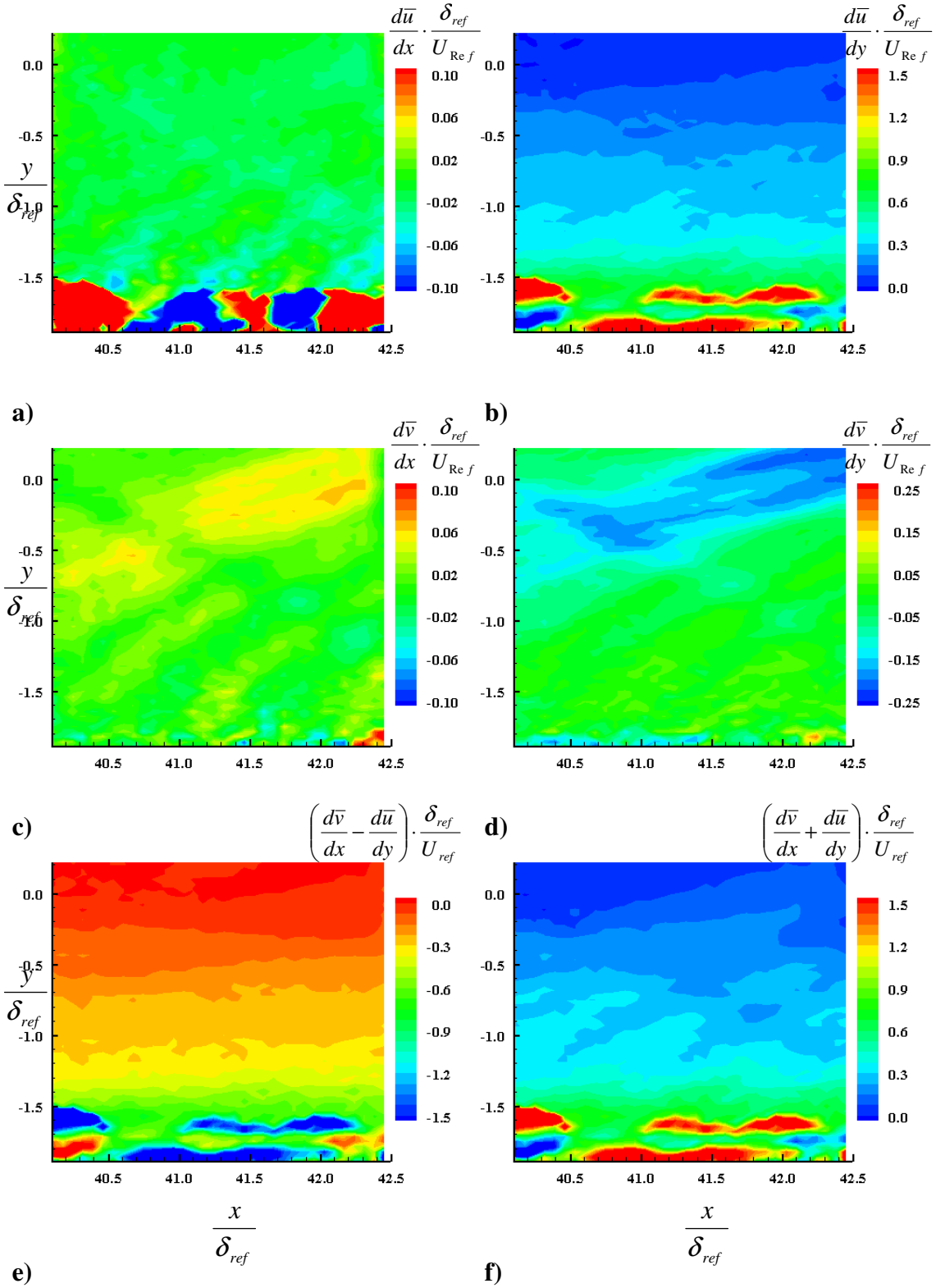

Figure 86: Velocity gradients of the SPG diamond roughness model at location 3

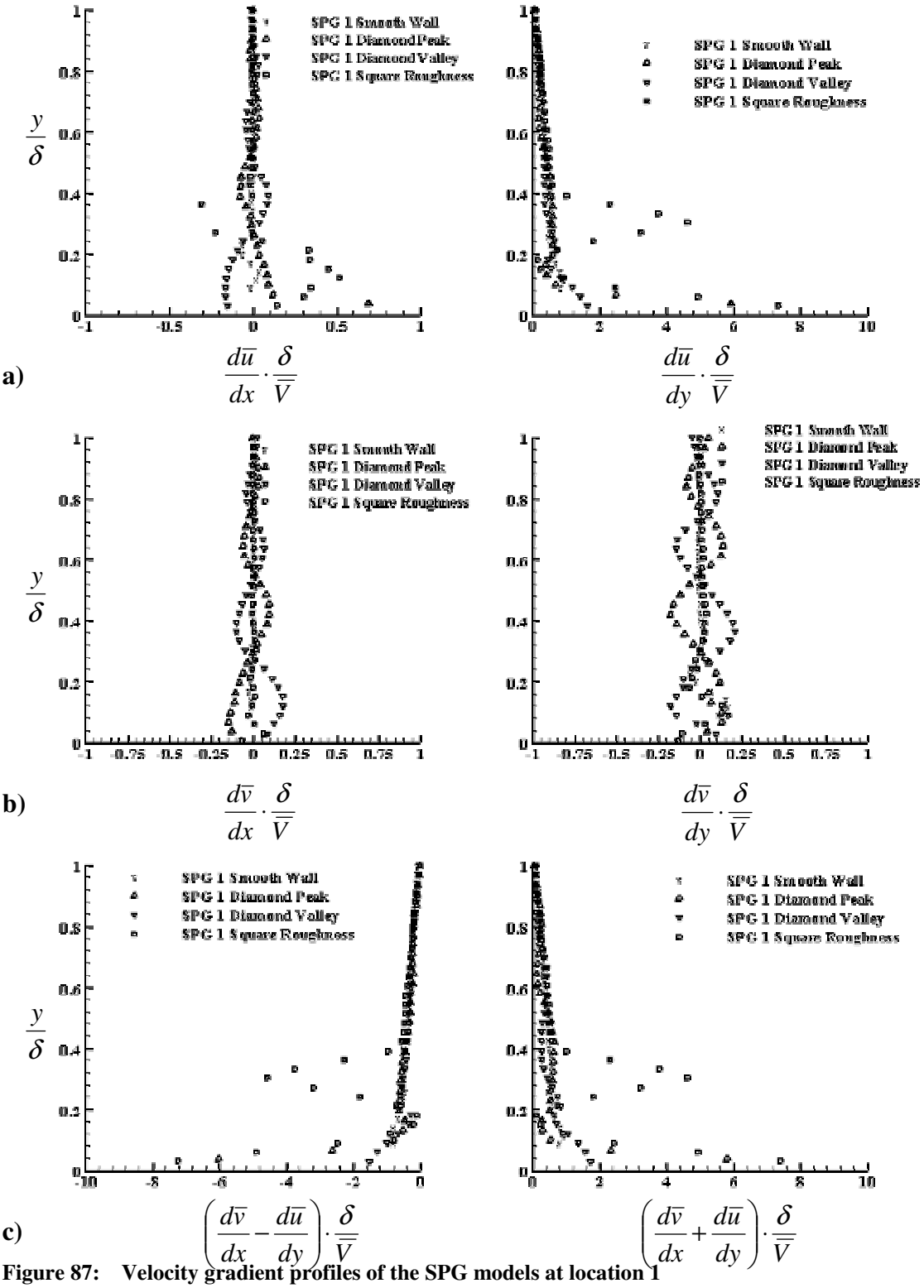

Figure 87: Velocity gradient profiles of the SPG models at location 1

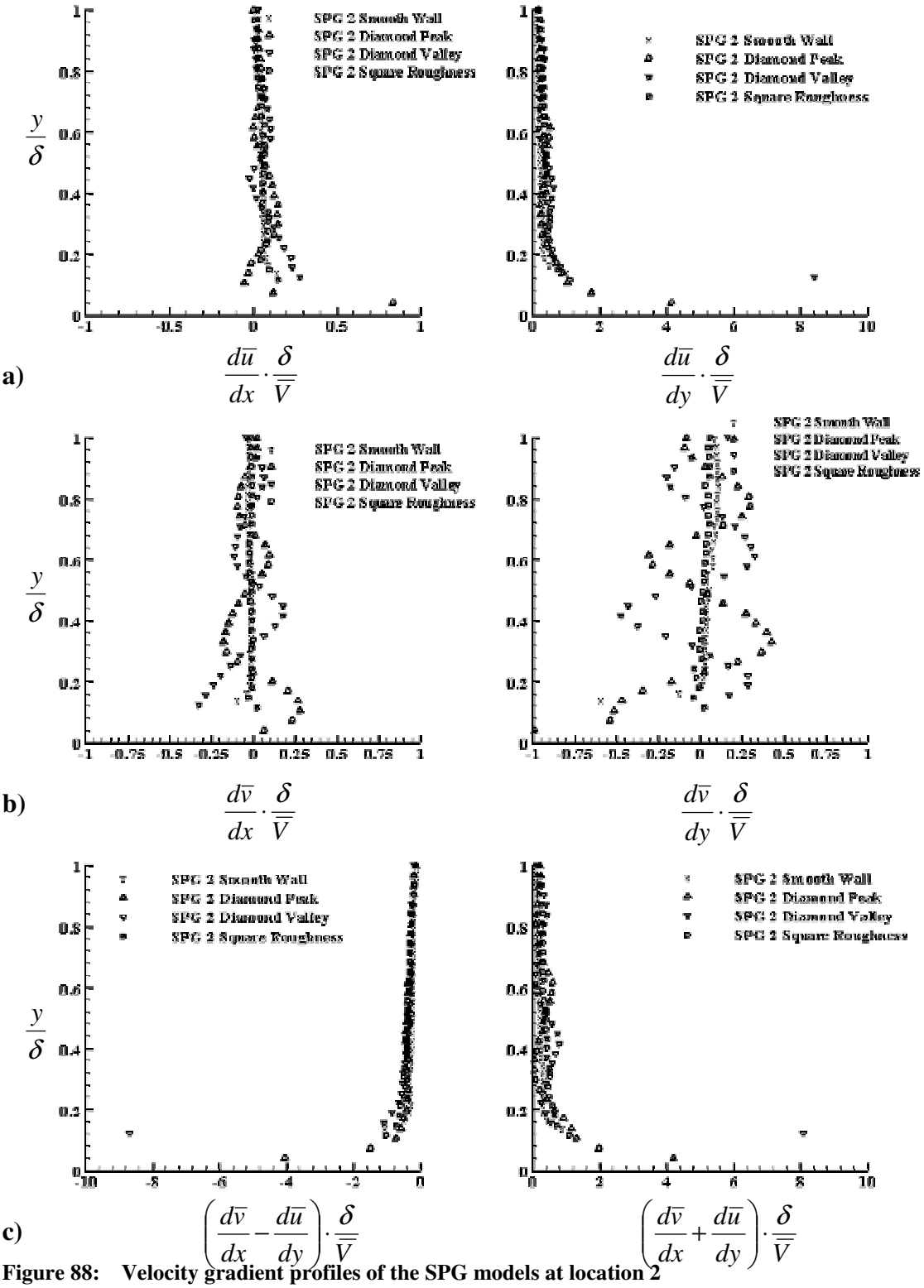

Figure 88: Velocity gradient profiles of the SPG models at location 2

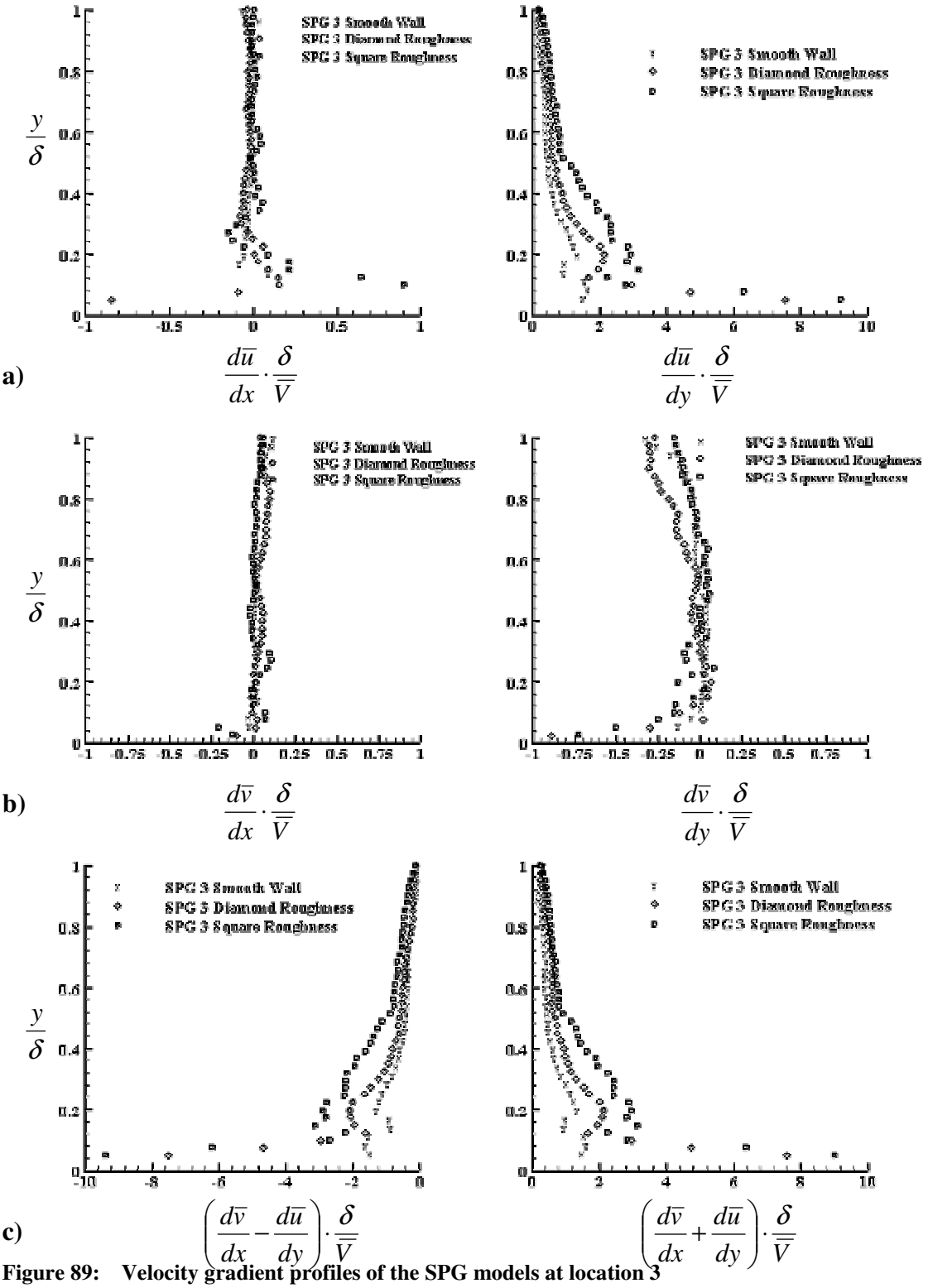

Figure 89: Velocity gradient profiles of the SPG models at location 3

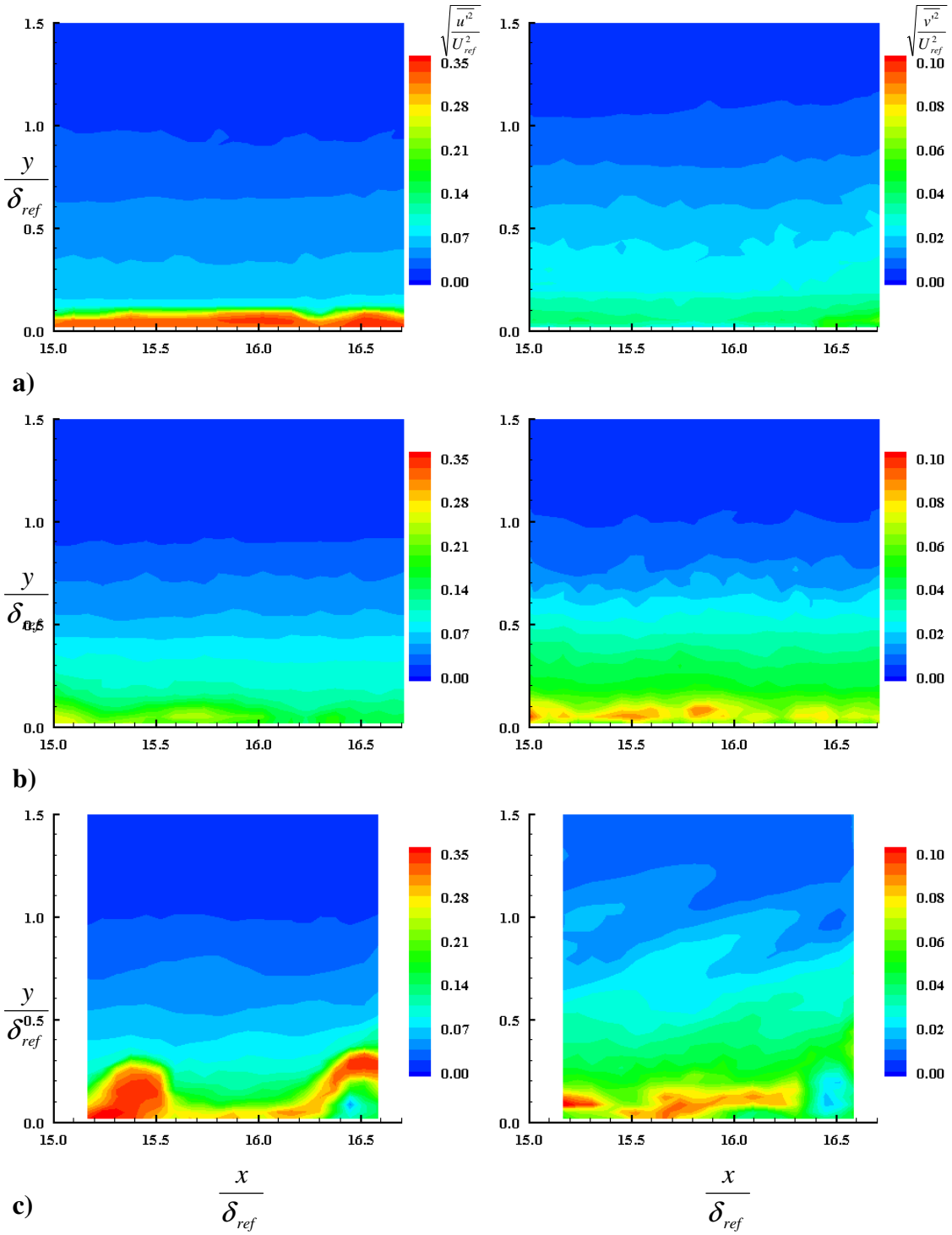

Figure 90: ZPG turbulence intensity at the 1st location for a) smooth, b) square, and c) diamond roughness

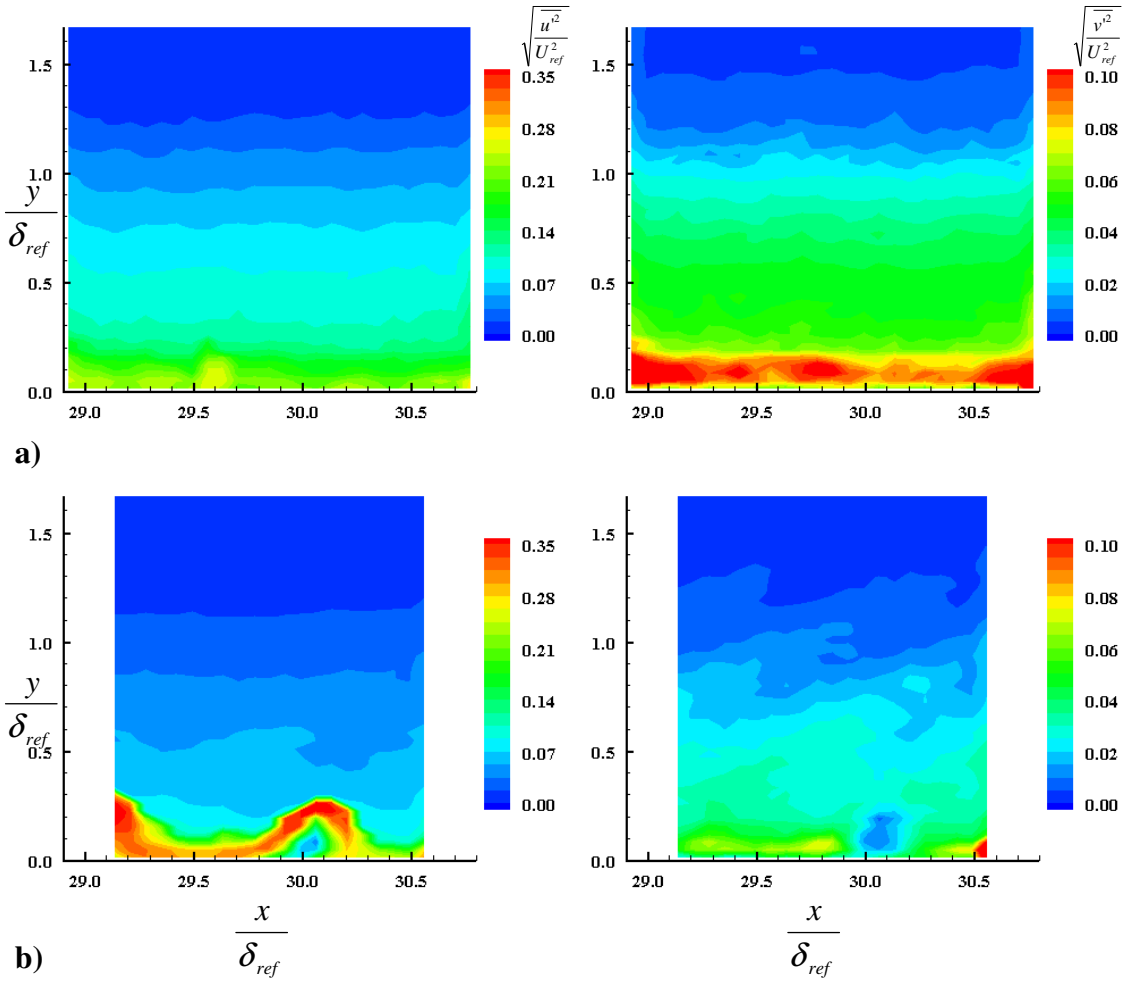

Figure 91: ZPG turbulence intensity at the 2nd location for a) square and b) diamond roughness

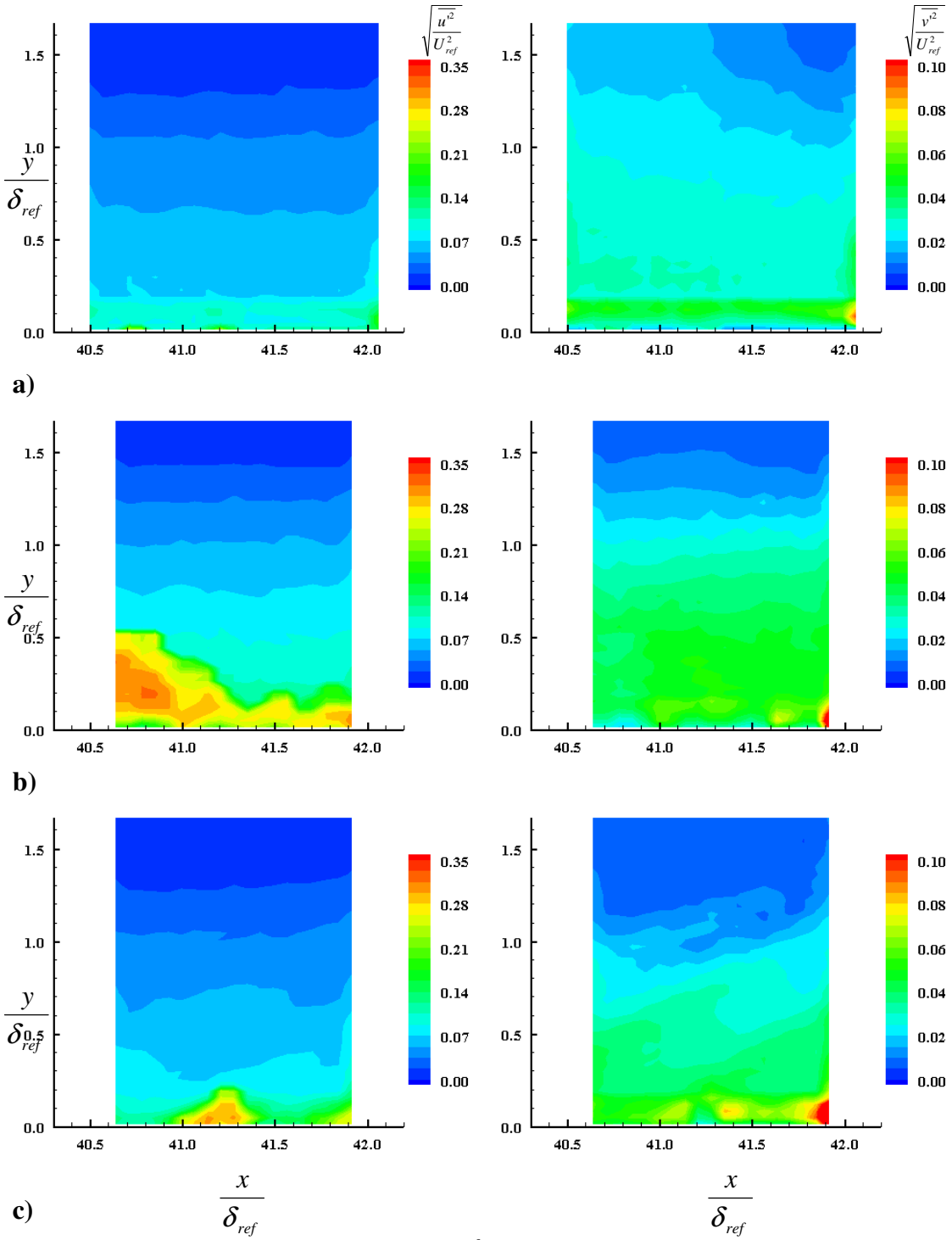

Figure 92: ZPG turbulence intensity at the 3rd location for a) smooth, b) square, and c) diamond roughness

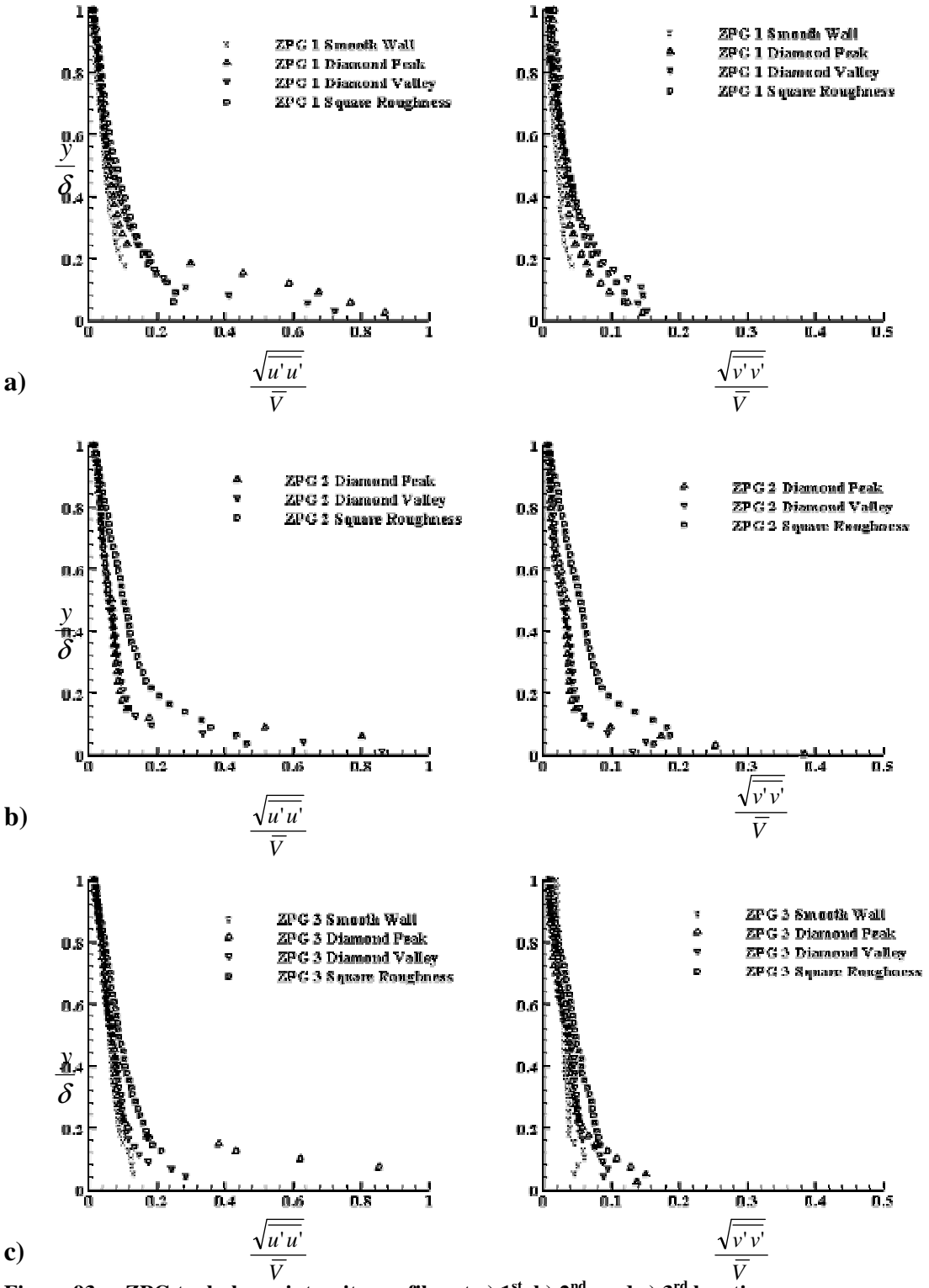

Figure 93: ZPG turbulence intensity profiles at a) 1st, b) 2nd, and c) 3rd locations

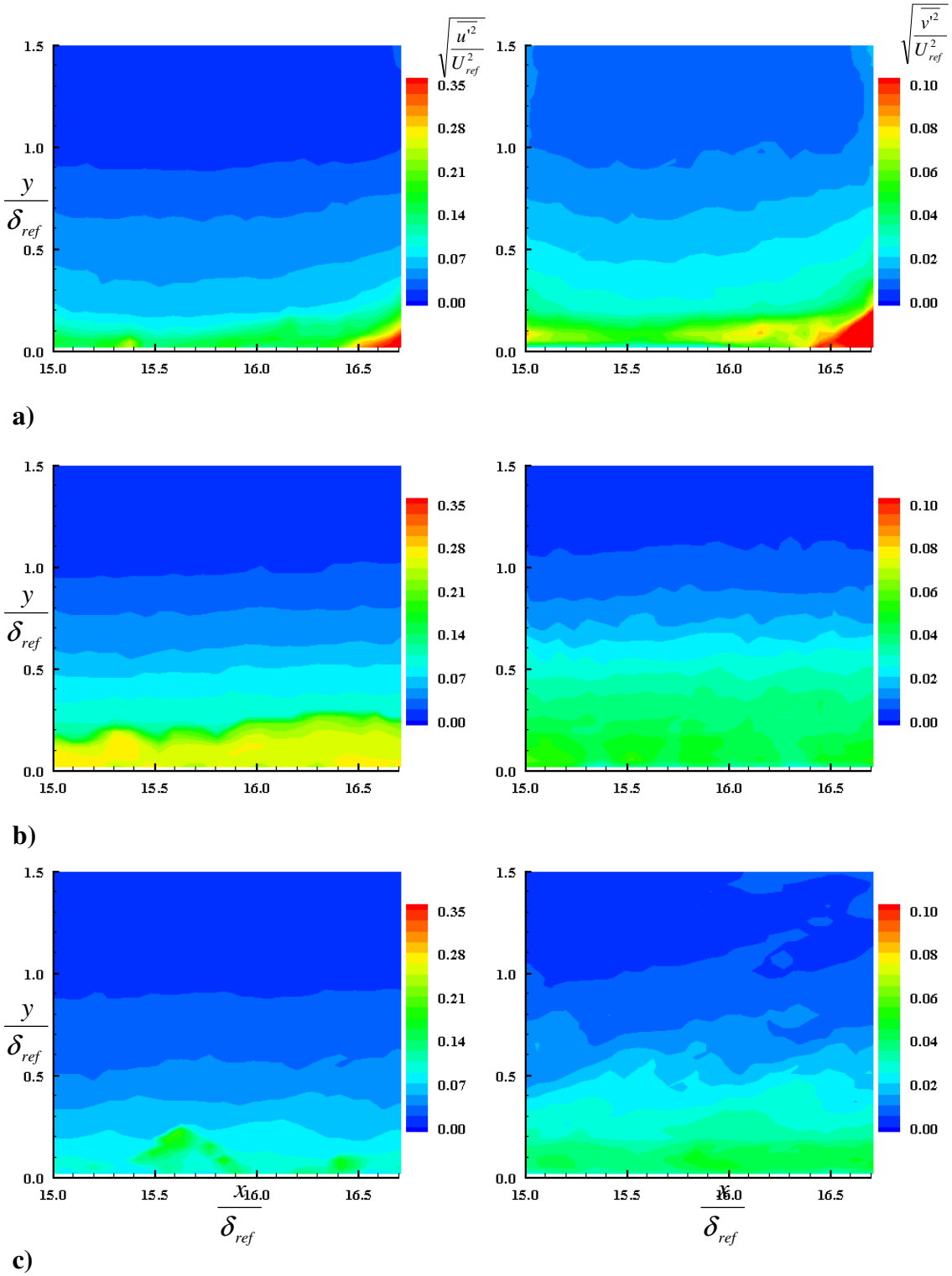

Figure 94: WPG turbulence intensity at the 1st location for a) smooth, b) square, and c) diamond roughness

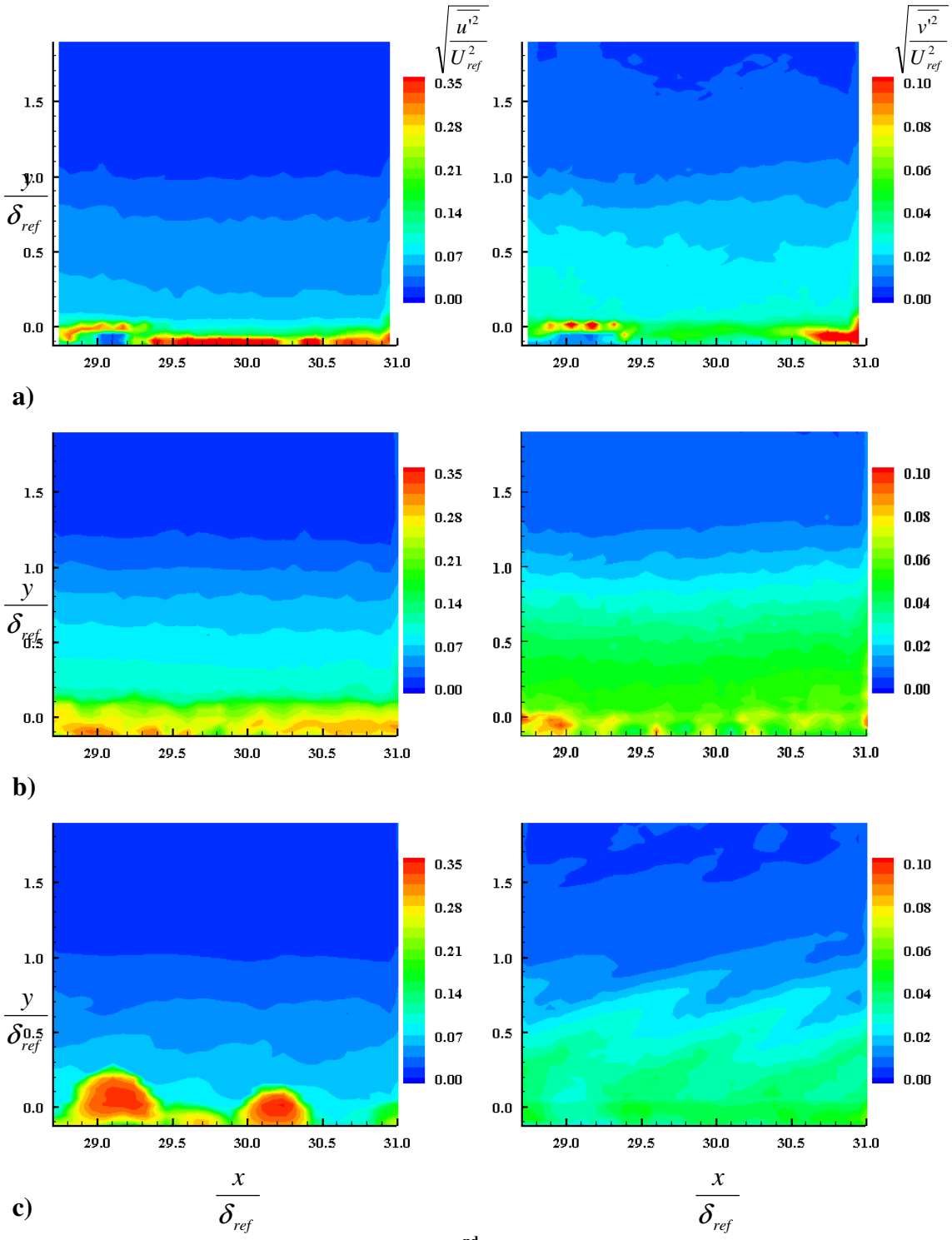

Figure 95: WPG turbulence intensity at the 2nd location for a) smooth, b) square, and c) diamond roughness

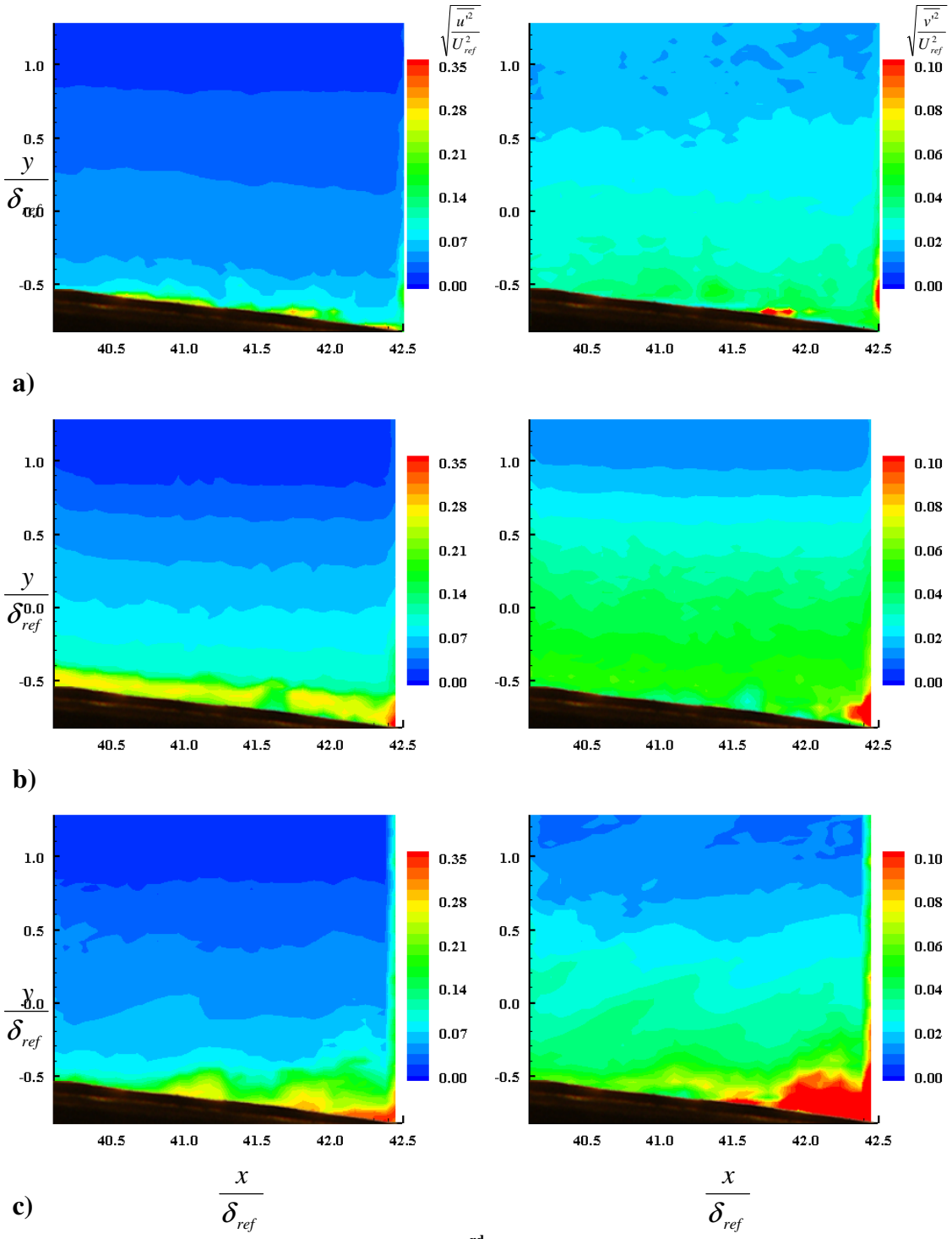

Figure 96: WPG turbulence intensity at the 3rd location for a) smooth, b) square, and c) diamond roughness

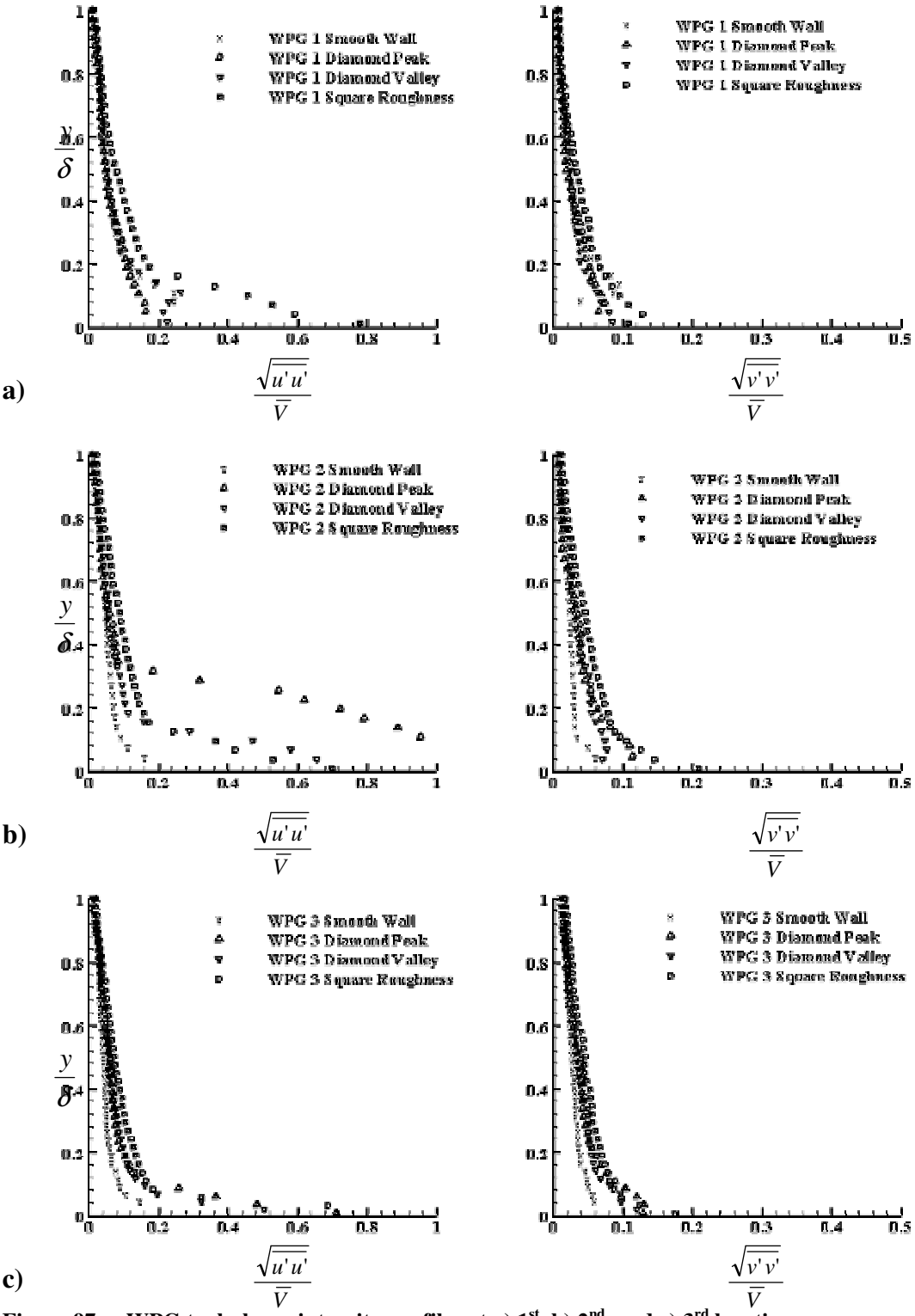

Figure 97: WPG turbulence intensity profiles at a) 1st, b) 2nd, and c) 3rd locations

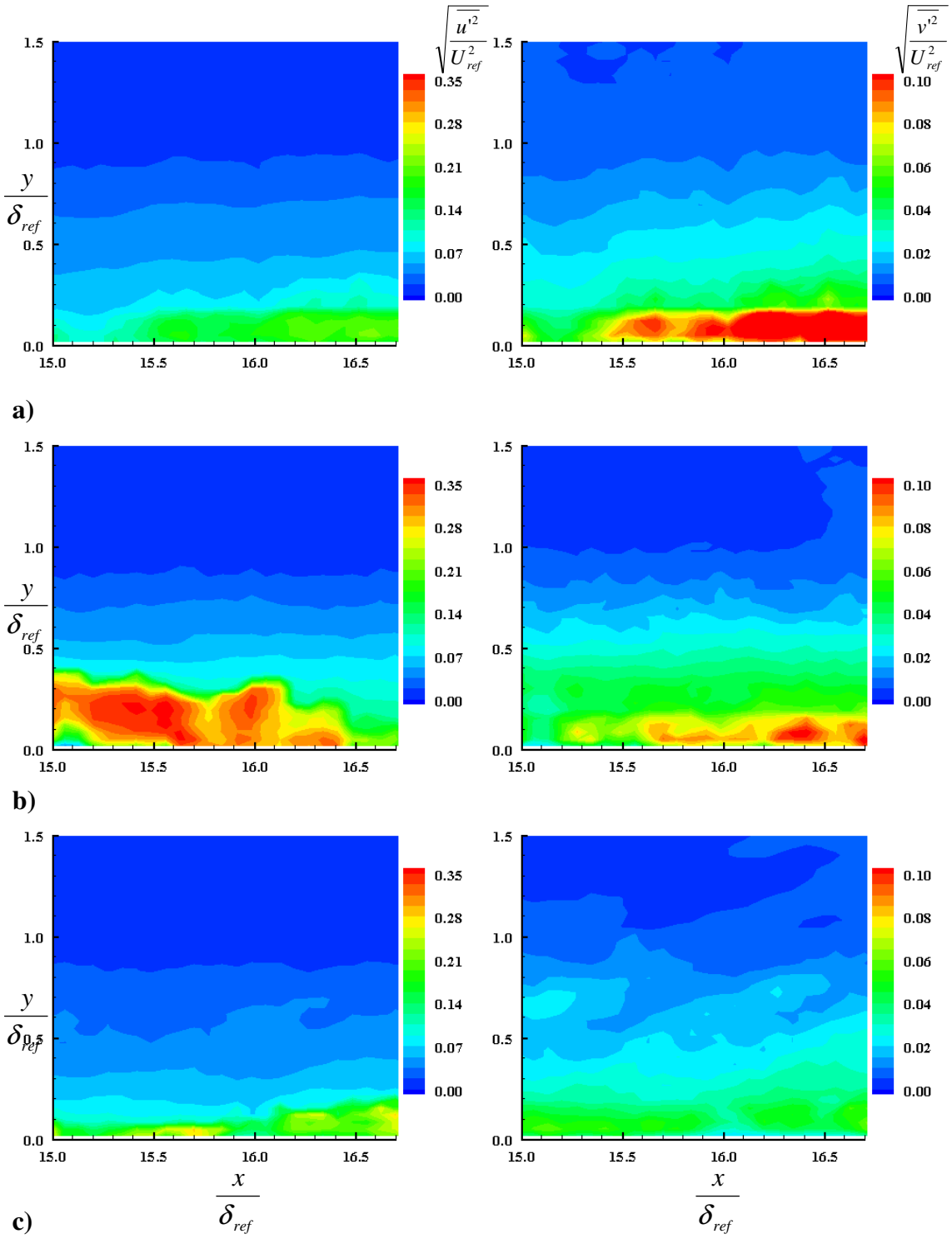

Figure 98: SPG turbulence intensity at the 1st location for a) smooth, b) square, and c) diamond roughness

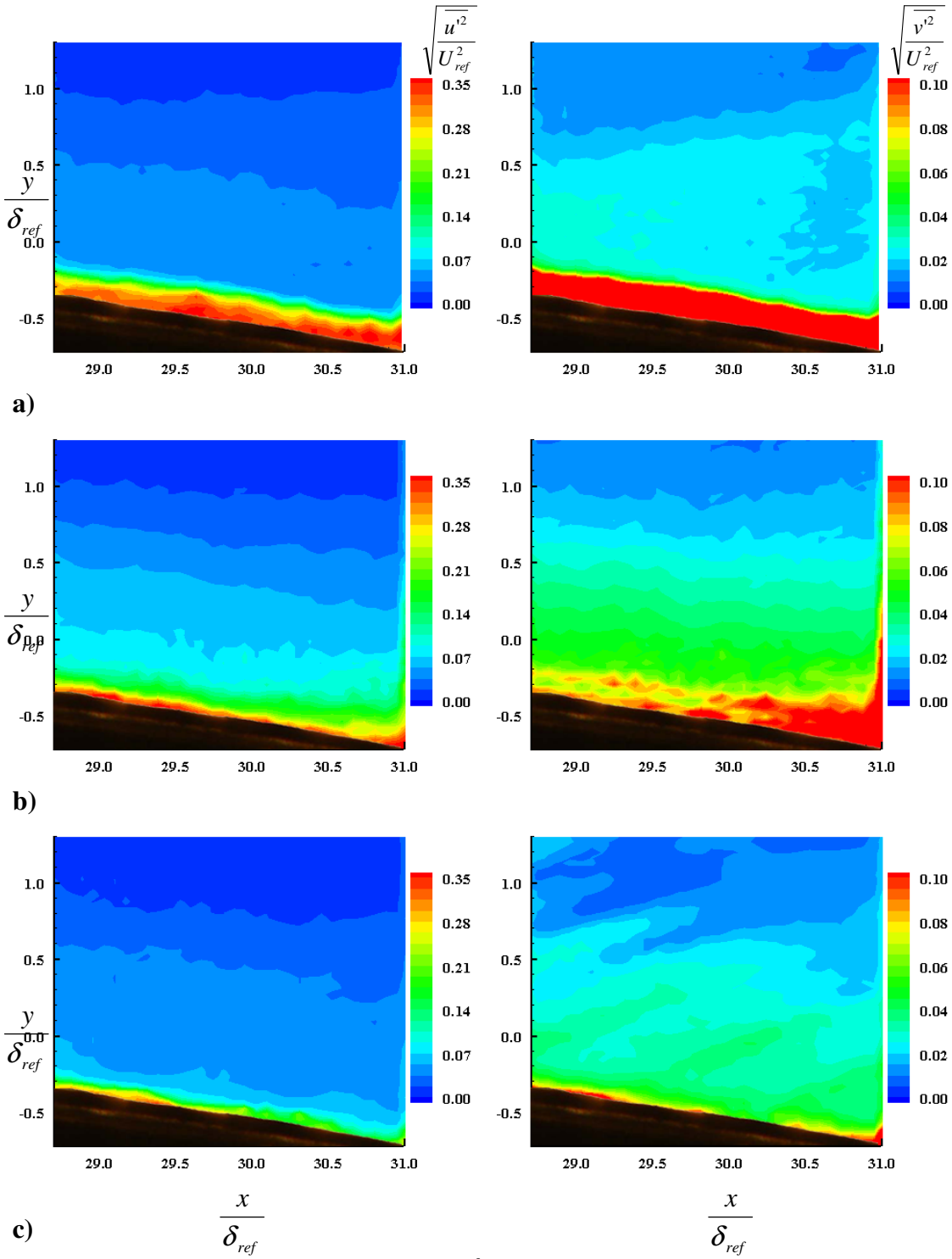

Figure 99: SPG turbulence intensity at the 2nd location for a) smooth, b) square, and c) diamond roughness

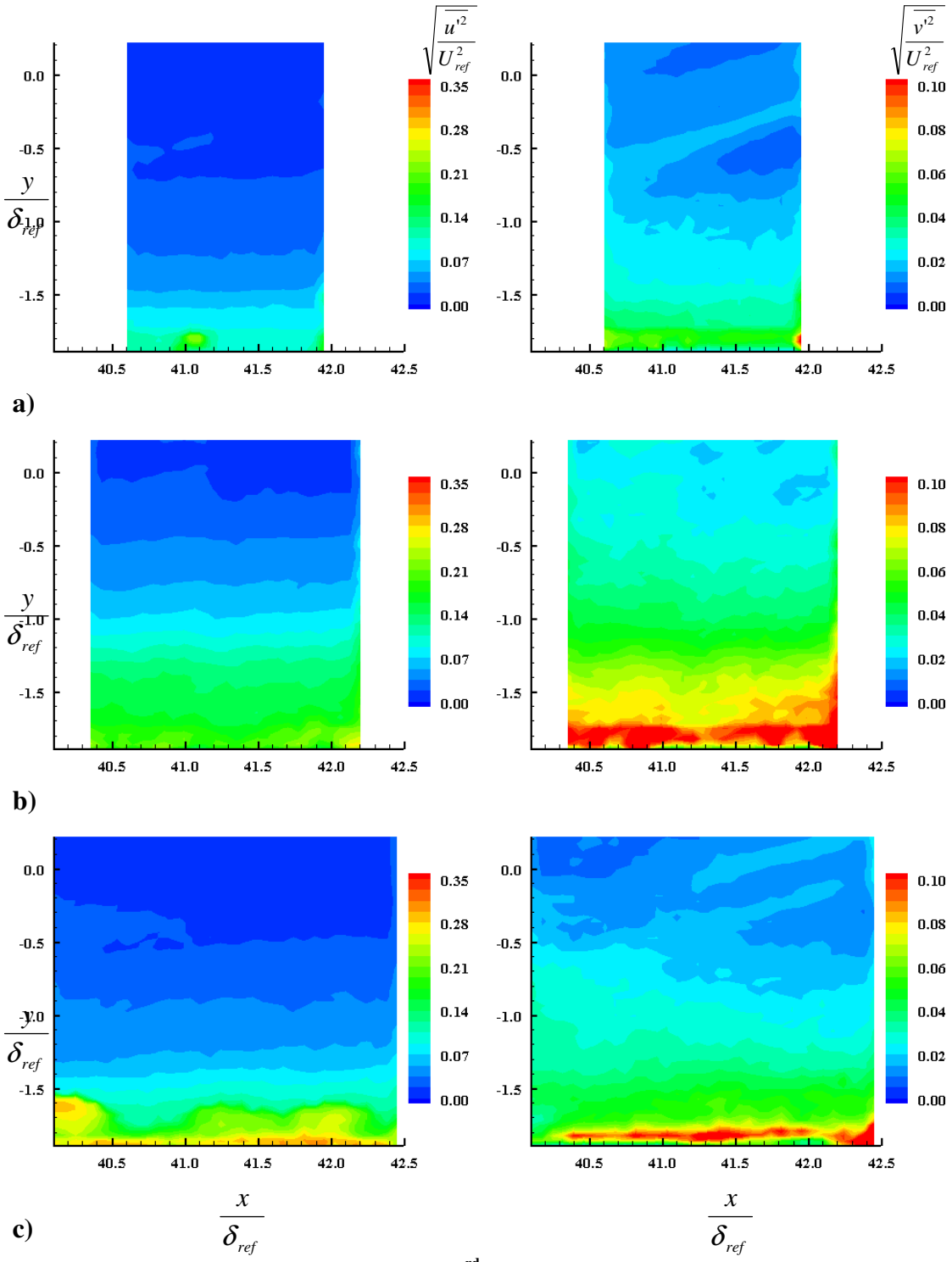

Figure 100: SPG turbulence intensity at the 3rd location for a) smooth, b) square, and c) diamond roughness

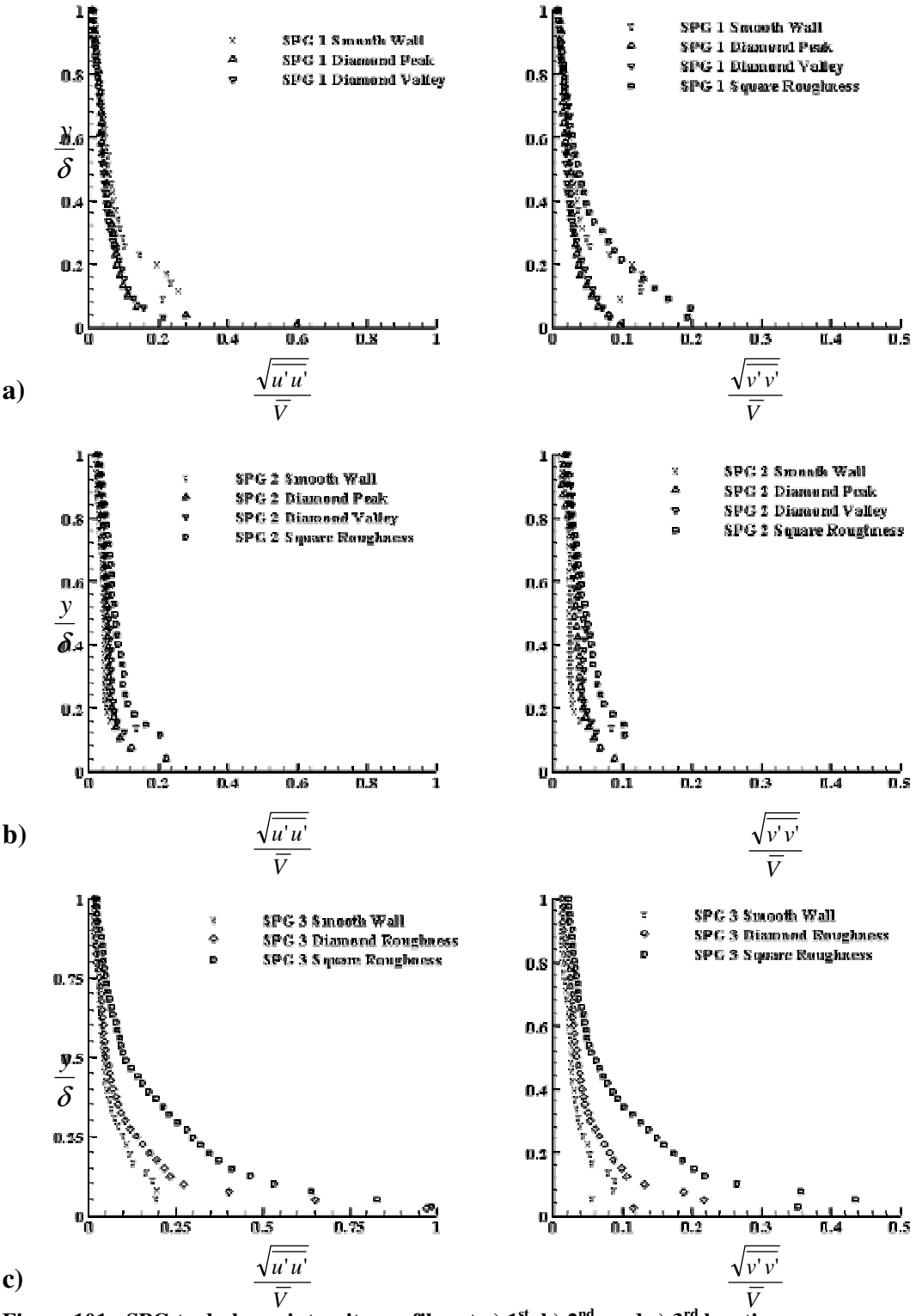

Figure 101: SPG turbulence intensity profiles at a) 1st, b) 2nd, and c) 3rd locations

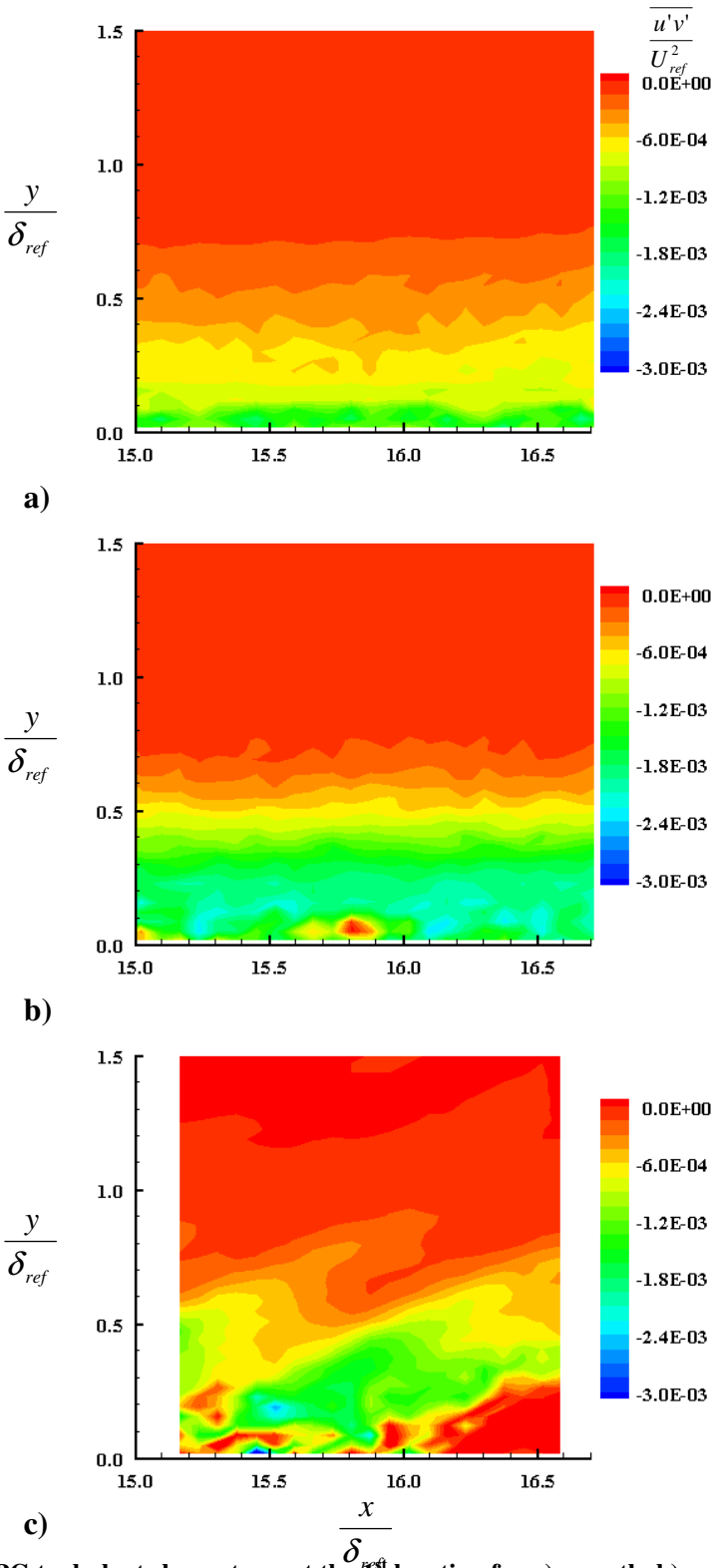

Figure 102: ZPG turbulent shear stress at the 1st location for a) smooth, b) square, and c) diamond roughness

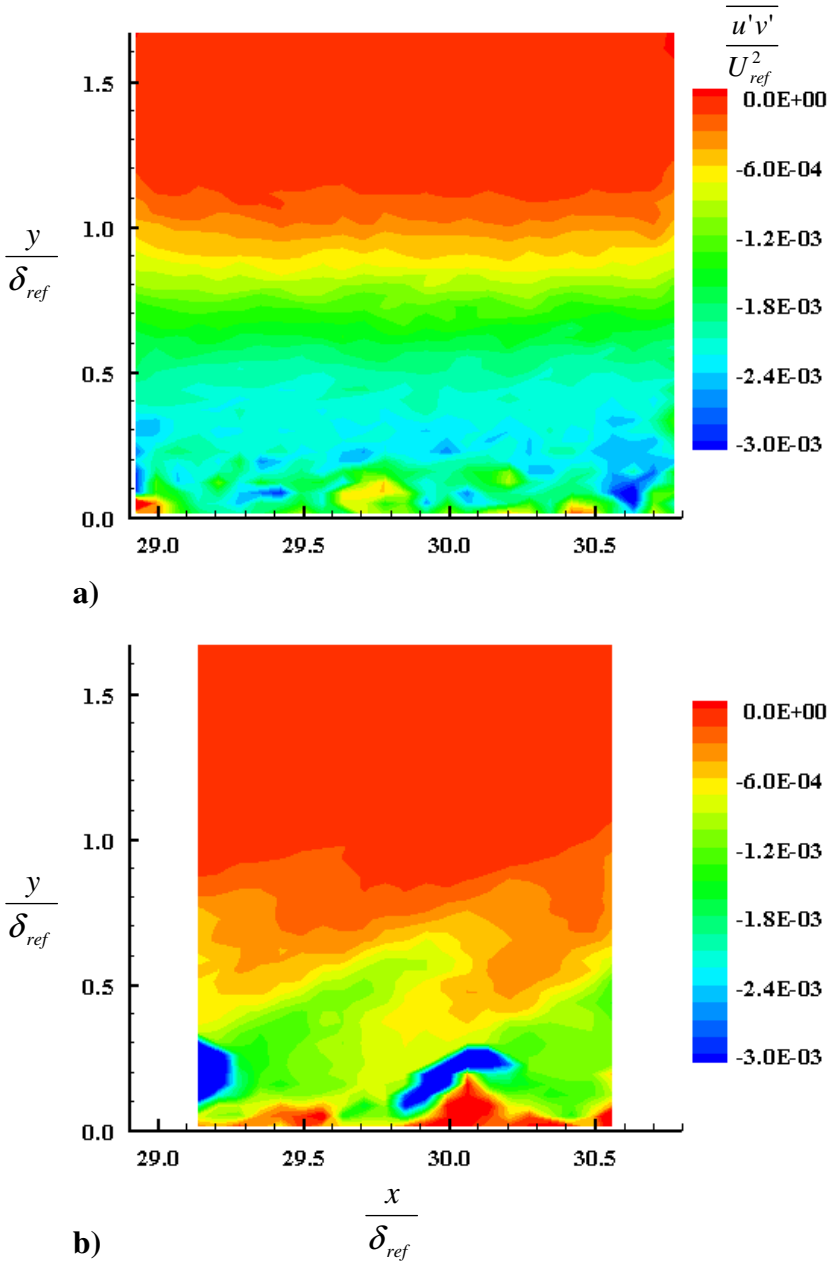

Figure 103: ZPG turbulent shear stress at the 2nd location for a) square and b) diamond roughness

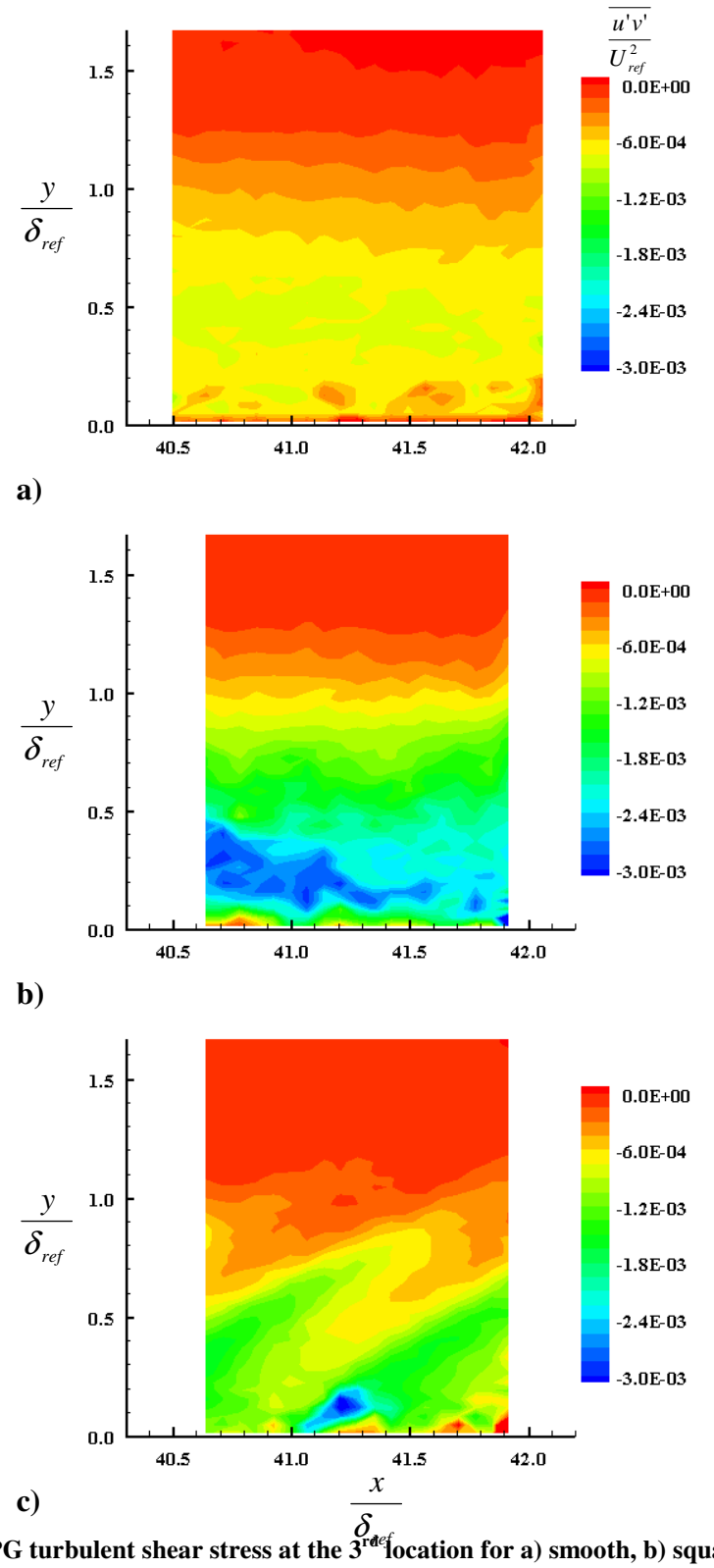

Figure 104: ZPG turbulent shear stress at the 3rd location for a) smooth, b) square, and c) diamond roughness

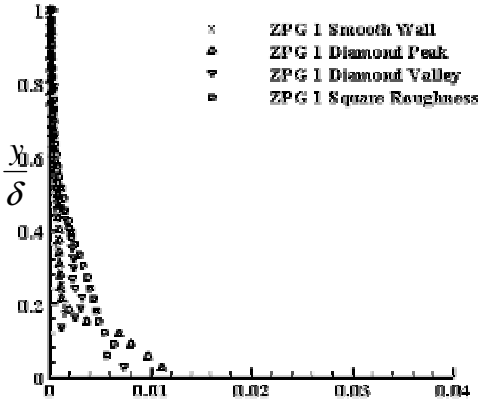

a)

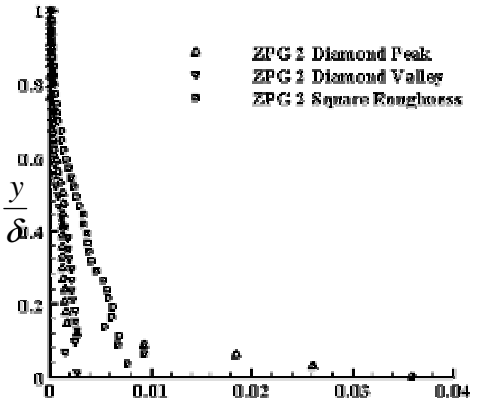

b)

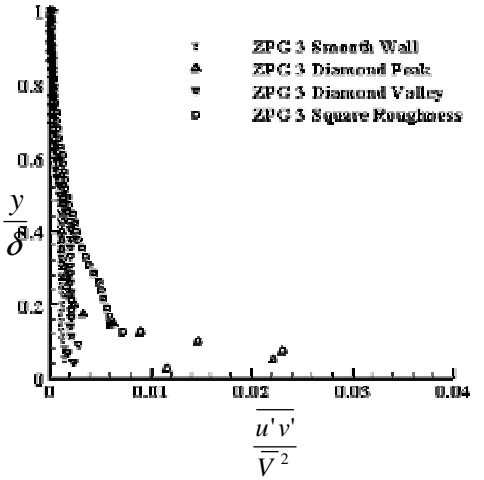

c)

Figure 105: ZPG turbulent shear stress at the a) 1st, b) 2nd, and c) 3rd locations

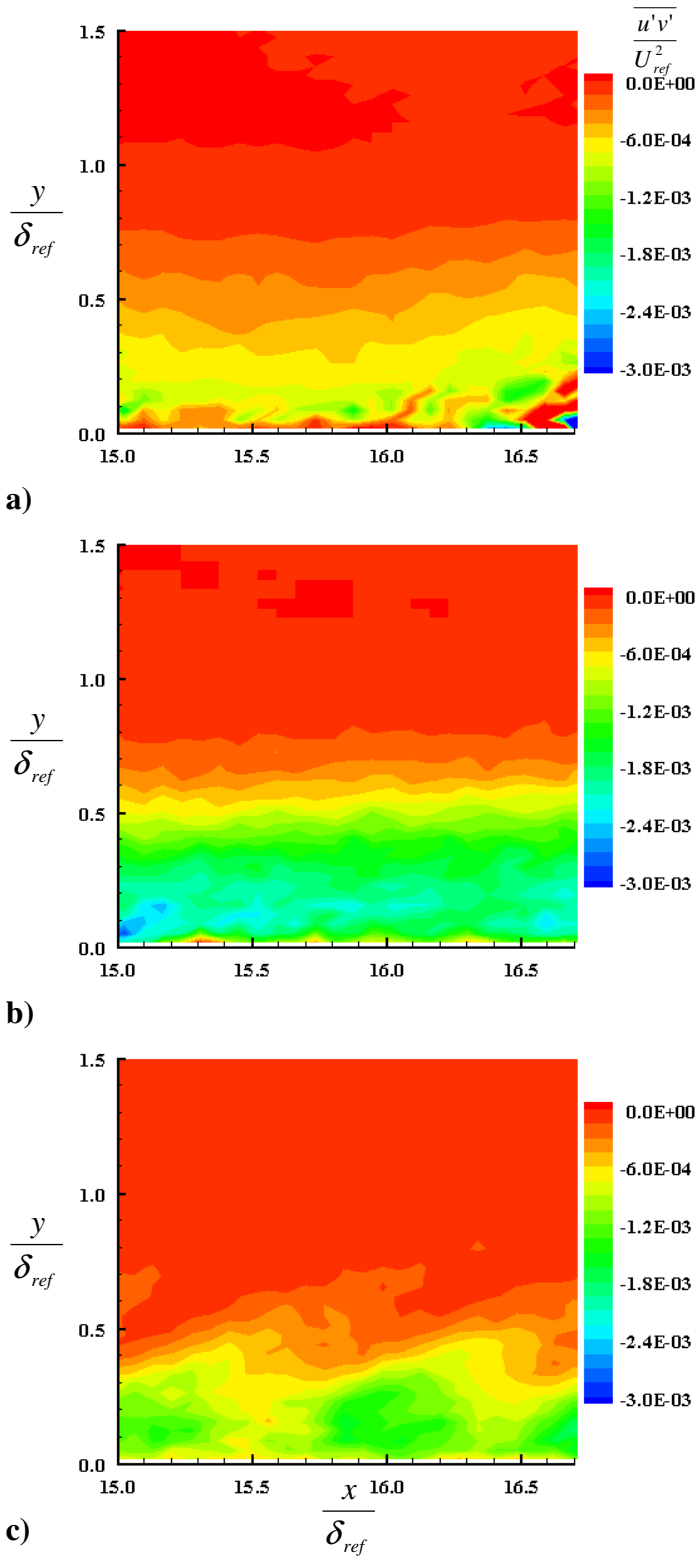

Figure 106: WPG turbulent shear stress at the 1st location for a) smooth, b) square, and c) diamond roughness

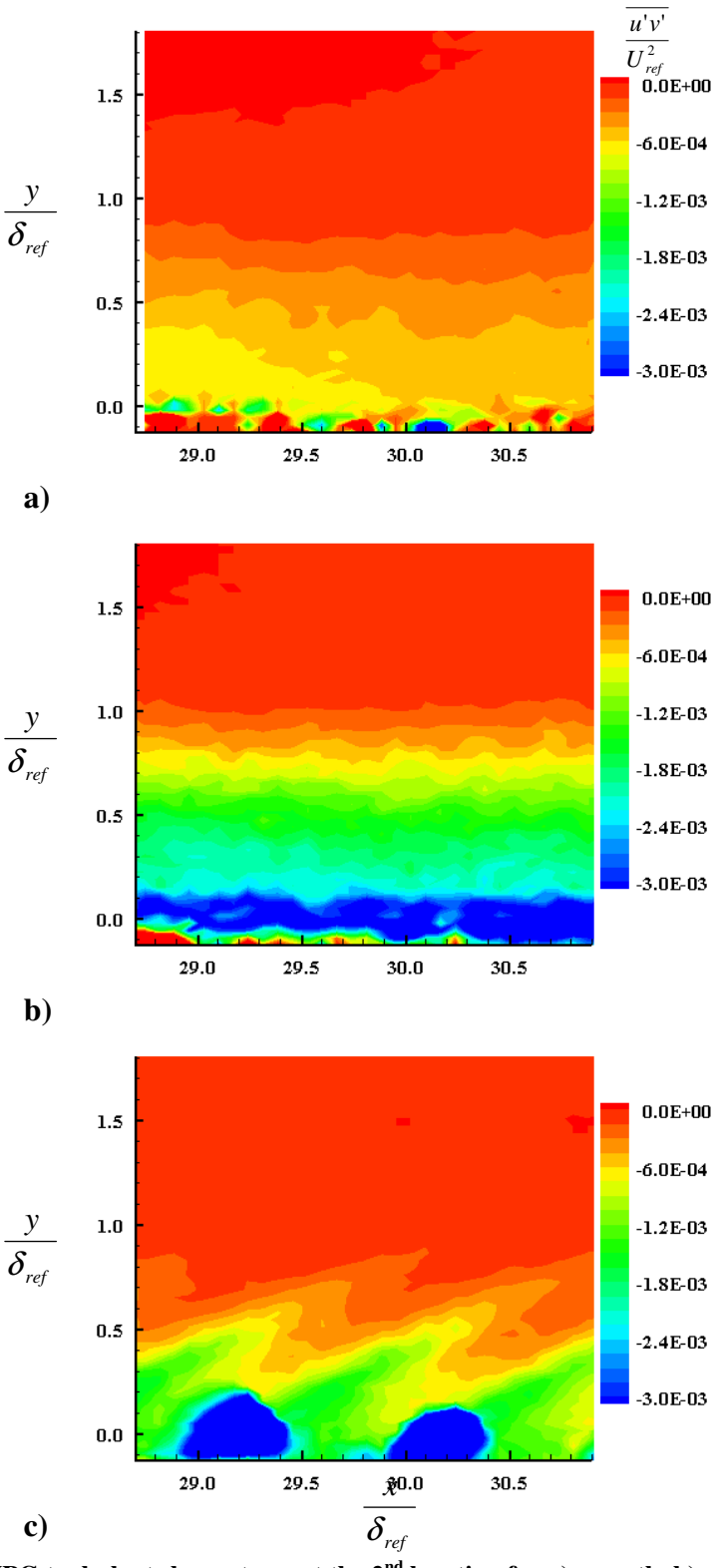

Figure 107: WPG turbulent shear stress at the 2nd location for a) smooth, b) square, and c) diamond roughness

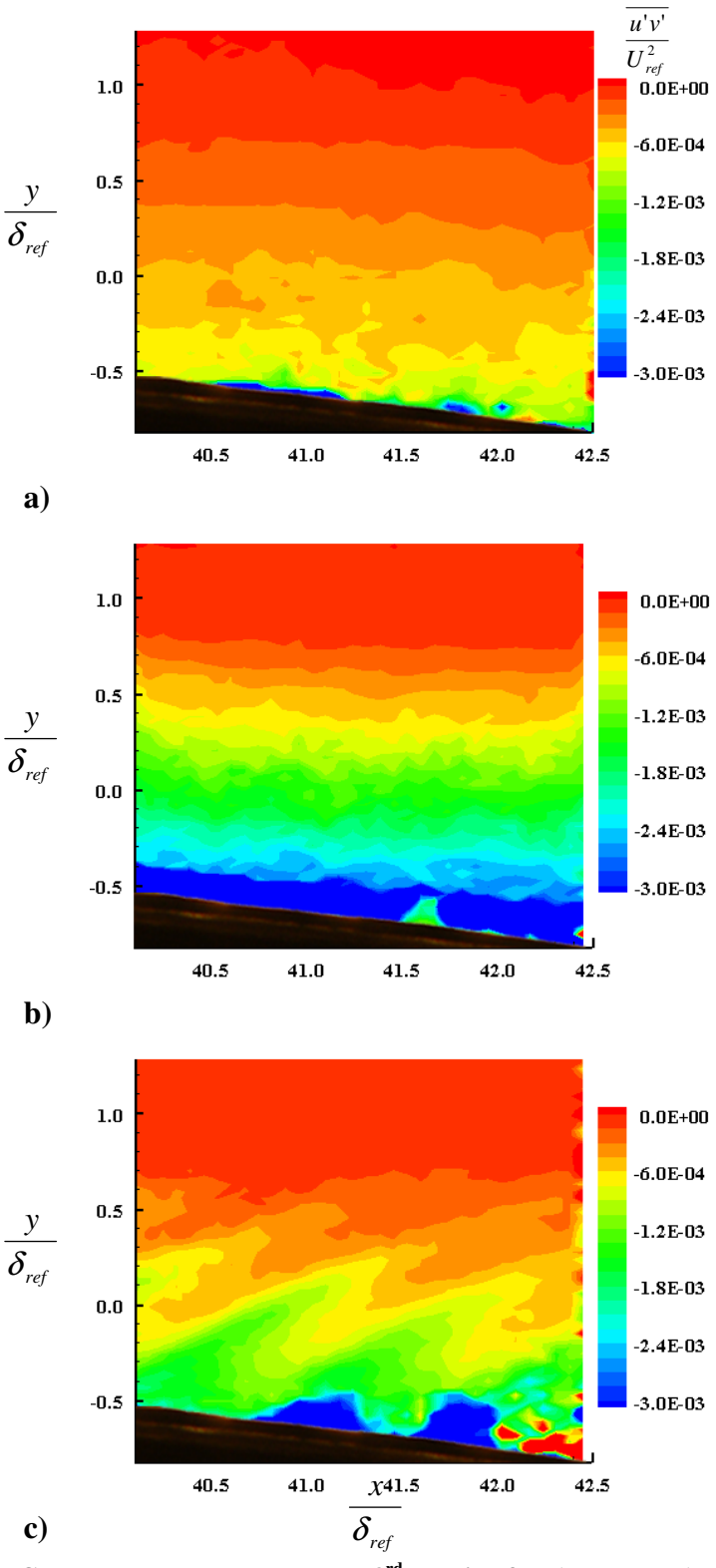

Figure 108: WPG turbulent shear stress at the 3rd location for a) smooth, b) square, and c) diamond roughness

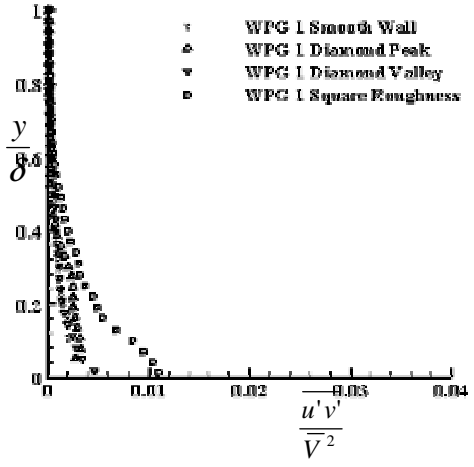

a)

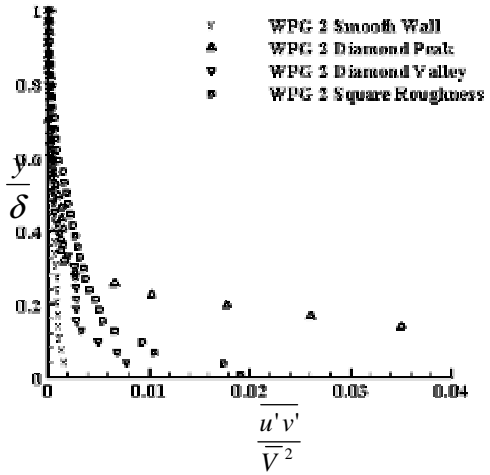

b)

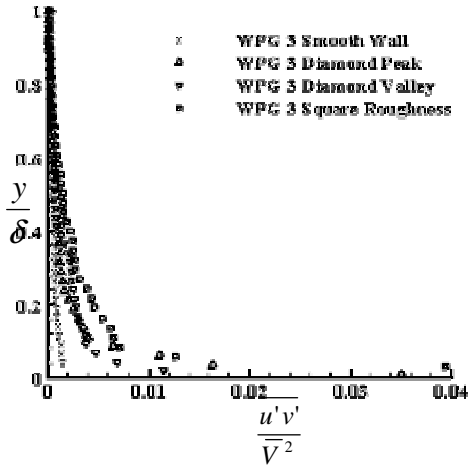

c)

Figure 109: WPG turbulent shear stress at the a) 1st, b) 2nd, and c) 3rd locations

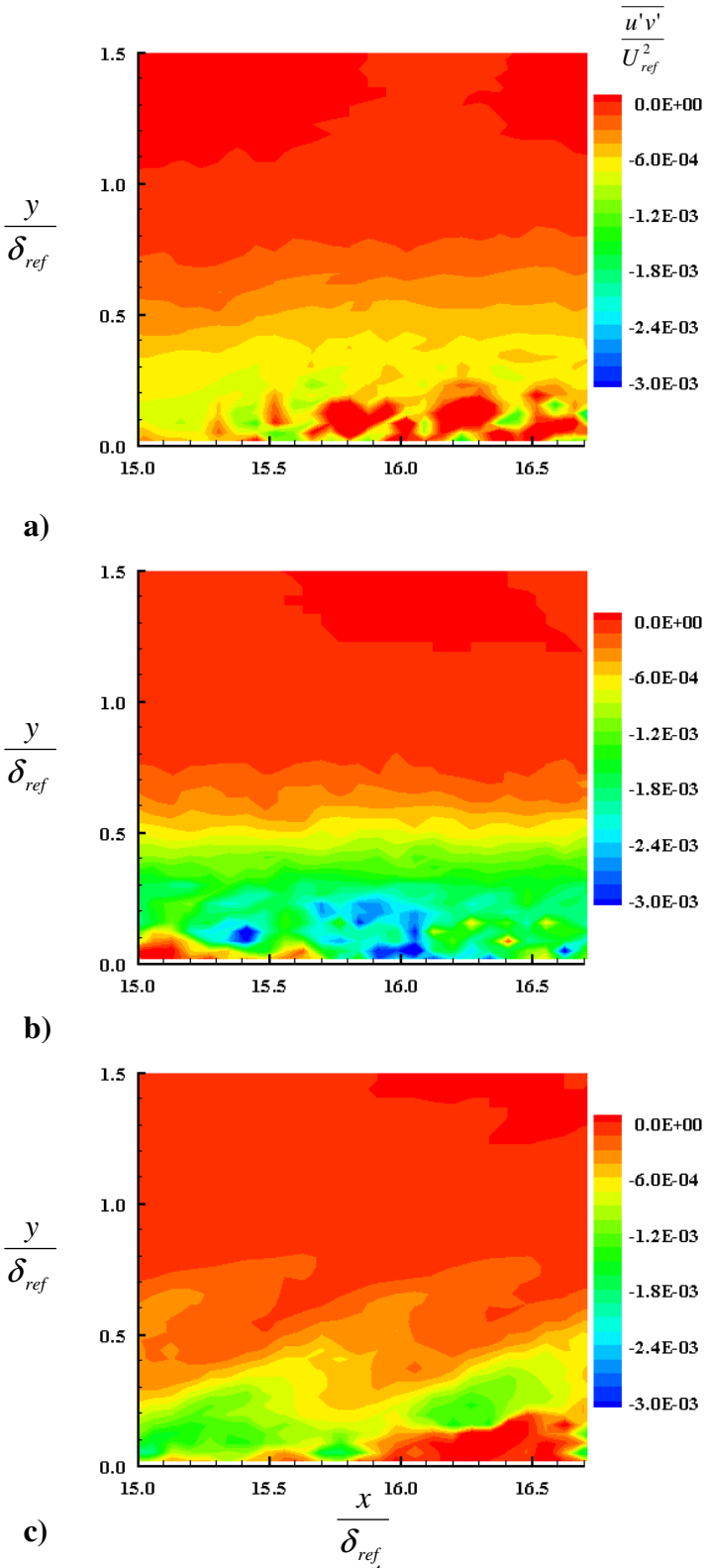

Figure 110: SPG turbulent shear stress at the 1st location for a) smooth, b) square, and c) diamond roughness

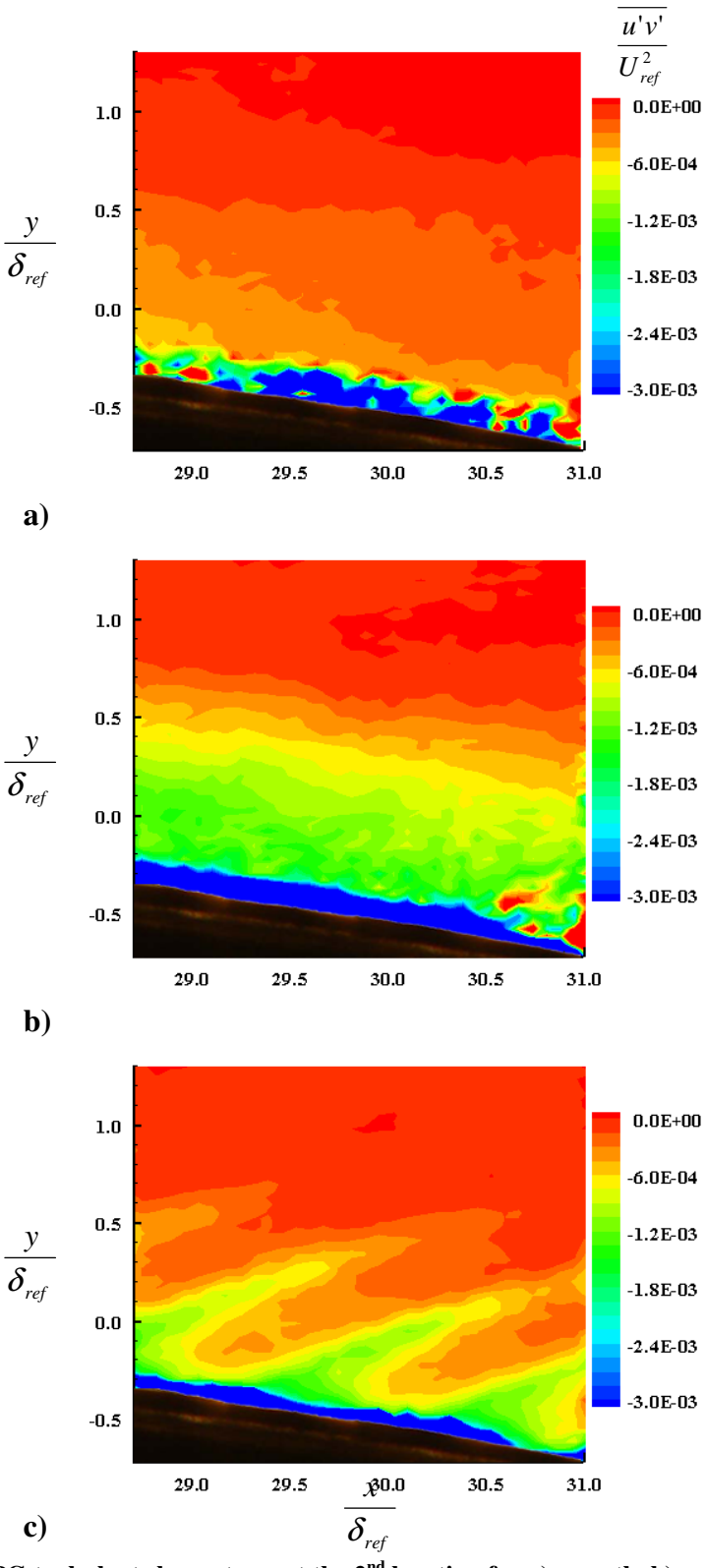

Figure 111: SPG turbulent shear stress at the 2nd location for a) smooth, b) square, and c) diamond roughness

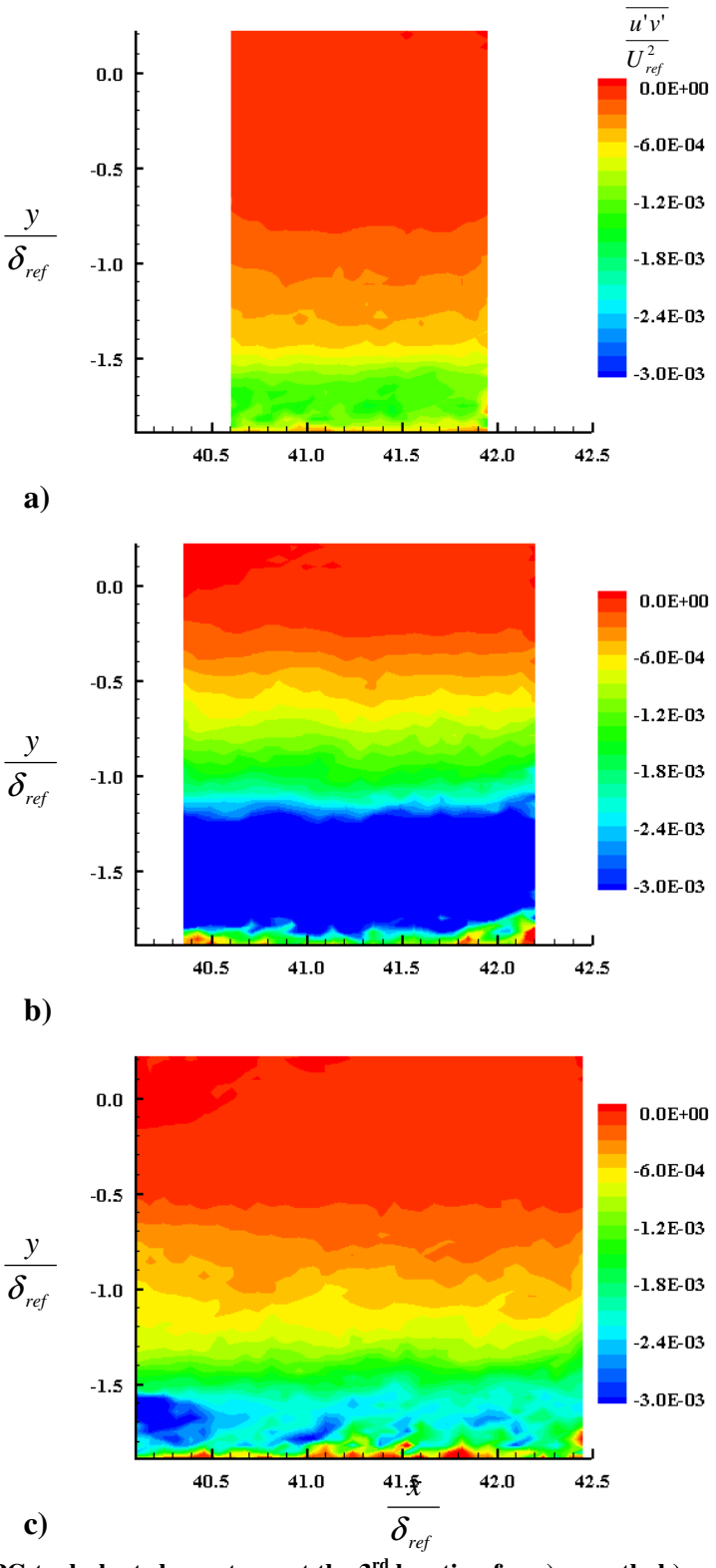

Figure 112: SPG turbulent shear stress at the 3rd location for a) smooth, b) square, and c) diamond roughness

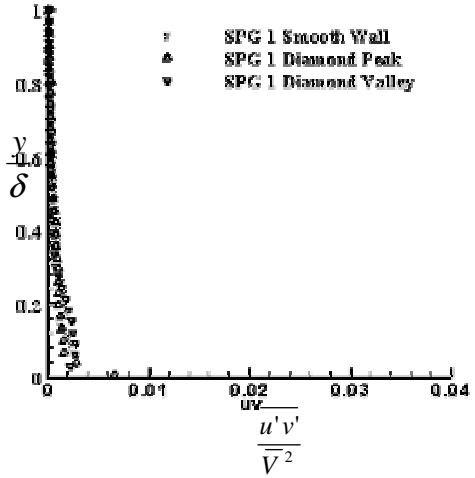

a)

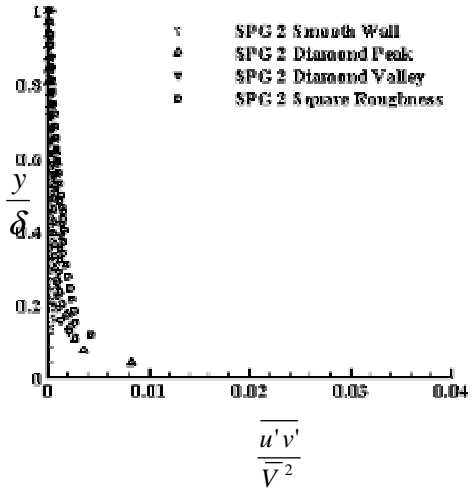

b)

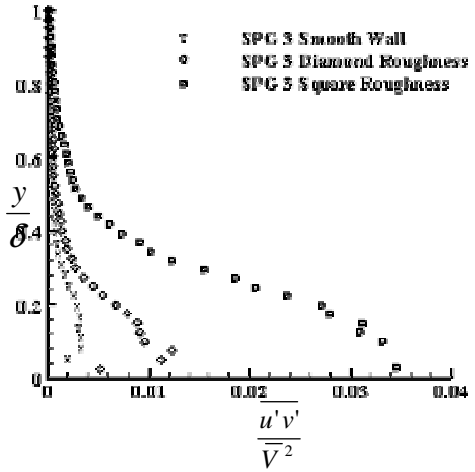

c)

Figure 113: SPG turbulent shear stress profiles at a) first, b) second, and c) third test locations.

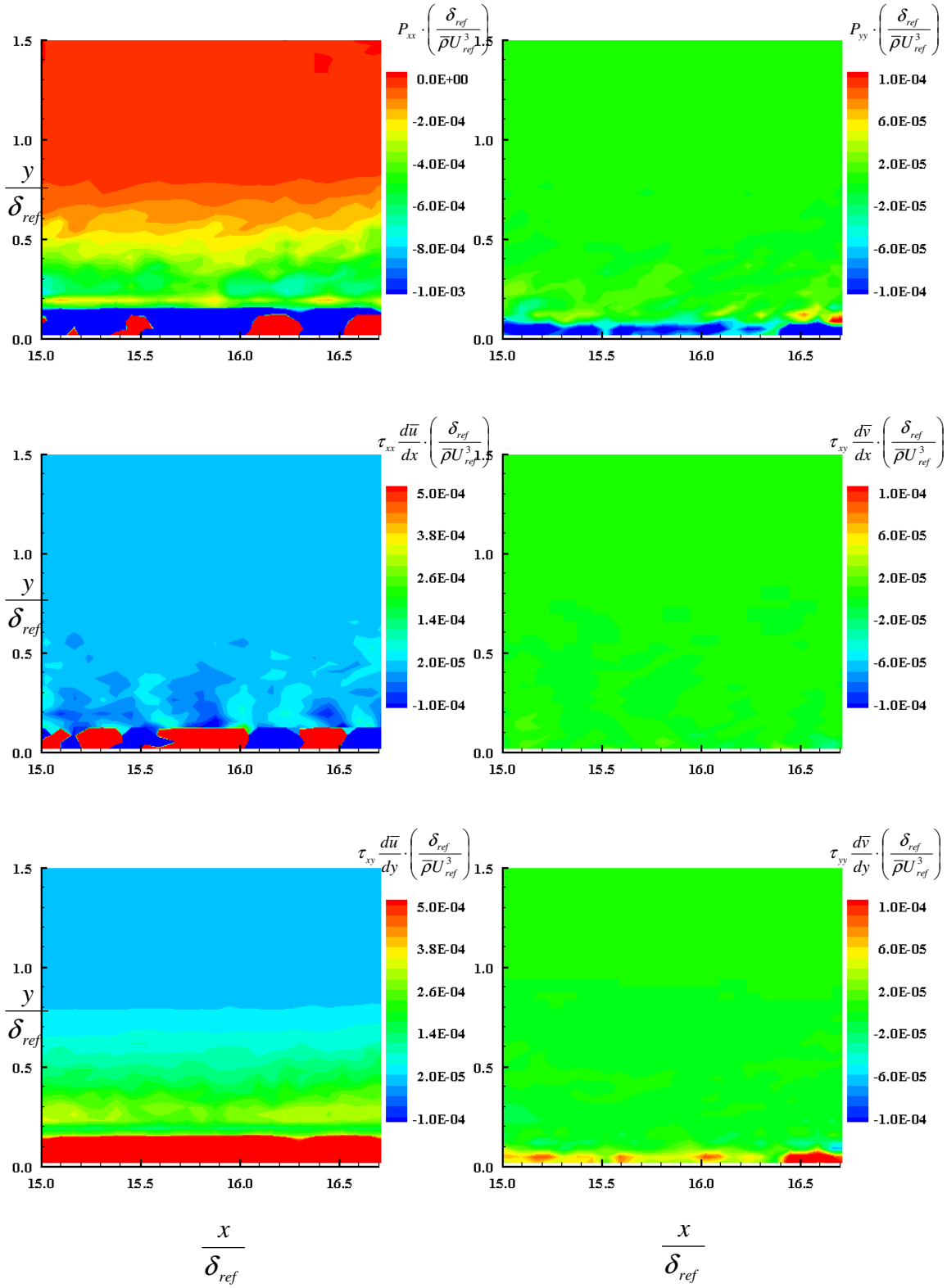

Figure 114: Smooth wall ZPG plot of P_{xx}, P_{yy} and their components at location 1

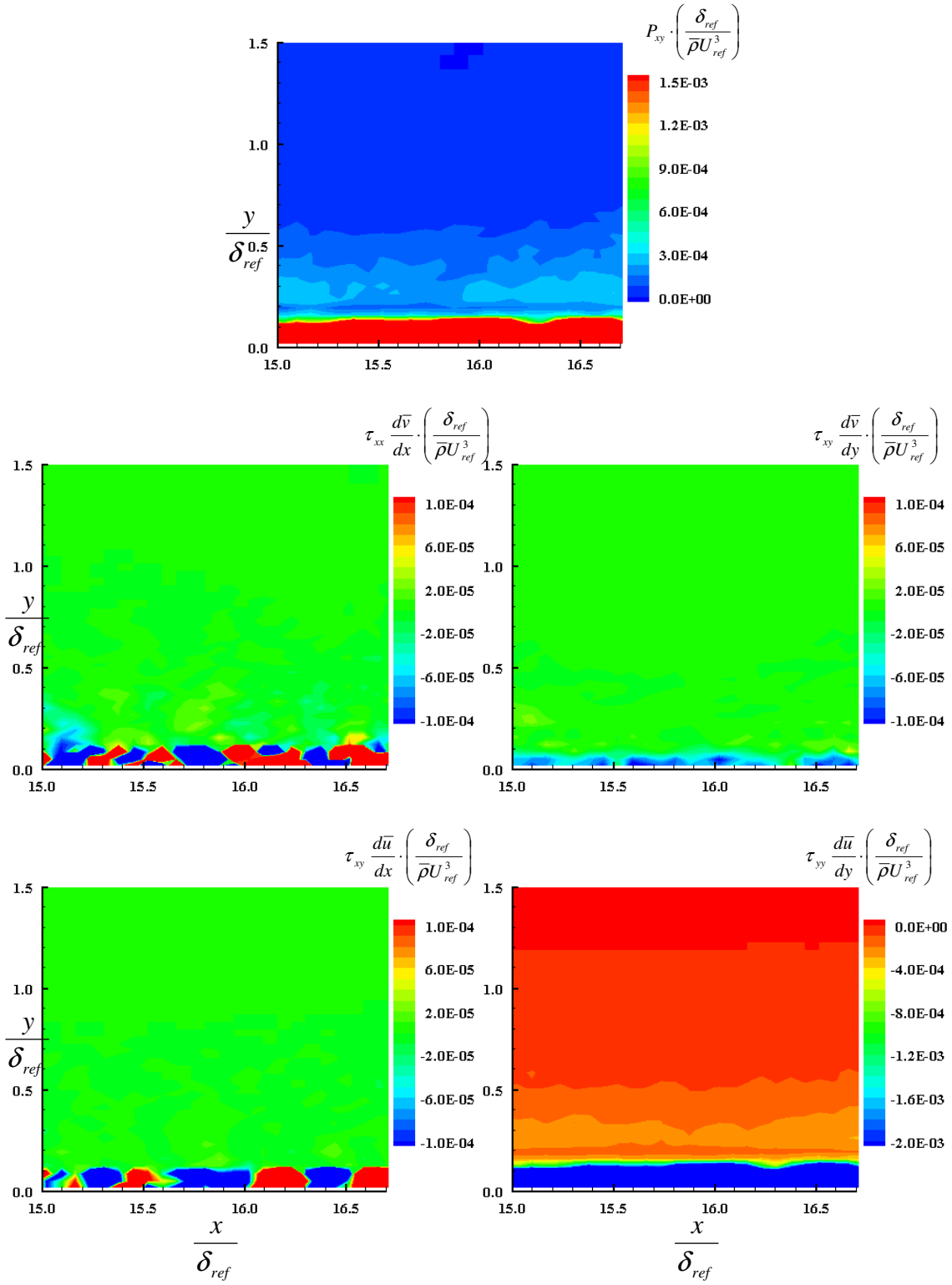

Figure 115: Smooth wall ZPG plot of P_{xy} and its components at location 1

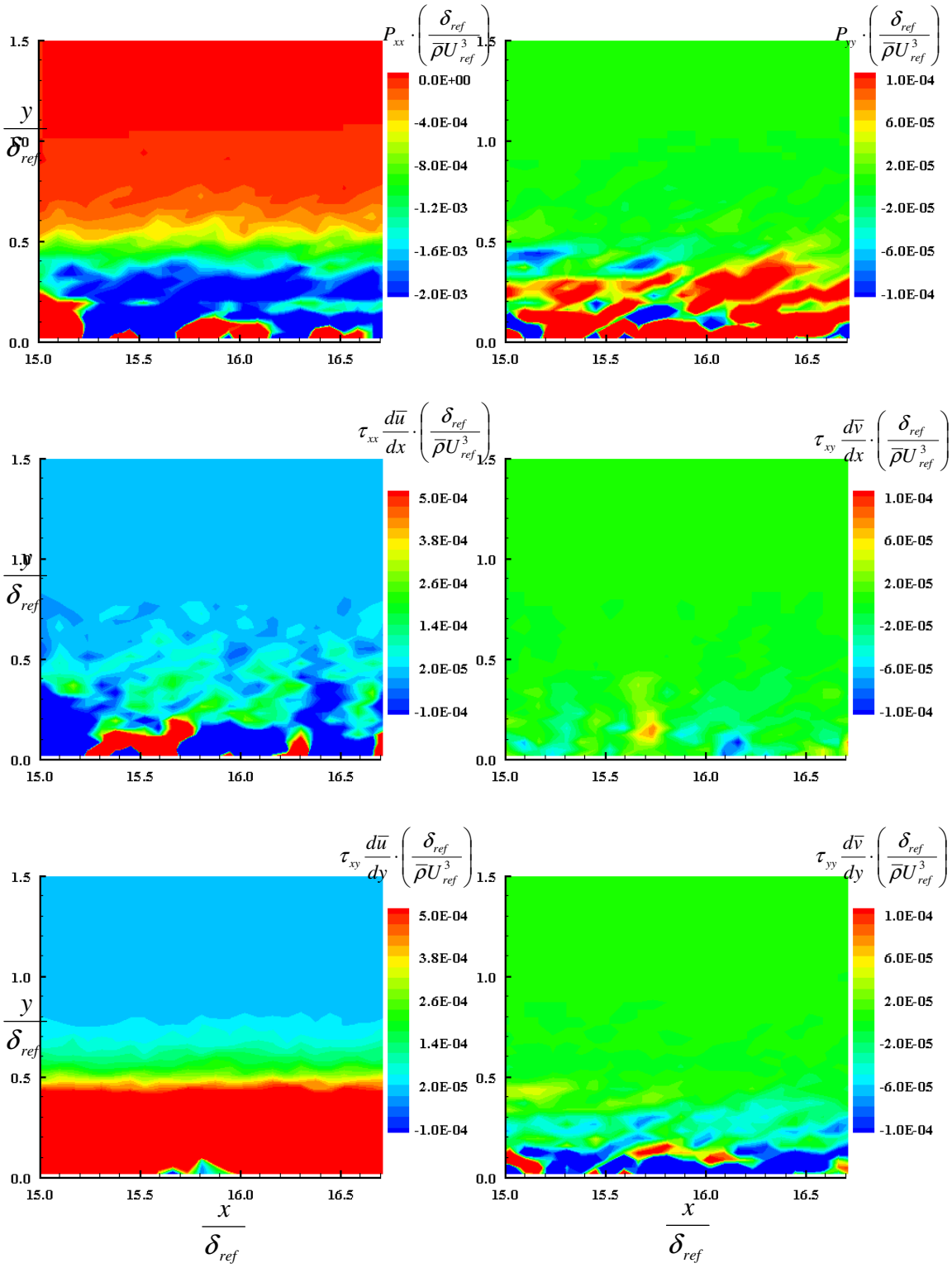

Figure 116: Square roughness ZPG plot of P_{xx}, P_{yy} and their components at location 1

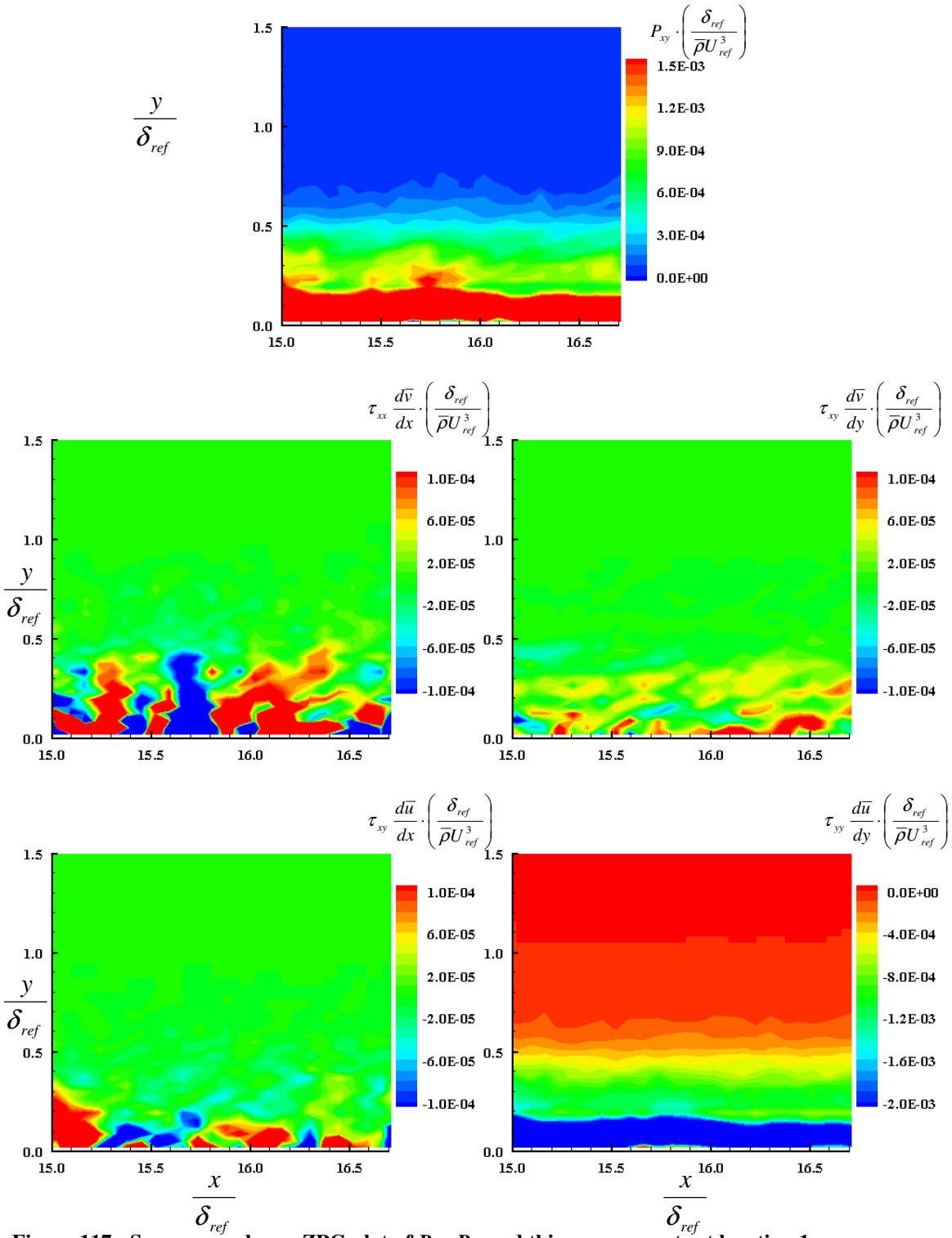

Figure 117: Square roughness ZPG plot of P_{xx}, P_{yy} and thier components at location 1

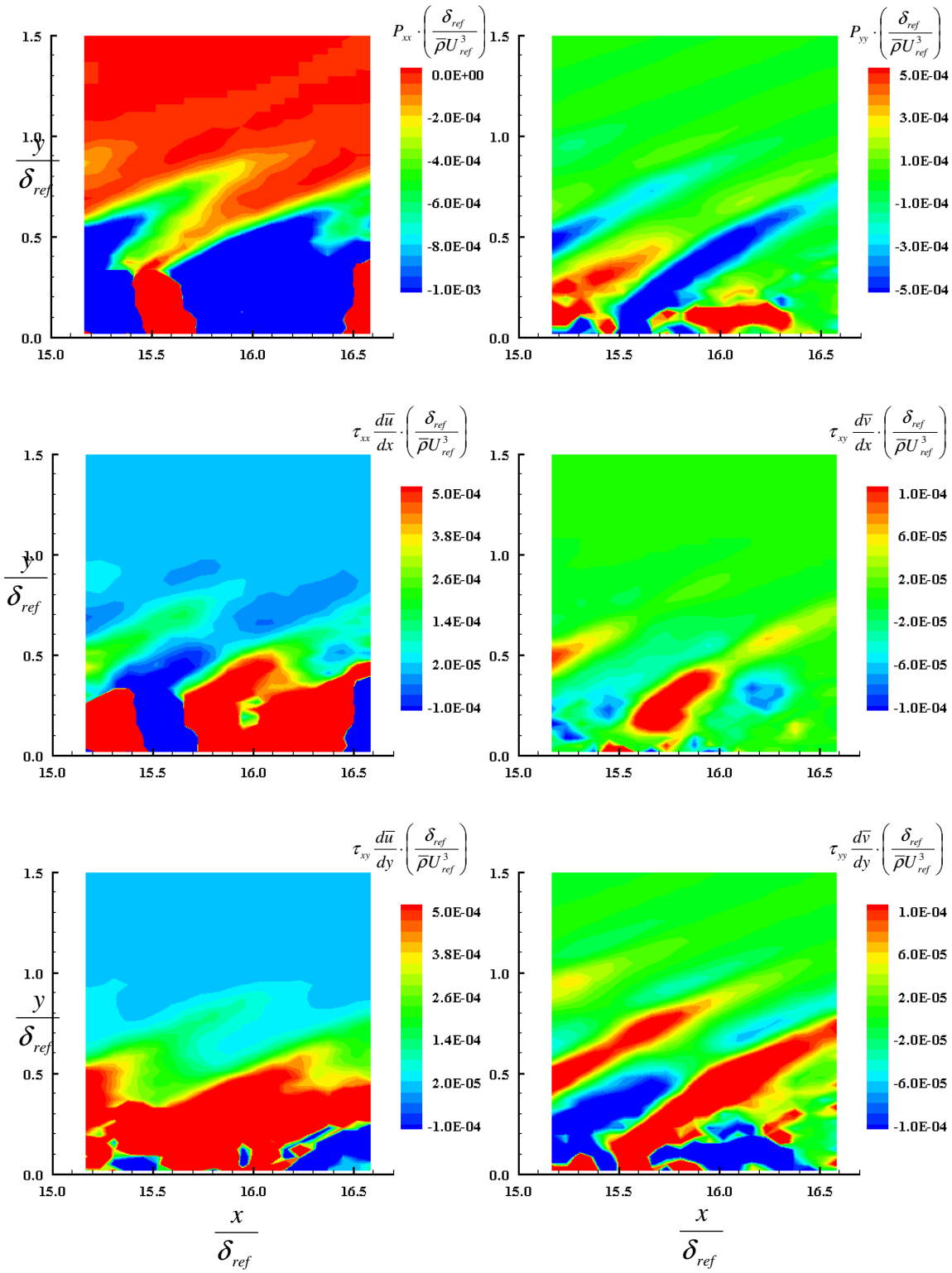

Figure 118: Diamond roughness ZPG plot of P_{xx}, P_{yy} and their components at location

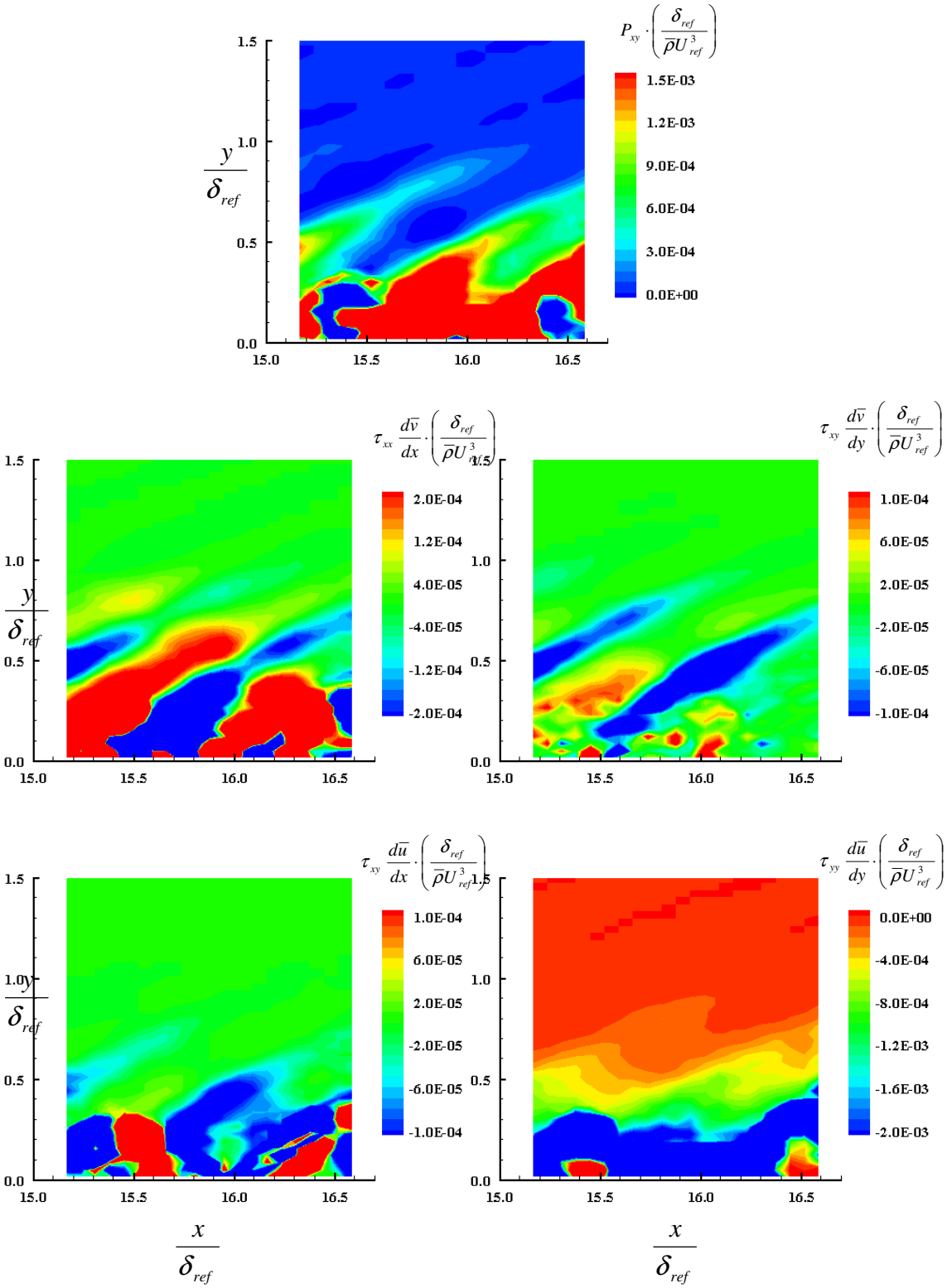

Figure 119: Diamond roughness ZPG plot of P_{xy} and its components at location 1

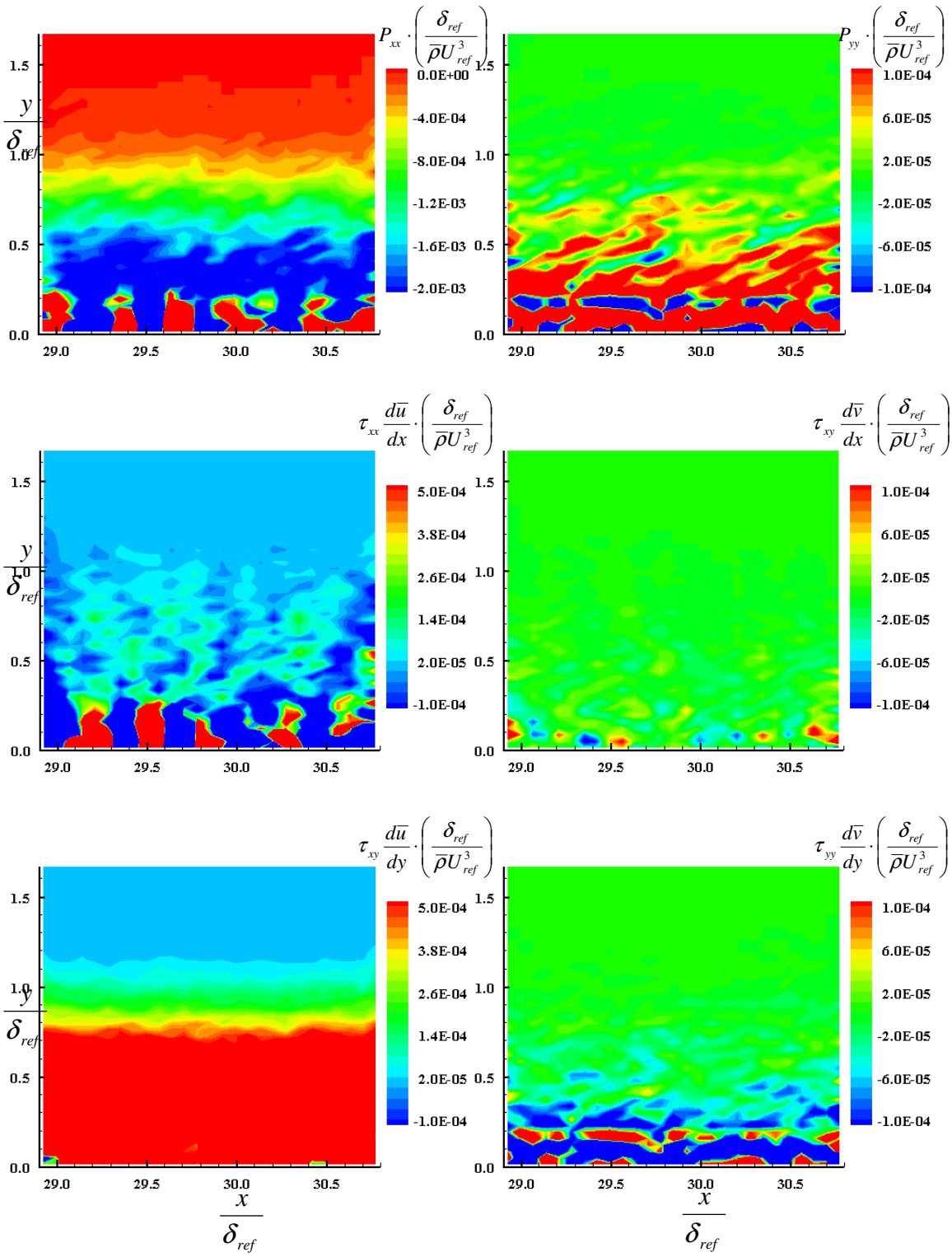

Figure 120: Square roughness ZPG plot of P_{xx}, P_{yy} and their components at location 2

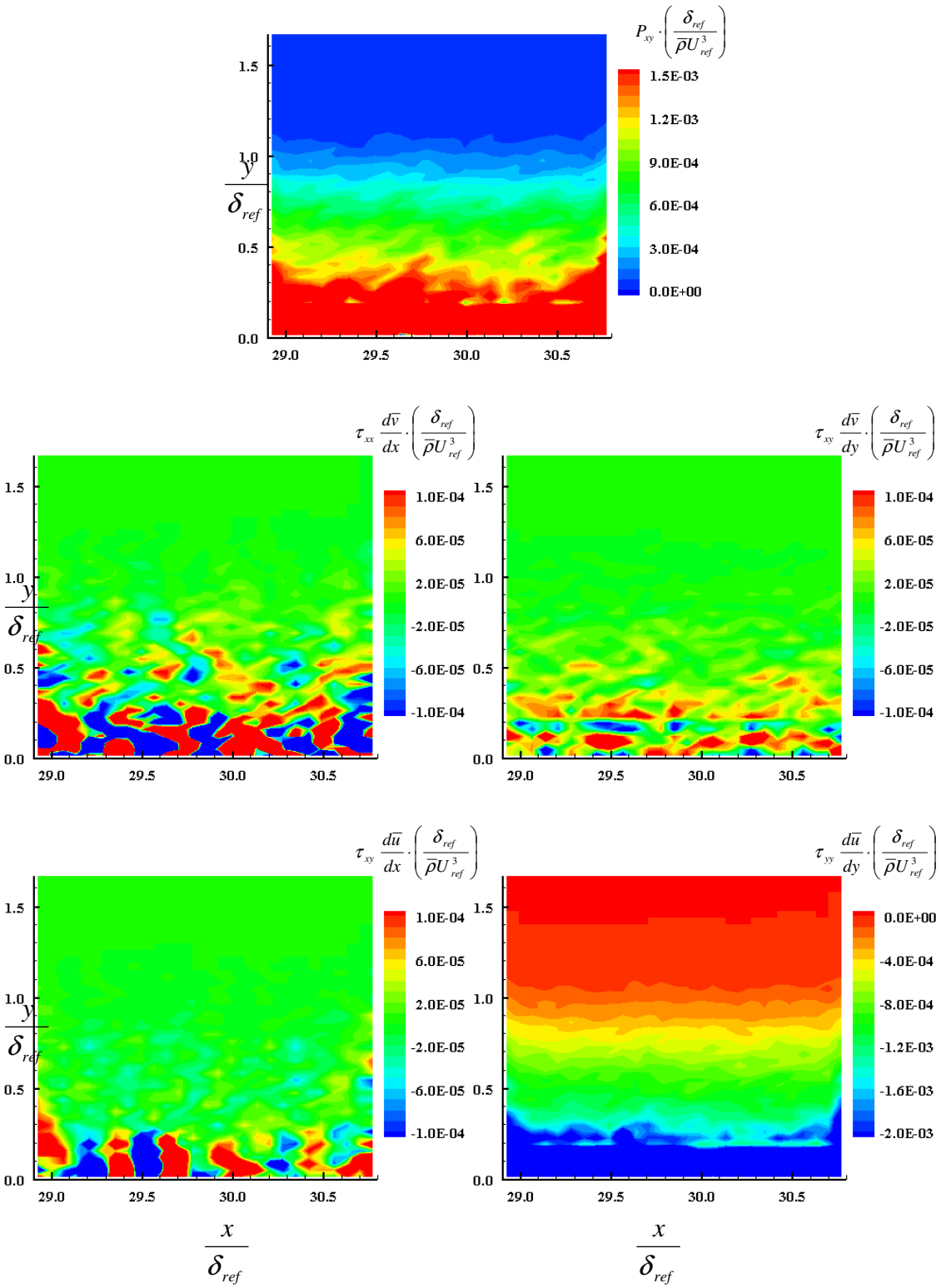

Figure 121: Square roughness ZPG plot of P_{xx}, P_{yy} and their components at location 2

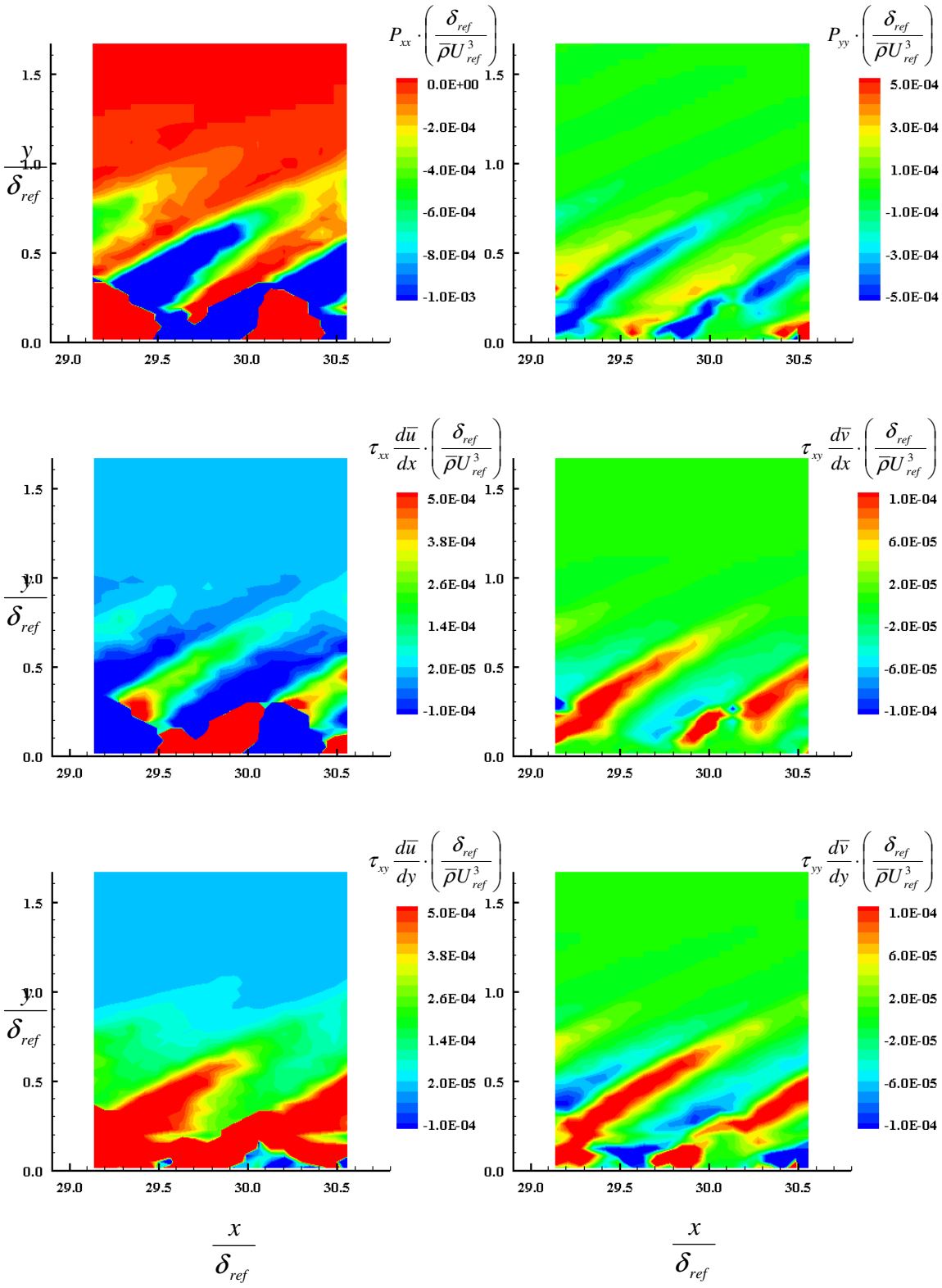

Figure 122: Diamond roughness ZPG plot of P_{xx}, P_{yy} and their components at location 2

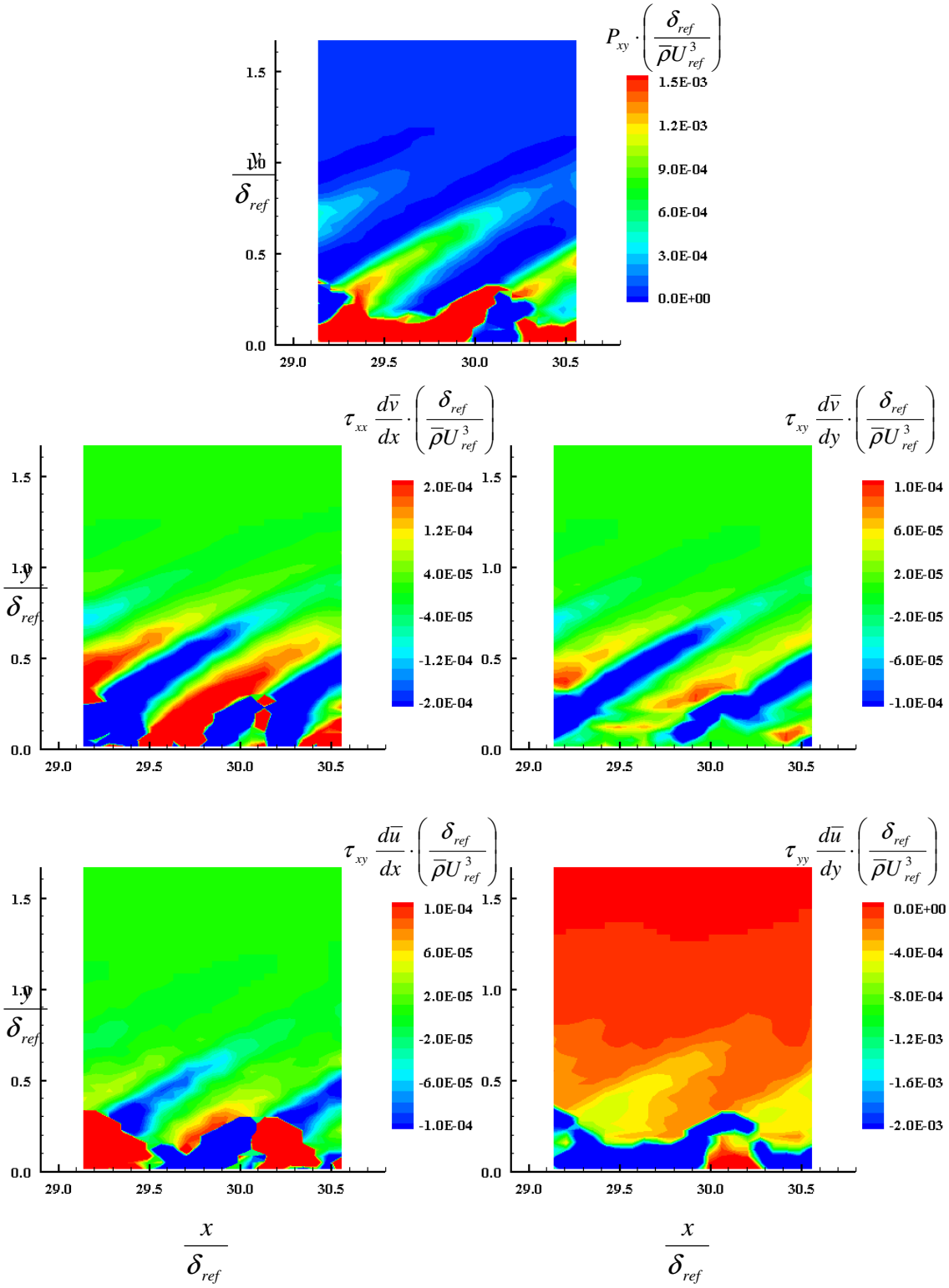

Figure 123: Diamond roughness ZPG plot of P_{xx}, P_{yy} and their components at location 2

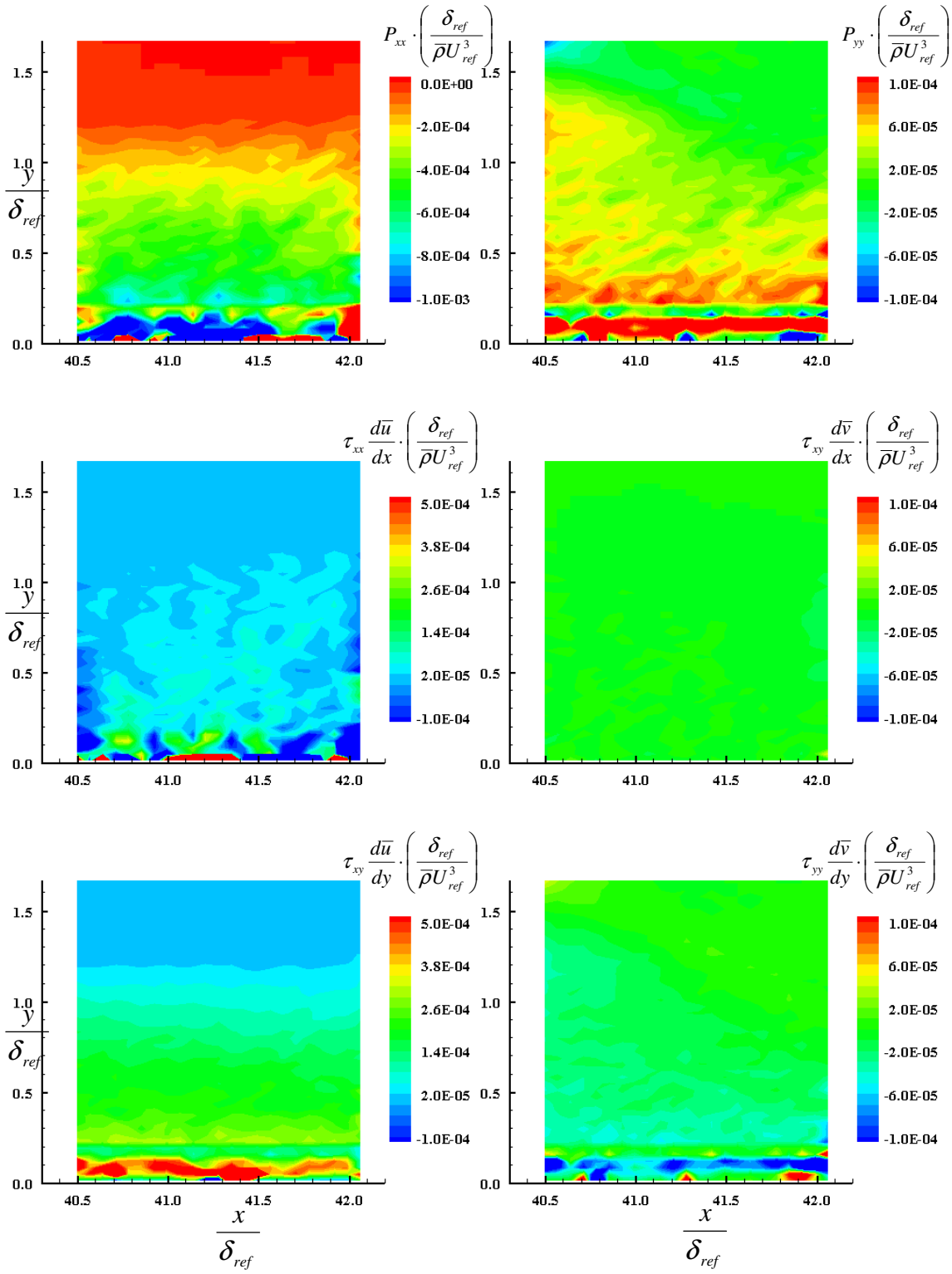

Figure 124: Smooth wall ZPG plot of P_{xx}, P_{yy} and their components at location 3

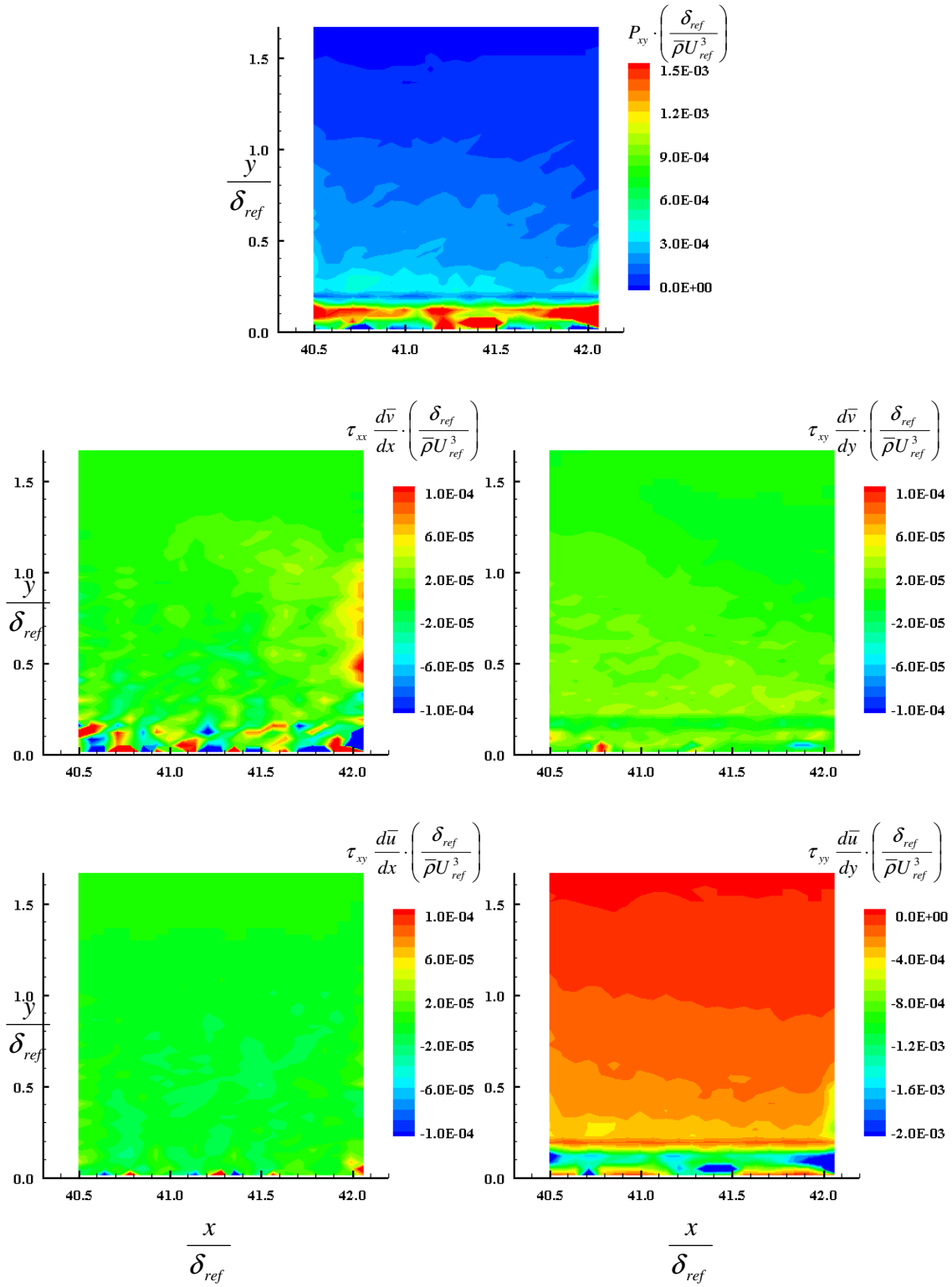

Figure 125: Smooth wall ZPG plot of P_{xy} and its components at location 3

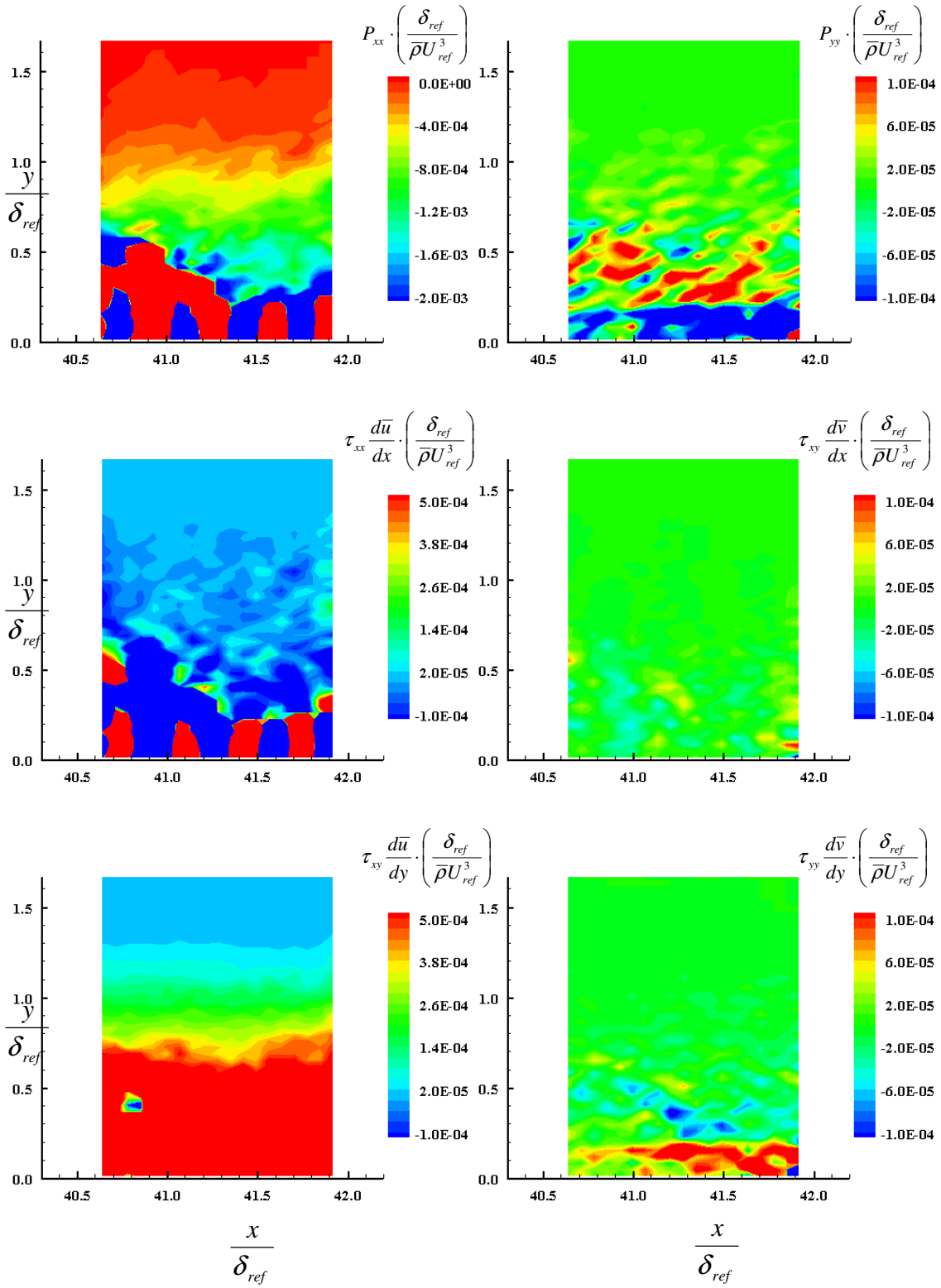

Figure 126: Square roughness ZPG plot of P_{xx}, P_{yy} and their components at location 3

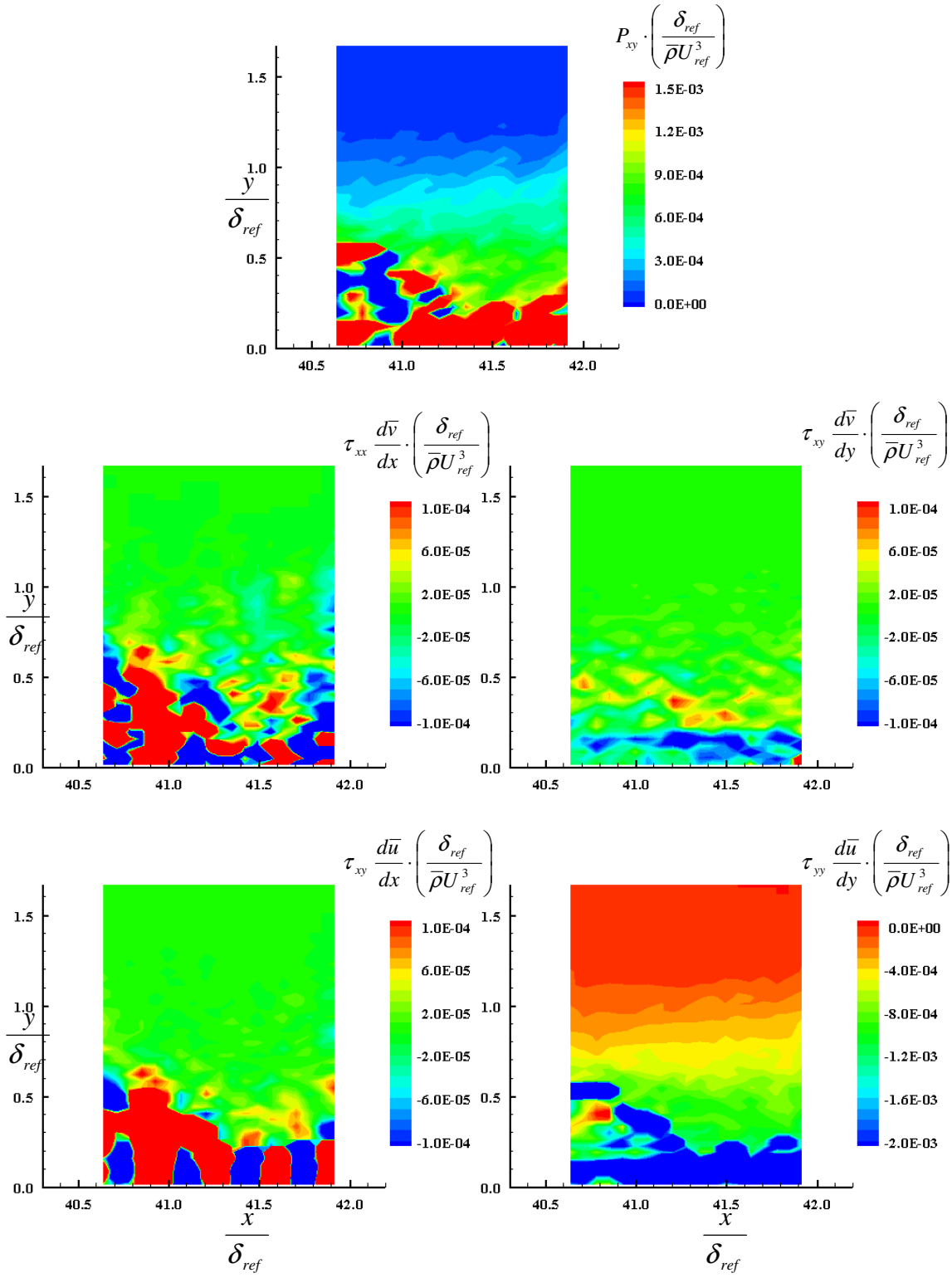

Figure 127: Square roughness ZPG plot of P_{xy} and its components at location 3

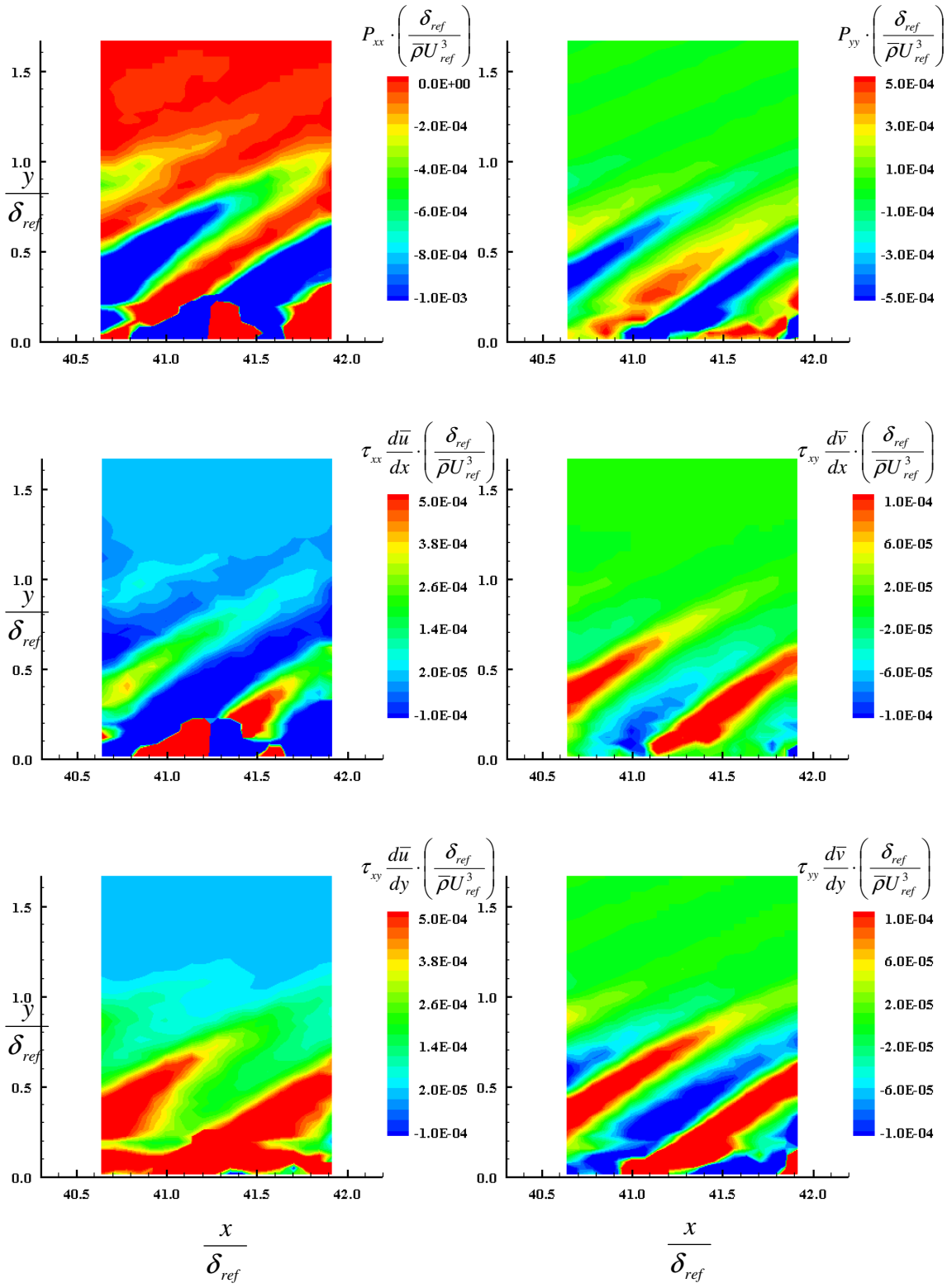

Figure 128: Diamond roughness ZPG plot of P_{xx}, P_{yy} and their components at location 3

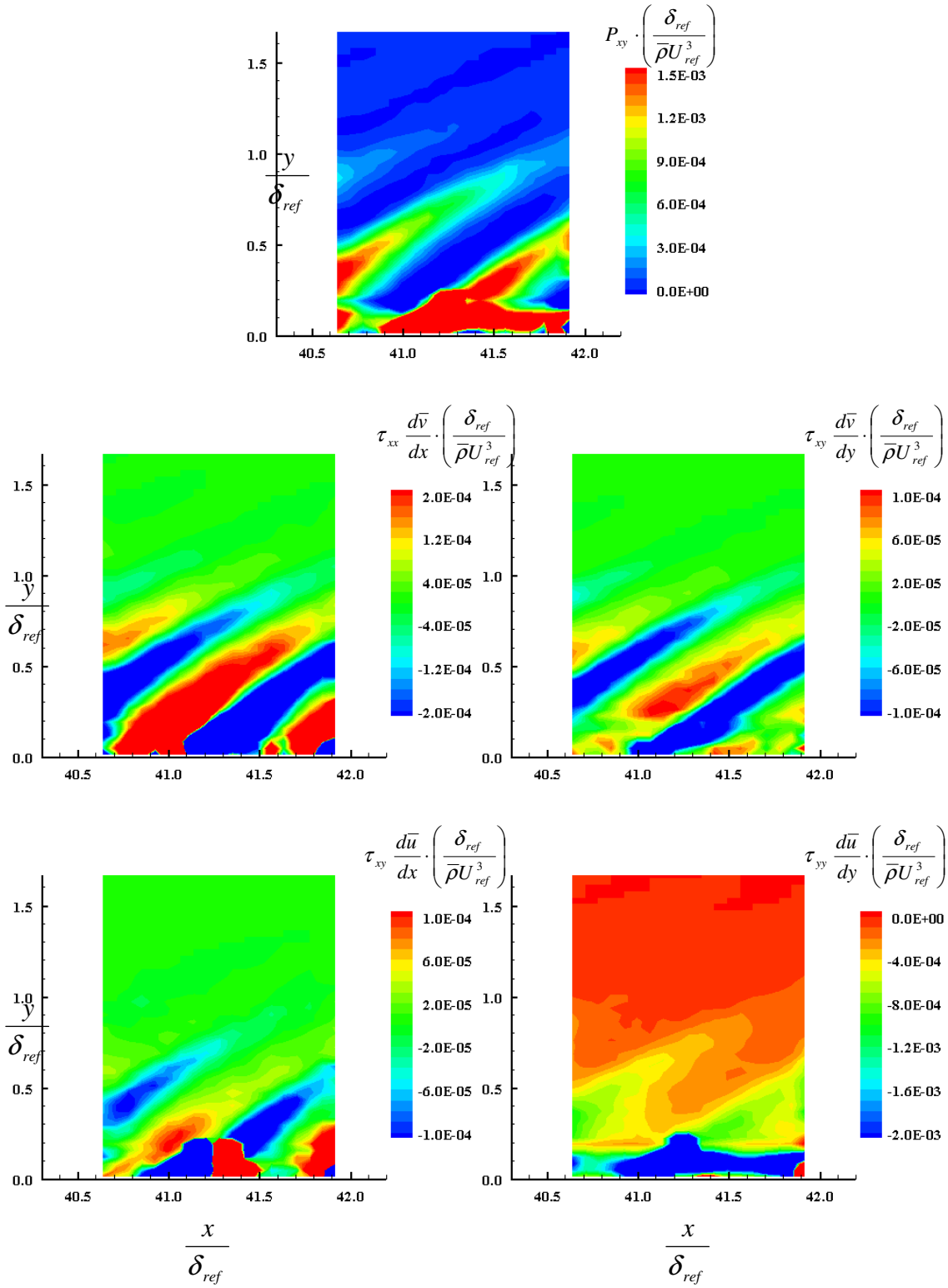

Figure 129: Diamond roughness ZPG plot of P_{xy} and its components at location 3

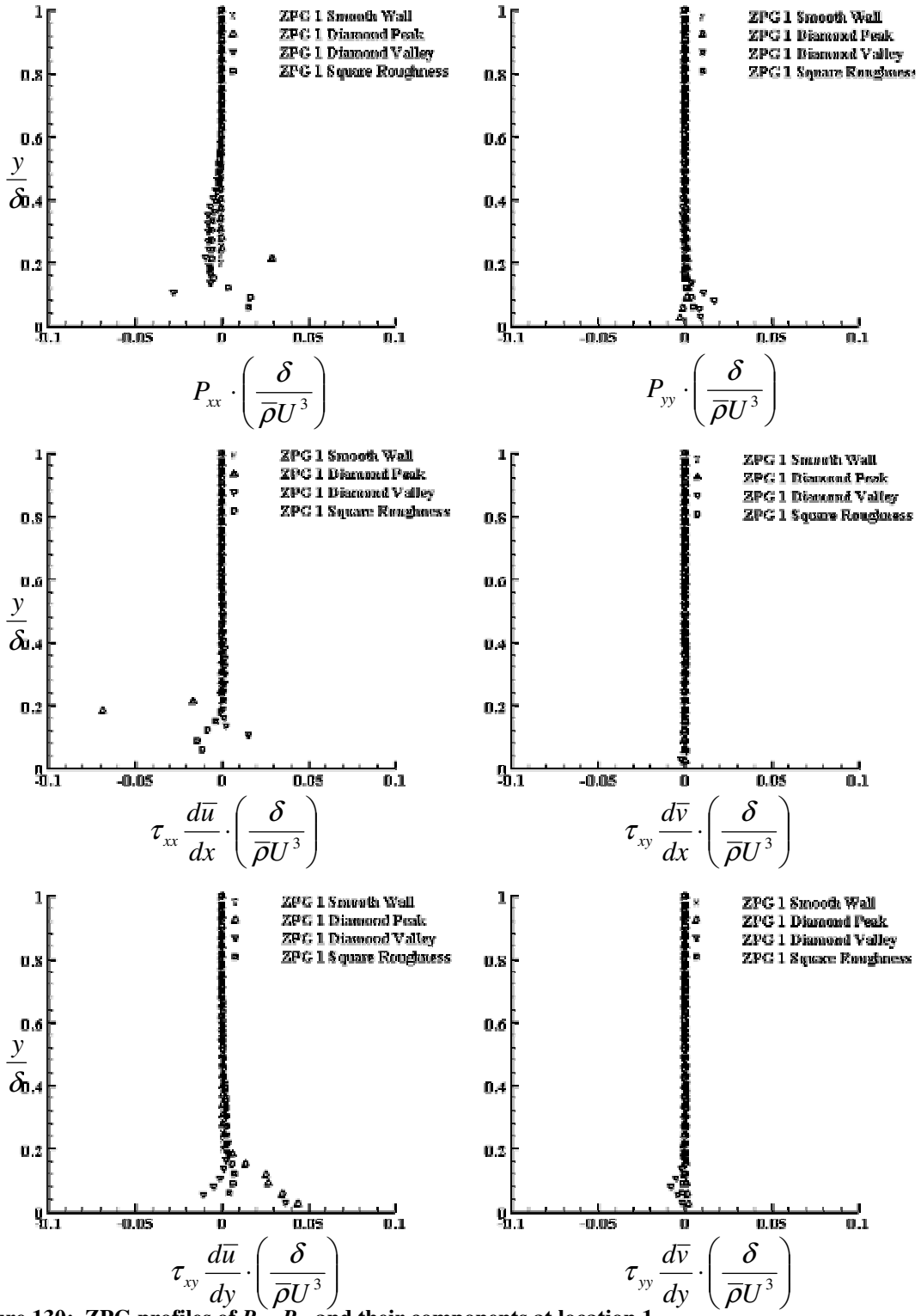

Figure 130: ZPG profiles of P_{xx}, P_{yy} and their components at location 1

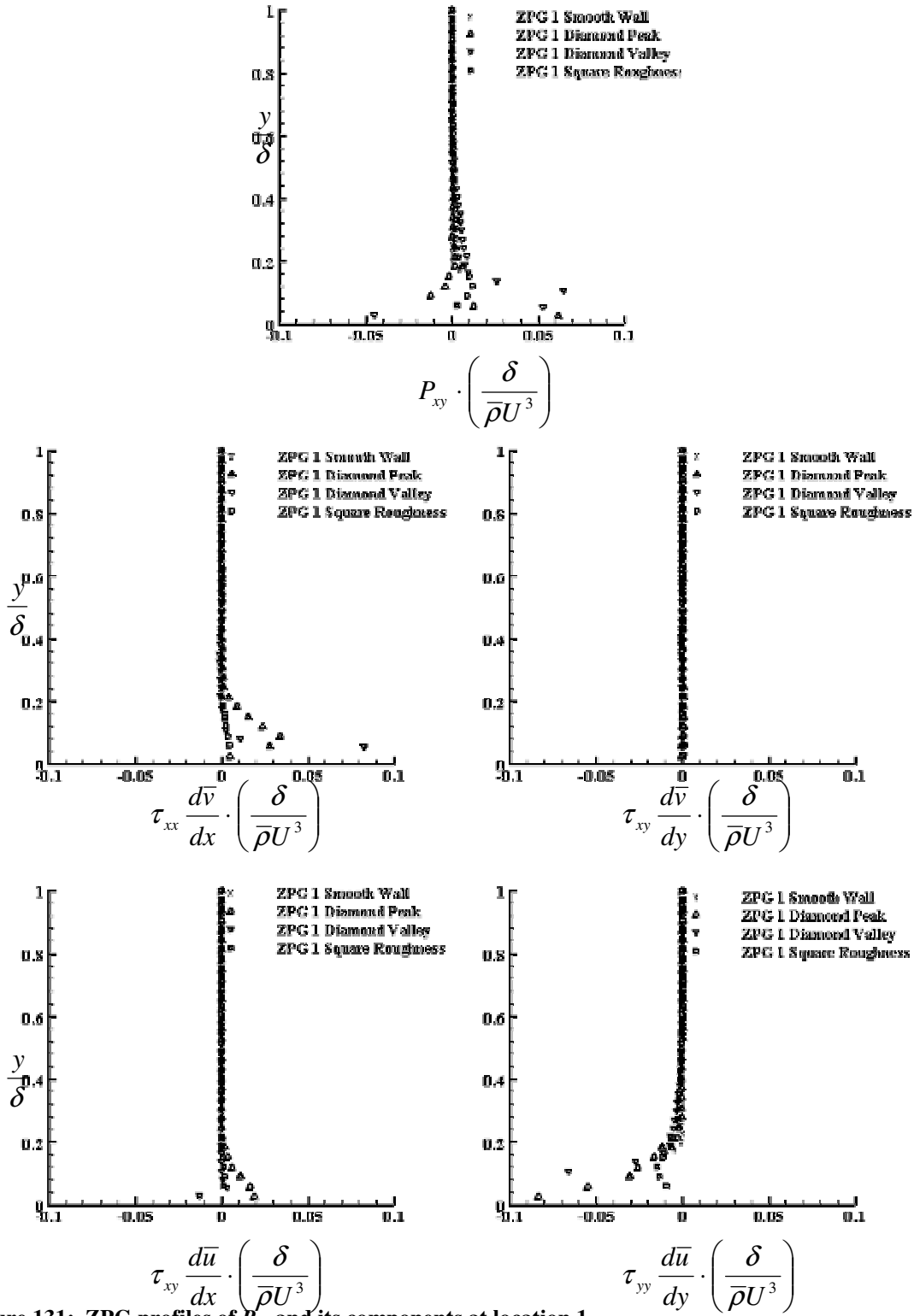

Figure 131: ZPG profiles of P_{xy} and its components at location 1

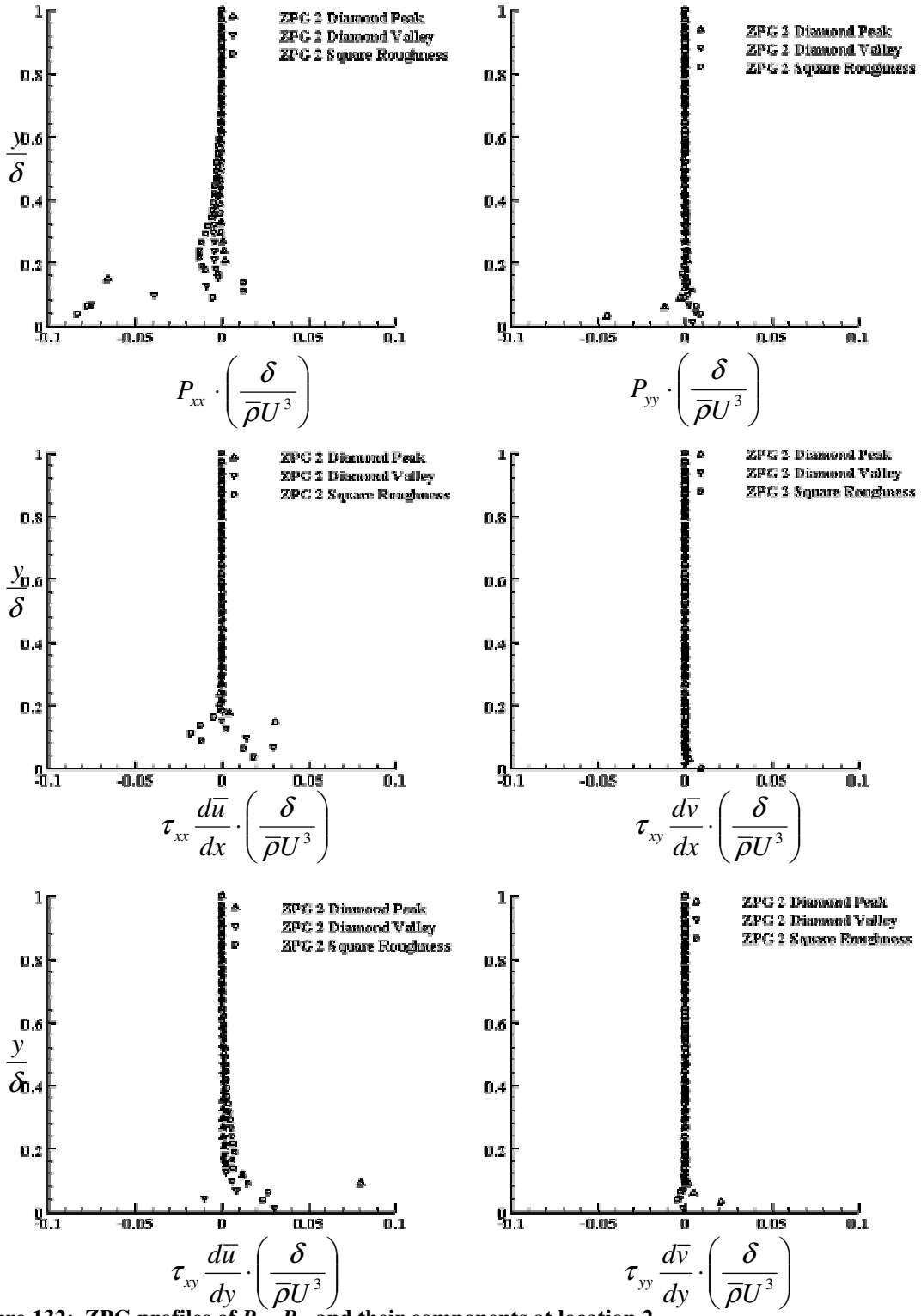

Figure 132: ZPG profiles of P_{xx}, P_{yy} and their components at location 2

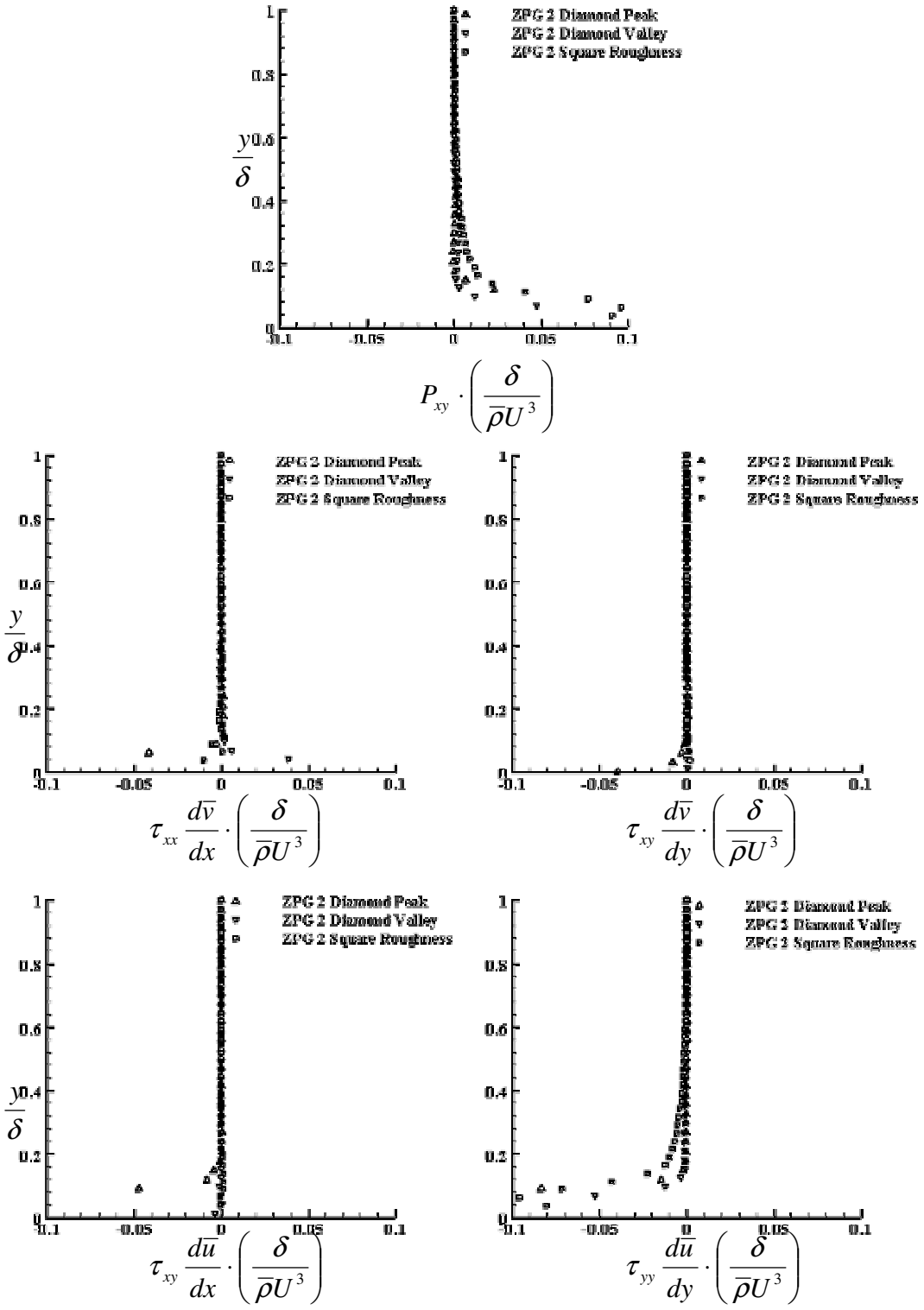

Figure 133: ZPG profiles of P_{xy} and its components at location 2

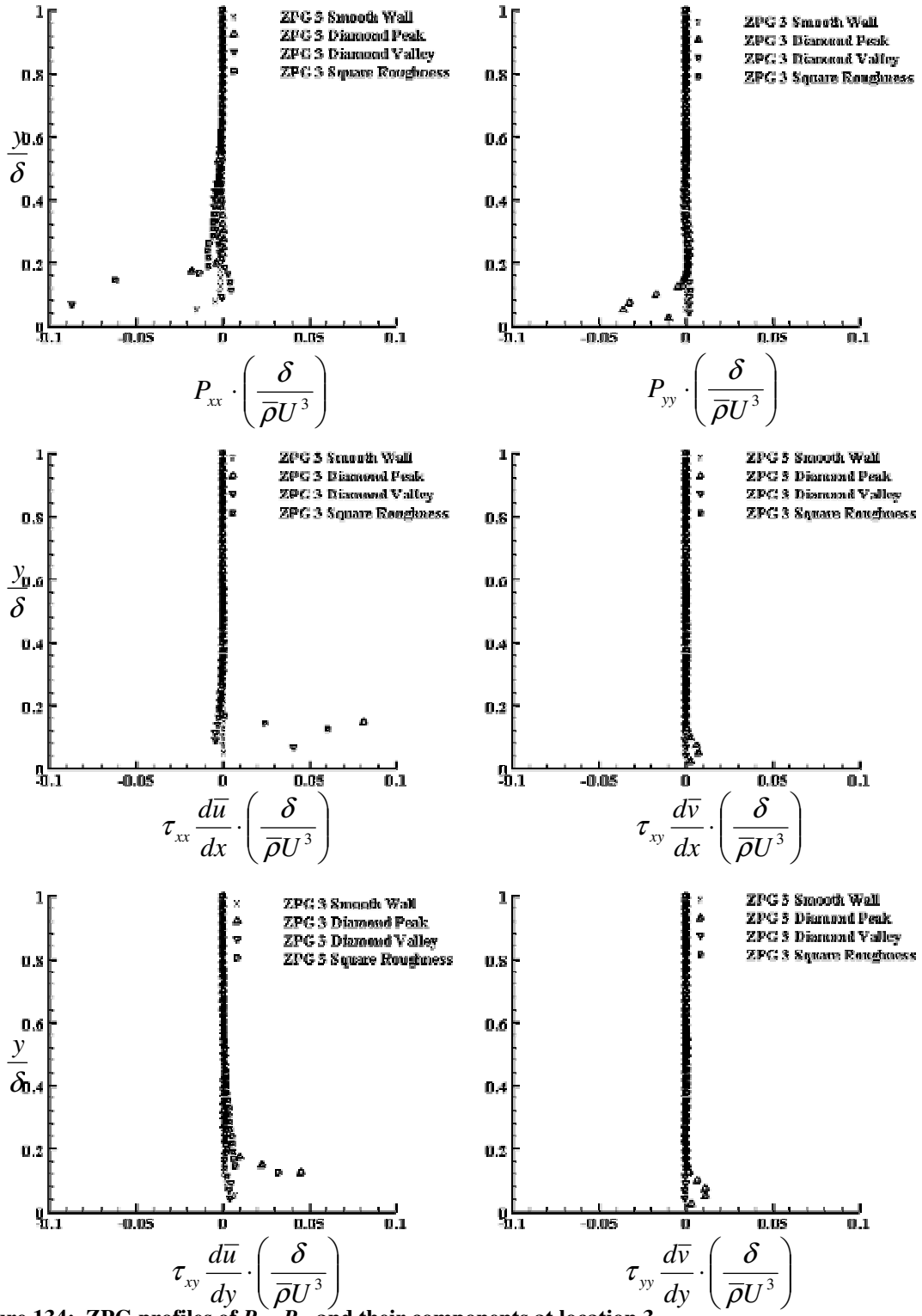

Figure 134: ZPG profiles of P_{xx}, P_{yy} and their components at location 3

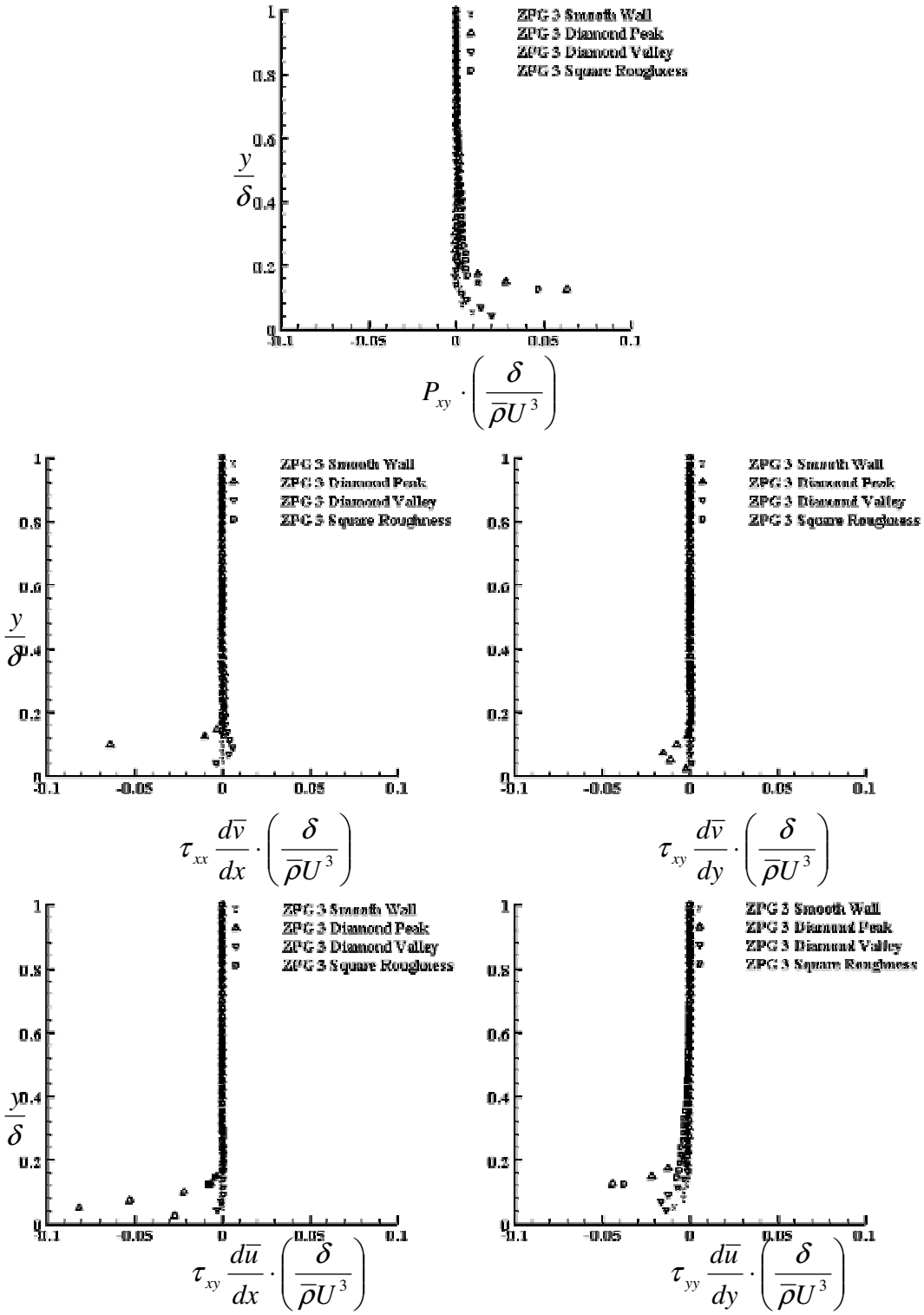

Figure 135: ZPG profiles of P_{xy} and its components at location 3

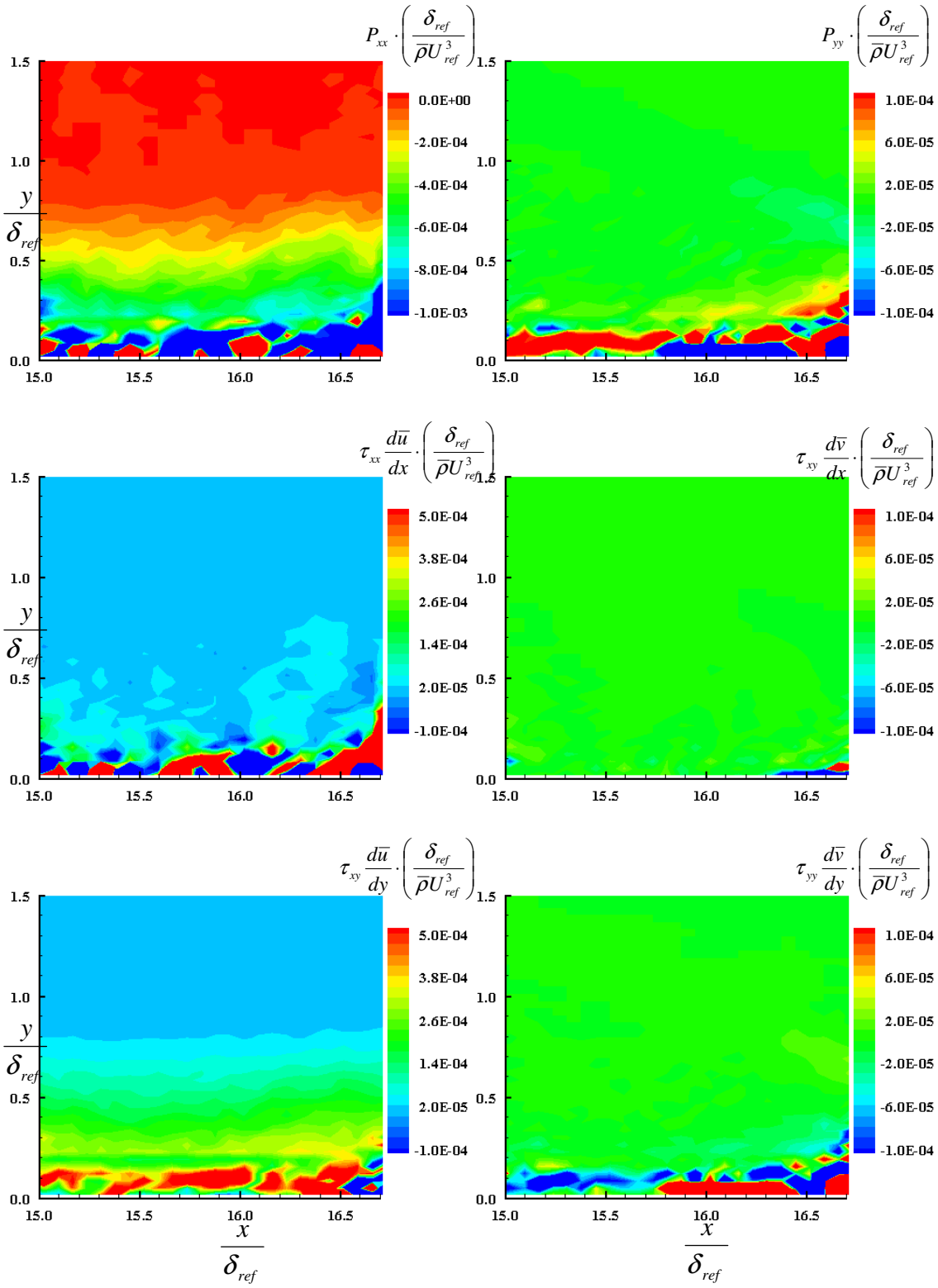

Figure 136: Smooth wall WPG plot of P_{xx}, P_{yy} and their components at location 1

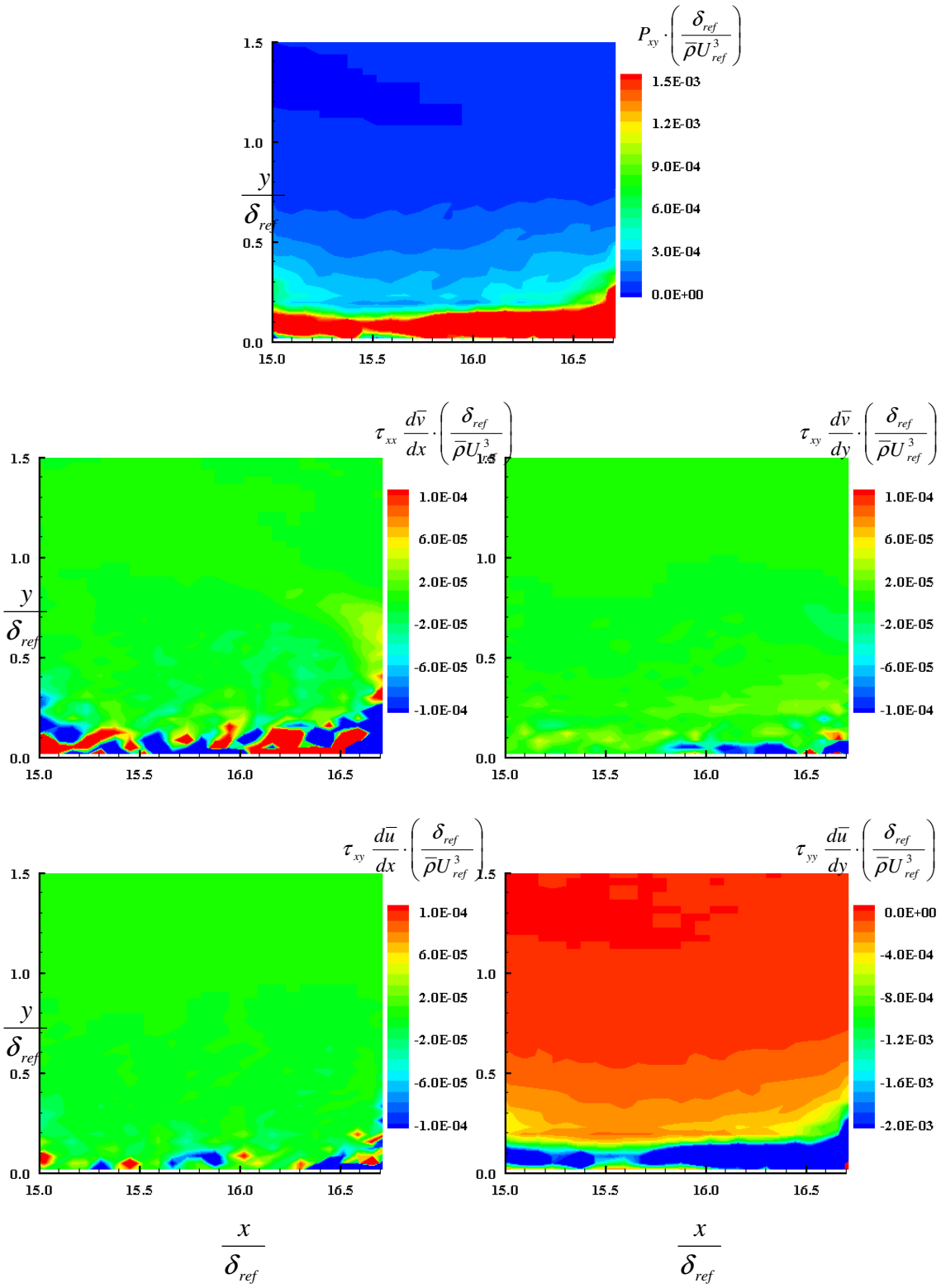

Figure 137: Smooth wall WPG plot of P_{xy} and its components at location 1

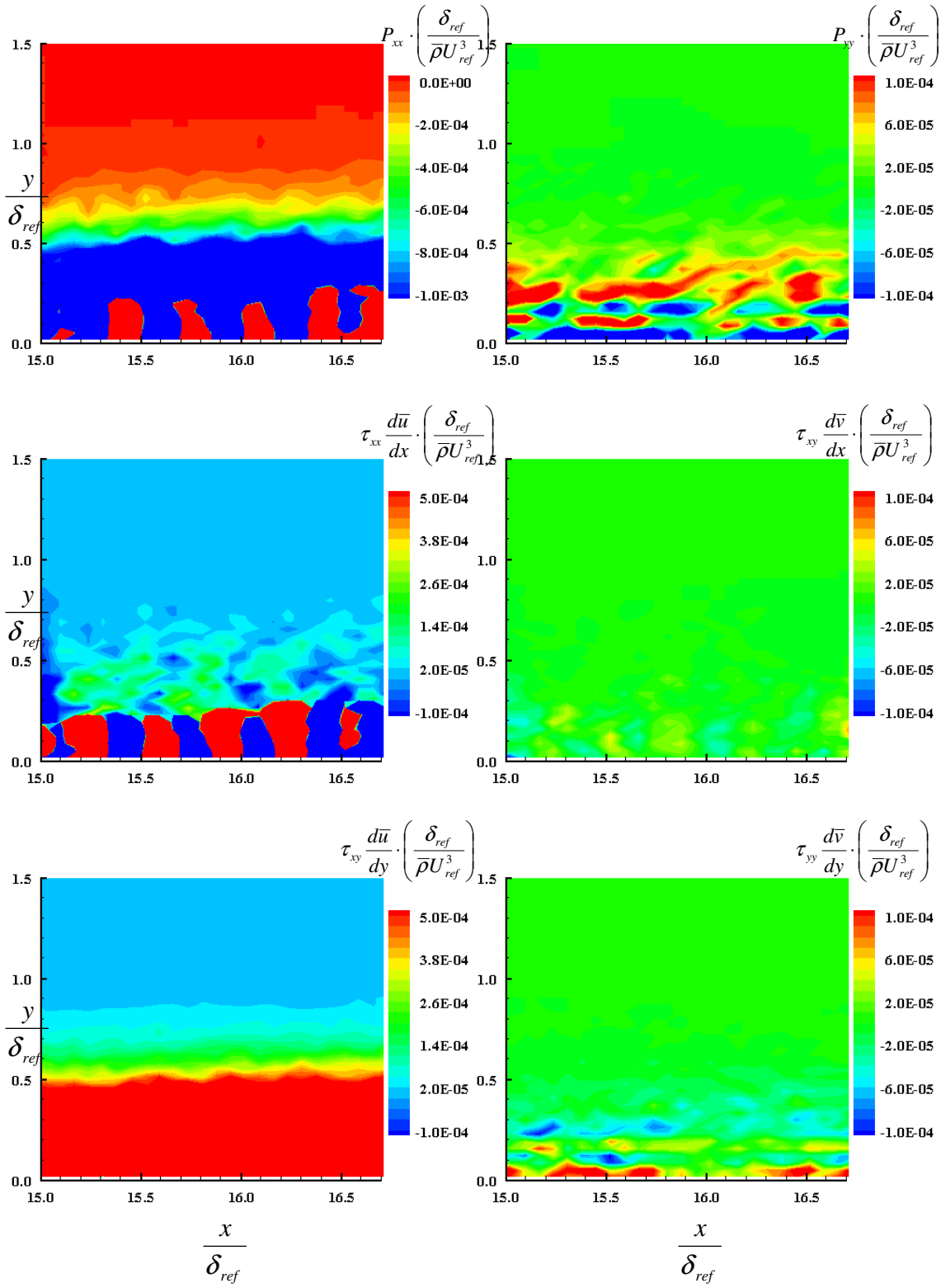

Figure 138: Square roughness WPG plot of P_{xx}, P_{yy} and their components at location 1

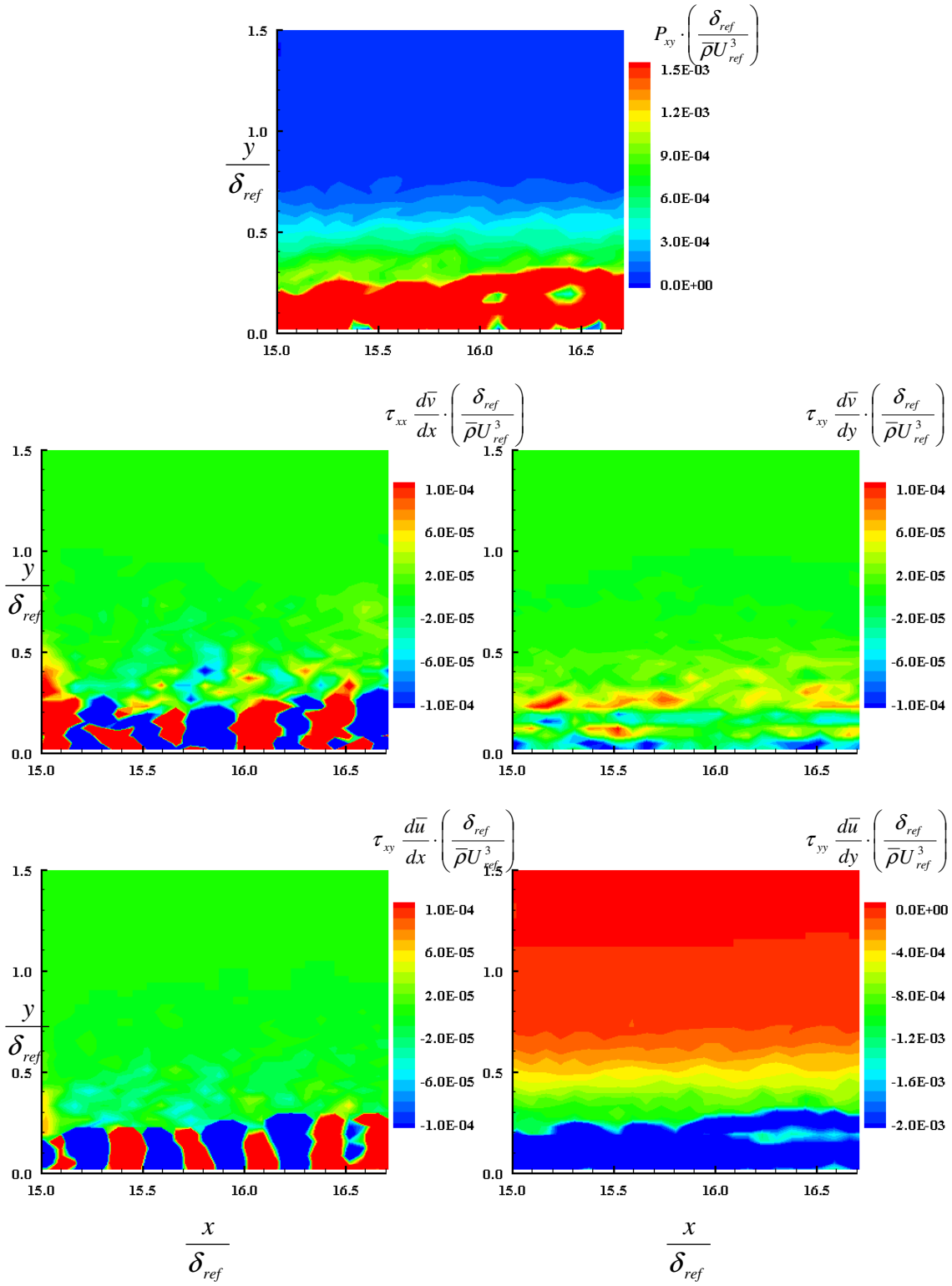

Figure 139: Square roughness WPG plot of P_{xy} and its components at location 1

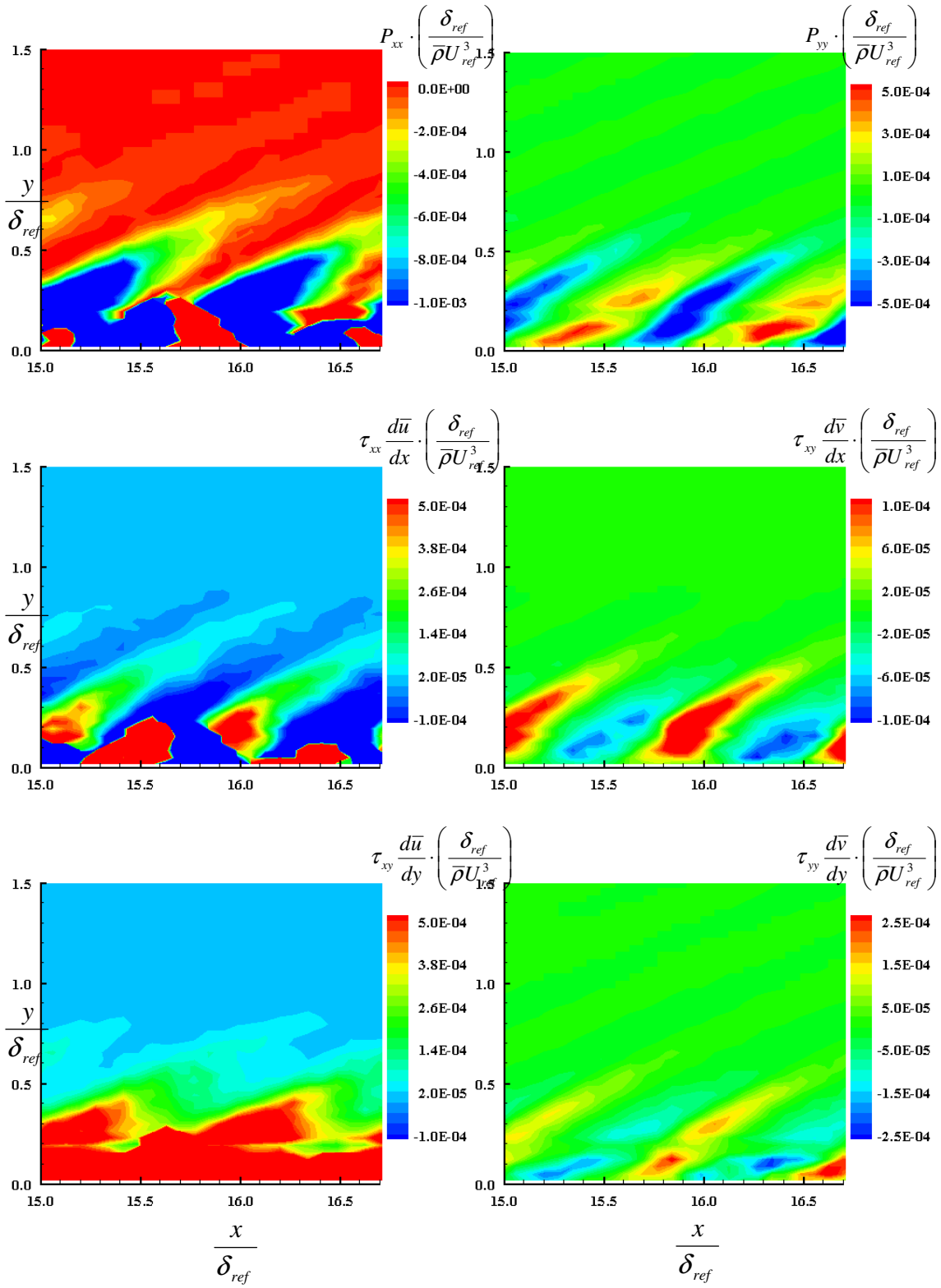

Figure 140: Diamond roughness WPG plot of P_{xx}, P_{yy} and their components at location 1

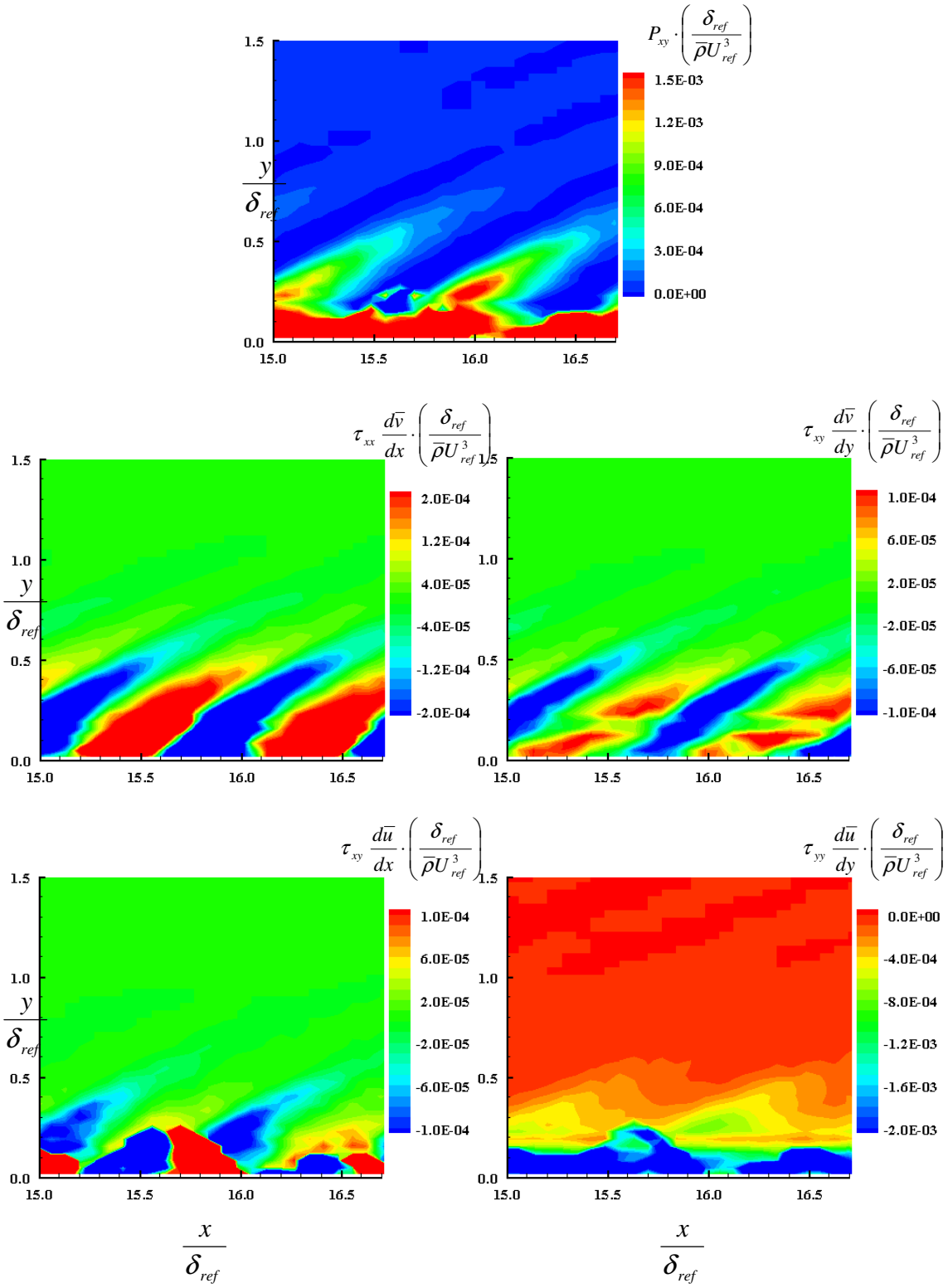

Figure 141: Diamond roughness WPG plot of P_{xy} and its components at location 1

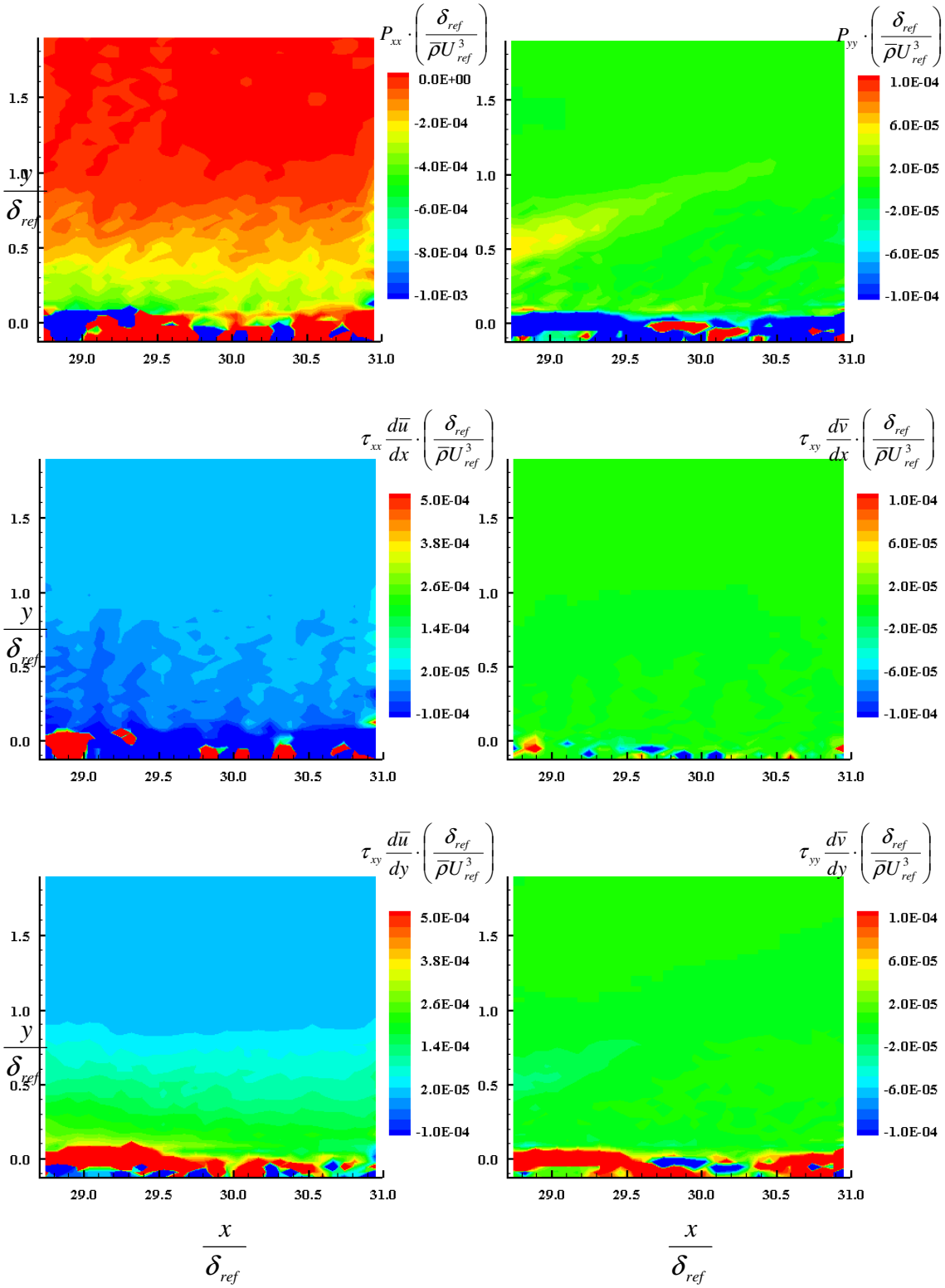

Figure 142: Smooth wall WPG plot of P_{xx}, P_{yy} and their components at location 2

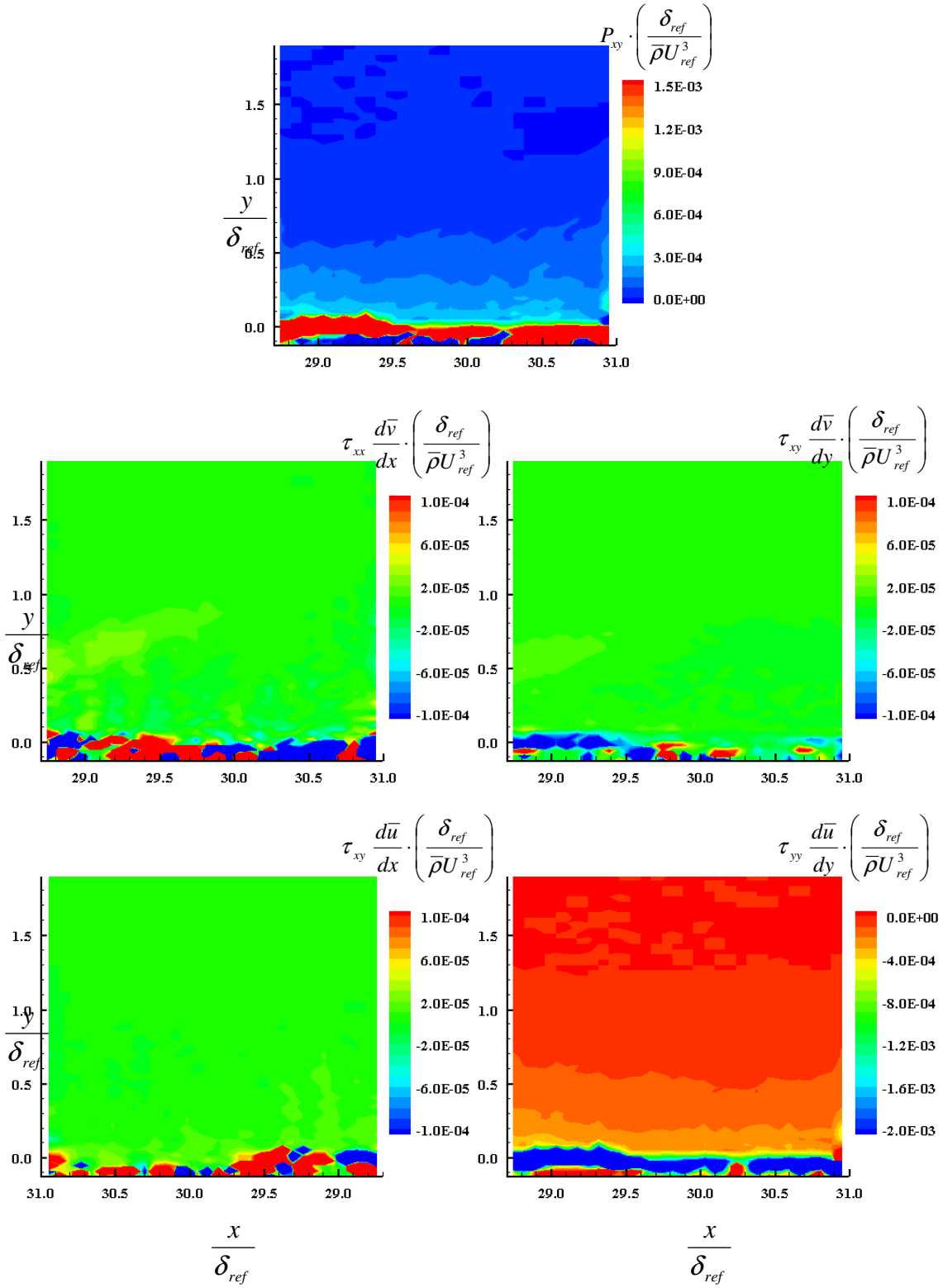

Figure 143: Smooth wall WPG plot of P_{xy} and its components at location 2

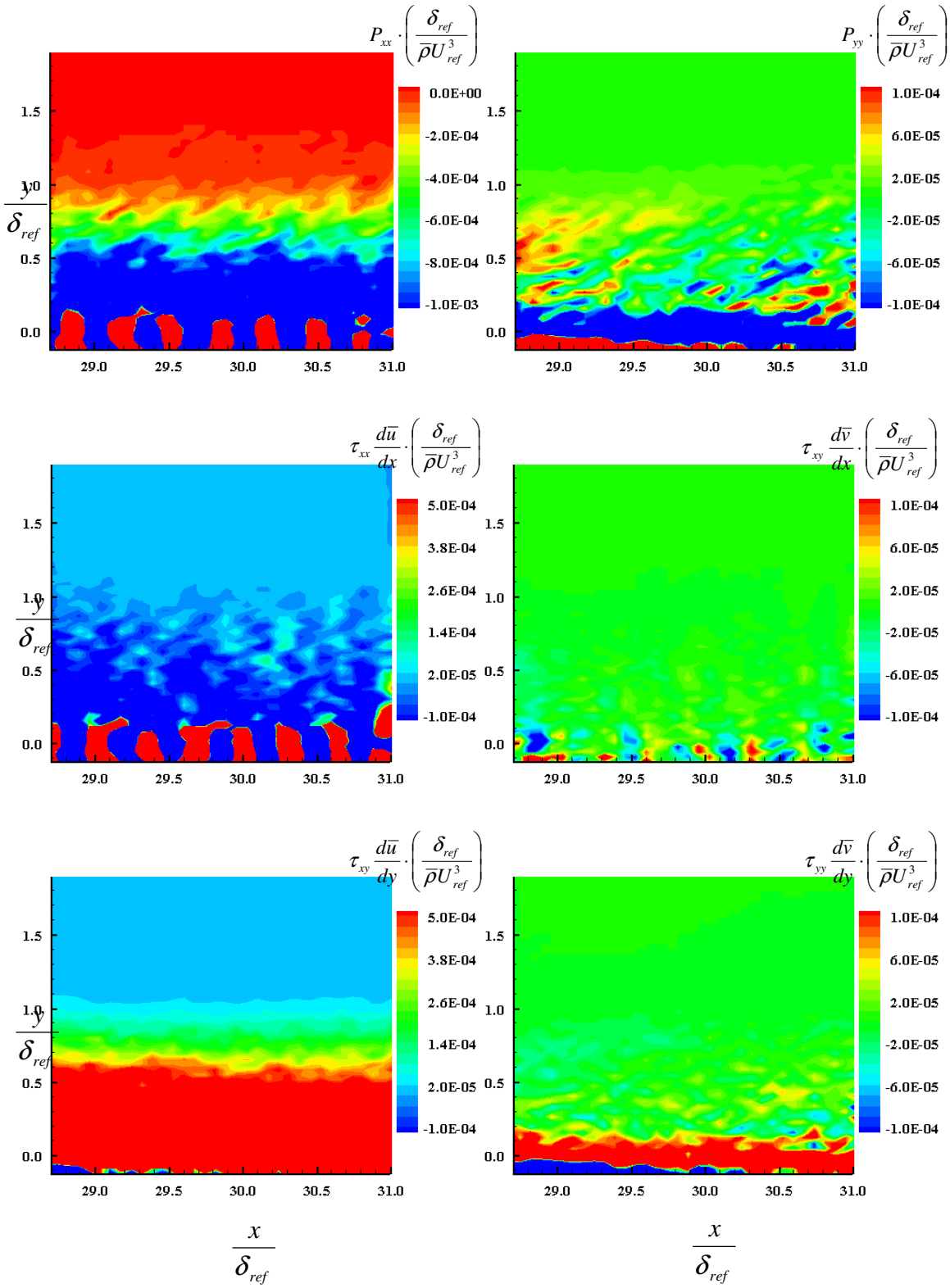

Figure 144: Square roughness WPG plot of P_{xx}, P_{yy} and their components at location 2

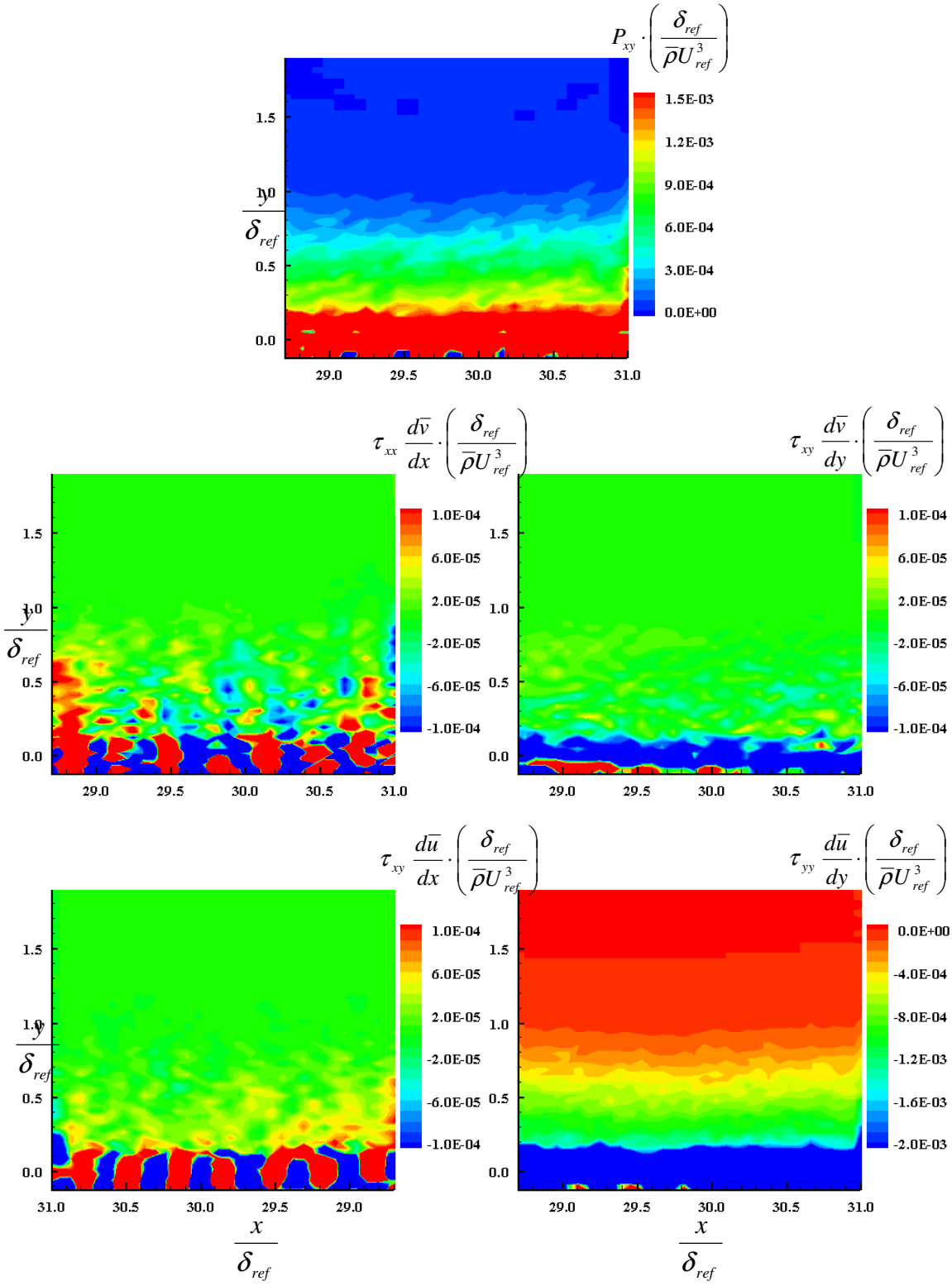

Figure 145: Square roughness WPG plot of P_{xy} and its components at location 2

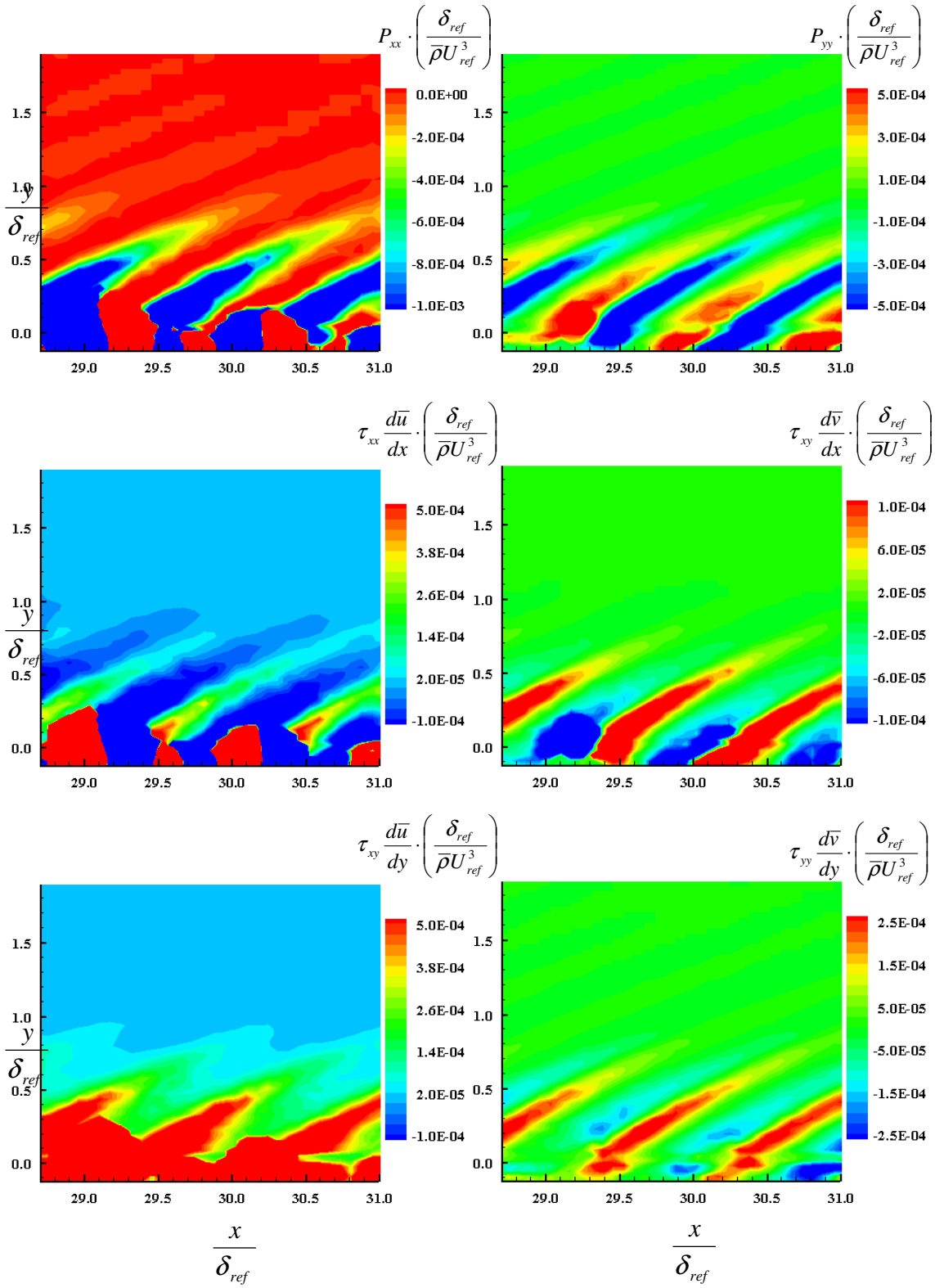

Figure 146: Diamond roughness WPG plot of P_{xx}, P_{yy} and their components at location 2

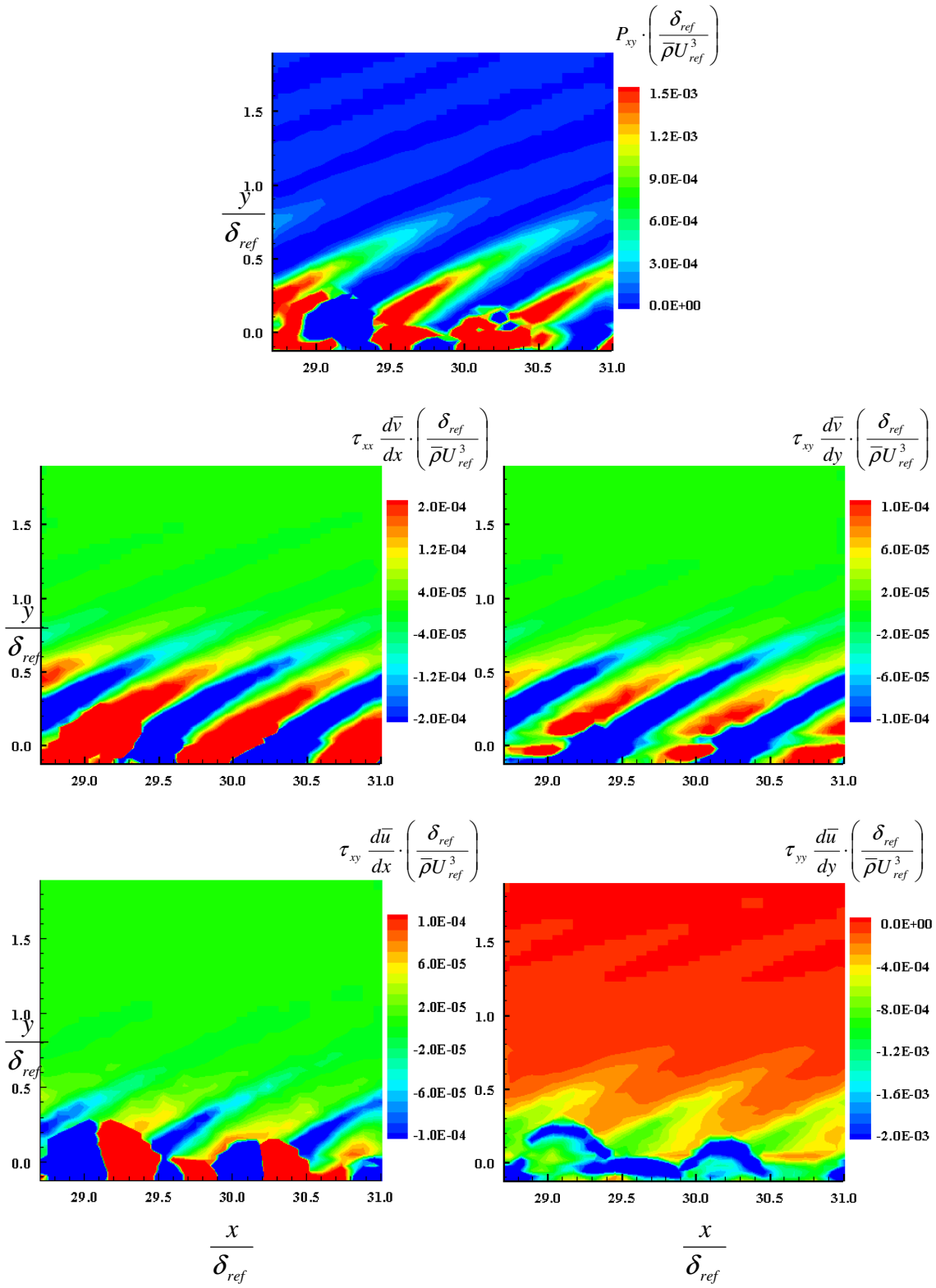

Figure 147: Diamond roughness WPG plot of P_{xy} and its components at location 2

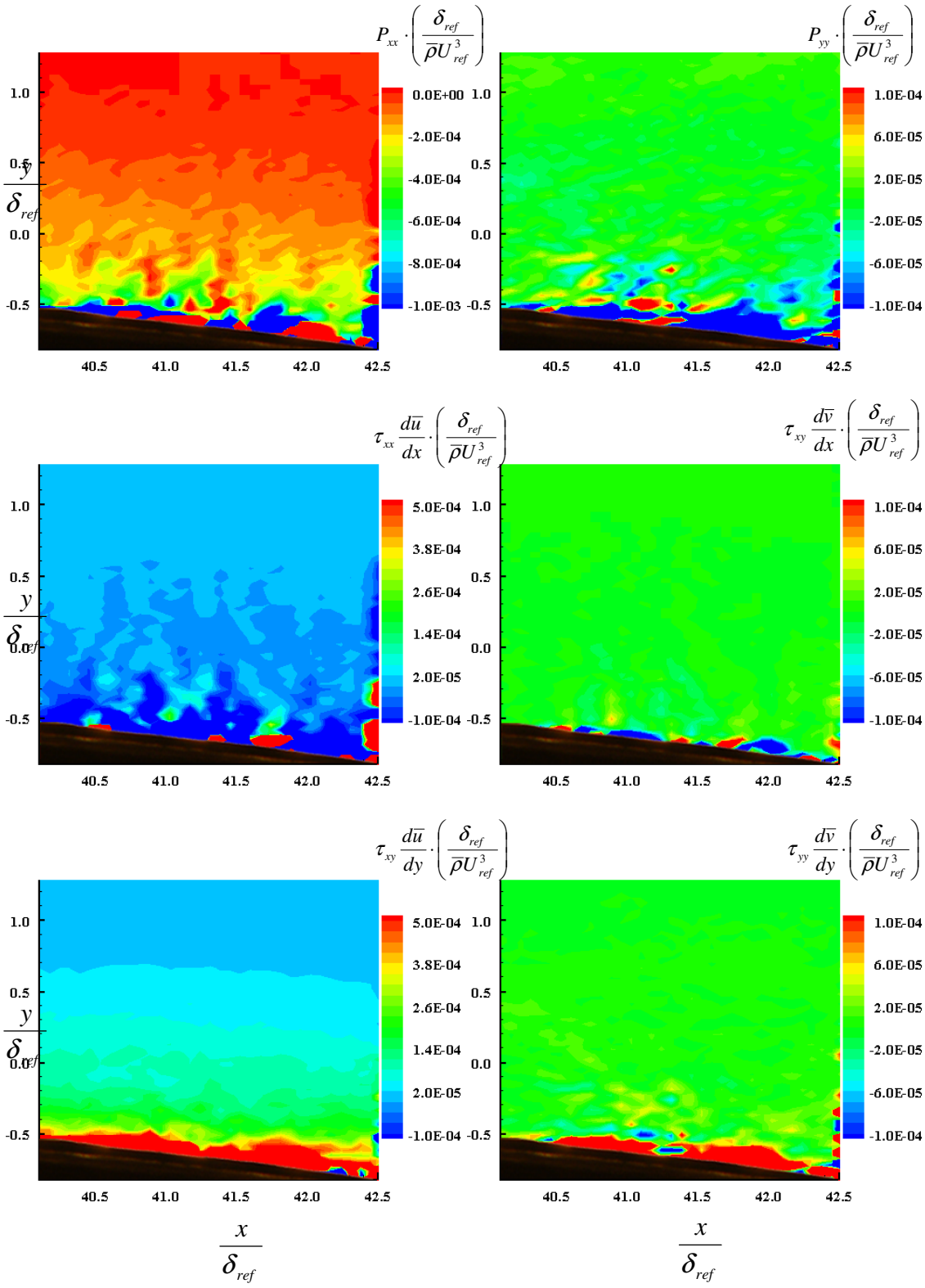

Figure 148: Smooth wall WPG plot of P_{xx}, P_{yy} and their at location 3

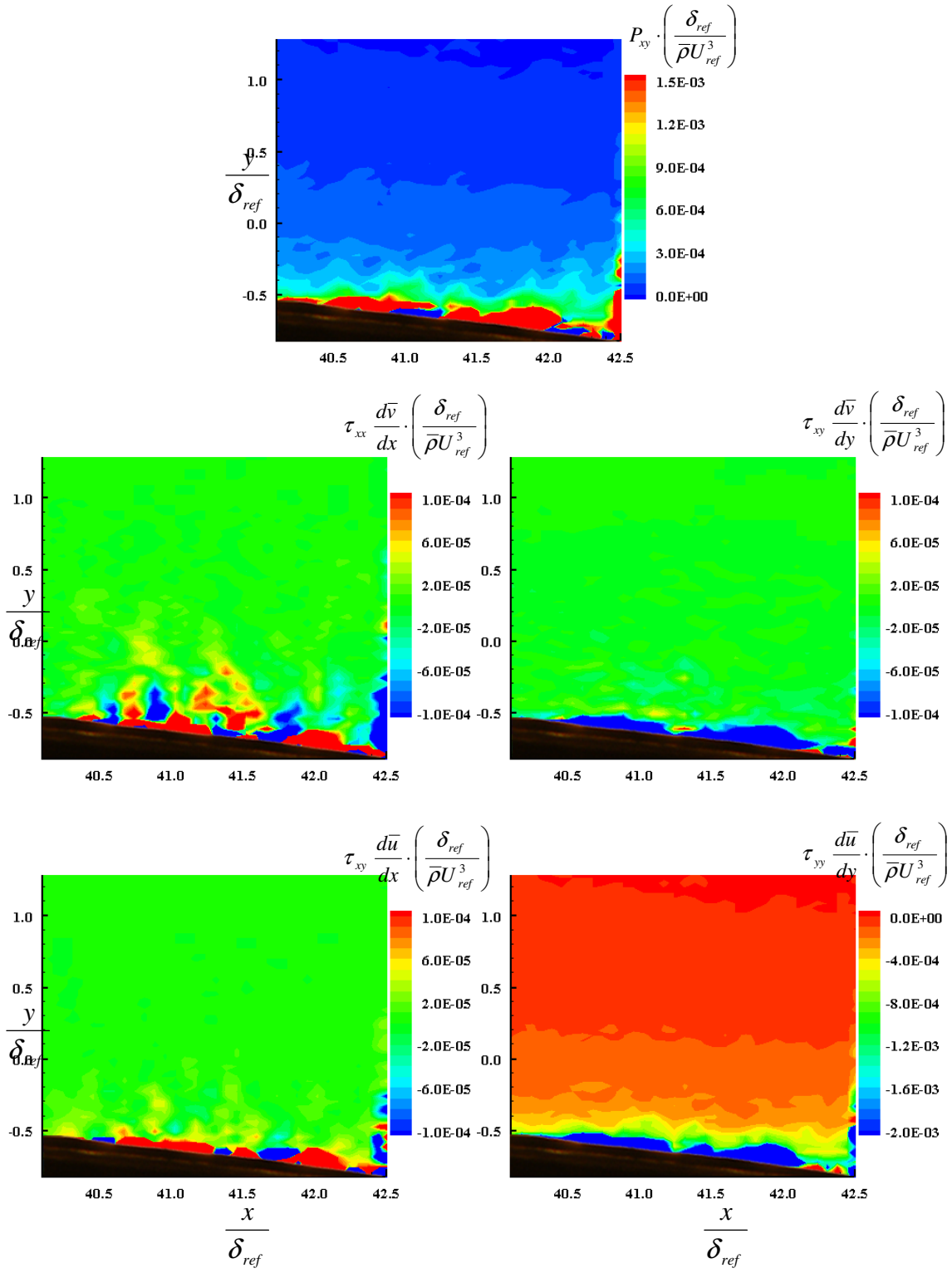

Figure 149: Smooth wall WPG plot of P_{xy} and its components at location 3

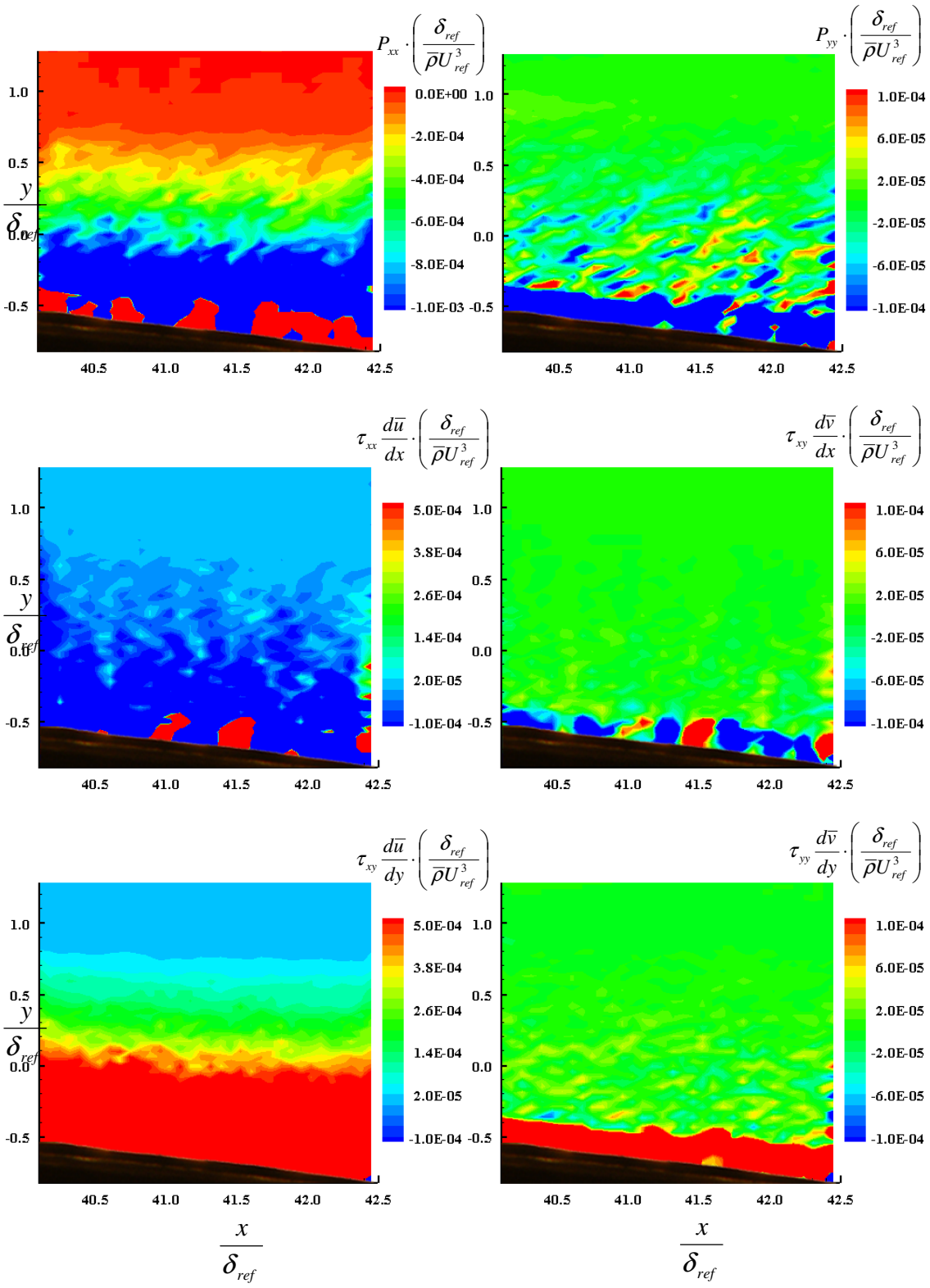

Figure 150: Square roughness WPG plot of P_{xx}, P_{yy} and their components at location 3

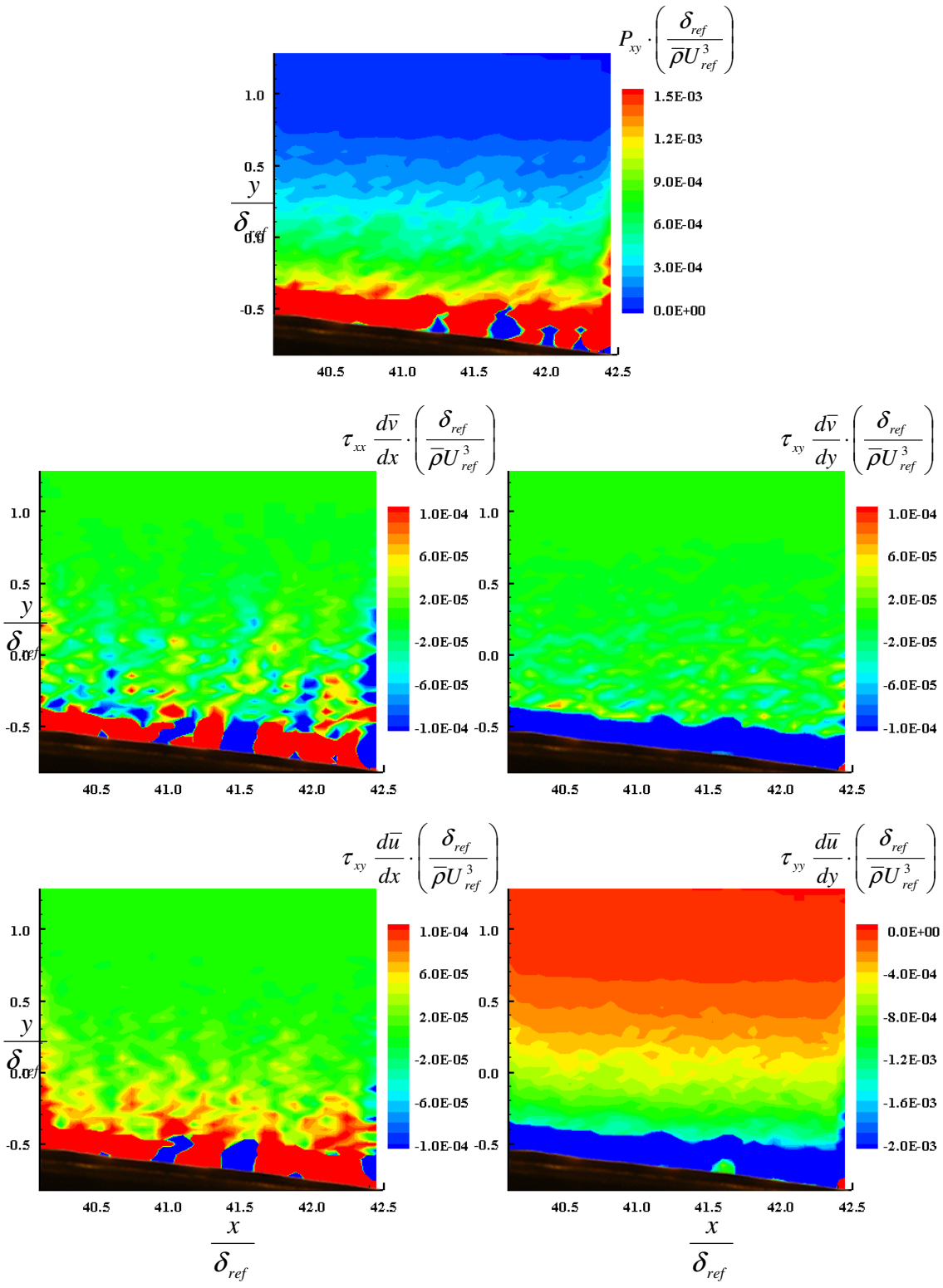

Figure 151: Square roughness WPG plot of P_{xy} and its components at location 3

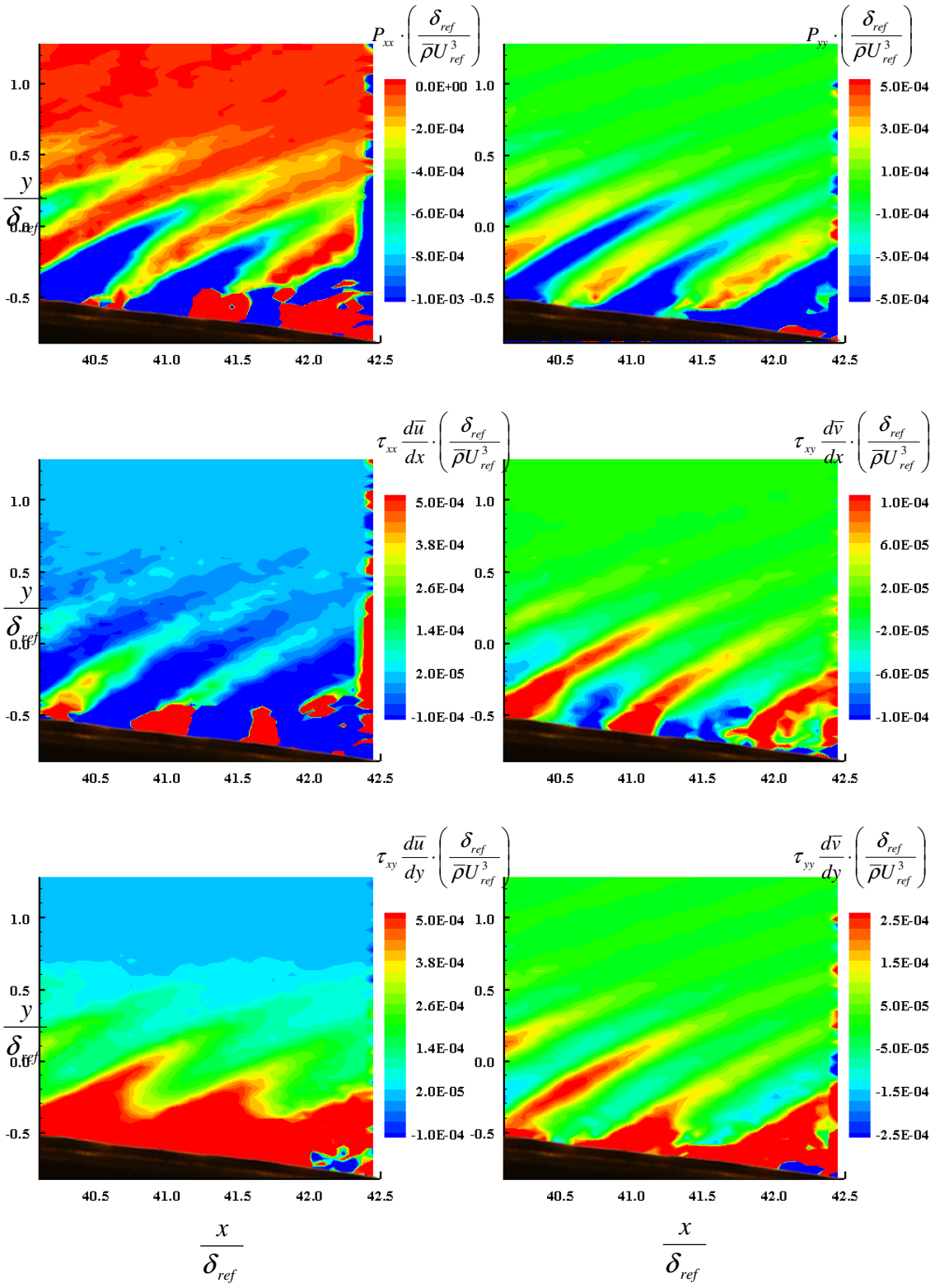

Figure 152: Diamond roughness WPG plot of P_{xx}, P_{yy} and their components at location 3

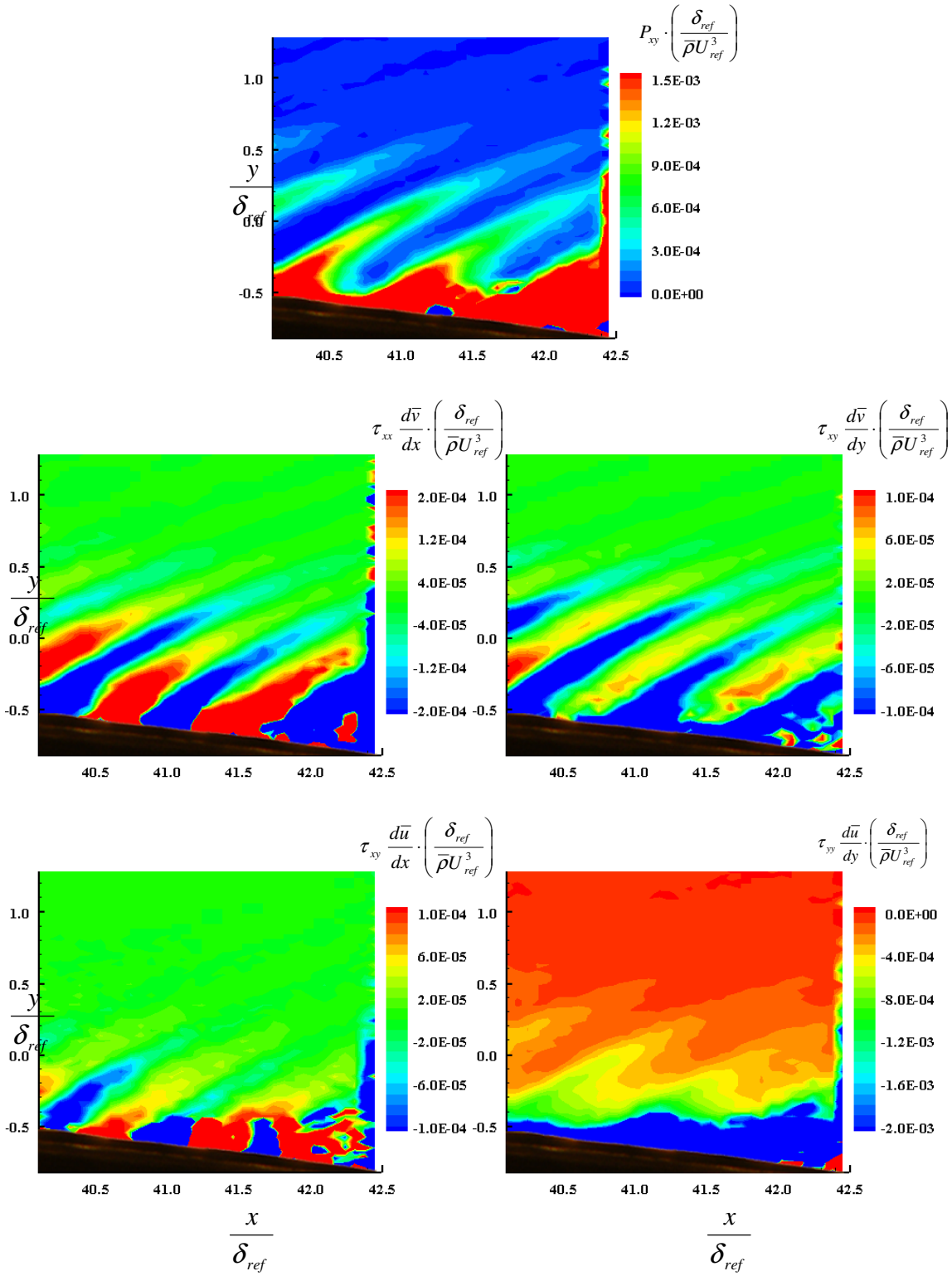

Figure 153: Diamond roughness WPG plot of P_{xy} and its components at location 3

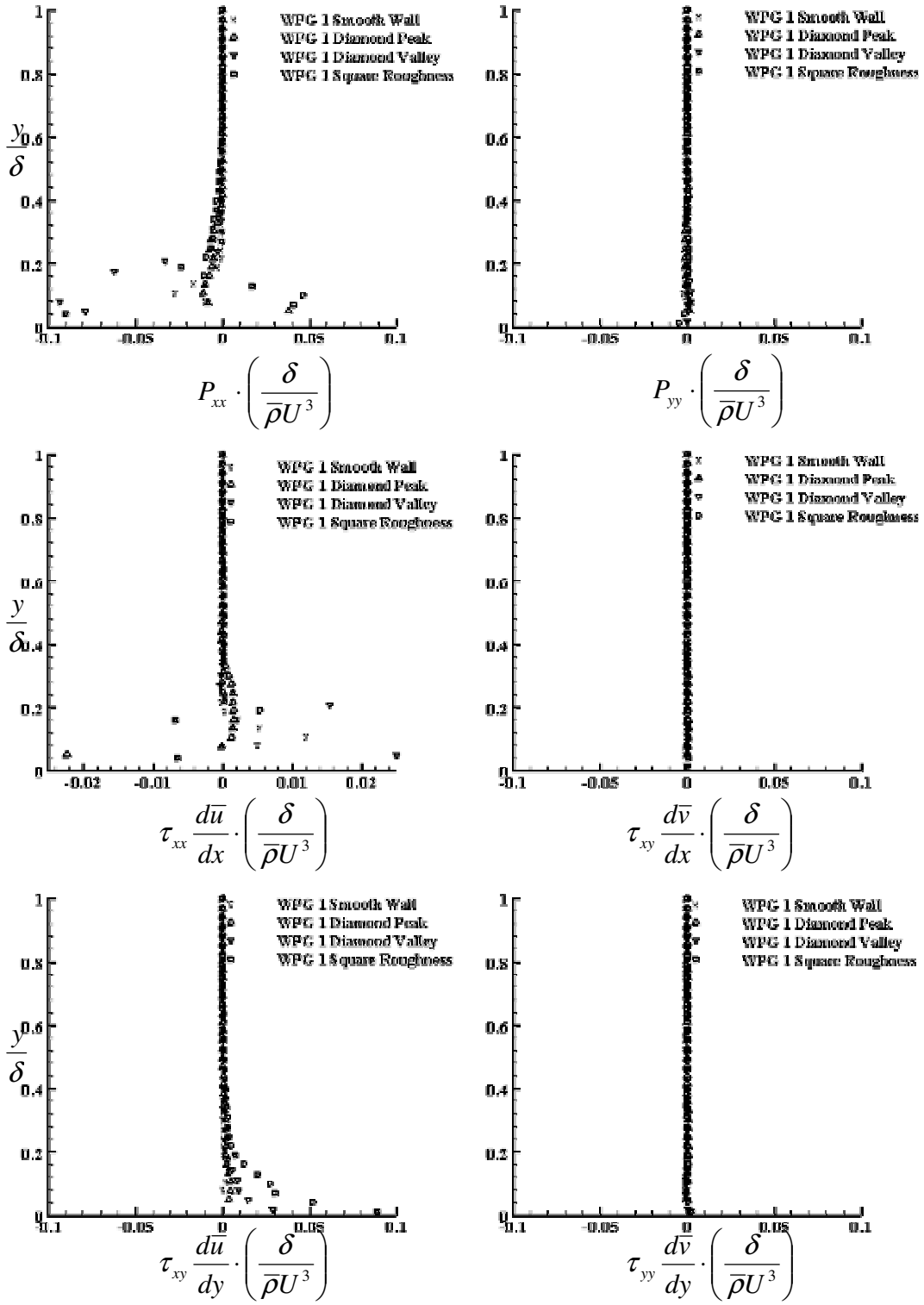

Figure 154: WPG profiles of P_{xx}, P_{yy} and their components at location 1

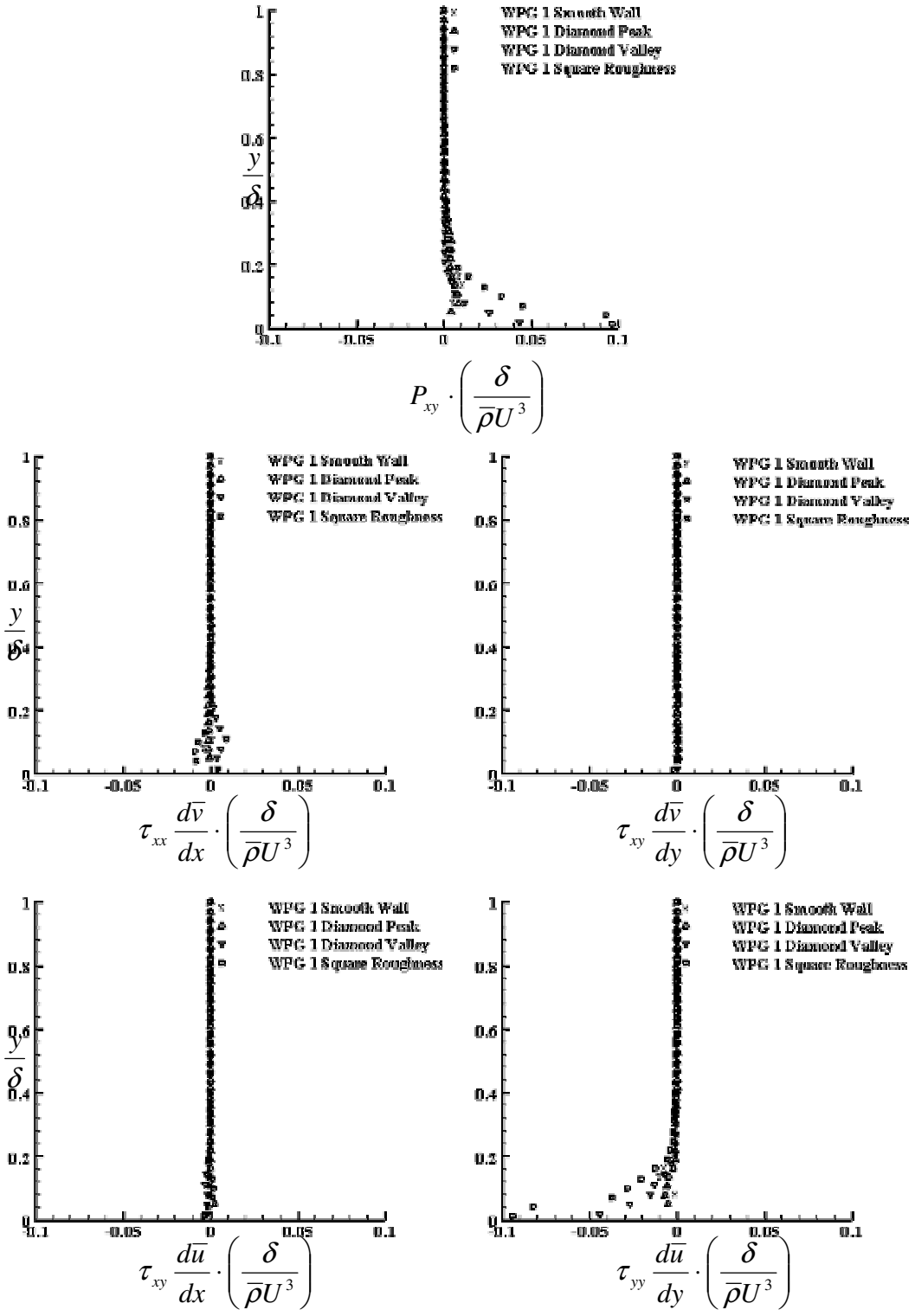

Figure 155: WPG profiles of P_{xy} and its components at location 1

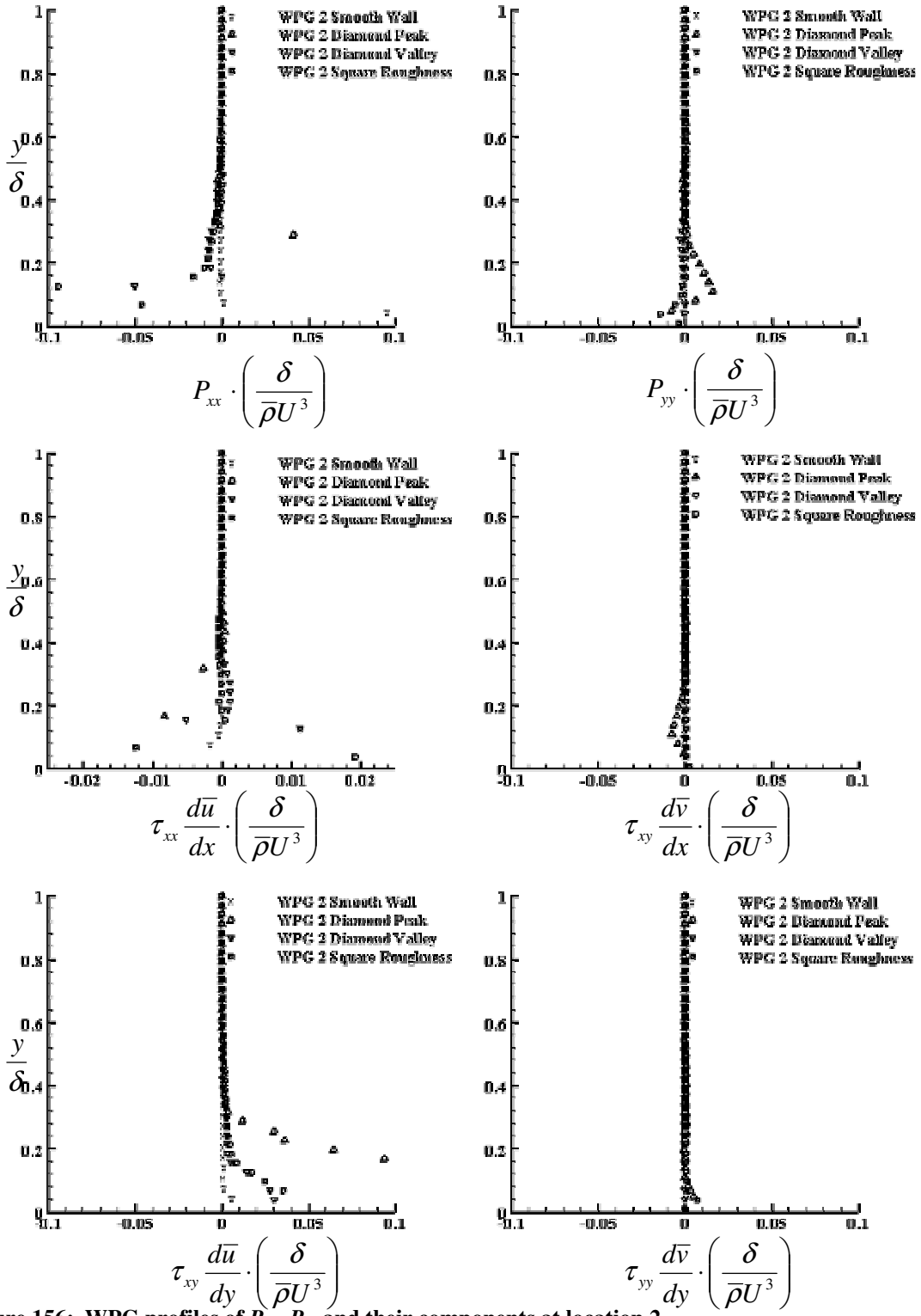

Figure 156: WPG profiles of P_{xx}, P_{yy} and their components at location 2

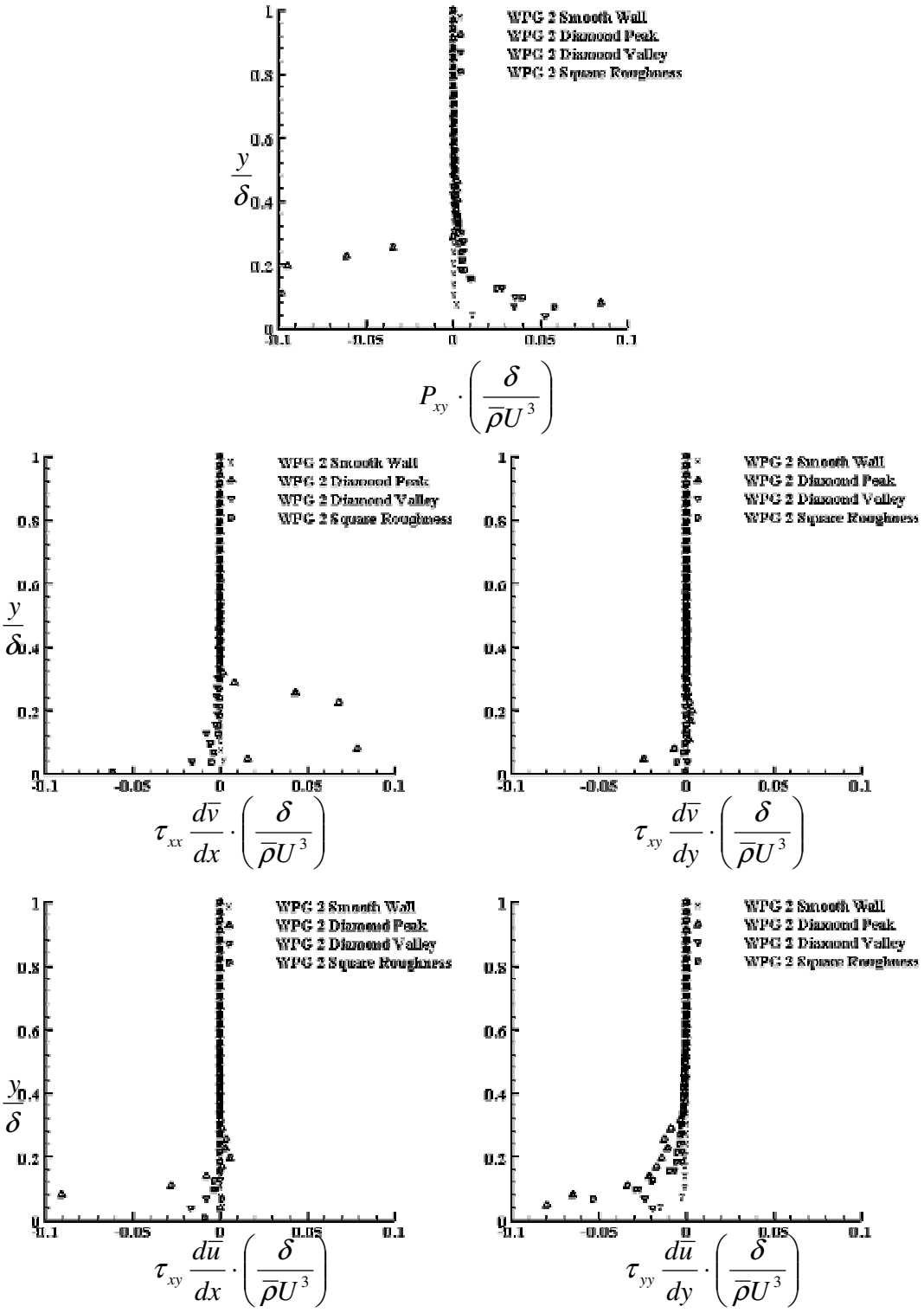

Figure 157: WPG profiles of P_{xy} and its components at location 2

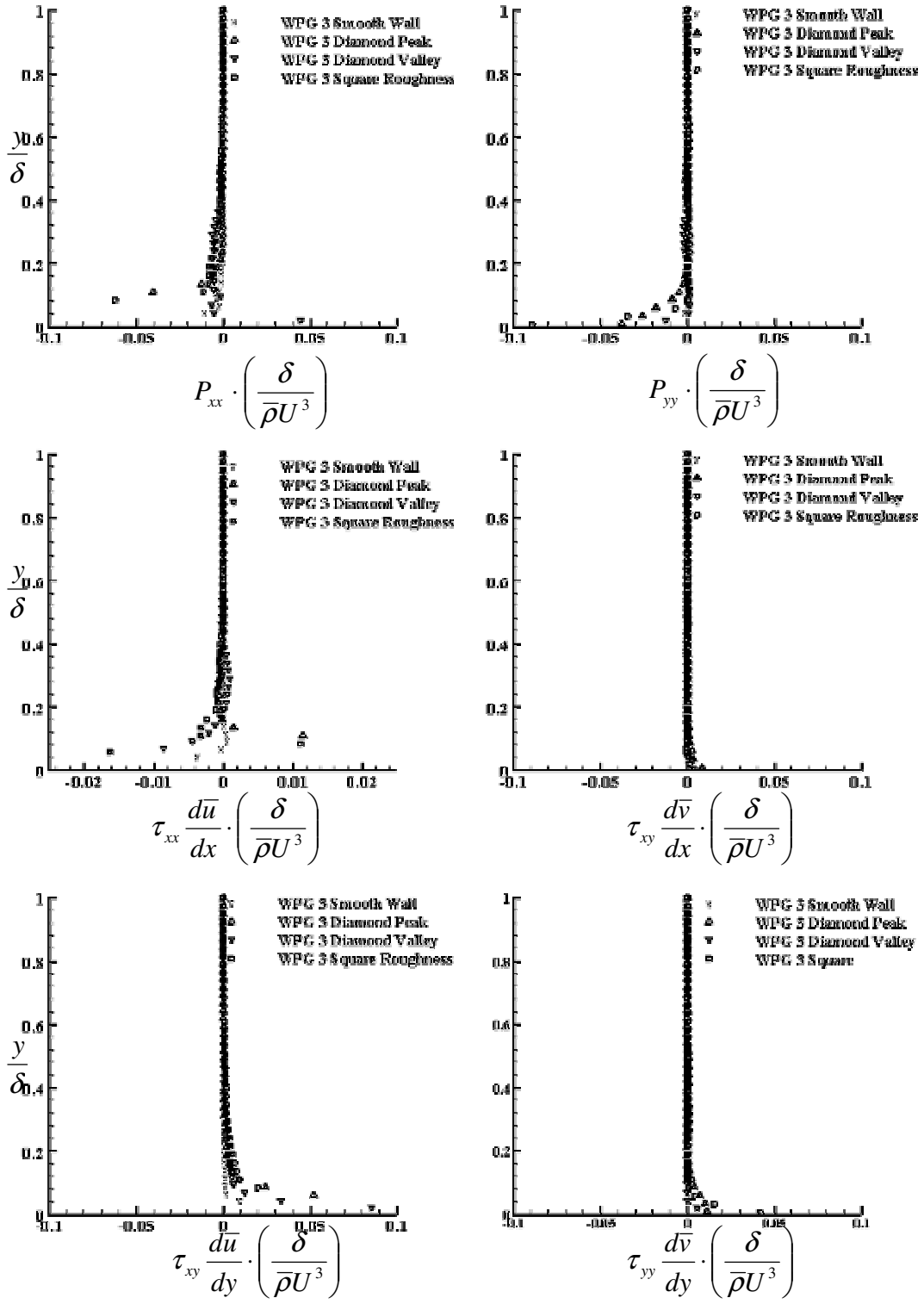

Figure 158: WPG profiles of P_{xx}, P_{yy} and their components at location 3

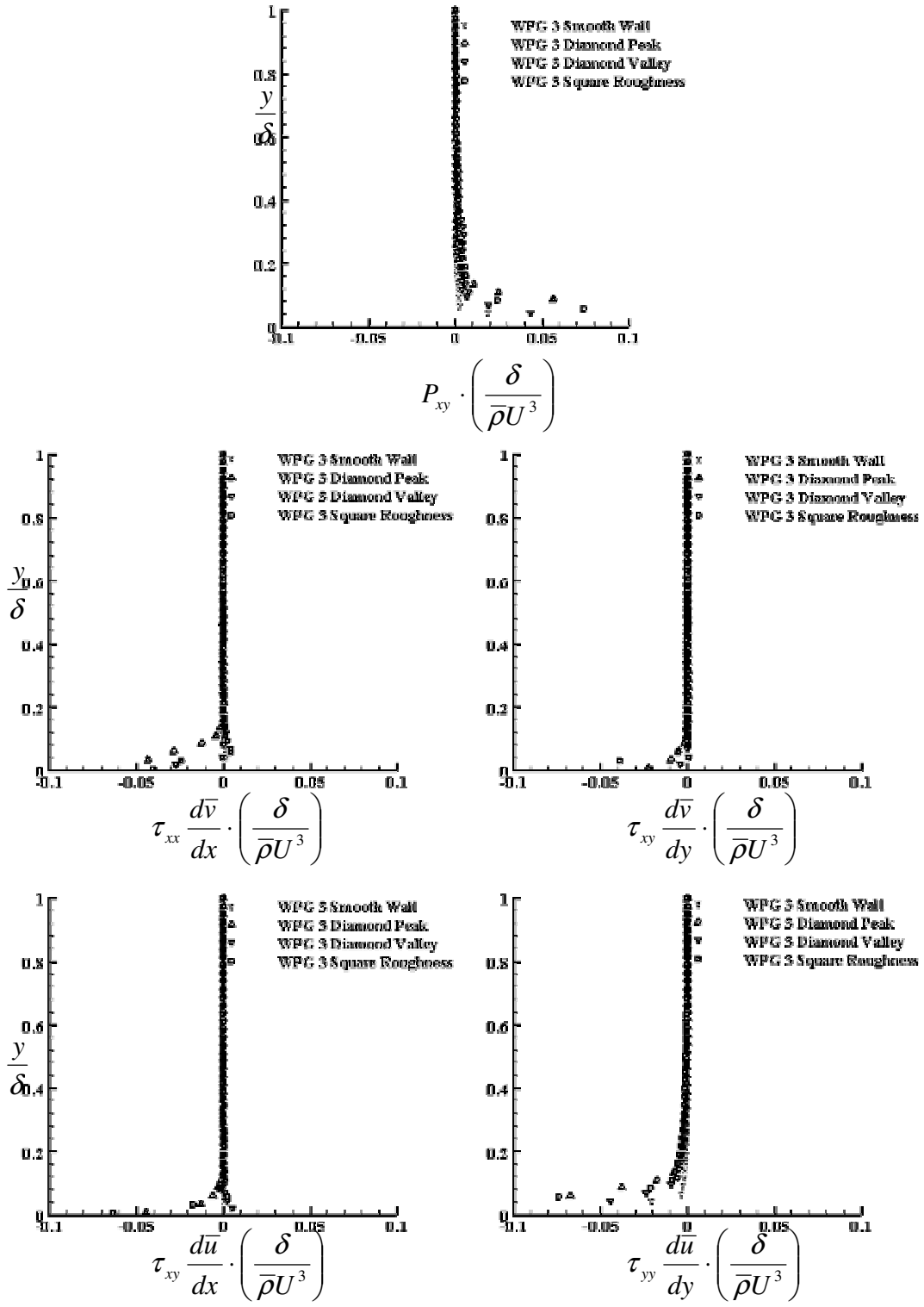

Figure 159: WPG profiles of P_{xy} and its components at location 3

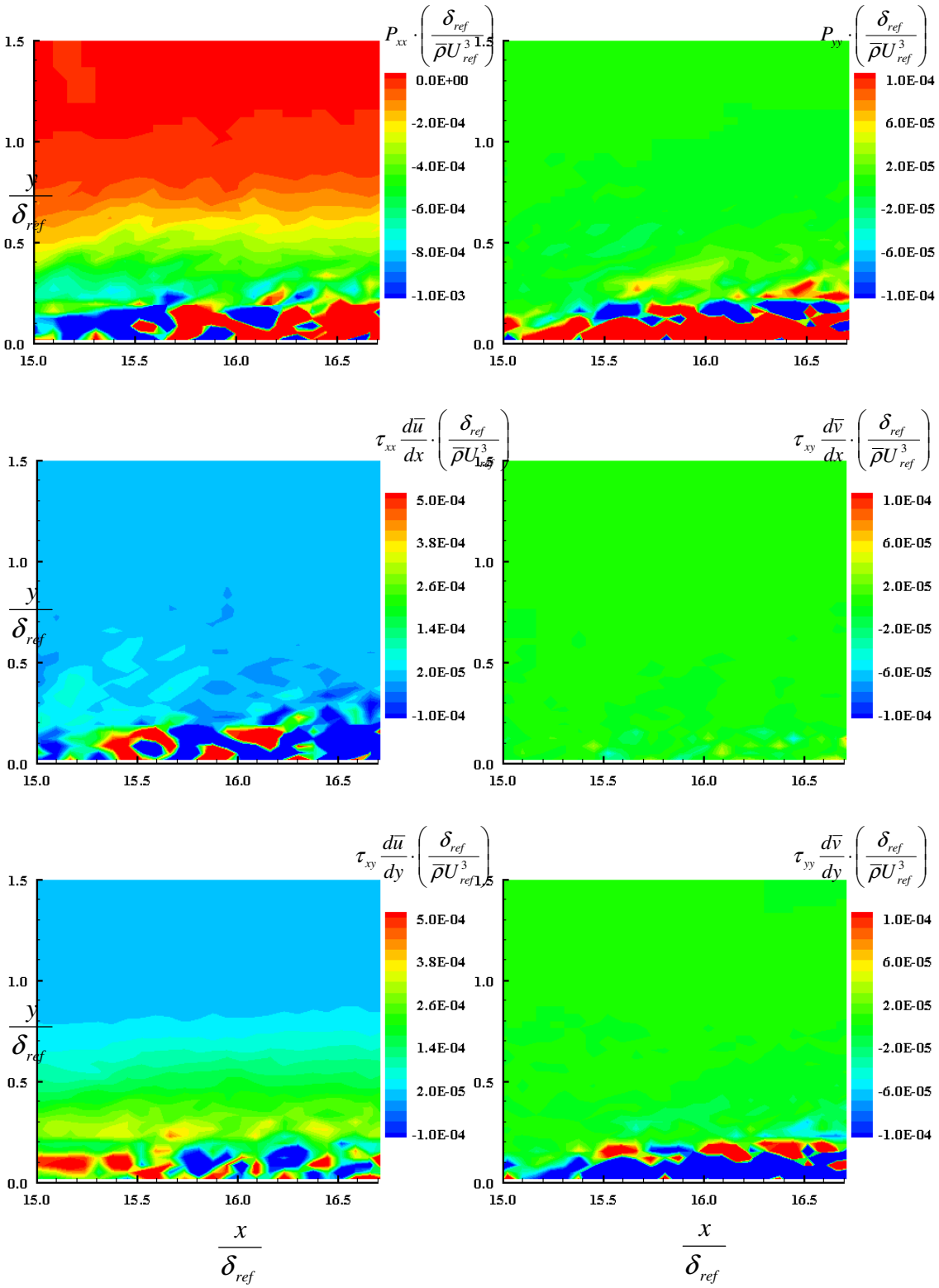

Figure 160: Smooth wall SPG plot of P_{xx}, P_{yy} and their components at location 1

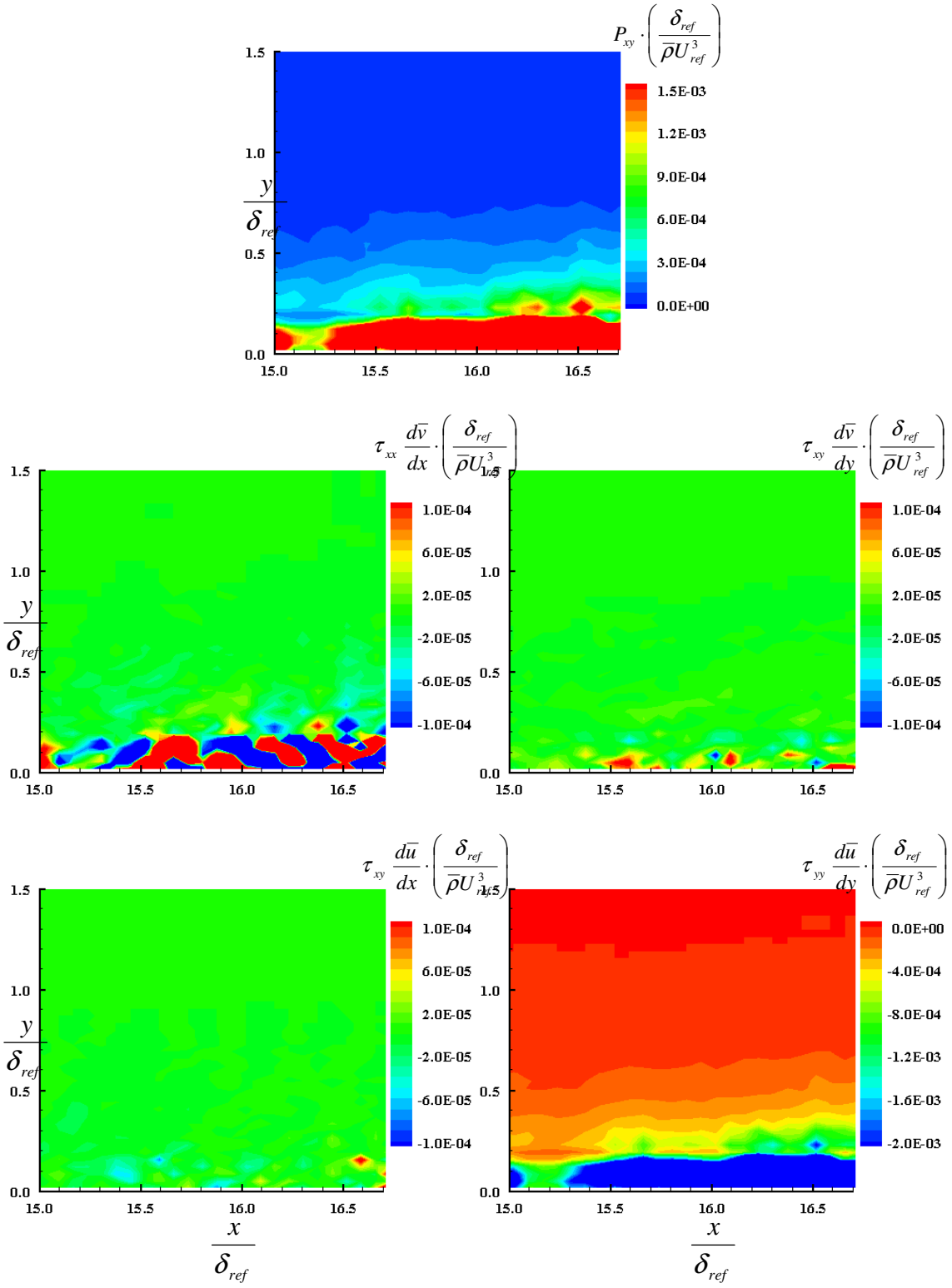

Figure 161: Smooth wall SPG plot of P_{xy} and its components at location 1

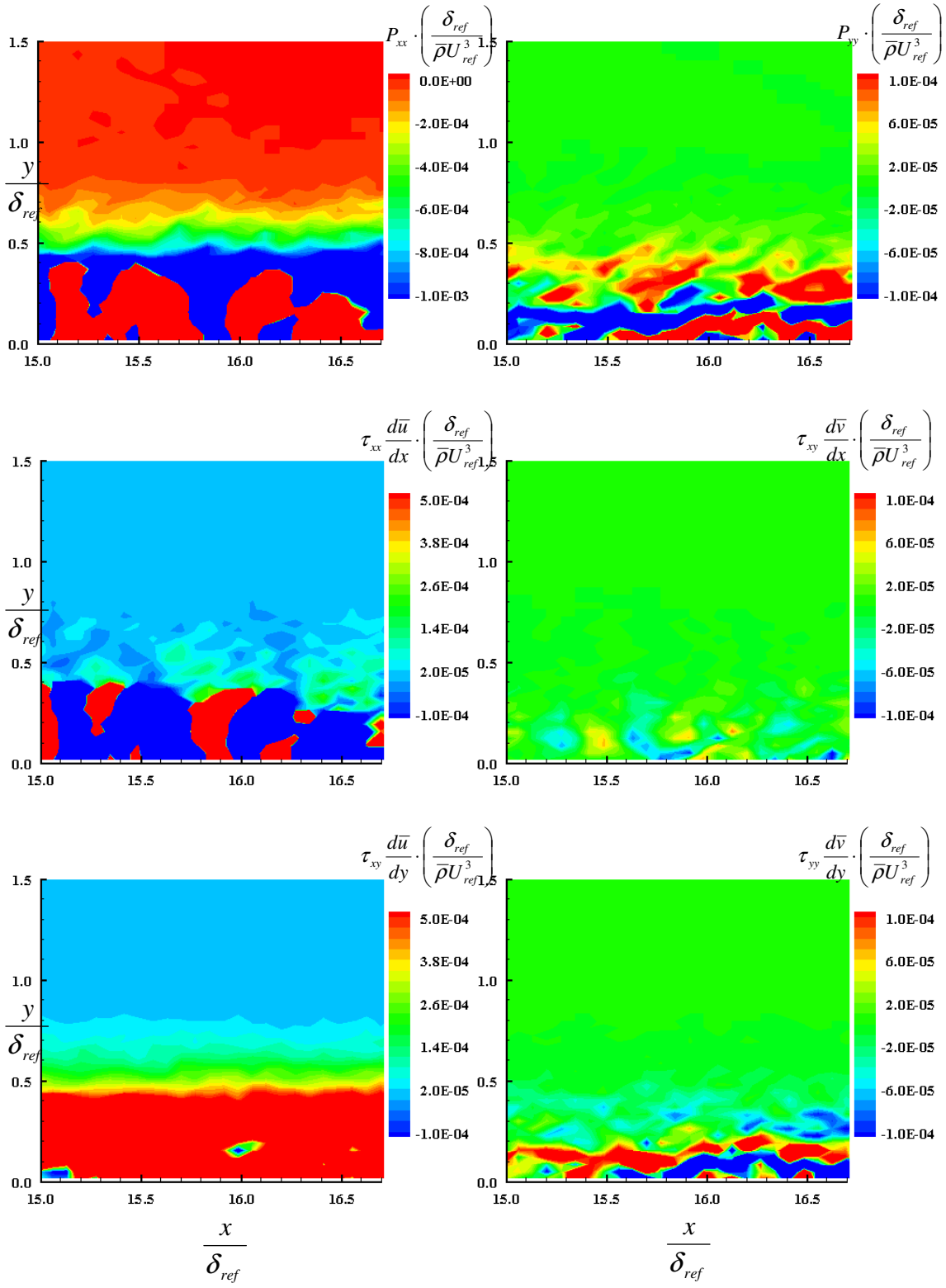

Figure 162: Square roughness SPG plot of P_{xx}, P_{yy} and their components at location 1

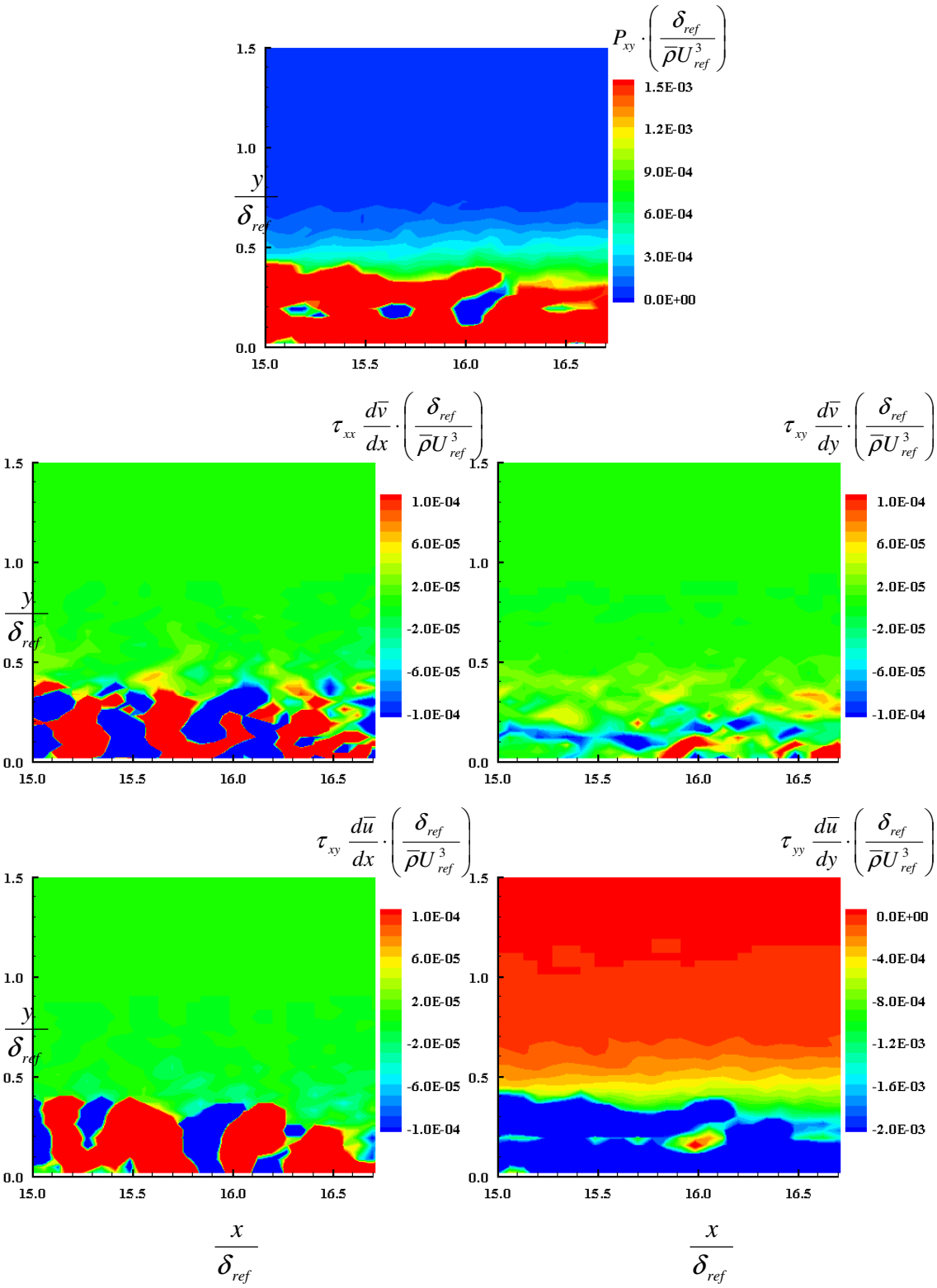

Figure 163: Square roughness SPG plot of P_{xy} and its components at location 1

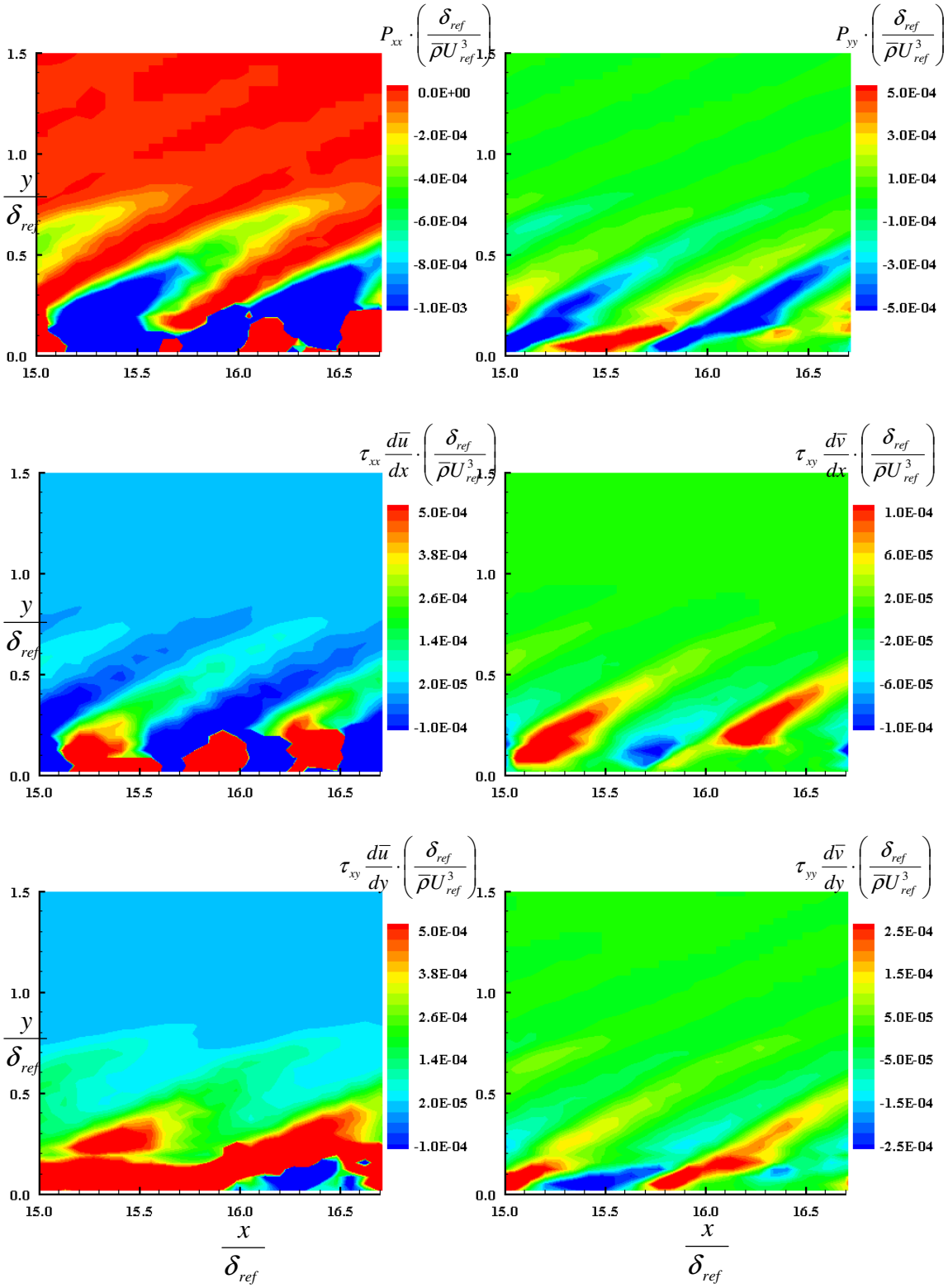

Figure 164: Diamond roughness SPG plot of P_{xx}, P_{yy} and their components at location 1

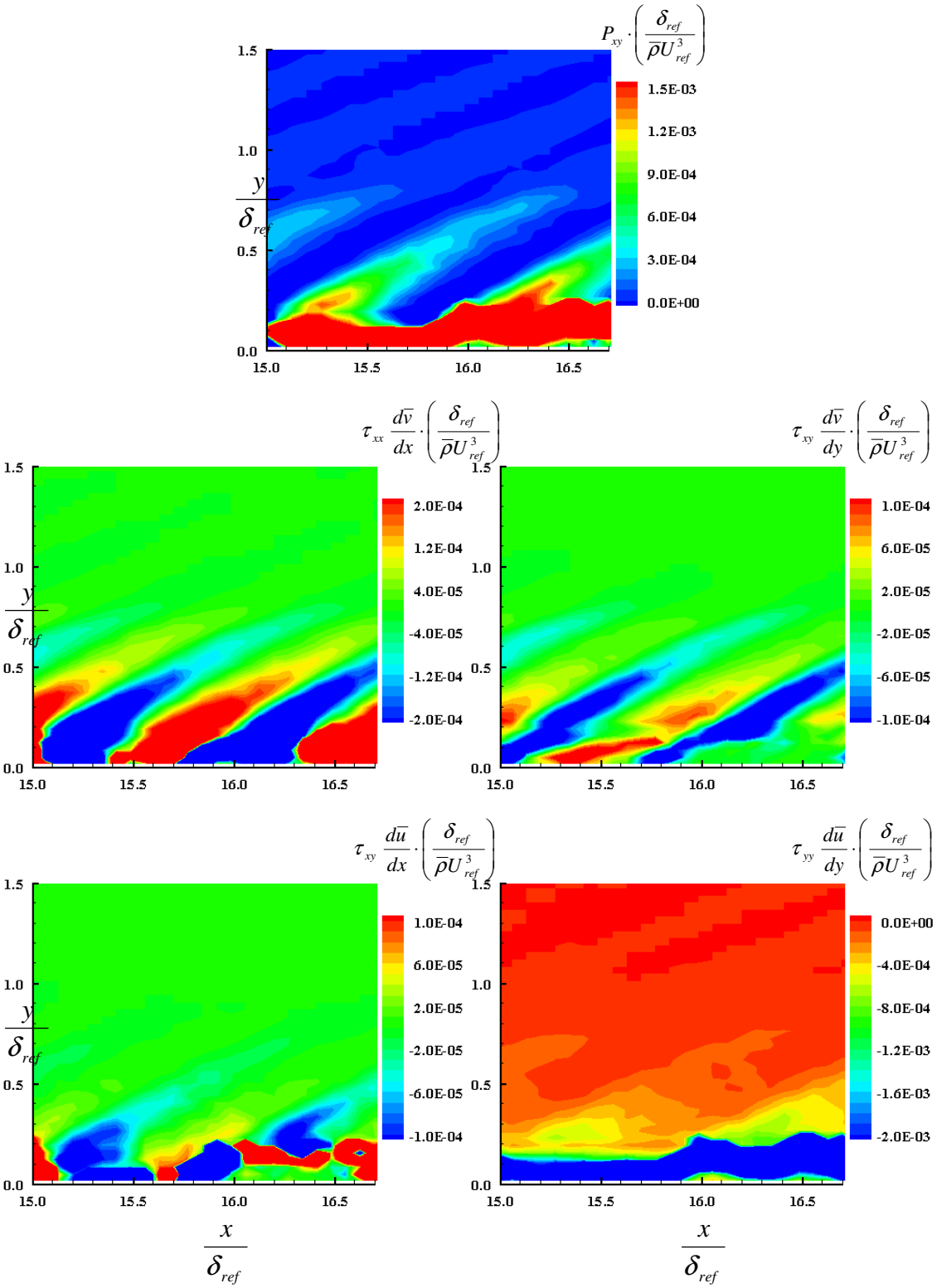

Figure 165: Diamond roughness SPG plot of P_{xy} and its components at location 1

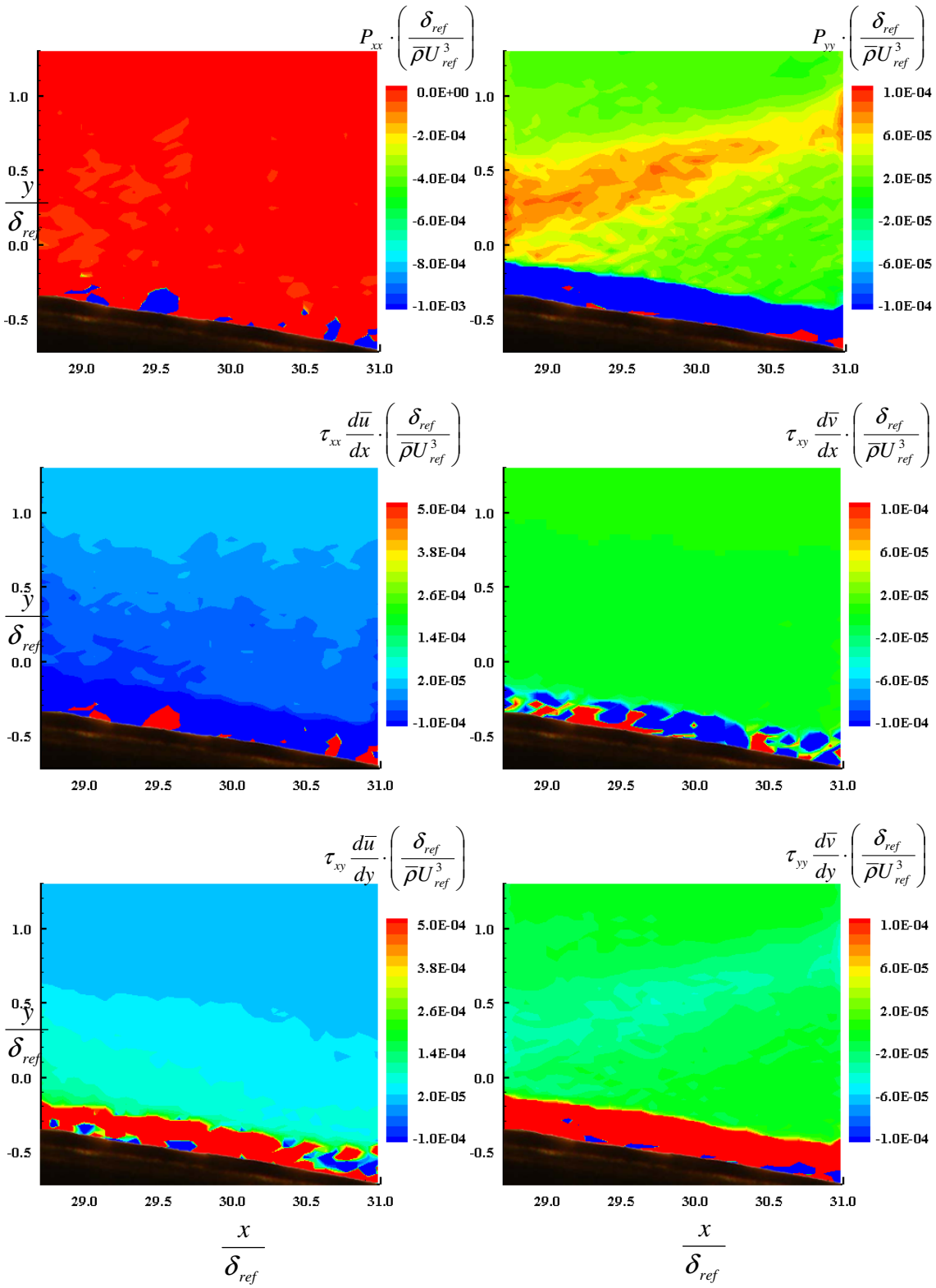

Figure 166: Smooth wall SPG plot of P_{xx}, P_{yy} and their components at location 2

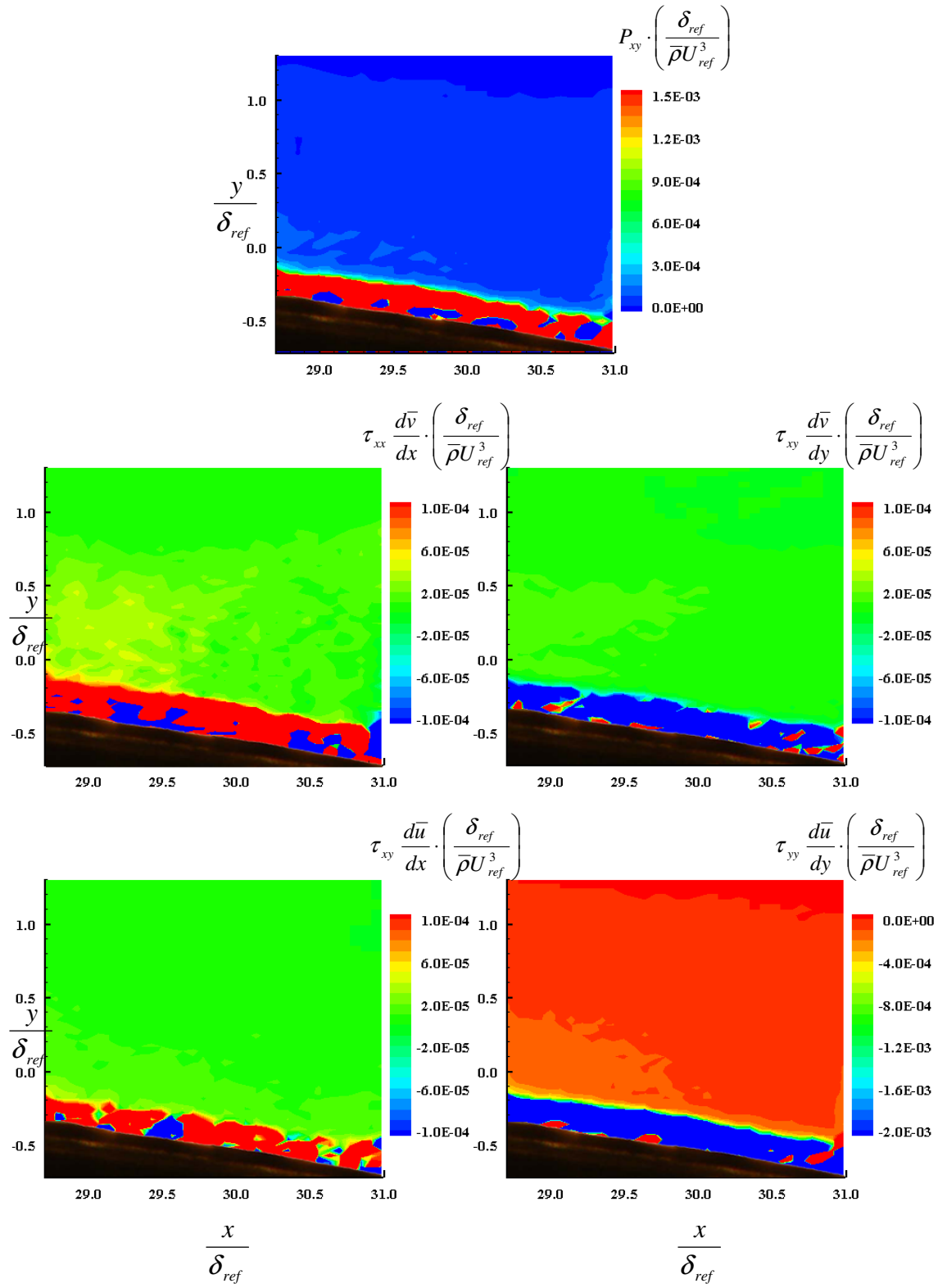

Figure 167: Smooth wall SPG plot of P_{xy} and its components at location 2

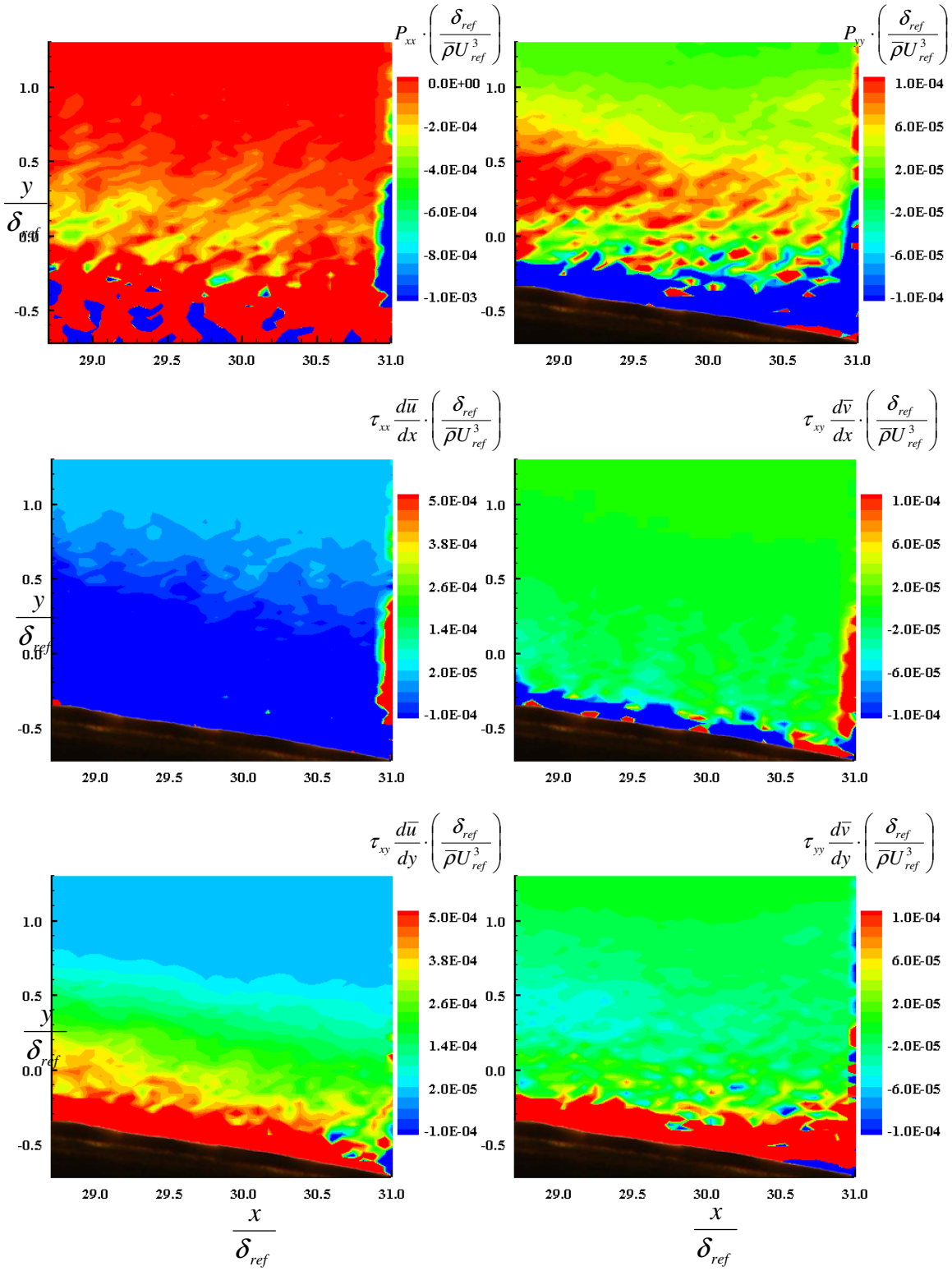

Figure 168: Square roughness SPG plot of P_{xx}, P_{yy} and their components at location 2

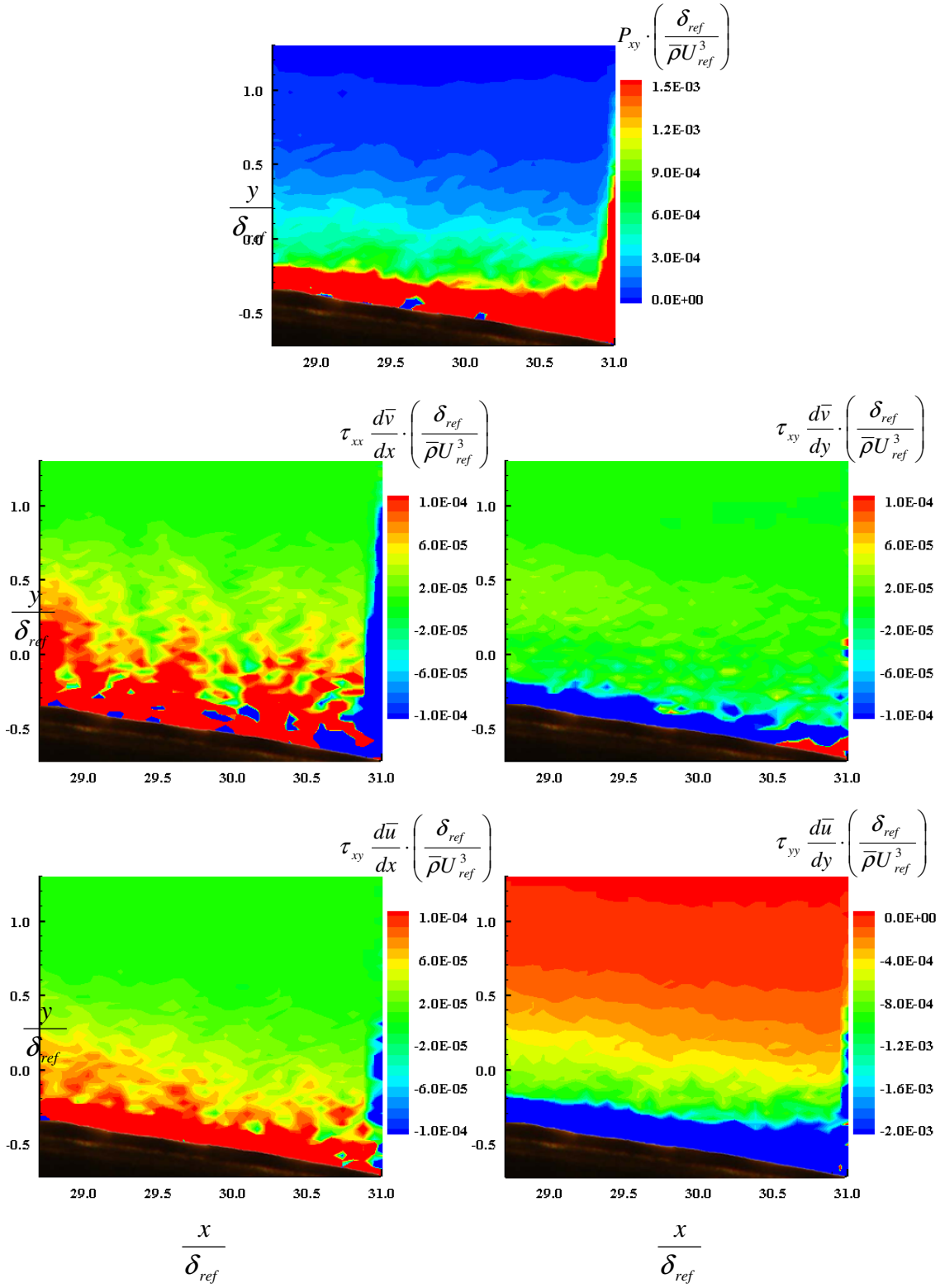

Figure 169: Square roughness SPG plot of P_{xy} and its components at location 2

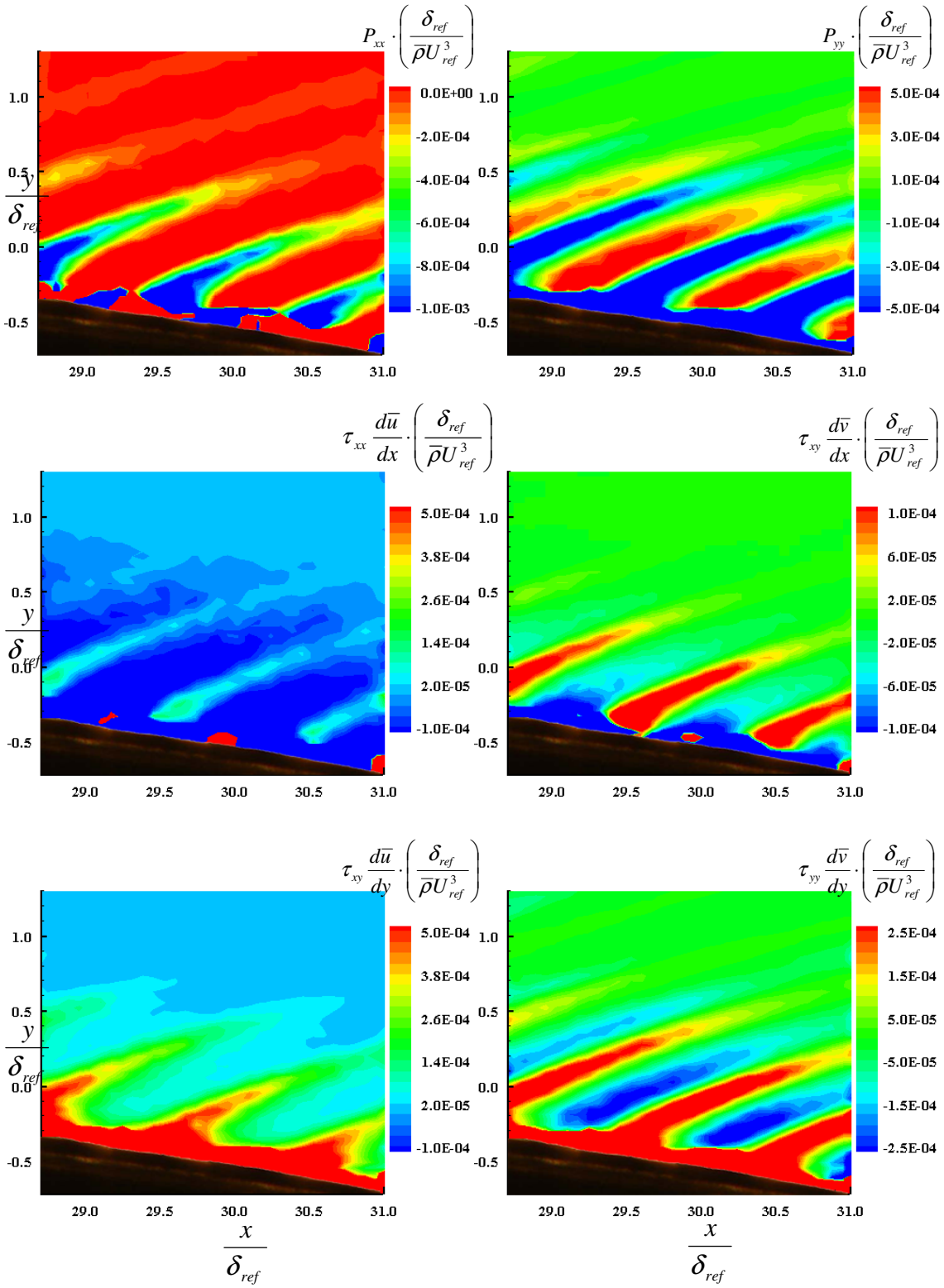

Figure 170: Diamond roughness SPG plot of P_{xx}, P_{yy} and their components at location 2

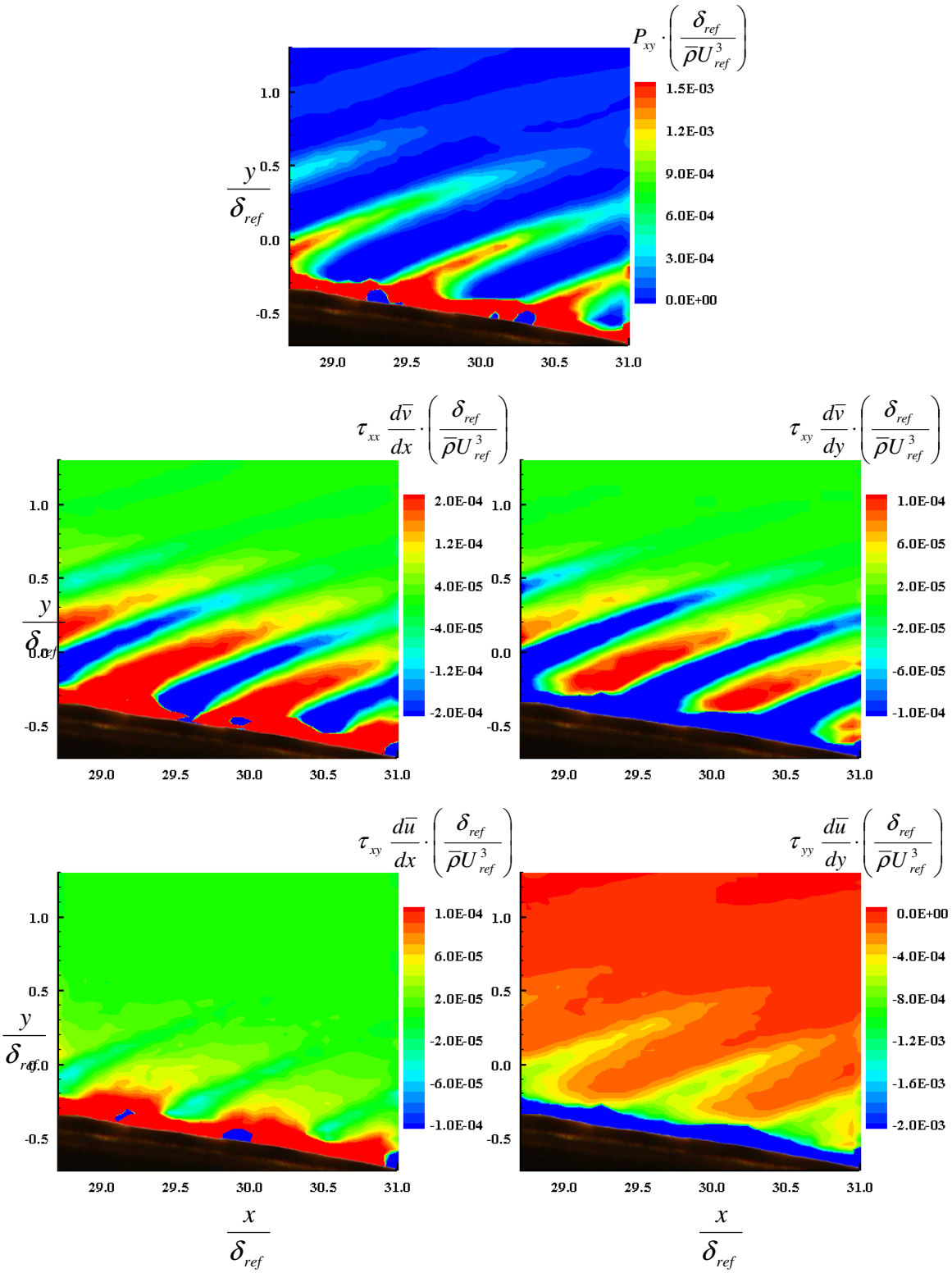

Figure 171: Diamond roughness SPG plot of P_{xy} and its components at location 2

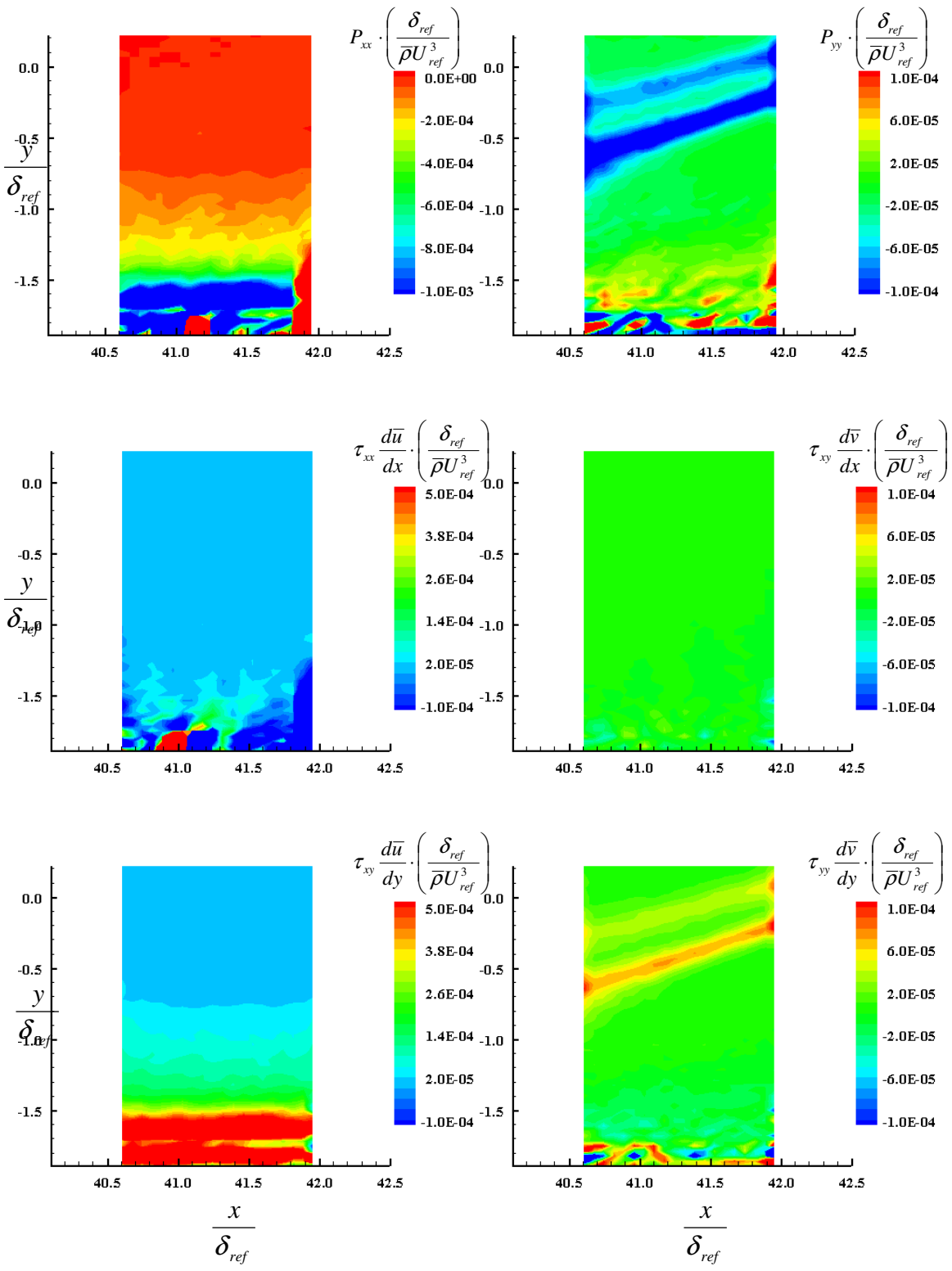

Figure 172: Smooth wall SPG plot of P_{xx}, P_{yy} and their components at location 3

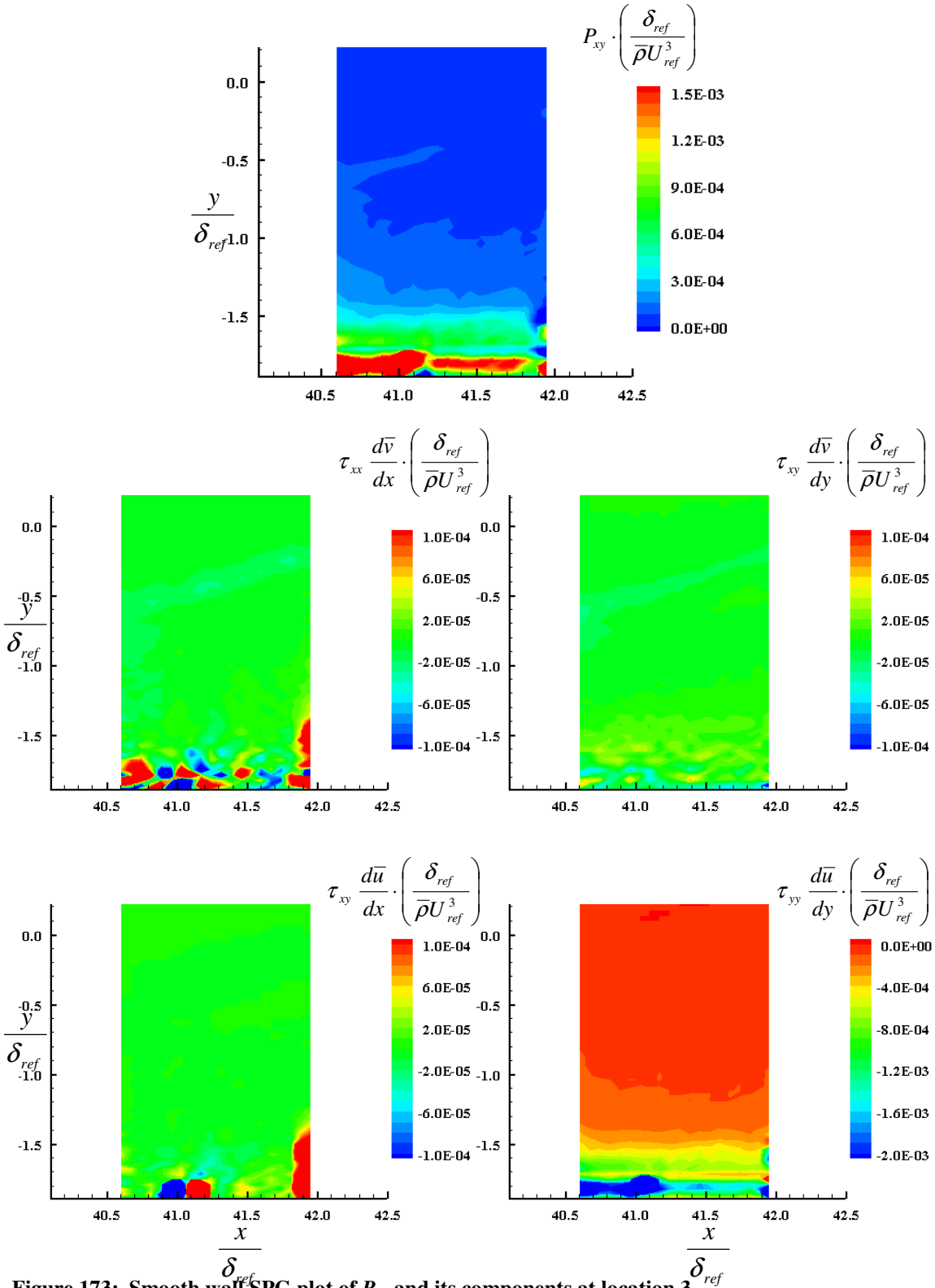

Figure 173: Smooth wall SPG plot of P_{xy} and its components at location 3

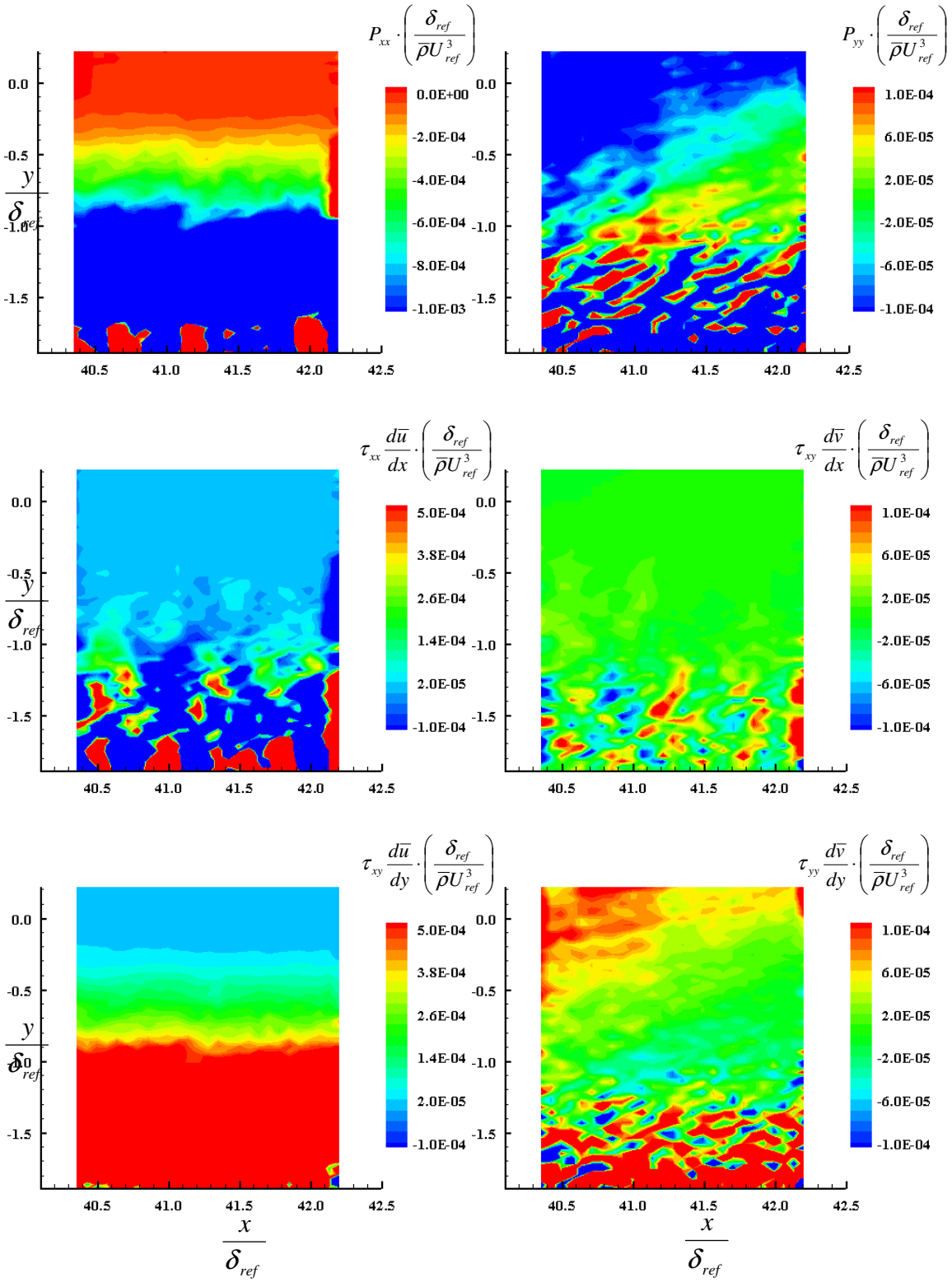

Figure 174: Square roughness SPG plot of P_{xx}, P_{yy} and their components at location 3

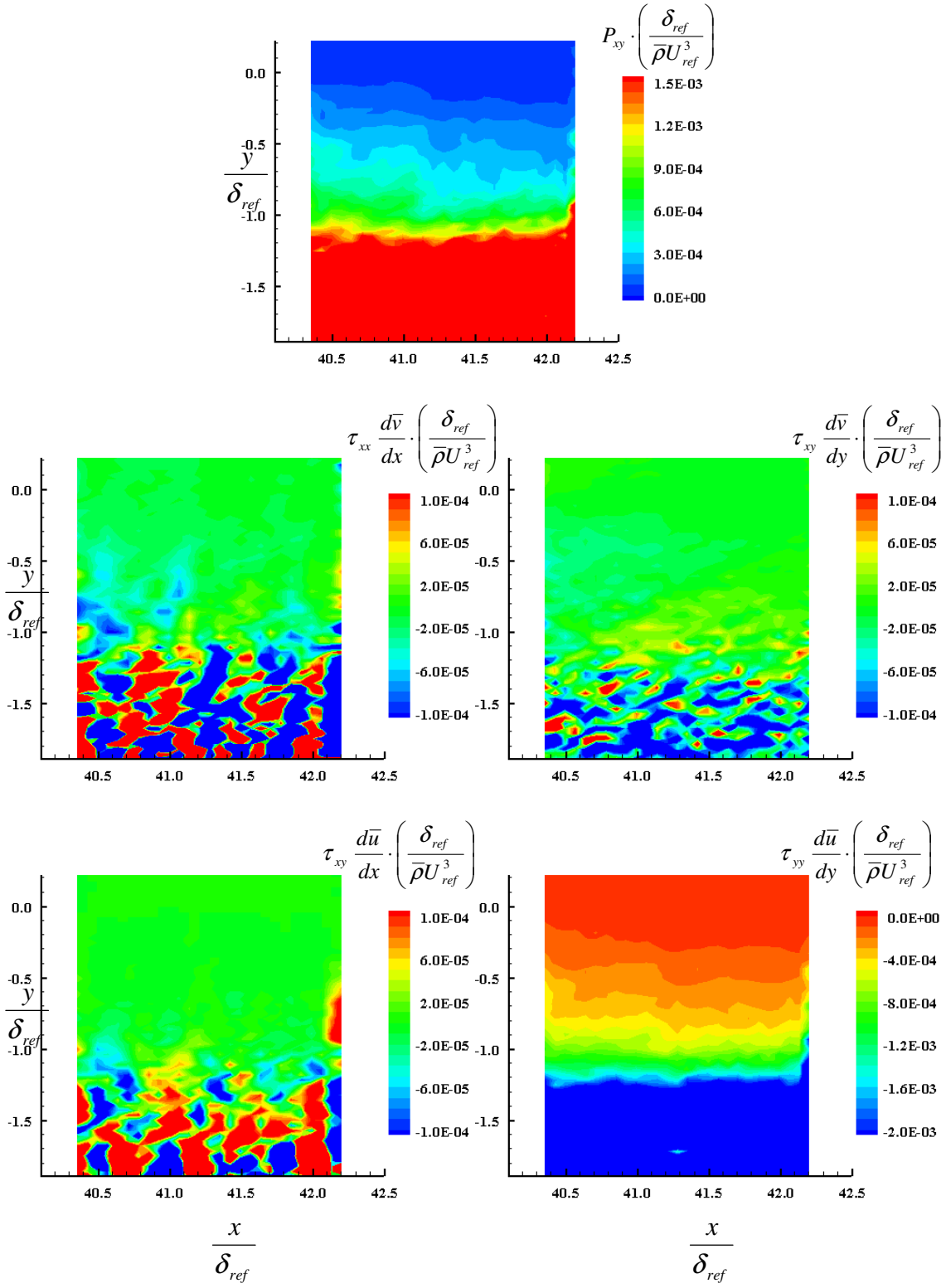

Figure 175: Square roughness SPG plot of P_{xy} and its components at location 3

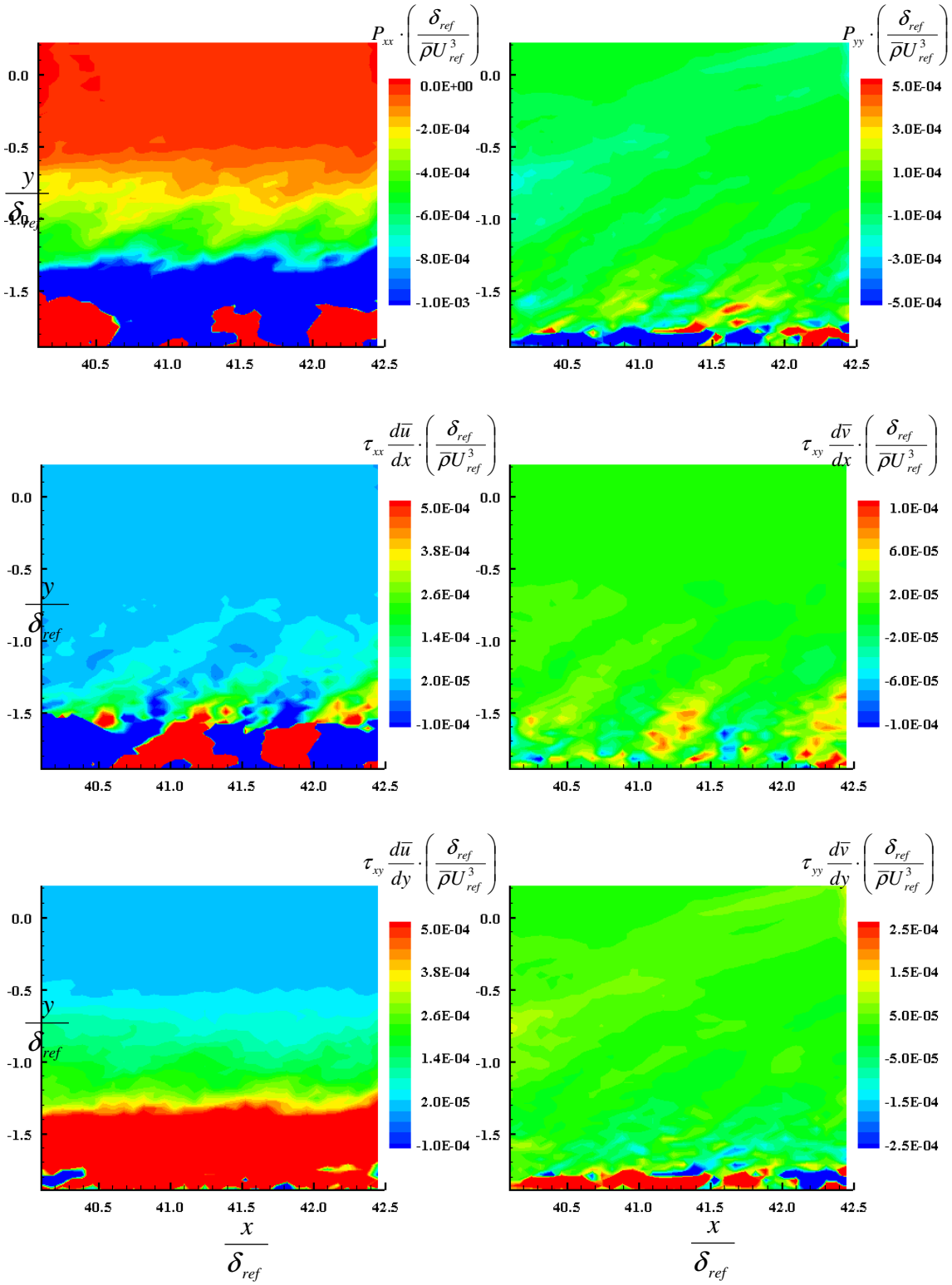

Figure 176: Diamond roughness SPG plot of P_{xx}, P_{yy} and their components at location 3

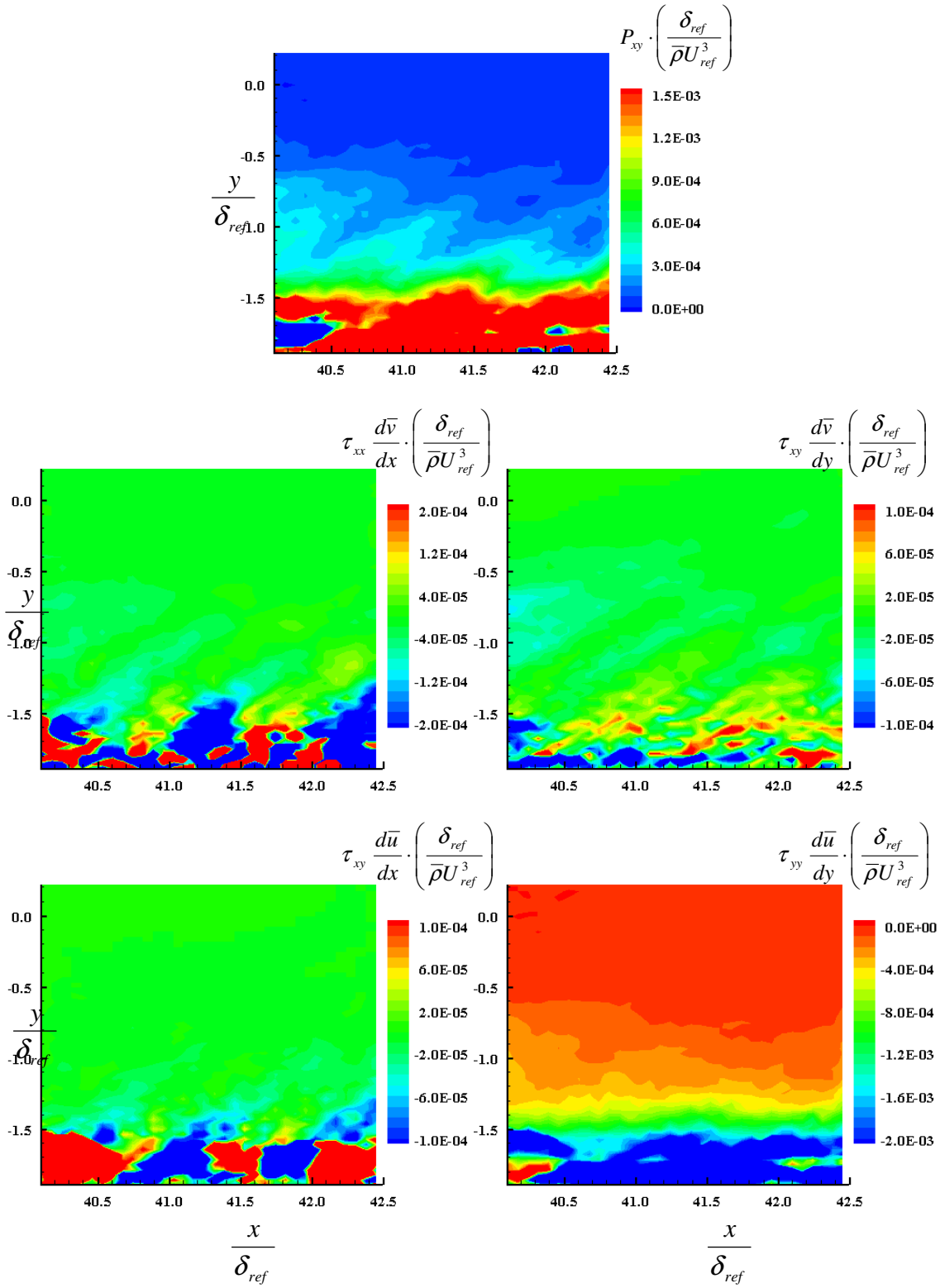

Figure 177: Diamond roughness SPG plot of P_{xy} and its components at location 3

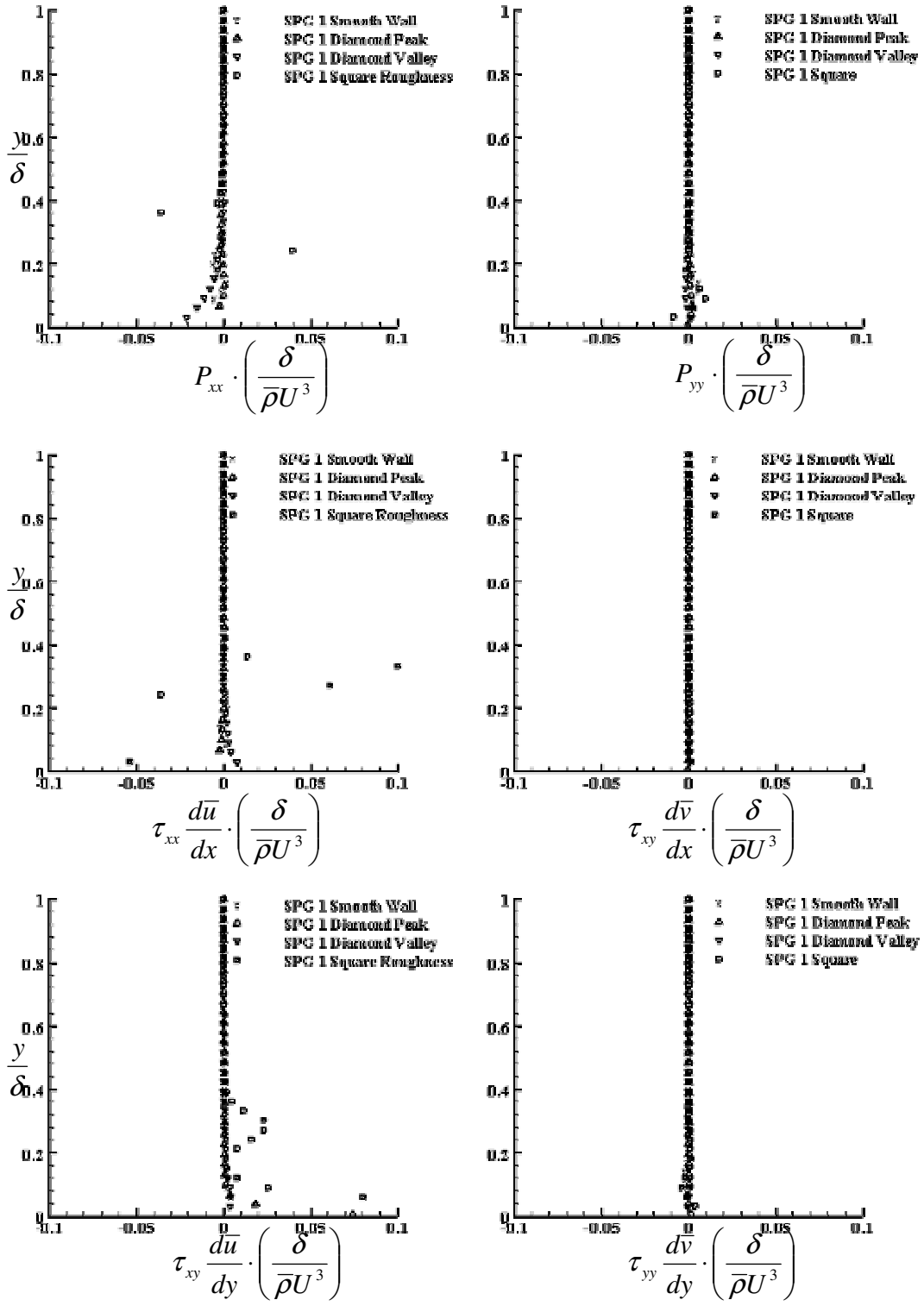

Figure 178: SPG profiles of P_{xx}, P_{yy} and their components at location 1

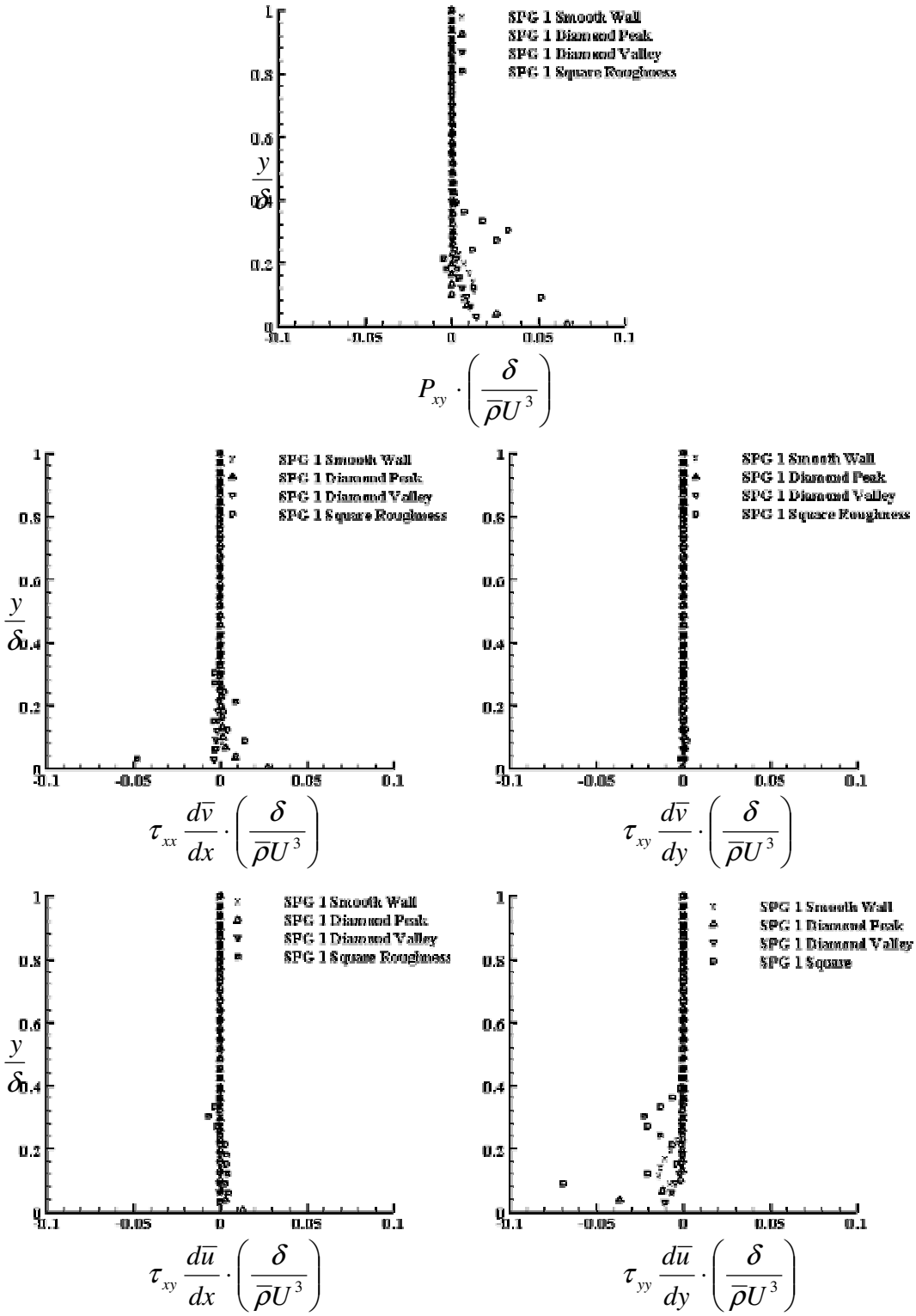

Figure 179: SPG profiles of P_{xy} and its components at location 1

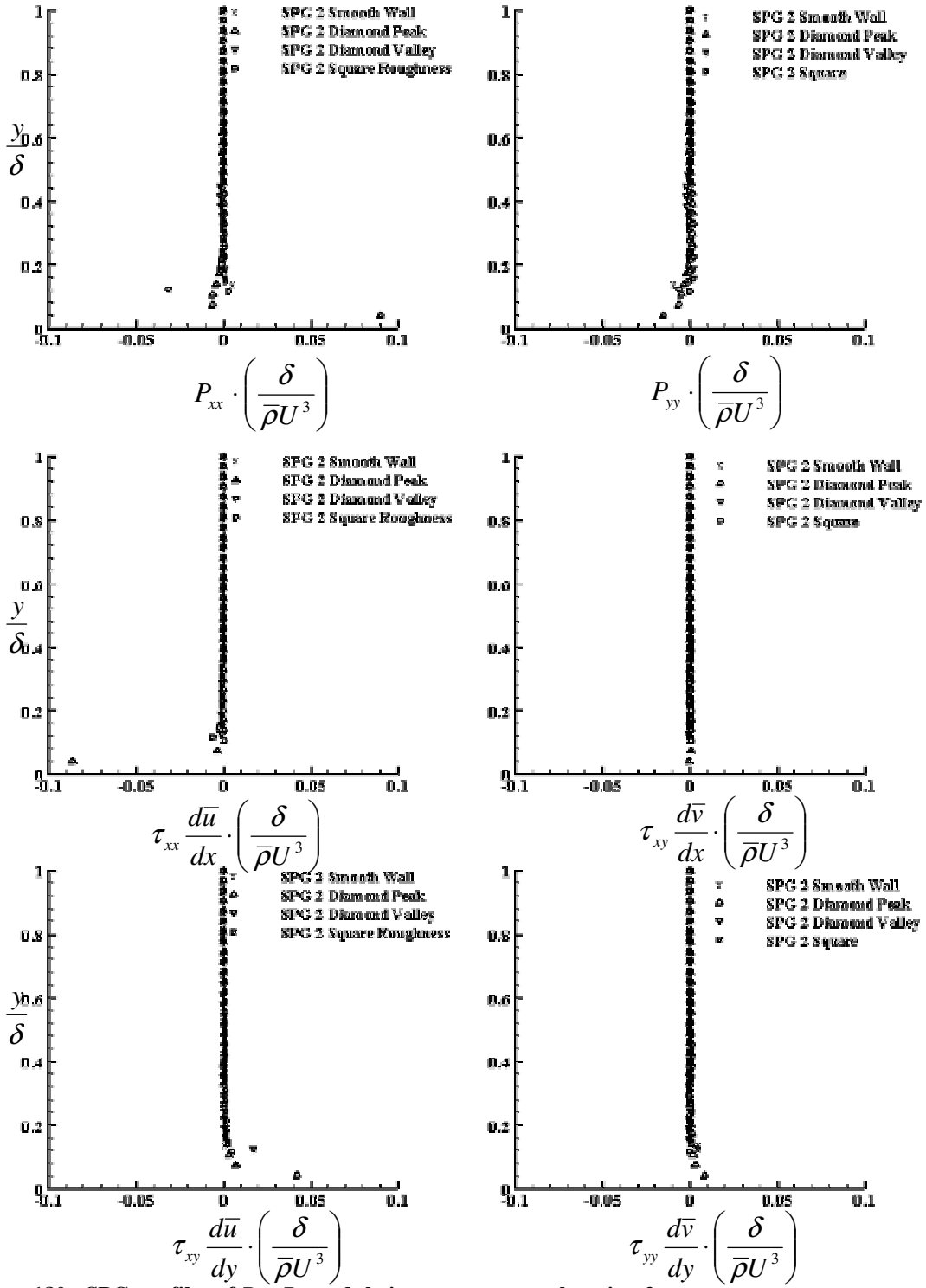

Figure 180: SPG profiles of P_{xx}, P_{yy} and their components at location 2

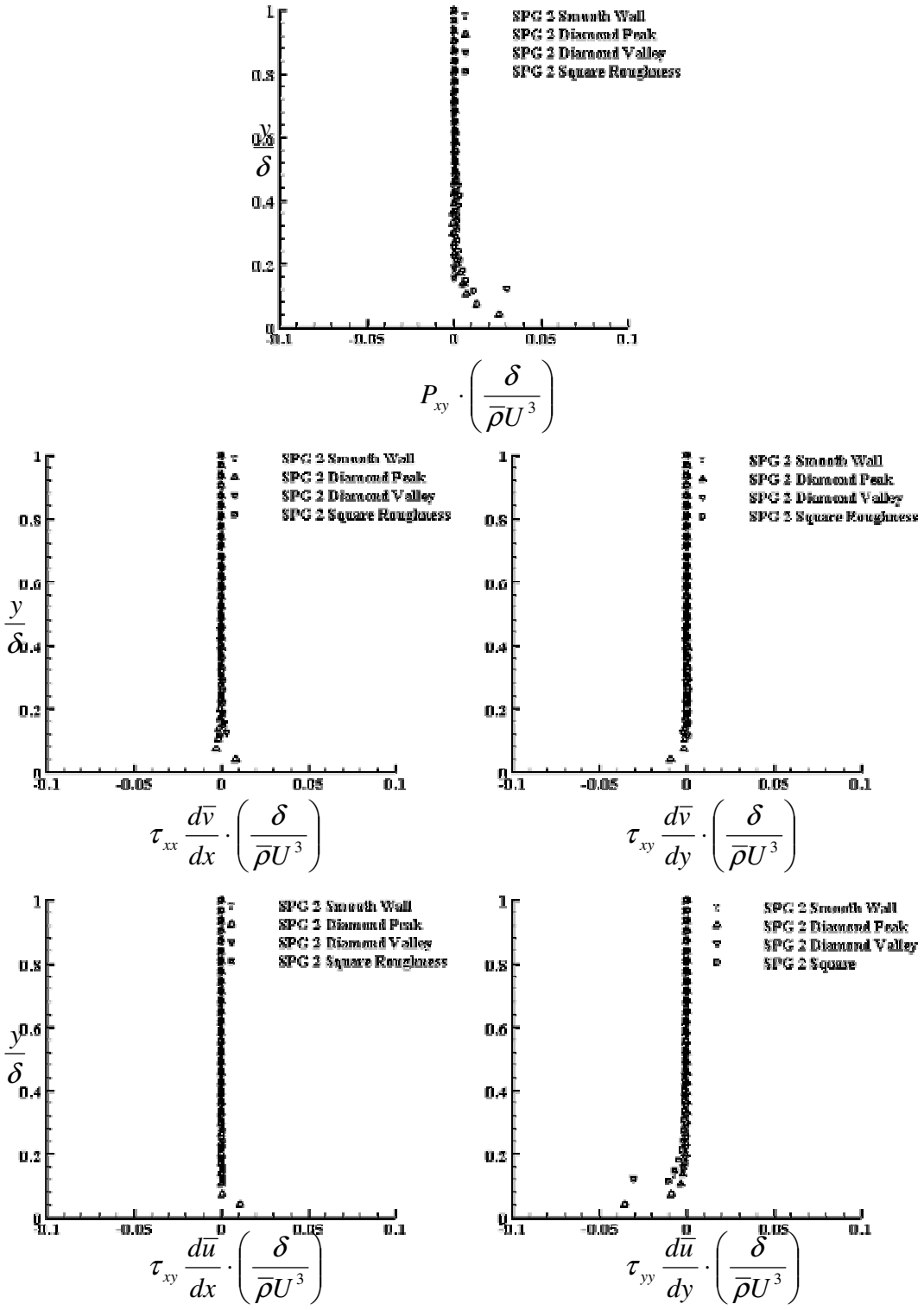

Figure 181: SPG profiles of P_{xy} and its components at location 2

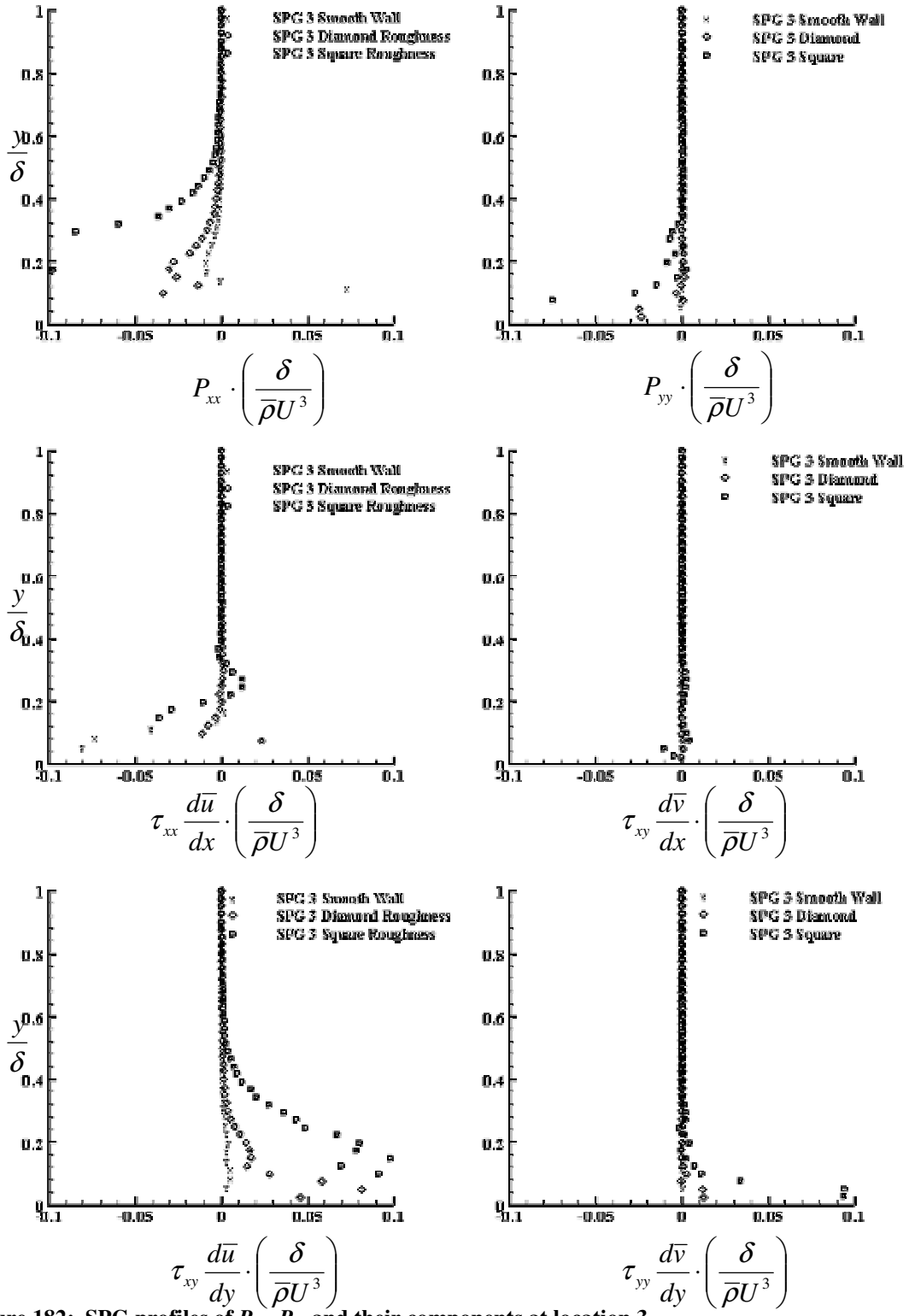

Figure 182: SPG profiles of P_{xx}, P_{yy} and their components at location 3

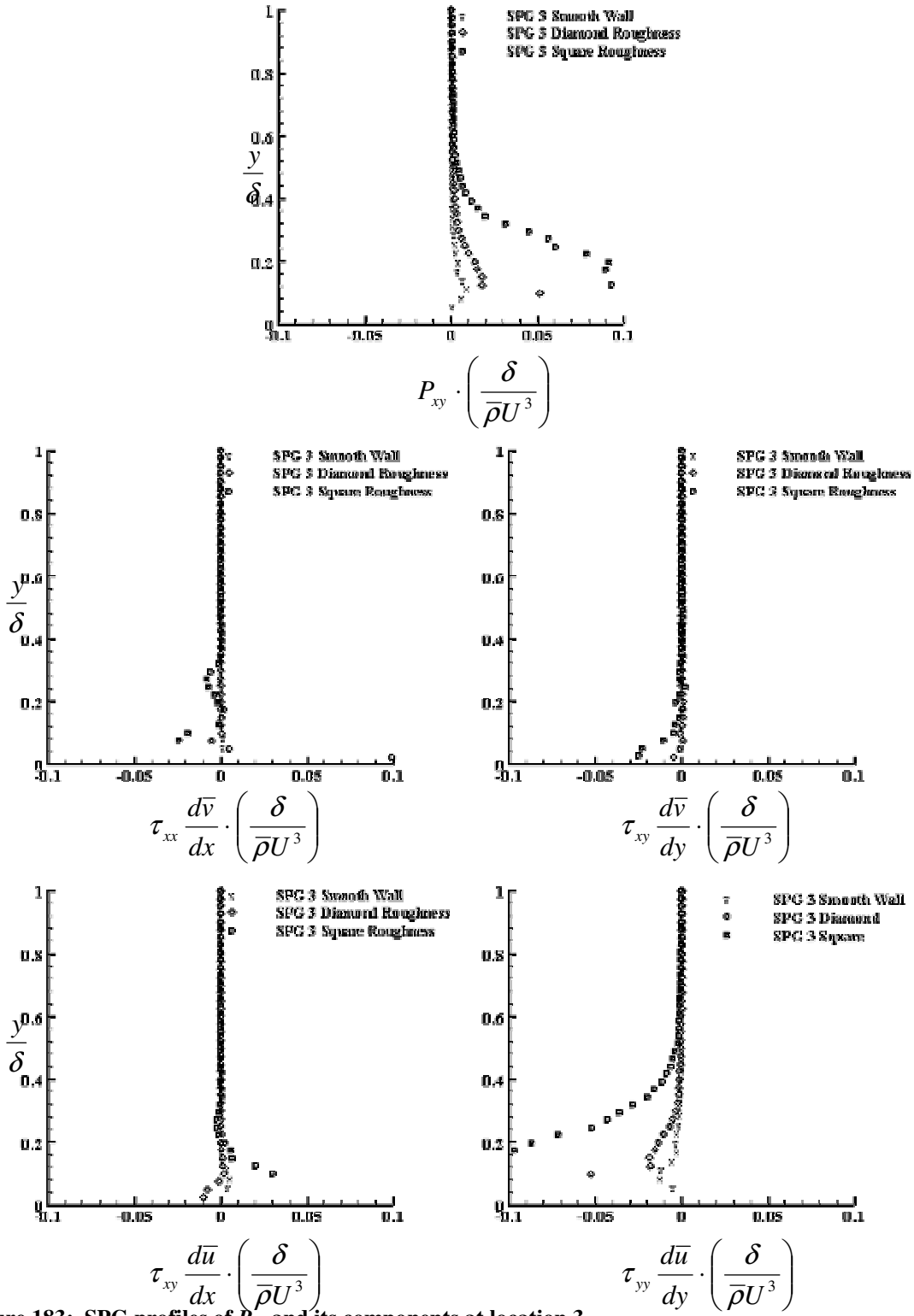

Figure 183: SPG profiles of P_{xy} and its components at location 3

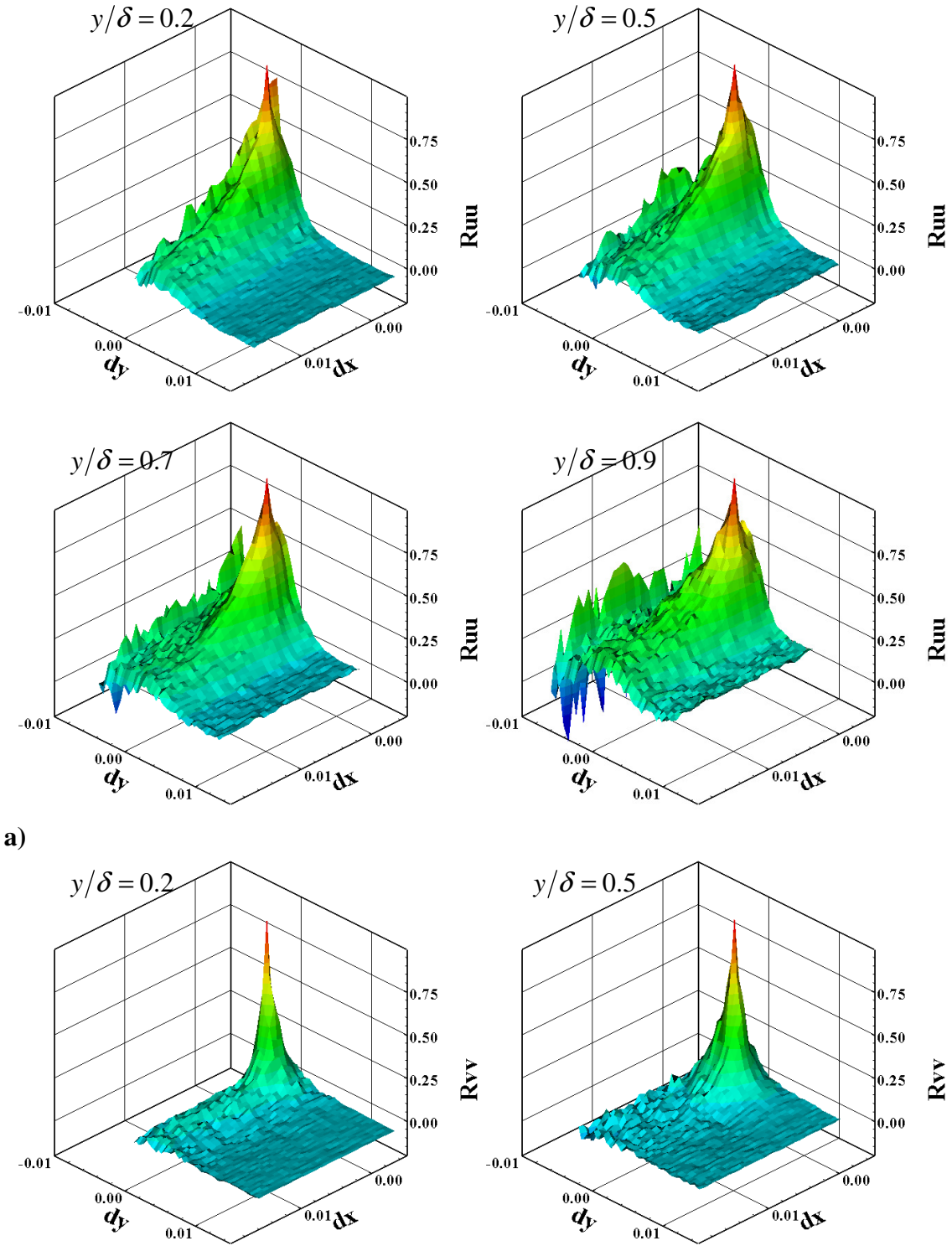

Figure 184: Correlation maps for the ZPG smooth wall model at the 1st location: a) *u'* auto, b) *v'* auto c) and cross

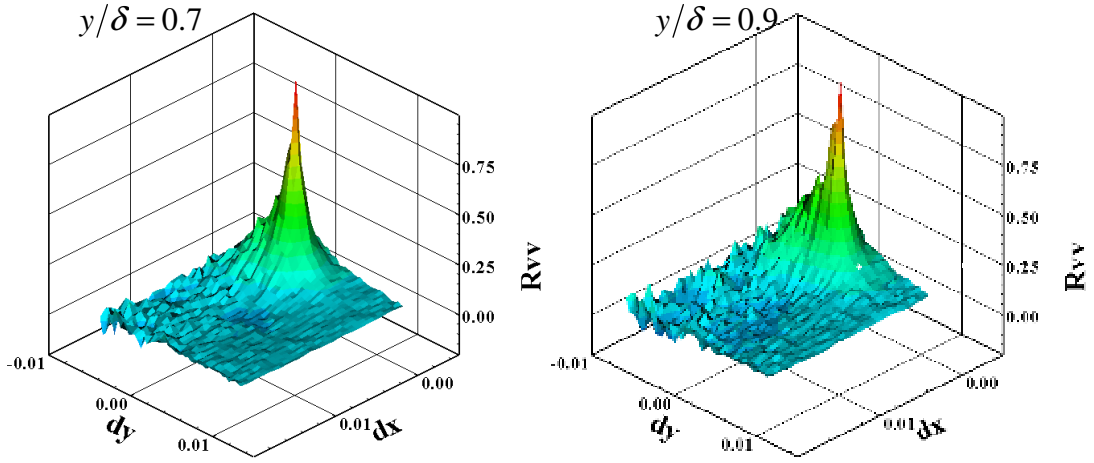

b)

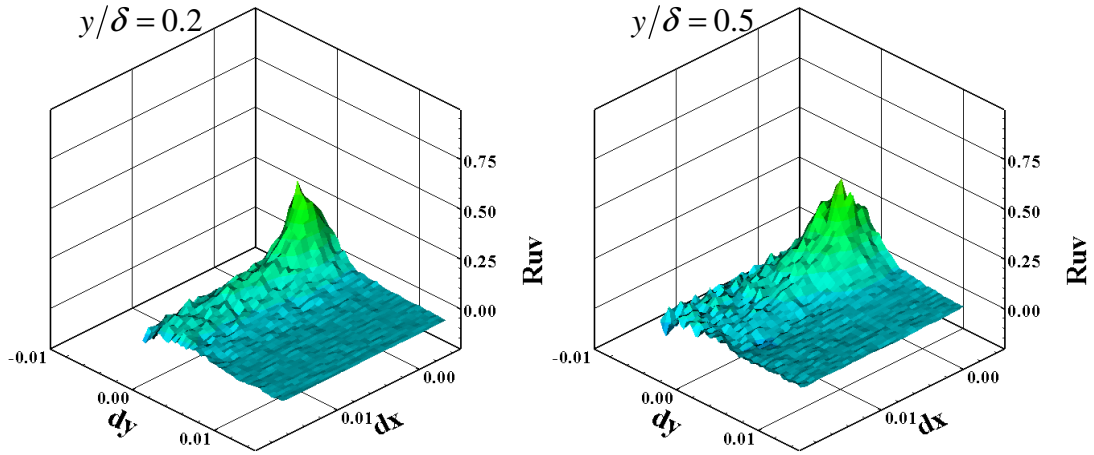

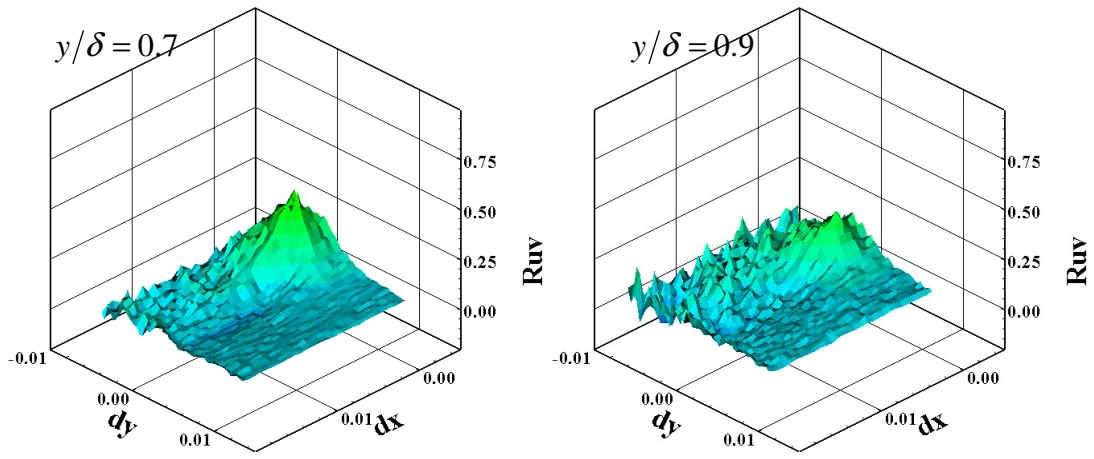

c)

Figure 184: Continued

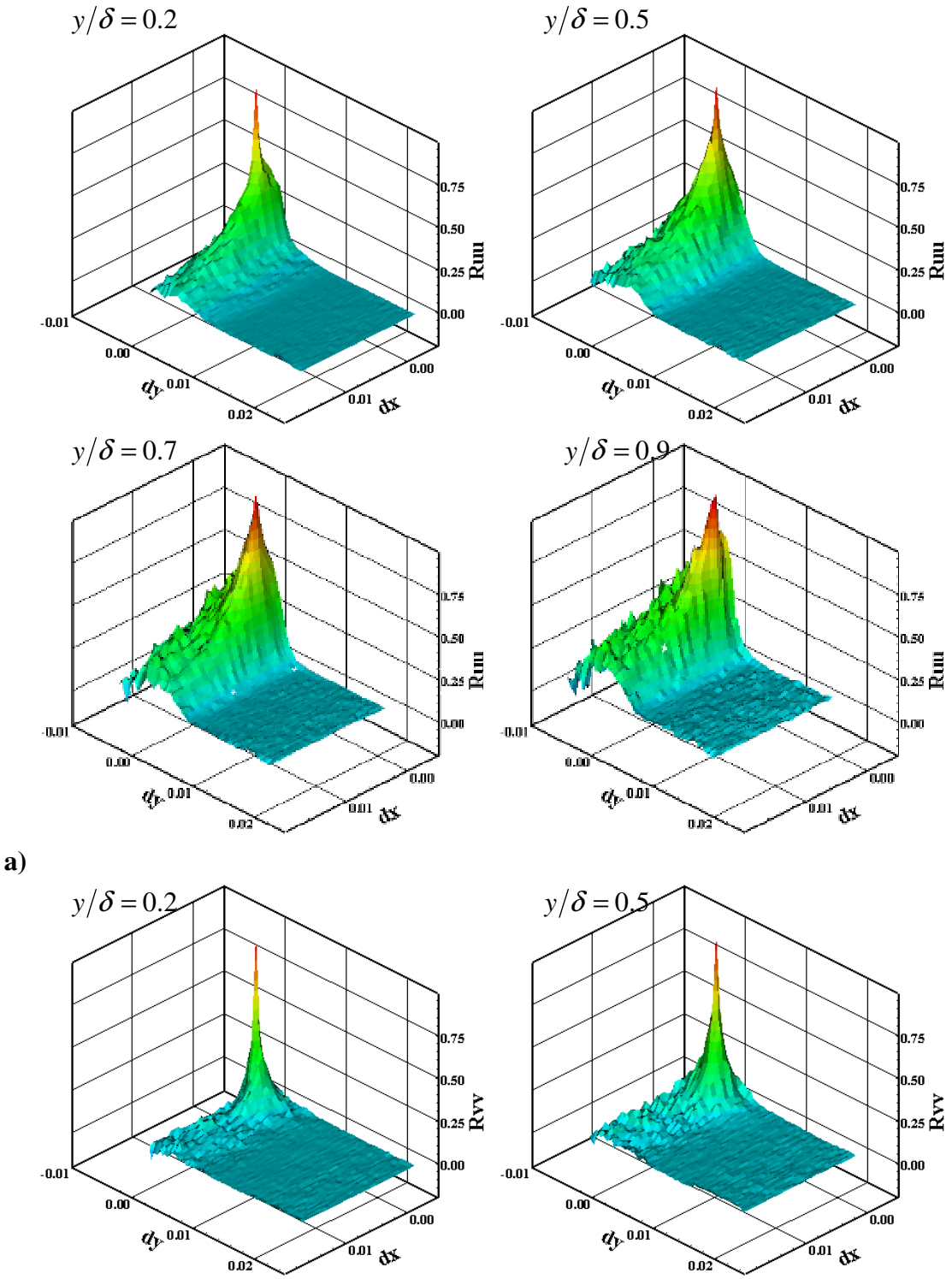

a)

Figure 185: Correlation maps for the ZPG square roughness model at the 1st location: a) *u'* auto, b) *v'* auto c) and cross

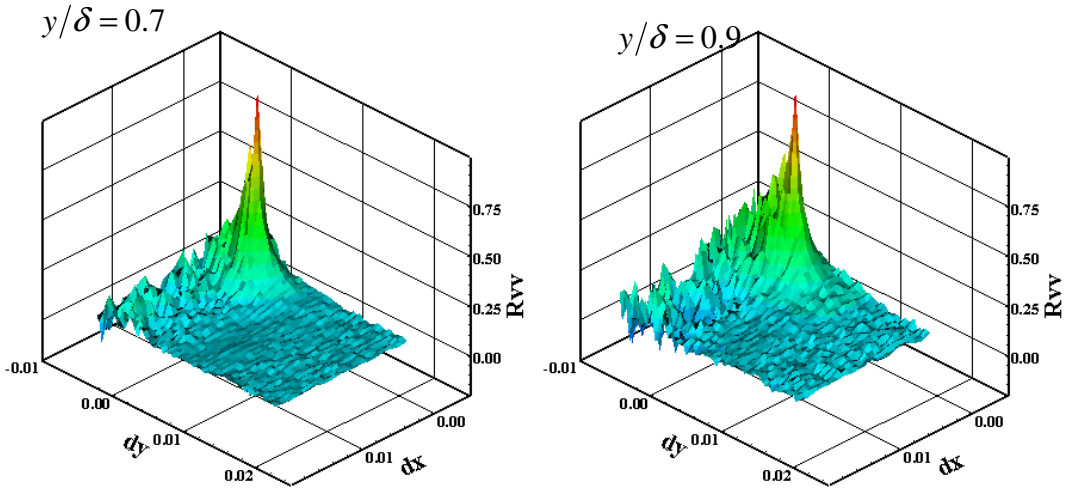

b)

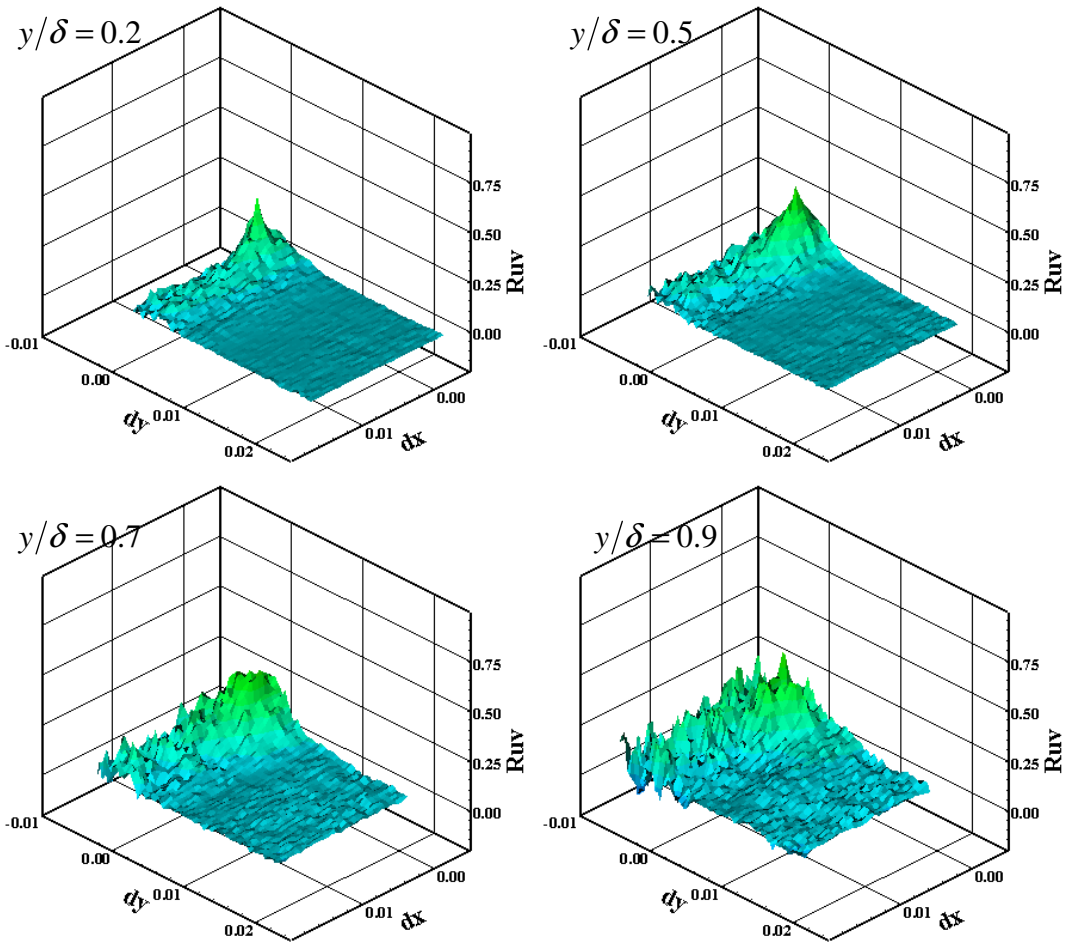

c)

Figure 185: Continued

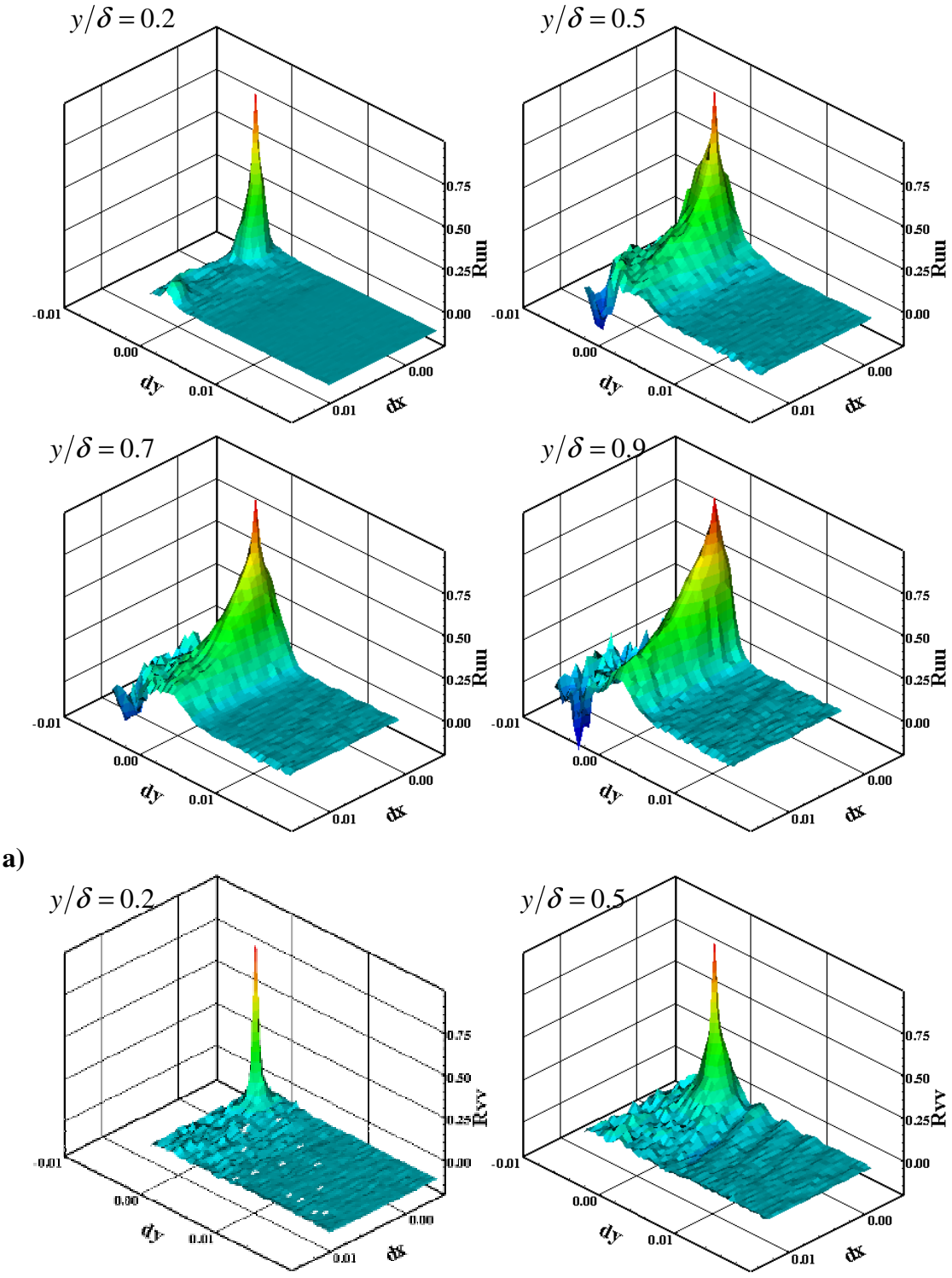

Figure 186: Correlation maps for the ZPG diamond roughness model at the 1st location: a) *u'* auto, b) *v'* auto c) and cross

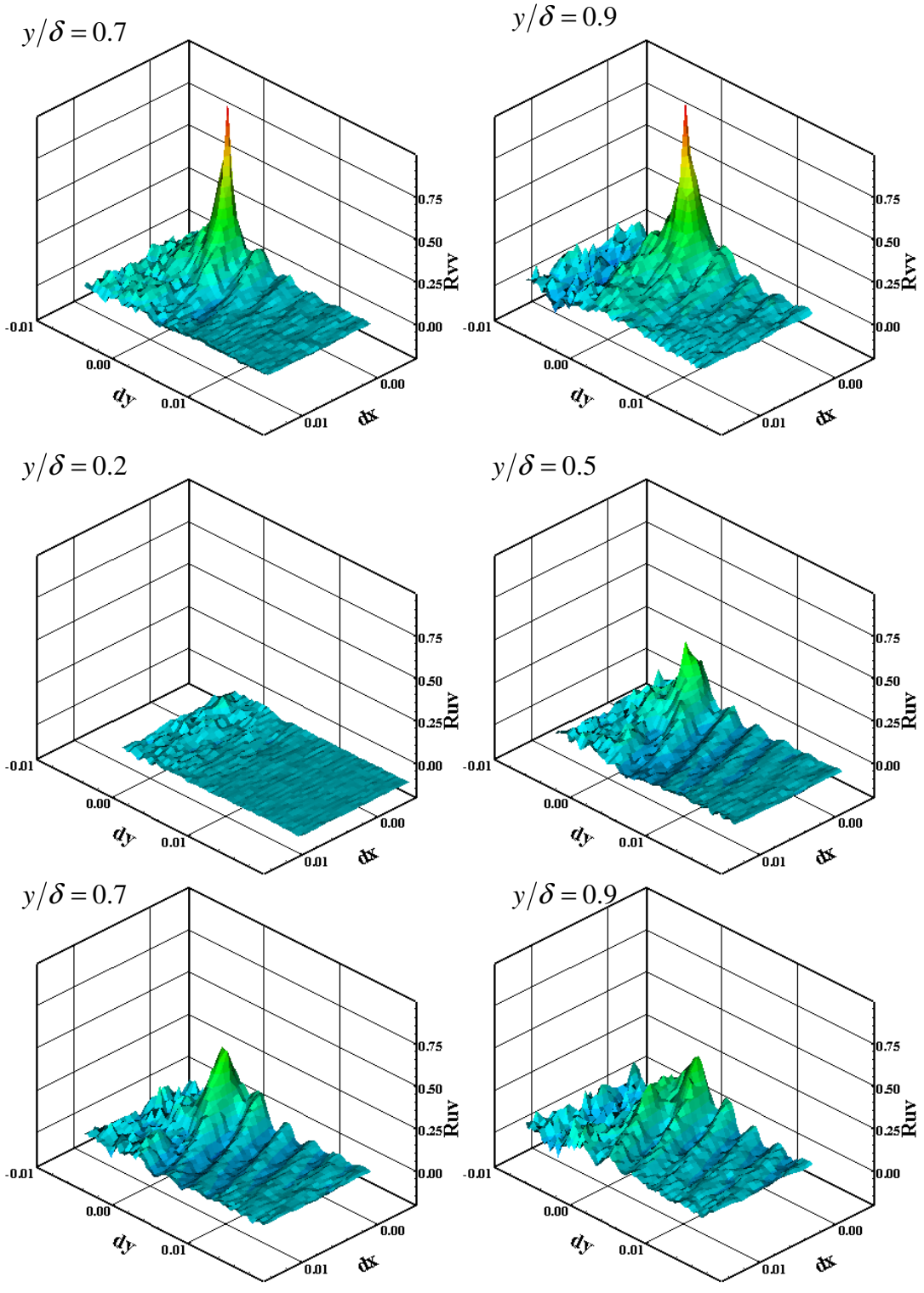

Figure 186: Continued

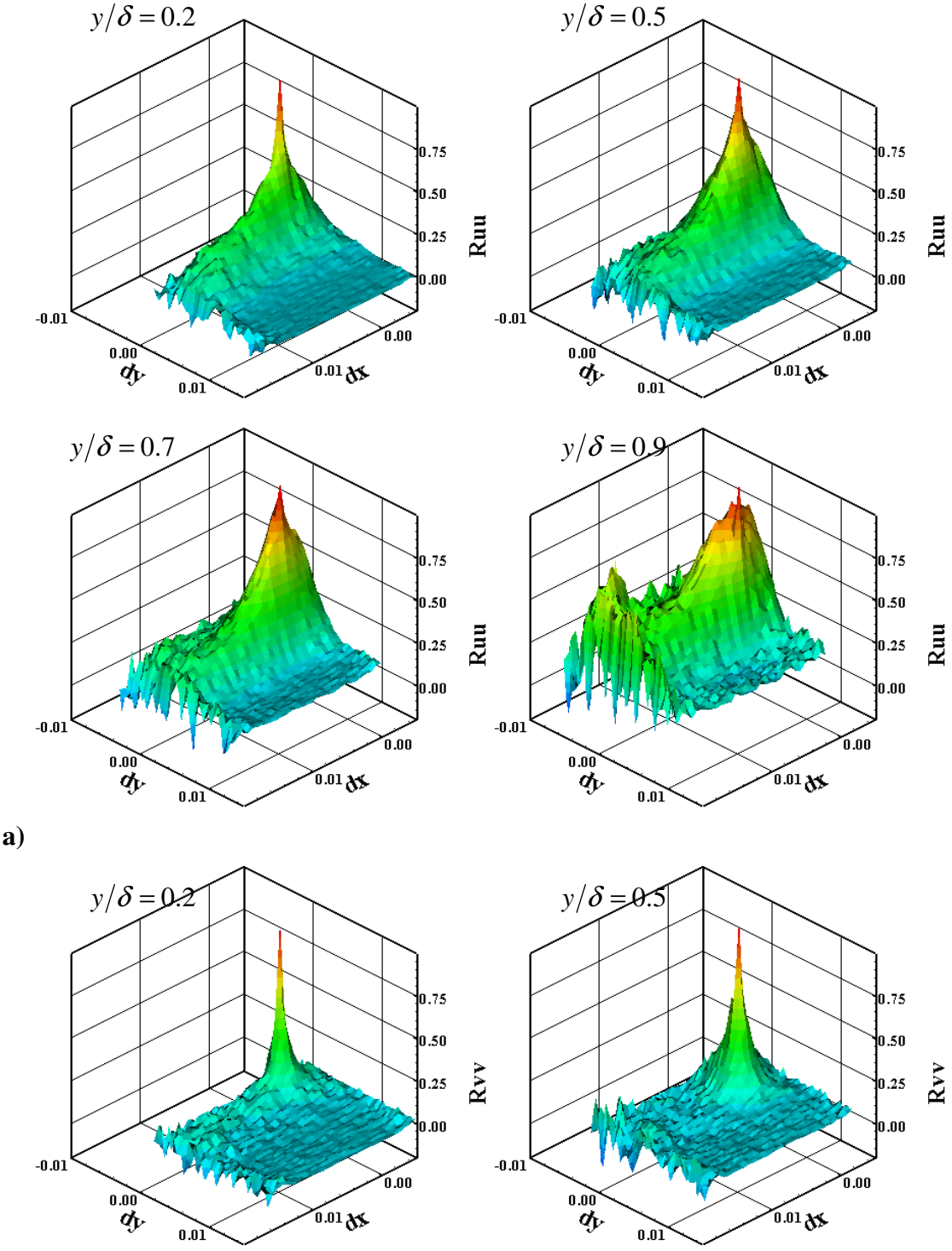

Figure 187: Correlation maps for the WPG smooth wall model at the 1st location: a) *u'* auto, b) *v'* auto c) and cross

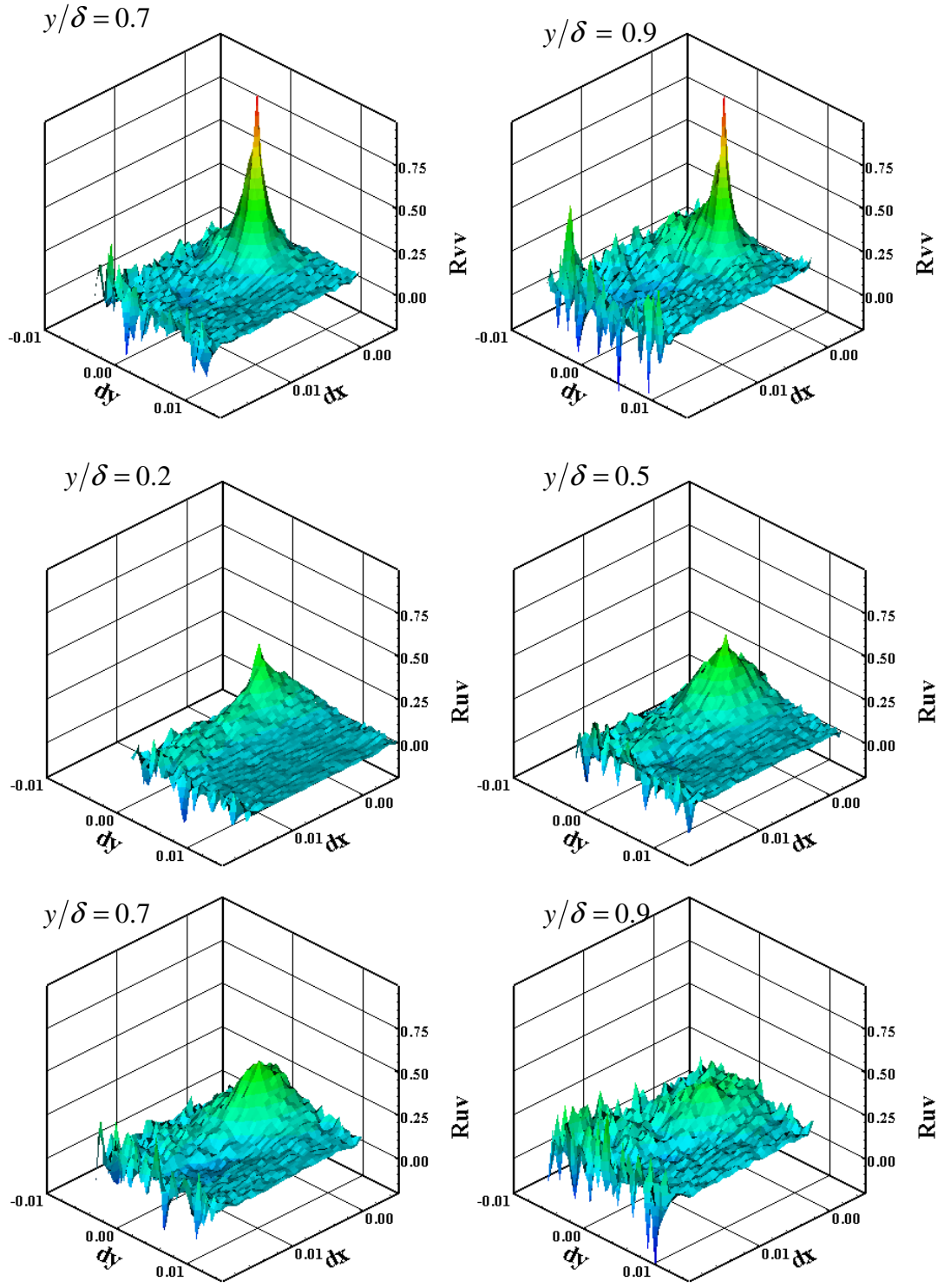

Figure 187: Continued

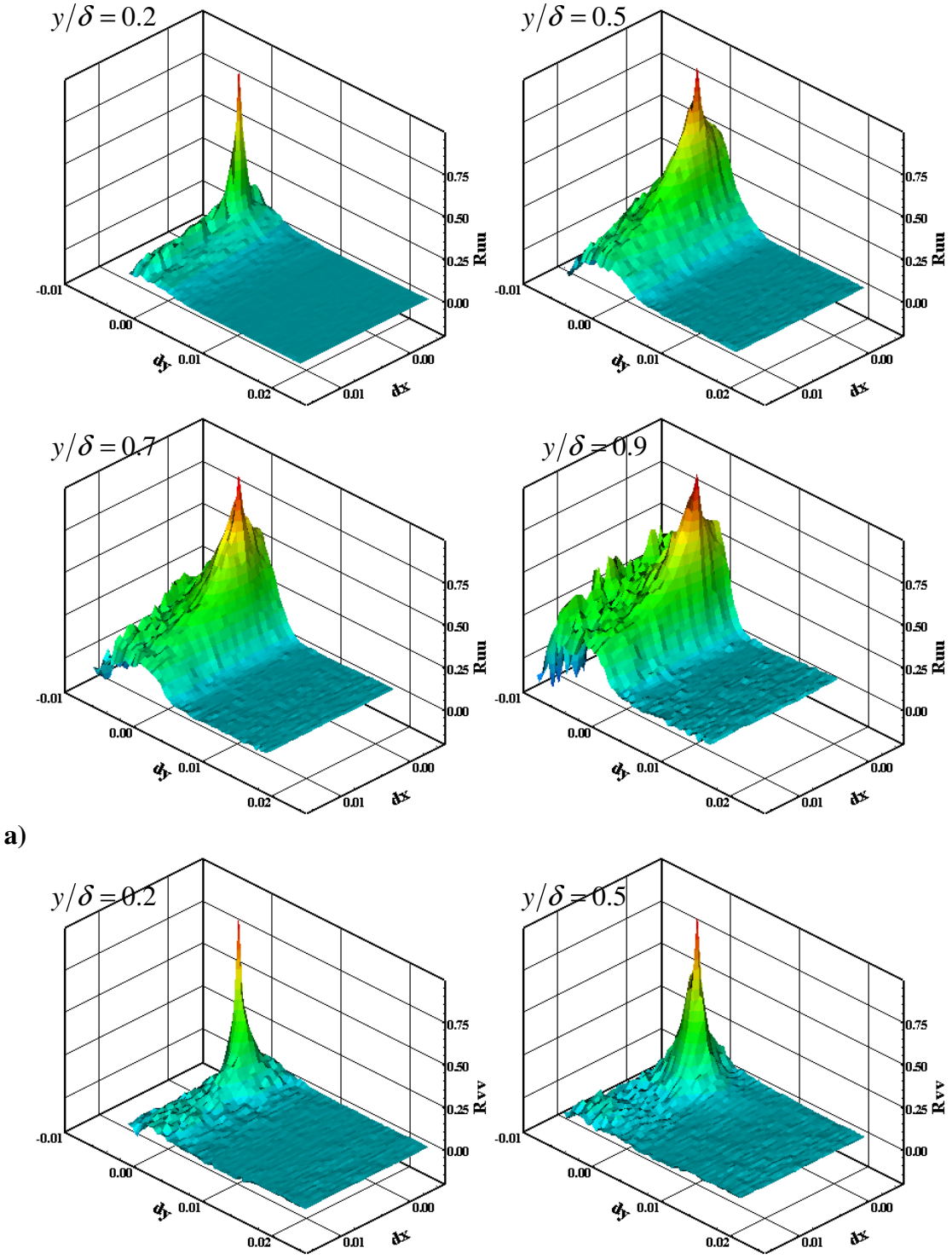

a)

Figure 188: Correlation maps for the WPG square roughness model at the 1st location: a) *u'* auto, b) *v'* auto c) and cross

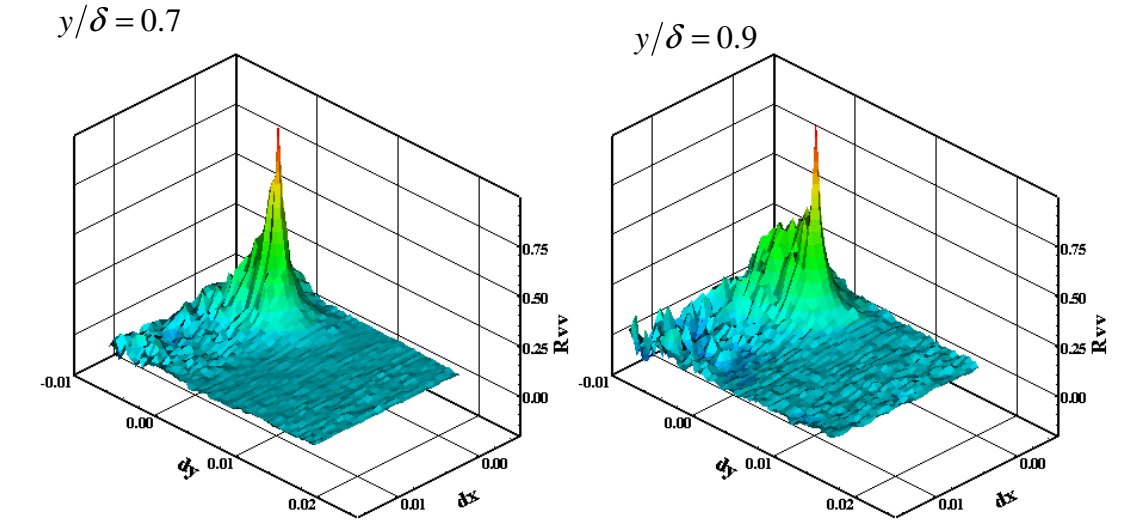

b)

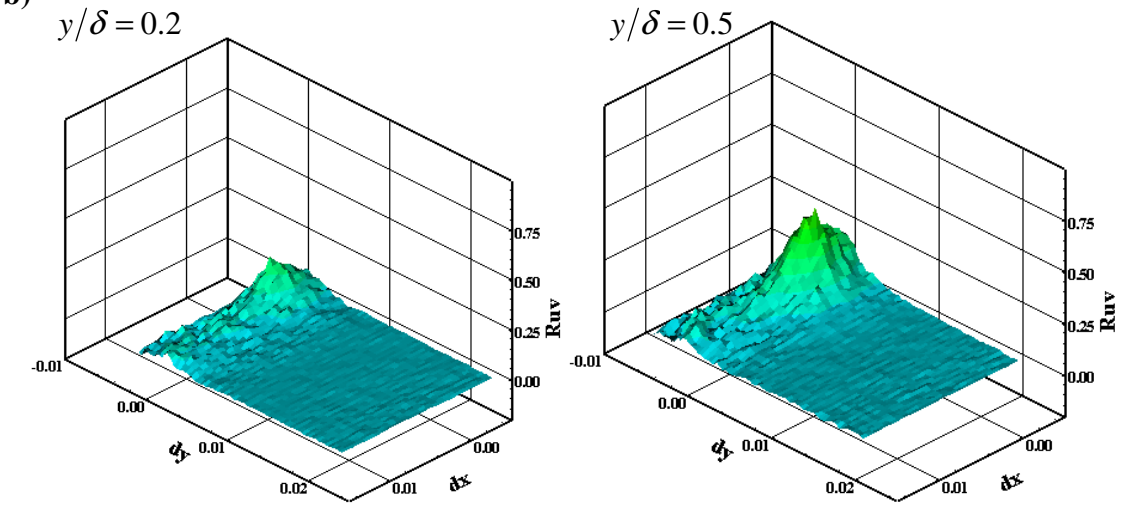

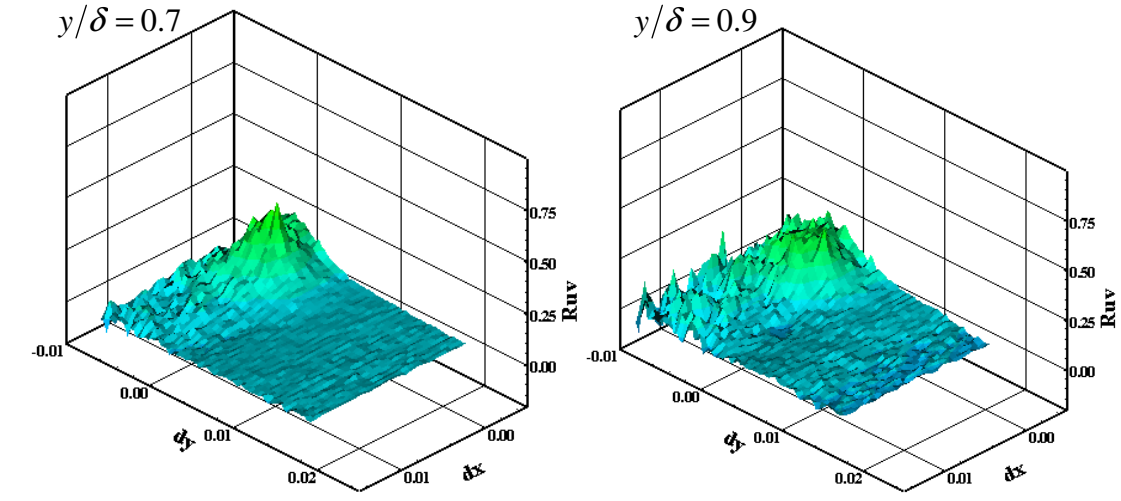

c)

Figure 188: Continued

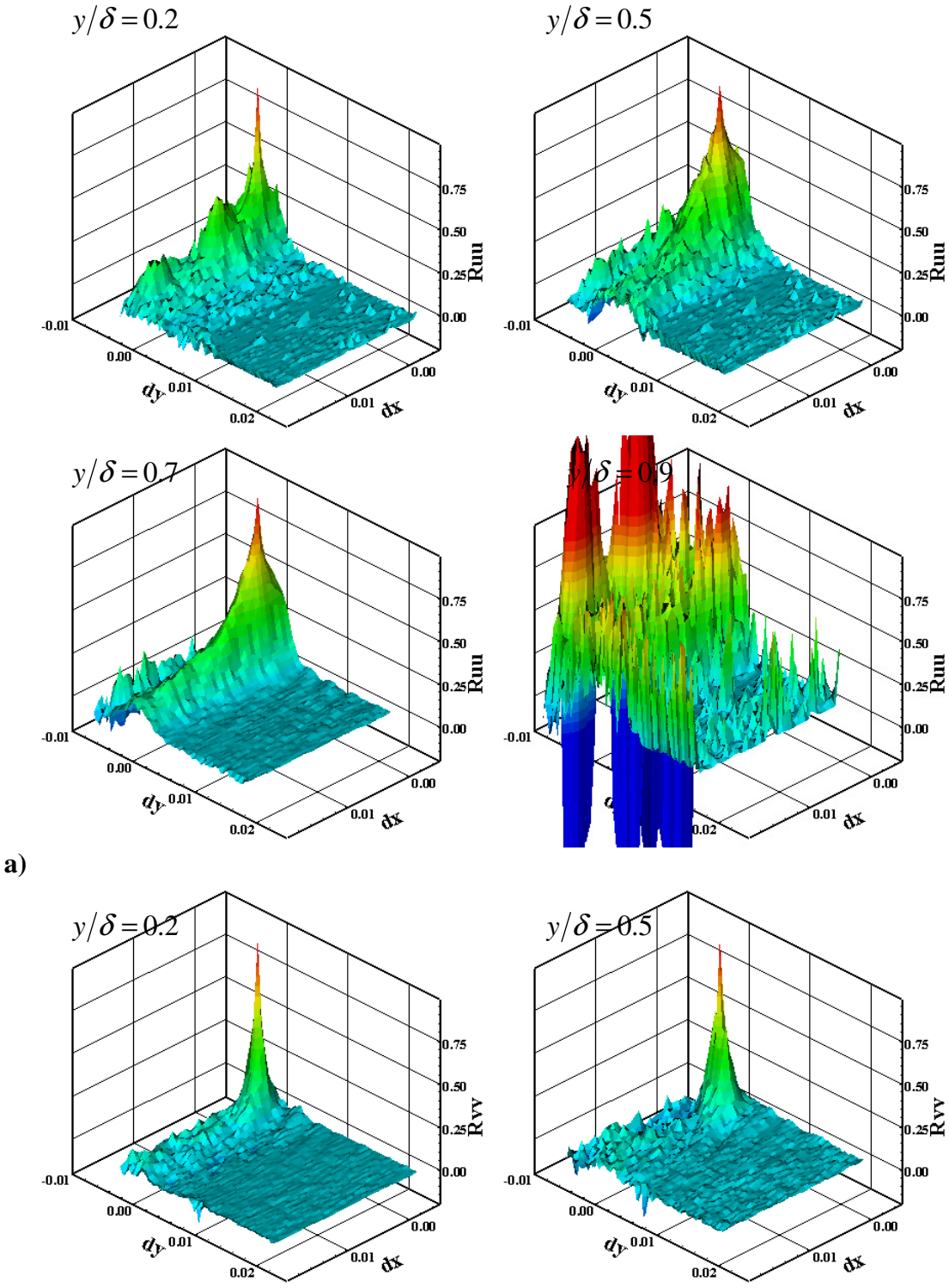

Figure 189: Correlation maps for the WPG diamond roughness model at the 1st location: a) *u'* auto, b) *v'* auto c) and cross

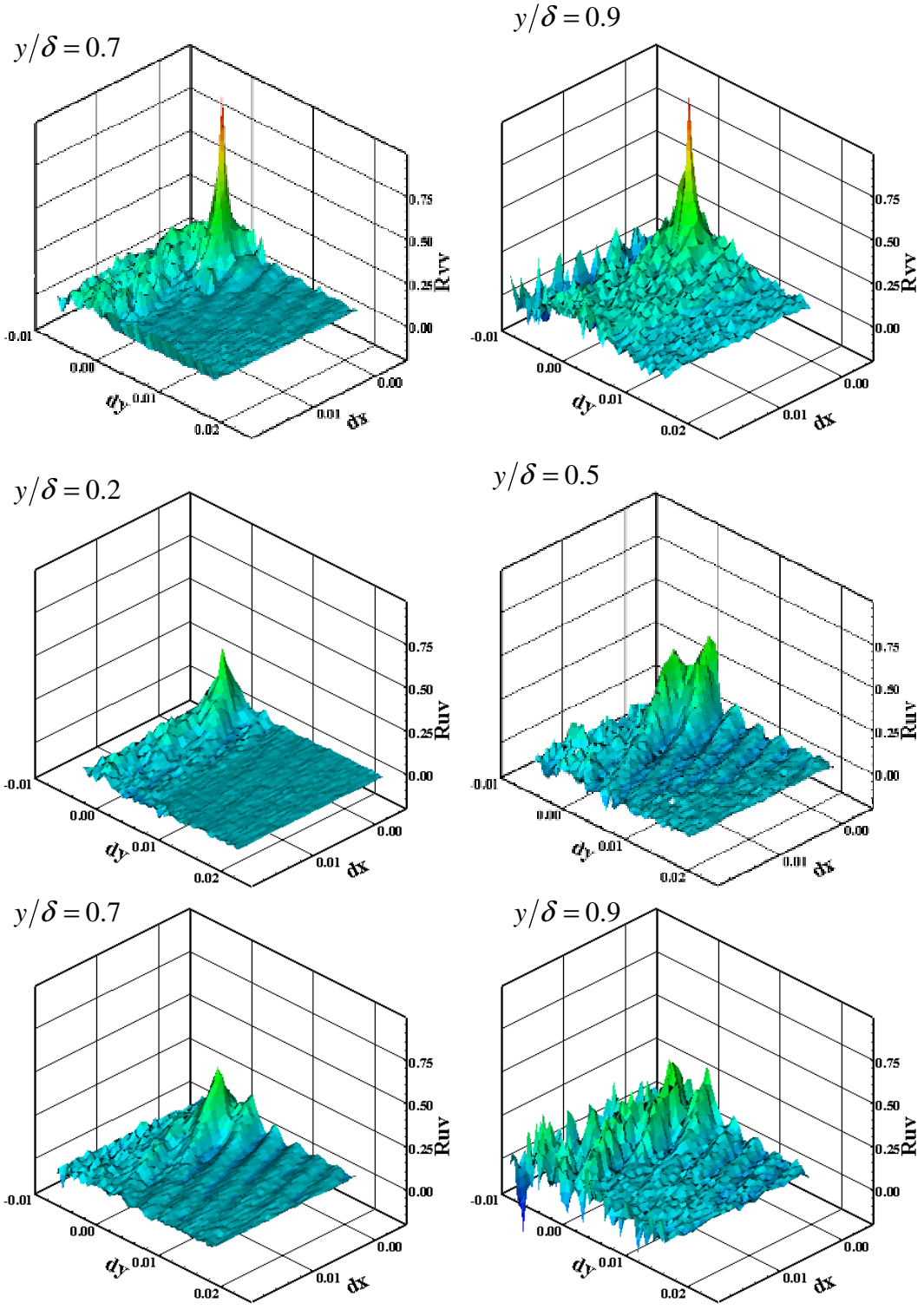

Figure 189: Continued

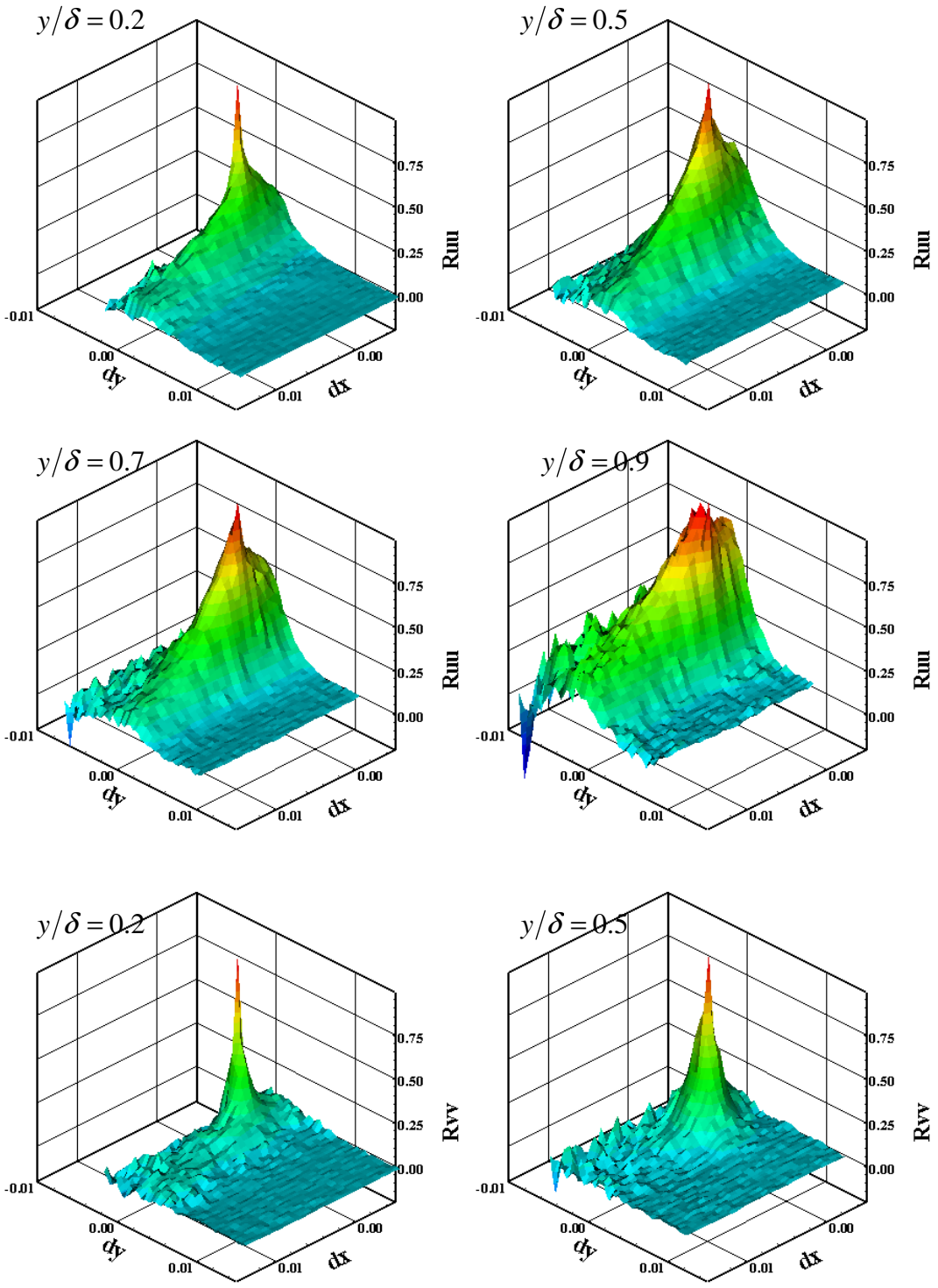

Figure 190: Correlation maps for the SPG smooth wall model at the 1st location: a) *u'* auto, b) *v'* auto c) and cross

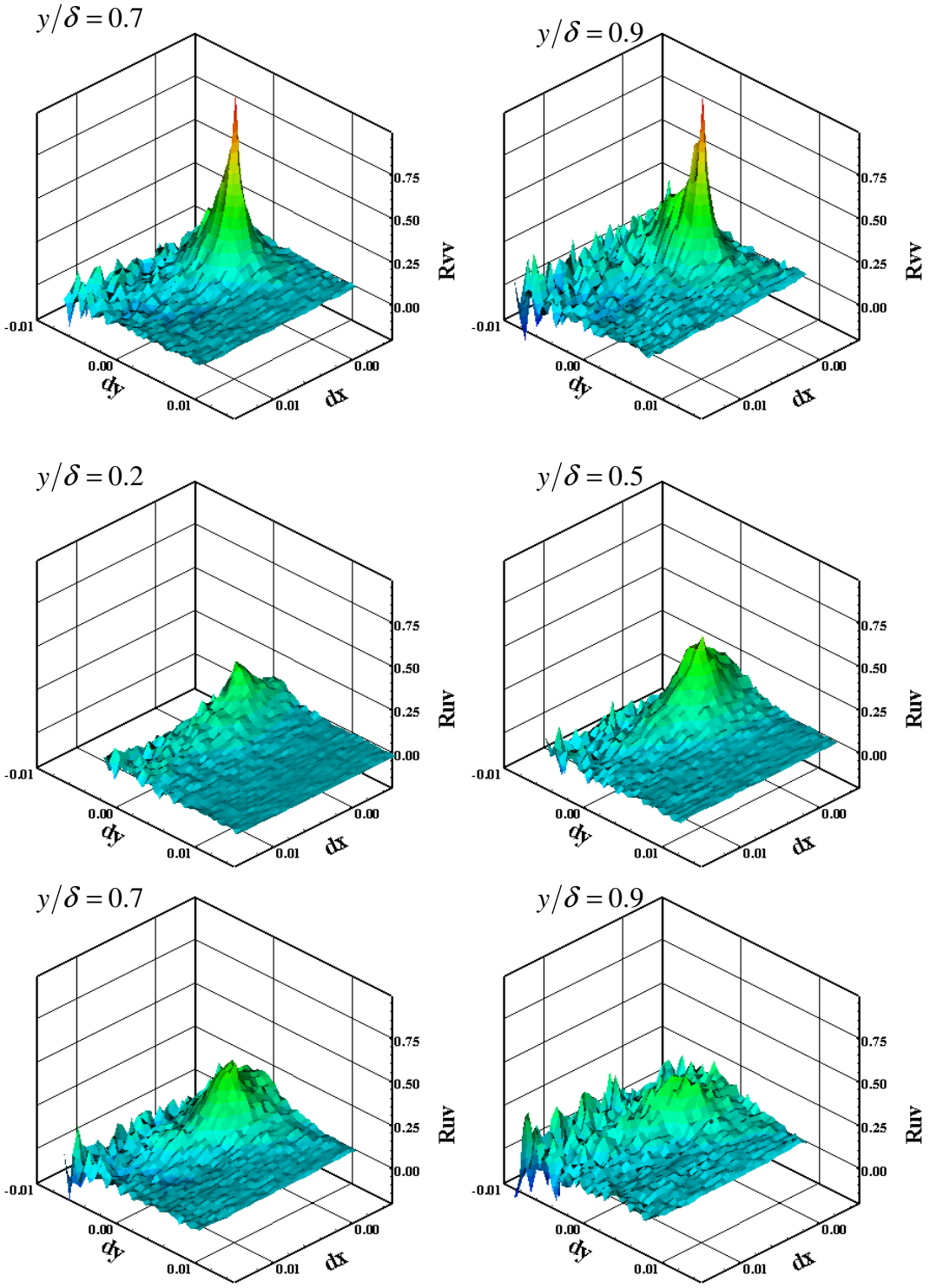

Figure 190: Continued

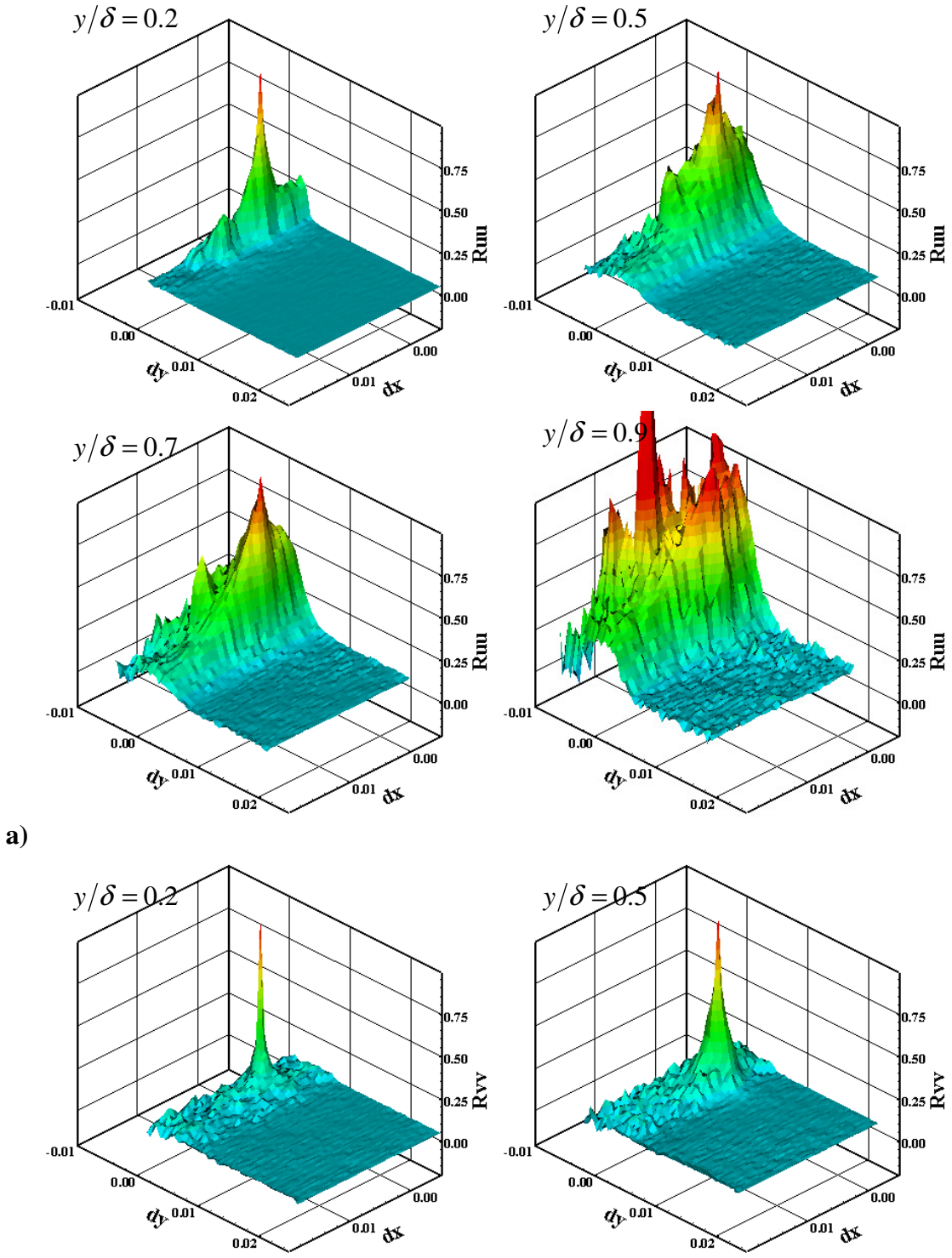

Figure 191: Correlation maps for the SPG square roughness model at the 1st location: a) *u'* auto, b) *v'* auto c) and cross

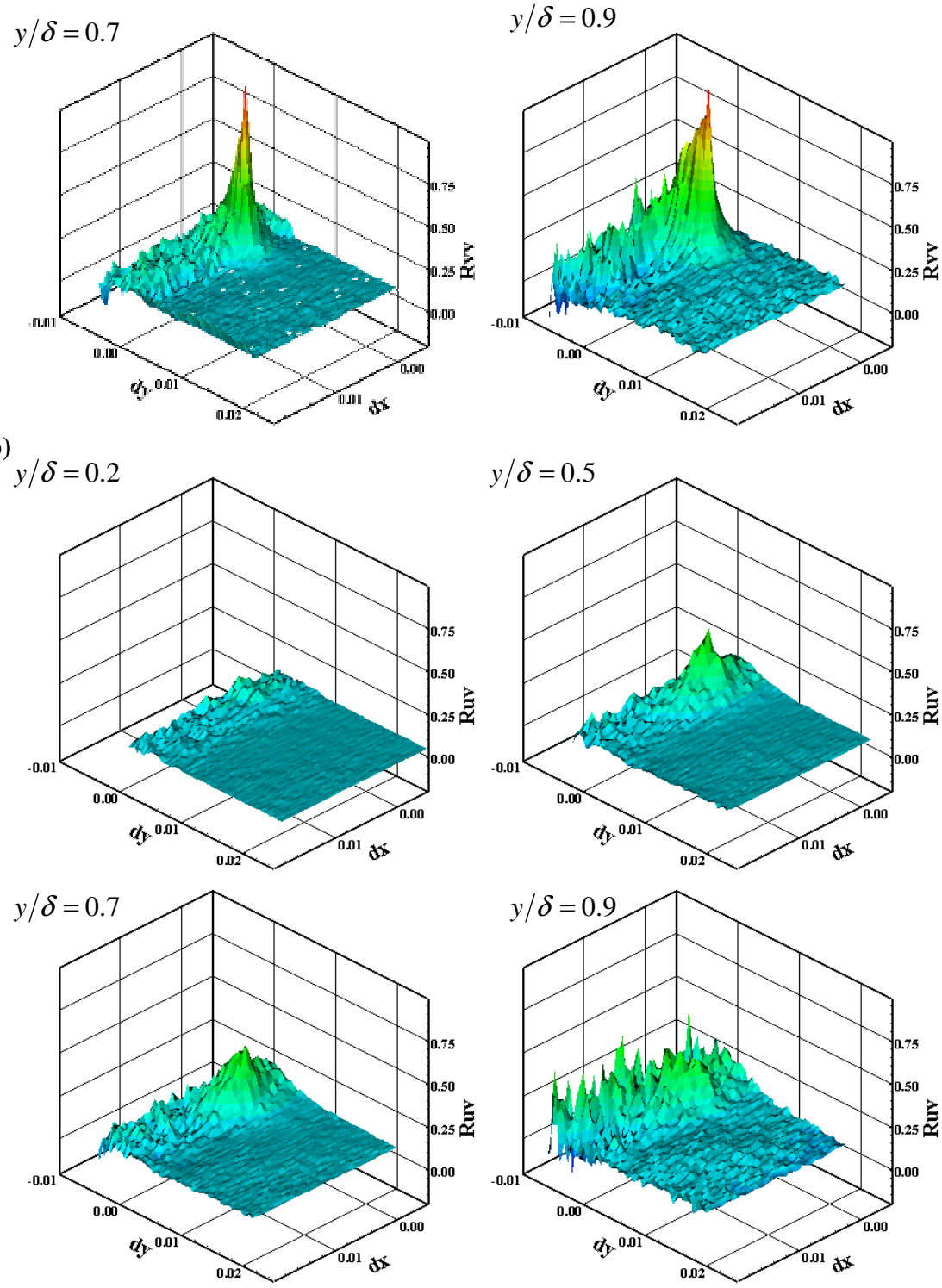

Figure 191: Continued

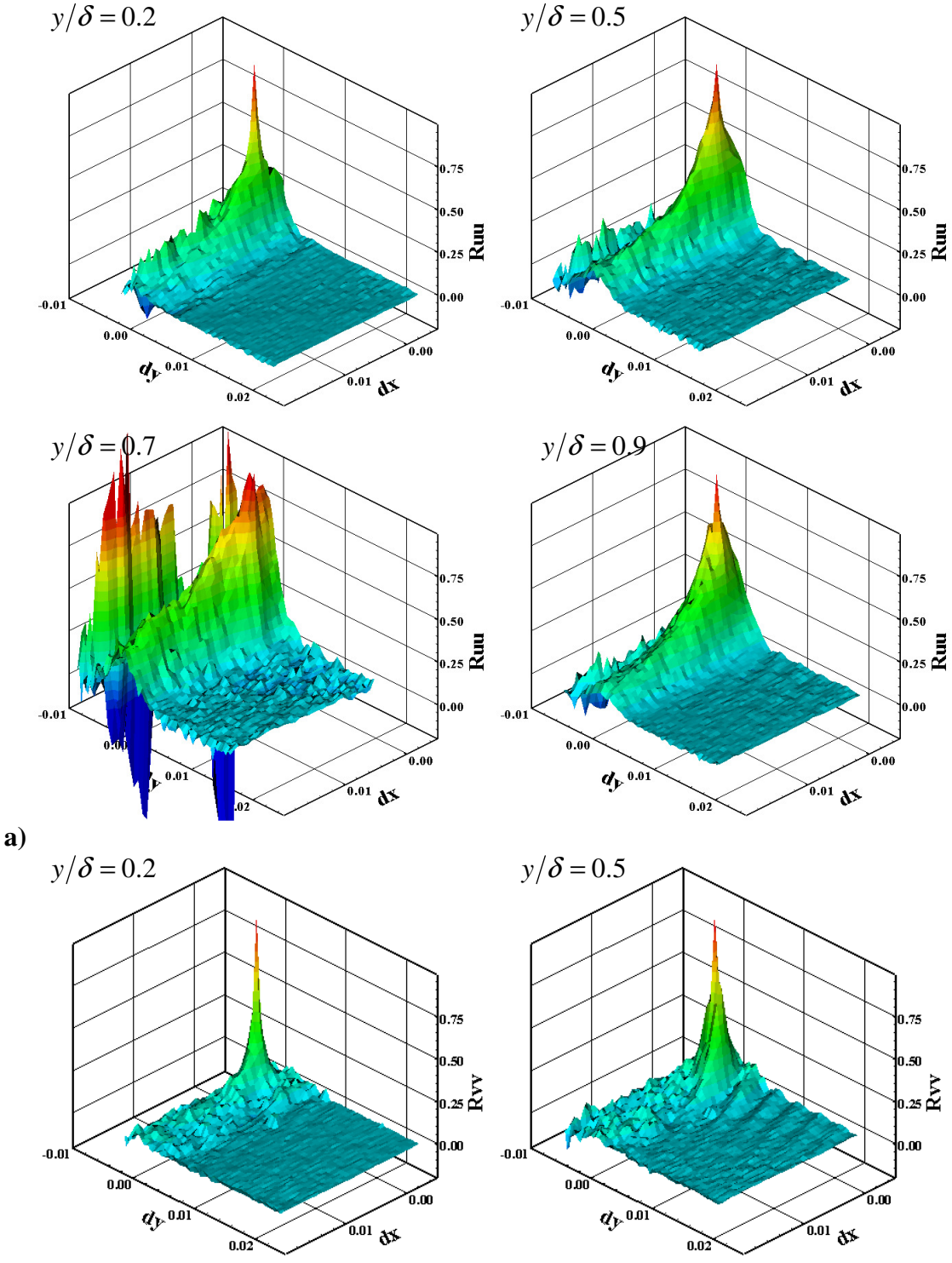

Figure 192: Correlation maps for the SPG diamond roughness model at the 1st location: a) *u'* auto, b) *v'* auto c) and cross

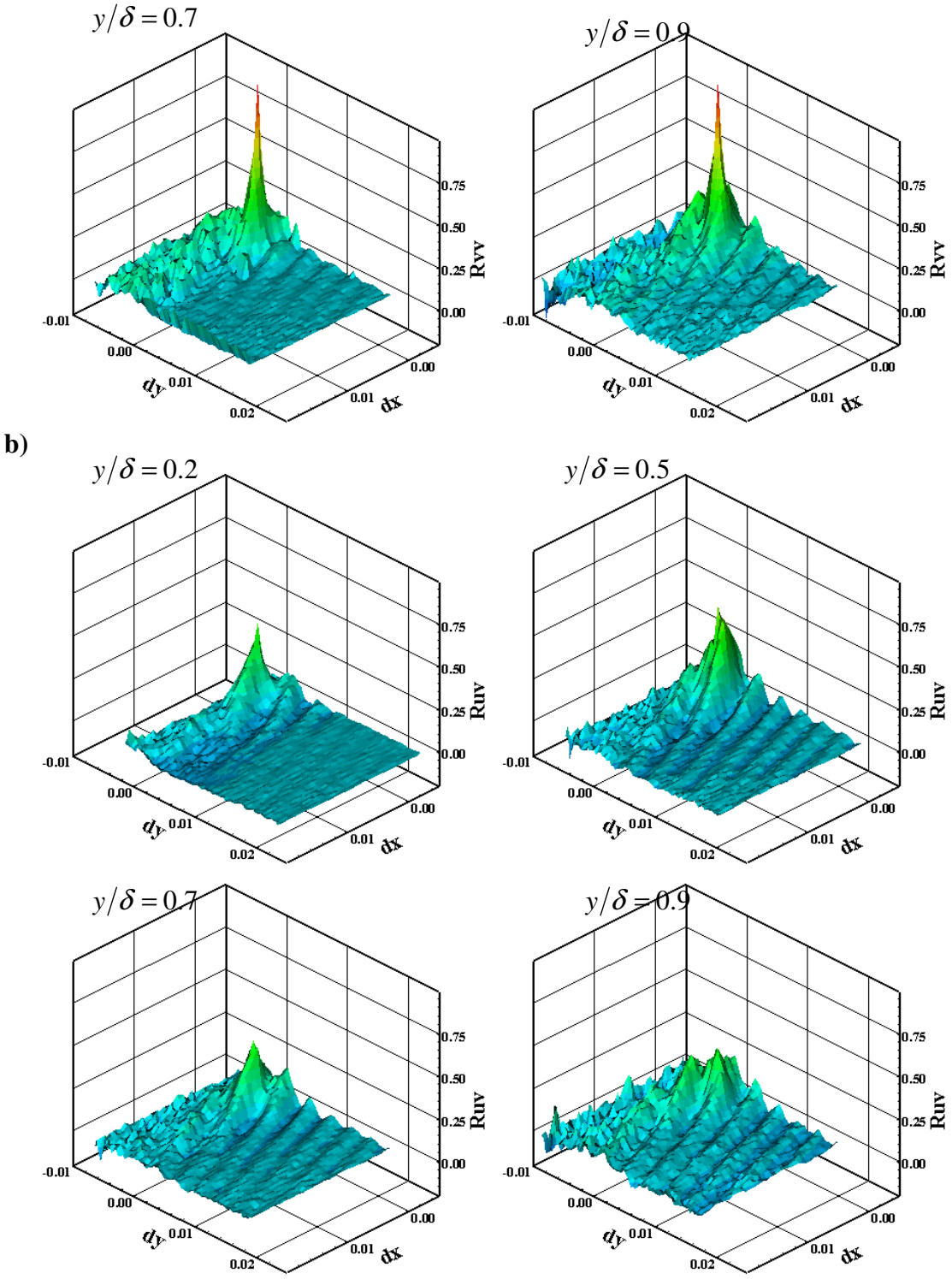

Figure 192: Continued

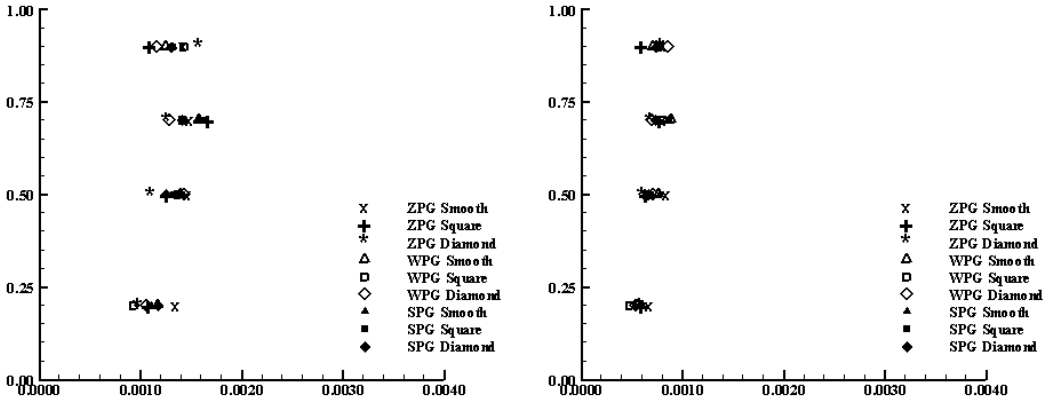

a)

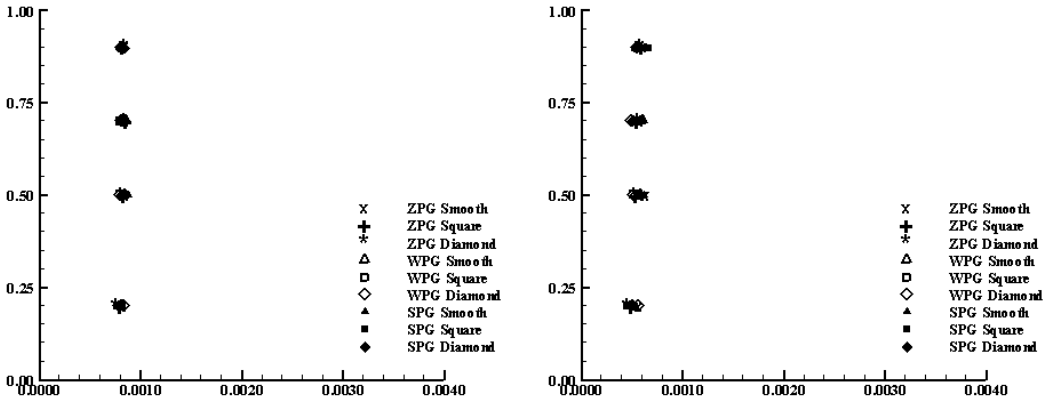

b)

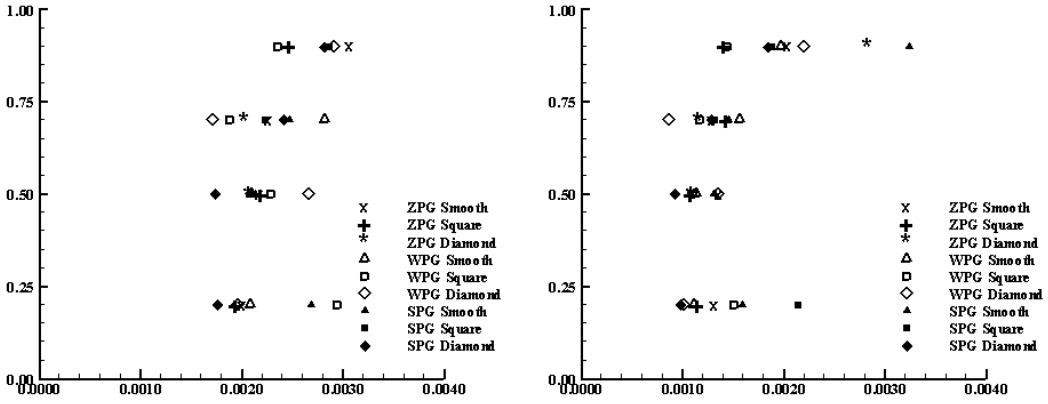

c)

Figure 193: *x* and *y* Taylor microscales for the first test location: a) *u'* auto, b) *v'* auto c) and cross-correlations

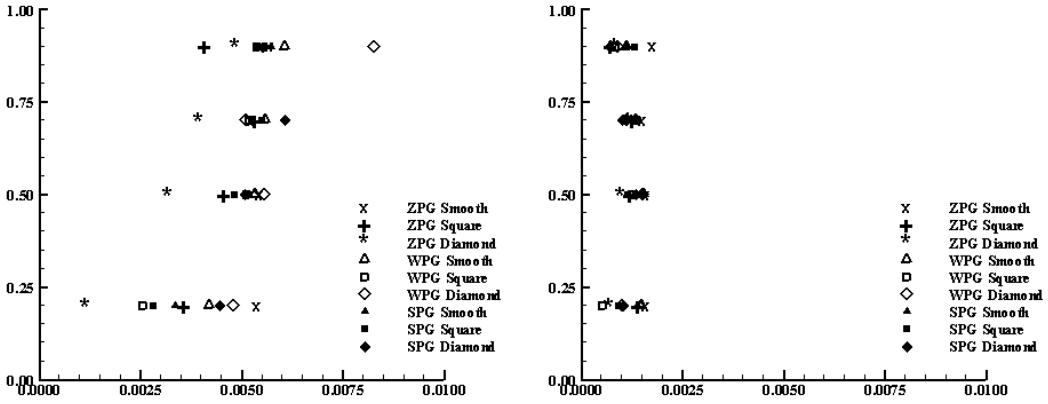

a)

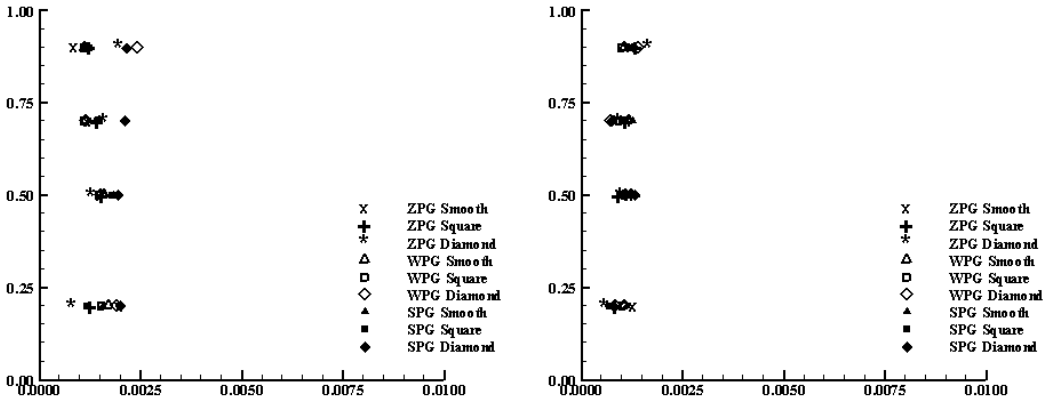

b)

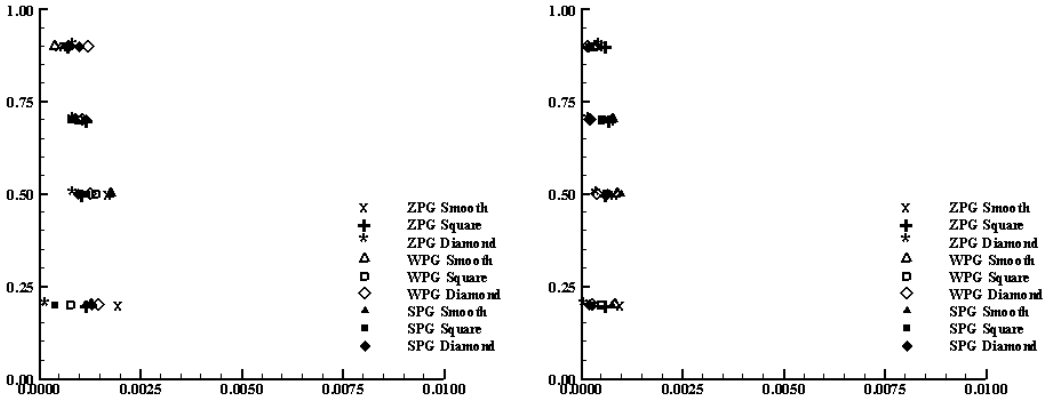

c)

Figure 194: *x* and *y* integral length scales for the 1st test location: a) *u'* auto, b) *v'* auto c) and cross-correlations

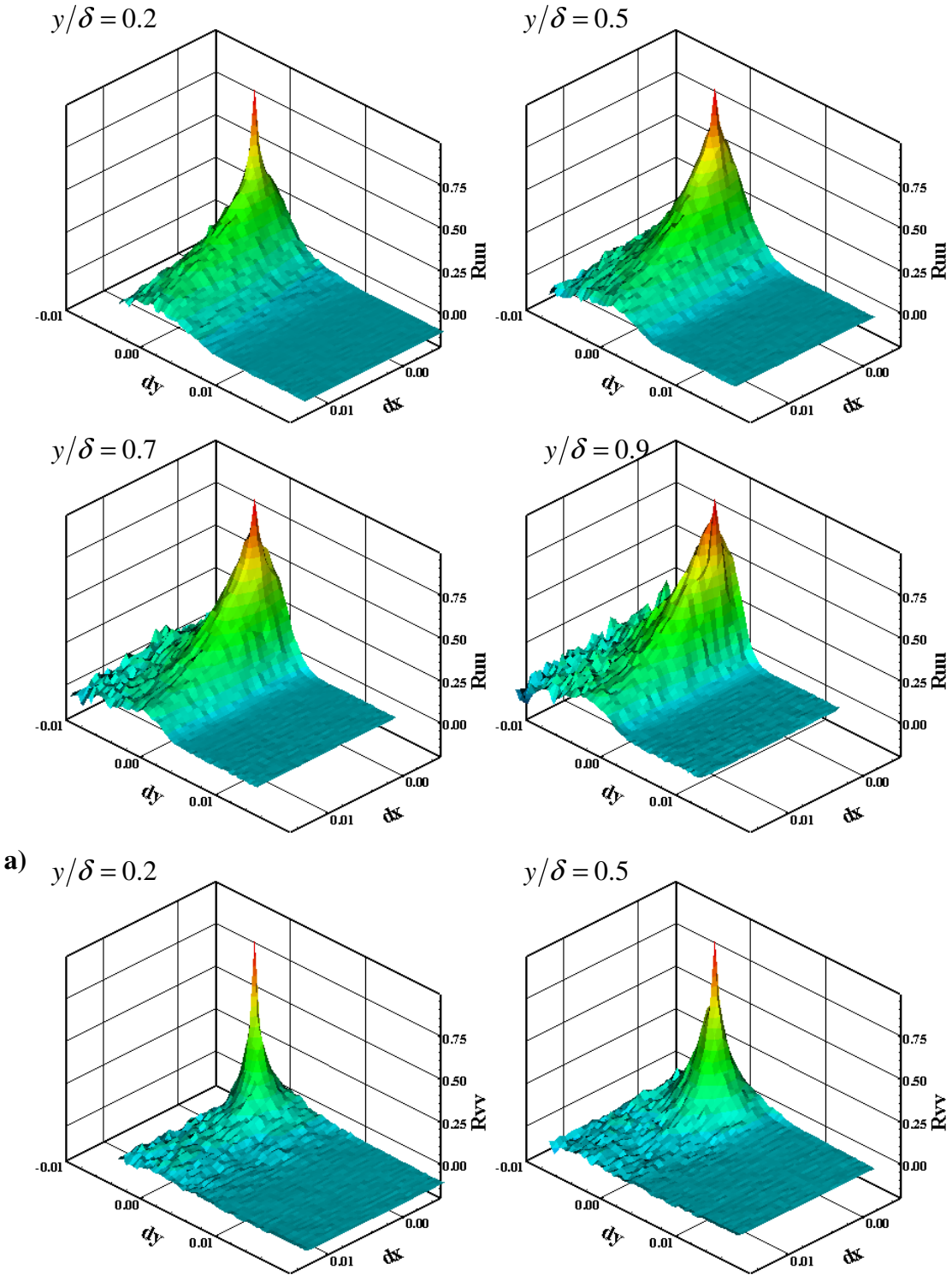

Figure 195: Correlation maps for the ZPG square roughness model at the 2nd location: a) *u'* auto, b) *v'* auto c) and cross

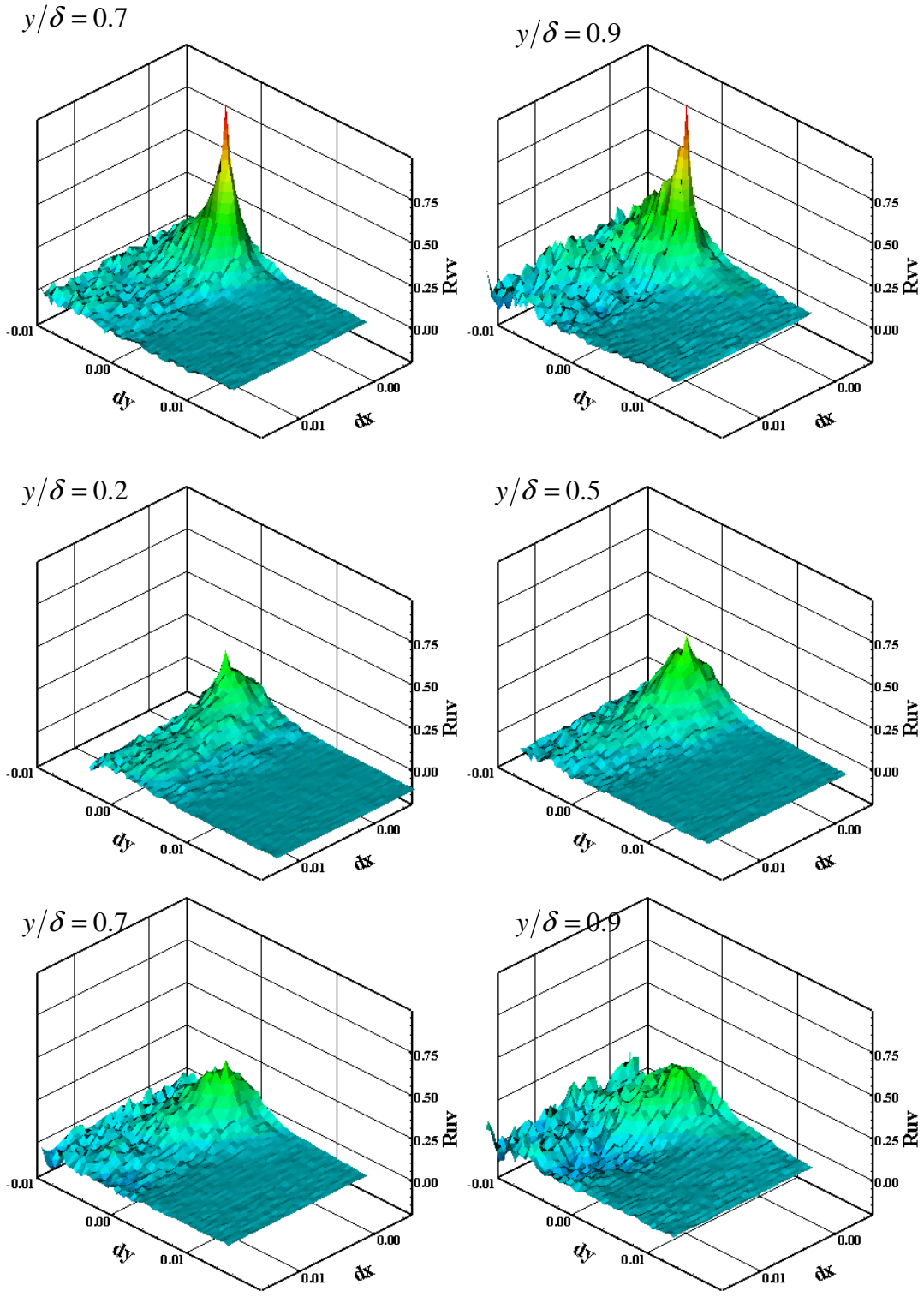

Figure 195: Continued

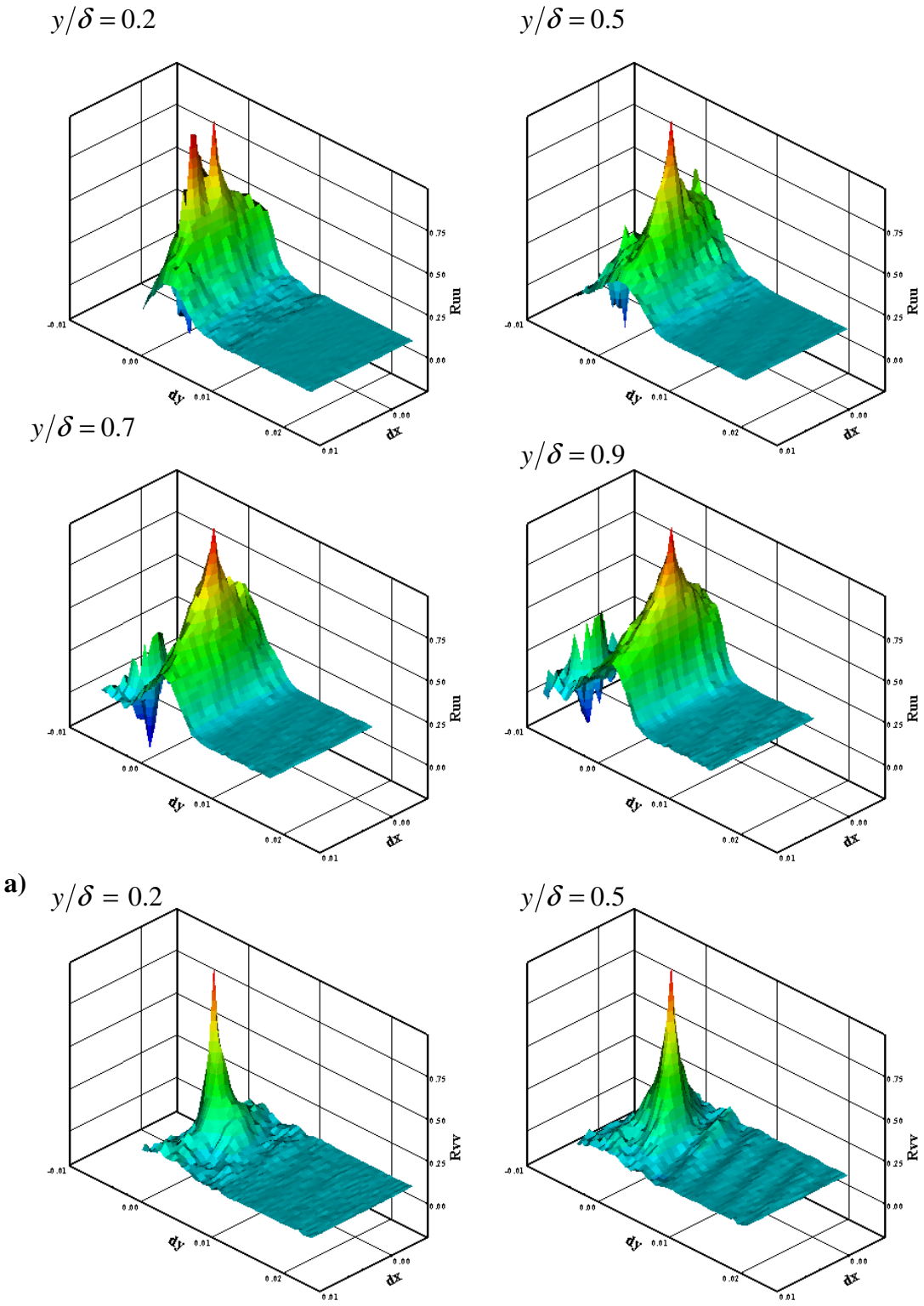

Figure 196: Correlation maps for the ZPG diamond roughness model at the 2nd location: a) *u'* auto, b) *v'* auto c) and cross

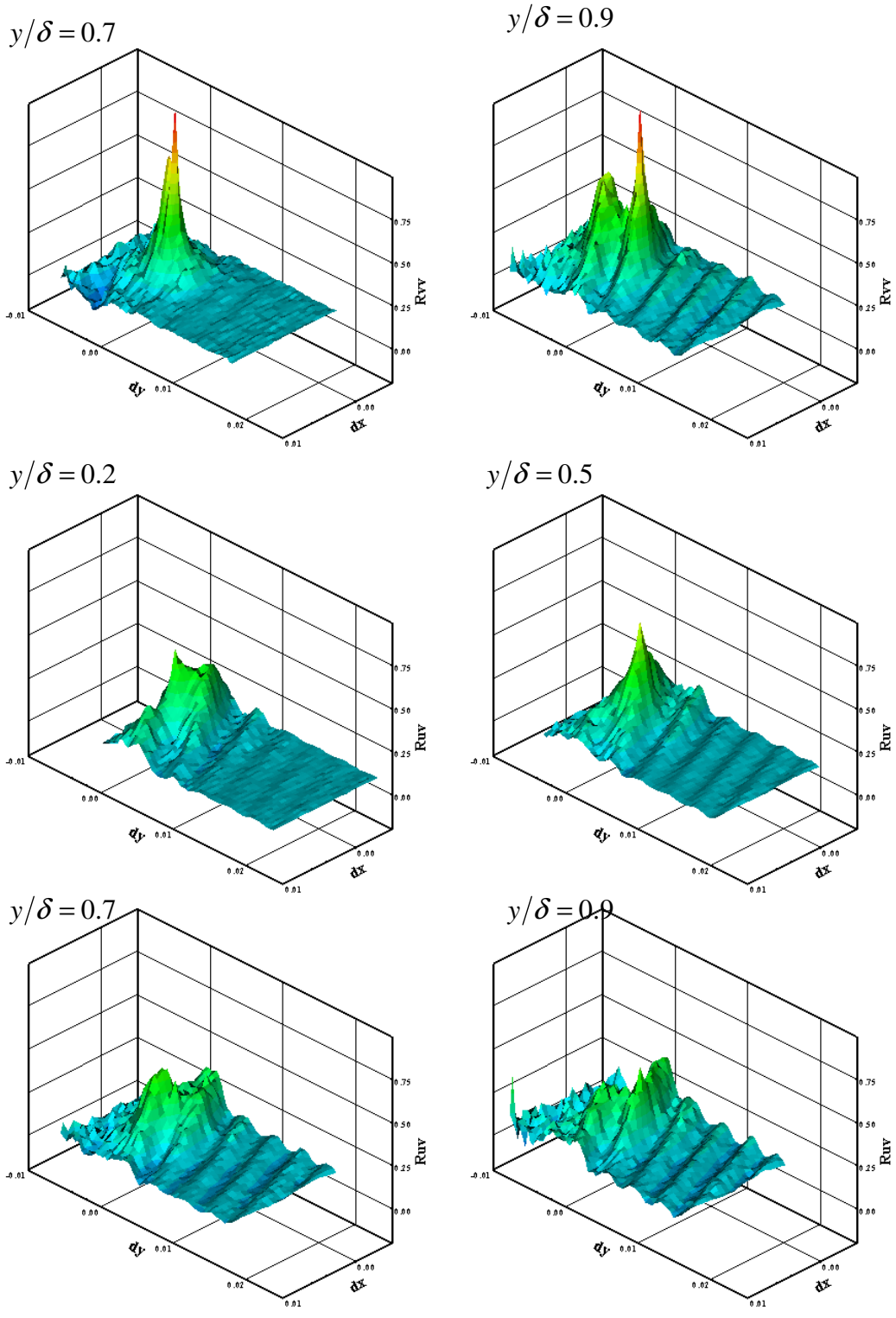

Figure 196: Continued

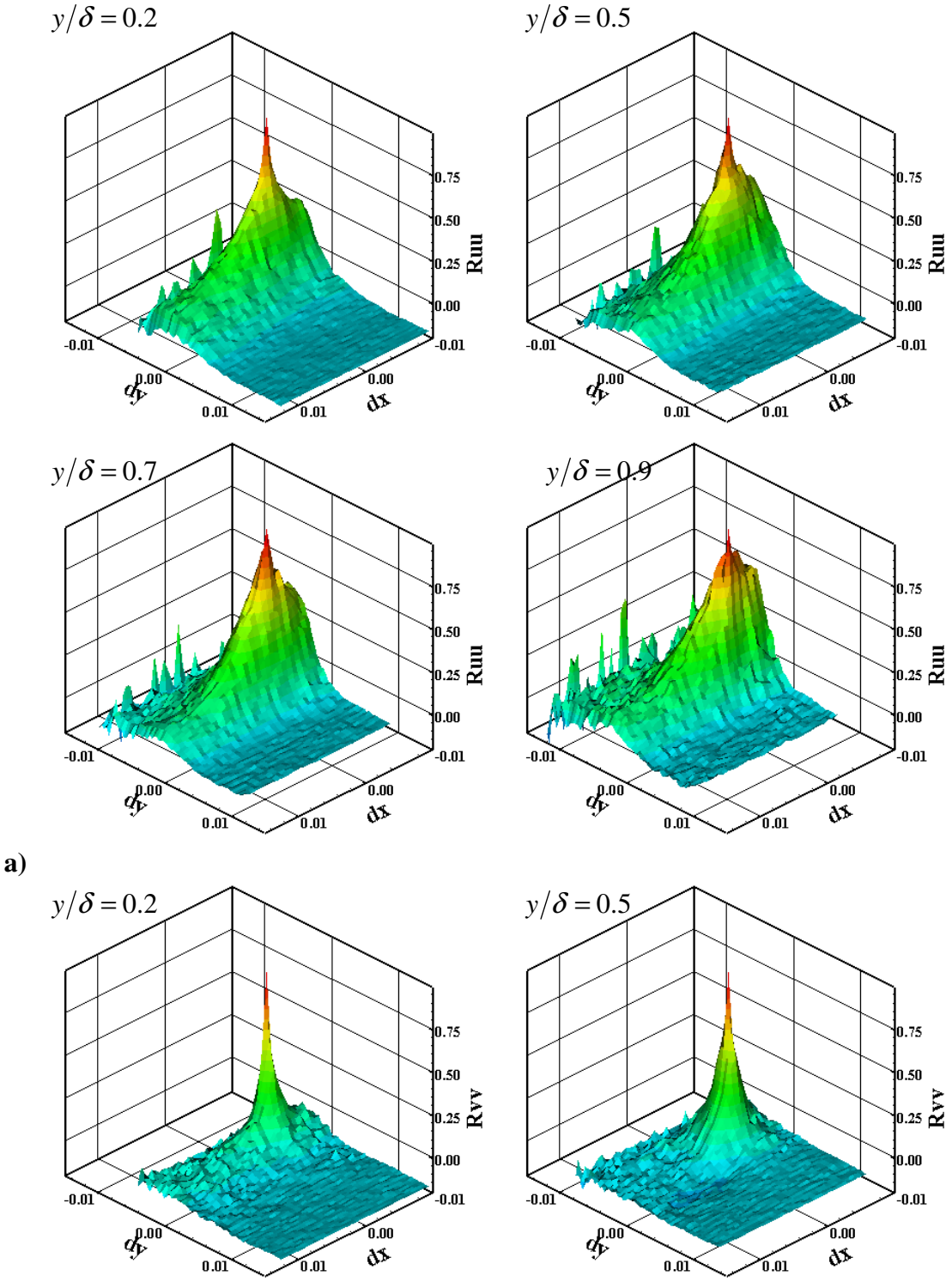

Figure 197: Correlation maps for the WPG smooth wall model at the 2nd location: a) *u'* auto, b) *v'* auto c) and cross

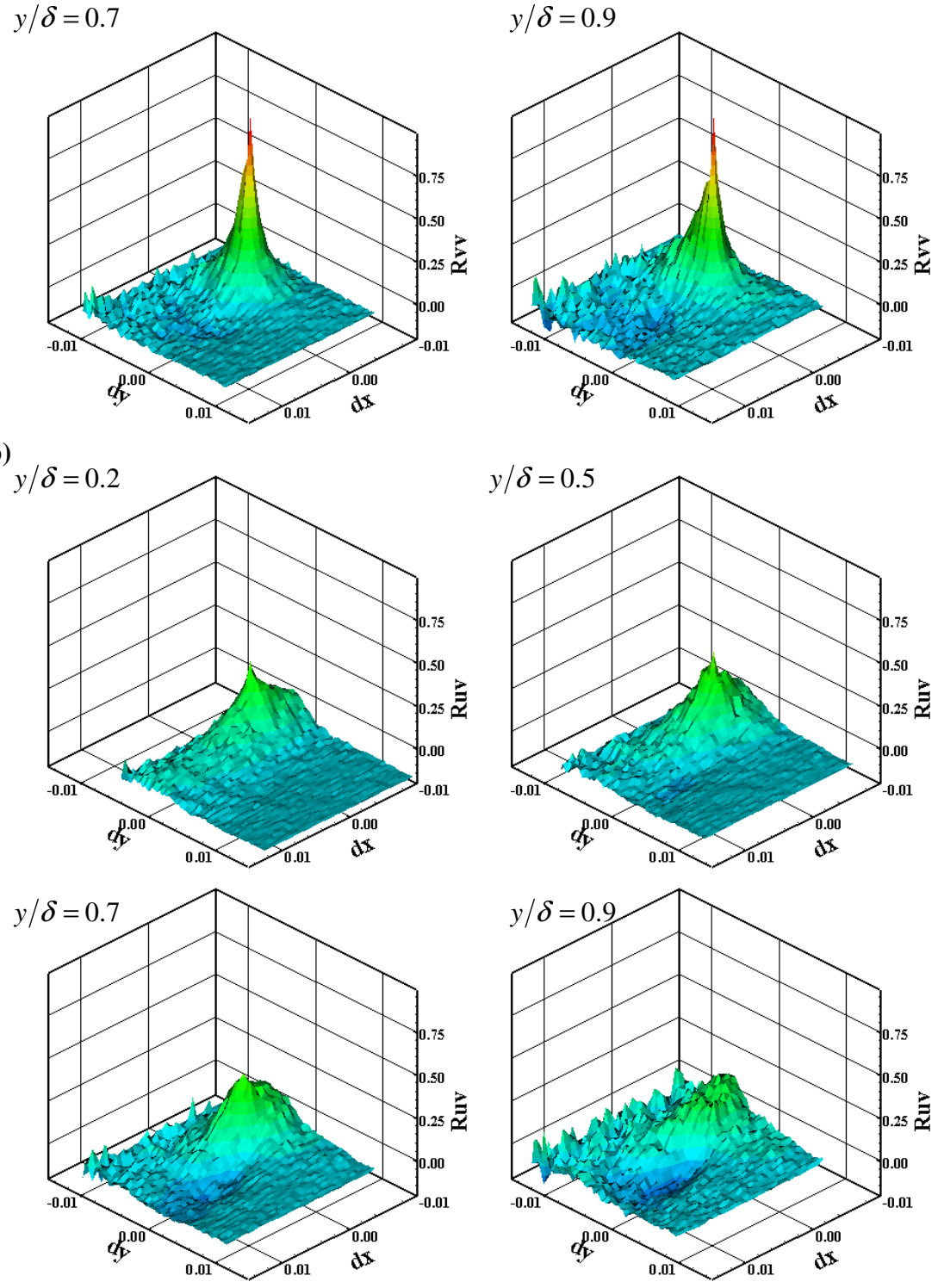

Figure 197: Continued

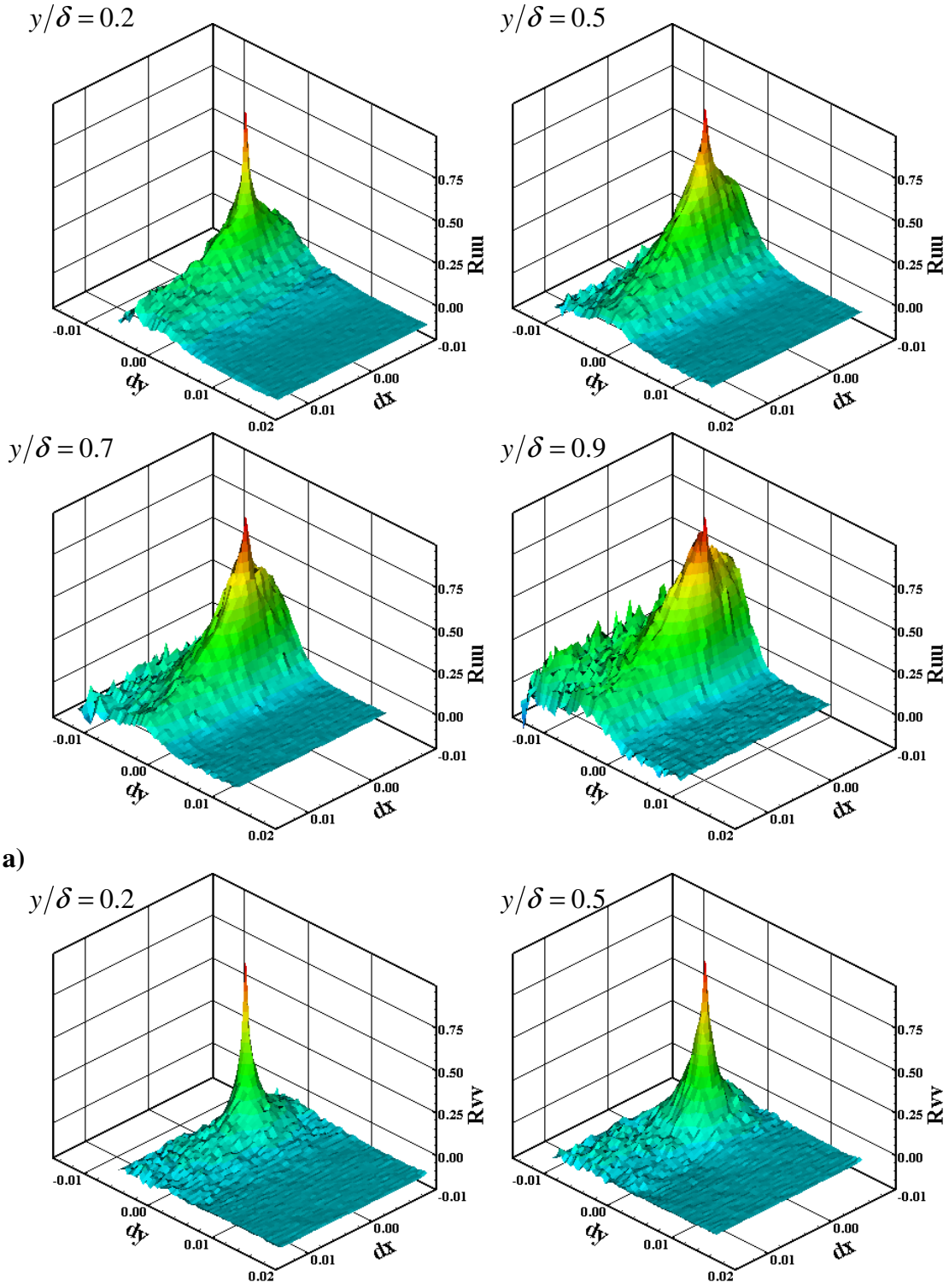

Figure 198: Correlation maps for the WPG square roughness model at the 2nd location: a) *u'* auto, b) *v'* auto c) and cross

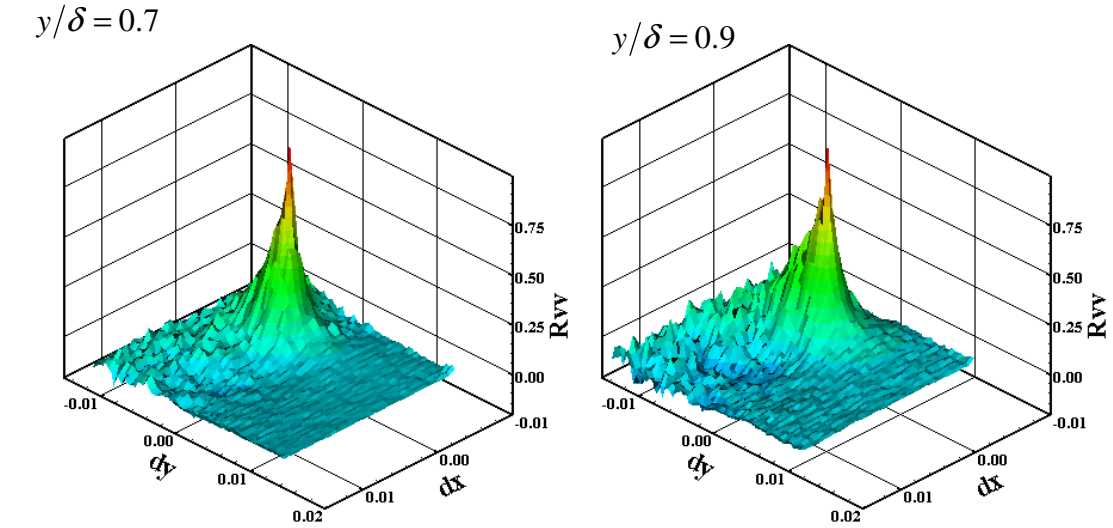

b)

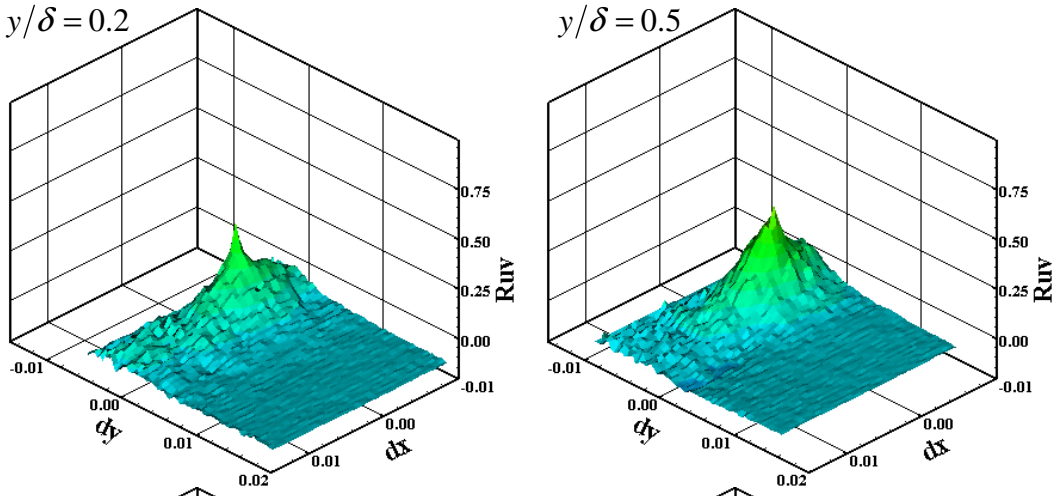

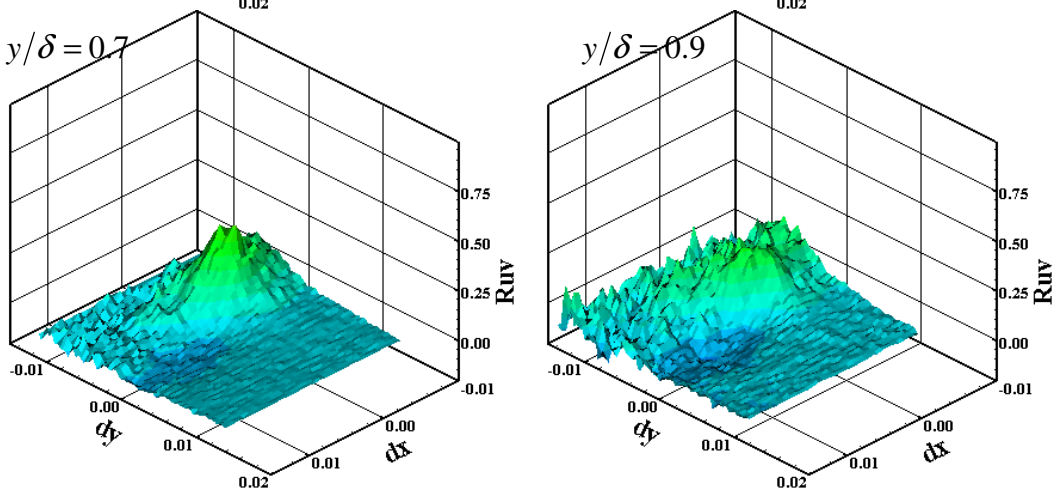

c)

Figure 198: Continued

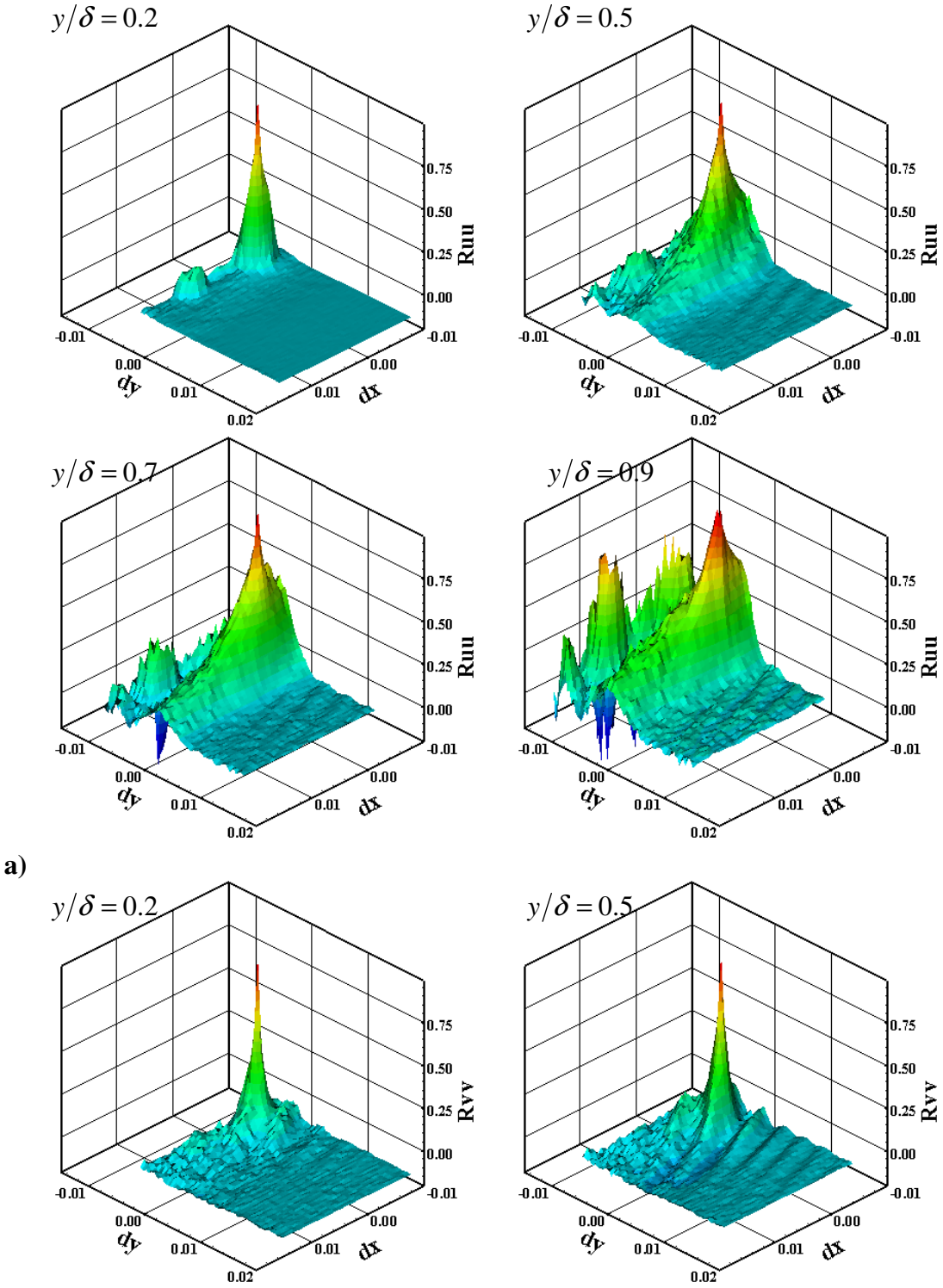

a)

Figure 199: Correlation maps for the WPG diamond roughness model at the 2nd location: a) *u'* auto, b) *v'* auto c) and cross

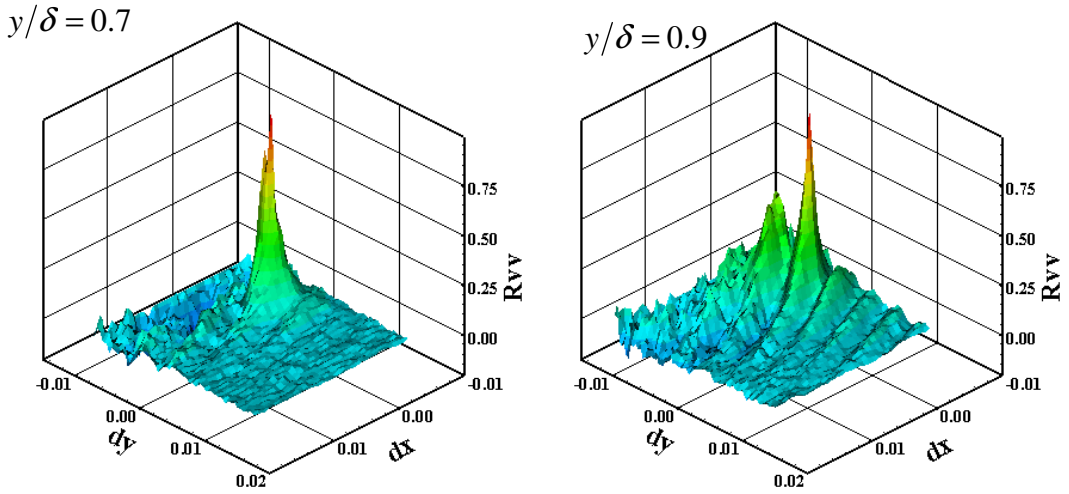

b)

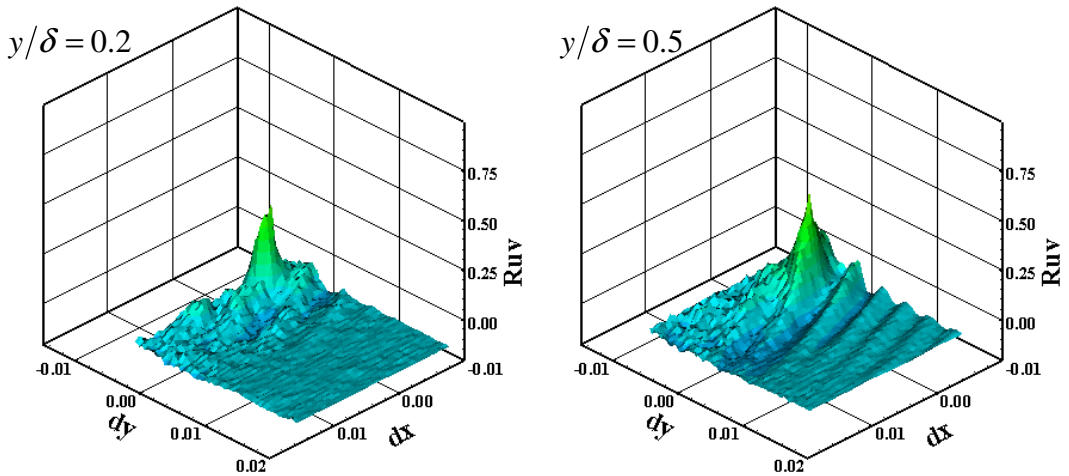

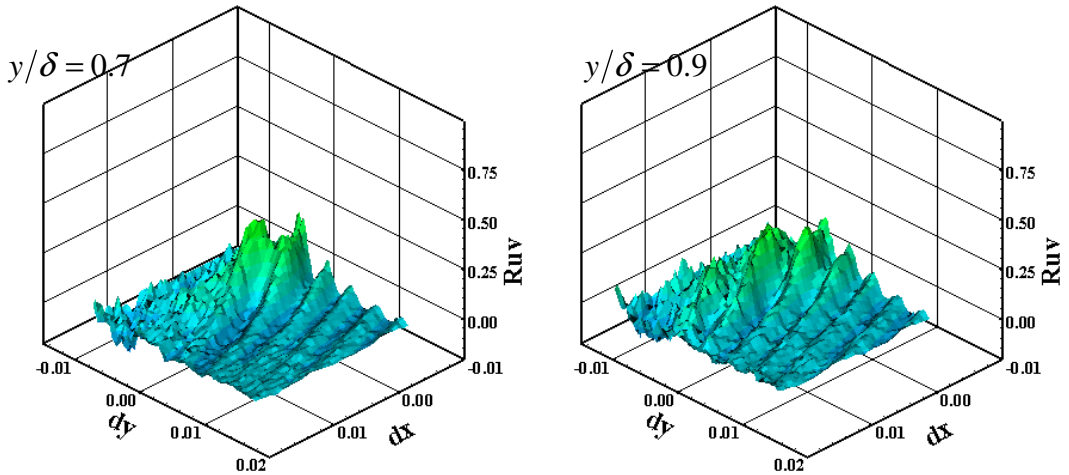

c)

Figure 199: Continued

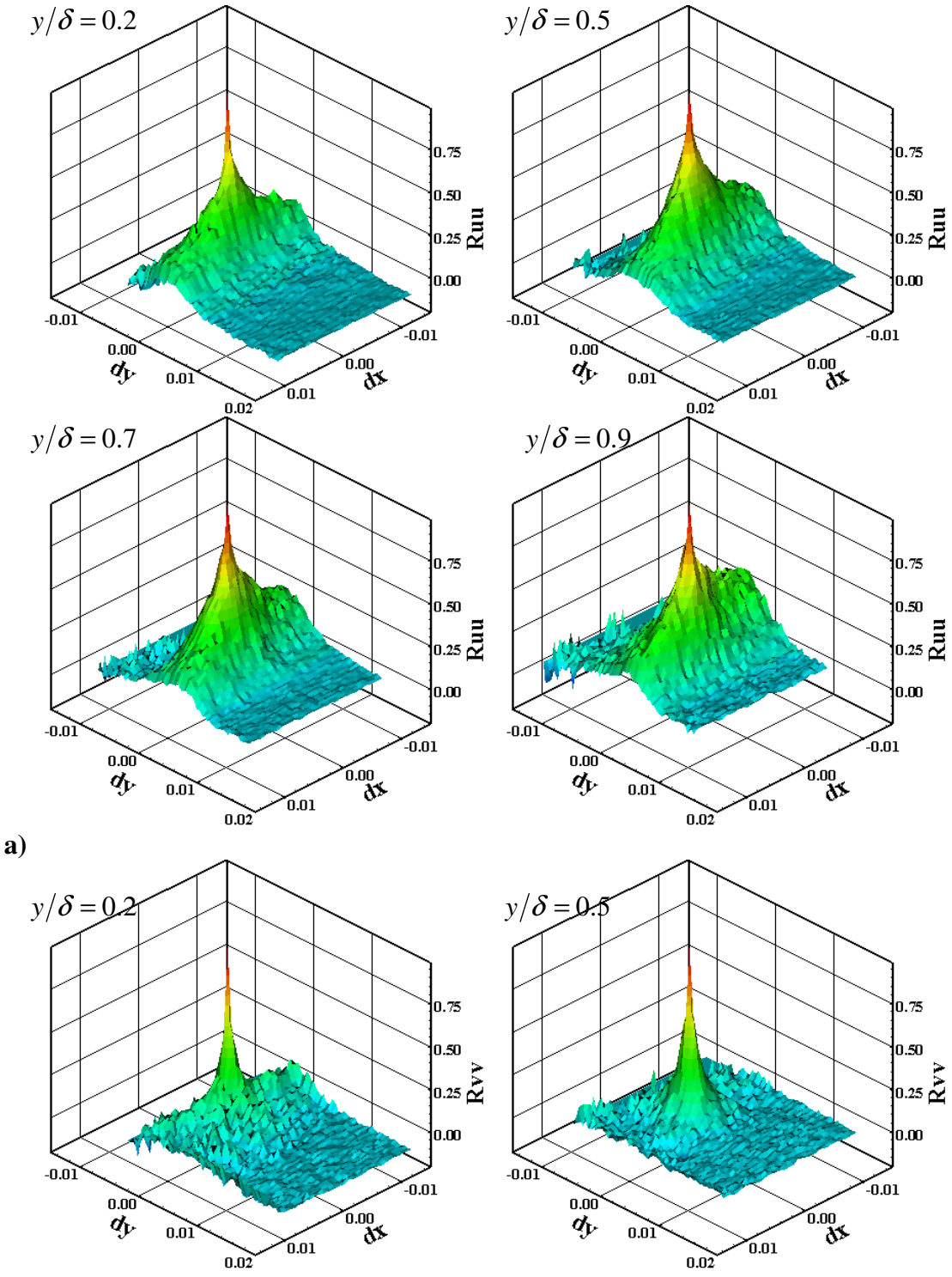

Figure 200: Correlation maps for the SPG smooth wall model at the 2nd location: a) *u'* auto, b) *v'* auto c) and cross

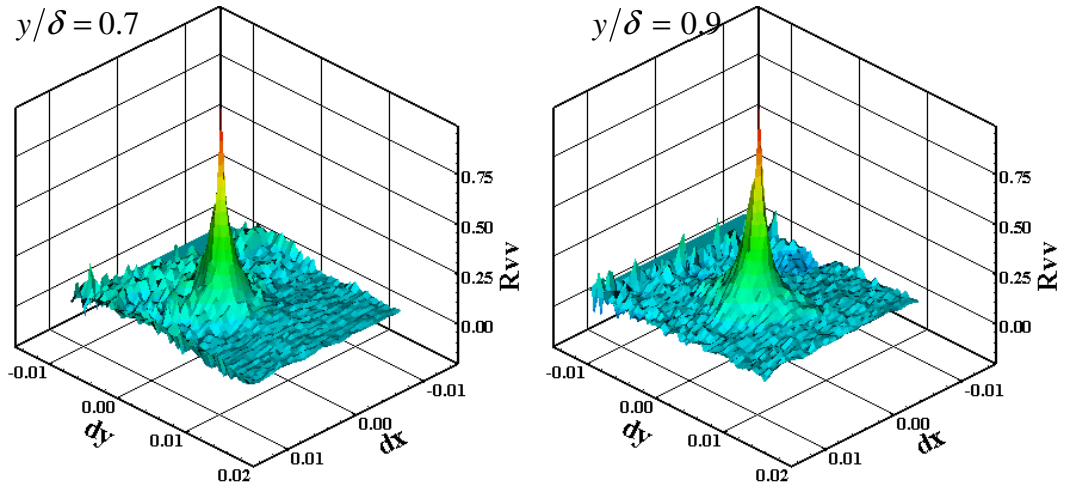

b)

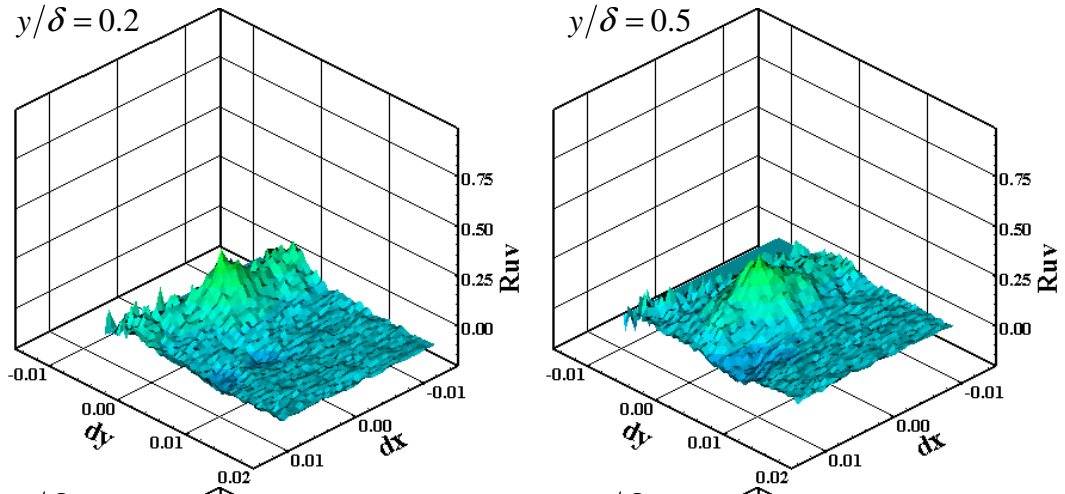

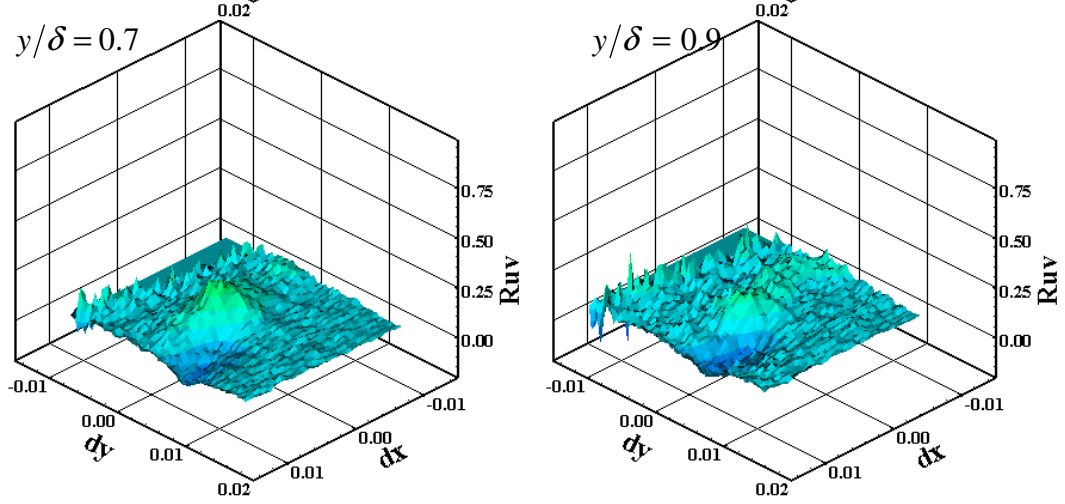

c)

Figure 200: Continued

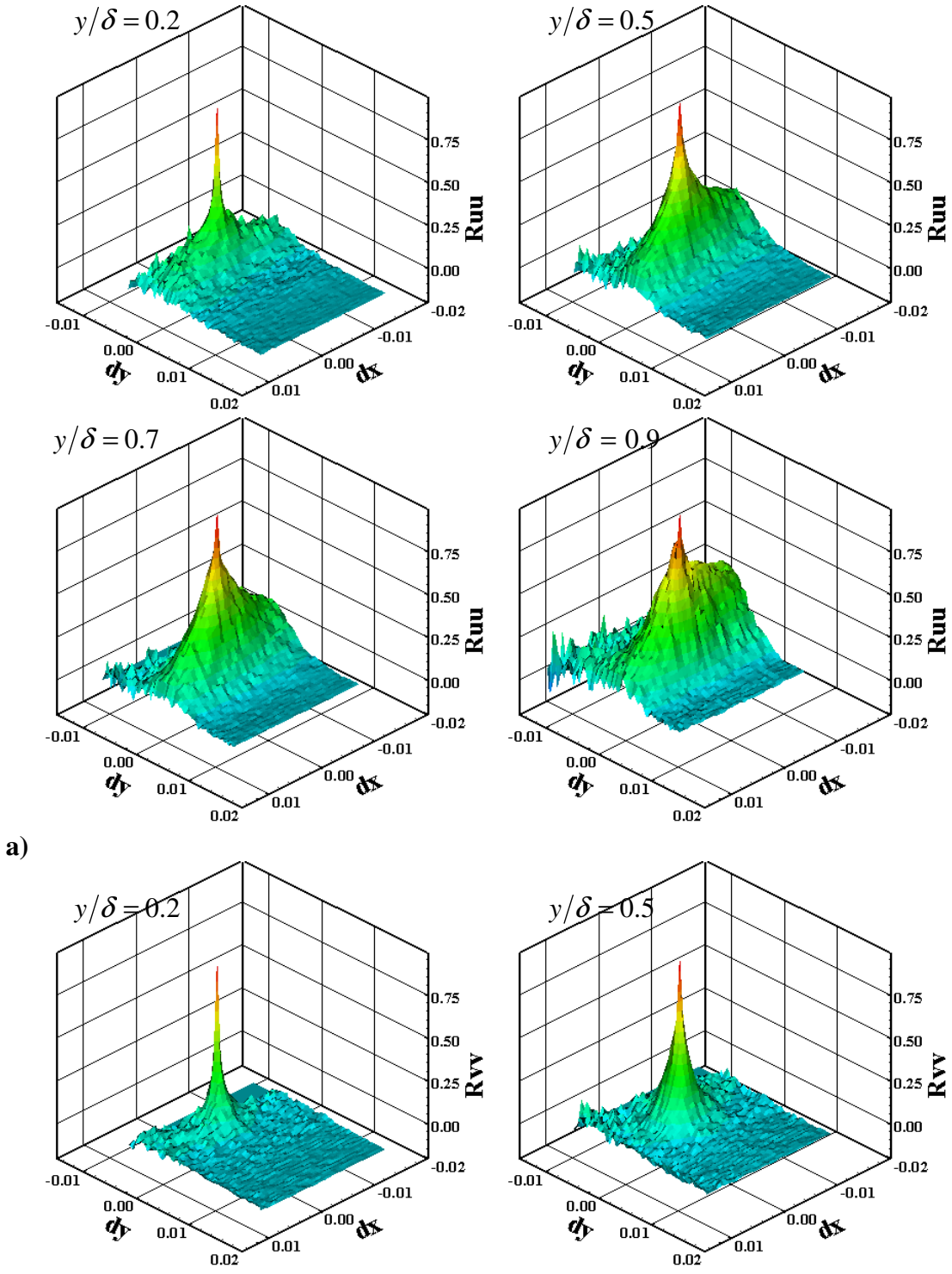

Figure 201: Correlation maps for the SPG square roughness model at the 2nd location: a) *u'* auto, b) *v'* auto c) and cross

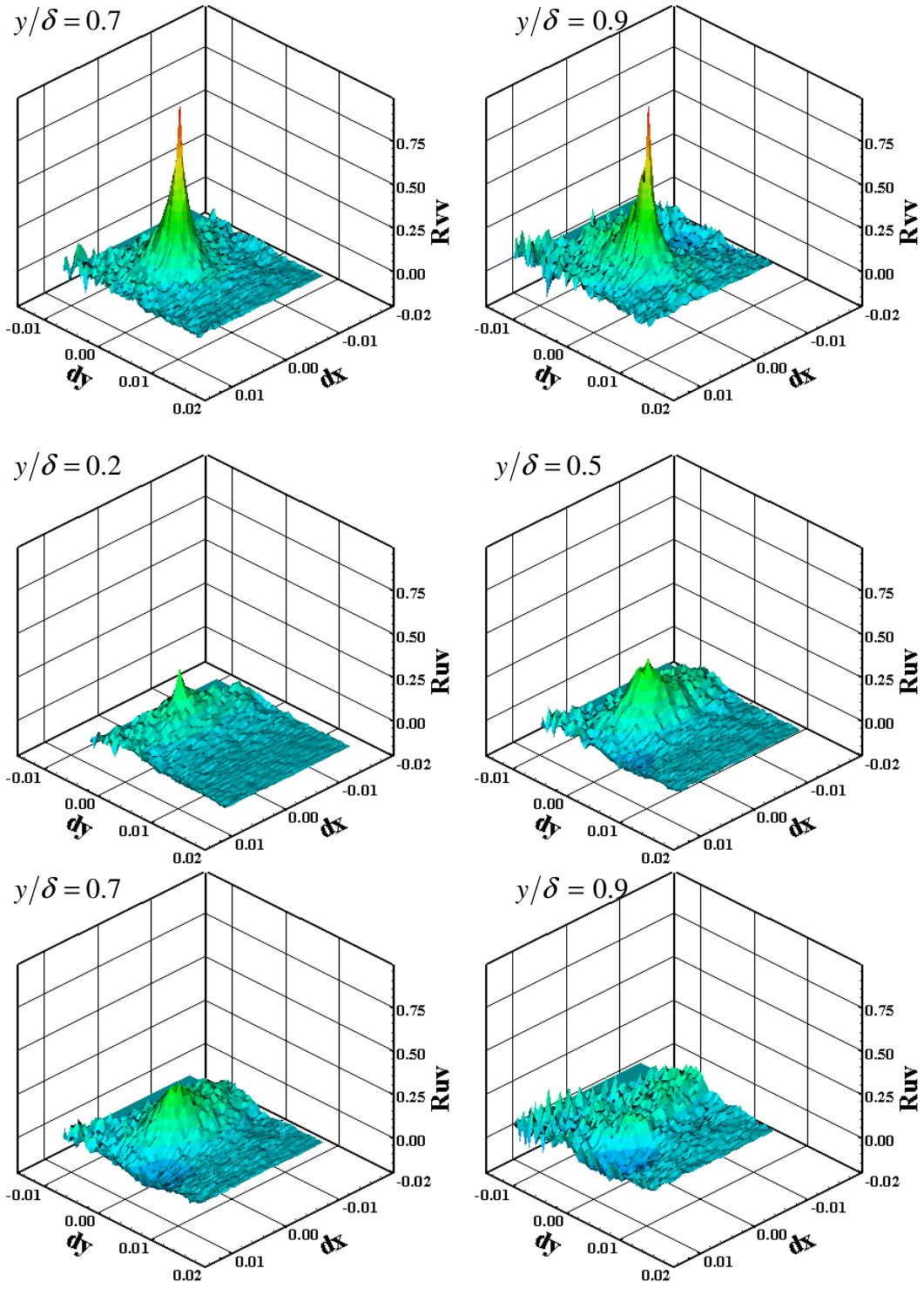

Figure 201: Continued

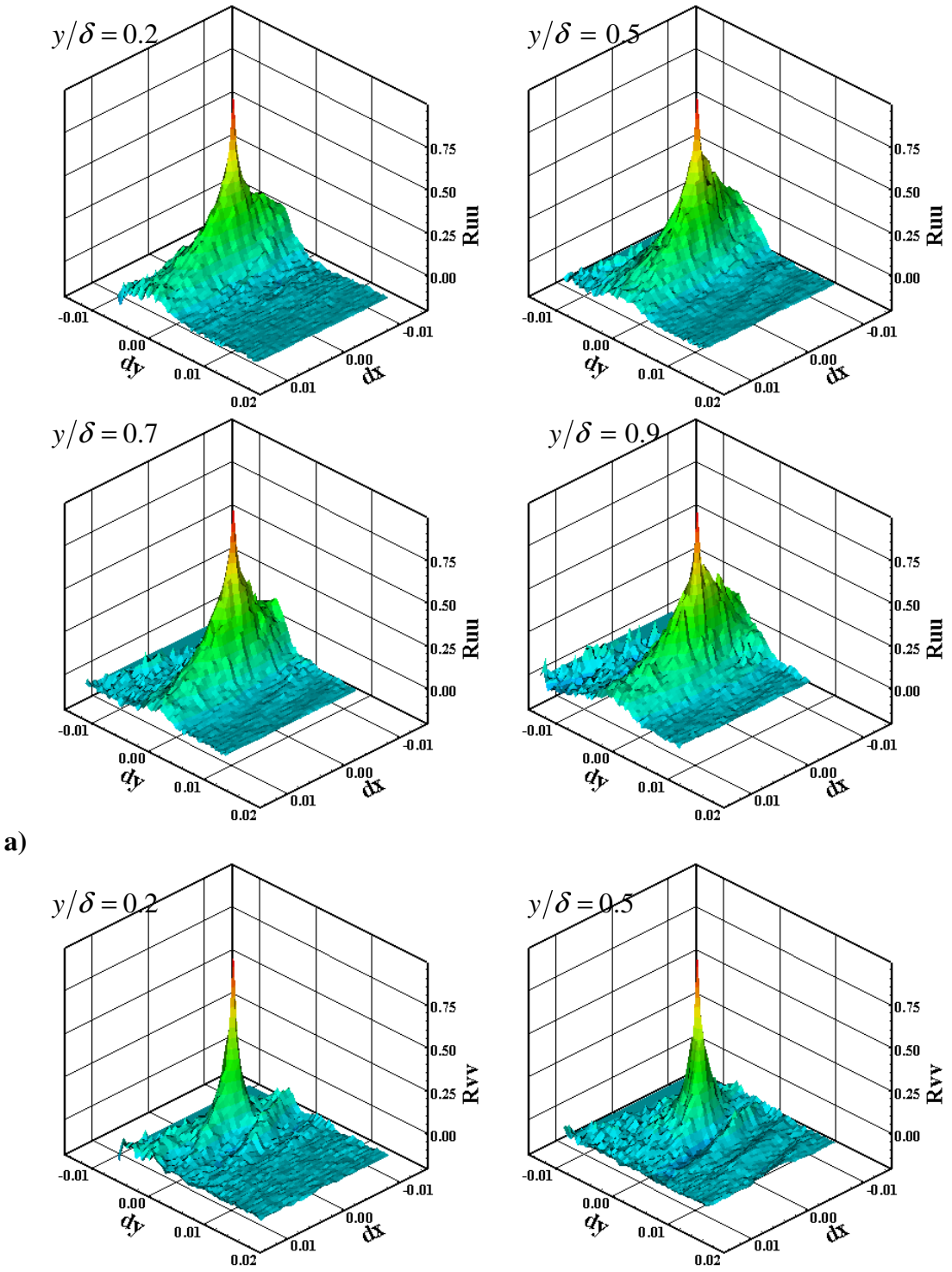

a)

Figure 202: Correlation maps for the SPG diamond roughness model at the 2nd location: a) *u'* auto, b) *v'* auto c) and cross

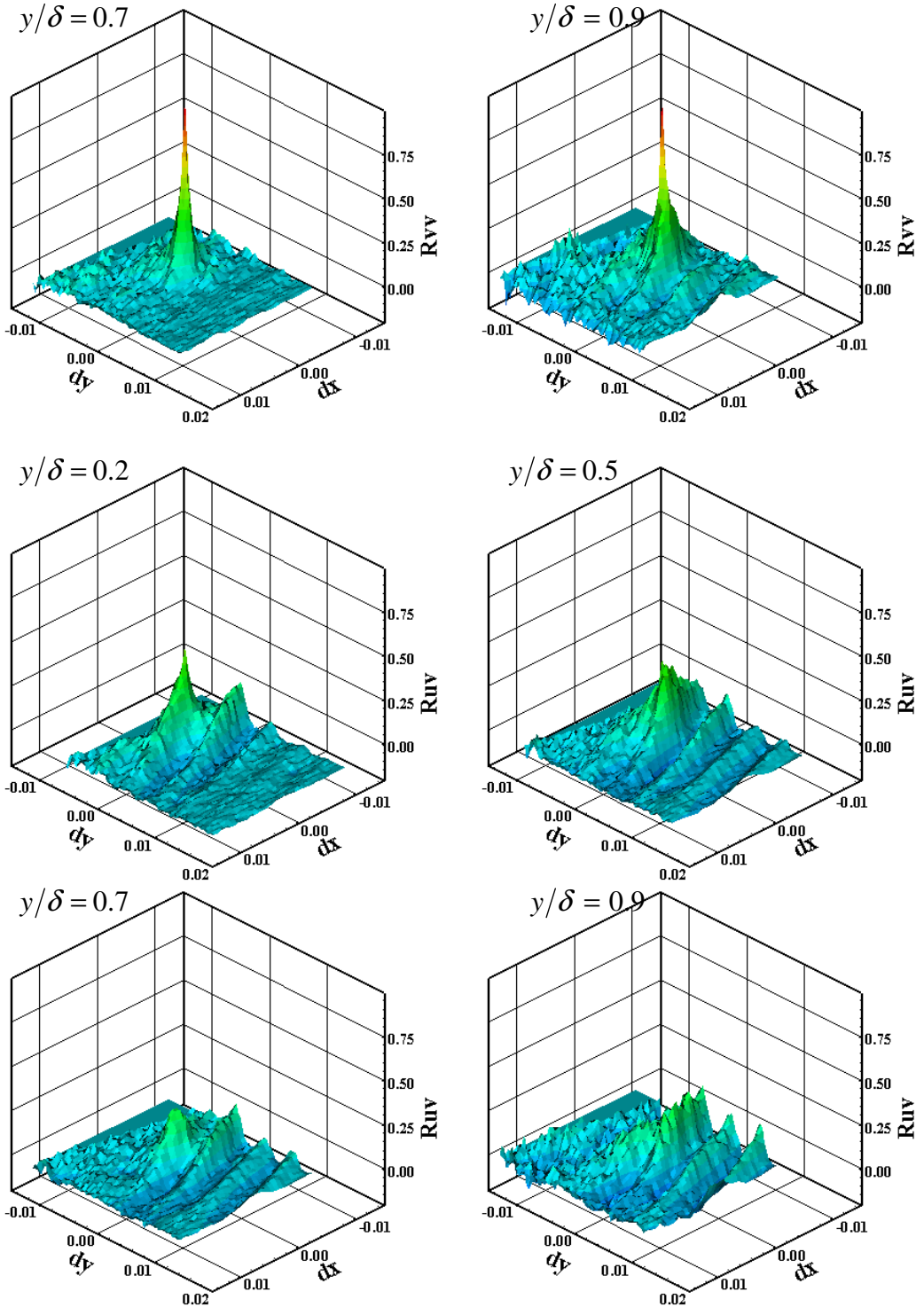

Figure 202: Continued

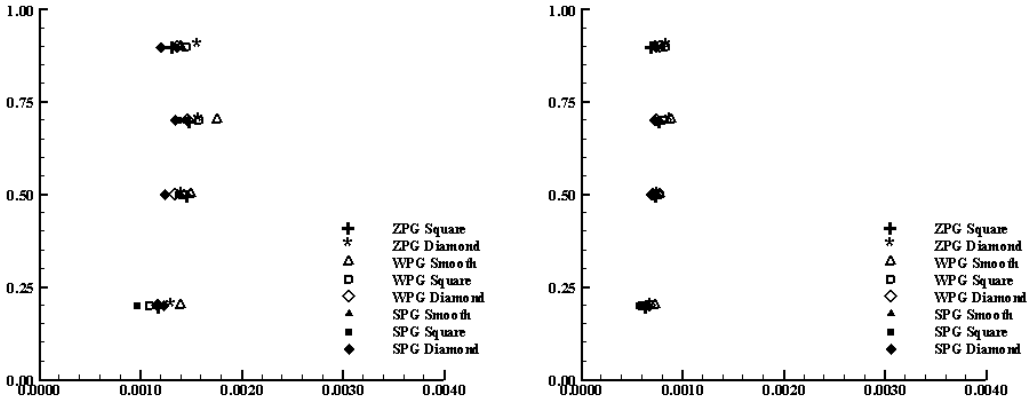

a)

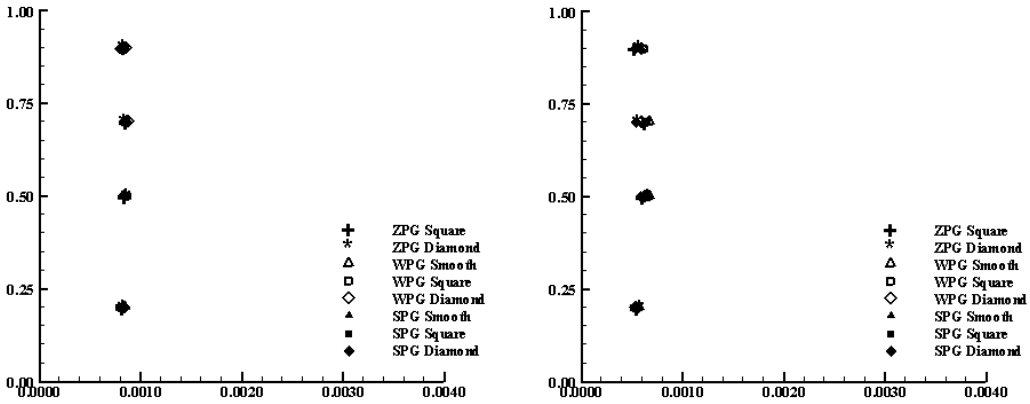

b)

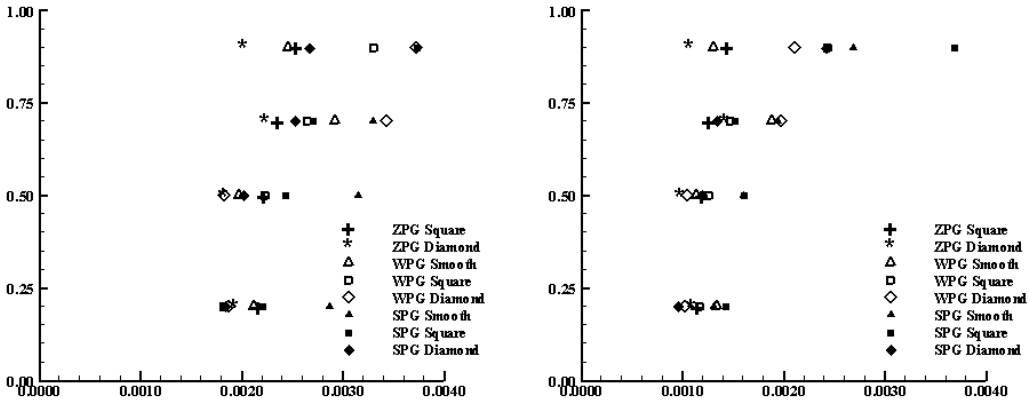

c)

Figure 203: *x* and *y* Taylor microscales for the 2nd test location: a) *u'* auto, b) *v'* auto c) and cross-correlations

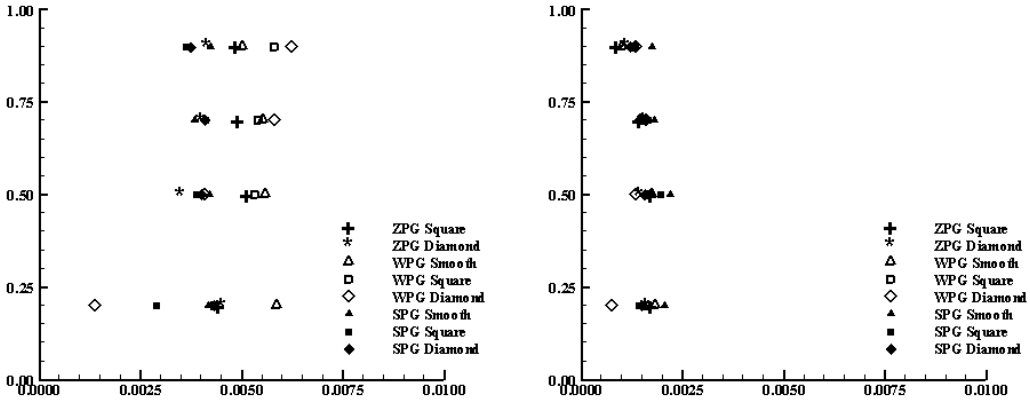

a)

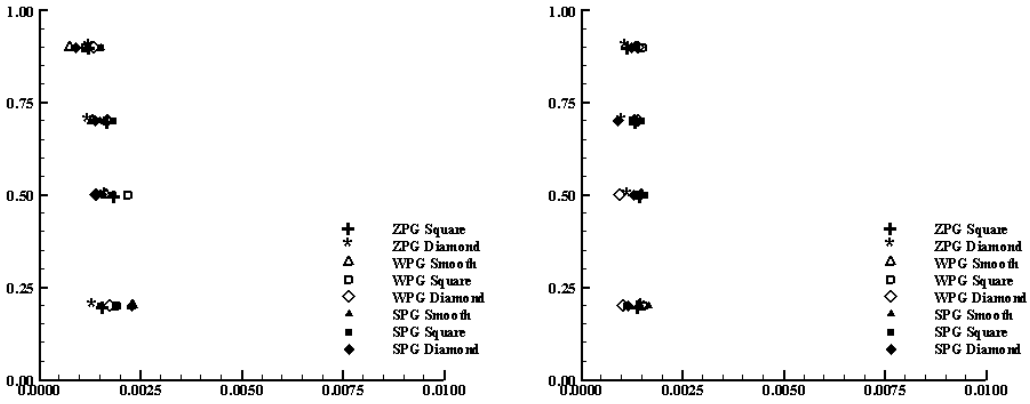

b)

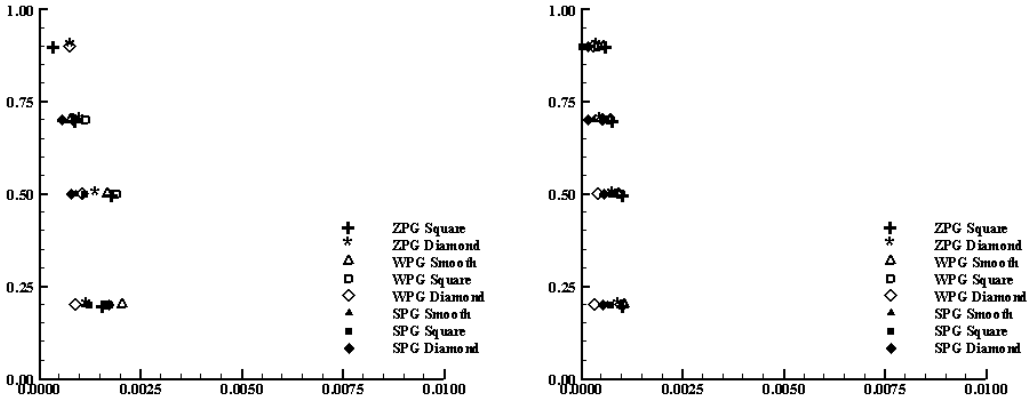

c)

Figure 204: *x* and *y* integral length scales for the 2nd test location: a) *u'* auto, b) *v'* auto c) and cross-correlations

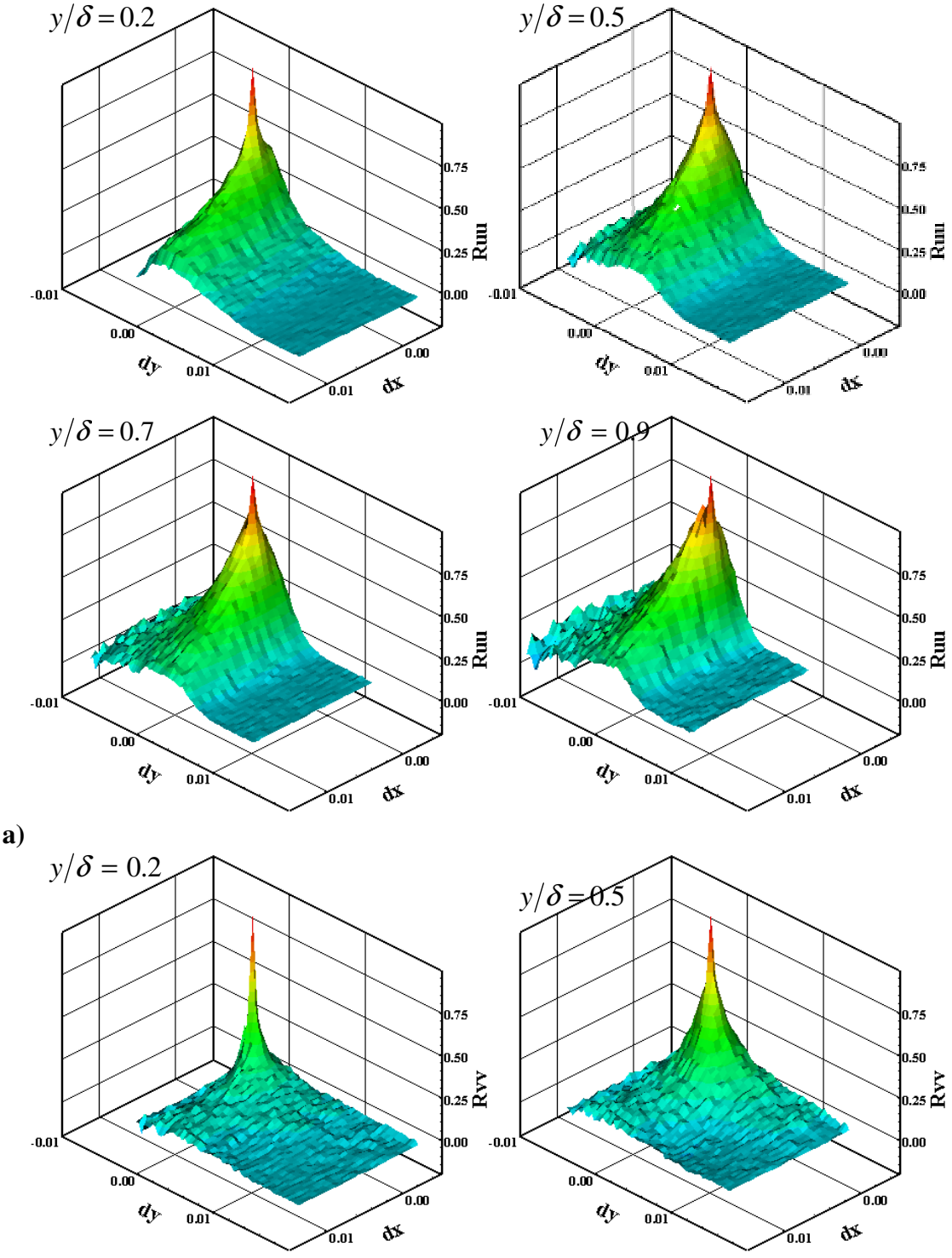

Figure 205: Correlation maps for the ZPG smooth wall model at the 3rd location: a) *u'* auto, b) *v'* auto c) and cross

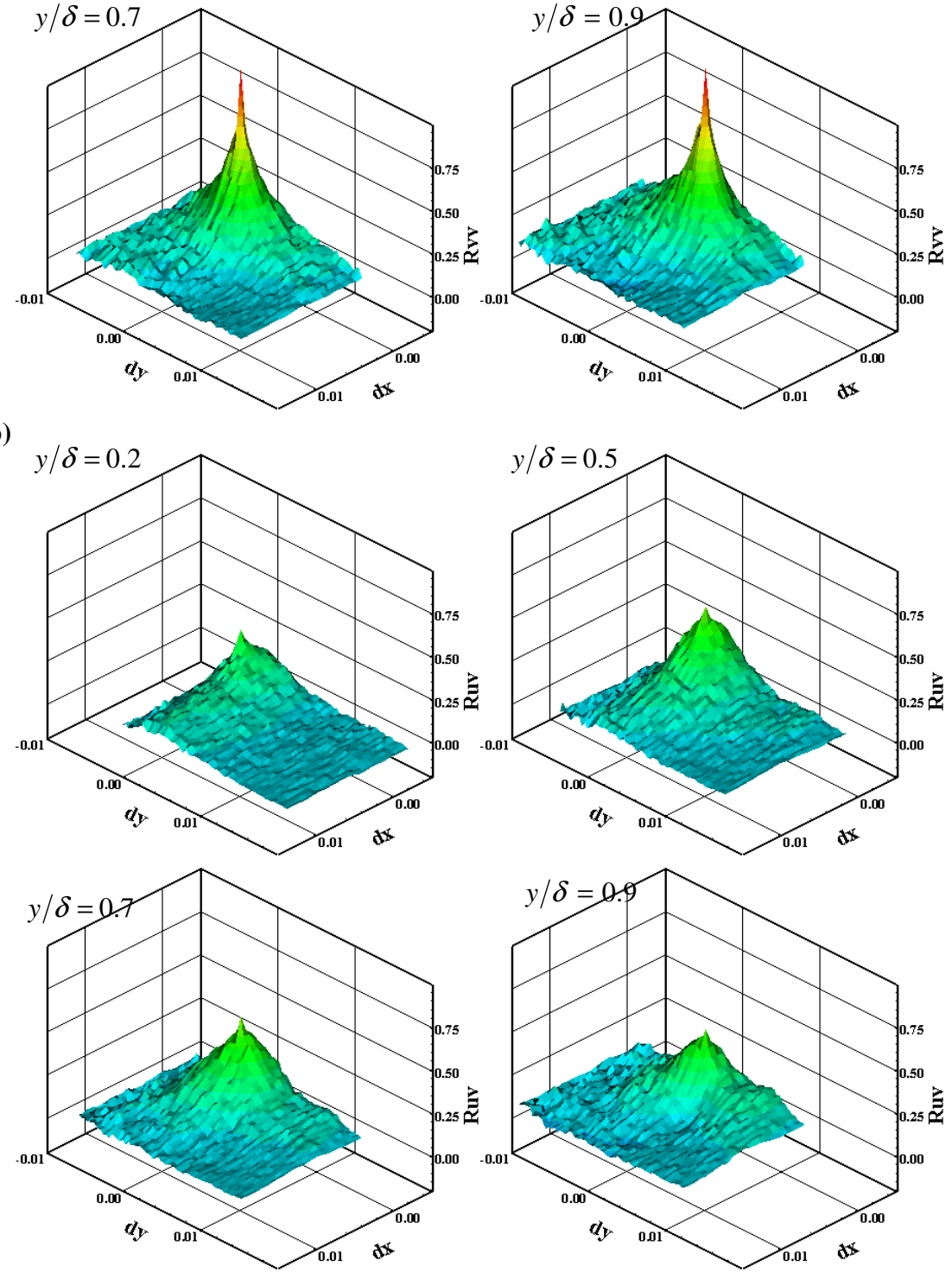

Figure 205: Continued

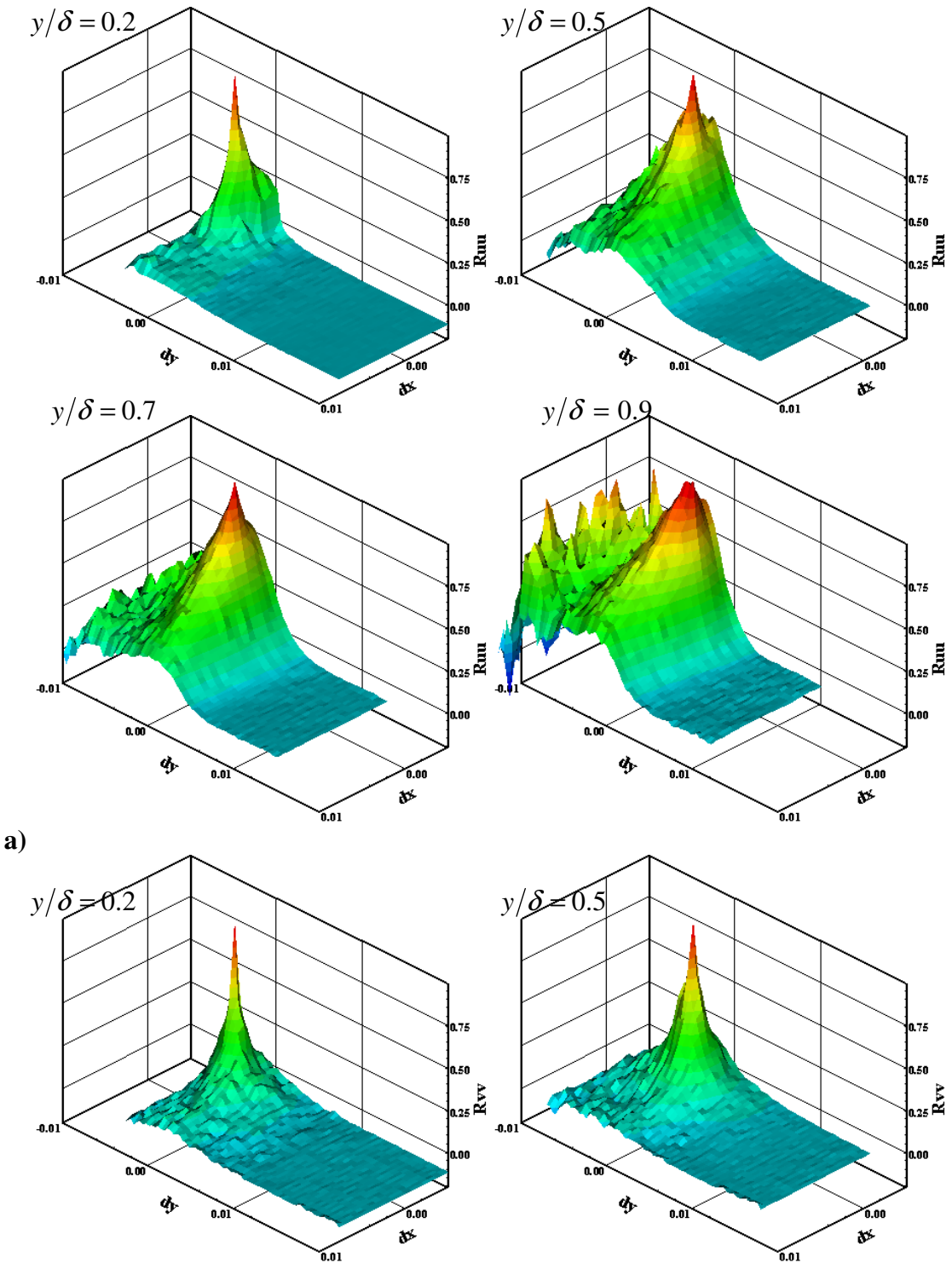

Figure 206: Correlation maps for the ZPG square roughness model at the 3rd location: a) *u'* auto, b) *v'* auto c) and cross

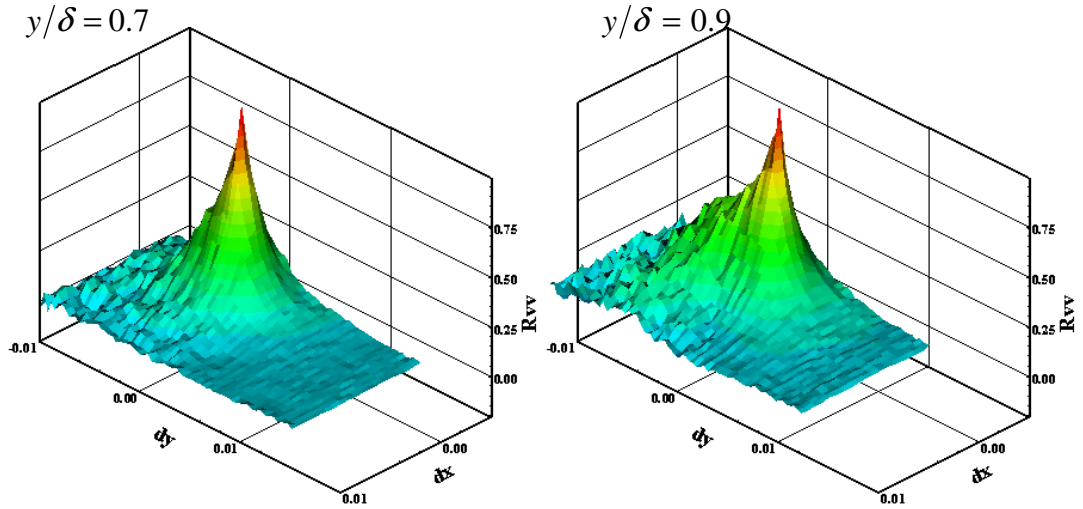

b)

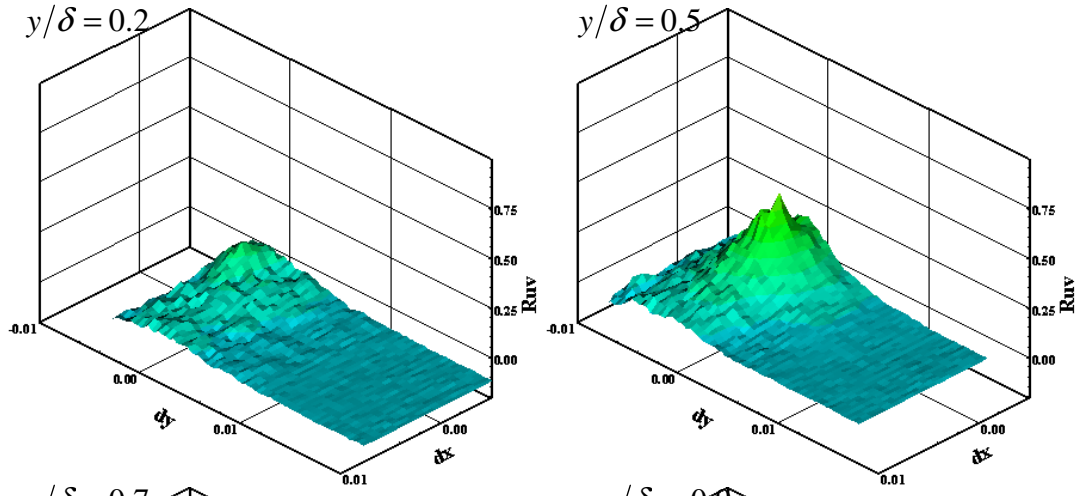

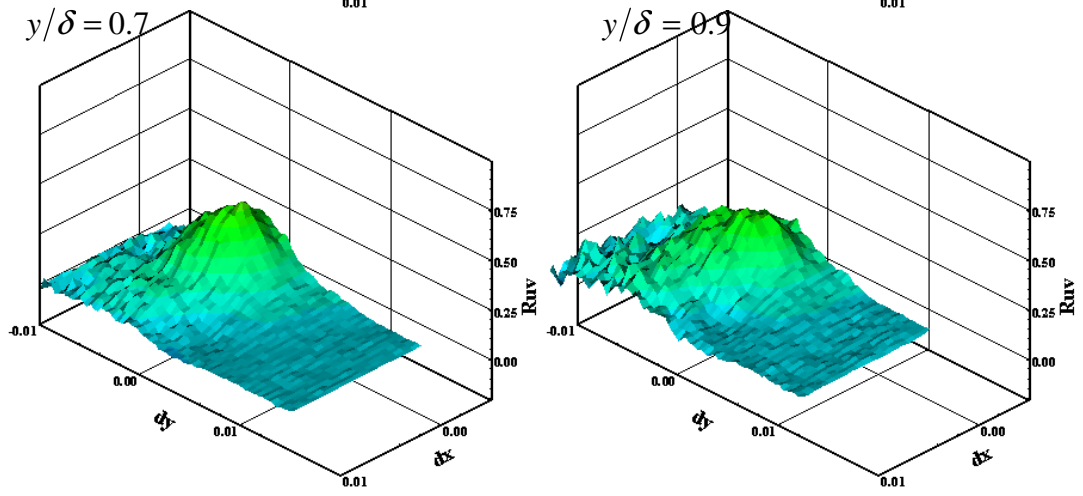

c)

Figure 206: Continued

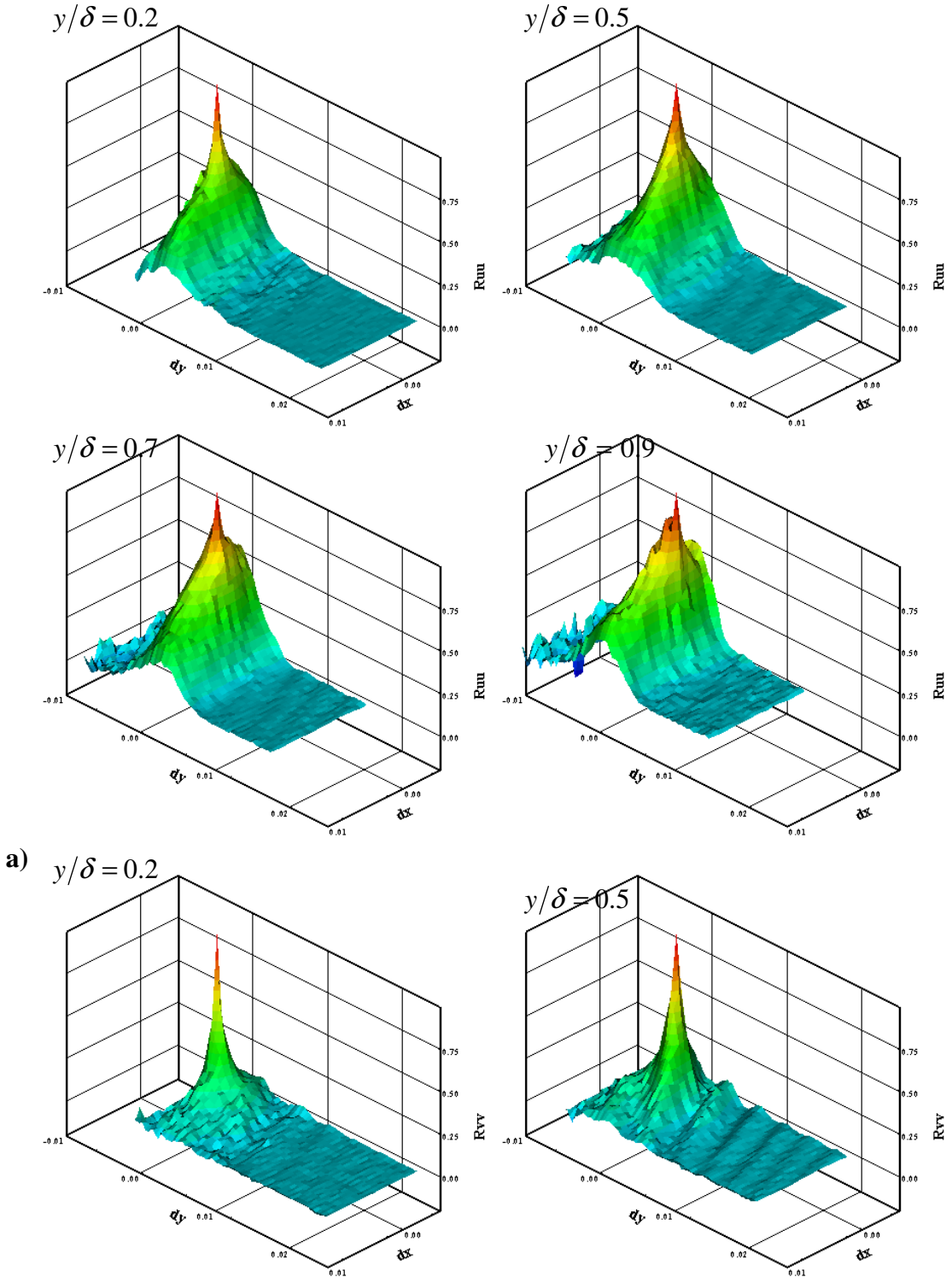

Figure 207: Correlation maps for the ZPG diamond roughness model at the 3rd location: a) *u'* auto, b) *v'* auto c) and cross

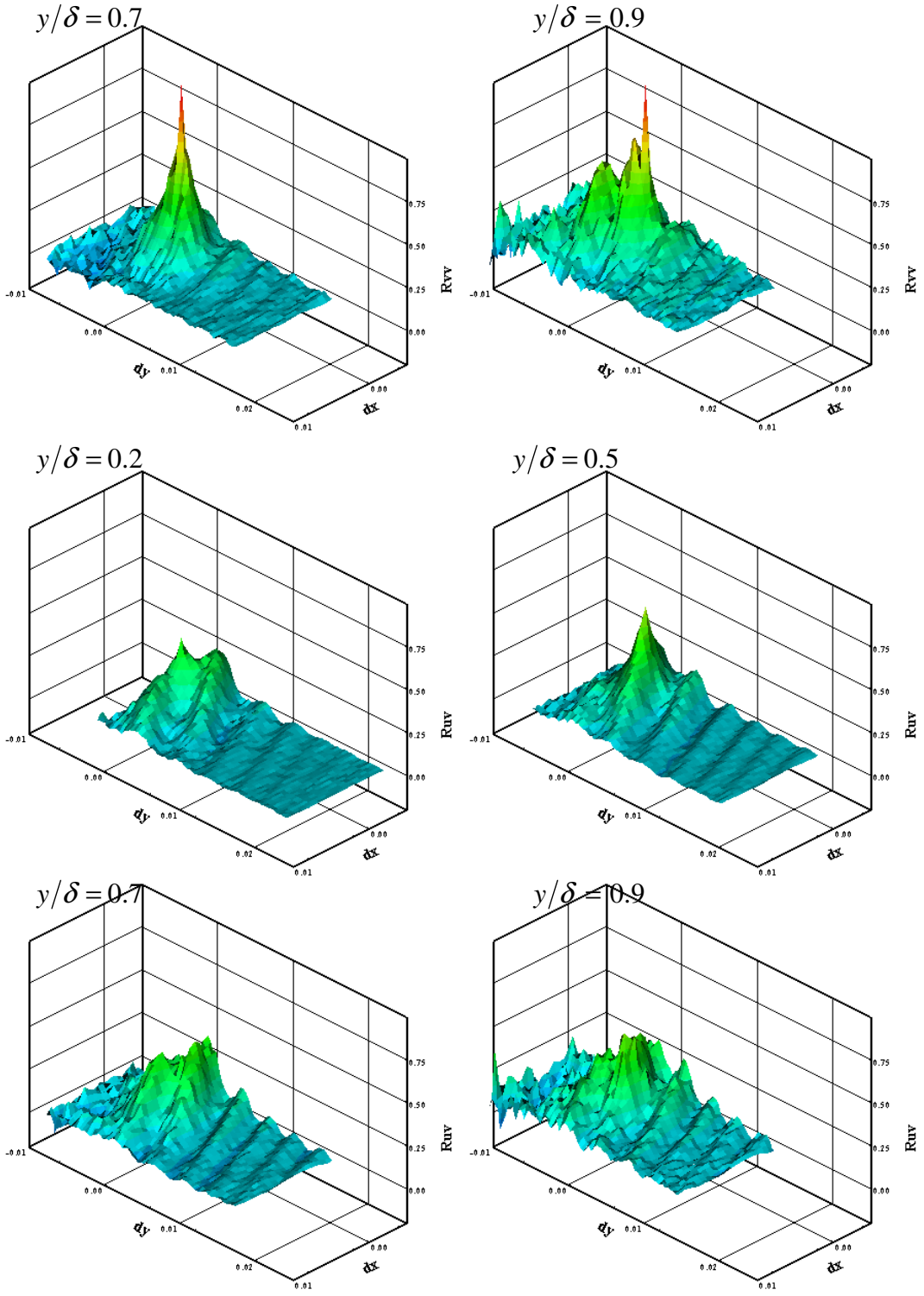

Figure 207: Continued

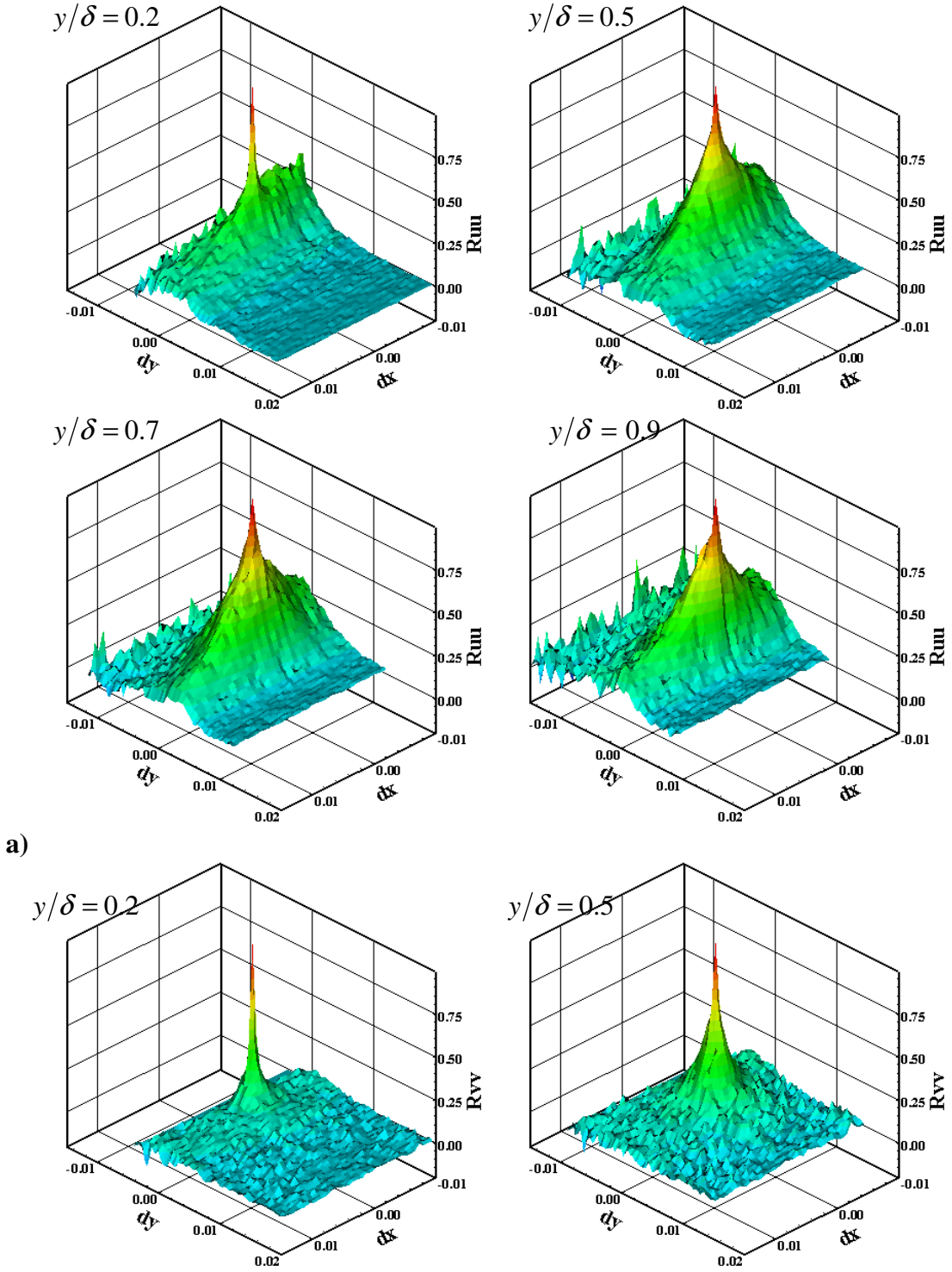

Figure 208: Correlation maps for the WPG smooth wall model at the 3rd location: a) *u'* auto, b) *v'* auto c) and cross

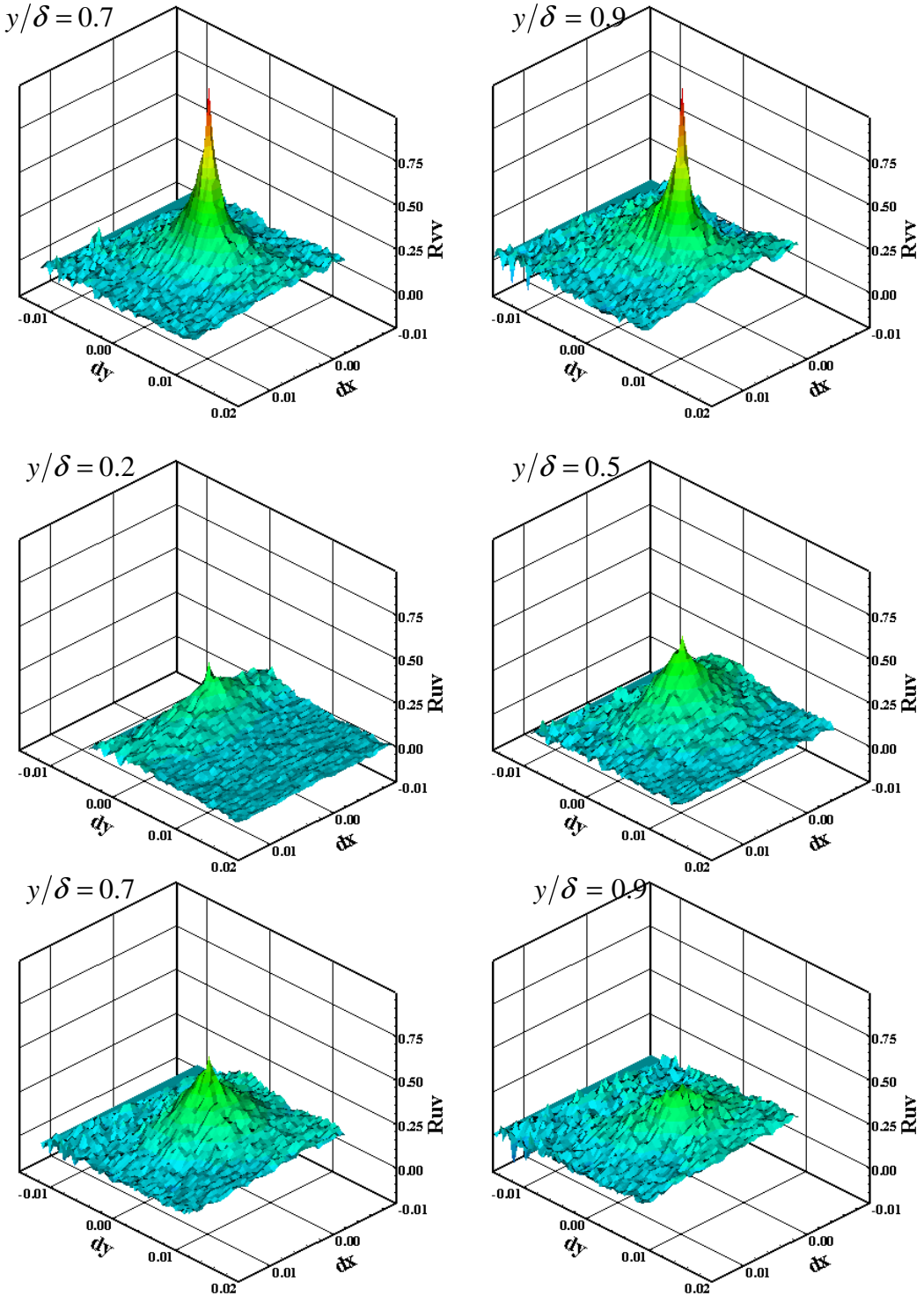

Figure 208: Continued

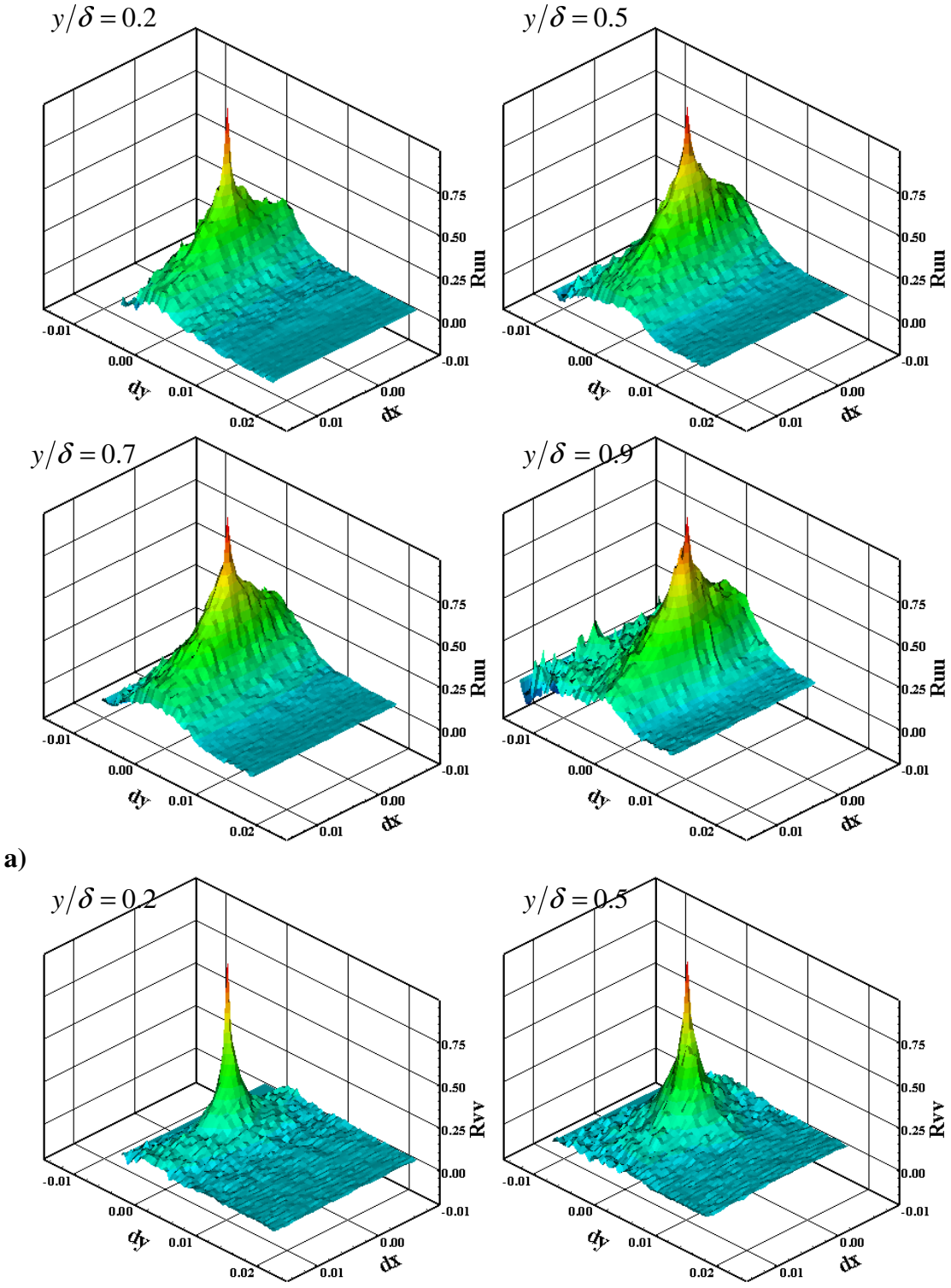

Figure 209: Correlation maps for the WPG square roughness model at the 3rd location: a) *u'* auto, b) *v'* auto c) and cross

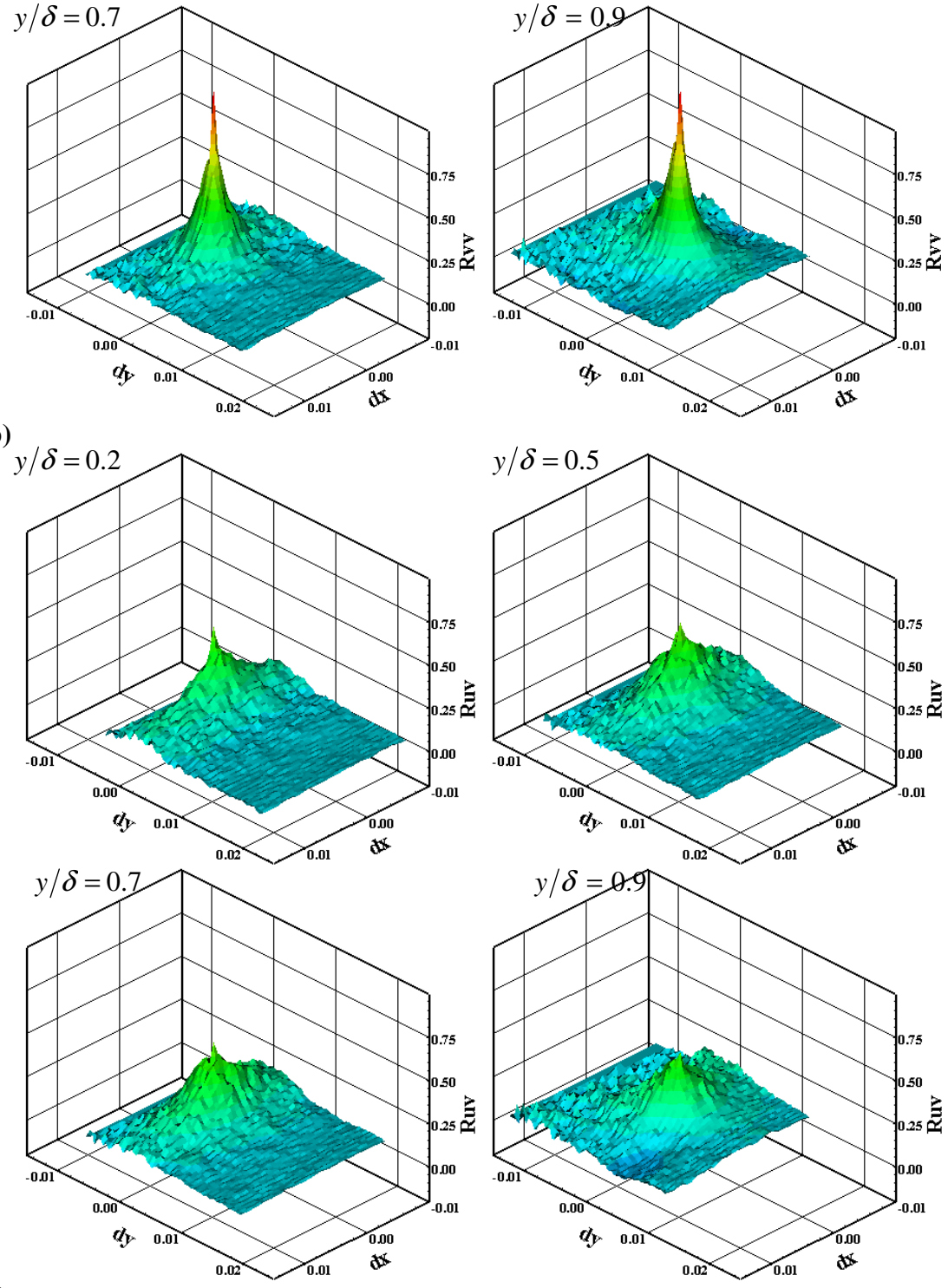

Figure 209: Continued

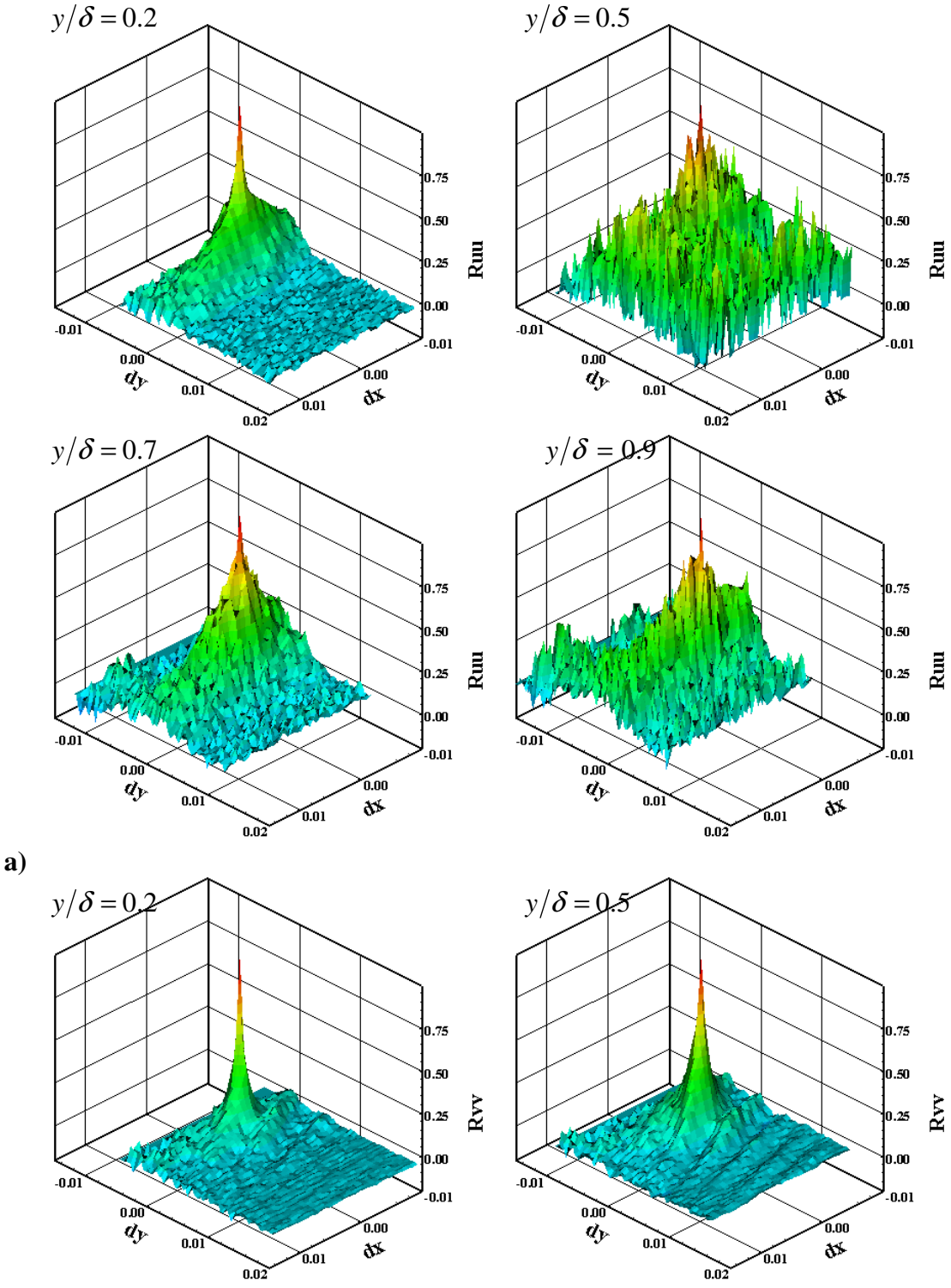

a)

Figure 210: Correlation maps for the WPG diamond roughness model at the 3rd location: a) *u'* auto, b) *v'* auto c) and cross

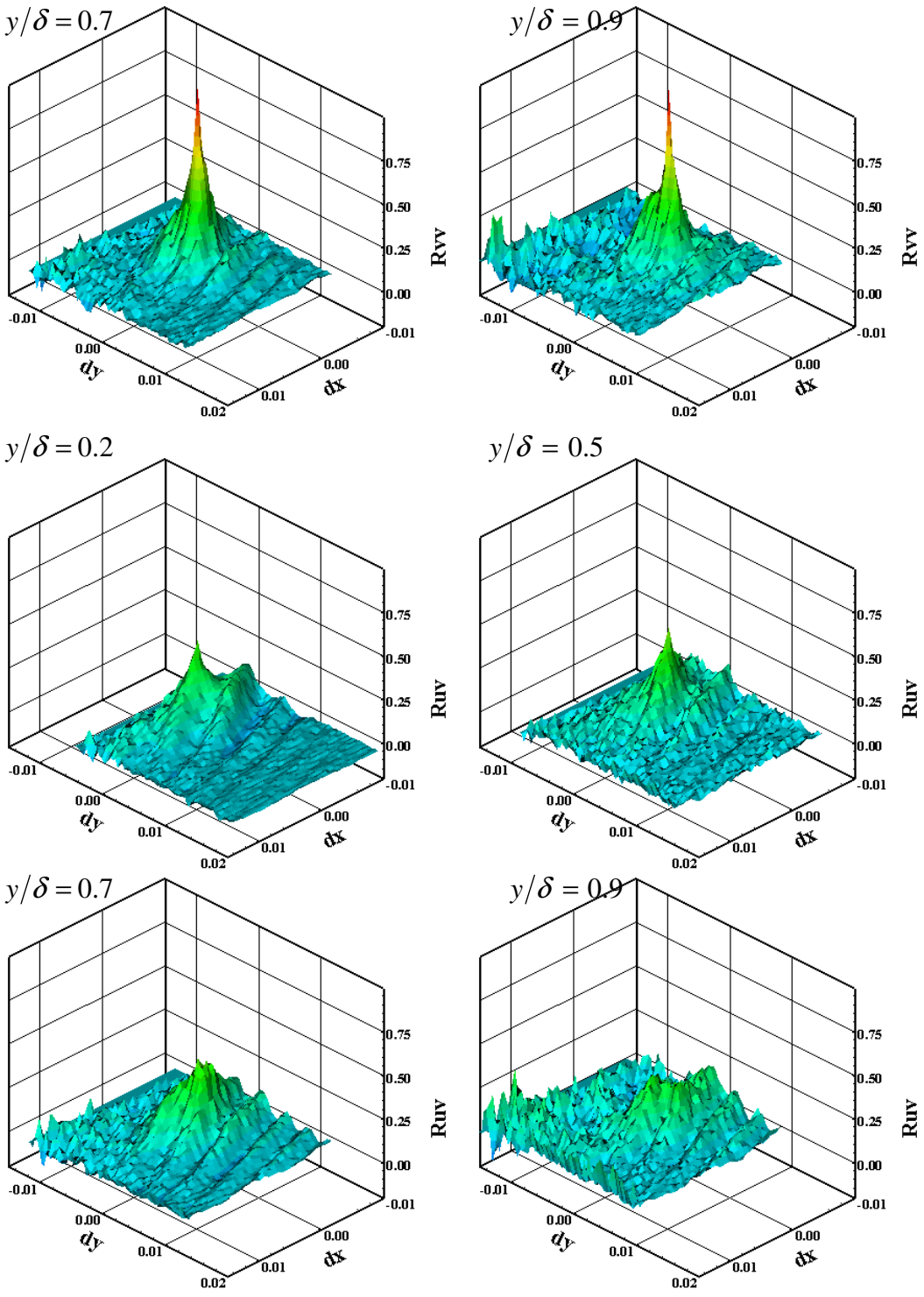

Figure 210: Continued

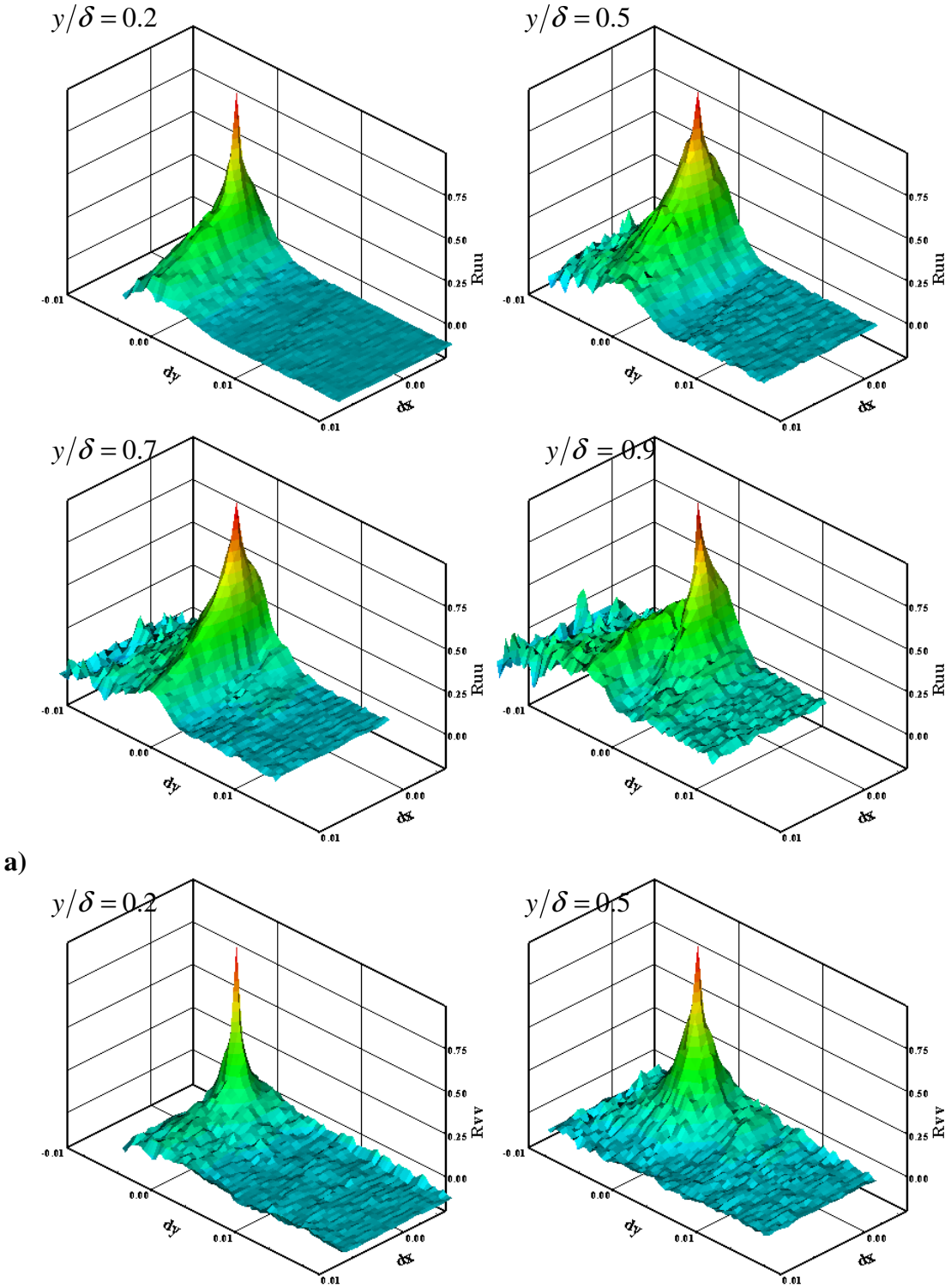

Figure 211: Correlation maps for the SPG smooth wall model at the 3rd location: a) *u'* auto, b) *v'* auto c) and cross

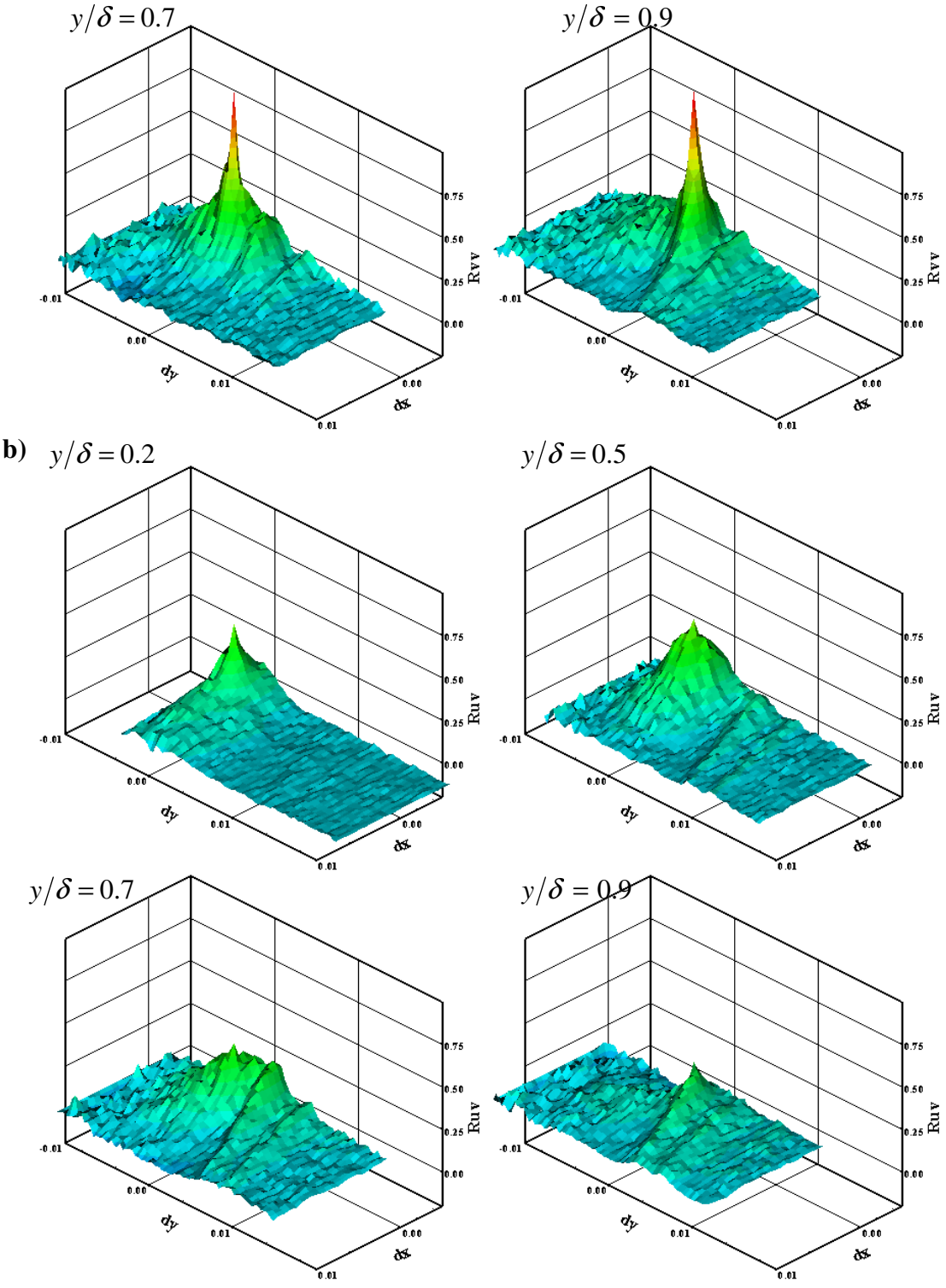

Figure 211: Continued

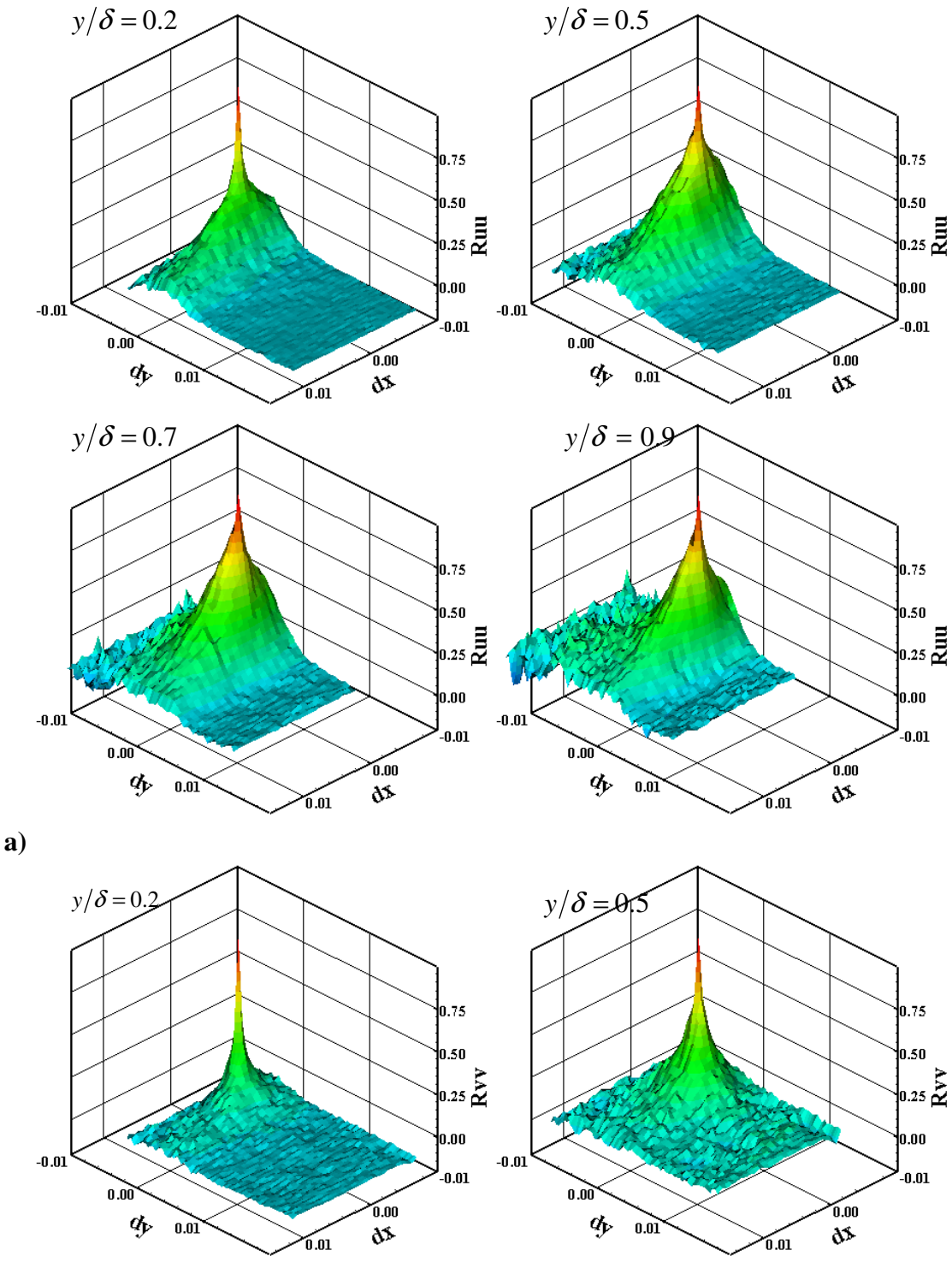

Figure 212: Correlation maps for the SPG square roughness model at the 3rd location: a) *u'* auto, b) *v'* auto c) and cross

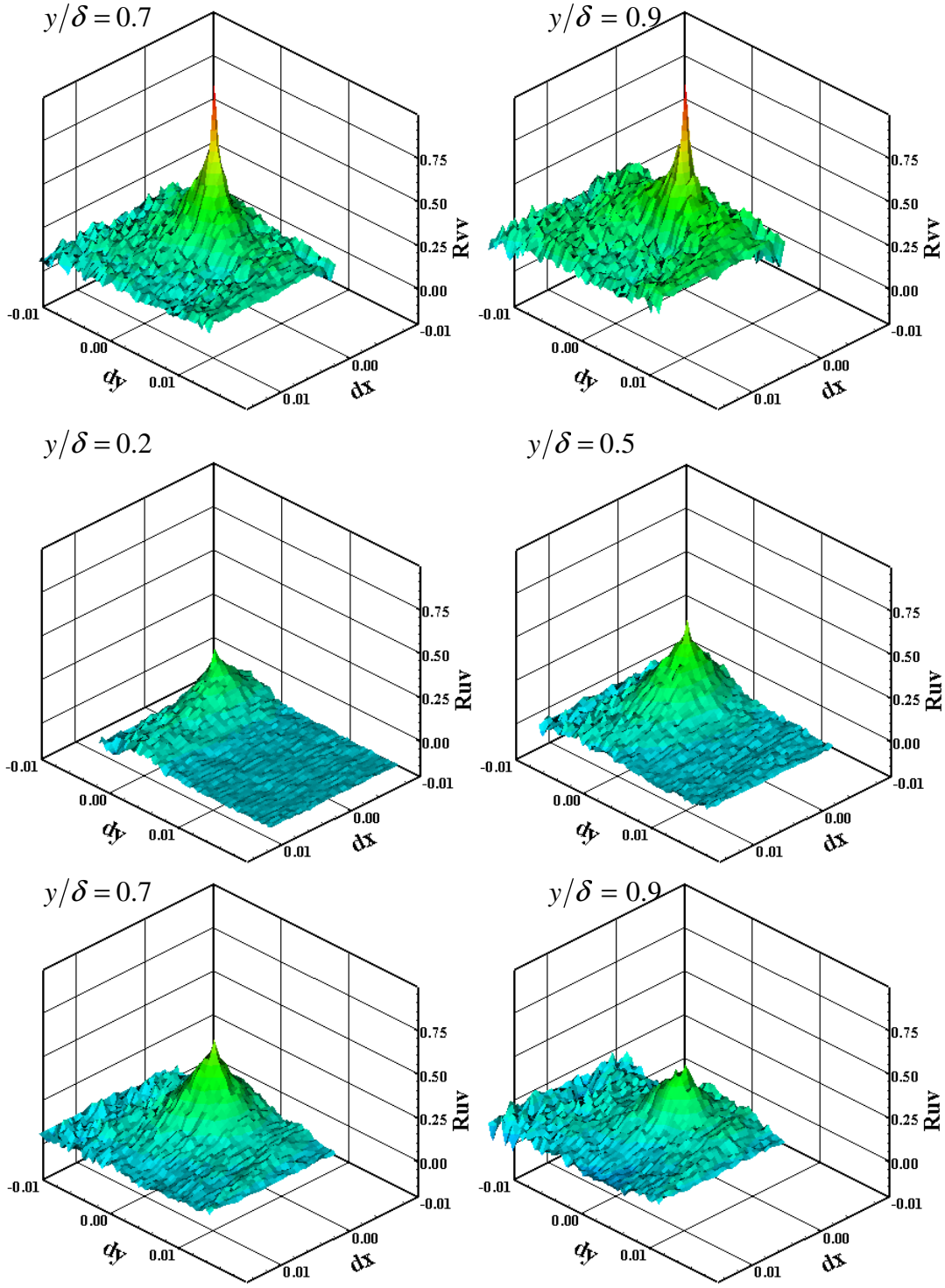

Figure 212: Continued

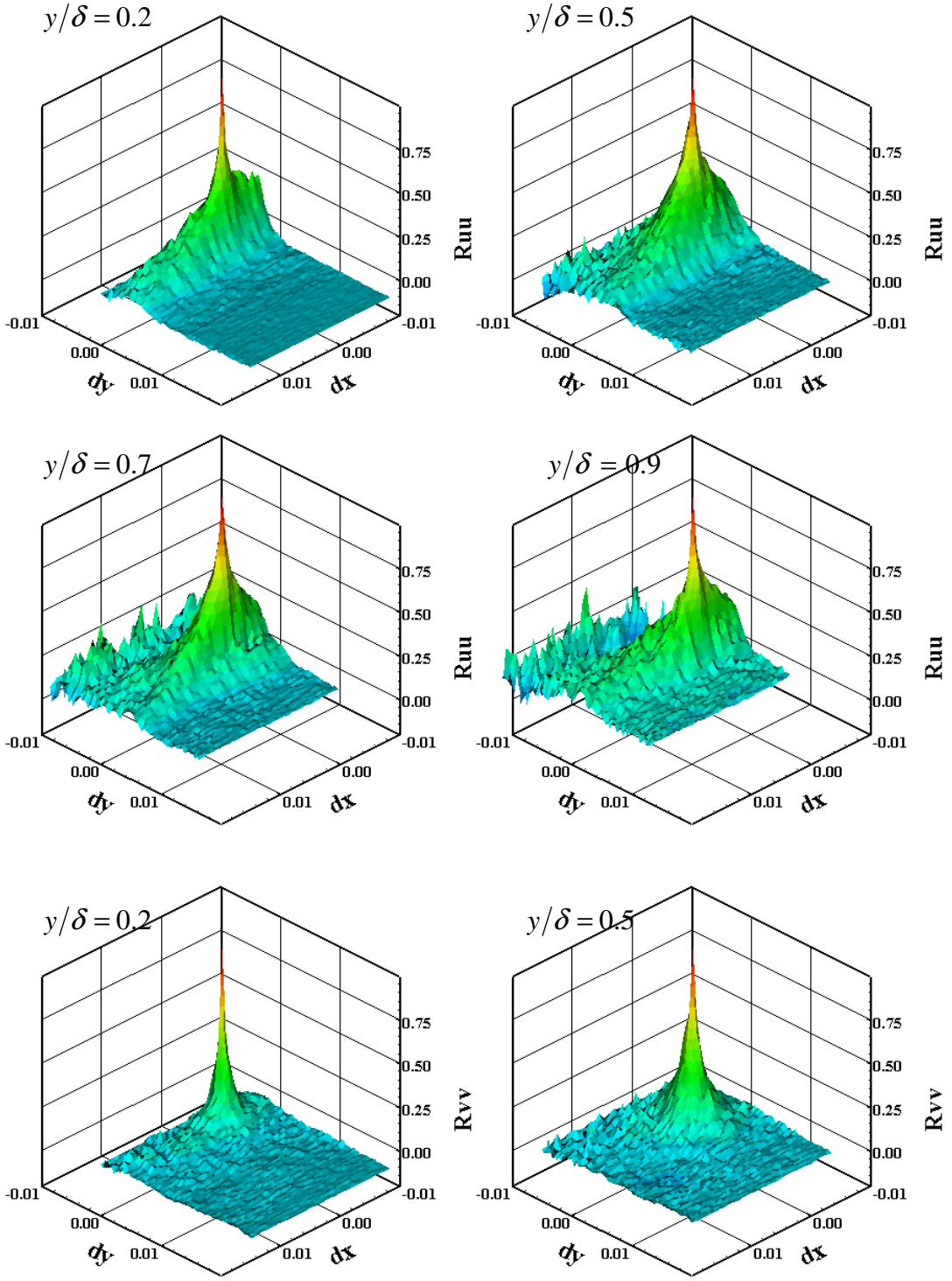

Figure 213: Correlation maps for the SPG diamond roughness model at the 3rd location: a) *u'* auto, b) *v'* auto c) and cross

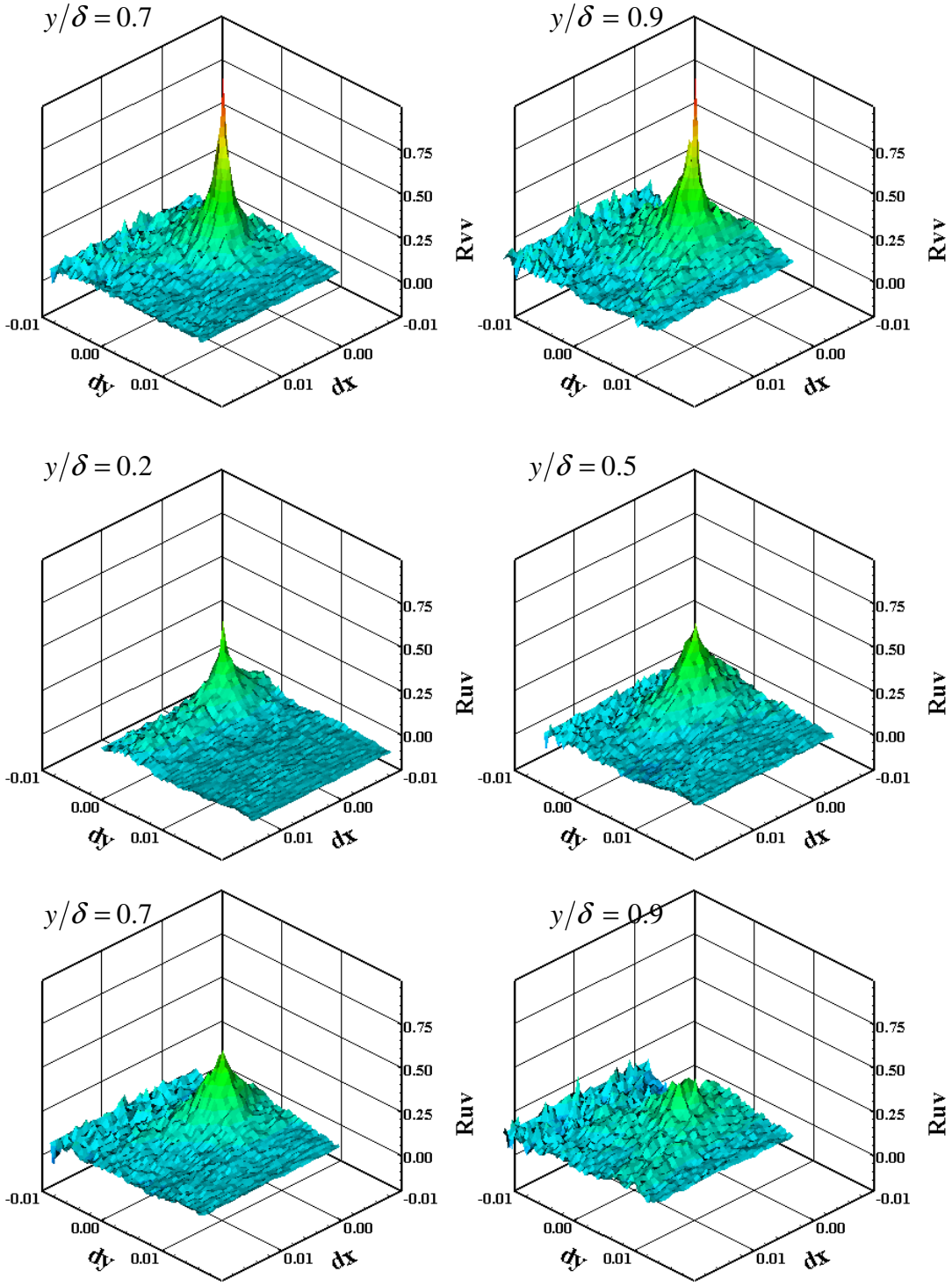

b)

c)

Figure 213: Continued

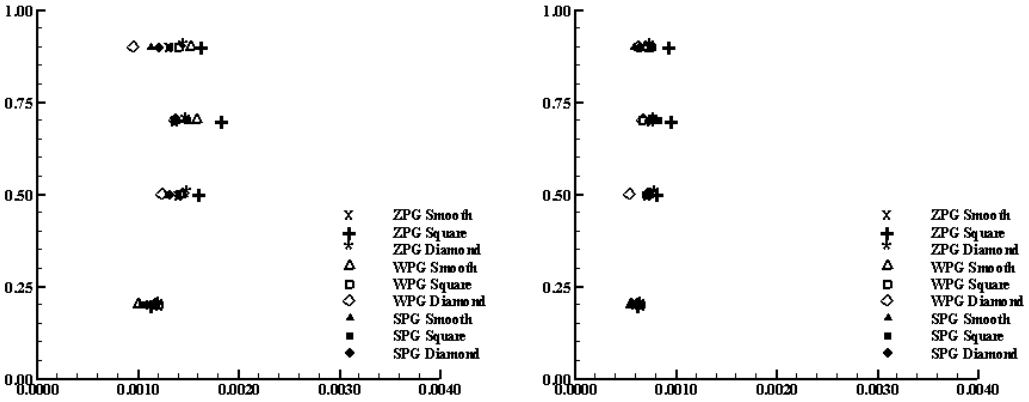

a)

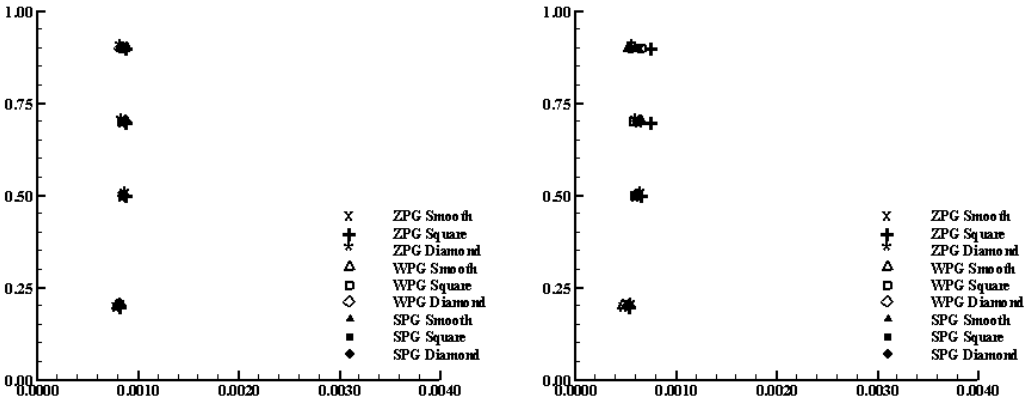

b)

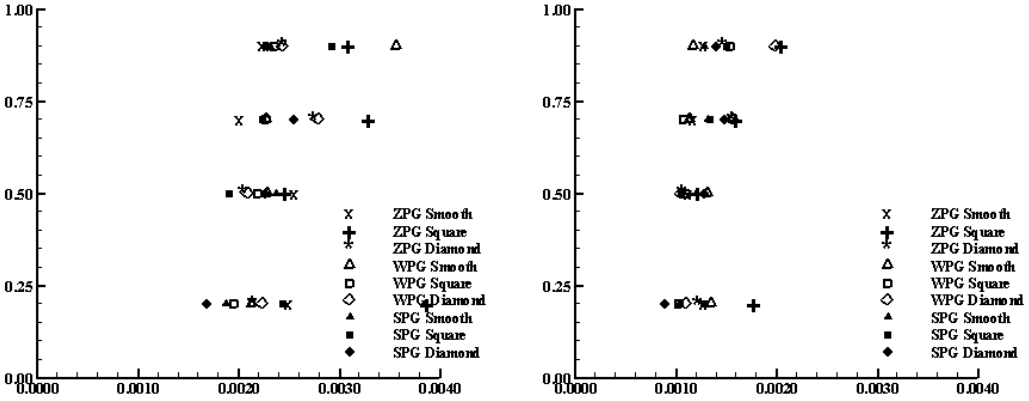

c)

Figure 214: *x* and *y* Taylor microscales for the 3rd test location: a) *u'* auto, b) *v'* auto c) and cross-correlations

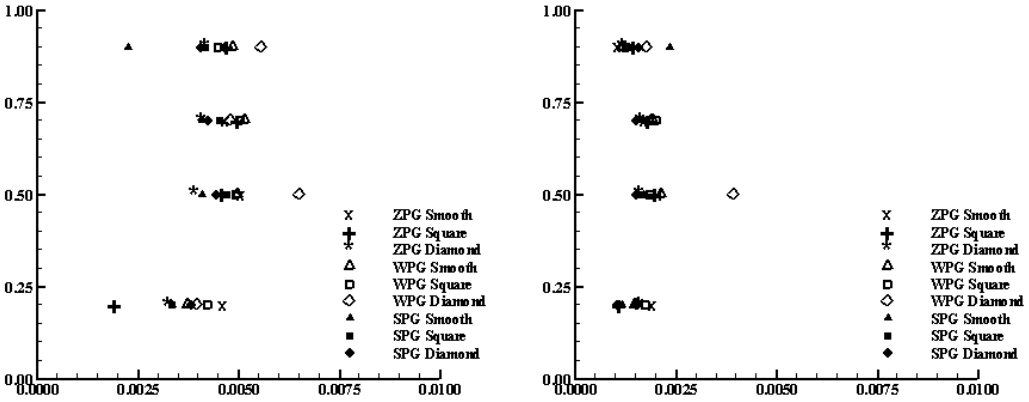

a)

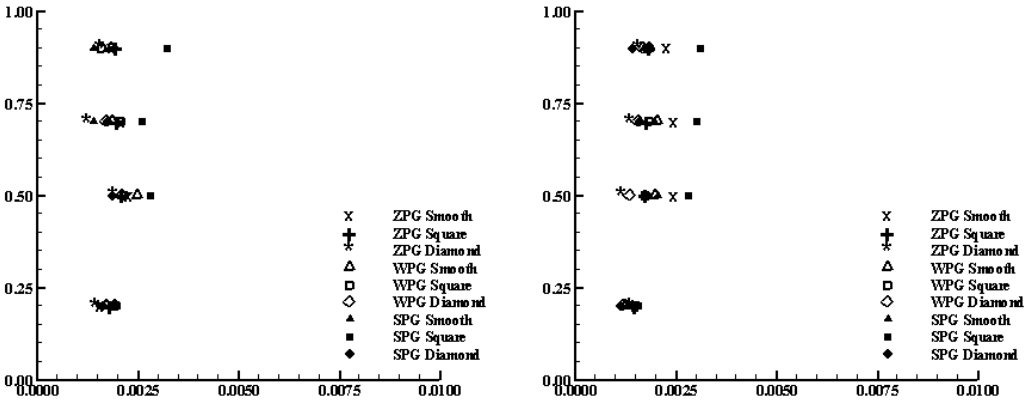

b)

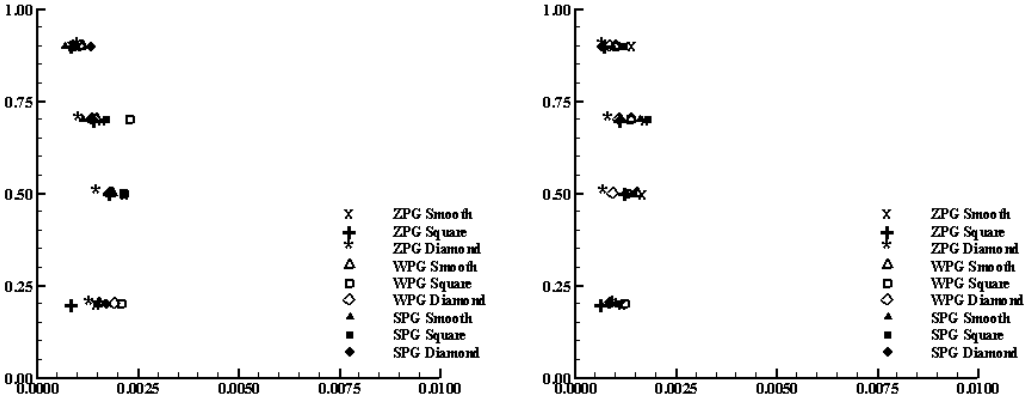

c)

Figure 215: *x* and *y* integral length scales for the 3rd test location: a) *u'* auto, b) *v'* auto c) and cross-correlations

VITA

Name:	Isaac Wesley Ekoto
Address:	Department of Aerospace Engineering, Texas A&M University, MS 3141, College Station, TX. 77843
Email Address:	ekoto@tamu.edu
Education:	B.S., Mathematics, Fayetteville State University, 2000 Ph.D., Aerospace Engineering, Texas A&M University, 2006